AGH UNIVERSITY OF SCIENCE
AND TECHNOLOGY
FACULTY OF ENERGY AND FUELS

PHD THESIS

Modified natural and synthetic aluminosilicates as the novel catalysts of selective catalytic reduction of nitrogen oxides with ammonia

Modyfikowane naturalne i syntetyczne glinokrzemiany jako nowe katalizatory selektywnej redukcji tlenków azotu amoniakiem

Agnieszka Szymaszek-Wawryca

Thesis Supervisor: Dr hab. Monika Motak, Prof. AGH

Thesis Co-supervisor: Dr inż. Bogdan Samojeden

Kraków 2023

Oświadczam, świadoma odpowiedzialności karnej za poświadczenie nieprawdy, że niniejszą pracę doktorską wykonałam osobiście i samodzielnie, oraz że nie wykorzystałam źródeł innych niż wymienione w pracy.

Agnieszka Szymaszek-Wawryca

The research presented in this PhD thesis was carried out on Faculty of Energy and Fuels at AGH University of Science and Technology and on ITQ Instituto de Tecnología Química of Universitat Politècnica de València (UPV) and Conejo Superior de Investigaciones Cientificas (UPV – CSIC).

Podziękowania

Pragnę złożyć serdeczne podziękowania wszystkim osobom, które przyczyniły się do powstania niniejszej pracy doktorskiej.

Z całego serca dziękuję i wyrażam nieskończoną wdzięczność mojemu Mężowi oraz Rodzicom, za nieocenione wsparcie, szczególnie w najtrudniejszych dla mnie chwilach na naukowej ścieżce prowadzącej do ukończenia studiów oraz pracy doktorskiej. Dziękuję także Przyjaciołom, za cierpliwość i każde dobre słowo wypowiedziane szczególnie wtedy, gdy było mi ono najbardziej potrzebne.

Pani Promotor, Dr hab. Prof. AGH Monice Motak dziękuję za czuwanie nad moją działalnością naukowo-badawczą. Promotorowi pomocniczemu, Dr inż. Bogdanowi Samojeden dziękuję za wskazówki dotyczące przygotowania niniejszej dysertacji.

W sposób szczególny dziękuję Dr Urbano Díaz za poświęcony czas, wsparcie merytoryczne, liczne konsultacje oraz możliwość wykorzystania zaawansowanej infrastruktury badawczej w ITQ Instituto de Tecnología Química Universitat Politècnica de València (UPV). Bez nich moja praca doktorska w przedstawionej formie nigdy by nie powstała. Dziękuję również wszystkim Pracownikom ITQ za liczne porady i wskazówki udzielone podczas realizowanych przeze mnie badań oraz miłą atmosferę pracy.

Wyrażam również wdzięczność Januszowi Guzera za pomoc w pracach laboratoryjnych oraz okazanie wsparcia w (niestety nieuniknionych) małych i większych niepowodzeniach.

Dziękuję także każdemu, z kim miałam możliwość prowadzenia wspólnych badań naukowych. Niestety, nie sposób wymienić wszystkich z osobna, niemniej, każda współpraca była dla mnie wspaniałą okazją do zdobycia nowych doświadczeń i ukształtowania mnie jako młodego naukowca.

Acknowledgements

I would like to express my sincere thanks to all those who contributed to the creation of this doctoral thesis.

I wholeheartedly thank and express my infinite gratitude to my Husband and Parents, for their invaluable support, especially when I needed it in the most difficult moments on my scientific path. I would also like to thank my Friends, for their patience and help that I could always count on.

I would like to thank the Supervisor, Prof. Monika Motak, for the supervision of my scientific and research activities throughout the period of my doctoral studies. I also express gratitude to the Co-supervisor, Dr. Eng. Bogdan Samojeden, for the tips on the preparation of this dissertation.

In a particular way, my thanks go to Dr. Urbano Díaz, for his time, substantive support, numerous consultations, and the opportunity to use the advanced research infrastructure at ITQ Instituto de Tecnología Química Universitat Politècnica de València (UPV). Without them, my dissertation in its present form would never have existed. I would also like to thank all of the Co-workers from ITQ, for their advice, guidance, and assistance during my multiple visits there.

I am also grateful to Janusz Guzera, for his help during my daily laboratory works and for expressing his support in some (unfortunately inevitable) small or bigger failures.

I would also like to show my gratitude to everyone with whom I collaborated and had the opportunity to conduct joint research during my doctoral studies. Unfortunately, it is impossible to mention all of them separately, nevertheless, each particular cooperation was a great chance for me to gain some new experience and shape me as a young scientist.

Table of contents

List of abbreviations

ABS – ammonium bisulfates

AC – activated carbon

ads – adsorption from the solution method

AS – ammonium sulfates

CL – clinoptilolite

cop – co-precipitation method

DeNO$_x$ – NO_x reduction technologies

EB – electron beam irradiation

EDTA – ethylenediaminetetraacetic acid

EEA – European Environment Agency

EPA – US Environmental Protection Agency

E-R – Eley-Rideal mechanism

EU – European Union

FT-IR – Fourier-transform infrared spectroscopy

H$_2$-TPR – temperature-programmed reduction with hydrogen

HC-SCR – selective catalytic reduction with hydrocarbons

HEU – heulandite

HT - hydrotalcite

ICP-OES – inductively coupled plasma optical emission spectroscopy

impr – impregnation method

IUPAC – International Union of Pure and Applied Chemistry

LDHs – layered double hydroxides

L-H – Langmuir-Hinshelwood mechanism

MAS-NMR – magic angle spinning nuclear magnetic resonance spectroscopy

MOFs – metal-organic frameworks

MWW – Mobile Twenty Two

NH_3-SCR – selective catalytic reduction with ammonia

NH_3-TPD – temperature-programmed desorption of ammonia

NO_x – nitrogen oxides (sum of NO and NO_2)

NSCR – non-selective catalytic reduction

OSHA – Occupational Safety and Health Administration

PAHs – polyacrylic aromatic hydrocarbons

PCHs – porous clay heterostructures

PILCs – pillared interlayer clays

SEM – scanning electron microscopy

SNCR – selective non-catalytic reduction

TGA – thermogravimetric analysis

UV-Vis – ultraviolet-visible spectroscopy

VOCs – volatile organic compounds

XPS – X-ray photoelectron spectroscopy

XRD – X-ray diffraction

Abstract

Nitrogen oxides (NO_x) emitted during combustion of fossil fuels are responsible for deterioration of environment's quality. Selective catalytic reduction with ammonia (NH_3-SCR) is generally considered as the leading technology used to abate excessive production of nitrogen oxides by stationary and mobile sources. However, some problems related to the commercial vanadium-based catalyst limit efficiency of the process, therefore, new solutions are continuously in search. Despite the interest in the application of modified zeolites, only few studies have investigated natural clinoptilolite and hierarchical layered MCM-22 as the substitutive catalysts of NH_3-SCR.

Thereby, this study aimed to prepare two series of catalysts supported on natural clinoptilolite or synthetic zeolite MCM-22 and test the materials in NH_3-SCR. Iron as an active phase was introduced by co-precipitation, adsorption from the solution, or impregnation method in order to compare the influence of the modification procedure on the physicochemical and catalytic properties of the zeolites. Besides, two representatives of each series were promoted with copper or cerium. The catalysts were characterized via ICP-OES, low-temperature N_2 sorption, XRD, SEM, TEM, NH_3-TPD, H_2-TPR, TGA, FT-IR, XPS, and UV-Vis. The catalytic tests on the fresh or SO_2-poisined samples were conducted using model gas mixture containing equal concentrations of nitrogen oxide and ammonia. Additionally, two of the most active samples were tested in the presence of various concentrations of SO_2 in the gas mixture.

It was found that clinoptilolite-supported catalysts exhibited superior high-temperature activity, while the samples with MCM-22 were more active in low-temperature range. The effect was assigned to the speciation of iron in two different zeolitic frameworks. Additionally, the influence of the modification method on the physicochemical features was determined by the type of zeolite: the most beneficial for clinoptilolite was co-precipitation (FeClin cop), while for MCM-22 it was adsorption from the solution (FeMCM22 ads). Concentration of N_2O generated during the reaction was considerably lower for MCM-22-supported catalysts, which was most likely caused by high-temperature decomposition of nitrous oxide over iron sites of higher nuclearity. In contrast, for clinoptilolite-supported samples emission of the by-product increased linearly with the reaction temperature.

Introduction of Cu shifted the temperature window of FeClin cop to lower values, however, it had no remarkable effect on FeMCM22 ads. In contrast, modification with Ce limited NO reduction of both Fe-zeolites as a consequence of the active phase clustering and promotion of the side reactions, such as oxidation of NH_3 and generation of N_2O.

The investigations on the influence of SO_2 on the catalytic performance of Cu-promoted Fe-zeolites indicated that exposition of the materials on sulfur dioxide limited high-temperature activity. Such result was linked with the formation of copper (II) and iron (III) sulfates, thus pore- and active centers-blockage. In general, comparing to FeCuMCM22 ads, FeCuClin cop was more resistant to the poisoning with SO_2, probably due to its stronger acidic character. However, the emission of N_2O for SO_2-poisoned FeCuClin cop was higher. Last, but not least, the inhibiting effect of sulfur dioxide was more pronounced while SO_2 was present in the gas mixture during the reaction. Importantly, in such conditions, FeCuMCM22 ads showed slightly better activity than FeCuClin cop. Nevertheless, generation of N_2O for the former catalyst in the presence of SO_2 was remarkably higher. Moreover, it was observed that the gradually increasing concentration of SO_2 from 200 to 800 ppm did not change NO conversion noticeably, regardless the type of the support.

Abstrakt w języku polskim

Emisja tlenków azotu (NO_x) podczas spalania paliw kopalnych wpływa na znaczne pogorszenie się jakości środowiska. Jedną z najlepszych dostępnych technik wykorzystywanych w celu ograniczenia produkcji NO_x ze źródeł stacjonarnych i mobilnych jest selektywna redukcja katalityczna amoniakiem (NH_3-SCR). Niemniej jednak, pewne istotne problemy związane z komercyjnym katalizatorem wanadowym procesu znacznie ograniczają jego efektywność. Z uwagi na to, poszukuje się alternatywnych, lepszych katalizatorów przemysłowych. Pomimo bardzo dużego zainteresowania zastosowaniem modyfikowanych zeolitów, naturalny klinoptylolit i hierarchiczny, warstwowy zeolit MCM-22 wciąż nie zostały szczegółowo zbadane jako substytucyjne katalizatory NH_3-SCR.

Wobec powyższego, celem niniejszej pracy było przygotowanie dwóch serii katalizatorów, wykorzystując naturalny klinoptylolit lub syntetyczny zeolit MCM-22 i przetestowanie ich w reakcji NH_3-SCR. Aby zbadać wpływ metody nanoszenia fazy aktywnej na właściwości fizykochemiczne i katalityczne, żelazo zostało wprowadzone do zeolitów poprzez współstrącanie, adsorpcję z roztworu lub metodę pierwszej wilgotności. Próbki wykazujące najwyższą konwersję NO zostały dodatkowo zmodyfikowane miedzią lub cerem. Otrzymane katalizatory scharakteryzowano za pomocą metod takich jak ICP-OES, niskotemperaturowa sorpcja N_2, XRD, mikroskopia SEM i TEM, NH_3-TPD, H_2-TPR, TG, FT-IR, XPS oraz UV-Vis. Testy katalityczne przeprowadzono na świeżych lub zatrutych SO_2 próbkach, z wykorzystaniem modelowej mieszanki gazowej zawierającej równe stężenia tlenku azotu i amoniaku. Dodatkowo, dwie próbki wykazujące najwyższą aktywność katalityczną przetestowane zostały w obecności różnych stężeń SO_2 w mieszance gazowej.

Zaobserwowano, że katalizatory na nośniku w formie klinoptylolitu wykazały zadowalającą aktywność w zakresie wysokotemperaturowym, natomiast próbki zawierające MCM-22 były bardziej aktywne w niskiej temperaturze procesu. Efekt ten spowodowany jest specjacją żelaza wprowadzonego do dwóch różnych sieci zeolitowych. Metody modyfikacji żelazem miały także odmienny wpływ na dany typ zeolitu: w przypadku klinoptylolitu najbardziej korzystna była metoda współstrącania (FeClin cop), natomiast dla MCM-22 była to adsorpcja z roztworu (FeMCM22 ads). Stężenie N_2O w gazie po reakcji katalitycznej było znacznie niższe w przypadku katalizatorów na nośniku MCM-22, co

spowodowane było prawdopodobnym rozkładem tlenku azotu (I), katalizowanym w wysokiej temperaturze przez oligomeryczne struktury żelazo-tlenowe. Z drugiej strony, w przypadku próbek zawierających klinoptylolit, produkcja N_2O wzrastała liniowo wraz z temperaturą reakcji.

Wprowadzenie miedzi jako promotora przesunęło okno aktywności FeClin cop w kierunku niższej temperatury, natomiast nie miało znacznego wpływu na zdolności katalityczne FeMCM22 ads. W przeciwieństwie do Cu, modyfikacja cerem zmniejszyła konwersję NO niezależnie od typu nośnika, co było konsekwencją agregacji żelazowych centrów aktywnych i katalizowania reakcji ubocznych, takich jak utlenianie NH_3 czy produkcja N_2O.

Badania wpływu SO_2 na aktywność katalityczną materiałów promowanych miedzią wykazały, że wstępne zatruwanie obniża aktywność próbek w zakresie wysokiej temperatury. Spadek konwersji NO niezależnie od nośnika katalizatora spowodowany był formowaniem się siarczanu (VI) miedzi (II) lub siarczanu (VI) żelaza (III) i blokowaniem porów oraz centrów aktywnych. W porównaniu do FeCuMCM22 ads, FeCuClin cop wykazał wyższą odporność na zatruwanie przez SO_2, co spowodowane było silniejszym charakterem kwasowym klinoptylolitu. Z drugiej jednak strony, emisja N_2O dla aktywniejszej próbki była wyższa. Negatywny wpływ SO_2 na przebieg reakcji katalitycznej był silniejszy po bezpośrednim wprowadzeniu tlenku siarki (IV) do mieszanki gazowej. Co istotne, w takich warunkach FeCuMCM22 ads wykazał wyższą aktywność od FeCuClin cop, z jednocześnie wyższą produkcją N_2O. Dodatkowo, zaobserwowano, że stopniowy wzrost stężenia SO_2 od 200 do 800 ppm nie ma wpływu na konwersję NO, niezależnie od typu nośnika.

Chapter I: Literature review

1. The problem of nitrogen oxides emission

1.1 General information about nitrogen oxides emission

The last decades have witnessed a dynamic development of the industrial processes, which increased the demand for energy production. Therefore, the rapid growth of urbanization resulted in the extensive combustion of fossil fuels [1,2]. As presented in **Figure 1,** in 2022 the world primary consumption of energy by source involved mainly coal, natural gas, and oil. Hence, one of the most adverse consequences of the proceeding industrialization is the emission of hazardous air pollutants.

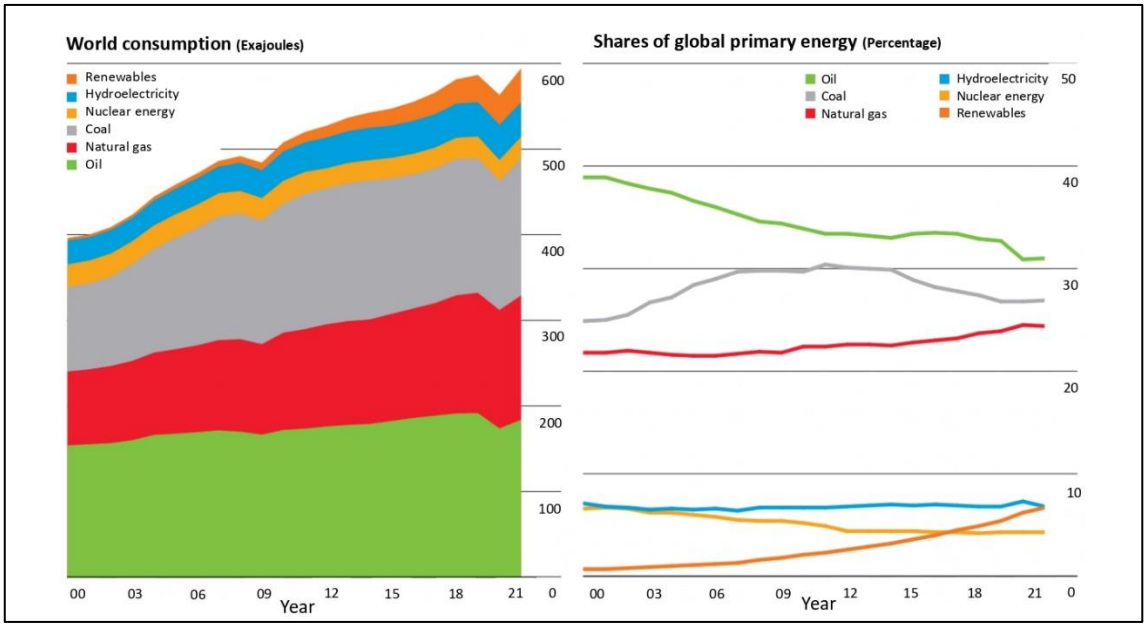

Figure 1. World primary energy consumption by source in 2022 (reproduced image basing on [1])

The World Health Organization (WHO) defined "air pollution" as the chemical composition of air, which may have a negative influence on the health of humans, animals, plants, and other components of the environment (such as water, soil, climate) [3]. While the quantity of the gaseous or particulate substances exceeds the background level, air can be considered as polluted [4]. The common contamination produced during the incineration processes are carbon dioxide (CO_2), carbon monoxide (CO), unburned hydrocarbons (HC), particulate matter (PM), sulfur oxides (SO_x), and nitrogen oxides (NO_x) [5]. Among them, nitrogen oxides exhibit alarmingly bad influence on the quality of air.

Nitrogen oxides, regarded as "NO_x" consist of nitric oxide (NO) and nitrogen dioxide (NO_2). Normally, the mixture of NO_x in the combustion exhausts contains around 95-97% of NO and 3-5% of NO_2 [6]. Due to the fact that NO present in the atmosphere is rapidly oxidized to NO_2, the environmental protection regulations normally treat NO_x as NO_2 [7]. Another adverse compound that belongs to the group of nitrogen oxides is nitrous oxide (N_2O). In the opposite to NO_x, its lifetime in the atmosphere can exceed even 100 years. Moreover, greenhouse effect of N_2O is around 300 times higher than that of carbon dioxide. However, the emission of nitrous oxide is significantly lower in comparison to the mixture of NO and NO_2 [7,8].

The formation of nitrogen oxides during the incineration processes results from the introduction of N_2 together with O_2 into the combustion zone. Alternatively, chemical groups containing nitrogen can be present in the fuel [9]. The pathway of the conversion of atmospheric nitrogen to nitrogen oxides is called "thermal" and was firstly described by Zeldovich, Frank-Kamenetskii, and Sadovnikov [7]. It comprises of the chain reactions described by **Equations (1-3)** (where * corresponds to a radical)**:**

$$N_2 + O^* \rightarrow NO + N^* \quad \textbf{(1)}$$

$$N^* + O_2 \rightarrow NO + O^* \quad \textbf{(2)}$$

$$N^* + OH^* \rightarrow NO + H^* \quad \textbf{(3)}$$

In the mechanism, the radicals of nitrogen and oxygen (N* and O*, respectively) are usually generated at high temperature, thus the reaction takes place above 1400 °C [10]. The majority of NO_x is formed according to this mechanism, since the temperature is exceeded in the most of the combustion processes. Additionally, the emission of thermal NO_x increases exponentially at higher temperature. "Thermal" nitrogen oxides are formed usually as the result of the combustion of fuels lean in nitrogen-containing species [11].

On the other hand, the mechanism of the generation of "feed" or "fuel" NO_x, derived from nitrogen present in the fuel is not completely understood. However, there is a general agreement that it depends on the characteristics of the fuel and its state of matter [9].

Furthermore, nitrogen oxides that are not produced according to Zeldovich mechanism and do not belong to the group of "feed" NO_x are known as "prompt" or "fast" NO_x. This group is formed by

the reaction of the fragments of fuel molecules with N_2 from the atmosphere. Typically, CH radicals interact with N_2 to form HCN, which is quickly decomposed to NO_x, CO_2, and H_2O. The mechanism strongly depends on the flame profile and occurs predominantly during low-temperature combustion of enriched gas mixtures. Additionally, it has usually the lowest contribution to the total emission of nitrogen oxides [9,11].

1.2 Main sources of nitrogen oxides emission

The anthropogenic sources of global NO_x emission can be divided into stationary and mobile. Stationary sources are related to the combustion systems (boilers, engines) that provide energy production for various purposes. There are two types of stationary NO_x emitters: point sources and area sources. The former ones are related to one emitter placed in the specific location, while the latter correspond to the group of multiple emitters in a certain area. On the other side, mobile sources can be categorized to on-road and non-road [12]. The complete picture of the global NO_x emission categories are presented in **Figure 2.**

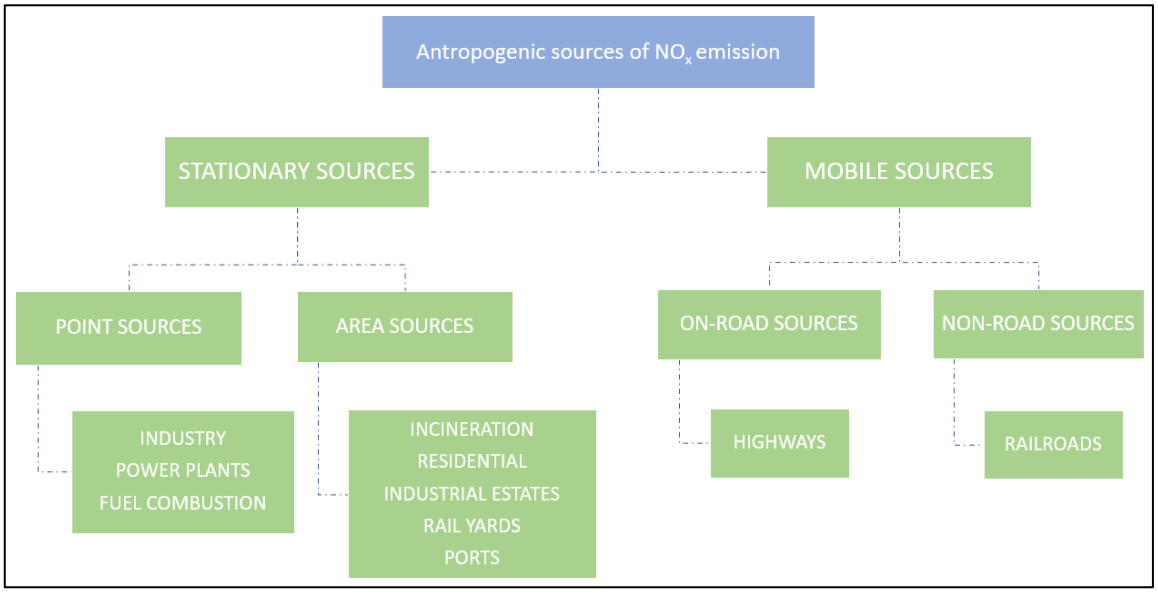

Figure 2. Schematic representation of the main sources of global NO_x emission [12]

As illustrated in **Figure 3,** the majority of anthropogenically-produced NO_x comes from mobile sources (58%), mainly trucks, passenger cars, motorcycles (on-road) or locomotives, marine vessels, lawn, garden and snow equipment etc. (non-road) [13,14]. Furthermore, combustion of various fuels in stationary sources contributes to 29% of the global NO_x emission. The greatest amount of nitrogen

oxides is produced in power, chemical, manufacturing and cement plants, refineries, foundries and others. Typically, NO_x at these facilities are produced by certain fuel-burning systems, such as boilers, burners, gas generators, kilns, furnaces, smelters, or incinerators [15].

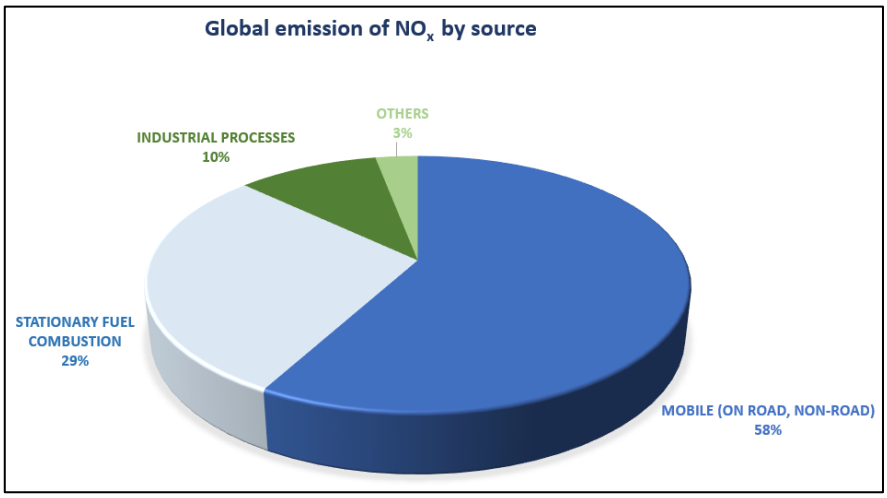

Figure 3. Global emission of NO_x by source [12]

More specifically, the standard scopes of NO_x concentration in the flue gas emitted by selected stationary sources are presented in **Table 1.** One should note that the given values are indicative and depend on many factors, such as the type of fuel, combustion conditions, construction of the combusting unit, etc.

Table 1. Concentration of NO_x emitted by the selected stationary sources [15]

Source of emission	**NO_x concentration ($mg \cdot m^{-3}$)**
Power plant	300-1000 (depending on the fuel used)
Waste incinerator	200-500 (depending on the composition of wastes)
Sintering machines in steelmaking	200-350
Glass production	1200-3000
Spray-drying towers in ceramic powder industry	300-1000

According to the recent reports, China has the largest contribution into the global emission of NO_x which is on average 21 546 Gg per year. It was estimated that this amount is almost doubled in relation to the annual production of nitrogen oxides by the United States (14 687 Gt) and European Union (10 974 Gt) [16]. In fact, in 2010 the Chinese government obliged to reduce 10% of NO_x emission

during the "12th Five-Year Plan". However, due to the intensive economic growth of the country, it was almost impossible to fulfil the commitment [17]. The significant decrease of the Chinese emissions of NO_x was noted in 2020, due to the outbreak of COVID-19 pandemic. Only in the first quarter of 2020 the production of nitrogen oxides was lower by 28.1%, comparing to the same period in 2019 [18].

Limiting solely to the emission of nitrogen oxides in European Union and Poland, the newest report on the development of EU-28 (28 Member States of European Union) emissions within 1990-2019, showed that the emission of nitrogen oxides has been gradually decreasing since 2005. The year is considered as the base and comparative for the emission reduction under National Emission reduction Commitments (NEC) Directive [19]. The reproduced data of NO_x emission from various EEA Sectors between 2005 and 2019 for EU-28 and Poland are presented in **Figure 4** and **Figure 5,** respectively.

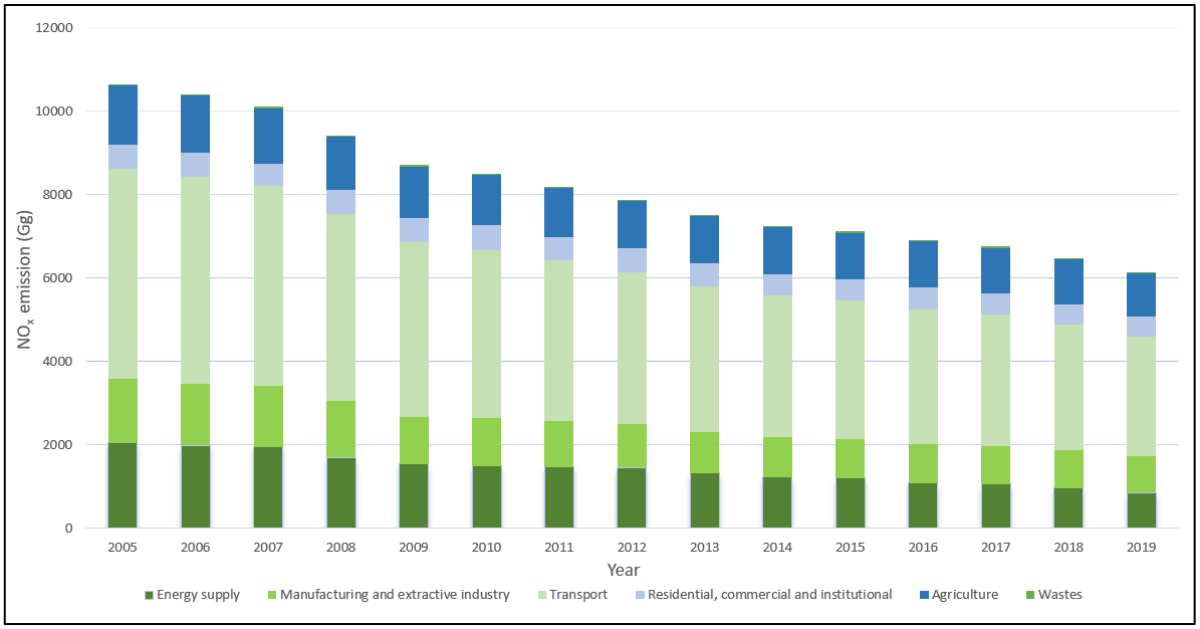

Figure 4. EU-28 NO_x emission from various sectors between 2005 and 2019 (reproduced data of EEA)

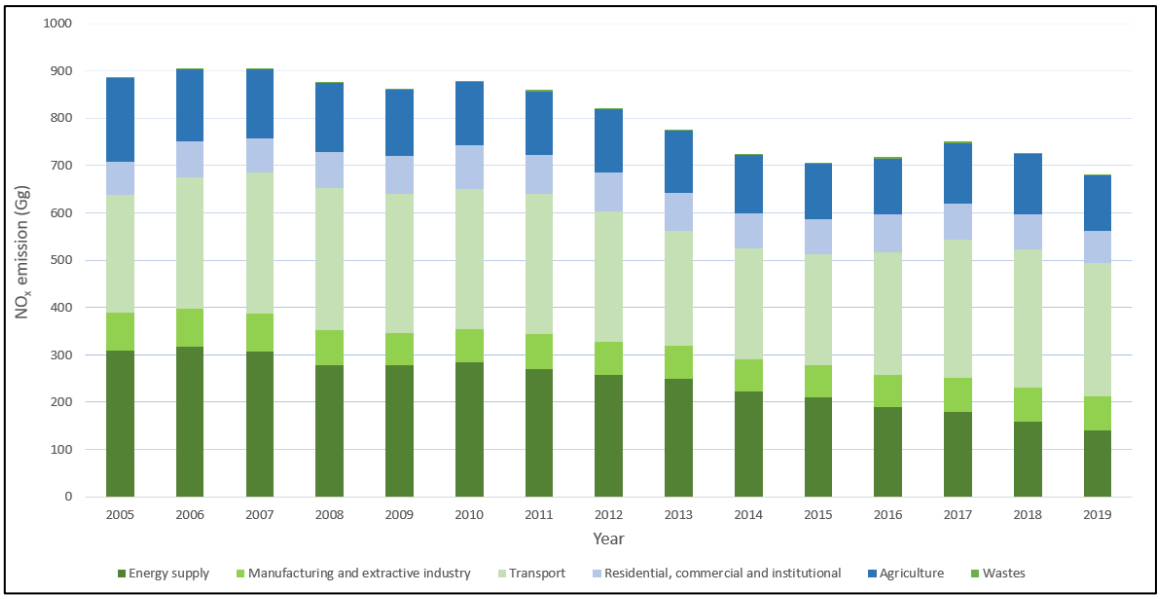

Figure 5. NO_x emission in Poland from various sectors between 2005 and 2019 (reproduced data of EEA)

It can be noticed that both in EU-28 and in Poland, the majority of NO_x is emitted from transport. However, in the case of EU-28, there is a pronounced trend of the total emission reduction, which in 2019 reached about 42%, comparing to 2005. On the other hand, Poland managed to reduce only 23% of the total NO_x emission. Besides, the contribution of the energy sector in Poland is significantly greater comparing to EU-28. The difference in the reported numbers can be explained by the combustion of tons of fossil fuels to produce energy, which contributes to the increased generation of NO_x.

1.3 Environmental consequences of nitrogen oxides emission

The presence of nitrogen oxides results in the deterioration of the quality of the environment and above all, contributes to the formation of secondary pollution. First of all, NO can be very easily oxidized to NO_2. Subsequently, nitrogen dioxide reacts with H_2O and forms nitric acid (HNO_3), which is a component of acid rain. As the very adverse environmental problem, acid rains poison agricultural crops, damage plants and buildings, and cause corrosion [20]. Besides, nitrogen oxides contribute to the destruction of ozone layer, which is a biological barrier for living organisms against harmful UV radiation [21]. Additionally, NO_x form particular matter (PM) in the reactions with other contamination of air [22]. Another phenomena related to the presence of nitrogen oxides in the atmosphere is photochemical, “Los Angeles” smog. Among others, it consists of nitric acid, ozone, aldehydes and occurs while ultraviolet light reacts with NO_x and unburnt hydrocarbons. Photochemical smog directly

affects humans health, for instance by the growth of lung cancer [23]. Moreover, the photolysis of NO_2 contributes to the formation of tropospheric ozone, considered as hazardous photochemical oxidant [24].

Despite the fact that nitrogen oxides have an adverse impact on the quality of the environment, their direct influence on humans health still remains under intensive studies. According to the recent literature reports, nitric oxide is less toxic than nitrogen dioxide. In general, NO can cause irritation of eyes or throat. However, as a radical, it reacts rapidly with oxygen and forms NO_2. On the contrary, the long term exposure on nitrogen dioxide is associated with respiratory illnesses, such as asthma [25]. Moreover, there is a strong evidence that children chronically exposed on the impact of NO_2 have a reduced function of lungs in adulthood [26]. Interestingly, the studies carried out by Wing et al. [27] evidenced that NO_2 emitted by road transport contributes to the increased level of cortisol [27].

1.4 Legal regulations of nitrogen oxides emission

Due to the detrimental influence of nitrogen oxides on the environment, the governments around the world implemented stringent regulations to restrain their excessive emission. The first legislations, implemented in Ventura County (California) in 1969, were related to the emission from the industrial boilers [28]. Subsequently, the United States Clean Air Act of 1970 enacted for the first time the limits for NO_x emission from vehicles [29]. Since then, the majority of the developed countries around the world started to realize their emission abatement policy.

The first measures for improving air quality in the countries of the European Union (EU) were implemented parallelly to those of the United States. The majority involved purification of the fossil fuels before combustion or the control of the pollution emission.

During the 1990s, the EU continued to compile and adopt a series of regulations on the management and assessment of air quality. As a result, specific, binding targets were set in order to abate the emission levels [30]. Nowadays, one of the most important act is the Directive (EU) 2016/2284 of the European Parliament and of the Council of 14 December 2016 on the reduction of national emissions of certain atmospheric pollutants (amending Directive 2003/35/EC and repealing Directive 2001/81/EC). The document was a result of the long-term objective of the EU to significantly decline the emission indicators. According to the Directive (EU) 2016/2284, the Member States have to limit

the annual emissions (among others, NO_x) in accordance with the national commitments applicable from 2020 to 2029 and since 2030 onwards [31]. Another highly significant act is Directive 2010/75/EU of the European Parliament and of the Council of 24 November 2010 on industrial emissions (integrated pollution prevention and control) [19]. According to the document, the limits of NO_x from stationary sources can be different, depending on the type of incinerated fuel. In general, the EU Member States committed to reduce 42% of NO_x emission within 2020-2029 and 63% starting from 2030 (comparing to 2005).

According to the publication of European Environment Agency (EEA) that reported the status of National Emission reduction Commitments for 2020, the emission of the four main pollutants (NO_x, volatile organic compounds, NH_3, and SO_2) declared by the Member States were below the respective ceilings since 2012 [32]. However, the progress made in that field is still insufficient to fulfill the commitments imposed for 2020-2029 and 2030 onwards. Considering NO_x emission, all Member States are in compliance with the ceilings since 2016. Nonetheless, according to the 2020 Report from the Commission of the European Parliament and the Council on the progress made on the implementation of Directive (EU) 2016/2284 on the reduction of national emissions of certain atmospheric pollutants, great majority of countries still does not meet the emission requirements for 2020-2030 [33,34]. What is more, according to EEA publication on the measures to reduce emissions of air pollutants and greenhouse gases, one of the major challenges for the Member States will be to reduce the emission of NO_x to the required level to 2030. In the case of the current EU regulations, the limits of industrial NO_x emissions depend on the boiler size and the age of the unit. The restrictions with the distinction of the selected parameters are collected in **Table 2.**

Table 2. NO_x emission limits for coal-fired boilers according to current European Union regulations [35]

Boiler size	**NO_x emission limit (mg · Nm^{-3})**	
	Existing installations	New installations
Large	150	85
Medium	180	100
Small	270	150

In order to meet the restrictions set by the Directive, the EU Member States are required to follow the specific operating conditions of the industrial processes. The supporting information is collected in the reference "Best Available Techniques (BAT)" document (BREFs) [36]. Additionally, in 2018 the European Commission presented a strategic vision called "A Clean Planet for all", which helped to develop a long-term strategy to meet the strict demands of the political regulations under the Paris Agreement (2015) after 2020. Another supporting document that includes the solutions of air quality improvement is "Masterplan for a Competitive Transformation of EU - Energy-intensive Industries Enabling a Climate-neutral Circular Economy by 2050", prepared by the High-Level Group on Energy-Intensive Industries [37].

Except the Directives [19,31], in Poland the emission of air pollutants (including nitrogen oxides) is regulated by the "Act of 17 July 2009 on the system to manage the emissions of greenhouse gases and other substances" (Journal of Laws of 2018, item 1271, as amended). Corresponding to the EEA document on the National Emission reduction Commitments for 2020, Poland has been meeting the strict legislations set by the EU Member States since 2016. Nevertheless, it still remains one of the greatest emitters of NO_x in EU. Besides, it does not fulfill the projected compliance for 2020-2030 and onwards and is under very high risk of non-decreasing the emission to the required levels [33,34].

1.5 Methods of stationary NO_x emission abatement

The abatement of nitrogen oxides emission from stationary sources can be realized by various methods, belonging to two separated groups: primary ("pre-combustion", "in-furnace") or secondary ("post-combustion", "tail-end") [6].

The aim of the "in-furnace" techniques is to prevent the formation of nitrogen oxides during incineration process, for example by purification of the fuel from nitrogen, lowering excess of air, temperature adjustment, fuel staging, or flue gas recirculation [38]. This group includes cheaper, however, significantly less effective solutions that reduce NO_x emission level by 30 - 70% [39].

In the group of "post-combustion" methods, wet and dry techniques can be distinguished. The idea of wet techniques is to install a scrubber columns for NO_x adsorption in alkaline solutions [40]. Dry methods can be classified into selective catalytic reduction with ammonia (NH_3-SCR) [41] or

hydrocarbons (HC-SCR) [42], non-selective catalytic reduction (NSCR) [43], selective non-catalytic reduction (SNCR) [44], adsorption [45], or electron beam irradiation (EB) [46]. The main drawback of the adsorption method is storage of the removed nitrogen oxides in the adsorptive medium, thus generation of secondary wastes. The other of the above mentioned methods aim to decompose NO_x, which is much more advantageous for industrial applications. Non-selective catalytic reduction is a mature technique based on the reaction between nitrogen oxides with other components of the flue gas. The major limiting factor of that technology is deactivation of the catalyst by its sintering and formation of fly ash deposits [47]. Selective non-catalytic reduction method is based on the reaction between NO_x and the reducing agent in the absence of the catalyst. Thus, in this case, satisfactory conversion of nitrogen oxides can be obtained only in very high temperature range (850 – 1100 °C) [48]. Similarly to SNCR, electron beam irradiation does not demand the application of catalyst. However, in the case of NO_x-rich exhausts, industrial EB installations need to be very complex and expensive [49].

Currently, the most widespread method used for NO_x emission abatement is selective catalytic reduction with ammonia in the presence of oxygen [50]. The process exhibits highly satisfactory efficiency and provides almost 90% of nitrogen oxides reduction. The main reaction of NH_3-SCR assumes the interaction between NO and the reducing agent and formation of N_2 and H_2O. The process takes place on the surface of the catalyst, thus its apparent activation energy ($\boldsymbol{E_A}$) is much lower in comparison to SNCR [44]. Nowadays, selective catalytic reduction with ammonia plays a crucial role in the majority of the industrial installations which contribute to NO_x emissions.

2. Selective catalytic reduction of nitrogen oxides (SCR)

2.1 Chemistry of selective catalytic reduction with ammonia (NH_3-SCR)

Selective catalytic reduction of nitrogen oxides with ammonia (NH_3-SCR) is the most widespread technique used to comply the current NO_x emission limits. The technology is relatively mature, since the first catalytic systems appeared in the 1970s in Japan. Due to the high efficiency, SCR reactors were systematically implemented on the international scale in electric power plants burning fossil fuel [51].

NH_3-SCR is an "end-of-pipe" removal technique that involves the reaction between NO_x and a reducing agent, injected ahead of the catalytic bed. The principle of the process is the use of an appropriate reductant, which reacts specifically with nitrogen oxides, instead of the excess of oxygen in the exhaust gas [52]. The desired products of the reaction are molecular nitrogen and water vapor. Preferably, the role of the reducing agents is played by N-containing chemical compounds, such as ammonia [53], urea [54], ammonium carbonate [55], ammonium carbamate [56], or amines [57]. According to the present knowledge, hydrocarbons may be also used as alternative reducing agents in SCR process [58,59]. Since ammonia is difficult and dangerous to store, in most of the practical applications urea or ammonium salts are used. Due to that, the inceptive step of NH_3-SCR is the injection of the urea solution into the flue gas and its time- and space-determined stepwise thermal decomposition. The chain reactions that produce ammonia from urea are described by **Equations (4-6),** while the overall urea decomposition, given by **Equation (7**) corresponds to the sum of **(1-3):**

$$NH_2 - CO - NH_{2\,(aqueous)} \rightarrow NH_2 - CO - NH_{2\,(molten)} + H_2O_{\,(gas)} \quad \textbf{(4)}$$

$$NH_2 - CO - NH_{2\,(molten)} \rightarrow NH_{3\,(gas)}) + HNCO_{\,(gas)} \quad \textbf{(5)}$$

$$HNCO_{\,(gas)} + H_2O \rightarrow NH_{3\,(gas)} + CO_{2\,(gas)} \quad \textbf{(6)}$$

$$NH_2 - CO - NH_{2\,(aqueous)} + H_2O_{\,(gas)} \rightarrow 2\,NH_{3\,(gas)} + CO_{2\,(gas)} \quad \textbf{(7)}$$

The first step (**1**) involves evaporation of water from the urea solution, yielding molten urea. Subsequently, $(NH_2)_2CO$ is thermolyzed into the equimolar mixture of ammonia and isocyanic acid (**2**). Finally, isocyanic acid undergoes hydrolysis on the surface of SCR catalyst to produce ammonia and carbon dioxide (**3**) [52,60]. Thus, thermal decomposition of urea generates 2 moles of NH_3 from 1 mol

of $(NH_2)_2CO$. As the typical molar ratio of NO_x to NH_3 in SCR reactions is 1 : 1, the stoichiometric balance of NO_x to the injected urea is maintained on the level of 1 : 2.

In the case of NH_3-SCR, the temperature of the total conversion of NO_x is usually in range of 300 – 400 °C [61]. It was reported that application of this technique can provide even up to 90% of nitrogen oxides reduction [62]. However, it is strongly influenced by type of the catalyst used in the system.

In general, due to the fact that the mixture of NO_x consists in 90% of NO, the key reaction of SCR is described by **Equation (8):**

$$4\ NH_3 + 4\ NO + O_2 \rightarrow 4\ N_2 + 6\ H_2O \qquad \textbf{(8)}$$

The reaction is called as "standard" SCR and the presence of required amount of O_2 is vital to provide appropriate course of the reaction. The very initial experiments over SCR process with isotopically labeled reactants confirmed that oxygen vacancies are reoxidized more rapidly by O_2 than by NO, which promotes the overall reaction rate [63]. Besides, the oxygen content in the exhausts should be strictly controlled to avoid undesirable oxidation of ammonia, which decreases the catalytic activity by the consumption of the reducing agent and yields secondary pollution, such as N_2O [64].

Alternatively, while oxygen is not present in the gas mixture, the process is significantly slower and follows the reaction represented by **Equation (9):**

$$4\ NH_3 + 6\ NO \rightarrow 5\ N_2 + 6\ H_2O \qquad \textbf{(9)}$$

What is more, so-called "fast" SCR reaction, described by **Equation (10)**, has the lowest activation energy and the highest rate below 200 °C [65]. It takes place when the feed gas contains equimolar concentrations of NO and NO_2:

$$4\ NH_3 + 2\ NO + 2\ NO_2 \rightarrow 4\ N_2 + 6\ H_2O \qquad \textbf{(10)}$$

While the concentration of NO_2 exceeds NO, nitrogen dioxide can react with ammonia, as shown by **Equation (11)**:

$$8\ NH_3 + 6\ NO_2 \rightarrow 7\ N_2 + 12\ H_2O \qquad \textbf{(11)}$$

The process is called “slow” SCR, however, according to the literature, it exhibits similar reaction rate to the “standard” type of reaction [66,67].

Taken together, the reaction rate of NH_3-SCR and its course is strongly determined by the composition of the purified exhausts. One of the consequences of the interactions between NO, NO_2, O_2, NH_3, and H_2O is formation of many side-products. Most of the competing reactions do not influence directly the conversion of nitrogen oxides, but may significantly affect the selectivity to nitrogen. Considering the above mentioned, NH_3-SCR process is characterized by complicated chemistry and its mechanism in various conditions is still under discussion.

2.2 Parallel and competing reactions of NH_3-SCR

Apart from the reactions represented by **Equations (8-11),** there is a number of undesired interactions between the molecules taking part in NH_3-SCR. Despite the fact, that “selective” refers to the reactivity of NO_x with NH_3 instead of oxygen, there are some inevitable reactions in the system, such as selective ammonia oxidation (SCO), described by **Equation (12):**

$$4\ NH_3 + 3\ O_2 \rightarrow 2\ N_2 + 6\ H_2O \qquad \textbf{(12)}$$

Alternatively, NO conversion can be significantly decreased due to the oxidation of NH_3 to NO, according to the reaction represented by **Equation (13)**:

$$4\ NH_3 + 5\ O_2 \rightarrow 4\ NO + 6\ H_2O \qquad \textbf{(13)}$$

The occurrence of ammonia oxidation reaction is usually more pronounced in the high temperature range and strongly depends on the type of the applied catalysts [68].

The term “selective” refers also to the products of the NH_3-SCR reaction. Except the desired N_2 and H_2O, other nitrogen-containing species can be formed during the process. One of the most adverse for the environment is N_2O [69]. It was reported that formation of N_2O occurs usually at intermediate temperature of SCR (230 – 350 °C) [70], which is presented by **Equations (14-16):**

$$4\ NH_3 + 4\ NO + 3\ O_2 \rightarrow 4\ N_2O + 6\ H_2O \qquad \textbf{(14)}$$

$$6\ NH_3 + 8\ NO_2 \rightarrow 7\ N_2O + 9\ H_2O \qquad \textbf{(15)}$$

$$4\ NH_3 + 4\ NO_2 + O_2 \rightarrow 4\ N_2O + 6\ H_2O \qquad \textbf{(16)}$$

Moreover, nitrous oxide can be also produced directly from NO [71], according to **Equations (17-18):**

$$2\ NO \rightarrow N_2O + ½\ O_2 \quad \textbf{(17)}$$

$$3\ NO \rightarrow N_2O + NO_2 \quad \textbf{(18)}$$

The analysis of N_2O formation was investigated in the research performed by Zhu et al. [69]. The temperature-programmed measurements with isotopically labeled ($^{18}O_2$, $H_2{}^{18}O$, $^{15}N^{18}O$, and ND_3) indicated that formation of N_2O involves one molecule of NH_3 and one of NO. Besides, both NO and gaseous O_2 participate in the generation of nitrous oxide. The presented results indicated that the abatement of N_2O production can be provided exclusively by the control of flue gas composition.

Another side-reactions occurring during NH_3-SCR on the industrial scale involve participation of sulfur dioxide (SO_2). One of the most undesired and challenging processes in the low temperature range of SCR is attributed to the oxidation of SO_2 to sulfur trioxide (SO_3). The subsequent interaction of SO_3 with ammonia or ammonium species on the catalyst surface generates ammonium sulfates (NH_4HSO_4) and ammonium bisulfates ($(NH_4)_2SO_4$), according to the reactions described by **Equations (19-20):**

$$SO_3 + NH_3 + H_2O \rightarrow NH_4HSO_4 \quad \textbf{(19)}$$

$$SO_3 + 2\ NH_3 + H_2O \rightarrow (NH_4)_2SO_4 \quad \textbf{(20)}$$

Additionally, SO_2 can also react with H_2O present in the exhausts, forming sulfuric acid upon reaction presented by **Equation (21):**

$$SO_3 + H_2O \rightarrow H_2SO_4 \quad \textbf{(21)}$$

All of the products of **reactions (19-21)** can cause considerable damages of the equipment of the catalytic system due to pressure drops within the monolith surface or strongly corrosive effect [72–74].

2.3 Mechanisms of NH_3-SCR

In recent decades, various possible mechanisms of NH_3-SCR reaction have been proposed. The very initial research on the process reported a number of pathways and even more factors influencing the dynamic behavior of the reagents [75–78]. In general, NH_3-SCR is a redox-type reaction in which nitrogen oxide and ammonia participate in the reduction, while oxygen is required for the re-oxidation of the active site [79]. The process follows Mars-van-Krevelen mechanism, which assumes electron

transfer between the adsorbed elements and the catalysts surface [80]. In situ UV-vis spectroscopy studies conducted during NH_3-SCR over V_2O_5-TiO_2 revealed that V^{5+} are predominant species. On the other hand, the amount of V^{4+} is negligible and appears only due to the reduction during the catalytic reaction. Low amount of V^{4+} was explained by quick re-oxidation of the species to V^{5+} by molecular oxygen [81,82]. Despite extensive research in the field of NH_3-SCR pathway, there is a number of unclear issues, such as the type of reaction mechanism, contribution of Brönsted and Lewis acid sites, intermediates formed during the reaction, role of oxygen, or rate-determining steps of the process.

Eley-Rideal mechanism of NH_3-SCR

There is a general consensus that the crucial step of the heterogeneous catalytic process is the adsorption of the reacting molecules on the catalyst surface. In the case of NH_3-SCR, there are two mostly recognized reaction pathways, described in the scientific literature. The first one, reported in the pioneer studies of Inomata et al. [76] assumes that NH_3 strongly adsorbs on Brönsted or Lewis acid site and reacts with gaseous NO. The model is classified as Eley-Rideal (E-R) mechanism [83] and has been confirmed by the great number of research on NH_3-SCR over various catalysts [84–87]. Typical E-R mechanism assumes formation of NH_4^+ on Brönsted site or adsorbed ammonia species on Lewis site.

Inomata et al. [76] declared that the reaction is determined by strong adsorption of ammonia on Brönsted acid site and the reaction pathway over V_2O_5 is represented by **Equations (22-26):**

$$NH_3 + V^{5+}\text{–}OH \rightarrow V^{5+}\text{–}ONH_4^+ \quad \textbf{(22)}$$

$$V^{5+}\text{–}ONH_4^+ + V^{5+}\text{=}OH \leftrightarrow V^{5+}\text{–}ONH_3H^+\text{–}O\text{–}V^{4+} \quad \textbf{(23)}$$

$$V^{5+}\text{–}ONH_3H^+\text{–}O\text{–}V^{4+} + NO \rightarrow N_2 + H_2O + V^{4+}\text{–}OH + V^{5+}\text{–}OH \quad \textbf{(24)}$$

$$2\ V^{4+}\text{–}OH \rightarrow H_2O + V^{3+} + V^{5+}\text{=}OH \quad \textbf{(25)}$$

$$O_2 + 2\ V^{3+} \rightarrow 2\ V^{5+}\text{=}O \quad \textbf{(26)}$$

First step involves equilibration of NH_3 on V-OH groups, acting as Brönsted acid sites **(Equation 22).** Afterwards, ammonia is activated on vanadyl species and forms active complex **(Equation 23).** Finally, the active complex reacts with gaseous NO to form N_2 and H_2O **(Equation 24).** The mechanism is terminated by re-oxidation of the active site to the initial oxidation state **(Equations 25-26).** The

proposed chain of reactions is in agreement with the assumption that N_2 molecule generated in NH_3-SCR is formed from one mole of NH_3-derived and one mole of NO-derived nitrogen atom [88].

In contrast to Inomata and co-workers, Ramis et al. [88] proposed for the first time *amide-nitrosamide* mechanism, claiming that ammonia is adsorbed on Lewis acid site. The reaction scheme on V_2O_5 as the exemplary active phase can be described by **Equations (27-29),** while **Equations (30-31)** reflect re-oxidation of the active site:

$$NH_3 + V^{5+}{=}O \rightarrow V^{4+}\text{-}NH_2 + OH^- \quad \textbf{(27)}$$

$$V^{4+}\text{–}NH_2 + NO \rightarrow V^{4+}\text{–}NH_2NO \quad \textbf{(28)}$$

$$V^{4+}\text{–}NH_2NO \rightarrow V^{4+} + N_2 + H_2O \quad \textbf{(29)}$$

$$2\ V^{4+} + ½\ O_2 \rightarrow 2\ V^{5+} + O^{2-} \quad \textbf{(30)}$$

$$2\ OH^- \rightarrow H_2O + O^{2-} \quad \textbf{(31)}$$

NH_3-SCR on Lewis acid site according to E-R mechanism involves chemisorption and activation of NH_3 to surface amide species (-NH_2), resulting in the reduction of metal active site **(Equation 27).** Subsequently, amide moieties react with gas-phase NO to form nitrosamide intermediates (-NH_2NO) **(Equation 28).** Decomposition of -NH_2NO generates N_2 and H_2O **(Equation 29)**, while the active site is re-oxidized by gas-phase oxygen **(Equations 30-31)**.

Qu et al. [89] identified the reaction pathway of NH_3-SCR over cerium-niobium catalysts and postulated that when NO_2 is involved into the reaction cycle, fast SCR is likely to occur. In this case, the reaction scheme, starting from the adsorption of NH_3 on Lewis acid site, can be described by **Equations (32-35)** (where ֍ is Lewis acid site and ○ is O_2 adsorption site)**:**

$$NH_3 + ֍ \rightarrow NH_2\text{-}֍ + H^+ \quad \textbf{(32)}$$

$$½\ O_{2\ (gas)} + ○ \rightarrow O\text{-}○ \quad \textbf{(33)}$$

$$NO + O\text{-}○ \rightarrow ○\text{-}NO_2 \quad \textbf{(34)}$$

$$2\ NH_2\text{-}֍ + NO + ○\text{-}NO_2 \rightarrow 2\ N_2 + 3\ H_2O \quad \textbf{(35)}$$

One should note that regardless the type of acid site, Eley-Rideal mechanism is characteristic for the catalysts showing excellent NH_3 adsorption capacity [90]. Most research confirmed that E-R dominates for vanadia-based and zeolite-supported catalysts, as the result of weak interaction between the fully oxidized catalyst surface and NO [91,92]. In the case of E-R mechanism, several side reactions can

occur, such as non-selective reduction of NO to N_2O and oxidation of NH_3 to NO or N_2 [93]. Among them, NH_3 oxidation becomes dominant at higher temperature, at which E-R mechanism takes place. The generalized Eley-Rideal reaction pathway of NH_3-SCR, with the formation of N_2 or N_2O and H_2O, is schematically depicted in **Figure 6.**

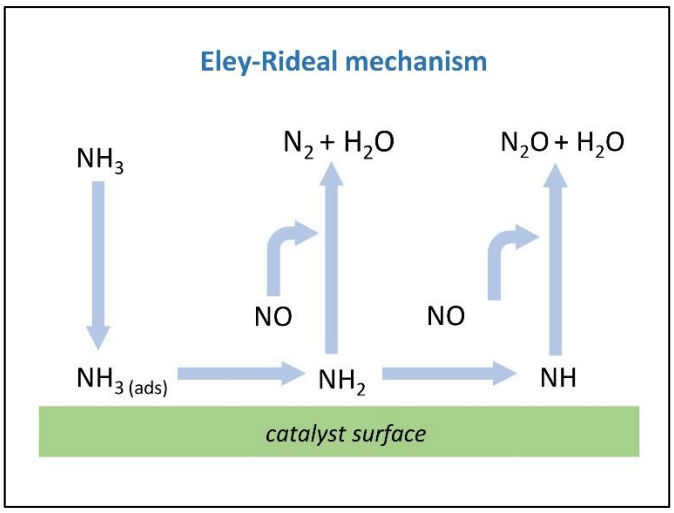

Figure 6. Schematic representation of Eley-Rideal mechanism (considered as "acid circle")

Langmuir-Hinshelwood mechanism of NH_3-SCR

In contrast to Inomata et al. [76] and Ramis et al. [88], Komatsu and co-workers [94] proposed simultaneous adsorption of NO and NH_3 on the active centers during NH_3-SCR. Generally, this reaction pathway is preferable for the catalysts exhibiting high NO and O_2 adsorption capacity [90]. According to the kinetic studies, the rate-determining step in this case is formation of oxidized N-containing species on the catalyst surface, after chemisorption of NO and O_2. This type of reaction mechanism is known as Langmuir-Hinshelwood (L-H) [83]. The scheme of L-H includes mainly Lewis acid sites and follows **Equations (36-41)** (where ♦ and ● represent adsorption sites for NO and NH_3) [95]**:**

$$O_2 + 2\,♦ \leftrightarrow 2\,♦\text{-}O \quad \textbf{(36)}$$

$$NO + ♦ \leftrightarrow ♦\text{-}NO_2 \quad \textbf{(37)}$$

$$NH_3 + ● \leftrightarrow ●\text{-}NH_3 \quad \textbf{(38)}$$

$$●\text{-}NH_3 + ♦\text{-}O \rightarrow ●\text{-}NH_2 + ♦\text{-}OH \quad \textbf{(39)}$$

$$●\text{-}NH_2 + ♦\text{-}NO_2 \rightarrow N_2 + H_2O + ●\text{-}♦ \quad \textbf{(40)}$$

$$2\,♦\text{-}OH \leftrightarrow H_2O + ♦\text{-}O + ♦ \quad \textbf{(41)}$$

Qu et al. [89] analyzed the pathway of Langmuir-Hinshelwood mechanism and observed formation of various surface nitrate species, presented schematically in **Figure 7.** The authors proposed the reaction scheme represented by **Equations (42-45)** (where * is a metal active site):

$$NO_{(gas)} + *=O + \tfrac{1}{2}\, O_2 \rightarrow *=O_2=NO \quad \textbf{(42)}$$

$$NO_{(gas)} + 2*=O \rightarrow *\text{-}O\text{-}(NO)\text{-}O\text{-}* \quad \textbf{(43)}$$

$$NH_{3\,(gas)} + *=(O_2)=NO \rightarrow *=(O_2)=NO\text{-}NH_3 \quad \textbf{(44)}$$

$$NH_{3\,(gas)} + *\text{-}O\text{-}(NO)\text{-}O\text{-}* \rightarrow *\text{-}O\text{-}(NO\text{-}NH_3)\text{-}O\text{-}* \quad \textbf{(45)}$$

The results showed that bidentate nitrate (produced via **Equation 42**) and bridging nitrate (produced via **Equation 43**) are not involved in the reaction at 200 °C, due to their high thermal stability. However, the presence of monodentate nitrates (*=O-NO_2) dramatically enhanced catalytic activity. The result was ascribed to its affinity to ammonia and low thermal stability of ammonium nitrates.

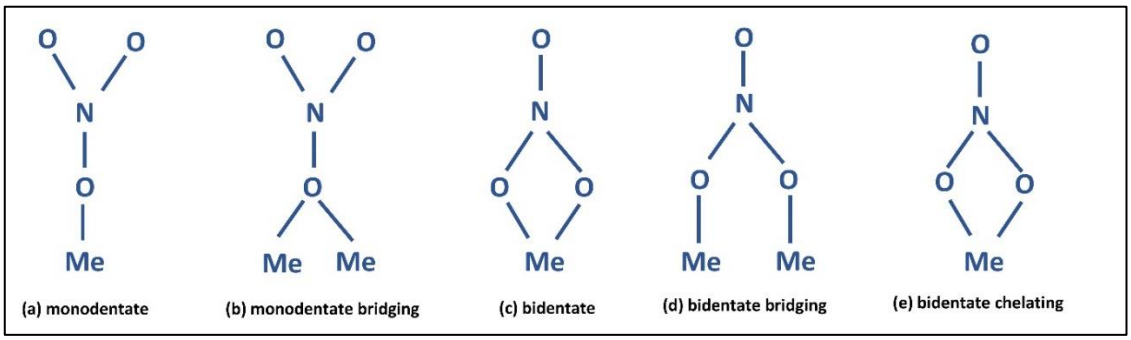

Figure 7. Examples of nitrate species generated during NH_3-SCR on metal sites of catalysts (based on [96]

Liu et al. [90] conducted *in situ* FT-IR studies of the adsorbed NO_x species, generated by co-adsorption of NO and O_2 on the surface of tube-shaped Mn-Ni-Ti solid solutions. Since NO interacts mainly with Lewis active sites, the presence of Brönsted acidity allowed unhampered adsorption of NH_3 molecules. Surface reactions between NO and NH_3 resulted in the formation of various intermediates, such as monodentate nitrates, bidentate nitrates, bridging nitrates or free nitrate ions. Thus, it was concluded that the reaction followed Langmuir-Hinshelwood mechanism. Likewise, Yang et al. [97] postulated that surface interaction between NO and NH_3 forms -NH_4NO_3 intermediates in the temperature range of 100-260 °C. These species were reported to produce N_2 and H_2O according to two pathways: reduction by gas-phase NO and decomposition to N_2 and H_2O **(Equation 46)** or surface reaction with NO and NH_3, followed by the formation of NH_4NO_2 and its decomposition to N_2 and H_2O **(Equations 47-48)** (where * represents metal active site)**:**

$$*\text{-}NH_4NO_{2\ (ads)} + NO + O_2 \rightarrow 2\ N_2 + 3\ H_2O + 2\ H^+ \quad \textbf{(46)}$$

$$NO_3^-{}_{(ads)} + NO + e^- \rightarrow 2\ NO_2^-{}_{(ads)} \quad \textbf{(47)}$$

$$NO_2^-{}_{(ads)} + NH_4^+{}_{(ads)} \text{ or } NH_{3\ (ads)} + *- \rightarrow NH_4NO_{2\ (ads)} \rightarrow N_2 + H_2O \quad \textbf{(48)}$$

Langmuir-Hinshelwood mechanism was reported to occur mostly on supported Fe_2O_3, CuO, MnO_x, or CeO_2 catalysts [89]. It is primarily due to the oxygen vacancies, which react with O_2 molecules and elevate the concentration of surface oxygen species, responsible for oxidation of NO on the catalyst surface. The schematic representation of Langmuir-Hinshelwood mechanism of NH_3-SCR reaction is showed in **Figure 8.**

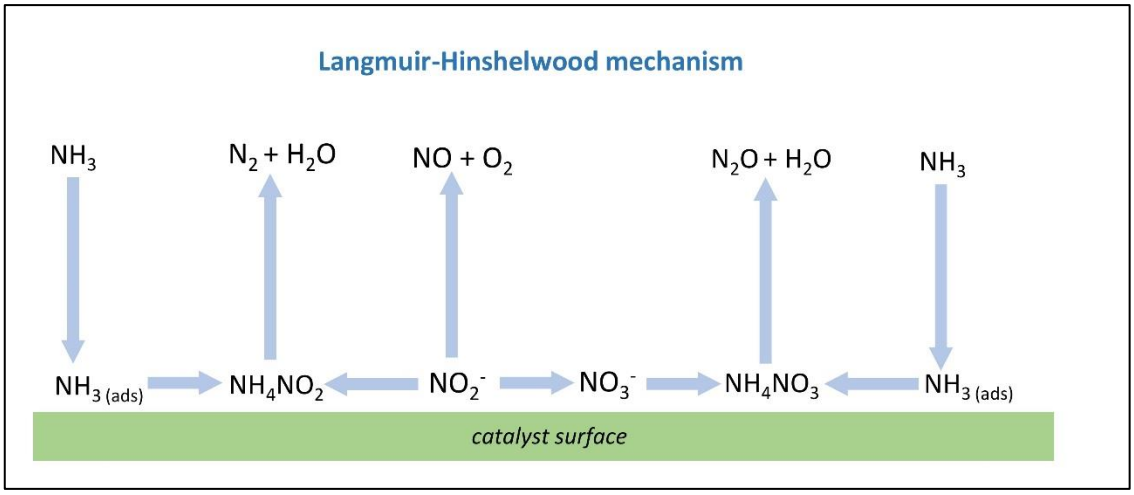

Figure 8. Schematic representation of Langmuir-Hinshelwood mechanism (considered as "redox cycle")

Coexistence of Eley-Rideal and Langmuir-Hinshelwood mechanisms during NH_3-SCR

Most of the studies, which aimed to analyze the respective contribution of E-R and L-H mechanisms, agree that the reaction pathway depends on the temperature. In general, regardless the type of the catalyst, above 200 °C, NH_3-SCR follows Eley-Rideal mechanism. The effect is caused by the activation of the adsorbed NH_3 species at high temperature [84]. On the other hand, below 200 °C, Langmuir-Hinshelwood is reported to have a greater contribution. It is ascribed to the lower energy barrier of the reaction [90]. Thus, it was found that L-H is more likely to occur, in comparison to E-R [95]. However, various factors, such as concentration of substrates, products, and by-products can dramatically change the mechanism [92].

In some cases, clear identification of the reaction mechanism is exceptionally complicated. For example, Kijlstra et al. [98] proposed that NH_2- species generated after NH_3 adsorption can either react

with gaseous NO (E-R mechanism) or form nitrate intermediates with the adsorbed NO (L-H mechanism), as presented by **Equations (49-55)** (where * represents metal active site):

$$O_2 + 2* \leftrightarrow 2*\text{-}O \quad \textbf{(49)}$$

$$NH_3 + * \leftrightarrow *\text{-}NH_3 \textit{ (Lewis acid site)} \quad \textbf{(50)}$$

$$NO + *\text{-}O \leftrightarrow *\text{-}O\text{-}NO \textit{ (bridged and monodentate nitrite)} \quad \textbf{(51)}$$

$$*\text{-}O\text{-}NO + *\text{-}O \rightarrow *\text{-}NO_3 + * \textit{ (bridged nitrate)} \quad \textbf{(52)}$$

$$*\text{-}NH_3 + *\text{-}O \rightarrow *\text{-}NH_2 + *\text{-}OH \quad \textbf{(53)}$$

$$\mathbf{*\text{-}NH_2 + NO \rightarrow N_2 + H_2O + * \text{ (E-R mechanism)}} \quad \textbf{(54)}$$

$$\mathbf{*\text{-}NH_2 + *\text{-}O\text{-}NO \rightarrow N_2 + H_2O + *\text{-}O + * \text{ (L-H mechanism)}} \quad \textbf{(55)}$$

$$2\ *\text{-}OH \leftrightarrow H_2O + *\text{-}O + * \quad \textbf{(56)}$$

Therefore, coexistence of the two mechanisms, usually related to the nature of the catalyst, makes it much more difficult to resolve the reaction pathway with high accuracy.

Dependence of NH_3-SCR pathway on the type of acid sites

One of the key factors determining the mechanism of NH_3-SCR is acidic character of the catalyst. The studies performed so far confirmed strong relationship between the activity and acidity of NH_3-SCR catalysts [81,99,100]. However, the debate on the type of sites and intermediates formed during the reaction is still opened.

Early studies in this area, conducted by Topsøe et al. [78], proved that Brönsted sites are the most important for NH_3 adsorption and successful NO reduction over V_2O_5-TiO_2. This conclusion was supported by linear correlation between the amount of surface NH_4^+ intermediates and the overall NH_3-SCR activity. Basing on the results of *in situ* FT-IR studies, the authors proposed NH_3-SCR pathway on Brönsted acid sites, following E-R mechanism, described by **Equations (57-62):**

$$V^{5+}\text{-}OH + NH_{3\ (gas)} \leftrightarrow V^{5+}\text{-}ONH_4 \quad \textbf{(57)}$$

$$V^{5+}\text{-}ONH_4 + V^{5+}{=}O \leftrightarrow V^{5+}\text{-}ONH_3H^+\text{–}O\text{-}V^{4+} \quad \textbf{(58)}$$

$$V^{5+}\text{-}ONH_3H^+\text{–}O\text{-}V^{4+} + NO \rightarrow V^{5+}\text{-}OH\text{-}NH_2NO\text{-}H\text{-}O\text{-}V^{4+} \quad \textbf{(59)}$$

$$V^{5+}\text{-}OH - NH_2NO - H\text{-}O\text{-}V^{4+} \rightarrow N_2 + H_2O + V^{5+}\text{-}OH + V^{4+}\text{-}OH \quad \textbf{(60)}$$

$$2\ V^{4+}\text{-}OH \rightarrow H_2O + V^{3+} + V^{5+}{=}O \quad \textbf{(61)}$$

$$2\ V^{3+} + O_2 \rightarrow 2\ V^{5+}{=}O \quad \textbf{(62)}$$

First step of the reaction **(Equation 57)** involves exothermic adsorption of gaseous ammonia on surface vanadyl groups (V^{5+}-OH) and formation of tetrahedral NH_4^+ adsorbate, without any energy barrier. Transformation of the adsorbed ammonia involves participation of V^{5+}=O and the step is regarded as "*activation of ammonia*", before the reaction with NO **(Equation 58).** Subsequently, gaseous NO approaches NH_4^+ species to form -NH_2NO intermediate **(Equation 59)**. The intermediate decomposes to form N_2 and H_2O with simultaneous generation of V^{5+}-OH and V^{4+}-OH **(Equation 60).** The reduced vanadyl species, V^{4+}-OH and V^{3+} are re-oxidized to redox sites, V^{5+}=O (**Equations 61-62).** Additionally, it was found that the amount of Brönsted acid sites increases with the increasing content of the active phase, while increasing temperature implies the decline of Brönsted acidity [100].

In contrast to the above mentioned, Ramis et al. [101] postulated that catalysts containing only Lewis acidity exhibit satisfactory catalytic activity in NH_3-SCR. Besides, *in situ* DRIFTS analysis confirmed that the stability of Lewis centers remains constant, regardless temperature of the reaction. The authors proposed that NH_3-SCR on Lewis acidic centers consists of the steps described by **Equations (63-66):**

$$[O=V^{5+}O_3] + NH_{3\,(gas)} \rightarrow [O=V^{4+}O_2(–OH)(–NH_2)] \quad \textbf{(63)}$$

$$[O=V^{4+}O_2(–OH)(–NH_2)] + NO \rightarrow [O=V^{4+}O_2(–OH)(–NH_2–NO)] \quad \textbf{(64)}$$

$$[O=V^{4+}O_2(–OH)(–NH_2–NO)] \rightarrow N_2 + H_2O + [O=V^{4+}O_2(–OH)] \quad \textbf{(65)}$$

$$4\,[O=V^{4+}O_2(–OH)] + O_2 \rightarrow 2\,H_2O + 4\,[O=V^{5+}O_3] \quad \textbf{(66)}$$

It was postulated that gaseous ammonia adsorbs on Lewis acid site and forms surface -NH_2 species, simultaneously reducing vanadia sites **(Equation 63).** The amide species subsequently react with gas-phase NO and produce surface nitrosamide intermediates (NH_2NO) **(Equation 64),** which decompose to N_2 and H_2O **(Equation 65).** The catalytic cycle is completed by re-oxidation of the reduced vanadia site by O_2 **(Equation 66).**

However, the study was based on the artificial generation of Lewis acidity under vacuum conditions. Thus, it was impossible for the authors to analyze the contribution of NH_4^+ species, removed in the reaction conditions. More recent studies on the participation of Lewis acidity in NH_3-SCR were performed by Gruber et al. [102] and Marberger at al. [81]. They confirmed that Lewis acid sites have significant contribution to the reaction mechanism. The findings on the significance of Lewis acidity in

NH_3-SCR are supported by Qu et al. [89] as well. The authors claimed that although both Brönsted and Lewis sites contribute to the reaction, the number and thermal stability of the latter centers is significantly higher. Additionally, it was declared that Lewis acid sites were responsible mainly for E-R mechanism.

On the contrary, Zhu et al. [103] proposed that for V_2O_5-WO_3-TiO_2 both types of acid sites contribute to NH_3-SCR activity. However, their relative population is determined by the content of the active phase and temperature of the reaction. The authors have drawn the general conclusion that the overall activity of the catalyst was determined by NH_4^+ adsorbed on Brönsted sites, however, NH_3 coordinated to Lewis centers exhibited higher specific activity. Additionally, participation of both acidic centers is correlated with other compounds present in the gas stream, such as H_2O. The simplified reaction mechanisms on Brönsted and Lewis acid sites on V_2O_5 as the exemplary active phase are presented in **Figure 9.**

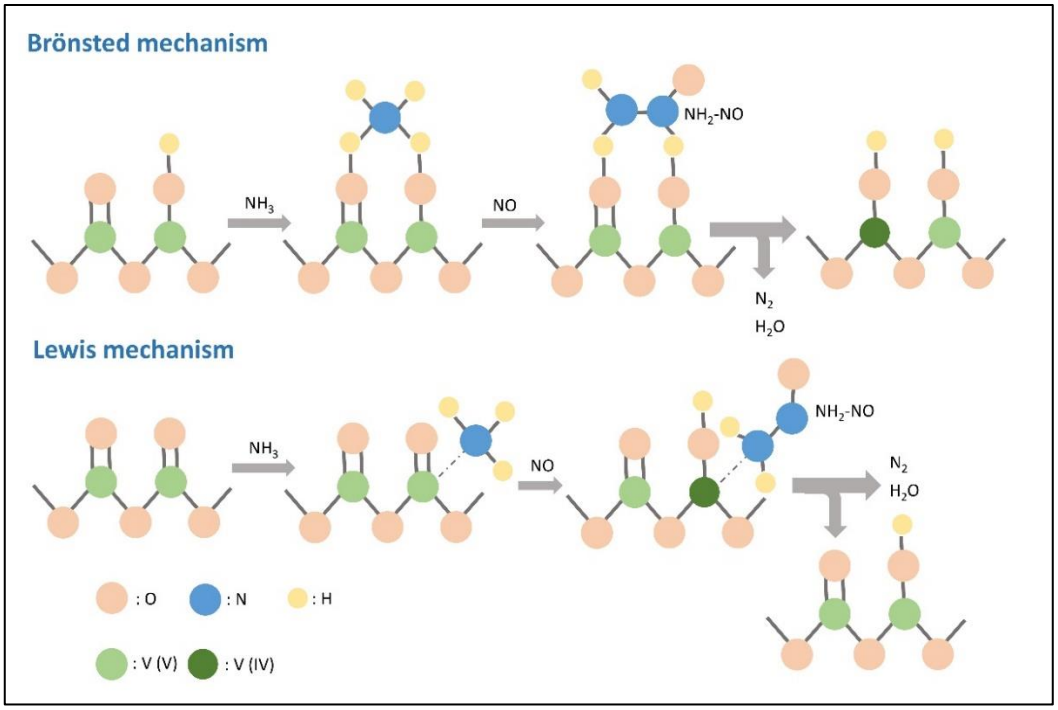

Figure 9. Schematic NH_3-SCR reaction pathway on Brönsted and Lewis acid site of V_2O_5 as the exemplary active phase (based on [104])

2.4 Selective catalytic reduction of nitrogen oxides with hydrocarbons (HC-SCR)

The last decades have witnessed an increased interest in the application of various hydrocarbons (HC) as the reducing agents of industrial SCR systems. The method is especially preferable for SCR

installations which aim to purify exhausts from lean-burn engines working in an excess-oxygen environment (diesel compression ignition, lean-burn gasoline direct injection) [105]. The pioneering research on HC-SCR was published by Held et al. [106] and Iwamoto et al. [107] and concerned copper-exchanged ZSM-5 as the efficient catalyst of the process.

Hydrocarbons, such as volatile organic compounds (VOCs) and polyacrylic aromatic hydrocarbons (PAHs) are emitted to the atmosphere simultaneously with NO_x. Therefore, the use of HC in SCR is both practicable and cost-efficient, since they are already the part of the flue gas [108,109]. Presently, methane [110], propane [111], and propylene [112] are the most common HC reducing agents. However, aromatic compounds are lately studied as well [109]. Normally, the specific hydrocarbon determines temperature window and type of intermediates produced during the reaction [113,114].

Intensive studies on the suitable catalysts of HC-SCR distinguished various materials active in the process. The most satisfactory catalytic performance was obtained for Cu, Co, Fe, Ni, Ag, and Pt, supported on high-silica zeolites (FER, MFI, MOR) or metal oxide catalysts supported on Al_2O_3, TiO_2, SiO_2, and CeO_2 [108]. Besides, ceria-zirconia mixed oxides [109] or porous clay heterostructures modified with Fe [112] ensured the highest conversion of NO and satisfactory selectivity to N_2.

There are various mechanisms of HC-SCR described in the literature and the probability of each of them depends on the reducing agent and reactivity of the catalytic system in the certain temperature region. One of the proposed reaction pathways assumes adsorption of NO and HC, their dissociation on the catalyst surface, and subsequent reaction. The produced intermediates, such as CH_3NO, CH_3NO_2, CH_3NON_2 are continuously decomposed, leading to the formation of N_2 [115]. Another mechanism of HC-SCR presumes oxidation of the reducing agent adsorbed on the catalyst surface, its reaction with gaseous NO_2, and production of isocyanates (NCO^-). NCO^- species are transformed to NH_3, thus, HC-SCR mechanism is switched to NH_3-SCR [116].

The HC-SCR reaction pathway over the mostly studied Cu-ZSM-5 catalyst was thoroughly described by Li and Guan [114]. The authors conducted *in situ* DRIFTS studies of SCR reaction in the excess of oxygen with propane and propene. The authors recognized different reaction pathways for the reducing agents, caused by diversified oxidation activity and adsorption of the reactants on Brönsted acidic sites. For propane (C_3H_8-SCR), the initial step of the reaction was adsorption of NO-O_2 and the

nitrate species were the most abundant and active reaction intermediates. The competitive adsorption of NO and propane precluded activation of C_3H_8 on the catalyst surface. Therefore, the schematic reaction pathway (without real stoichiometry) of C_3H_8-SCR, described by **Equations (67-71),** have been proposed:

$$NO_{(gas)} + O + 2\,H^+ \rightarrow \text{-}NO^+_{(ads)} + H_2O \quad \textbf{(67)}$$

$$\text{-}NO^+_{(ads)} \rightarrow Me^{n+}\text{-}NO^{\gamma+}_{(ads)} \quad \textbf{(68)}$$

$$Me^{n+}\text{-}NO^{\gamma+}_{(ads)} + O_{(ads)} \rightarrow Me^{n+}\text{-}NO_{3\,(ads)} \quad \textbf{(69)}$$

$$\text{-}NO_{3\,(ads)} + C_3H_{8\,(gas)} \rightarrow \text{-}H + C_3H_7\text{-}NO_3 \quad \textbf{(70)}$$

$$C_3H_7\text{-}NO_3 + O_{2\,(gas)} \rightarrow N_2 + CO_2 + H_2O \quad \textbf{(71)}$$

First step of the reaction **(Equation 67)** consists of the adsorption of NO and formation of $\text{-}NO^+$ intermediate. Interaction of $\text{-}NO^+$ with the adjacent metal site results in the formation of $Me^{n+}\text{-}NO^{\gamma+}$ with simultaneous charge transfer **(Equation 68).** Oxidation of the unstable $\text{-}NO^{\gamma+}$ species to $\text{-}NO_3$ **(Equation 69)** and reaction of $\text{-}NO_3$ with gaseous propane recovers the Brönsted center **(Equation 70)**, while oxidation of the produced $C_3H_7\text{-}NO_3$ yields the mixture of N_2, CO_2, and H_2O **(Equation 71).** Continuous reduction of NO to N_2 during the reaction is provided by constant formation of $Me^{n+}\text{-}NO_3$ species on the catalyst surface.

Alternate mechanism of NO reduction was proposed for propene. In this case, the first and the most important step of the reaction involves adsorption and activation of C_3H_6 on the Brönsted site of metal cation. In the case of Cu-ZSM-5, propene adsorbed on the acidic center can be oxidized by the neighborhood Cu^{2+}, according to the reaction described by **Equation (72):**

$$Cu^{2+} + \text{-}C_3H_6 \rightarrow Cu^+\text{-}C_xH_y \quad \textbf{(72)}$$

Re-oxidation of Cu^+ to Cu^{2+}, according to **Equation (73)** is provided by the surface active oxygen:

$$Cu^+\text{-}C_xH_y + O_{(ads)} \rightarrow Cu^{2+} + \text{-}C_xH_y + H_2O \quad \textbf{(73)}$$

The most important intermediates of C_3H_6-SCR are adsorbed amine species, which react with NO or NO_2 to finally form N_2 and H_2O. The schematic mechanism of C_3H_6-SCR (without true stoichiometry) can be presented by **Equations (74-82):**

$$NO_{(gas)} + O_{(ads)} \rightarrow NO_{2\,(gas)} \quad \textbf{(74)}$$

$$C_3H_{6\,(gas)} + O_{(ads)} \rightarrow \text{-}C_xH_{y\,(ads)} + H_2O \quad \textbf{(75)}$$

$$-C_xH_{y\ (ads)} + NO_{2\ (gas)} \rightarrow -C_xH_yO_{z\ (ads)} + -NCO \quad \textbf{(76)}$$

$$-NCO_{\ (ads)} + O_{\ (ads)} \rightarrow N_2 + CO_2 \quad \textbf{(77)}$$

$$-NCO_{\ (ads)} + NO \rightarrow N_2 + CO_2 \quad \textbf{(78)}$$

$$-NCO_{(ads)} + H_2O \rightarrow -NH_2 + CO_2 \quad \textbf{(79)}$$

$$-NH_{2\ (ads)} + NO \rightarrow N_2 + H_2O \quad \textbf{(80)}$$

$$-NH_{2\ (ads)} + NO_2 \rightarrow N_2 + H_2O \quad \textbf{(81)}$$

$$-C_xH_yO_z + O_{(ads)} \rightarrow CO_2 + H_2O \quad \textbf{(82)}$$

After adsorption of C_3H_6, the produced surface species ($-C_xH_y$) **(Equation 75)** are oxidized by an oxidant (for example NO_2) to yield $-C_xH_yO_z$ **(Equation 76).** Reduction of NO_2 results in the formation of -NCO species, which can generate N_2 and CO_2 **(Equations 76-78)** or hydrolyze to $-NH_2$ **(Equation 79)**, regarded as the most active reaction intermediates. Reaction between $-NH_2$ and NO or NO_2 results in the formation of N_2 and H_2O **(Equations 80-81)**, while the adsorbed $-C_xH_yO_z$ species are further oxidized to CO_2 and H_2O by the surface oxygen **(Equation 82)**. Two possible reaction pathways over metal-exchanged ZSM-5 with propane or propene are depicted in **Figure 10.**

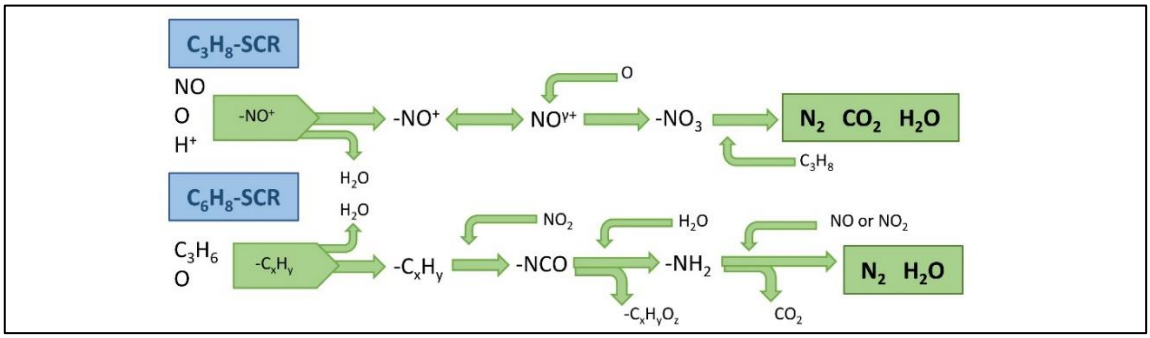

Figure 10. Schematic reaction pathways of SCR with propane (C_3H_8) or propene (C_3H_6) (based on [114])

The presented investigations proved that the key factors controlling the mechanisms of C_3H_8-SCR and C_3-H_6-SCR is Brönsted acidity and oxidative features of the catalyst. Additionally, several studies have shown that the Si/Al molar ratio and co-existence of CO or H_2 in the gas stream have a crucial influence on the catalytic performance of Cu-ZSM-5 in HC-SCR [105,117].

2.5 Alternative reducing agents of SCR

Selective catalytic reduction with ammonia or with hydrocarbons enables to obtain high conversion of NO_x. However, there are some limitations of these methods, such as “ammonia slip” for NH_3-SCR or poor low-temperature activity of HC-SCR [118]. According to the present knowledge,

ammonia (or its derivatives) and hydrocarbons can be replaced in SCR systems by alternative reducing agents. A number of studies reported that H_2 and/or CO are suitable compounds to effectively remove the majority of NO_x from the exhausts [119]. The comprehensive description of the advances in H_2-SCR and CO-SCR was provided in the literature reviews of Hamada et al. [120] and Gholami et al. [121].

CO-SCR reaction was studied by Yan et al. [122] who performed DFT study over $LaMnO_3$ perovskite. The authors proposed the reaction pathway of N_2 formation consisting of three steps, described by **Equations (83-86):**

$$2NO_{(ads)} \rightarrow N_2O_{2\,(ads)} \quad \textbf{(83)}$$

$$N_2O_{2\,(ads)} + CO_{(ads)} \rightarrow N_2O_{(ads)} + CO_{2\,(ads)} \quad \textbf{(84)}$$

$$N_2O_{(ads)} \rightarrow N_{2\,(ads)} \quad \textbf{(85)}$$

$$CO_{(ads)} + O_{(ads)} \rightarrow CO_2 \quad \textbf{(86)}$$

In the first step **(Equation 83),** the adsorbed NO undergoes bimolecular reaction to produce intermediate N_2O_2, which is subsequently reduced by the adsorbed CO molecules to N_2O **(Equation 84).** At least, N_2O is reduced to N_2, while CO is oxidized to CO_2 **(Equations 85-86).** Among various catalytic systems investigated for CO-SCR, supported transition metal oxides, especially Cu-catalysts, exhibit the highest activity [121].

Over the last years, the focus has also shifted to the application of hydrogen as the alternative reducing agent of SCR [120,123,124]. Most of the catalytic systems for H_2-SCR uses metals of platinum group (for example Pt and Pd) supported on metal oxides, perovskites, or mesoporous silica [120].

There are two general reaction mechanisms of H_2-SCR. The first one assumes simultaneous adsorption and dissociation of NO, facilitated by the adsorbed H_2. Appropriate concentration of O_2 in the gas removes the excess of H_2, thus, hinders the undesirable formation of NH_3. The second mechanism is related to the oxidation-reduction mechanism with the formation of nitrate and NH_3 or NH_4^+ [125]. In this case, N_2 is produced by the surface reaction between NH_4^+ species and NO + O_2, while NO_3^- or NO_2^- species yield mainly N_2O through the reaction with the adsorbed H_2 [118]. It was confirmed that the mechanism of H_2-SCR is determined by the chemical character of the catalyst support: basic supports are capable to adsorb NO_3^- and NO_2^- intermediates, while acidic ones stabilize active phase and adsorb ammonia molecules [118]. Besides, H_2-SCR reaction pathway is correlated with

the temperature of the process. Komatrubara [126] conducted a study of H_2-SCR over Pt-AlMCM-41 catalyst with the excess of oxygen and found that both mechanisms (NO surface dissociation and NH_3 formation) participated in the reaction pathway. The authors recognized the following temperature regions of the H_2-SCR (1) 40-100 °C **(Equations 87-88)**; (2) 77-177 °C **(Equations 89-91)**; and (3) 177-377 °C **(Equations 92-94):**

(1) 40-100 °C – adsorption and dissociation of NO into N and O, formation of N_2O upon the reaction with the adsorbed NO**,** removal of $O_{(ads)}$ upon the reaction with gaseous H_2:

$$2\ NO \rightarrow N_2O + O_{(ads)} \quad \textbf{(87)}$$

$$O_{(ads)} + H_2 \rightarrow H_2O \quad \textbf{(88)}$$

(2) 77-177 °C – formation of intermediate NH_3 upon the reaction between NO and H_2, NH_3-SCR of NO_x with the formed NH_3:

$$2\ NO + 5\ H_2 \rightarrow 2\ NH_3 + 2\ H_2O \quad \textbf{(89)}$$

$$4\ NO + 4\ NH_3 + O_2 \rightarrow 4\ N_2 + 6\ H_2O \quad \textbf{(90)}$$

$$4\ NO + 4\ NH_3 + 3\ O_2 \rightarrow 4\ N_2O + 6\ H_2O \quad \textbf{(91)}$$

(3) 177-377 °C – formation of intermediate NH_3 upon the reaction between NO and H_2 **(31)** and its selective oxidation to N_2 or N_2O:

$$2\ NO + 5\ H_2 \rightarrow 2\ NH_3 + 2\ H_2O \quad \textbf{(92)}$$

$$4\ NH_3 + 3\ O_2 \rightarrow 2\ N_2 + 6\ H_2O \quad \textbf{(93)}$$

$$2\ NH_3 + 2\ O_2 \rightarrow N_2O + 3\ H_2O \quad \textbf{(94)}$$

Despite the fact that H_2 seems to be an attractive alternative for NH_3 or hydrocarbons, its implementation still needs more investigations. Although the approach of the H_2 application is interesting, the majority of H_2-SCR catalysts is active in narrow temperature window and sensitive for the poisoning with CO. Additionally, still more research is required to establish the participation of NH_3-SCR in the mechanism of H_2-SCR and the influence of some gaseous impurities (SO_2 or H_2O) on the efficiency of H_2-SCR.

3. The commercial V_2O_5-TiO_2 catalyst and its limitations

3.1 Typical composition of the catalyst

The most common catalyst used in NH_3-SCR installations in power plants supplied by fossil fuels is vanadium-titanium-based system, V_2O_5 – TiO_2 promoted with tungsten or molybdenum (WO_3, MoO_3, respectively). In the most cases, the catalyst provides around 90% of NO conversion and satisfactory selectivity to N_2, especially above 300 °C [127–129]. The support of the catalyst, TiO_2 in a form of anatase, exhibits relatively high specific surface area and well-developed pore system. The active phase consisting of monolayer V_2O_5 species delivers active centers for the catalytic reaction [130]. The addition of WO_3 as a promoter facilitates the formation of Lewis and Brönsted acidity, improves SO_2 resistance and durability of the catalyst [64,131]. Additionally, some of the industrial catalytic systems contain small additions of SiO_2, which was reported to enhance high-temperature stability and resistance to the poisoning effect of SO_2 [132].

3.2 Operating problems of the commercial V_2O_5-TiO_2 catalyst

Despite the fact that the commercial vanadium-based catalyst exhibits relatively high NO conversion in the temperature region of 300-450 °C, there are some issues, which limit its efficient work. First of all, relatively fast deactivation of the system requires to change the catalytic layers every 2 - 3 years [133]. Avoiding the replacement of the old or spent catalysts may result in serious problems, such as ammonia slip [134]. Since the catalyst accounts to 30-50% of the overall cost of industrial SCR installations, it significantly increases the total expenses of the catalytic unit [135]. Results reported by Kiełtyka et al. [136] suggest that the activity of V_2O_5-TiO_2 used in a coal-fired power plant with biomass co-firing decreased by 10% after 2000 h of operation, while after 5000 h it reduces to 20%. In the case of straw-fired boilers, the deactivation rate can reach even 1% per one day of work [137].

In general, the deactivation of the V_2O_5- TiO_2 system can be divided into mechanical, chemical, and thermal [138]. Chemical deactivation concerns poisoning of the catalysts with chemical compounds, usually present in the exhausts (alkali metals, sulfur trioxide). Mechanical deactivation concerns the damage of the catalyst surface and its attrition upon uneven flue gas distribution and velocity [139]. At least, thermal deactivation is related to the irreversible sintering of anatase into rutile. Since the latter

exhibits significantly lower specific surface area, the phase transition is highly undesirable [140]. High operating temperature can also result in volatilization of vanadium or tungsten (in the WO_3-promoted catalyst), and as a consequence, lower activity and narrower temperature window [141–143]

The operating obstacles related to the application of V_2O_5- TiO_2 on the industrial scale are described in detail in the research papers [129] and [134], while the following subsection is focused only on the most important reasons of the chemical deactivation of V_2O_5- TiO_2. All of the mentioned points highlight the aspects that have to be taken into account to design chemical composition of the novel NH_3-SCR catalyst. The common deactivating factors and processes, together with the possible solutions are illustrated in **Figure 11.**

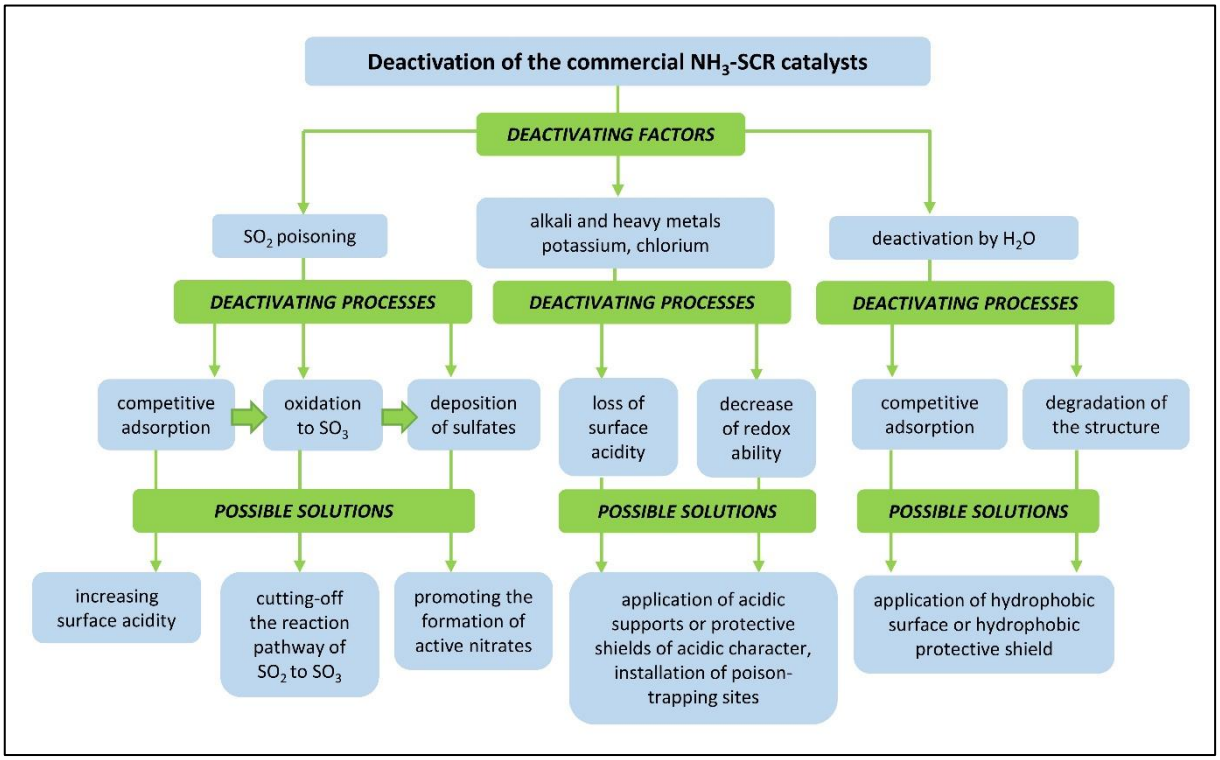

Figure 11. The factors, processes, and possible solutions related to the deactivation of commercial catalysts of NH_3-SCR

3.2.1 Narrow temperature window

The significant drawback of the commercial vanadium-based system is its narrow temperature window. The standard temperature of the industrial flue gas reaches maximum 300 °C, depending on the work stability of the boiler. Therefore, the efficient NH_3-SCR catalyst should exhibit satisfactory activity in the range of 100-300 °C, which is below the optimum of V_2O_5-TiO_2 [144]. In order to provide

appropriate temperature window and avoid additional costs for the re-heating of the exhausts, the catalyst is usually placed in so-called “high dust” configuration, before flue gas desulphurization unit (FGD) and electrostatic precipitator (ESP) [145,146]. In the most of cases, this solution helps to increase the reaction temperature. However, the catalyst is exposed to the harmful impact of sulfur oxides (SO_x), deactivation by alkali metals present in the fly ash, or non-metallic compounds, such as arsenic or lead [99,147–149].

3.2.2 Poisoning and deactivation with sulfur oxides

Sulfur oxides belong to the group of strong poisons of NH_3-SCR catalysts, including the commercial vanadium-based system [150]. The deactivating effect is caused by the interaction of SO_2 with vanadium species at the temperature below 300 °C. It is due to the fact that V_2O_5 exhibits relatively high catalytic activity in the oxidation of SO_2 to SO_3 [151,152]. Early findings of Svachula et al. [153] and Dunn et al. [154] on the influence of SO_2 on the conversion of NO_x over honeycomb V_2O_5-TiO_2 proved that NO_x can facilitate oxidation of SO_2 to SO_3. The effect is especially strong in the low-temperature range, when NO_x concentration is high. More recent studies carried out by Xu et al. [155] proved that conversion of SO_2 to SO_3 increases linearly with the increasing reaction temperature.

In general, V_2O_5-TiO_2 can be deactivated by sulfur compounds upon two pathways. The first one assumes the reaction between SO_3 generated during catalytic oxidation and gaseous NH_3 and H_2O. The resulting ammonium bisulfates (ABS, NH_4HSO_4) and ammonium sulfates (AS, $(NH_4)_2SO_4$) block the pores of the catalytic material and hinder the diffusion of the reactants into the active centers [156]. Besides, the compounds form deposits in the cold equipment, downstream of the SCR reactor, lead to corrosion. Ammonium sulphates and bisulphates can also accumulate in air-preheater and cause pressure drops and its clogging [157–159]. All of these effects seriously affect economic and safe operations of NH_3-SCR units of fossil fuel-fired power plants. However, several studies have found that AS and/or ABS can be decomposed under appropriate conditions [156,160,161]. Thus, this type of deactivation is at least partially reversible.

The second route of deactivation with sulfur species concerns interaction with SO_2 and metallic active centers to form thermally stable sulfates [162–164]. The species significantly affect redox

properties of the catalyst, inhibiting the catalytic reaction. In-situ experimental investigation performed by Guo et al. [165] proved that metal sulfate species are formed rather upon the interaction of SO_3 with titania, than with vanadium. The study presented Du et al. [166] further corroborate with this hypothesis, explaining the mechanism of metal sulphates formation. According to the authors, TiO_2 provides the surface for SO_2 adsorption, while vanadium monomers and dimers are responsible for SO_2 oxidation to SO_3. The temperature of metal sulfates decomposition is relatively high (in most cases, up to 500 °C) [167]. Thus, regeneration of the catalyst by thermal treatment would result in the significant loss of the active material. Therefore, poisoning of the catalytic systems by metal sulfates is irreversible and stands as a considerable, unsolved problem.

What is interesting, some studies confirmed that exposition of the catalyst to small amounts of SO_2 can have a positive impact on the catalytic performance [168,169]. Hence, the commercial catalyst usually contains 0.5-1 wt.% of sulfur in order to generate SO_4^{2-} species that act as a reservoir for the adsorbed NH_3 [170]. Therefore, the role of sulfate groups in the commercial NH_3-SCR catalyst has attracted a considerable attention in the recent years. Nevertheless, the beneficial influence of sulfation is still unclear and remains under research.

3.2.3 Poisoning with particulate matter compounds

Apart from sulfation, high-dust-positioned catalyst is also susceptible to the deactivation by the components of fly ash, such as alkali metals [148]. Large concentration of these compounds is characteristic for the fly ash produced by coal-fired power plants. The amount is even higher while renewable energy sources, like biomass are combusted [137]. Deactivation character of these compounds is related to their basic character and affinity to the acidic sites. Interaction of the metals of I or II group of periodic table with the V^{5+}-OH Brönsted acidic sites results in their consumption and reduced NH_3 adsorption capacity of the catalyst. Most research on the deactivation of V_2O_5-TiO_2 by basic compounds assumed the formation of alkali-vanadium compounds ($NaVO_3$, KVO_3, $RbVO_3$) on its surface. As a result, the catalyst undergoes irreversible chemical and structural changes and loss of catalytic activity [137,147,171]. Additionally, Moradi et al. [172] postulated that the inhibiting effect increases at the elevated reaction temperature. Besides, the latest investigation of Lei et al. [173] and

Tang et al. [174] confirmed that the deactivation can be also related to the decreased reducibility and hindered polymerization of vanadium species, caused by alkaline metals.

What is more, the catalyst placed before EP is exposed to other trace elements, for example lead oxide (PbO) [149,175]. PbO is typically present in the exhaust gas emitted by the solid waste incineration, rather than in the flue gas produced by the combustion of fossil fuel [169]. As a typical heavy metal present in the flue gas, lead has a severely poisoning impact on NH_3-SCR catalyst, decreasing its activity even by 50% [176,177]. Jiang et al. [177] postulated that lead species accelerate transformation of V^{5+} species to V^{4+} which results in the reduction of Brönsted acidity and denitrification efficiency. Except of the acidic properties, the presence of PbO results in significant changes of redox abilities of the vanadium species, disturbing the course of the catalytic reaction. Additionally, the lead oxide particles adsorbed on the active sites of the catalyst are the barrier to the free diffusion of the reagents through the porous structure [134,178].

Another trace element that causes deactivation of the commercial catalyst placed in the "high-dust" position is arsenic (As), usually present in a form of oxide (Al_2O_3) or dimer (Al_4O_6) [179]. Its concentration in the industrial exhausts typically oscillates around 1 $\mu g \cdot m^{-3}$ – 10 $mg \cdot m^{-3}$, depending on the incinerated fuel [180]. Poisoning effect of arsenic involves reaction of As^{5+} with the vanadium oxide that results in the occupation of the active sites of the catalyst. Additionally, relatively small molecules of Al_2O_3 can easily diffuse through the inner structure of the catalyst and clog the micropores [180]. Kong et al. [181] presented two possible mechanisms of V_2O_5-TiO_2 poisoning with As: by the formation of As_2O_3 and its oxidation to As_2O_5 deposits (1) or generation of As^{5+} isolated cations at the expense of vanadium species, occupied by As_2O_3 or As_2O_5 (2). Moreover, according to the authors, transformation of As_2O_3 to As_2O_5 is promoted by pentavalent vanadium species that are reduced to V^{4+}. Both routes of deactivation by As involve the participation of surface active oxygen, which is an essential factor in the catalytic cycle of NH_3-SCR [182].

The most recent developments, presented by Lu et al. [180] have led to the conclusion that deactivation of V_2O_5-TiO_2 in coal-fired power plants strongly depends on the position of the catalyst in the installation. The authors postulate that the catalyst placed in the "high dust" position suffers from the poisoning of physical nature, while "tail end" placement results rather in chemical deactivation.

3.2.4 Toxicity of the components

In the industrial conditions, vanadium and tungsten can be easily released to the environment by volatilization. The effect is commonly observed in the case of mobile applications of the vanadium-based catalytic system [183]. Vanadium is especially dangerous for human health due to its carcinogenic character, confirmed by International Agency for Research on Cancer [184]. Thus, the Occupational Safety and Health Administration (OSHA) set the ceiling limits of the exposure for the respirable dust and fumes of V_2O_5 to 0.5 mg $\cdot$ m^{-3} and 0.1 mg $\cdot$ m^{-3}, respectively [163]. On the other hand, the investigation of the carcinogenic or mutagenic effect of tungsten is still in progress. However, the element was included by the US Environmental Protection Agency (EPA) to the Priority Testing List, which collects compounds that are potentially toxic [185]. Therefore, the design of the novel NH_3-SCR catalysts should include substitution of the active phase and the promoters with non-toxic chemical compounds.

4. Review of the novel catalysts for NH_3-SCR

All of the complications related to the application of V_2O_5-TiO_2 on the industrial scale are the motivation for the research and development of new catalytic systems or improvement of the existing ones. Considering the problems described in **subsection 3.2**, the vanadium-based system should be replaced with better one, free from all the mentioned drawbacks. It is especially required for the new catalyst to:

- be active in NH_3-SCR process under oxidizing atmosphere and insensitive to the changes of O_2 concentration in the flue gas,
- be selective to N_2 and non-selective to the greenhouse N_2O,
- have a stable structure, regardless the operating conditions,
- be inactive in the reaction of catalytic ammonia oxidation,
- have wide temperature window,
- be resistant to deactivation with SO_2, alkali metals, and other contamination of flue gas,
- be resistant to deactivation with H_2O [86].

Therefore, in the recent years the studies have shifted to the application of alternative materials, potentially active in NH_3-SCR process. The great effort made in this field resulted in the progressing development of the substitutive catalytic systems. The special focus was directed into supported metal oxides which are deprived of the drawbacks exhibited by the commercial catalyst. In their systematic literature review, Han et al. [186] and Liu et al. [65] described comprehensively the materials that recently have attracted the biggest attention. The following section involves the examples of promising alternative catalysts, which can be potentially implemented on the commercial scale.

4.1 Modified layered aluminosilicates

In recent decades, natural layered aluminosilicates have received a growing interest as the materials important for the industry. The representatives of the cationic minerals can be used as adsorbents [187] or elements of composites [188]. Normally, natural clay minerals are composed of ultrathin aluminosilicate layers of around 1 nm thickness. Each layer consists of one or two (for 1:1 and 2:1 type, respectively) O-Si- O tetrahedral sheets and one O- Al (Mg)-O octahedral sheet, of around

100 × 100 nm in width and length, respectively [188]. The layered structure is stabilized by hydrogen bonds and electrostatic forces. Isomorphous replacement of Al^{3+} by Mg^{2+} ions in the octahedral sheets results in the negative charge, which is compensated by various interlayer cations, such as Na^{+} or Ca^{2+} [189,190]. The peculiar layered structure of natural cationic clays provides considerable ion exchange capacity. Specific surface area of the materials can be easily increased using mineral acids [191,192]. The significant advantages of natural clays are abundance in the environment and non-toxicity. What is more, their unique structural features allow to tailor materials for various catalytic applications [189,193], including NH_3-SCR [194]. Schematic structure of the of natural layered clay minerals is depicted in **Figure 12.**

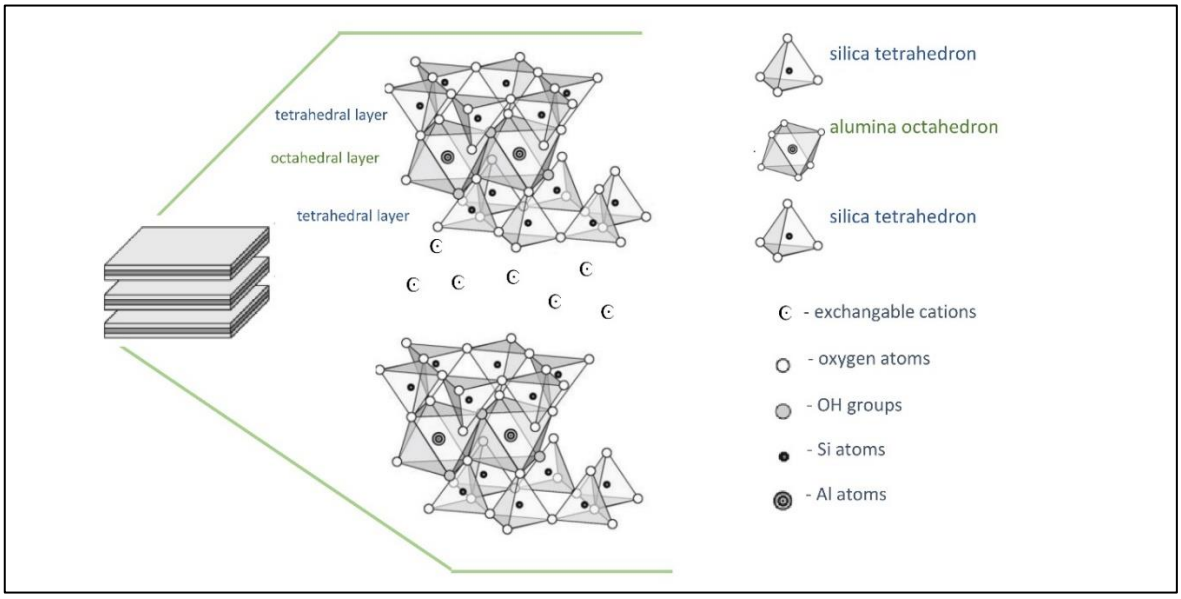

Figure 12. Schematic molecular structure of layered clays on the example of montmorillonite (based on [195])

The great contribution to the research on the catalytic activity of modified clays in NH_3-SCR was made by the group of Chmielarz and co-workers [190,196–198]. The authors pointed out that the catalytic properties of layered clays can be enhanced upon acid treatment [197] or intercalation with various metal oxides [198]. The first method is based on the ion-exchange of interlayer charge-balancing cations for hydrogen cation at the boiling point of the acid [199]. The resulting clay exhibits higher specific surface area, enhanced porosity, and more acid centers [187]. Additionally, acid treatment can increase NH_3-SCR potential of some clays, which contain catalytically active species in octahedral sheets [200,201]. Chmielarz et al. [197] concluded that the treatment of vermiculite with mineral acids,

such as HCl and H_2SO_4 resulted in leaching of Al^{3+}, Mg^{2+}, and Fe^{3+} cations on the external surface of the clay. Consequently, various forms of Fe^{3+} sites became easily accessible active sites for NH_3-SCR reaction. Besides, the authors reported that the specific surface area of the clay can increase even 20-30 times upon acid treatment, depending on the applied acid.

The second essential method of modification is intercalation (pillaring) provided by ion-exchange properties of the layered clays [202]. The procedure is based on the exchange of the charge-compensating cations for bigger metal polyoxocations (oligocations). Introduction of the polyoxocations is preceded by the swelling of the clay with water molecules, to extend the interlayer distance. Calcination of the intercalated clay results in the formation of thermally stable metal oxide pillars [203]. The obtained materials, called "pillared interlayer clays (PILCs)" exhibit specific surface areas of 150-350 $m^2 \cdot g^{-1}$ and mainly microporous structure. What is more, the presence of specific pillars has a direct influence on the catalytic performance, since they can deliver additional acid sites. In general, the most common pillars are Al_2O_3, TiO_2, ZrO_2, or Fe_2O_3 [196,204,205]. Chmielarz et al. [198] compared $DeNO_x$ activity of montmorillonite pillared with SiO_2, SiO_2–Al_2O_3, and SiO_2-TiO_2. According to the study, SiO_2-TiO_2 facilitated formation of well-dispersed isolated Cu^{2+} and Fe^{3+} cations, which improved catalytic activity in NH_3-SCR, especially below 300 °C. One of the disadvantages of PILCs is that their structure is stable only to 400-450 °C. The limited thermal stability can lead to the collapse of the pillared layers at higher temperature and deactivation of the modified clay [203].

Preparation of more stable pillars is possible trough more complex routes, for example surfactant-directed methods, reported for the first time in 1995 [206]. The resulting materials, called porous clay heterostructures (PCHs) exhibit surface areas up to 1000 $m^2 \cdot g^{-1}$, micro-mesoporosity, and considerable acidity. However, the final features of PCHs strongly depend on the specification of the parent clay [207]. Preparation procedure of PCHs starts from the ion-exchange of cationic alkylammonium surfactants and alkylamine co-surfactants with the interlayer cations. In the next steps, the source of silica is introduced into the solution, hydrolyzed, and condensed around organic template. Calcination or extraction results in the removal of the template and formation of silica pillars [208]. The structure of PCHs is reported to be more thermally stable than that of PILCs [209].

4.2 Modified activated carbon

Carbon-based materials were reported to be promising precursors of NH_3-SCR catalysts [210–213]. Activated carbon (AC) is regarded as very advantageous for denitration processes, due to the high adsorption capacity facilitated by well-developed pore system and high specific surface area [214]. Moreover, the existence of surface oxygen-rich groups can potentially contribute to the increased SO_2-poisoning resistance [215,216]. The schematic porous structure of activated carbon is schematically showed in **Figure 13.**

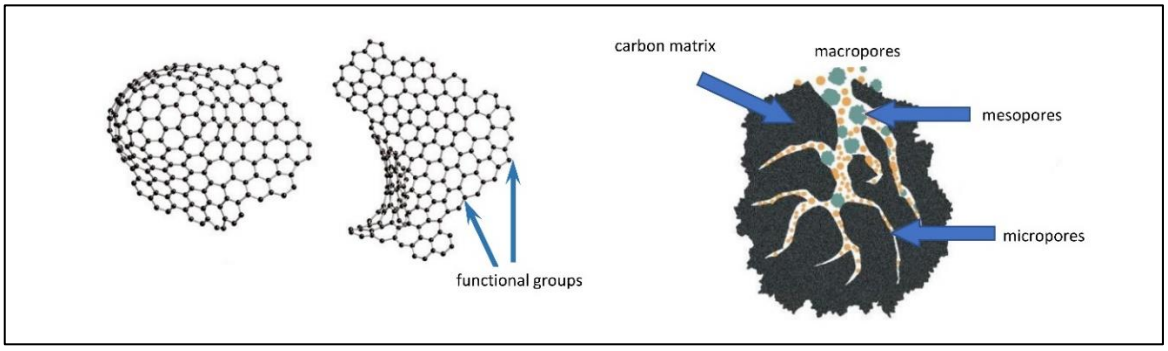

Figure 13. The graphical structure of activated carbon with specific types of pores (based on [217])

The structure and surface chemistry of carbonaceous materials is complicated and depends on many factors. Thus, the issue has become a central point in the scientific investigations. The great number of research on the application of activated carbon and carbon-derived materials in NH_3-SCR is related to structural modifications [213,218,219]. Most of them involve introduction of heteroatoms, such as oxygen (O), nitrogen (N), phosphorous (P), sulfur (S), or boron (B) [213,218,220]. In general, such modifications enable to tailor the electron donor-acceptor features of the carbonous matrix. Oxygen is one of the common heteroatoms present on the edges of carbonic layers. The catalytic performance of activated carbon in NO conversion strongly depends on the number and kind of O-groups. This correlation is ascribed to the fact that oxygen groups play a role of adsorption sites for NO and NH_3 molecules. Guo et al. [221] oxidized activated carbon with nitric acid and investigated the chemistry of the formed functional groups. The analysis revealed that generation of the type of oxygen groups was strongly determined by the pretreatment temperature. The performed NH_3-SCR catalytic tests indicated that carboxyl, anhydrite, and phenol groups had a promoting effect on catalytic activity. On the other hand, several studies have found nitrogen species to enhance NH_3-SCR performance of activated carbon

[151,213,222,223]. The promotional effect takes place due to the increased surface basicity and creation of extra-delocalized electrons that facilitate adsorption of NO and O_2 and formation of NO_2. Recently, Li et al. [222] modified activated carbon with the solution of $NH_3 \cdot H_2O$ or nitric acid (HNO_3) in order to enhance its catalytic activity in NH_3-SCR. On the basis of X-ray photoelectron spectroscopy (XPS), performed before and after catalytic reaction, the authors postulated that the introduced pyridine and pyrrole groups, and quaternary oxygen participated in the surface reaction. Yao et al. [223] explained that these structures supplied the material with unpaired electrons, crucial for the adsorption and oxidation of NO during NH_3-SCR. Saad et al. [213] performed a double modification of activated carbon using nitric acid (HNO_3) to increase specific surface area and urea to introduce N-groups. Besides, Ce was used as the active phase of the catalyst. The reported outcomes proved that the highest concentration of HNO_3 resulted in the development of new pore systems, while introduction of Ce increased NO conversion, comparing to the samples impregnated only with urea.

In fact, deposition of chemical surface groups can increase catalytic potential of activated carbon in NH_3-SCR. However, it can be even more enhanced by the introduction of transition metals, such as iron (Fe) [224], manganese (Mn) or cerium (Ce) [211,223,225]. However, in some cases introduction of transition metals can result in the formation of carbon-metal deposits, which hinder diffusion of the gas molecules through the pores.

The activated carbon-based materials also attracted a growing attention as the catalysts for simultaneous removal of NO_x and SO_2 [216,226,227]. According to Guo et al. [228], the presence of NO facilitates adsorption and elimination of SO_2. However, higher SO_2/NO ratio restricts the adsorption of NO and decreases the efficiency of NH_3-SCR. Furthermore, Saad et al. [212] analyzed NH_3-SCR catalytic performance of Cu-modified activated carbon poisoned with SO_2. The authors suggested that deactivating effect was mainly caused by the formation of thermally-resistant $CuSO_4$. Additionally, the catalytic activity of around 90% exhibited by the fresh Cu-AC was significantly limited after poisoning with SO_2 and regeneration.

Despite the promising performance of AC-based materials in NH_3-SCR, still, they are not free from some drawbacks. The work by Ren et al. [229] indicated that HNO_3-treated activated carbon modified with Mn and Ce were completely and irreversibly deactivated by KCl and Al_2O_3. Moreover,

Su et al. [230] observed severe deactivation of Mn-Ce-AC catalyst by PbO. Both authors ascribed the deactivating effect to the pore clogging and deposition of the poisoning compounds on the functional surface groups of activated carbon. In some aspects modification with strongly oxidizing agents can result in the formation of catalytically inactive groups [221] or excessive weight loss of the carbonous precursor. Additionally, carbonous support can be preferentially decomposed in the high temperature range of the reaction, which affects stability of the catalyst. This inhibiting effect can be suppressed by its mixing with binders and shaping. However, such procedures negatively affect adsorption capability of activated carbon [231].

4.3 Metal oxide catalysts

The interest in the application of metal oxide catalysts is related to their satisfactory activity in the low-temperature range of NH_3-SCR. Metal oxide catalyst can act as catalysts itself (single metal oxide catalysts), be mixed with other metal oxides (multi metal oxide catalysts) or be supported on other metal oxide (supported metal oxide catalysts) [232]. According to the literature, the oxides of transition metals show the highest catalytic activity in NH_3-SCR [233–235].

Single metal oxide catalysts

One of the very promising metal oxide that can be applied in NO reduction process is iron oxide (Fe_2O_3). The most advantageous feature of Fe_2O_3 catalyst is its low activation energy ($\boldsymbol{E_A}$) of 28.32 kJ · mol^{-1} [236], therefore competitive to V_2O_5-TiO_2, which is 85 kJ · mol^{-1} [237]. Besides, Fe_2O_3 exhibits high specific surface area and crystallinity [238]. Due to the fact that iron is a multivalent atom, it can form various stable oxides, such as α-Fe_2O_3 (haematite), γ-Fe_2O_3 (maghemite) or Fe_3O_4 (magnetite) [239]. Results reported in the literature suggest that the certain surface of iron oxide determines its catalytic performance in NO reduction. Liu et al. [240] provided a thorough comparison of α-Fe_2O_3 and γ-Fe_2O_3 activity in NH_3-SCR. It was observed that γ-Fe_2O_3 was more active (95% NO conversion) than α-Fe_2O_3 (85% NO conversion) at 250 °C. The authors ascribed this effect to the abundance of hydroxyls and defect oxides available on the surface of γ-Fe_2O_3. Additionally, Yao et al. [241] demonstrated that Fe_3O_4 shows very poor catalytic activity of around 15% at 400 °C.

Among single metal oxide catalysts, manganese oxide (MnO_x) was found to be promising in NH_3-SCR as well. Similarly to iron oxide, the activity-determining features in this case are Mn oxidation state, specific surface area, and crystallinity [242]. Considering various oxidation states of manganese, it was reported that MnO_2 and Mn_2O_3 are the most active in NO reduction, while the lowest NO conversion is obtained for MnO. The effect is directly related to the amount of surface-active oxygen species that are essential in the mechanism of NH_3-SCR. Likewise Fe_2O_3, Mn_2O_3 can be present in various phases, such as α or β [95]. Tang et al. [243] compared NO conversion and N_2O production for α-Mn_2O_3 and β-Mn_2O_3 during NH_3-SCR at 150 °C. Basing on the obtained outcomes, the authors postulated that despite higher NO conversion obtained for β-Mn_2O_3, the material was more selective to N_2O. This effect was assigned to higher NH_3 adsorption capacity of β-Mn_2O_3, resulting in the abundance of adsorbed N-species, actively reacting with gaseous NO to form nitrous oxide.

Multi-metal oxide catalysts

Multi-metal oxide catalysts (or composite catalysts) have gained a growing attention mainly due to synergistic effect of various metals on the activity and selectivity in the catalytic reactions. In this case, typically one metal modifies electronic and structural features of the another.

The studies have shown that Fe_2O_3- and CeO_2-based catalysts exhibit unusual catalytic performance in NH_3-SCR reaction. The fact can be explained by the combination of high oxygen storage capacity of CeO_2 and very good redox ability of Fe_2O_3. Liu et al. [244] postulated that due to smaller radius of Fe, it can form solid solution with CeO_2 with the improved redox properties. However, there is a general agreement that the performance of the catalysts is strictly determined by the preparation procedure. Ma et al. [245] analyzed the influence of the synthesis method on the catalytic and physicochemical properties of FeO_x-CeO_2 mixed oxides. It was found that the highest NO conversion was obtained by the materials prepared by microemulsion method (MM) and sol-gel method (SG). The authors ascribed this effect to the highest specific surface area of the (MM) sample and enhanced redox and oxidizing properties of (SG) sample. Due to that, besides satisfactory denitration ability, the catalysts were regarded as active in direct oxidation of NH_3 to N_2O.

Side reactions during NH_3-SCR over γ-Fe_2O_3-containing catalysts were motivation to find a path to increase selectivity to N_2 and avoid unnecessary consumption of the reducing agent. For example. Yang et al. [246] declared that Fe_2O_3-TiO_2 mixed oxide shows declined redox activity of the active species and facilitates high-temperature performance. Several studies proved that Fe_2O_3-WO_3 mixed oxides exhibit very good denitration performances, especially because of structurally- and chemically-promoting impact of tungsten on iron oxide [235,247].

Except of bimetallic oxides, the catalyst can also consist of more components. The good example of multi-metal oxide catalysts was presented by Stahl et al. [248]. The authors observed synergistic effect of Fe, W, and Ce oxides as the constituents of NH_3-SCR catalyst. It was postulated that combination of Ce and W can promote dispersion of Ce^{3+} ions and improved chemisorption of oxygen during the catalytic reaction. The multi-metallic oxide Fe-W-Ce catalyst exhibited broad temperature window of 250-500 °C. Thus, after the addition of W and Ce, the activation energy decreased and NO to NO_2 oxidation was improved. Besides, the material showed satisfactory resistance to SO_2 and/or H_2O in the gas stream. After elimination of the inhibiting agents, the catalytic activity was almost totally restored.

Layered double hydroxides

The catalytic potential and physicochemical character of metal oxides depend on the preparation procedure. This fact is especially pronounced for the catalysts derived from layered double hydroxides (LDHs), known also as anionic clays. LDHs are a type of materials in which the positively charged, stacked layers are balanced by the interlayer anions. The general chemical formula of LDHs is described by **Formula (95):**

$$Me_{1-x}^{2+}\, Me_x^{3+}\, (OH)_2]^{x+} \left(A_{\frac{x}{n}}^{n-}\right) \cdot y\, H_2O \qquad \textbf{(95)}$$

where Me^{2+} corresponds to divalent metal cations (for example Mg^{2+}, Ni^{2+}, Cu^{2+}, Co^{2+}, Zn^{2+}), while Me^{3+} is attributed to trivalent metal cations (such as Al^{3+}, Mn^{3+}, Fe^{3+}, Ga^{3+}), and A^{n-} is an organic or inorganic anion (for instance Cl^-, CO_3^{2-}, NO_3^-, CH_3COO^-) [145,249]. One of the most widespread LDHs is

hydrotalcite (HT). The material reflects brucite structure, however, it exhibits positive charge due to the partial substitution of Mg^{2+} with Al^{3+}. Therefore, HT consists of edge-sharing $Mg(OH)_6$ and $Al(OH)_6$ octahedra. The positive charge of the layers, resulting from the isomorphous substitution of Mg^{2+} with Al^{3+} is balanced by anions, typically CO_3^{2-}. Calcination at high temperature transforms LDHs to the solid solution of mixed metal oxides and spinels [250,251]. Schematic structure of layered double hydroxides, on the example of hydrotalcite, is illustrated in **Figure 14.**

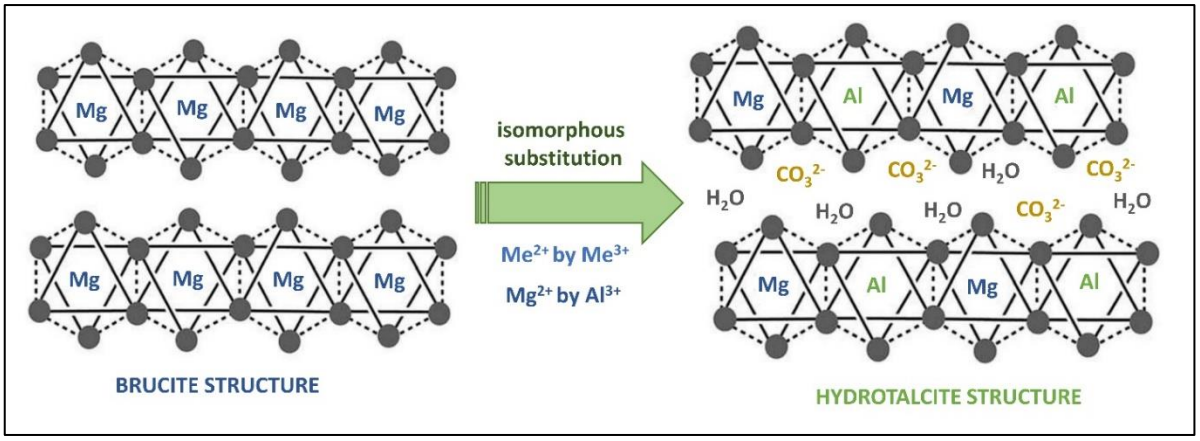

Figure 14. Schematic representation of the formation of hydrotalcite from brucite (based on [251])

Recently, LDHs have attracted a growing attention as the precursors of novel NH_3-SCR catalysts, due to three major reasons. First of all, atomic scale dispersion and reduced particle size of the active species improves catalytic activity. Secondly, the ions are mutually bounded, which results in high thermal stability. Thirdly, wide range of possible compositions of LDHs opens many new paths to prepare catalysts with the desired features. For example, Wang et al. [252] analyzed FeNi mixed oxides derived after calcination of LDHs at various temperatures (400, 500, 600 °C). It was observed that LDHs treated at 500 °C exhibited superior catalytic performance and the widest temperature window of 210-360 °C. The effect was due to the formation of well-dispersed FeO_x-NiO_x species, beneficial for low-temperature activity and $NiFe_2O_4$ phase, active in high-temperature range. Wierzbicki et al. [145] prepared Cu-Co-Mn LDHs by co-precipitation method and obtained mixed metal oxides after calcination at 500 °C. Alternatively, manganese was introduced into the LDHs precursor by ion-exchange with Mn-EDTA solution. The results indicated that both the content of Mn and the method of its introduction determined the catalytic performance, especially in the case of selectivity. It was noted that introduction of manganese by ion-exchange resulted in the formation of well-dispersed metal

cations, contributing to the low emission of N_2O. On the contrary, the sample with the highest concentration of the active phase, prepared by co-precipitation method was the most active, however, it suffered from poor selectivity to N_2.

4.4 Metal-organic frameworks

Metal-organic frameworks (MOFs) are a class of hybrid, crystalline and porous materials, which consist of metal ions (or metal-containing clusters) coordinated to organic ligands. The crystalline MOFs share some properties with zeolites, such as large internal surface area or uniform pore size. Additionally, the framework and pore structures, as well as crystallinity nature of MOFs can be easily tailored by the introduction of various metals and organic linkers [253,254]. The fascination in the application of MOFs in the number of processes is related to their advantageous structural features. High specific surface area of MOFs is usually abundant in the easily available active centers, while uniform porosity provides shape-selectivity. Besides, the co-existence of well-developed texture and homogeneous dispersion of metal ions and organic linkers enhances catalytic potential of MOFs in many reactions [254]. The preparation procedures involve mainly solvothermal, hydrothermal, or seeded-growth method, microwave irradiation, and sonication synthesis [254]. The synthesis method has a crucial impact on the morphology of MOFs. In general, the unlimited combinations of metals and organics lead to the numerous of various MOFs structures. The schematic unit cells of the selected MOFs (MOF-5, MIL-53, HKUST-1, BTC, and UiO-67) are presented in **Figure 15** [65].

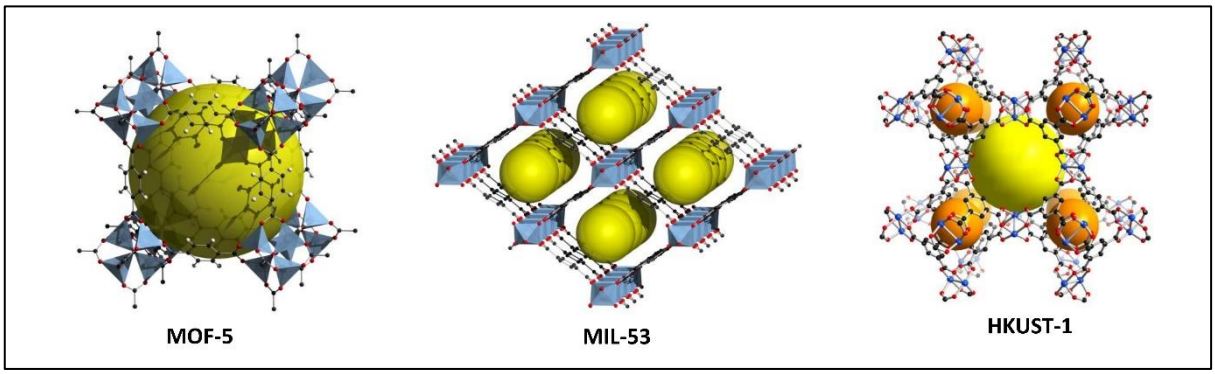

Figure 15. Structures of unit cells of selected MOFs: MOF-5, MIL-53, and HKUST-1 (yellow and orange spheres represent pore volume, oxygen atoms – red bullets, carbon atoms – black bullets, hydrogen – white bullets, metal atoms – blue bullets, tetrahedrons – functional linkers) [255–257]

Since investigations on the application of MOFs in NH_3-SCR started quite latterly, there are only few papers describing their catalytic performance in the process. Predominantly, MOFs-based NH_3-SCR catalysts can be divided into three groups: single metal MOFs (1), hybrid MOFs (2), and MOFs used as the catalyst support (3) [65]. Li et al. [258] has provided the first analysis of the catalytic performance of Cu-BTC in NH_3-SCR. The authors reported satisfactory activity of the material in NO reduction between 220-280 °C. The result was assigned to the structure abundant in unsaturated Cu sites. In spite of this result, the catalyst had low thermal stability, which affected the MOFs structure already at 300 °C. Similar results, related to the temperature window and thermal stability were obtained by Wang et al. for Cu-MOF [259]. Unsatisfactory heat resistance was a motivation for more in-depth research over more stable MOFs. Sun et al. [260] claimed that the thermal stability of Ni-MOF maintained up to 440 °C, thus, in low- and high-temperature range of NH_3-SCR. As a matter of fact, Ni-MOF exhibited almost 90% of NO conversion between 200-400 °C. However, according to the research, such result can be obtained only after thermal pre-treatment at strictly controlled conditions.

Preparation of bimetallic MOFs is more rare, comparing to single metal-MOFs. However, the presence of two active metals can provide synergistic catalytic properties. In general, introduction of more than one metal results in different features and usually, improves catalytic performance and stability. Smolders et al. [261] incorporated Ce or the mixture of Ce and Zr into the frameworks of MOFs, UiO-66, and CAU-24. Application of bimetallic active phase resulted in the formation of Zr_5Ce metal clusters, which enhanced redox properties and thermal stability. Nevertheless, the authors observed hindered re-oxidation of the prepared MOFs-based catalysts, ascribed to the lack of oxygen vacancies on their surface. Wang et al. [262] proposed that ceria nanoparticles can be encapsulated in the structure of MIL-100(Fe). According to the study, introduction of CeO_2 expanded the temperature window during NH_3-SCR to 196-300 °C. The effect was ascribed to the elevated amount of surface active oxygen, which facilitated the formation of NO_2 and promoted fast mode of NH_3-SCR.

Ultimately, MOFs were reported to be highly porous supports of NH_3-SCR catalysts. Especially, Mn-modified metal-organic frameworks attracted considerable attention [263,264]. In their 2017 study, Zhang et al. [263] compared Mn deposited on UiO-66 by wet impregnation or mechanical mixing. The investigation revealed that the former method had a beneficial influence on the distribution of

manganese sites within UiO-66 framework. It was declared stable operation of the catalyst and structure retention, even in the presence of SO_2 and H_2O. However, one should note that the authors focused only on the low-temperature range of NH_3-SCR. Sun et al. [264] investigated the potential of MIL-125(Ti) as the support for Mn in NH_3-SCR. According to their research, the unique structure of the support was beneficial for uniform dispersion of Mn^{4+} species. Additionally, it facilitated Mn^{4+}/Mn^{3+} redox cycle and hindered oxidative properties of MnO_x aggregates. Since MIL-125(Ti) doped with Mn showed around 90% of NO conversion within 175-425 °C, it seems to be one of the most promising MOFs-based catalysts of NH_3-SCR.

On the other side, MOFs-based catalysts are not deprived of some significant drawbacks that can considerably limit their application in NH_3-SCR on the industrial scale. First of all, usually, the synthesis of MOFs is expensive, especially comparing to zeolite-supported catalysts [265]. One of the biggest disadvantages of MOFs is their limited thermal stability. Harsh conditions of industrial processes, such as high temperature or the presence of poisoning agents leads to the irreversible structural destructions, migration of the metal species from the accessible surface, and rapid deactivation above 300 °C [264]. In fact, the tunable pore structure provides high specific surface area, abundance in the active sites, and size selectivity. However, the inherent microporosity of MOFs can hinder efficient mass transfer during the catalytic reaction [254]. Therefore, the present knowledge and progress in the application of MOFs in NH_3-SCR still demands more in-depth research.

5. Zeolites

5.1 Structure of zeolites

Zeolites are well-known crystalline solids that established a “gold standard” in many important industrial catalytic processes, such as separation, adsorption, and catalysis [266–268]. Up to date, 255 zeolitic framework structures, with the unique three-letters codes were accepted by the Structural Commission of the International Zeolite Association [269]. However, according to the literature, theoretically, the number of possible zeolitic frameworks is practically unlimited [270].

Zeolites are crystalline materials consisting of $[AlO_4]^{5-}$ and $[SiO_4]^{4-}$ tetrahedrons. These tetrahedrons, with Si or Al located centrally are known as the “primary building units” (PBU). The

tetrahedrons can be also arranged into larger structures, so-called “secondary building units” (SBU). The adjacent $[SiO_4]^{4-}$ and $[AlO_4]^{5-}$ tetrahedrons are bonded by oxygen atoms located in the corners [271]. Specific orientation of oxygen in the framework determines development of voids and pores, which form channels and cages between the Si- and Al-blocks, as presented in **Figure 16(a).** The type of zeolite can be determined by the pore size opening and the pores can be divided into small (8-membered ring), medium (10-membered ring), large (12-membered ring) and extra-large (>12-membered ring) [272].

The consequence of the formation of internal structure is the development of internal and external surface area. In the case when each tetrahedron of the framework contains silicon as the central atom, the overall structure is neutrally charged, as depicted in **Figure 16(b).** On the other hand, zeolite frameworks can also exhibit negative charge, due to the presence of cations of the valency lower than 4+, such as Al^{3+} or Fe^{3+}. Thus, zeolites can accommodate the compensating extra-framework cations in ion-exchange positions, for example NH_4^+, H^+, Na^+, K^+, Ca^{2+}, Mg^{2+} [273]. The schematic structure of low-silica zeolite, accommodating Na^+ cations is presented in **Figure 16(c).**

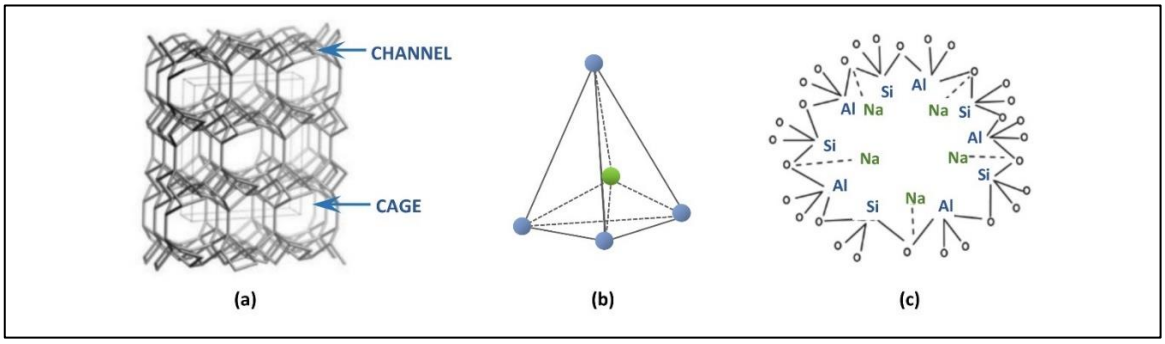

Figure 16. Typical structure of zeolite with three-dimensional cages and channels (a), three-dimensional representation of a tetrahedron with centrally located silicon or aluminium atom (c)

Considering the presence of charge-balancing metal cations and Si and Al tetrahedrons, the zeolites can be generally described by the **Formula (96)**:

$$Me_{2/n}O \cdot Al_2O_3 \cdot x\,SiO_2 \cdot y\,H_2O \qquad \textbf{(96)}$$

where *Me* is an alkaline or alkali earth atom, *n* is the charge of *Me* atom, *x* is the number of Si tetrahedrons, and *y* is the number of water molecules. Furthermore, the structure of zeolite, based on the crystal unit cell (with SiO_2 and Al_2O_3 as variables) is represented by the **Formula (97)**:

$$Me_{a/n}\ (AlO_2)_a\ (SiO_2)_b \cdot c\ H_2O \qquad \textbf{(97)}$$

where *a* and *b* are total numbers of Al and Si tetrahedra, respectively, per unit cell, while *c* is the number of water molecules per unit cell [274].

As above mentioned, zeolites can accommodate not only cations and water molecules, but also small organic compounds. The zeolitic lattice is exceptionally stable, providing almost unlimited ion-exchange properties and reversible dehydration of the structure [273]. The ions and molecules in the cages are loosely bonded. Therefore, introduction of catalytically active species into zeolites by ion-exchange is relatively easy. What is more, the presence of microporosity within the tetrahedral frameworks provides the same order of pore size as the kinetic diameters of small molecules. Thus, zeolites are called as "molecular sieves", useful in separation and filtration processes [275,276]. Shape-selectivity of zeolites is beneficial for many catalytic applications as well [203,277]. Nevertheless, taking into consideration narrow diameters of micropores, usefulness of specific zeolite in the catalytic reaction is evaluated basing on the pore size.

All in all, the unique zeolitic structure provides fascinating properties of the materials. However, the specific features of the materials are determined also by their chemical composition and may vary according to their origin. High sorption capacity depends on the void volume and size of the pore openings, while ion-exchange properties are influenced by the number and nature of exchangeable extraframework cations. Additionally, the dimension of the channel system and pore openings determine catalytic performance of specific zeolite in a catalytic reaction. Thus, although more than 250 zeolite structures have been discovered so far, less than 20 of them were commercialized. Some of the most common are BEA, CHA, FAU, FER, MFI, and MOR. Additionally, there is still a little agreement if natural of synthetic zeolites have better potential to be used on the large scale.

5.2 Acidity of zeolites

Acidity is one of the most important features of zeolites. The investigations on this feature started at the end of the 1950s and it was described in the literature in 1964, after enacting the patent for a zeolite-based catalyst of selective cracking [278].

Generally, there are two types of acidic sites: Brönsted and Lewis. The Brönsted theory assumes an acid as *a donor of proton*, while a base as *an acceptor of proton.* According to the theory, during acid-base reaction a proton is transferred to a base with the formation of so-called *conjugate base*, according to **Equation (98):**

$$A - H + B^{-} \leftrightarrow A^{-} + B - H \quad \textbf{(98)}$$

$$acid + base \leftrightarrow conjugate\ base + acid$$

More comprehensive theory on the acidic properties of substances was proposed by Lewis, who postulated that any compound with a vacant orbital, able to accept a pair of electrons, can be classified as an acid. On the contrary, a base has an unshared pair of electrons. In line with Lewis theory, acid-base reaction involves formation of the covalent bond between the electron pair of base and the vacant orbital of acid, according to **Equation (99)** (the upper band represents an electron pair):

$$A + \bar{B} \leftrightarrow AB \quad \textbf{(99)}$$

Therefore, it can be concluded that a Brönsted acid is not a Lewis acid, since the accepted proton from Brönsted acid bonds to the base, releasing basic species. However, a Brönsted base is also a Lewis base, due to its capability to donate unshared electron pair to a proton [279]. Some of the possible acid sites on the surface of zeolites are showed in **Figure 17.**

Considering the presence of SiO_4 and AlO_4 tetrahedra and charge-balancing cations, the presence of acid sites in zeolites can be explained as it follows:

- proton, as a charge-balancing cation binds itself to bridge oxygen connected to Al and forms hydroxyl group (OH^-), acting as a *proton donor*, thus Brönsted acid site,
- compensation cations and extraframework Al atoms with at least one free valence, such as $Al(OH)^{2+}$, $Al(OH)_2^{+}$, AlO^{+}, $(Al_2O_2OH)^{+}$, $(Al_2O)^{4+}$, AlOOH, or $Al(OH)_3$ can act as *acceptors of the electron pair*, thus Lewis acid site [279].

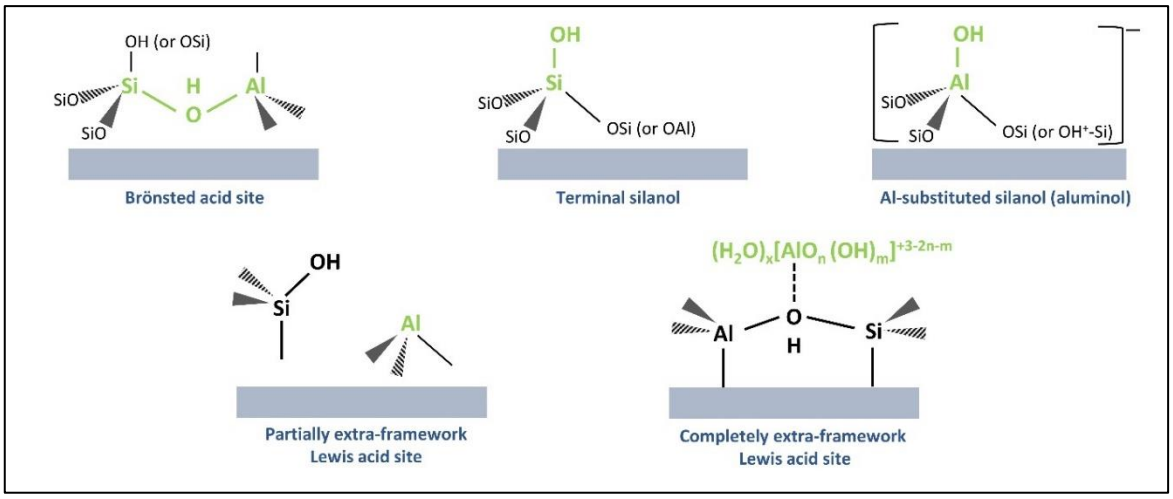

Figure 17. Schematic representation of the selected possible acid sites present in zeolites (based on [277])

Additionally, new Brönsted and Lewis acid sites in zeolites can be also generated, according to various methods listed in **Table 3.** One should note that introduction of Lewis acid sites usually affects the amount of Brönsted sites, for example during mild steaming of zeolite.

Table 3. Possible methods to generate Brönsted and Lewis acid sites in zeolites [279]

Generation of Brönsted acid sites	**Generation of Lewis acid sites**
(1) ion-exchange of H^+ with charge-balancing metal cation	(1) dehydration at high temperature
(2) ion-exchange of NH_4^+ with charge-balancing metal cation followed by calcination	(2) mild steaming with the dislodge of Al from regular framework positions
(3) reduction of metal cations to lower oxidation state, generating surface protons	
(4) ion-exchange with polyvalent cations, which generate protons through partial hydrolysis of water molecules	

Crystalline nature of zeolites facilitates dispersion of acid sites, which are especially strong in high-silica variants (Si/Al > 10) [280]. Typically, zeolites possess both Brönsted and Lewis acidity and sometimes their identification is complicated. It is caused mainly by their interconversion, for example by dihydroxylation of Brönsted site, leading to the formation of Lewis site, involving Si and Al in three-fold coordination [279]. Both types of acid centers can be located inside the pores or on the external surface of a zeolite [281]. Practically, Brönsted acid sites are easier to determine, comparing to Lewis

centers. Typically, a comprehensive characterization of acidic properties of zeolites can be performed using three procedures:

- spectroscopic techniques (FT-IR, ^{1}H or ^{27}Al MAS-NMR) – evaluation of the strength of O-H bonds in hydroxyl groups,
- calorimetry, temperature programmed desorption – quantification of the interaction between basic probe molecules and the acid site,
- catalytic test reactions, which require specific strength and density of acid sites [277,279].

However, none of the above mentioned techniques is able to provide information about the strength, number, density and accessibility of the active sites itself. Currently, only combination of various methods allows to characterize acidic features of zeolites in detail.

5.3 Natural zeolites

Natural zeolites are formed at relatively low temperature, in many kinds of geological environments, such as lake sediments, alkaline deserts, ash ponds, or marine sediments. The minerals can be also generated over the years, as crystals in small cavities of metamorphic rocks, or as volcanic glass or tuffs, altered by the reactions with saline waters. In 1950s, it was discovered that zeolitic crystals deposited in volcanic tuffs are filled with water, which can be easily removed by heating. Furthermore, the dehydrated crystals possessed the structure of honeycombs, consisting of 2-10 Å pores, of the order of few atoms [273]. The general formula of natural zeolites is depicted by the **formula (100):**

$$(Li, Na, K)_p\ (Mg, Ca, Sr, Ba)_q\ [Al_{(p+2q)}Si_{n-(p+2q)}O_{2n} \cdot m\ H_2O \qquad \textbf{(100)}$$

where p is the number of monovalent metal ions, q is the number of divalent metal ions, n is the half of the number of oxygen atoms and m is the number of water molecules [282].

Natural zeolite-rich rocks, which contain more than 50% of the pure zeolitic phase are usually used on industrial scale. Price of the materials depends on the content of pristine zeolite in the rock and its physicochemical properties, such as particle size, specific surface area, or surface character. Besides, natural zeolites can also contain catalytically active species or chemical character desired for the specific process [274,283]. The U.S. Geological Survey reported in 2021 that the price of zeolite-rich rocks per

ton was in range of $50-$300 in the last five years, while the world production of natural zeolites in 2020 was estimated to ca. 1.1 million tons [284]. Among natural zeolites, clinoptilolite and chabazite are among the most widely used, especially for water treatment or agricultural applications [285].

Despite the number of advantages of natural zeolites, the materials are not deprived of some drawbacks. One of the major downsides is contamination, commonly present in the zeolite-rich rocks. In some cases, it is almost impossible to remove the admixtures of other minerals and completely isolate pure zeolitic phase from the deposit. Moreover, the type of contamination depends on the source and origin of the parent rock. Thus, it is hard to determine accurate composition of the isolated zeolite. Besides, the presence of quartz or amorphous glass precludes application of naturally-derived zeolites in the processes which require purity and uniformity of the materials [282].

Information about zeolite origin and framework type is sufficient to determine its structural and chemical properties, which have a direct impact on its characteristics. In order to systematize the natural zeolite minerals, they have been classified into families. The examples of the natural zeolite frameworks and their visualizations are presented in **Table 4** and **Figure 18,** respectively.

Table 4. Selected industrially important natural zeolites and their structural parameters [269]

Zeolite family	**Chemical formula**	**Accessible volume (%)**	**Idealized cell data (Å)**	**Channel dimensions (Å)**
Chabazite **(CHA)**	$\lvert Ca_6(H_2O)_{40}\rvert_{1/3}$ $[Al_{12}Si_{24}O_{72}]_{1/3}$	17.27	**Trigonal;** a = 13.7 c = 14.8	3.8 × 3.8
Faujasite **(FAU)**	$\lvert (Ca, Mg, Na_2)_{29}(H_2O)_{240}\rvert$ $[Al_{58}Si_{134}O_{384}]$	27.42	**Cubic;** a = 24.3	7.4 × 7.4
Heulandite **(HEU)**	$\lvert Ca_4(H_2O)_{24}\rvert[Al_8Si_{28}O_{72}]$	9.42	**Monoclinic;** a = 13.7 b = 17.6 c = 14.8	3.1 × 7.5 3.6 × 4.6 2.8 × 4.7
Mordenite **(MOR)**	$\lvert Na_8(H_2O)_{24}\rvert[Al_8Si_{40}O_{96}]$	12.27	**Orthorhombic;** a = 18.8 b = 20.5 c = 7.5	6.5 × 7.0 2.6 × 5.7

Phillipsite **(PHI)**	$\lvert K_4(Ca, Na_2)_4\ H_2O)_{24}\rvert_{1/2}$ $[Al_{12}Si_{20}O_{64}]_{1/2}$	9.89	**Orthorhombic;** a = 9.9 b = 14.1 c = 14.0	3.8 × 3.8 3.0 × 4.3 3.2 × 3.3

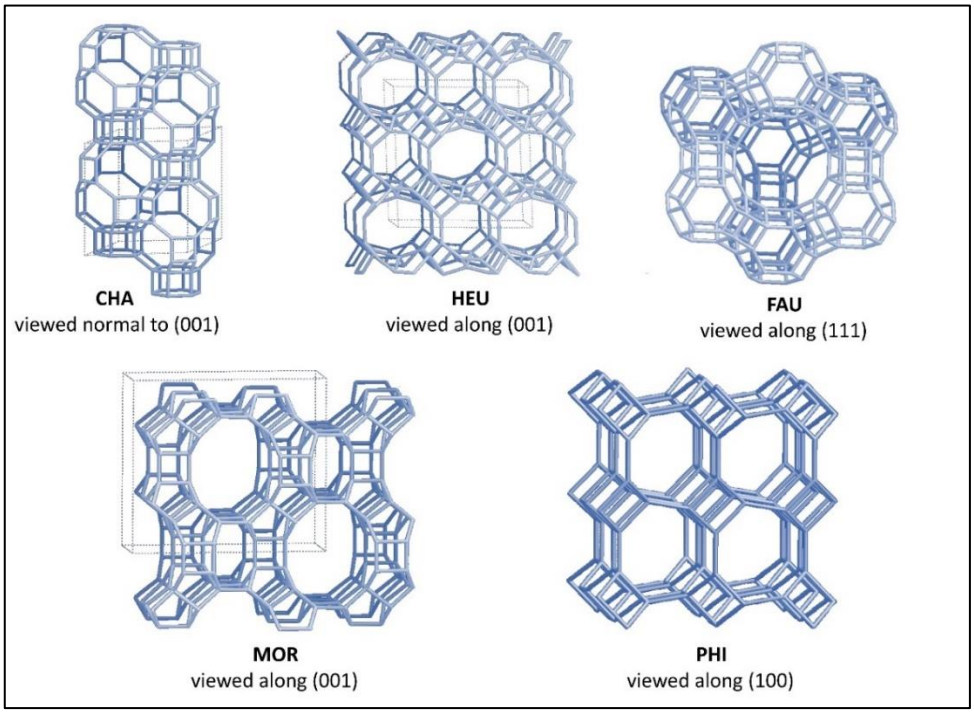

Figure 18. Schematic visualization of selected frameworks of natural zeolites [269]

5.4 Clinoptilolite as the representative of natural zeolites

The outstanding and unique properties of natural zeolites make them very useful materials in the number of industrial and environmental applications. One of the representatives of this group is clinoptilolite (CL), belonging to the heulandite (HEU) class of zeolites [286]. It is estimated that more than 90% of the world's production of zeolites is clinoptilolite. Both heulandite and clinoptilolite are three-dimensional zeolites, exhibiting microporosity and containing water molecules and cations in ion-exchange positions [287]. X-ray diffraction (XRD) analysis indicated that the unit cell parameters of CL and HEU are very similar [287]. HEU-type framework consists of the $T_{10}O_{20}$ SBU, illustrated schematically in **Figure 19.** The SBU are connected and form long chains along (102) plane. The (102) chains are laterally linked and generate dense (010) silicate layers. The parallel layers are joined and form two-dimensional structure with three systems of channels: tetrahedron, 10-MR, 8-MR along (001), and 8-MR along (100), with the extraframework population and pores of approximately 7 Å [288].

Heulandite series were divided by the Subcommittee on Zeolites of the International Mineralogical Association into species based on the dominant cation present in the channel. Thus, HEU-Ca, HEU-Na, HEU-K, HEU-Sr, and HEU-Ba can be distinguished and their occurrence depends on the environmental conditions [286].

One should note that although CL and HEU have isomorphic framework structure, their chemical formula is different: $(Na, K, Ca_{0.5})_{10}$ $(Al_{10}Si_{26}O_{72}) \cdot 24\ H_2O$ (with Si/Al ca. 2.6) for HEU and $(Na, K, Ca_{0.5})_{5.4}$ $(Al_{5.4}Si_{30.6}O_{72}) \cdot 20\ H_2O$ (with Si/Al ca. 5.7) for CL. Besides, the molar ratio of Si to Al is < 4 for heulandite, while clinoptilolite exhibits Si/Al > 4. Since the materials exhibit various Si/Al ratio and the content of different ions, the spectroscopic properties and unit-cell parameters of the materials are not identical [286,289]. Besides, clinoptilolite and heulandite show different thermal stability. It was observed, that the structure of CL was not destroyed even after 12 h-lasting heating at 750 °C, while the phase transitions of heulandite takes place already at 250-300 °C [290]. Due to the fact that thermal stability is a crucial factor, which decides about industrial applications of the materials, clinoptilolite seems to be much more attractive candidate for the commercial use, comparing to heulandite.

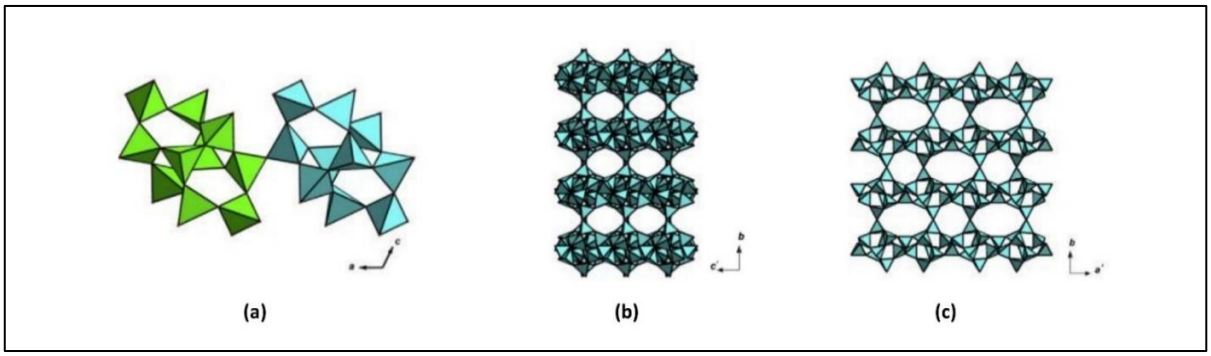

Figure 19. Characteristic for heulandite, two corner-sharing $T_{10}H_{20}$ units (a) and HEU-type framework viewed down: (100) (b) and (001) (c) (reproduced basing on [286])

Clinoptilolite (CL) is among the most abundant zeolites occurring in nature, especially in altered volcanic tuffs and saline or in alkaline-lake deposits [291]. On the average, parent rocks contain around 50-80% of the clinoptilolite phase [289,292]. Clinoptilolite can be found in various areas around the world, for example in China, Iran, Ukraine, Slovakia, Greece, Russia, New Zealand, Argentina, Colombia, and the United States. Thus, chemical composition of clinoptilolite is correlated with its origin, as presented in **Table 5.**

Table 5. Chemical composition (wt.%) of selected clinoptilolite fractions derived from various regions of the world

Origin	SiO_2	Al_2O_3	CaO	K_2O	Na_2O	Fe_2O_3	MgO	LOI*	Reference
Australia	68.26	12.99	1.37	4.11	0.64	1.37	0.83	10.43	[293]
China	75.71	13.66	0.33	1.70	6.82	1.11	0.58	0.09	[294]
Colombia	63.31	14.90	5.48	1.98	-	4.51	1.30	8.52	[295]
Iran	68.17	11.05	3.93	1.11	0.64	0.53	0.62	13.95	[287]
Greece	68.25	13.19	0.76	1.66	4.12	1.41	1.14	9.47	[296]
Slovakia	64.97	9.88	1.39	2.93	2.49	1.44	0.32	16.58	[297]
Ukraine	67.29	12.32	3.01	2.76	0.66	1.26	0.29	12.41	[298]
United States	76.18	13.66	0.31	1.65	6.52	1.12	0.54	0.02	[294]

*LOI – loss of ignition

Natural clinoptilolite is present in a form of microscopic crystals of 2-20 μm in size and its network consists of all kinds of pore sizes. The primary porosity of CL is determined by the cavities and channels, while the secondary porosity results from meso- and macropores [289]. Formation of mesopores in clinoptilolite is due to the splitting of CL crystallites, while macroporosity is generated by the voids between the crystals and various grains of minerals present in the parent rock [299]. Mesoporosity of clinoptilolite is especially attractive for practical applications, since it provides transporting channels, active sites for catalytic reactions, and adsorption centers for larger molecules. The illustration of clinoptilolite framework with the polyhedrons and the channel systems are presented in **Figure 20.**

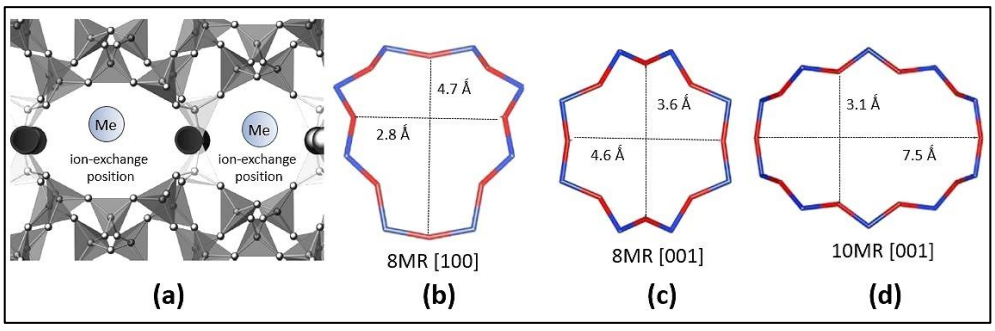

Figure 20. Schematic framework of clinoptilolite (a) and its channels: 8-member rings (b) and (c), 10-member rings (d) (based on [289,300])

From the following considerations, it can be concluded that porous structure of clinoptilolite exhibits heterogeneous nature. On the basis of N_2 adsorption-desorption measurements at 77 K, Mansouri et al. [287] suggested that clinoptilolite contains mainly microporosity represented by nanotubic system. In the mesoporous range, the authors detected slot pores of ca. 2.3 nm. Similarly to the chemical composition, the specific surface area of clinoptilolite depends on the origin and formation conditions. For the natural, non-modified zeolite it oscillates around 14-30 $m^2 \cdot g^{-1}$ [296,298]. As already mentioned, one of the most important features of clinoptilolite, which provides an opportunity of its application in many industrially important processes is high thermal stability. Apart from that, the resistance of the zeolite to mechanical crush is above 7 MPa [300]. Besides, high ion-exchange capacity of CL not only enables to use the material in the elimination of toxic compounds, but also allows to introduce active species while the zeolite is used as a support of a catalyst. Another great advantage of clinoptilolite is its high acidity, desired in many reactions. Therefore, clinoptilolite was recognized as an advantageous support for the catalysts of p-nitrophenol hydrogenation [301], synthesis of acetylsalicylic acid [289], or as an adsorbent for the elimination of radioactive compounds [300,302].

Although clinoptilolite exhibits attractive structural properties, in the majority of cases its satisfactory performance in adsorption and catalytic depends on the initial modifications. Commonly, CL is pretreated with acid, base, or surfactants [303]. The pretreatment procedures are usually applied to dissolve some natural contamination and enhance the physicochemical properties or to remove pore-blocking impurities. As a result, the zeolite is more useful for the purification processes, due to the increased specific surface area and improved pore size distribution. The substitutive name of acid or base treatment is “activation”, since interaction between the aluminosilicate surface and the solution of the certain chemical character results in the generation of new centers, useful in specific process. For instance, pretreatment with acid was confirmed not only to enhance textural properties of zeolite, but also to decrease the content of Al [304]. Besides, the controlled dealumination of clinoptilolite generates new sub-micropores (with the diameter of 0.7-2 nm) and mesopores [305]. On the contrary, modification with alkaline medium results in the preferential extraction of Si from the zeolitic framework, hence, increase of aluminum content and the acidic character [306]. Kussainova et al. [307] investigated the efficiency of Pb^{2+} adsorption on the raw and acid-modified clinoptilolite. The authors reported that after

pretreatment with 85% phosphoric acid (H_3PO_4), ions such as K^+, Ca^{2+}, Mg^{2+}, and Al^{3+} were exchanged with H^+ cations and OH^- groups. Thus, acidic character of the material was significantly improved. Additionally, it was observed that the size of voids and channels and the specific surface area increased after modification with H_3PO_4, which enhanced molecular sieve properties of the zeolite and its adsorption capacity. Castro de Souza and co-workers [304] used NaOH for the pretreatment of clinoptilolite under various conditions, with regard to time of contact, temperature and concentration of the sodium hydroxide solution. The authors found that the modification with NaOH only slightly changed the specific surface area of clinoptilolite, however, it increased the secondary mesoporosity in the selected samples. Additionally, too high concentration of the alkaline solution can lead to the decreased crystallinity or even total collapse of the zeolitic framework. According to the literature, apart from acids and bases, clinoptilolite can be modified with salts. However, according to Stocker et al. [308] in contrast to NaCl, both HCl and NaOH significantly influenced Si/Al molar ratio and increased the specific surface area of the material.

Alternative method to change the properties of natural zeolites, which brings about much less structural damages and crystallinity loses is ammonium exchange-calcination procedure. The aim of the method is to transform zeolite into NH_4^+- form at mildly acidic conditions. Thermal treatment of the ammonium-zeolite at around 450-500 °C results in the decomposition of NH_4^+ groups and formation of the protonated zeolite of acidic character [306]. Clinoptilolite modified by ammonium exchange-calcination method was confirmed to be an effective catalyst of selective catalytic reduction with propane [309] or ammonia [295] and cracking of oilsands bitumen [310].

Except of the treatment with inorganic substances, clinoptilolite can be modified with organic compounds, including cationic surfactants [311] or polymers [312]. Generally, this kind of modification forms bilayer-like structure, which alters the charge of zeolitic surface from negative to positive. Therefore, adsorption of anions is provided by the positive charge, while non-polar organic compounds can be sorbed by the organic-rich layer [313]. One of the most commonly used organic agents for clinoptilolite modification is hexadecyltrimethylammonium ion (HDTMA) [292]. It was found that surfactant-modified clinoptilolite effectively removes chromate, nitrite, selenite, or sulfate anions. Besides, the framework of these materials remain stable even at extreme values of pH [313,314]. Except

of HDTMA, other surfactants, such as *N*-cetylpyridinium or cetyltrimethylammonium ion (CTMA) were used as modifying agents of clinoptilolite [303]. The advantageous alternative of surfactants to broaden the practical applications of clinoptilolite are polymers, such as polyethylenimine [315], polyaniline [316], polypyrrole [317], or chitostan [312]. It was confirmed, that the coexistence of multiple-functional polymeric groups and clinoptilolite in such materials facilitates removal of dyes from aqueous solutions, improves adsorption capacity of radioactive species, and elimination of heavy metal cations from wastewater [292].

Taken together, physicochemical parameters of natural clinoptilolite which determine its potential to be used on an industrial scale are correlated both with its origin and with the performed modifications. The selected commercial applications of natural clinoptilolite pretreated by various methods are summarized in **Table 6.**

Table 6 Exemplary application of modified clinoptilolite in the environmentally significant processes

Process	**Form of clinoptilolite/modification method**	**Reference**
Photodegradation of oil refinery wastewater treatment	nanoparticles of SnS_2-ZnS/clinoptilolite composite	[318]
Removal of Cu^{2+}, Cr^{3+}, Fe^{3+}, from wastewater from graphic industry	non-modified	[319]
Removal of Ni^{2+} from water solutions	micro- or nanopowders modified with dimethylglyoxime	[320]
Removal of Pb^{2+} from acidic medium	non-modified acid-activated	[307]
Removal of NH_4^+ ions from water solutions	activated in alkali media, homogenized under ultrasonic irradiation, reduced in the extract of green tea	[321]
	non-modified	[322]
Removal of radioactive compounds	non-modified	[323]
Electrochemical sensor of amitriptyline detection in wastewater	Fe^{3+}-exchanged clinoptilolite mixed with graphite and casted on the surface of glassy carbon electrode	[324]
Drug delivery	surfactant-modified	[325]

Detoxification of the organisms	surfactant-modified	[326]
Selective catalytic reduction of NO_x with hydrocarbons	H-clinoptilolite clinoptilolite modified with Mn_xO_y nanoparticles	[309] [111]
Selective catalytic reduction of NO_x with ammonia	Fe^{3+}-modified clinoptilolite	[295,327,328]

5.5 Synthetic zeolites

In contrast to the majority of natural zeolites, synthetic zeolites possess uniform chemical composition, highly crystal lattice structure, and determined pore size. One of the great advantages of synthetic zeolites over natural zeolites is that their properties can be adapted on the synthesis level. The first known synthetic zeolite, Levynite, was obtained in 1862 by Charles Sainte-Claire de Ville [329]. Since then, the attention of scientists was directed not only to the synthesis of the analogues of natural zeolites, but also to the development of new zeolitic phases, characterized by various structures and chemical compositions. Nowadays, the number of methods are used for the preparation of zeolites, for example:

- hydrothermal synthesis (at normal or higher pressure) [330],
- fusion method [331],
- alkali activation [332],
- microwave-assisted synthesis [333].

Among the above mentioned, hydrothermal synthesis is the most commonly used, since it reflects the natural conditions of zeolites formation. In general, the method is conducted in the temperature range of 80-350 °C, it requires Si and Al precursors, and alkaline solution of pH > 8.5. As prepared synthesis pot is transported to autoclaves and aged for the certain time. Aging involves a series of physicochemical changes of the mixture of precursors, such as dissolution, condensation, gelatinization, and finally, crystallization [334]. Type of the formed zeolitic framework is determined by the following factors:

- synthesis temperature,
- pressure,

- concentration of the reagents in the synthesis pot,
- chemical character of the synthesis pot (pH),
- activation process,
- application of organic templates,
- time of ageing,
- content of Si and Al in the slurry of their precursors [273].

Strict control of these factors enables to obtain well-known zeolitic phases. It was reported that high temperature and elevated pressure results in the formation of the mixture of analcime, zeolite P, and hydroxysodalite in various proportions. The phases formed below 100 °C involve mainly zeolite X, while high proportion of Al (Si/Al < 1) in the synthesis pot yields zeolite A. What is more, temperature has a crucial influence on the crystal size. In general, at lower temperature, smaller and not fully developed crystals are formed. Porosity of the synthetic zeolites can be regulated by the addition of organic templates, which act as structure directing agents. Removal of organic molecules during thermal treatment generates the desired shape of framework and opened zeolitic structure [334,335].

Another very important factor is the molar ratio of silica to alumina in zeolites (Si/Al). The increase of Si/Al (from 0.5 to infinity) induces significant changes of other parameters, for example it improves the resistance to acids, thermal stability, and hydrophobicity. However, other features, such as hydrophilicity, cation concentration, and density of the acidic sites declines with the increasing Si/Al parameter. In relation to the content of Si, zeolites can be classified as:

- "high silica" with Si/Al molar ratio higher than 10,
- "intermediate silica" with Si/Al molar ratio between 1.5 and 10,
- "low silica" with Si/Al molar ratio of approximately 1 [274].

Normally, according to the rule of Loewenstein, the amount of $[SiO_4]^{4-}$ tetrahedra in the zeolite structure should be lower than $[AlO_4]^{5-}$ [271]. Additionally, in some of the zeolitic frameworks, Al can be isomorphously substituted by other elements, for instance Ti, Zr, or B. There are also purely silicious zeolites (Si/Al = ∞) [336].

Preparation of zeolites requires the substrates of high purity, special equipment, and high temperature. Moreover, synthetic zeolites are usually suitable for the certain commercial end users. Therefore, in this case, the production cost is considerably higher than the processing of their natural counterparts [334]. Thus, the worldwide value of the sale of synthetic zeolites oscillates around tens of billions of dollars [337].

Due to the high expenses of zeolites production, currently, the research is focused on the development of methods in which low-cost substrates can be used to obtained the desired products. Additionally, some of the novel ideas involve the replacement of pure chemicals by the natural silica sources, such as kaoline, haloisite, perlite, or pumice [334]. Alternatively, over the last years the focus has shifted to the recycling of waste materials. For example, in their 2021 review paper, Szerement et al. [271] offered a comprehensive overview of the contemporary applications of zeolites produced from fly ash in agriculture and environmental protection. On the whole, over 15 types of zeolite framework types can be synthesized from the coal fly ash. The type of the obtained framework is strongly correlated with the chemical and mineralogical composition of the fly ash. Additionally, one of the most valuable zeolite, ZSM-5 can be obtained from rice husk ash or municipal solid waste incineration [303]. It was reported that clay minerals can be easily dissolved in alkaline solutions and form zeolite frameworks [303]. Furthermore, García-Villén et al. [330] postulated that zeolites can be successfully produced from sanitary ware waste by hydrothermal method. The authors observed that formation of various zeolitic phases was correlated with time and temperature of the synthesis. The assemblage of the minerals produced at 100 °C included mainly zeolite P, Na-Faujasite, and sodalite, while natrolite and zeolite A were metastable phases, detected only for the synthesis pots aged for a longer time. For higher aging temperatures (150 and 200 °C) analcime and cancrinite were crystallized. Therefore, one of the limitations of the production of zeolites from wastes is their uncertain initial composition and the form of the final product. In fact, the use of waste materials is in agreement with the assumptions of circular economy, thus, seems to be an effective way to reduce the landfills size. However, one should note that wastes can contain some toxic elements, which limit their application in industry, especially in environmental processes [274].

Despite some disadvantages related to the price of synthetic zeolites, they are much more advantageous, comparing to the natural ones. It was confirmed that the adsorption capacity of zeolites A and X for the removal of heavy metal ions (for example Zn^{2+} or Cd^{2+}) is significantly higher than that of natural clinoptilolite [338]. Another superiority of synthetic zeolites are wider pores, which allow the adsorption of larger molecules and prevent pore blockage during catalytic reactions [335]. Moreover, chemical properties of synthetic zeolites can be easily controlled by the optimization of the Si/Al molar ratio. For example, low Si/Al value results in high polarity, sorption capacity, and acidic character [339]. On the contrary, highly-siliceous zeolites are preferred for reactions with a risk of water poisoning [334].

The commercial, laboratory-scale synthesis of zeolites from pure chemicals started in 1954 from the production of Linde "A" zeolite. The extensive research over the preparation procedure of synthetic zeolites resulted in obtaining polymorphic, large-pore and high-silica zeolite beta by G. T. Kerr and co-workers in the laboratories of Mobil Oil Corporation in 1967. It was demonstrated that zeolite beta can be used as an effective support of the catalysts of many important industrial processes, such as cracking, hydrocracking, isomerisation, or biomass conversion [340]. Since Si/Al molar ratio of zeolite beta was about three times of that of natural mordenite, the further investigations were focused on the development of novel, highly silicious materials [269]. The intensive investigations resulted in the reveal of numerous types of zeolitic frameworks denoted by the International Zeolite Association (IZA). Schematic frameworks of the selected synthetic zeolites are presented in **Figure 21,** while the examples of their possible commercial application are listed in **Table 7.**

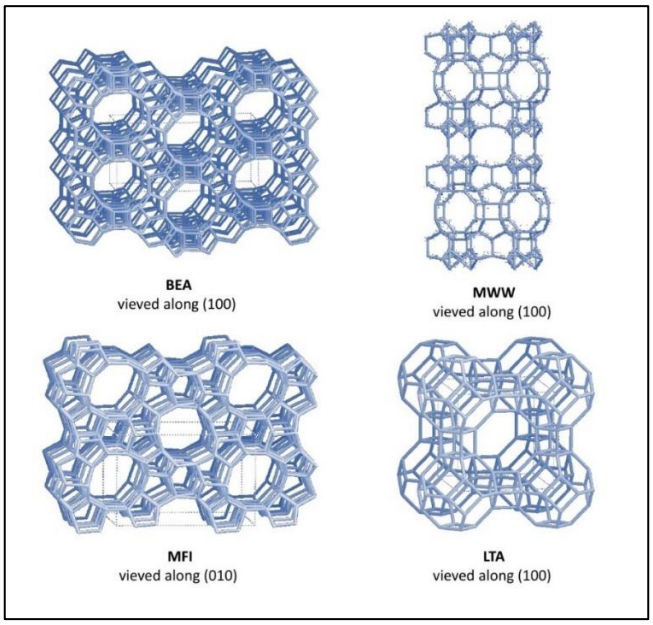

Figure 21. Schematic visualization of selected frameworks of synthetic zeolites [269]

Table 7. Selected types of synthetic zeolites and their possible commercial applications

Zeolite family	**Possible commercial application**	**References**
Zeolite beta **(BEA)**	alkylation reactions NH_3-SCR reaction	[341] [342]
SSZ-13 **(CHA)**	oxidation reactions (e.g. CO or NH_3) N_2O decomposition NH_3-SCR reaction	[343] [344] [345], [346]
SAPO-34 **(CHA)**	production of light olefins N_2O decomposition NH_3-SCR reaction	[347] [344] [348]
MCM-22 **(MWW)**	catalytic cracking dehydration reactions NH_3-SCR reaction	[349] [350,351] [352,353]
MCM-36 **(MWW)**	methanol oxidation dehydration reactions NH_3-SCR reaction	[354] [351] [353,355]
ITQ-2 **(MWW)**	methanol-to-olefin conversion removal of elemental mercury from exhausts NH_3-SCR reaction	[356] [357] [353]

ZSM-5 **(MFI)**	catalytic cracking aromatization reactions NH_3-SCR reaction	[358,359] [360] [361,362]
Zeolite A **(LTA)**	oxidation of methanol NH_3-SCR reaction	[363] [364,365]
Zeolite X **(FAU)**	CO_2 methanation purification of biogas	[366] [367]

5.6 Layered zeolites of MWW topology as the representatives of synthetic zeolites

Zeolites characterized by various types of frameworks belong currently to the major sources of innovations and breakthroughs in sorption and catalysis. The porous structures of these materials can be realized in two (2D zeolites) or three (3D zeolites) dimensions. The representative form of the group of 2D zeolites is MWW (**M**obil-t**W**enty-t**W**o) family.

The materials of MWW group are classified as zeolites, but they exhibit some unconventional physicochemical properties. Normally, zeolites are purely microporous, thus, their application in many catalytic reactions including bulk molecules is limited. First of all, both the access to the active centers and diffusion through narrow zeolitic channels is hindered. Secondly, even if the product of the reaction is formed, its residence time is increased due to the limited space for escape from the zeolite channel. Therefore, the molecules undergo secondary reactions or form deposits, deactivating the catalyst. On the contrary, MWW materials combine microporosity, characteristic for zeolites, and mesoporosity formed by pillaring or delamination. Due to that, they are categorized as hierarchical materials with superior structural features. In 2009, Perez-Ramirez et al. [368] introduced a concept of *hierarchical factor* (HF) and defined it as "the product of the relative micropore volume (V_{micro}/V_{total}) and the relative mesopore surface area (S_{meso}/S_{BET})". According to this definition, HF increases with the increasing mesopore surface area, without altering the volume of micropores. In general, layered zeolites are characterized by high values of HF, which is beneficial for many catalytic reactions. Thus, the increased mesopore volume and total surface area of MWW zeolites provide good access to the active centers.

Discovery of 2D zeolites is related to the synthesis of a framework related to MCM-22 zeolite with medium size of pores and internal supercages [369]. Furthermore, by adjusting the synthesis

conditions, it is possible to obtain 3D layered zeolites or 2D precursors. The former procedure results in the formation of 3D zeolite, MCM-49. Interruption of the crystallization of MCM-49 implies formation of MCM-56 phase with disordered agglomeration of MWW layers. On the contrary, the latter pathway involves synthesis of two-dimensional MCM-22 (P), which is the precursor used to prepare other MWW materials [370].

2D layered precursor MCM-22 (P)

MCM-22 (P) can be obtained by hydrothermal treatment of aluminosilicate gel of the desired composition, containing hexamethyleneimine (HMI) as the structure-directing agent. The synthesis is typically carried out in alkaline medium, with Na^+ used as the charge balancing cation. Highly crystalline precursor can be obtained for Si/Al between 15 and 17. While Si/Al in the synthesis pot exceeds the value of 70, MFI phase impurities can be formed. Hydrothermal crystallization proceeds at 135-150 °C and usually lasts 7-12 days (depending on Si/Al) [371]. Normally, the synthesis pot is aged in agitation conditions, since static crystallization results in the simultaneous formation of FER or MOR phases [372]. MCM-22 (P) consists of ordered, parallel zeolitic MWW monolayers of 2.5 nm thickness, disposed perpendicularly to axis *c*. The structure contains 2D 10-MR pore system, defined as "intralayer" with 5.5 × 4.0 Å sinusoidal channels. The intralayer channels in the precursor can be diagnosed in XRD pattern by the presence of (002) reflection, as presented in **Figure 22** [335,373,374].

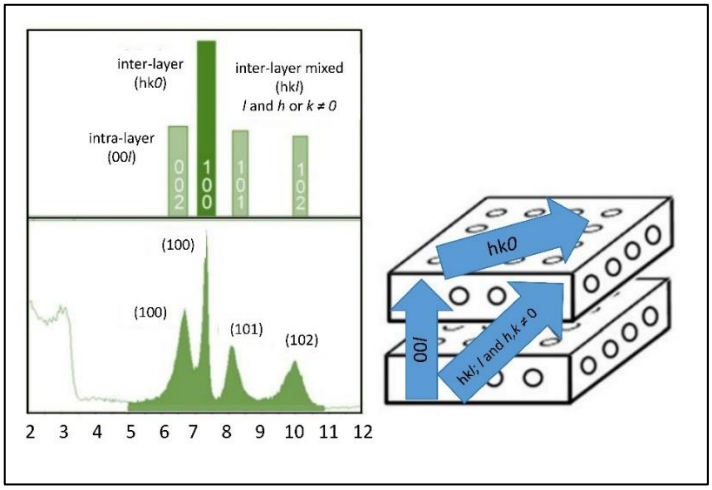

Figure 22. XRD pattern of the diagnostic region of MCM-22 (P) with the (002) reflection (based on [374])

Since the sheets are only electrostatically bonded by weak Van der Waals forces, it is possible to design various opened structures from only one precursor [375]. The topology of MCM-22 (P) is schematically illustrated in **Figure 23.**

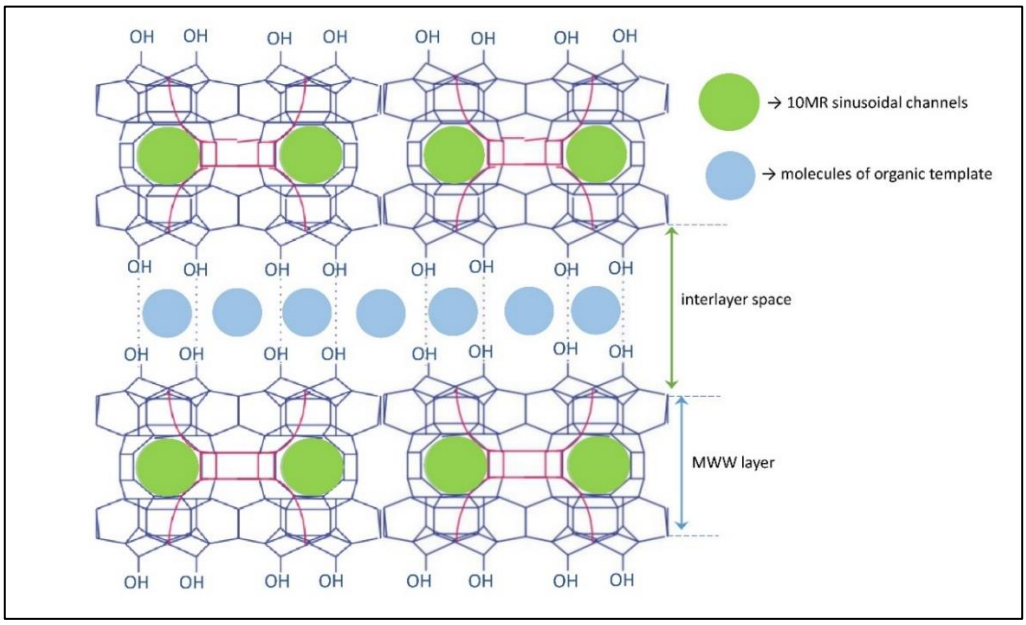

Figure 23. Schematic illustration of the topology of MCM-22 (P) (based on [335])

3D layered zeolite MCM-22

The first zeolite produced from the layered precursor was 3-dimensional MCM-22 [369,376]. Formation of the 3D framework of MCM-22 results from covalent condensation of the adjacent silanol groups (Si-OH) during thermal decomposition of the organic template. The collapse of the layers generates interlayer 12 MR pore system, with the windows of 5.1 × 4.0 Å, connecting large supercages of 18.2 × 7.1 Å [377]. Two independent pore systems of MCM-22 zeolite are presented in **Figure 24.**

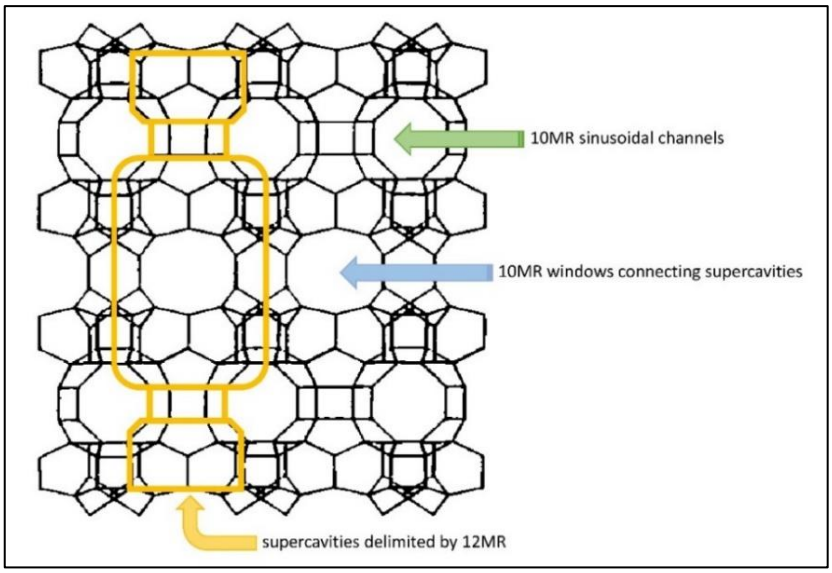

Figure 24. Schematic illustration of two independent pore systems of MCM-22 (based on [369])

Calcination of the precursor significantly changes physicochemical parameters of the material. First of all, condensation of 2D to 3D decreases the value of *c* cell parameter, form ca. 26.7 to 25.1 Å. Due to that, diffraction maxima with Miller index $l \neq 0$ and the (002) reflection move to higher range of 2θ. Additionally, calcination causes partial removal of aluminum from the framework. Thus, MCM-22 usually exhibits strongly acidic character, induced by the remaining hydroxyl groups [376]. Therefore, the material has been recognized as a promising catalyst for many important processes, such as Fischer-Tropsch synthesis [378], Friedel-Crafts alkylation of benzene [379], oxidation of organic compounds [380], dehydration of alcohols [351], or the capture of elemental mercury from the flue gas [381,382]. Additionally, recent studies on MCM-22 proved that modification with transition metals can considerably enhance its catalytic performance in NH_3-SCR [352,353] or HC-SCR [383].

Apart from MCM-22, other materials derived from 2D layered precursor have been intensively studied and described in the literature. The representatives of this group are MCM-36 (pillared zeolite), and ITQ-2 (swollen and delaminated precursor) [335,384]. The advantageous accessibility of the external surface resulted in the growing interest in the pillared and delaminated MWW zeolites.

Pillared layered zeolite MCM-36

MCM-36 is the first intercalated (pillared) zeolite, exhibiting both micro- and mesoporosity. The first step to prepare MCM-36 is swelling of MCM-22 (P) by the cationic exchange of the organic

surfactant molecules (typically $C_{16}TMA^{+}OH^{-}$), introduced into the interlayer space. Swelling process is determined by some important factors, especially chemical character of the solution. Positive result of swelling is obtained if pH of 10-13 is maintained during the procedure. High pH induces deprotonation of the surface silanols, thus, surfactant molecules can be easily attached to the MWW layers. The importance of basic character of the swelling solution is explained by low silanol density on MWW layers. Thus, at lower pH, the surfactant molecules would lay on the layers horizontally, causing little expansion of the structure. On the other side, the increased pH creates new SiO^{-} surface groups, which have strong affinity to the surfactant molecules [277]. Coulomb interactions between the long surfactant chains and surface SiO^{-} defects result in vertical alignment of the swelling agent molecules and expansion of the interlayer distance [384]. Normally, tetrapropylammonium hydroxide (TPAOH) is used as the auxiliary substance to maintain the required basicity of the swelling mixture. Successful swelling of the precursor can be confirmed by XRD patterns, due to the disappearance of the characteristic (002) reflection. On the contrary, the intense diffraction maximum, appearing in low-angles, indicates the increase of the interlayer distance, caused by the presence of $C_{16}TMA^{+}$ molecules. Separation of the adjacent MWW layers during the swelling step enables pillaring of the precursor. Intercalation is performed in an inert atmosphere, using tetraethyl orthosilicate (TEOS) as silica precursor. Subsequent hydrolysis and calcination results in the formation of stable SiO_2 pillars in the interlayer space [335,384]. The steps of MCM-36 synthesis and the final pillared structure of the zeolite are presented in **Figure 25.**

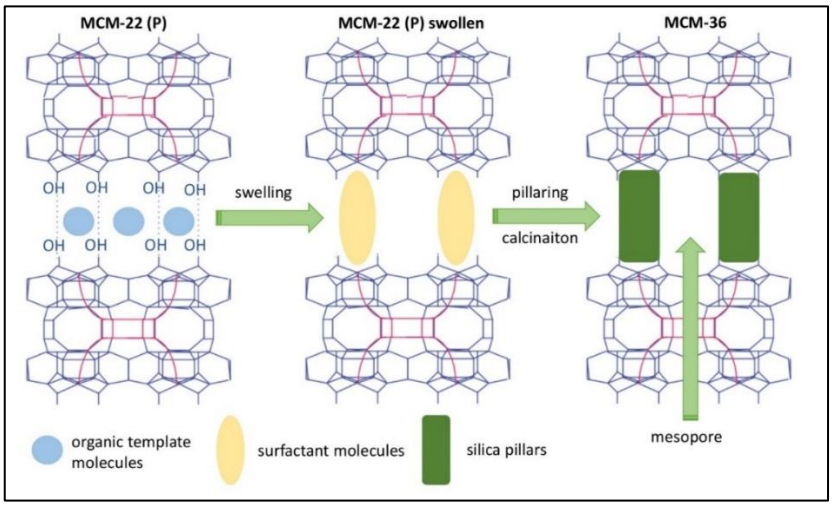

Figure 25. Scheme of the formation of MCM-36 structure (based on [385])

As illustrated in **Figure 25,** the 10MR channels in MWW layers of the precursor remain unchanged after swelling and pillaring. In contrast, 12MR supercages are absent, since the adjacent layers are not linked, as in the case of MCM-22. However, the effective pillaring with SiO_2 implies generation of mesopores with the diameter of 25-30 Å. The pore size facilitates accessibility to the internal acid sites of the materials, thus it is exceptionally advantageous for the number of catalytic processes. Barakov et al. [370] declared that among MCM-22, MCM-36, MCM-49, MCM-56, MCM-41 and beta zeolite, micro-mesoporous MCM-36 exhibited the highest selectivity in Prins-Friedel-Crafts reaction. Additionally, titanosilicate-pillared MCM-36 showed outstanding activity in epoxidation of olefins [386,387]. Nevertheless, in some cases SiO_2 can block the active centers of metal-modified MCM-36 and hinder the proceeding reaction. The problem can be solved by introduction of other pillaring oxides. Therefore, apart from silica, other metal oxide pillars were deposited in the interlayer space of MCM-36, for example TiO_2 [355], or the mixtures of Al_2O_3 with MgO, BaO, or SiO_2 [388,389]. Introduction of Al_2O_3 as pillars can generate Lewis or Brönsted acidity, due to the formation of silica-alumina clusters in the interlayer space. On the other hand, intercalation with alkaline oxides, such as MgO or BaO creates base properties. Thus, depending on the modification pathway, MCM-36 can be considered as acid-base bifunctional material.

Delaminated layered zeolite ITQ-2

Another important derivative of MCM-22 (P) is ITQ-2, the first exfoliated zeolite [390]. There are also other delaminated zeolites of MWW family, for example MCM-56 obtained in single-step [391]. Additionally, exfoliation of swollen precursors has been applied not only to MWW frameworks. For example, delamination of NSI-type materials results in the formation of ITQ-18 [392]. The term "exfoliation" is often used equivalently to "delamination" and both mean dispersion of the loose zeolitic layers in a liquid medium solution [277]. The idea of delaminated materials represents a concept of maximized accessibility and exposure of the zeolite layers to the reactants.

ITQ-2 consists of thin layers of ca. 0.25 Å thickness and possesses well-defined and high specific surface area of even 700 $m^2 \cdot m^{-2}$ in well-prepared samples [393]. In opposition to MCM-36, the sheets are disordered, forming so-called "house-of-cards" arrangement. Random stacking of the layers creates

mesoporosity, enabling the access of large molecules to the active sites, while ITQ-2 is used as a catalyst. The structure of ITQ-2 possesses zeolite characteristics with 10MR channels, running around so-called "cups". They have a size of ca. 7 Å deep and penetrate the MWW sheets from both sides. The cups are formed by 12MR apertures of ca. 7 Å and meet with each other at the center of each MWW layer, forming double 6MR window. 6MR window connects the cups bottom to bottom, generating smooth 10MR channel system inside the MWW sheets. ITQ-2 structure is schematically showed in **Figure 26.**

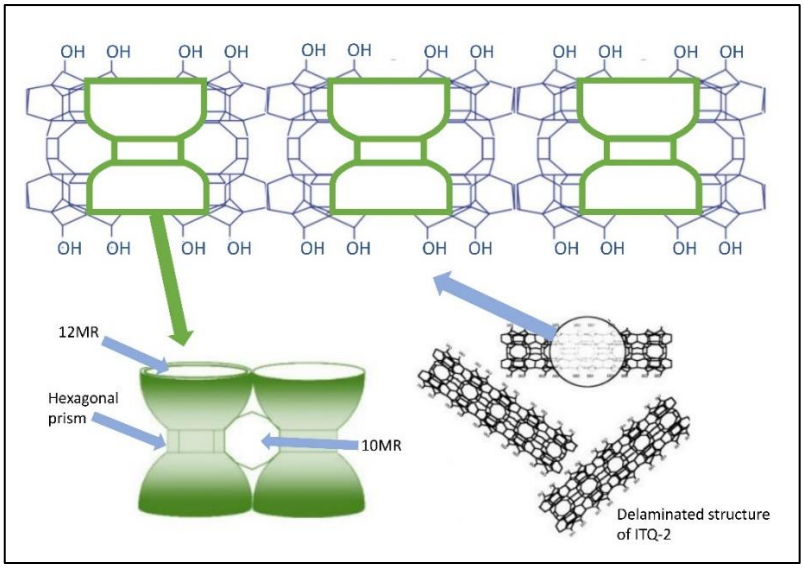

Figure 26. Schematic illustration of ITQ-2 structure (based on [335,390])

Preparation procedure of ITQ-2 starts from swelling, analogously to the synthesis of MCM-36. Typically, swelling solution contains alkylammonium molecules: $CTMA^+OH^-$ or tetrabutylammonium (TBA^+OH^-). In the case of ITQ-2 synthesis, it is crucial to control temperature and pH of the swelling process. Corma et al. [393] mentioned that pH lower than 12.5 and temperature below 50 °C prevents delamination. For higher values, the undesired formation of amorphous M41S materials occurs. During delamination process, the zeolitic layers of the swollen precursor are randomly separated. Usually, the step requires ultrasonic techniques to disorder MWW layers. Finally, pH of the slurry is decreased to around 2 by the addition of HCl and the material is centrifuged multiple times. Calcination of as-prepared zeolite at 540 °C removes the residual molecules of organic structure directing agents [335]. Both swelling and delamination processes can be followed by XRD technique, due to some remarkable changes occurring in the patterns of the modified zeolite. It is established that low-angle diffraction maxima in XRD patterns of MWW materials correspond to the ordering of layers and interlayer space.

Thus, during successful swelling, the distance between MWW sheets increases from 27 to 45 Å. Furthermore, the delaminated zeolite does not exhibit (001) and (002) reflections, characteristic for regular distribution of MWW layers, ordered perpendicularly to axis *c* [335]. ITQ-2 synthesis procedure with the corresponding XRD patterns of the intermediate phases are presented in **Figure 27.**

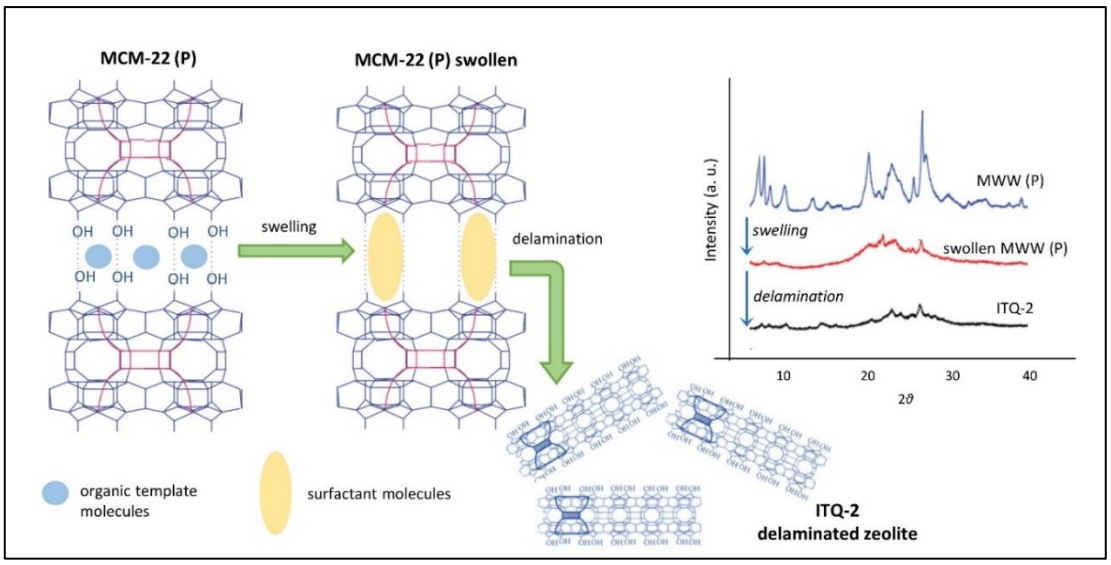

Figure 27. Schematic procedure of the synthesis of delaminated zeolite ITQ-2 (based on [335,390])

ITQ-2 has many uses in the field of catalysis, for example in biomass pyrolysis vapors [394–396]. Naqvi and Naqvi [397] compared the catalytic activity of various zeolites in deoxygenation of the vapors derived from biomass pyrolysis. The authors reported that ITQ-2, as the highly acidic and medium-pore size zeolite, exhibits high selectivity to aromatic compounds. Furthermore, Kweon et al. [398] compared Ni-MCM-22 and Ni-ITQ-2 as the catalyst of CO_2 reforming to methane. Delaminated structure and high external surface area of ITQ-2 facilitated dispersion of nickel cations, resulting in higher activity of Ni-ITQ-2 in the process. Apart from that, ITQ-2 was tested as the catalyst of cracking [399] or dehydroaromatization reaction [400]. Additionally, Rutkowska et al. [353] tested ITQ-2 as the representative of delaminated MWW zeolites in NH_3-SCR. Besides, Moreno-González et al. [401] investigated interaction of Cu^{2+} and alkanes on Cu-ITQ-2 during HC-SCR. However, application of ITQ-2 in SCR reaction has not been so far explored in depth.

Zeolites of MWW family - summary

The extensive research on MWW materials proved that the wide range of structural modifications enables to precisely tailor their properties. Chemical and mechanical stability, distribution of the active sites or concentration and strength of the acid sites can be easily adjusted to the desired level [277]. All of the factors are determined by the assembly of the MWW layers. Furthermore, the arrangement of the zeolitic sheets is correlated with the treatment of 2D precursor. The products of thermal treatment (MCM-22), pillaring (MCM-36) and delamination (ITQ-2) exhibit various physicochemical features, however all of them combine hierarchical pore structure and high density of acidic sites. In their review paper, Roth et al. [374] presented tabular classification of 3D zeolite frameworks with MWW topology. Reproduction of the proposed systematics, including the synthesis steps is presented in **Figure 28.**

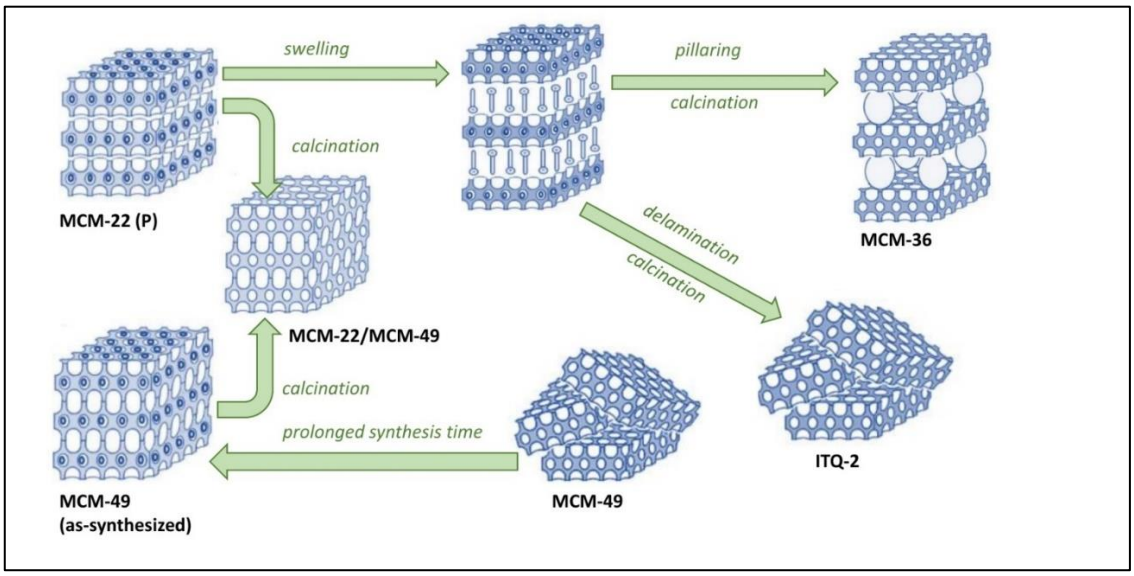

Figure 28. The pathways of the preparation of MWW zeolites (based on [335,374])

6. Zeolite-supported NH_3-SCR catalysts

Zeolites, as materials with ordered framework structures and high specific surface areas ensure dispersibility of the active components and promote the diffusion of the reactants. Distribution of the active phase in zeolites can be adjusted by the regulation of Si (in silicon-containing aluminophosphate zeolites) or Al (in aluminosilicate zeolites) content by the electrostatic stabilization effect [402]. Thus, modified zeolites are widely recognized as the precursors of active and selective catalysts of NH_3-SCR process [186,403]. The catalytic potential of zeolites results from their wide operation temperature range, surface acidity, and non-toxicity [404]. Therefore, ion-exchanged zeolites are among commonly investigated materials for vehicle NH_3-SCR applications, as the substitutes for three way catalytic converter, or industrial vanadia-based catalysts, used in stationary emission sources [405].

Development of zeolite-supported catalysts of NH_3-SCR started from the discovery of Iwamoto et al. [406]. In 1986, the authors recognized that ZSM-5 containing Cu^{2+} promotes catalytic decomposition of NO into N_2 and O_2. Soon after that, in 1990s, it was found that metal-exchanged ZSM-5 can selectively reduce NO to N_2 using hydrocarbons as reductants [407]. Successively, the studies on the application of zeolites in NH_3-SCR were focused on the catalytic potential of modified BEA [408] or FAU [409]. In fact, initially, the catalytic performance of these systems in NO reduction was limited. It was mainly caused by insufficient low-temperature activity, hydrocarbons fouling, low stability, and excessive NH_3 storage capacity. However, it was found that these problems can be overcame by the adjustment of pore sizes, simultaneously limiting the access of non-desired compounds to zeolite cages and their active centers. As ZSM-5 and BEA or FAU contain 10 and 12 oxygen atoms in the window, respectively, they are considered to be medium-pore materials. This type of pore opening enables the access of larger hydrocarbon molecules to the inner structure, implicating gradual deactivation of the catalyst. Hence, both modifications of the materials and the development of small-pore zeolites with 8 or less oxygen atoms in the window has become a hotspot of the future research.

Intensive studies on various zeolites led to the findings that the zeolite SSZ-13 and its silicoaluminophosphate structural analogue, SAPO-34, have a great potential in NH_3-SCR. Both of the zeolites are isostructural to CHA framework and their synthesis was reported for the first time in 1980s

[410,411]. Originally, the materials were designed for methanol to olefins process. However, in 2010 Kwak et al. [412] reported that Cu-SSZ-13 exhibits satisfactory NO conversion and great hydrothermal stability, combined with the resistance to poisoning with hydrocarbons. Furthermore, in 2011, Fickel et al. [413] recognized that Cu-SAPO-34 shows similar catalytic performance and hydrothermal stability to Cu-SSZ-13. As a result, both Cu-SSZ-13 and Cu-SAPO were commercialized in 2010 and are currently the typical choice for SCR catalysts in vehicle applications. The scheme of the chronological development of zeolitic materials used in commercial $DeNO_x$ systems, including NH_3-SCR is presented in **Figure 29.**

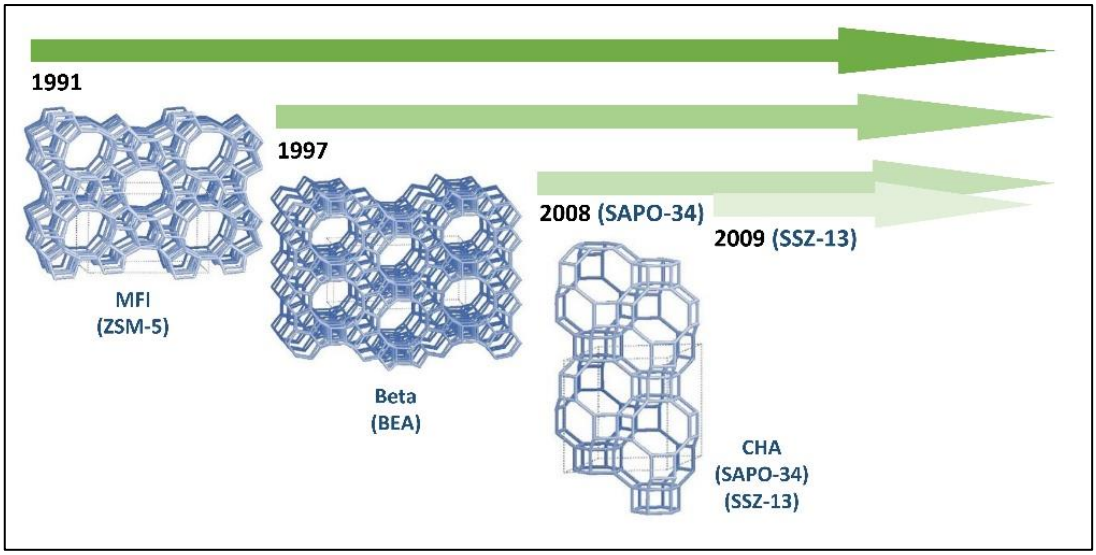

Figure 29. Scheme of chronological development of zeolitic materials applied for $DeNO_x$ industrial systems

Due to the complexity of the zeolitic structure and the diversity of the possible introduced metals, it is difficult to understand the active sites or mechanisms of NH_3-SCR in the zeolitic catalyst. Besides, the major challenge for the practical application of metal-exchanged zeolites in NH_3-SCR are their SO_2 tolerance and hydrothermal stability. Most current research is therefore aimed at overcoming these obstacles.. According to the large number of studies, among many catalysts supported on zeolites, Fe- and Cu-based catalysts show the best features, applicable in NH_3-SCR reaction [85,353,414].

7. Catalytic performance of Fe-zeolites in NH_3-SCR

Over the last ten years, the focus on new, zeolite-supported catalysts for NH_3-SCR has shifted to the application of iron-exchanged materials. The extensive investigations were motivated by environmentally-benign characteristics of iron, its low price, and prominent thermal stability. Additionally, as NH_3-SCR catalysts, the compounds of iron show excellent medium and high temperature activity and advantageous selectivity to N_2. Another advantage of Fe-zeolite catalysts is high oxygen storage capacity and oxygen mobility, caused by the facile redox equilibrium, $Fe^{3+} \leftrightarrow Fe_3O_4 \leftrightarrow Fe^{2+}$ [415]. Besides, the materials are resistant to the poisoning influence of H_2O and SO_2 at low temperature [416].

Great majority of the research has been focused on iron species incorporated into ZSM-5 structure, after the precursory work of Iwamoto et al. [406] on Cu-ZSM-5. It was found that Fe-ZSM-5 is much more active, exhibiting 100% of NO conversion in a broad temperature window of 350-500 °C. Besides, Fe-ZSM-5 is more selective to N_2 and more hydrothermally stable, comparing to Cu-ZSM-5 [417]. Nevertheless, application of Fe-ZSM-5 on industrial scale is limited by its inferior low-temperature activity, caused by high energy barrier of the reduction of iron species incorporated into the zeolite [85].

Except ZSM-5, other Fe-modified zeolite structures were tested in NH_3-SCR. Jabłońska et al. [418] compared catalytic characteristics of Fe-BEA catalysts prepared by ion-exchange or post-synthesis replacement of Al with Fe atoms. The authors declared that both of the materials exhibited satisfactory NO conversion, which was influenced by the speciation of iron. Besides, the results confirmed that Fe-BEA prepared by ion-exchange shows enhanced activity in N_2O decomposition above 450 °C. Generally, Fe-BEA are considered as more active and stable than Fe-ZSM-5. However, the materials do not maintain high activity and durability at hydrothermal conditions. According to Shwan and co-workers [419], hydrothermal aging of Fe-BEA results in declined NO conversion in the temperature range of 100-300 °C, while at higher temperature, the activity remains high. The authors ascribed this effect to the diminished NH_3 storage capacity and increased oxidation state of Fe, which enhanced the activity in non-selective oxidation of NO and ammonia. Nedyalkova et al. [420] postulated

that the problem of low hydrothermal stability of Fe-BEA could be partially solved by H_2-pretreatment of the catalyst. However, it was observed that the proposed procedure is limited by irreversible dealumination of the zeolite during hydrothermal aging.

Apart from ZSM-5 and BEA, other different synthetic and natural zeolites, such as clinoptilolite or chabazite have been investigated [421]. It occurred that modified clinoptilolite showed excellent performance in selective catalytic reduction of nitrogen oxides, similar to that of modified ZSM-5 [422]. The advantage of clinoptilolite, guaranteeing selective abatement of NO_x emission is its pore diameter of approximately 7 Å, thus, bigger than the estimated kinetic diameters of the reacting molecules [288]. One of the primary studies on the application of clinoptilolite in NH_3-SCR was conducted by Mishima et al. [423] in 1998. The authors prepared the anchored pellet catalyst using Zeo 3S (consisting mainly of clinoptilolite) by ion-exchange with HNO_3 to produce H-zeolite, followed by impregnation with vanadium cations. The pore diameter and the presence of vanadium cations facilitated the access of NH_3 and NO to the inner space of the zeolite and adsorption on Brönsted acid sites, respectively. Subsequently, the focus on the modification of clinoptilolite was directed into substitution of vanadium by other metals active in NH_3-SCR. In 2002, Long and Yang [424] compared the catalytic performance of Fe-modified mordenite, heulandite, beta, ferrierite, and chabazite zeolites. It was found that Fe-MOR and Fe-HEU exhibit the highest activity among the tested materials, exceeding that of the commercial vanadium-based system: NO conversion for these catalysts reached the value of 95-98% within 400-450 °C. The authors also observed that SO_2 and the mixture of SO_2 and H_2O enhanced NH_3-SCR activity of the catalysts. Furthermore, it was proposed that NO reduction over Fe-HEU involves the reaction between NO_2 and a pair of NH_4^+ ions, generation of active intermediates and reaction of the produced species with gas-phase NO. According to the analysis, the rate-determining step of the reaction was oxidation of NO to NO_2. Additionally, the presence of well-dispersed Fe^{3+} species deposited in the framework and extraframework sites provided adsorption of NO, N_2O_3, NO_2, and nitrate intermediates, while ammonia molecules were bonded to Brönsted acid sites. The catalytic potential of clinoptilolite in NH_3-SCR was also examined by Moreno-Tost et al. [425,426]. Their work published in 2004 concerned application of Cu-zeolite in NH_3-SCR. The catalyst exhibited significantly lower resistance to SO_2 poisoning, comparing to that with Fe. Afterwards, in 2005, the authors exceeded their studies

over metal-modified clinoptilolite and tested the zeolite with Ag and Zn. However, the metals were found to be almost inactive in NO conversion. As a result, further research over application of clinoptilolite in the process involved mainly Fe-clinoptilolite. In his 2007 study, Ates [421] modified three fractions of natural clinoptilolite with iron by ion-exchange method and tested the materials as catalysts of N_2O reduction with NH_3. The transition experiments indicated that the presence of active oxygen is related only to the deposited Fe species, while oxygen storage capacity depends on the type of iron sites, rather than on Fe loading. According to the results, only Fe^{2+} were responsible for oxygen storage capacity during the reaction. Additionally, NH_3-TPD measurements indicated that iron species are introduced instead of the charge-balancing Na^+ cations. Thus, the activity in the selective reduction of N_2O was provided mainly by isolated species in extraframework positions. Besides, it was found that modification with Fe enhances specific surface area and the total acidity of the material, due to the removal of impurities and exchange of charge-balancing cations with NH_4^+, respectively. One of the recent studies related to the application of Fe-clinoptilolite in NH_3-SCR was conducted by Gelves and co-workers [295]. The catalyst was tested under lean and hydrothermal conditions of NH_3-SCR in its natural, protonated, and Fe^{2+}- or Fe^{3+}-form. The authors postulated that the overall reaction mechanism was controlled by the presence of NO_2, produced by the oxidation of NO on Fe^{3+} sites. Besides, the activity of Fe^{3+} was superior in comparison to Fe^{2+}. However, due to the competitive adsorption of H_2O molecules and NO, the reaction was hindered in the presence of water. On the other hand, 5% mol of H_2O in the inlet stream improved the adsorption of NO_2 on the catalyst surface. Nevertheless, interaction with water resulted in the formation and adsorption of nitrous (HNO_2) and nitric acid (HNO_3) on the catalyst surface and further oxidation of NO. The results of the catalytic tests under hydrothermal conditions indicated that NO conversion decreases significantly only at 500 °C, after 30 h of the reaction. The effect was a combined result of dealumination, contraction of zeolite channels, and declined acidity and crystallinity of the material. Comparison of clinoptilolite modified with iron to other natural aluminosilicates was provided by the work published by Szymaszek et al. [327]. The authors tested iron-doped bentonite, vermiculite, and clinoptilolite in NH_3-SCR and found that the best candidate for the efficient catalyst is Fe-clinoptilolite. The results of the catalytic reaction performed over non-modified clinoptilolite were in line with that obtained by Gelves et al. [295] and proved that iron naturally present

in the zeolite can moderately reduce NO in the high-temperature region. What is interesting, the emission of N_2O, which is by-product of the reaction was below the detection limit in the whole tested temperature range. The result was supported by the work of Saramok et al. [328], which revealed that below 450 °C the ratio of inlet to outlet N_2O concentration is lower than 1. Thus, the material is active not only in $DeNO_x$, but also in DeN_2O process. As described above, clinoptilolite exhibits a promising potential as the catalyst of NH_3-SCR. However, despite the outstanding activity, comparable to the commercial synthetic zeolites, in some cases commercialization of natural clinoptilolite is still limited by the costs of homogenization and purification of zeolite-bearing tuffs. Nevertheless, the abundance in environment and low price are the premises why the material is a promising candidate for the new, substitutive commercial catalyst of NH_3-SCR process.

Simultaneously to the works carried out on medium-pore zeolites, intensive studies were conducted on small-pore SSZ-13 and SAPO-34. Motivation of the investigations on Fe-SSZ-13 and Fe-SAPO-34 was caused by commercialization of these zeolites doped with Cu as novel NH_3-SCR catalysts of diesel exhausts purification. One of the first research on Fe-SSZ-13 and Fe-SAPO as NH_3-SCR catalysts was published in 2012 by Ye et al. [427] and concerned comparison of the catalytic performance and resistance of the materials to hydrocarbon poisoning. The catalytic potential of small-pore Fe-CHA zeolites in NH_3-SCR was also intensively investigated by the group of Corma and co-workers [428,429]. Martín et al. [429] postulated that large cavities of the crystalline CHA structure can favor stabilization of iron cations. Moreover, small windows of 3.8 Å, which connect the cavities, preclude sintering of metal species, thus improve hydrothermal stability. The authors observed that Fe-CHA obtained by one-pot synthesis under alkaline conditions exhibited high NO conversion, dependent on Si/Al molar ratio. Additionally, excellent catalytic activity of Fe-SAPO-34 was confirmed by Andonova et al. [348], who found that NO conversion for this catalyst exceeds 80% in the temperature range of 300-600 °C. Consequently, the material was patented in 2015 as SCR catalyst for the reduction of NO_x from vehicle engine exhausts [430]. Additionally, Zhao et al. [431] reported that the addition of the controlled amount of Fe promotes the catalytic activity of Cu-SAPO-34 in NH_3-SCR. The authors found that 1 wt.% of Fe resulted in the reduction of bulk CuO surface species, thus, decreased NH_3 oxidation rate above 350 °C. What is more, the presence of isolated Fe^{3+} species enhanced high

temperature activity of the catalyst. On the other hand, introduction of 1.5 wt.% of iron implied the replacement of isolated Cu^{2+} with Fe^{3+} ions and aggregation of both species to CuO_x and Fe_xO_y clusters. As a result, high temperature activity of the material was reduced by the lower amount of isolated copper species and enhanced activity in NH_3 oxidation.

Application of CHA-type materials was undoubtedly a breakthrough in the improvement of hydrothermal stability and high activity of Fe-catalysts supported on zeolites. However, despite the fact that small-pore zeolites promote the formation of important intermediates (for example NH_4^+ pairs, acting as Brönsted acid sites), they can also decrease diffusion rate of the molecules, affecting the catalytic activity. Thus, the works on new, potentially active in NH_3-SCR materials were recently expanded to large-pore zeolites, such as MSE. Ryu et al. [432] synthesized UZM-35 zeolite with the pore system formed by one 12MR and two 10MR channels, belonging to MSE family. The authors modified the material with iron and compared its catalytic performance in NH_3-SCR to Fe-beta, Fe-LTA, and Fe-SSZ-13. It was observed that the fresh Fe-UZM-35 showed the highest conversion of NO among all tested materials in the entire tested temperature range. The effect was ascribed to the abundance of intrazeolitic isolated iron cations, contributing to low-temperature activity.

Several studies have found that large pore, layered zeolites of MWW topology have an excellent catalytic potential in NH_3-SCR. The first reported research on the application of these materials in selective catalytic reduction of NO with ammonia was reported in 1997 by Wu et al. [433]. According to the study, incorporation of iron into the framework of MCM-22 resulted in the formation of Si(OH)Fe species, thus, Brönsted sites of weak acidity. Despite low acidic character, it was remarked that below 350 °C the material showed higher NO conversion than that of Fe-MFI zeolites. Besides, in contrast to Fe-MFI, Fe-MCM-22 did not exhibit activity in non-selective NH_3 oxidation, due to the lack of aggregated iron oxide species. The next approach to the application of MWW zeolites in NH_3-SCR was reported only in 2015 by Rutkowska et al. [353]. The authors compared physicochemical and catalytic features of MCM-22, MCM-36, and ITQ-2 modified with iron or copper and tested the materials in NH_3-SCR. It was concluded that among the different arrangement of layers, the ordered micro-mesoporous structure and variety of iron species of Fe-MCM-22 contributed to the best catalytic performance. Additionally, Fe-ITQ-2 contained almost exclusively isolated Fe^{3+} cations, thus, its

delaminated structure was confirmed to promote incorporation of well-dispersed framework iron species. However, the authors declared that the presence of mononuclear Fe cations in Fe-ITQ-2 was responsible for significant decrease of NO conversion above 450 °C. The study by Grzybek and co-workers [434] offered an analysis of the catalytic performance of Fe-modified MCM-56, the representative of MWW zeolites with disordered layers. The authors claimed that acid treatment of the material will partially remove Al from the framework, thus, generate vacancies, which can be filled with heteroatoms, acting as Lewis acid sites. The results of NH_3-SCR tests indicated that HNO_3- or NH_4F/HF-treated MCM-56 modified with iron exhibited minimum 92% of NO conversion and more than 99% selectivity to N_2 above 400 °C. Such catalytic behavior was ascribed to the presence of monomeric iron cations and small aggregates of iron oxide, which limited ammonia oxidation in the tested temperature region. In 2020, Chen et al. [352] published their research on the catalytic activity of MCM-22 modified with iron by various methods. The authors obtained very good results of catalytic tests in low-temperature range for the material with iron introduced to the synthesis pot.

Therefore, the above-mentioned studies demonstrate that well-prepared and Fe-modified zeolites have a great catalytic potential in selective catalytic reduction of NO_x with ammonia. The summarized NH_3-SCR activities of Fe-catalysts supported on zeolites with various topologies are listed in **Table 8.**

Table 8. NH_3-SCR activity of the representative Fe-zeolite catalysts

Catalyst (topology)	**Channel system**	**Synthesis method**	**%Fe**	**Reaction conditions**	**Temp. window (°C)**	**NO_x conv.**	**Ref.**
Fe-ZSM-5 (MFI)	10MR	IE [a]	5	1000 ppm NO, 1000 ppm NH_3 10 vol.% O_2, 5 vol.% H_2O balance of N_2 GHSV = 52,000 h^{-1}	480-650	> 80%	[435]
Fe-beta (BEA)	12MR	IMP [b]	4	2500 ppm NO, 2500 ppm NH_3 2.5 vol.% O_2, balance of He WHSV = 24,000 $cm^3 \cdot h^{-1} \cdot g^{-1}$	230-530	> 80%	[436]
Fe-SSZ-13 (CHA)	8MR	IE	1.37	350 ppm NO, 350 ppm NH_3 14 vol.% O_2, 2.5 vol.% H_2O balance of N_2 GHSV = 200,000 h^{-1}	320-550	> 80%	[437]

Fe-SAPO-34 (CHA)	8MR	OPS [c]	1	350 ppm NO, 350 ppm NH_3 14 vol.% O_2, 5 vol.% CO_2 5 vol.% H_2O, balance of Ar	230-650	60-65%	[348]
Fe-UZM-35	12MR	IE	1.9	500 ppm NO, 500 ppm NH_3 5 vol.% O_2, 10 vol.% H_2O balance of N_2 GHSV = 100,000 h^{-1}	250-570	> 90%	[438]
Fe-Clin [e]	10MR	Ex [f]	3.2	400 ppm NO, 45 ppm NO_2, 400 ppm NH_3, 8 vol.% O_2, 0-5% H_2O, balance if Ar GHSV = 30,000 h^{-1}	325-475	> 80%	[295]
Fe-MCM-22	10MR	OPS	4.8	500 ppm NO, 500 ppm NH_3 5 vol.% O_2, balance of N_2 GHSV = 60,000 h^{-1}	190-490	> 80%	[352]
Fe-ITQ-2	12MR	IE	0.9	2500 ppm NO, 2500 ppm NH_3 2.5 vol.% O_2, balance of He T [d] = 373 g · h · mol^{-1}	280-480	> 80%	[353]

[a] : ion exchange, [b] : wet impregnation, [c] : one pot synthesis, [d] : space time of NO, [e] : clinoptilolite, [f] : extraction

7.1 Metal active sites in Fe-zeolites

The evaluation of the type, amount, and distribution of the active sites is a vital issue for better understanding of NH_3-SCR reaction mechanism over metal-exchanged zeolites. According to the present knowledge, the activity of Fe-zeolites in NO reduction is determined by the form of metal species in the catalyst [352,439]. It is generally accepted that iron can be present in zeolites in a form of isolated Fe^{2+} and Fe^{3+} cations (either isomorphously substituted in framework positions or in cationic positions in zeolite channels), binuclear or oligonuclear $Fe_xO_y(OH)_z$ clusters, nanoparticles of iron oxide, or bulk particles of iron oxide, located at the surface of the zeolite crystals [440]. Different forms of iron deposited in zeolitic structure, on the example of Fe-ZSM-5, are presented in **Figure 30.**

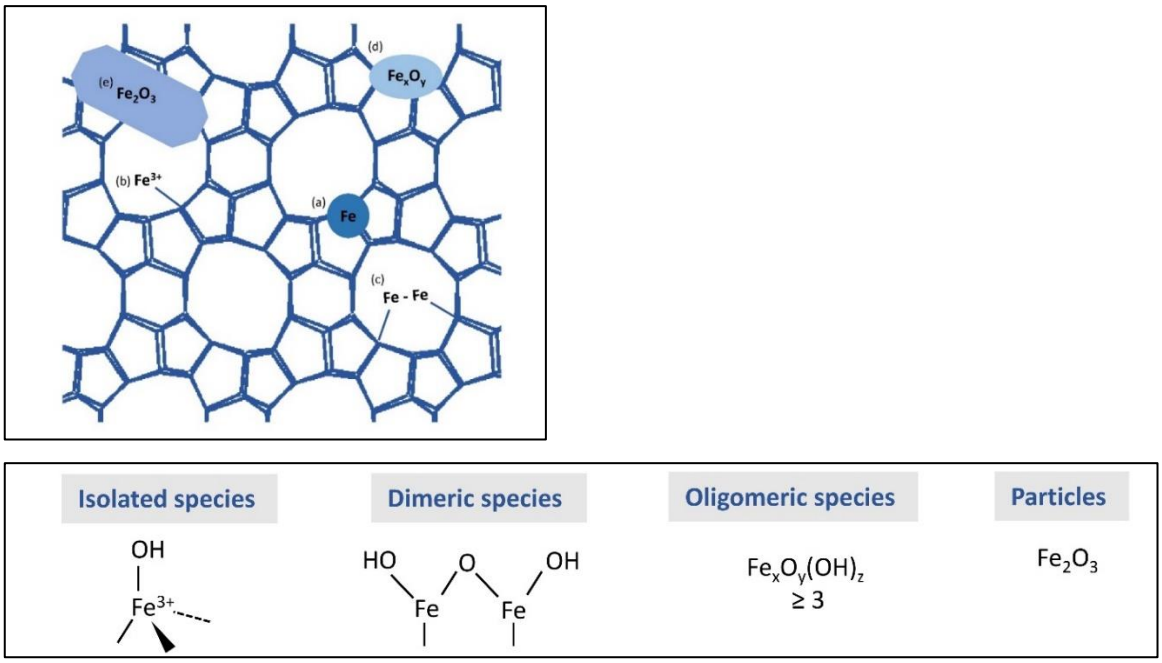

Figure 30. Schematic representation of various Fe species identified in the structure of Fe-ZSM-5: isomorphously substituted isolated cations in framework positions (a) isolated cations in cationic positions in zeolite channels (b), binuclear (or oligonuclear iron complexes in extraframework positions (c), iron oxide nanoparticles (≤ 2 nm) (d), large particles of iron oxide (≤ 25 nm) located at the zeolite surface (d) (based on [440])

Catalytic activity of various forms of iron in zeolites was intensively investigated in the recent years. In 2010, Brandenberger et al. [439] correlated the quantity of monomeric and clustered forms of iron with catalytic performance of Fe-ZSM-5 in NH_3-SCR. The results confirmed that various forms of active sites determine the overall activity of the catalyst and their behavior is correlated with temperature of the reaction. In general, in low-temperature region (below 300 °C) NO conversion was taking place mainly on the dispersed isolated Fe^{3+} cations and monomeric $[Fe(OH)_2]^+$, while activity in the region of 300-500 °C was determined by dimeric $[HO\text{-}Fe\text{-}O\text{-}Fe\text{-}OH]^{2+}$, oligomeric, and partially uncoordinated iron sites on the surface of aggregated Fe_2O_3 clusters. When the temperature exceeded 500 °C, Fe_2O_3 particles promoted NH_3-SCR reaction. The differences in the catalytic activity of iron sites was ascribed to different activation energies of the species. Basing on the estimation of the apparent activation energies ($\boldsymbol{E_A}$) from Arrhenius plot, it was found that for the monomeric species $\boldsymbol{E_A}$ = 36.3 kJ · mol^{-1}, while for dimeric species $\boldsymbol{E_A}$ = 77.0 kJ · mol^{-1}. Besides, the authors analyzed the relationship between nuclearity of iron moieties and NH_3 oxidation activity. Monomeric iron sites were not active in the reaction up to 500 °C, while the oligomers oxidized ammonia from 350 °C. The activity pattern of

different iron species with the turnover frequencies (***TOF*** - number of converted NO molecules per second per iron atom) proposed by Kröcher and Brandenberger [440] is presented in **Table 9.**

Table 9. Turnover frequencies (TOF) of various iron species (reproduced basing on [440]

	TOF (s^{-1})			
Temperature	**Isolated species**	**Dimeric species**	**Oligomeric species**	**Iron oxide particles**
200 °C	7 ± 0.5	≤ 1 [b]	-	-
250 °C	15 ± 0.5	2 ± 1 [b]	-	-
300 °C	28 ± 2	8 ± 5	-	-
350 °C	45 ± 2 [a]	27 ± 10	-	-
400 °C	74 ± 4 [a]	58 ± 13	active	-
450 °C	153 ± 8 [a]	270 ± 80 [b]	active	27

[a] Extrapolated from an Arrhenius plot at 200, 250, and 300 °C
[b] Extrapolated from an Arrhenius plot at 300, 350, and 400 °C

In general, generation of N_2 and H_2O from nitrate species during NH_3-SCR is promoted by the reduction of Fe^{3+} to Fe^{2+} or the oligonuclear Fe_xO_y to Fe_2O_3. For example, Shi et al. [441] prepared Fe-beta catalyst and obtained high catalytic activity in the broad temperature window of 250-500 °C. The authors assigned this result to the formation of Fe^{2+}-NH_2 intermediates, which reacted with gaseous NO to form N_2 and H_2O.

The research on the nature of the iron sites was expanded by Gao et al. [442], who analyzed the effect of iron loading on the formation of iron species and catalytic activity. Similarly to Brandenberger et al. [439], the authors concluded that various forms of iron are active in particular temperature regions. Additionally, it was observed that for the analyzed iron contents (0.27-1.20 wt.%) the apparent activation energy did not change, thus, all of the samples contained the same forms of iron.

The coordination environment of iron active sites in zeolites have been intensively studied as well. According to the general agreement, the coordination number of Fe in zeolites used in NH_3-SCR is 4 and it can increase to 5 after adsorption of NO by the formation of [Fe^{2+}-OH-N=O] complexes [443]. What is more, the form of iron sites in zeolites is strongly correlated with the preparation procedure of

the catalyst [352,429,436]. Boroń et al. [436] modified beta zeolite by two-step post-synthesis, ion-exchange, and wet impregnation method. On the basis of Mössbauer spectroscopy, it was found that Fe-BEA zeolites contained mainly pseudo-tetrahedral Fe^{3+} species, ≡Fe (III)-O(H)-Si≡. Besides, the ion-exchanged and impregnated samples were the most active, due to the co-existence of pseudo-tetrahedral sites with strongly acidic ≡Al(III)-O(H)-Si≡.

Another important issue related to the iron species concerns its spatial distribution in the zeolitic structure. Ellmers et al. [444], investigated the location of Fe in the framework of ZSM-5 and proved that it has a crucial impact on catalytic activity in NH_3-SCR. Their analysis confirmed that the isolated Fe^{3+} species in 10MR, so-called α sites, are active in standard conditions of NH_3-SCR, while Fe^{3+} in so-called β and γ positions in 6MR and 5MR, respectively, enhance the activity of fast NH_3-SCR.

The proceeding developments in Fe-exchanged zeolites confirmed that iron species change the acidic characteristics of the materials. NH_3-TPD studies conducted by Brandenberger et al. [435] on Fe-ZSM-5 proved that introduction of iron significantly reduced the amount of Brönsted acid sites. The effect was explained by the replacement of H^+ by Fe atoms. What is interesting, this phenomena was observed only for the samples in which Fe/Al was below 0.4. On the other hand, for higher Fe/Al ratios, the majority of iron is present in a form of more aggregated particles. The dependence of the concentration of various acid sites on the deposition of various loadings of Fe was also observed by Jabłońska et al. [418] for BEA zeolite. In line with Brandenberger et al. [435], it was confirmed that introduction of Fe reduced Brönsted acidity, in favor of the population of Lewis sites.

7.2 Preparation procedures of Fe-zeolite catalysts for NH_3-SCR

One of the crucial factors, regulating distribution of the active sites and determining the catalytic performance of metal-exchanged zeolites in catalytic reactions, including NH_3-SCR, is preparation procedure. In the case of iron, two main groups of methods have been reported in the literature: post-synthesis treatment and isomorphous substitution (one-pot synthesis) [352]. The preparation methods of Fe-zeolite catalysts with the corresponding iron precursors and the synthesis conditions are presented in **Table 10.**

Table 10. NH_3-SCR activity of representative Fe-zeolite catalysts

Catalyst	Fe loading (wt.%)	Preparation procedure	Fe source	Conditions of Fe introduction	Ref.
Fe-MCM-22	1.0	wet ion-exchange	$FeSO_4$	Stirring in a solution of $FeSO_4$ at 85 °C for 6 h, washing with distilled water, calcination at 550 °C for 6 h	[353]
Fe-HBEA	1.0 - 4.0	incipient wetness impregnation	$Fe(NO_3)_3$	$Fe(NO_3)_3$ was dropped onto HBEA and the mixture was stirred at room temperature for 24 h, then the suspension was stirred in evaporator at 80 °C for 2 h until water was completely removed	[436]
Fe-ZSM-5	3.5	solid-state ion exchange	$FeCl_3$	Mixing of H-ZSM-5 with a suitable amount of anhydrous $FeCl_3$ in a ball mill for 1 h, heating at 600 °C in a flow of N_2 for 2 h, washing with alkali solution to neutralize HCl, washing with deionized water, calcination at 550 °C in air	[445]
Fe-ZSM-5	0.29-0.78	chemical vapour deposition	$FeCl_3$	Mechanical mixing of H-ZSM-5 with $FeCl_3$ in a glove box, heating at 650 °C in N_2 atmosphere for 2.5 h, cooling to room temperature, washing with deionized water, calcination at 650 °C for 5 h in a flow of 20% O_2 in N_2	[446]
Fe-ZSM-5	0.67	steaming extraction	$Fe(NO_3)_3$	Fe-ZSM-5 zeolite with isomorphously substituted Fe^{3+} species was calcined at 550 °C for 10 h, converted into H-form, steamed at ambient pressure in a flow of N_2, followed by the exposure to a mixture of H_2O in N_2 at 600 °C for 5 h	[447]
Fe-MCM-22	4.8	one-pot synthesis	$Fe(NO_3)_3$	$Fe(NO_3)_3$ was added as the precursor of iron into the synthesis gel, which was subsequently hydrothermally treated	[352]
Fe-SSZ-13	6.25	one-pot synthesis	$FeSO_4$	$FeSO_4$ was added as the precursor of iron into the synthesis gel, which was subsequently hydrothermally treated	[448]

The most important post-synthesis methods are wet ion-exchange [353], incipient wetness impregnation (or impregnation) [436], solid-state ion exchange [344], chemical vapour deposition (CVD) [446], or steaming extraction of isomorphously substituted Fe-zeolite [447]. Typically, in order to avoid oxidation of Fe^{2+} to Fe^{3+} and undesired oligomerization of the species, it is necessary to perform the modification of Fe-zeolite catalysts under N_2 atmosphere [429]. Apart from the formation of oligomers, the oxidized Fe^{3+} ions tend to agglomerate into bulk clusters, leading to pore clogging. Besides, multiple treatments are required to efficiently utilize ion-exchange capacity of the zeolite. The highest rates of ion-exchange combined with the formation of isolated extraframework iron cations are obtained while well-soluble iron precursors are used, such as iron nitrate, iron sulfate, or iron chloride.

Avoiding of the above-mentioned complications related to wet-ion exchange can be realized by the application of alternative methods. The problem of uncontrolled amount of iron introduced by wet ion-exchange can be solved by the use of incipient wetness impregnation, which guarantees the precise loading of the active phase. On the other hand, in this case, it is impossible to avoid agglomeration of iron species and formation of bigger particles on the external surface of the zeolite. Alternatively, chemical vapor deposition of volatile precursors of Fe (for example $FeCl_3$) was reported to achieve successful deposition of isolated metal species on acidic sites of the zeolite. Iwasaki et al. [446] observed that Fe-ZSM-5 prepared by CVD method contained high amount of well-dispersed iron cations and successful substitution of the framework Brönsted protons with Fe^{3+}. On the contrary, Schwidder et al. [449] observed that in the case of CVD, formation of isolated iron species is possible only for low iron loadings, not exceeding 0.3 wt.%.

Solid-state ion exchange (SSIE) is based on physical mixing of H- or NH_4-zeolite powder with a metal salt (usually chloride). The uniform mixtures are obtained by ball milling or crushing with agate mortar. Solid state interaction, accompanied by the evolution of HCl and NH_4Cl, occurs during thermal treatment in air, inert atmosphere, or vacuum. Rauscher et al. [450] prepared Fe-ZSM-5 using SSIE and calcined the material either in aerobic (oven) or anaerobic (vacuum) conditions. In general, the materials calcined in vacuum exhibited higher concentration of Brönsted acid sites and activity toward N_2O decomposition. The biggest advantages of SSIE are the control of metal loading and crystal size and reproducibility of the modification procedure [451].

Active metal centers can be also incorporated into framework or extraframework positions of the zeolite structures on the level of hydrothermal synthesis. This type of modification is known as one-pot synthesis. The method ensures homogeneous metal dispersion within the zeolitic structure, which is especially important for the materials with high Si/Al ratios, for which metal cations can be poorly charge-balanced [429]. Additionally, direct hydrothermal synthesis of metal-zeolites eliminates the need for post-synthetic modifications, thus reduces the number of modification steps. One-pot synthesis of The Fe-zeolites, such as MCM-22, SAPO-34, ZSM-5, or BEA, were recently studied by several research groups [352,429,452,453].

The preparation procedure is strictly correlated with the NH_3-SCR catalytic activity of iron zeolites. Iwasaki et al. [446] identified the quantity of Fe active sites introduced into ZSM-5 by impregnation, SSIE, and CVD with various loadings of the metal. It was found that the most effective technique to obtain satisfactory NO conversion was chemical vapor deposition, due to the highest rate of the substitution of Brönsted sites by Fe^{3+} and abundance of iron monomers, dimers, and oligocations. In their two papers concerning the catalytic behavior of Fe-BEA in NH_3-SCR, Boroń et al. [436,454] compared the efficiency of wet ion-exchange, incipient wetness impregnation, and two-step post synthesis methods for Fe deposition. Higher catalytic activity was observed for the materials modified by impregnation and ion-exchange and the authors assigned this result to the presence of acidic framework sites, which were almost absent in the structure of acid-treated sample. Analogous post-synthesis procedure was adopted by Jabłońska et al. [418], who additionally observed increased production of N_2O for the material modified with HNO_3 in comparison to ion-exchanged Fe-BEA. The effect of preparation strategies for Fe-MCM-22 was also examined by Chen et al. [352]. The authors comprehensively compared the factors influencing catalytic activity of one-pot synthesized, ion-exchanged, impregnated, solid state ion-exchanged, and mechanical mixed Fe-zeolite. The highest NO conversion in the temperature range of 200-500 °C, together with almost 100% selectivity to N_2 was obtained for one-pot synthesized sample. At the same time, the other materials exhibited typical behavior for iron-exchanged zeolites, showing increased activity in the reaction above 250 °C.

Apart from the preparation method, conditions of the synthesis also affect the activity of Fe-exchanged zeolites, for example calcination temperature or synthesis atmosphere. Liu et al. [455]

prepared Fe-SSZ-12 and analyzed the influence of the calcination temperature on NH_3-SCR activity of the catalyst. It was found that calcination below 550 °C results in the formation of more isolated Fe^{3+} species and acid sites, thus, higher catalytic activity in low-temperature region and better NH_3 adsorption capacity. Calcination above 500 °C implied gathering of the isolated forms of iron and formation of dimeric and oligomeric clusters, active in the high-temperature range. Another factor influencing the catalytic behavior of zeolites is synthesis atmosphere. According to the general agreement, N_2 atmosphere facilitates the formation of highly reducible Fe^{3+} species, active in the low- and medium temperature range of NH_3-SCR [456].

7.3 Mechanism of NH_3-SCR on Fe-zeolites

Fundamental understanding of the mechanism of NH_3-SCR on Fe-zeolite catalysts have been in scope of the research for many years. The main difficulty in the explanation of the reaction mechanism results from the dynamic changes of multiple types of iron species. Despite the consensus on the active sites participating in NH_3-SCR reaction, there are still some discussions on the reaction pathway on various catalysts. As described in **subchapter 2.3,** selective catalytic reduction of NO with ammonia follows Langmuir-Hinshelwood or Eley-Rideal mechanism, in low- and high- temperature range, respectively [402].

Since the active intermediates of L-H and E-R are different, identification of the particular mechanism can be realized by recognition of the transition states of the reacting molecules. Hence, considerable effort has been devoted to monitor the mechanism of NH_3-SCR over Fe-exchanged zeolites using *operando* techniques, such as applied electrical impedance spectroscopy (IS) and diffuse reflection infrared Fourier transformation spectroscopy (*in situ* IS-DRIFTS) [457–459].

The reaction pathway of standard and fast NH_3-SCR over Fe-zeolites was proposed in the work by Jiang and Lobo [460]. The scheme, summarizing this analysis, is presented in **Figure 31.**

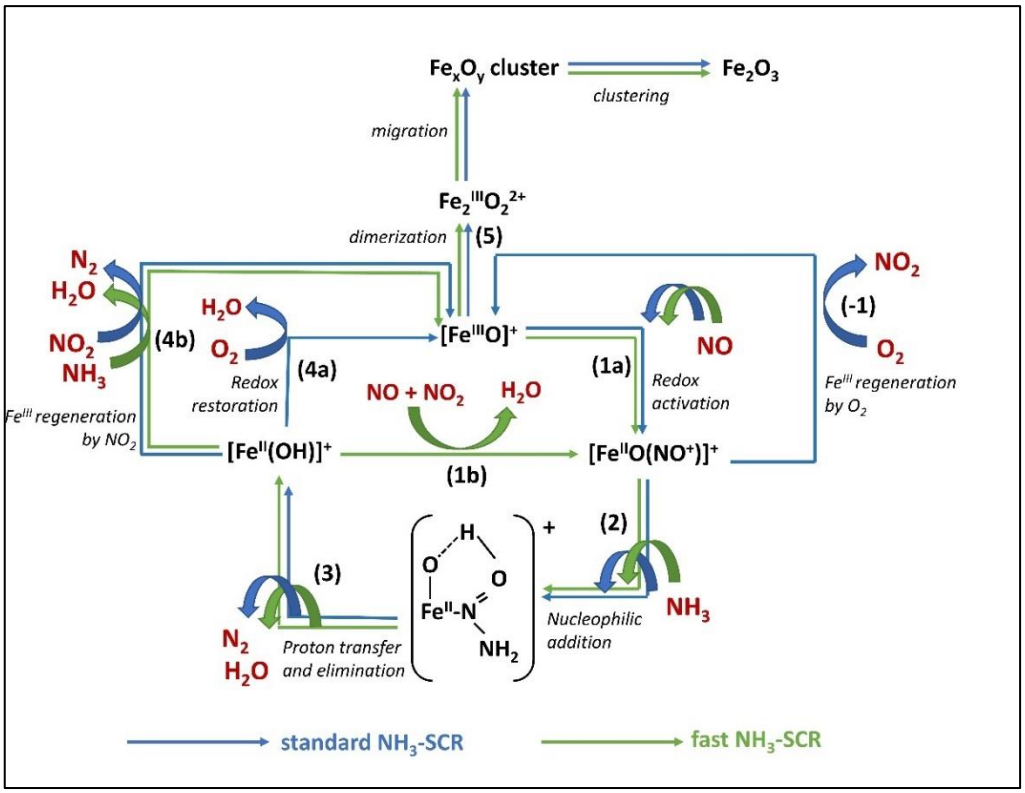

Figure 31. Schematic representation of the mechanism of standard and fast NH_3-SCR reaction over Fe-zeolites proposed by Jiang and Lobo [460]

The authors based their study on the fact that Fe forms strong complexes with NO and weak complexes with NH_3, which corresponds to Langmuir-Hinshelwood mechanism. Besides, it was assumed that iron is strongly coordinated with the framework oxygen of zeolites. Therefore, the structure and composition of zeolite can alter the ability of Fe sites to coordinate with other ligands. The possible intermediate complexes formed during NH_3-SCR on Fe-zeolites, included in the further considerations are presented in **Figure 32.**

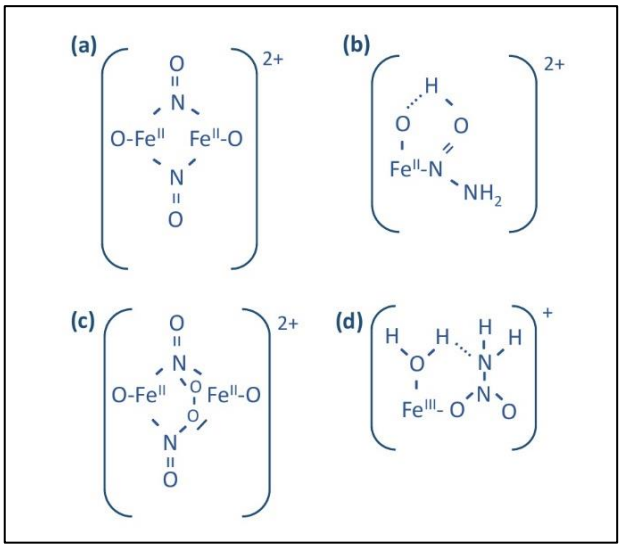

Figure 32 Intermediate complexes formed on iron-based zeolites during NH_3-SCR

NH_3-SCR over Fe-zeolites starts from the generation of dimeric complex: $[Fe^{II}O(NO^+)$-$(NO^+)OFe^{II}]^{2+}$ (showed in **Figure 32a**) with two nitrosyl groups, bridging with two Fe sites. Production of the complex is provided by the redox reaction between gas-phase NO and active sites, $[Fe^{III}O]^+$ or $[Fe^{III}(OH)_2]^+$ (reaction **1a in Figure 31**). Subsequently, nucleophilic reaction between the nitrosyl group (NO^+) of $[Fe^{II}O(NO^+)$-$(NO^+)OFe^{II}]^{2+}$ complexes and electron-rich NH_3 generates $[Fe^{II}O(N(OH))$-$NH_2]^+$ intermediates (presented in **Figure 32b),** as depicted by **reaction 2 in Figure 31.** Afterwards, H^+ attached to the oxygen atom of nitrosyl group is transferred to the oxygen bonded to iron and forms $[Fe^{III}(OH)]^+$. As a result, nitrosamide (NH_2NO) is eliminated from the complex and it decomposes thermally into N_2 and H_2O. Alternatively, the decomposition can occur on Brönsted site, as presented by **reaction 3 in Figure 31.**

Regeneration of the $[Fe^{III}O]^+$ active center or the intermediate $[FeO(NO^+)]^+$ can proceed according to several pathways, dependent on the gas composition and reaction temperature. Below 250 °C, $[Fe^{III}O]^+$ can be restored through the formation of nitrosyl bridged dimeric Fe complexes, generated by the reaction between $[Fe^{II}O\text{-}NO]^+$ complexes with gas-phase O_2, as presented by **reaction -1 in Figure 32.** This kind of mechanism is suggested due to the common formation of bridged dimeric complexes of iron, since the process is 4-electron redox reaction, unlikely to occur on one iron center. The regeneration of $[Fe^{III}O]^+$ centers, marked in **Figure 31 as (-1)** is presented in detail in **Figure 33.**

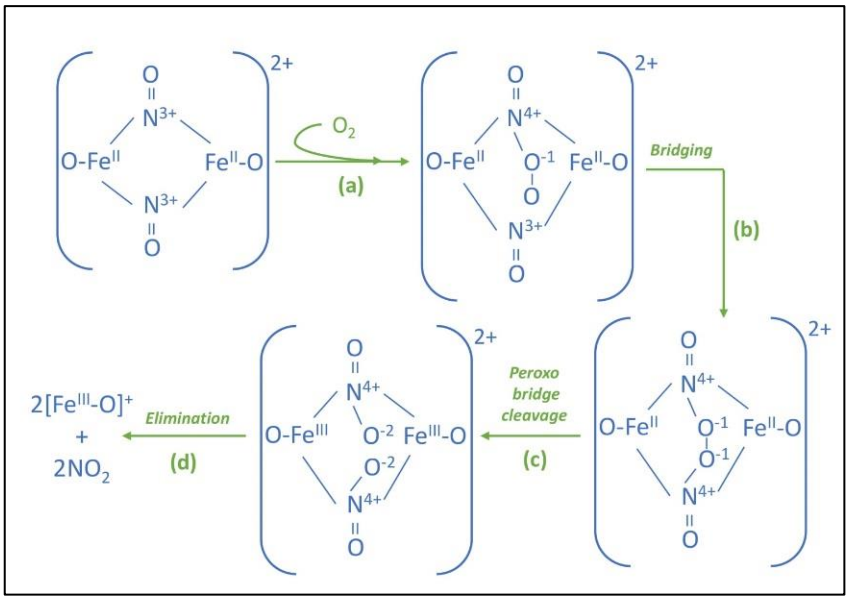

Figure 33. Elementary steps of regeneration of $[FeO]^+$ with the release of NO_2 proposed by Jiang and Lobo [460]

Typically, the regeneration pathway starts from the reaction between O_2 with the dimeric complex, $[Fe^{II}O(NO^+)\text{-}(NO^+)OFe^{II}]^{2+}$ and consequent formation of an intermediate peroxynitrite, $(N(O)O_2^-$, FeO-N(O)O_2) **(Figure 33a).** The intermediate reacts with nitrosyl group and generates a dimer with unstable N-O-O-N linkage by the transfer of two electrons of nitrogen atoms to oxygen atoms from N-O-O-N. As a consequence, the oxidation state of nitrogen atoms in nitrosyl groups is changed to 4+ oxidation state **(Figure 33b).** Afterwards, O-O bond cleaves and two Fe^{II} are oxidized to Fe^{III}, and two electrons are transferred to oxygen atoms by nitrogen atoms in nitrosyl groups **(Figure 33c).** Subsequently, two molecules of NO_2 are eliminated from the complex **(Figure 33d).** In general, in standard NH_3-SCR reaction, regeneration of Fe^{III} involves the participation of O_2 and depends on the reaction temperature. Below 250 °C, the dominant pathway of Fe^{III} regeneration is based on the oxidation of dimeric $[Fe^{II}O(NO^+)]^+$ to two $[Fe^{III}O]^+$. Therefore, Fe-zeolites which contain or form dimeric Fe species are easily regenerated below 250 °C, thus, exhibit higher reaction rates in this temperature range. In contrast, above 250 °C, the monomeric $[Fe(OH)]^+$ species are the dominant moieties. Hence, oxidation of $[Fe(OH)]^+$ to $[Fe^{III}O]^+$ is considered as the main regeneration reaction in this temperature region.

Low-temperature activity of NH_3-SCR catalysts is among the most important issues for the practical applications of the catalysts. Since Fe-zeolites exhibit high NO conversion in medium and high temperature region, various methods are studied to enhance their low-temperature activity. The efficient

way to improve catalytic performance of these materials below 300 °C is to increase NO_2/NO molar ratio to 0.5, to induce the occurrence of fast SCR reaction [457]. This effect was assigned to the altering of reaction paths by coordinating of NO_2 with Fe centers, which causes significant changes in the concentration of reacting intermediates [460].

As presented in **Figure 31,** under fast NH_3-SCR conditions, $[Fe^{II}OH]^+$ species can react with NO or NO_2 to form $[FeO(NO^+)]^+$ or regenerate $[Fe^{III}O]^+$ species **(reactions 1b** and **-1**, respectively). In the case of fast NH_3-SCR, below 250 °C, NO and NO_2 are bond to divalent $[Fe^{II}(OH)]^+$ to form $[FeO\text{-}NO]^+$ **(reaction 1 in Figure 31)**. Afterwards, $[Fe^{II}(OH)]^+$ reacts with NH_3 to directly generate N_2 and H_2O. Above 250 °C, $[Fe^{II}OH]^+$ is proposed to be oxidized by NO_2 in the presence of ammonia **(reaction 4b in Figure 31)**. The elementary steps of the reaction are given in **Figure 34.**

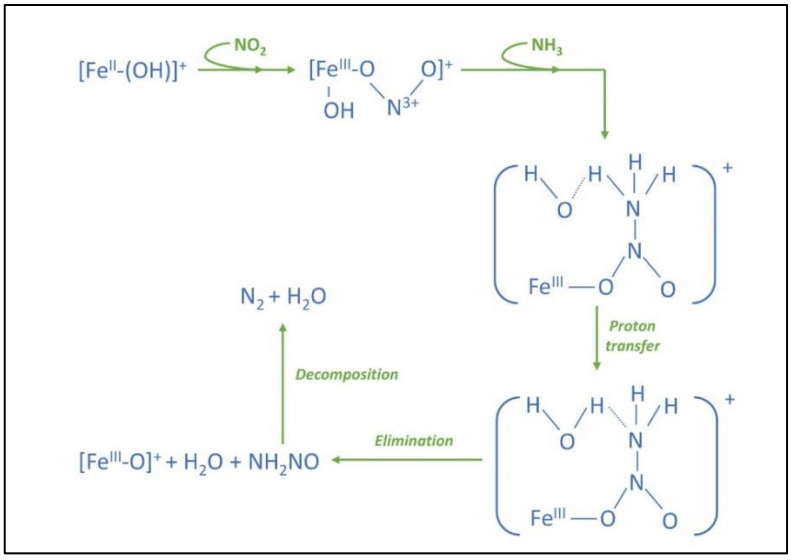

Figure 34. Elementary steps of the reaction of regeneration of $[FeO]^+$ by NO_2 in the presence of NH_3 proposed by Jiang and Lobo [460]

First step of the pathway illustrated in **Figure 34** involves coordination of NO_2 with $[Fe^{II}(OH)]^+$ to form $[Fe(OH)\text{-}NO_2]^+$, in which Fe is oxidized to +3, while nitrogen is reduced to +3. Afterwards, $[Fe(OH)\text{-}NO_2]^+$ interacts with NH_3 to form $[Fe(OH)\text{-}NO_2\text{-}NH_3]^+$, which decomposes to $[Fe^{III}O]^+$, N_2, and H_2O. Therefore, NO_2 can fasten NH_3-SCR process by the rapid regeneration of the active $[Fe^{III}O]^+$ species. The reactions described above and presented schematically in **Figures 31-33** are listed in the **Equations (101-115).**

Reaction (1a)	$[Fe^{III}O]^+ + NO \rightarrow [Fe^{II}O(NO^+)]^+$	**(101)**
Reaction (-1)	$2[Fe^{II}O(NO^+)]^+ \rightarrow [Fe^{II}O\text{-}(NO^+)_x]_2^{2+}$	**(102)**
	$[Fe^{II}O\text{-}(NO^+)_x]_2^{2+} + O_2 \rightarrow [Fe^{II}_2O_2(N_2O_4)_x(O_2)_x]^{2+}$	**(103)**
	$[Fe^{II}_2O_2(N_2O_4)_x(O_2)_x]^{2+} \rightarrow 2\,[Fe^{III}O]^+ + 2\,NO_2$	**(104)**
Reaction (1b)	$2\,[Fe^{II}(OH)]^+ + NO + NO_2 \rightarrow 2\,[Fe^{II}O]^+ + 2\,NO_2$	**(105)**
Reaction (2)	$[Fe^{II}O(NO^+)]^+ + NH_3 \rightarrow [Fe^{II}(OH)NONH_2]^+$	**(106)**
Reaction (3)	$[Fe^{II}(OH)NONH_2]^+ \rightarrow [Fe^{II}(OH)]^+ + NH_2NO$	**(107)**
	$NH_2NO \rightarrow N_2 + H_2O$	**(108)**
Reaction (4a)	$4\,[Fe^{II}(OH)]^+ + O_2 \rightarrow 4\,[Fe^{III}O]^+ + 2\,H_2O$	**(109)**
Reaction (4b)	$[Fe^{II}(OH)]^+ + NO_2 \rightarrow [Fe^{III}(OH)(NO_2)]^+$	**(110)**
	$[Fe^{III}(OH)(NO_2)]^+ + NH_3 \rightarrow [Fe^{III}(OH)NO_2NH_3]^+$	**(111)**
	$[Fe^{III}(OH)NO_2NH_3]^+ \rightarrow [Fe^{III}(H_2O)(O)(NONH_2)]^+$	**(112)**
	$[Fe^{III}(H_2O)(O)(NONH_2)]^+ \rightarrow [Fe^{III}O]^+ + NH_2NO + H_2O$	**(113)**
	$NH_2NO \rightarrow N_2 + H_2O$	**(114)**
Reaction (5)	$2\,[Fe^{III}O]^+ \rightarrow [Fe_2O_2]^{2+} \rightarrow Fe_xO_y \rightarrow Fe_2O_3$	**(115)**

One of the characteristic phenomena of fast NH_3-SCR over Fe-zeolites is formation of N_2O [461]. In general, nitrous oxide can be formed by iron-zeolite catalysts when NO_2/NO_x radio exceeds 0.5. Typically, when NH_3 and NO_2 adsorbed on the catalyst surface interact with each other to form NH_4NO_3, NO conversion is inhibited by the pore blockage. Further decomposition of ammonium nitrate species around 200 °C results in the formation of N_2O, as presented by **Equations (116-117):**

$$2\,NH_3 + 2\,NO_2 \rightarrow N_2 + NH_4NO_3 + H_2O \quad \textbf{(116)}$$

$$NH_4NO_3 \rightarrow N_2O + 2\,H_2O \quad \textbf{(117)}$$

According to the general agreement, Brönsted acid sites (Si-(OH)-Al) in zeolites are very important for the formation of NH_4^+, which interact with surface nitrates and nitrites [457]. However, Brandenberger et al. [435] observed that Brönsted acid sites are not required for the adsorption and activation of ammonia and NH_3 is rather coordinated to Lewis acid sites: Fe^{3+} and Al^{3+}. Furthermore, as already mentioned, Li et al. [462] proposed that Brönsted acid sites in Fe-zeolites participate only in the acid-catalyzed decomposition of NH_4NO_2 to N_2 and H_2O.

On the other hand, the formation of NH_4^+ intermediates on Fe-zeolites, related to the interaction between NH_3 and NO, was regarded as the key factor to understand mechanistically NH_3-SCR reaction over these materials [457–459]. Chen et al. [458] used *in situ* electrical impedance spectroscopy (IS) and diffuse reflectance infrared Fourier transform spectroscopy (*in situ* IS-DRIFTS) to investigate surface processes occurring on Fe-ZSM-5 during NH_3-SCR. The authors claimed that the activity of the catalyst between 175 and 250 °C is related to the formation of highly mobile and reactive NH_4^+ intermediates. Additionally, higher reducibility of Fe species by the interaction between NH_3 and NO resulted in the formation of higher amount of NH_4^+, which promoted the reaction rate. The schematic pathway of the formation of NH_4^+ intermediate on iron sites, resulting in the formation of N_2 and H_2O is presented in **Figure 35.**

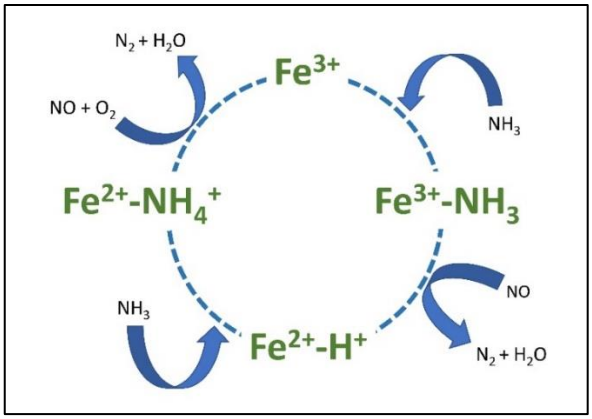

Figure 35. Schematic pathway of NH_4^+ formation in standard NH_3-SCR over Fe-ZSM-5 (based on [458])

In summary, NH_3-SCR over Fe-zeolites is a complicated process, influenced by various factors, such as reaction temperature, composition of the gas, and the produced intermediate species. The studies on the intermediates, representing different pathways of the reaction can help to evaluate the rate-determining steps of the reaction and promote the catalytic performance of Fe-zeolites in NH_3-SCR.

7.4 SO_2 poisoning of Fe-zeolites during NH_3-SCR

As described in detail in **subchapter 3.2,** sulfur oxides are among the most poisoning or even deactivating agents of NH_3-SCR catalysts working under the real operation conditions. Therefore, sulfur tolerance of metal-exchanged zeolite catalysts attracted much attention of the scientists [463–465]. In the case of zeolitic catalysts, it is commonly known that the systems with Cu are significantly less resistant to deactivation, comparing to Fe-zeolite catalysts [463,466,467].

In general, SO_2 can cause reversible and irreversible poisoning of metal-exchanged zeolite catalysts. The mechanism of poisoning with SO_2 is related to the reaction temperature, however, it is most prominent below 300 °C [85]. Additionally, it depends on the type of sulfur complexes formed during the interaction with the zeolitic framework or metal active sites [465]. Therefore, the identification of the active sites, which respond to the poisoning effect under real conditions is difficult. However, according to the general agreement, SO_2 changes the chemistry of metal active centers, simultaneously inhibiting adsorption and activation of NH_3 or NO. The types of poisoning with SO_2 are schematically presented in **Figure 36.**

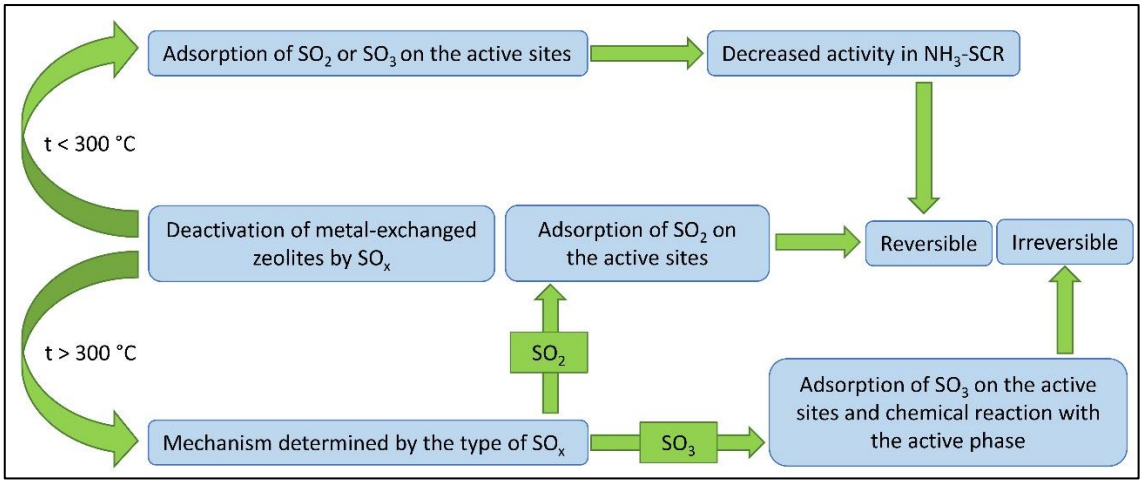

Figure 36. Possible pathways of metal-exchanged zeolites deactivation by SO_x

The strength of poisoning is also influenced by the chemistry of the zeolite. Ma et al. [468] proved that there is a significant influence of Si/(Fe + Al) molar ratio on the response to SO_2 present in the gas and zeolites of higher acidity are more resistant to the poisoning by SO_2. Additionally, lower activity resulted from the competitive adsorption of NO and SO_2 on the active centers. In general, in the presence of SO_2 low temperature activity is decreased by the deposition of surface ammonium sulfites and sulfates. In high temperature region, corresponding to the decomposition temperature of the sulfate species, the activity of the materials increases. Therefore, Fe-zeolites are reversibly poisoned with SO_2. The increased NO conversion in high temperature region was explained in 2000 by Long et al. [469] on the example of Fe-ZSM-5. The authors pre-treated the catalyst with the mixture of SO_2 and O_2 in He and noticed oxidation reaction of sulfur dioxide to SO_3. Consequent formation of iron sulfates on the catalyst surface resulted in the generation of S=O covalent bond with strong affinity to electrons.

Therefore, Lewis acidity of sulfated iron species enhanced the strength of Lewis acid sites. What is more, adsorption of H_2O on Lewis sites led to the formation of Brönsted acidity, which increased NH_3 adsorption capacity of the catalyst.

According to the above-mentioned, considering the influence of SO_2 on Fe-zeolite catalysts, the presence of H_2O in the gas cannot be omitted. In general, water is a typical component of flue gas, which shows a significant impact on the behavior of metal-exchanged zeolite catalysts. It competes with NH_3 to be adsorbed on the active sites and changes acidic properties of the materials [470]. Co-existence of SO_2 and H_2O in the exhausts causes formation of sulfuric acid (H_2SO_4) or other sulfur complexes. Liu et al. [465] investigated the correlation between catalytic activity of Fe-ZSM-5 and its exposure to the mixture of SO_2 and H_2O in the high temperature region of NH_3-SCR (> 500 °C). The authors observed that the poisoning effect of the gas impurities followed the order of $H_2O + SO_2 > H_2O \geq SO_2$. Basing on DFT calculations, it was proposed the deactivation pathway of the catalyst in the simultaneous presence of SO_2 and H_2O in the exhausts. First of all, water molecules adsorb and dissociate on the catalyst surface and generate hydroxyl groups, with a relatively low energy barrier, according to **Equation (118):**

$$[FeO]^+ + OH^- \rightarrow [FeO\text{-}OH] \qquad \textbf{(118)}$$

The second step involves sulfation of the surface through the adsorption of SO_2 on the ligand oxygen from Fe-O. Furthermore, the atom of H is captured by S=O bond derived from sulfur dioxide. Finally, chemically stable chelating bidentate HSO_4^-/SO_4^{2-} are formed on Fe-OH, according to **Equation (119):**

$$[FeO\text{-}OH] + SO_2 \rightarrow Fe\text{-}HSO_4 \qquad \textbf{(119)}$$

What is more, the studies confirmed that metal cations in zeolites increased the resistance to dealumination caused by the hydrolysis of Al-O bond and dislodgement of aluminum to non-framework positions after adsorption of H_2O. The mechanism of SO_2 and H_2O poisoning proposed by the authors is illustrated schematically in **Figure 37.**

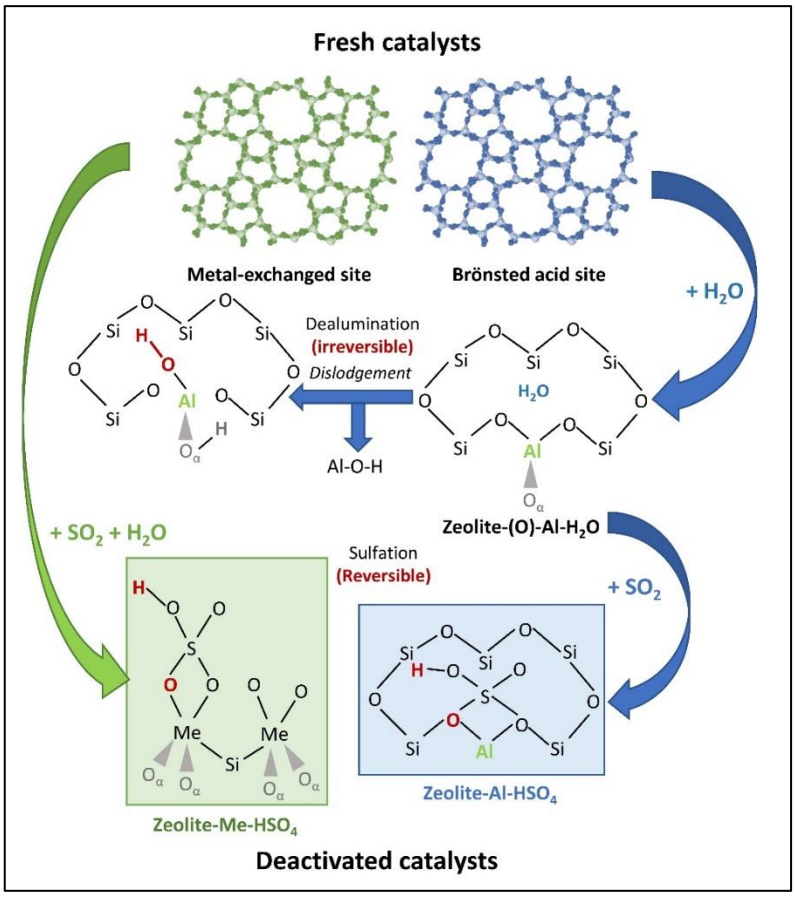

Figure 37. Schematic illustration of the poisoning mechanism of metal-exchanged zeolites with SO_2 and H_2O proposed by Liu and co-workers [465]

7.5 Promoters of Fe-zeolite catalysts of NH_3-SCR

Fe-zeolites promoted with Cu

Basing on the literature research on iron-exchanged zeolites, these materials are very promising high-temperature catalysts of NH_3-SCR. However, the improvement of their low-temperature activity is still a matter of ongoing research. In contrast to Fe, copper-exchanged zeolite catalysts exhibit high NO conversion rates below 300 °C [272,365,471]. Considering the difference between the activity of Fe- and Cu-zeolites in NH_3-SCR at various temperatures, combination of these two metals can significantly broaden the operating window of the catalysts [472]. The exemplary Fe/Cu-zeolite catalysts of NH_3-SCR with their catalytic performances are listed in **Table 11.**

The synergistic effect of Fe and Cu and their satisfactory performance as NH_3-SCR catalysts was confirmed for many zeolites, including ZSM-5 [473–475], zeolite beta [476,477], chabazite [474], SSZ-13 [345,478], or SAPO-34 [472]. In general, there are three main possibilities to combine copper-

and iron in zeolites: dual-layer catalysts, dual-brick catalysts, or zeolites containing the mixture of Cu and Fe.

Dual-layer catalysts of various configurations and parameters have been widely studied for the practical applications of metal-exchanged zeolites in NH_3-SCR [474,479]. Metkar et al. [474] conducted modeling NH_3-SCR studies over dual-layer Cu-CHA and Fe-ZSM-5, testing various sequential arrangement and thickness of the layers. It was found that over 90% of NO conversion was obtained when the catalytic system consisted of thinner layer of Fe-ZSM-5 on the top of thicker layer of Cu-CHA on the bottom. Such effect was explained by lower rate of NH_3 oxidation in the range of 400-450 °C for Fe-ZSM-5, which also determined its enhanced activity in high temperature range. Besides, the authors found that the increase of NO_2/NO_x ratio to 1 inducted fast NH_3-SCR, enhancing the overall catalytic activity, especially that of Fe-ZSM-5. On the other hand, the excess of NO_2 resulted in the formation of ammonium nitrate and N_2O, decreasing N_2 selectivity. In the same study, the authors compared dual-layer and dual-brick Cu-Fe catalysts and claimed that the former systems are superior due to better distribution of Cu and Fe washcoats within the monolith. On the contrary, the results obtained by Shakya et al. [479] indicated that dual-brick catalysts outperformed dual-layer ones. However, the effect can be observed only in the case of low values of space velocity.

The alternative for the above-mentioned systems are single-layer zeolites, thus, doped with the mixture of Fe and Cu of various ratios. These catalysts can be prepared using conventional methods, such as wet ion-exchange, solid-state ion-exchange, one-pot hydrothermal synthesis, or impregnation [480]. The synergistic effect of Fe and Cu and satisfactory catalytic performance is ascribed to their broad temperature window. Additionally, deposition of iron on the outer parts of zeolite crystals reduces intracrystalline mass-transfer limitations of Cu-zeolites [478].

Combination of Cu and Fe in zeolite-supported catalysts of NH_3-SCR was studied by Sultana et al. [473]. The authors observed that the addition of Cu to Fe-ZSM-5 enhanced reducibility of iron species, simultaneously shifting the NH_3-SCR temperature window to lower range. In fact, the presence of easily reducible metal species improves low temperature activity of the catalysts, however, it also facilitates oxidation ability. Therefore, it is important to control the amount of copper incorporated into Fe-zeolites, since its excess can result in the undesired NH_3 oxidation. It was found that not only copper,

but also iron loading plays an important role in the overall catalytic activity of Cu-Fe bimetallic zeolite catalysts. Wan and co-workers [345] proved that the increase of Fe content caused gradual disappearance of isolated Cu^{2+} species and formation of highly oxidizing Fe_2O_3 aggregates.

The interactions between Cu and Fe in NH_3-SCR was explained in detail by Zhang et al. [478] on the example of small-pore zeolite, SSZ-13. HRTEM, EPR, and H_2-TPR studies confirmed that copper was present in the sample in the form of monomeric Cu^{2+} ions, coordinated to three atoms of oxygen and provided low-temperature activity of the material. On the other hand, UV-Vis and EPR spectroscopy indicated that high-temperature activity was determined by Fe^{3+} monomers. Additionally, basing on the results of XPS, it was found that Cu^{2+} sites were located in the internal part of the zeolite crystals, while Fe^{3+} moieties occupied the outer surface of the material, which had a crucial influence on the selectivity of the catalyst to nitrogen.

Table 11. NH_3-SCR activity of bimetallic Fe- and Cu-zeolite catalysts

Catalyst	Metal loading	Preparation procedure	Temperature window	NO conversion	Ref.
Fe-Cu-ZSM-5	4 wt.% Fe 1 wt.% Cu	solid state ion exchange	250-475 °C	> 90%	[473]
Fe-Cu-BEA	1 wt.% Fe 1 wt.% Cu	wet impregnation	130-430 °C	70-80%	[476]
Fe-Cu-SSZ-13	0.09 wt.% Fe 0.13 wt.% Cu	one-pot synthesis of Cu-SSZ-13, ion-exchange of Cu-SSZ-12 with Fe precursor	200-600 °C	> 90%	[478]
Fe-MOR mixed with Cu-SAPO-34	3.7 wt.% Fe 0.75 wt.% Cu	ion-exchange of the zeolite with Fe or Cu precursor, mechanical mixing of the obtained zeolites in the weight ratio of 50:50	200-450 °C	> 80%	[472]

Fe-zeolites promoted with Ce

The promoting effect of cerium oxide (CeO_2) on the activity of metal-exchanged zeolite catalysts in NH_3-SCR process has been confirmed by the number of research [481–483]. CeO_2 is commonly used

as the promoter of Three Way Catalyst (TWC), which aims to oxidize CO and hydrocarbons and eliminate NO_x from the exhausts produced by internal combustion engine [484].

Although it was confirmed that pure CeO_2 shows relatively poor NH_3-SCR (around 40%) [485], ceria in metal-exchanged zeolite catalysts exhibits outstanding oxygen storage capacity, facilitates the formation of acid sites, and improves redox properties [481]. The oxygen storage capacity of ceria can be explained by the fact that the stoichiometric cubic structure of CeO_2 can release the mobile oxygen under reducing conditions. On the other hand, under oxidizing conditions, the partially reduced ceria can store oxygen in the vacancies produced under reducing conditions [481]. The reduction of Ce^{4+} to Ce^{3+} and formation of liable oxygen vacancies is schematically illustrated in **Figure 38.**

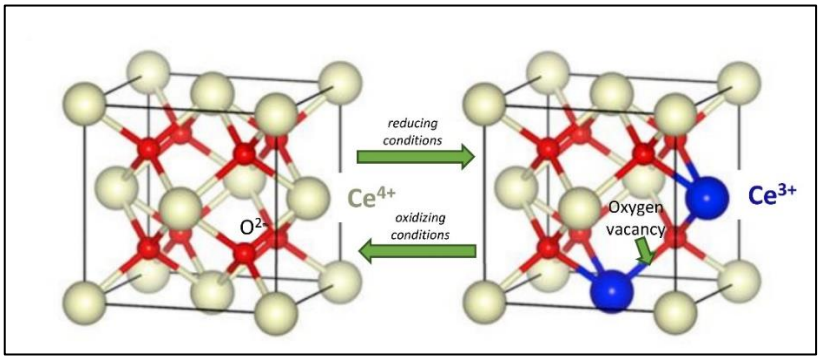

Figure 38. Cell structure of the stoichiometric CeO_2 (left) and CeO_2 with oxygen vacancies (right) (based on [481])

In general, ceria in the supported catalysts can be used as the active phase, promoter, or as the support [481]. In fact, as the catalyst support, CeO_2 exhibits many advantages, for example low reduction temperature or prominent adsorption of NO and NH_3 during the reaction. Nevertheless, ceria-supported catalysts are restricted by sintering and smaller specific surface area, comparing to other materials, e. g. zeolites. Therefore, recently, CeO_2 has gained an increasing attention as the potential component of metal-modified zeolites [482,483,486–489].

One of the first studies on the influence of Ce on the activity of zeolite catalysts in NH_3-SCR was presented by Carja et al. [488]. The authors proved that the addiction of Ce shifted the temperature window of Fe-ZSM-5 from 350 to 230 °C, with simultaneous N_2 selectivity of ca. 100% in the entire temperature range. This effect was explained by the formation of "Fe,Ce-oxo" cations, built into the Fe-O-Ce bridges, in which both metals reduce at similar temperature. Additionally, the stability tests indicated stable operation of the catalysts, even in the presence of SO_2 and H_2O. Further research

published in 2016 by Begum et al. [482] covered comprehensive comparison of the impact of various lanthanide metals on the catalytic activity of Fe-ZSM-5. The authors proved that Ce-promoted catalyst exhibited the best catalytic performance with NO conversion exceeding 95% within 300-500 °C. The incorporation of Ce resulted in the lowering of the energy barrier of the reaction by the formation of ultra-strong Lewis sites and Brönsted sites of moderate strength. Both of the above-mentioned studies involved introduction of the active phase by reflux method, which provided uniform dispersion of Fe and Ce within the zeolite. Alternative attempt to the catalyst synthesis was proposed by Chen et al. [489]. The authors prepared hierarchical Fe- ZSM-5@CeO_2 with inner iron phase and outer CeO_2 phase by the coating of the zeolite with polydopamine shell. Decoration of Fe-ZSM-5 with CeO_2 resulted in higher catalytic activity in comparison to the material prepared by mechanical mixing of Fe-zeolite with cerium oxide. Additionally, CeO_2 on the outer surface promoted the conversion of NO to NO_2, facilitating fast SCR reaction. Besides, the surface Ce^{4+} and active oxygen species adsorbed and activated NO, which selectively reacted with NH_3 according to Langmuir-Hinshelwood mechanism. Apart from iron-exchanged ZSM-5, the promoting effect of Ce was also confirmed for Cu-zeolites of CHA structure, such as Cu-SAPO-34 [487] and Cu-SSZ-13 [483]. One of the novel attempts to prepare the CeO_2-promoted material of zeolitic properties was presented by Yan et al. [486]. The authors synthesized Ce-$Si_5Al_2O_x$ catalyst derived from ultrasmall nanozeolite EMT and found that NO conversion for the material exceeds 95% in the temperature region of 270-540 °C. The satisfactory results were ascribed to the highly ordered bonding between aluminosilicate and cerium species, built into the structure.

The studies on the application of CeO_2 as the promoter indicated that ceria enhances the overall performance of the catalytic system. However, most of the studies have overlooked mixed oxides containing CeO_2 and there is still a gap in the research on the influence of ceria on metal-modified zeolites. Therefore, more analysis in this field is highly required. The NH_3-SCR catalytic performance of various Ce-promoted zeolites is summarized in **Table 12.**

Table 12. NH_3-SCR activity of metal-exchanged zeolite catalysts promoted with Ce

Catalyst	Metal loading	Preparation procedure	Temperature window	NO conversion	Ref.
Fe-Ce-ZSM-5	1.6 wt.% Fe 2.5 wt.% Ce	chemical vapor deposition	250-530 °C	> 80%	[488]
Fe-Ce-ZSM-5	0.7 wt.% Fe 0.5 wt.% Ce	reflux method [a]	250-500 °C	> 90%	[482]
Fe-ZSM-5@CeO_2	no data	polymerization of dopamine over Fe-ZSM-5, addition of Ce precursor to the synthesis pot	210-400 °C	> 80%	[489]
Cu-Ce-SSZ-13	4.0 wt.% Cu 1.0 wt.% Ce	incipient wetness impregnation	190-500 °C	> 80%	[483]
Cu-Ce-SAPO-34	6.8 wt.% Cu 0.4 wt.% Ce	one-pot synthesis	200-475 °C	> 80%	[487]

[a] dissolving of the metal precursor in 80 cm^3 of acetonitrile, addition of 5 g H-ZSM-5, stirring in a refluxing flask for 24 h, filtration, drying, calcination

7.6 Fe-zeolite catalysts for N_2O decomposition

Nitrous oxide (N_2O) has been recognized as the third most hazardous greenhouse gas with a global warming potential of ca. 310 times higher than that of carbon dioxide on a per mass basis. Therefore, besides the control of CO_2 emission, the abatement of nitrous oxide generation is also of great importance [490]. Nitrous oxide is produced mainly from anthropogenic sources, for instance the production of nitric and adipic acid or combustion of fossil fuels in stationary and mobile sources. Additionally, N_2O is responsible for the production of NO_x and ozone-layer depletion [491].

Nowadays, direct decomposition to N_2 and O_2 (called deN_2O) is considered to be the most efficient method to eliminate N_2O emission from stationary and mobile sources [490,492]. The reaction of N_2O decomposition is described by **Equation (120):**

$$2\ N_2O \rightarrow 2\ N_2 + O_2 \qquad \textbf{(120)}$$

At standard conditions, deN_2O process is highly endothermic and the activation energy for N_2O to be thermally decomposed is about 250 J · mol^{-1}. Thus, the reacting gas mixture has to be heated at least to 1000 °C to induce the process in the absence of the catalyst [434]. The most frequently proposed mechanism of N_2O decomposition is represented by **Equations (121-123)** (where ♣ represents an active site) [493]**:**

$$N_2O + ♣ \rightarrow N_2 + ♣\text{-}O \quad \textbf{(121)}$$

$$♣\text{-}O + N_2O \rightarrow N_2 + O\text{-}♣\text{-}O \quad \textbf{(122)}$$

$$O\text{-}♣\text{-}O \rightarrow ♣\text{-} + O_2 \quad \textbf{(123)}$$

In the mechanism, at least two active centers are required and the rate-determining step depends on the temperature region. The combined computational and experimental study conducted by Guesmi et al. [494,495] showed that in the presence of Fe-catalyst supported on zeolite, at low temperature, the reaction is controlled by the desorption of N_2, while above 430 °C the rate-determining step is N_2O dissociation. This mechanism was confirmed to occur by the transient response experiments, which showed that N_2 appears before O_2 in the temperature region of 500-575 °C [496].

Among various catalysts investigated for N_2O decomposition, Fe-containing zeolites are particularly advantageous, especially due to and their low cost and durability in the presence of O_2, NO, SO_2, or H_2O [490]. The N_2O decomposition rates over iron-exchanged zeolites is also determined by the zeolite topology and distribution of the active sites. Sklenak and co-workers [497] compared the catalytic performance of Fe-ferrite, Fe-ZSM-5, and Fe-beta zeolites and found that the activity order is as it follows: Fe-ferrite >> Fe-beta > Fe-ZSM-5. The superiority of Fe-ferrite was due to the accommodation of Fe^{2+} in β positions of two adjacent six-member rings. Additionally, the authors claimed that the β sites have to be surrounded by two atoms of Al in order to provide appropriate distribution of the active centers. On the other hand, the lowest activity of Fe-ZSM-5 was explained by unfavorable geometrical arrangement of two adjacent α sites and low concentration of Al surrounding the iron centers. The geometric requirements for the adsorption and activation of N_2O on Fe-exchanged zeolites have been also confirmed by Bols et al. [498].

Recently, several studies have found that layered zeolites of MWW topology modified with Fe are active in N_2O decomposition. Grzybek et al. [434] observed that Fe-MCM-56 exhibits 80% of N_2O

conversion at 600 °C. The behavior of the material in the reaction was ascribed to the presence of oligomeric iron species in α positions and generation of α oxygen, bonded to iron in the complexes. Similar results on the form of active iron sites were obtained by Rutkowska et al. [499] for MCM-22. The authors demonstrated that the formation of highly active oligocations was favored by the ion-exchange with $[Fe_3(OCOCH_3)_7OH \cdot 2\ H_2O]NO_3$.

Apart from zeolite topology, the activity of Fe-containing zeolites is determined by the type of iron species. According to Sklenak et al. [497], the presence of two adjacent Fe^{2+} is essential to provide high conversion of N_2O. At low concentrations of iron, isolated Fe^{2+}, $[FeO]^+$, and $[Fe(OH)_2]^+$ sites were confirmed to be the most active [500], while the multinuclear iron sites are prominent for high concentrations of the metallic phase [501]. The comprehensive explanation of the catalytic behavior of mononuclear and binuclear iron sites incorporated into ZSM-5 zeolite was investigated by DFT calculations and microkinetic modeling performed by Pidko et al. [502]. The superior activity of the binuclear sites is related to extraframework oxygen atoms placed near binuclear iron species, available for N_2O adsorption and activation. The importance of oligomeric iron species in catalytic decomposition of N_2O was also confirmed by Zhang et al. [491]. The authors found that the activity of Fe-SAPO-34 prepared by solid-state ion exchange is correlated with the precursor of iron, which is in agreement with the research of Rutkowska et al. [499]. The catalytic activity of the selected Fe-containing zeolites in N_2O decomposition is presented in **Table 13.**

Table 13. Catalytic activity of Fe-exchanged zeolite catalysts in catalytic N_2O decomposition

Catalyst	Metal loading	Preparation procedure	Temperature window	N_2O conversion	Ref.
Fe-ZSM-5	1.71 wt.%	solid state ion exchange	375-550 °C	> 90%	[451]
Fe-beta	0.89 wt.%	incipient wetness impregnation	400-600 °C	> 95%	[500]
Fe-SAPO-34	3.02 wt.%	solid state ion exchange	525-600 °C	> 80%	[491]
Fe-MCM-56	0.23 wt.%	acid treatment of MCM-56 with HNO_3, adsorption from the aqueous solution of FeC_2O_4	550-600 °C	70-80%	[434]
Fe-MCM-22	12.67 wt.%	ion-exchange with $[Fe_3(OCOCH_3)_7OH \cdot 2\ H_2O]NO_3$	475-600 °C	> 80%	[499]
Fe-ITQ-2	9.79 wt.%	ion-exchange with $[Fe_3(OCOCH_3)_7OH \cdot 2\ H_2O]NO_3$	500-600 °C	> 95%	[499]

Chapter II: Motivation and objectives of the studies

As it was highlighted and described in detail in the *Literature review* section, the increasing emissions of harmful contaminants resulting from the combustion of fossil fuels are one of the most significant environmental problems. Nitrogen oxides, which are primarily emitted from power plants, chemical industries, and transportation are considered as the main source of acid rain, photochemical smog, or ozone layer depletion. Moreover, their presence in the atmosphere generates global health implications, lowering the quality of life. In fact, selective catalytic reduction with ammonia, which is one of the most effective technologies for NO_x removal, can help to solve the problem of excessive emissions. Nevertheless, due to the important limitations related to the commercial catalysts of NH_3-SCR, it is required to find a new, active, ecological-friendly, and low-cost substitutive catalytic system.

Among the number of candidates for the precursors of the novel catalyst of NH_3-SCR, iron-modified zeolites are the most promising. According to the literature studies, there are several directions for the development of highly-efficient Fe-based zeolite catalysts for NH_3-SCR:

- the choice of the appropriate topology of the supporting zeolite to optimize the distribution of metal species and increase their stability, which would eventually broaden the NH_3-SCR temperature window, improve stability of catalysts, and resistance to poisoning with SO_2,
- the adjustment of the preparation procedure/modification method of the supporting zeolite, to provide high dispersion of the active phase within the zeolitic framework,
- the improvement of the catalytic performance by the introduction of another metal in a form of chemical or mechanical promoter.

Despite the interest in zeolite-supported catalysts, there are only few studies, which have briefly considered application of natural clinoptilolite or layered zeolites of MWW family as the precursors of NH_3-SCR catalysts. Therefore, the research tasks described in this work involved:

- preparation of Fe-catalysts supported on natural zeolite (clinoptilolite) or synthetic zeolite (MCM-22) by various methods (co-precipitation, adsorption from the solution, incipient wetness impregnation),

- promotion of the most active catalysts with copper or cerium introduced by incipient wetness impregnation,
- physicochemical characterizations of the supports and the selected catalysts,
- catalytic tests performed over the selected fresh and SO_2-poisoned catalysts using model gas mixture,
- time-on-stream stability tests of the selected catalysts in the presence of SO_2 in the model gas mixture.

The above-mentioned experiments aimed to:

- determine if heulandite-type structure of natural zeolite (clinoptilolite) or MWW-type structure (MCM-22) provides more advantageous distribution of iron for successful elimination of nitrogen oxides via NH_3-SCR and low emission of N_2O during the reaction,
- find the most catalytically-beneficial procedure to modify the zeolitic structure with iron,
- investigate the effect of copper or cerium on the physicochemical features and thus, catalytic performance of the selected Fe-catalysts,
- examine the catalytic behavior of the selected catalysts after poisoning or in the presence of SO_2 in the model gas mixture.

Chapter III: Experimental part

1. Methodology of the work

The experimental part of the presented studies includes synthesis of the new catalysts of selective catalytic reduction of nitrogen oxides with ammonia (NH_3-SCR), supported on natural or synthetic zeolite. The representative of natural zeolite used in the study contained 87 wt.% of clinoptilolite phase. The representative of the synthetic material was layered zeolite, MCM-22 belonging to the MWW family, prepared by hydrothermal synthesis. The natural and the synthetic zeolites were protonated and modified with transition metals using various methods.

The preparation of the catalysts started from transformation of the zeolites into hydrogen or sodium form using hydrochloric acid (HCl) in the case of clinoptilolite and sodium nitrate ($NaNO_3$) in the case of MCM-22. Despite the interest in the application of zeolites in NH_3-SCR, any of the conducted studies involved the analysis and comparison of the catalytic performance of Fe-clinoptilolite and Fe-MCM-22, prepared by various methods, in the reaction. Therefore, the zeolites were modified with iron, using three different methods:

- co-precipitation,
- adsorption from the solution,
- incipient wetness impregnation.

The intended concentration of iron in the catalysts was 5 wt.%. The investigation of three various procedures of iron deposition aimed to determine the method, which provided the most uniform and beneficial distribution of Fe in clinoptilolite and MCM-22. Besides, it was analyzed which zeolite (natural or synthetic) provides more advantageous support for Fe species.

Basing on the fact, that copper and iron exhibit synergistic behavior as bimetallic catalysts of NH_3-SCR, Fe-catalysts were promoted with Cu. On the other hand, to date, any of the published studies addressed the impact of Ce on the catalytic performance of Fe-clinoptilolite and Fe-MCM-22 in NH_3-SCR. Thus, the materials were doped with 1 wt.% of Cu or 0.7 wt.% of Ce by incipient wetness impregnation, in order to compare their catalytic performance in NH_3-SCR.

The physicochemical properties of Fe-catalysts and the catalysts promoted with Cu or Ce were analyzed using adequate instrumental techniques, such as: inductively coupled plasma atomic emission spectrometry (ICP-AES), X-ray diffraction (XRD), scanning electron microscopy (SEM), transmission electron microscopy in various modes (BF - bright-field, HAADF - high angle-annular dark field, HR - high resolution), N_2 adsorption-desorption studies at 77 K, temperature-programmed desorption of ammonia (NH_3-TPD), temperature-programmed reduction with hydrogen (H_2-TPR), thermogravimetry (TGA), Fourier transform infrared spectroscopy (FT-IR), X-ray photoelectron spectroscopy (XPS), and diffuse reflectance ultraviolet-visible spectroscopy ultraviolet-visible spectroscopy (UV-vis-DRS).

Catalytic performance of the catalysts in NH_3-SCR was investigated in the temperature range of 150-450 °C using model gas mixture, consisting of equal amounts of ammonia and nitrogen oxide, adequate amount of oxygen, and helium as an inert.

Since SO_2 is one of the most adverse gases present in the industrial exhausts, it is indispensable to examine resistance of the catalysts on its poisoning effect. Therefore, the materials, which exhibited the best catalytic performance in NH_3-SCR were poisoned with SO_2 and tested in NH_3-SCR. Moreover, selected materials were subjected to the stability "time-on-stream" catalytic tests using model gas mixture containing sulfur dioxide.

2. Synthesis of the catalysts

2.1 Modification of the natural clinoptilolite

Natural, micronized Ukrainian zeolite, consisting of 87 wt.% clinoptilolite (Calaya, Laboratorium Cosmeceuticum, Poland) was the precursor of natural zeolite-supported catalyst considered in the investigations. The chemical composition of the material (determined by X-ray fluorescence analysis) was as it follows: 0.8 wt.% of Na_2O, 0.8 wt.% of MgO, 12.1 wt.% of Al_2O_3, 74.7 wt.% of SiO_2, 2.1 wt.% of Fe_2O_3, 0.04 wt.% of SO_3, 3.2 wt.% of K_2O, 3.7 wt.% of CaO, 0.2 wt.% of TiO, and 0.07 wt.% of MnO. The sample of non-modified clinoptilolite was labelled as **Clin**. The raw zeolite was transformed into protonated form using hydrochloric acid (HCl) (36-38 wt.%, POCH), diluted to 15 wt.%. Hydrogenation procedure was conducted for 2 hours, under stirring conditions, at room temperature. Protonation was repeated three times in order to provide high level of ion-exchange with hydrogen

cations. Subsequently, the material was washed with distilled water until the complete removal of chloride anions (Cl^-). The presence of Cl^- was controlled by the addition of few drops of $AgNO_3$ to the residual filtrate. Afterwards, H-clinoptilolite was dried at 100 °C in air. The protonated clinoptilolite was labelled as **H-Clin**.

2.2 Synthesis of MCM-22

MCM-22 with Si/Al ratio of ca. 12 was obtained according to the procedure described by Corma et al. [376]. The molar composition of the synthesis gel was described by the formula **(124):**

$$\mathbf{SiO_2 : 0.02\ Al_2O_3 : 0.5\ HMI : 0.09\ NaOH : 45\ H_2O} \qquad \mathbf{(124)}$$

The synthesis mixture was prepared using sodium hydroxide (NaOH) (Sharlab), sodium meta-aluminate ($NaAlO_2$) (56% Al_2O_3, 37% Na_2O) (Carlo Erba Reagents) as the source of aluminum, Aerosil 200 (Evonik Rohm Gmbh) as the source of silica, hexamethyleneimine (HMI, 98 wt.%) (Sigma Aldrich, Merck KGaA) as the structure-directing agent, and deionized water. Typically, 0.375 g of NaOH and 0.375 g of $NaAl_2O_3$ were dissolved in 81.71 g of deionized water and stirred for 5 minutes at room temperature. Afterwards, 6 g of Aerosil 200, was slowly added to the mixture under stirring. Finally, 4.96 g of HMI was dropwise introduced into the solution and the resulting gel was mixed for 2 h. The obtained gel was crystallized in a teflon-lined, stainless-steel autoclave under rotation (60 rpm) at 150 ºC for 7 days. The solid product was filtered, washed several times to pH ca. 7.0, and dried overnight at 100 ºC in air. Finally, the material was calcined at the following temperature ramps: 100 ºC for 2h, 150 ºC for 2.5 h, 350 ºC for 3 h, and 580 ºC for 3 h. Before modification with iron, MCM-22 was rinsed several times with 0.04 M solution of $NaNO_3$ (Acros Organics) with the wt.% ratio of solid to liquid = 1/150. Afterwards, the Na-MCM-22 was dried overnight at 60 °C. The obtained support was labelled as **MCM22**.

2.3 Modification of the zeolites with iron

The zeolitic catalysts precursors were modified with iron by the post-synthesis procedures: co-precipitation, adsorption from the solution, and incipient wetness impregnation. The investigated

samples with their description and corresponding codes, used in the further chapters of the thesis are collected in **Table 14.**

2.3.1 Co-precipitation method

Co-precipitation procedure was adapted from the experiments carried out by Świderska-Dąbrowska et al. [297]. 5 g of the zeolitic support was mixed with the aqueous solution of 0.05 M $FeSO_4$ (Acros Organics) for 4 h at 50 °C and pH ca. 3 (adjusted using 1 M H_2SO_4). The amount of the Fe^{2+} solution was calculated adequately to precipitate 5 wt.% of the active phase into the structure of the catalysts. Afterwards, pH of the solution was elevated by the dropwise addition of 25 vol.% of aqueous solution of ammonia ($NH_{3\,(aq)}$). After that, the alkaline solution was stirred for 1 h. Subsequently, Fe-modified solids were filtered and washed with 500 cm^3 of distilled water. The obtained materials were dried overnight at 100 °C in air and then calcined in a muffle furnace, in air at 500 °C for 2 h. The zeolites modified with iron by co-precipitation method were labelled as **FeClin cop** and **FeMCM22 cop**, for natural and synthetic zeolite, respectively.

2.3.2 Adsorption from the solution method

Adsorption from the solution method was performed using aqueous solution of 0.05 M $Fe(NO_3)_3 \cdot 9\ H_2O$ (POCH). The amount of the Fe^{3+} solution used for the modification was calculated adequately to introduce 5 wt.% of the active phase into the structure of the zeolites. Typically, 5 g of the zeolite was stirred in the solution of iron nitrate at 60 °C for 24 h. Afterwards, the material was filtered, washed with distilled water, and dried overnight at 100 °C in air. Subsequently, Fe-zeolites were calcined in a muffle furnace, in air at 400 °C for 4 h. The zeolites modified with iron by adsorption from the solution method were labelled as **FeClin ads** and **FeMCM22 ads**, for natural and synthetic zeolite, respectively.

2.3.3 Incipient wetness impregnation method

Incipient wetness impregnation method was carried out using $Fe(NO_3)_3 \cdot 9\ H_2O$ (POCH) dissolved in deionized water. The adequate amount of the solution of the concentration providing 5 wt.% of the active phase in the zeolite was added dropwise on 5 g of the zeolitic support. After that, the material was carefully mixed with a spatula for several times and dried overnight at 100 °C in air.

Subsequently, Fe-modified zeolites were calcined in a muffle furnace, in air at 400 °C for 4 h. The zeolites modified with iron by incipient wetness impregnation method were labelled as **FeClin impr** and **FeMCM22 impr**, for natural and synthetic zeolite, respectively.

2.4 Modification of the catalysts with copper

In order to investigate the influence of copper on the catalytic properties of catalysts which exhibited the best catalytic performance, the materials were promoted with 1 wt.% of Cu using $Cu(NO_3)_2 \cdot 3\ H_2O$ (Acros Organics). Typically, the adequate amount of the aqueous solution of Cu^{2+} ions was introduced into Fe-modified zeolites by incipient wetness impregnation method. After that, the materials were carefully mixed with a spatula for several times and dried overnight at 100 °C in air. Subsequently, Cu-promoted catalysts were calcined in a muffle furnace, in air at 400 °C, for 4 h. The catalysts promoted with copper were labelled as **FeCuClin cop** and **FeCuMCM22 ads**.

2.5 Modification of the catalysts with cerium

In order to investigate the influence of cerium on the catalytic properties of the selected samples which exhibited the best catalytic performance, the materials were promoted with 0.7 wt.% of Ce using $Ce(NO_3)_3 \cdot 6\ H_2O$ (Acros Organics). Typically, the adequate amount of the aqueous solution of Ce^{3+} ions was introduced into Fe-modified zeolites by incipient wetness impregnation method. After that, the materials were carefully mixed several times with a spatula and dried overnight at 100 °C in air. Subsequently, Ce-promoted catalysts were calcined in a muffle furnace, in air at 400 °C, for 4 h. The catalysts promoted with cerium were labelled as **FeCeClin cop** and **FeCeMCM22 ads.**

Table 14. List of the investigated catalysts with their descriptions and corresponding codes

Sample code	Description of the sample
Clin	Non-modified natural zeolite
H-Clin	Protonated natural zeolite
FeClin cop	H-Clin modified with **Fe** by co-precipitation method
FeCuClin cop	H-Clin modified with **Fe** by co-precipitation method and promoted with **Cu**
FeCeClin cop	H-Clin modified with **Fe** by co-precipitation method and promoted with **Ce**
FeClin ads	H-Clin modified with **Fe** by adsorption from the solution method
FeClin impr	H-Clin modified with **Fe** by incipient wetness impregnation method
MCM22	Sodium form of MCM-22
FeMCM22 cop	MCM22 modified with **Fe** by co-precipitation method
FeMCM22 ads	MCM22 modified with **Fe** by adsorption from the solution method
FeCuMCM22 ads	MCM22 modified with **Fe** by adsorption from the solution method and promoted with **Cu**
FeCeMCM22 ads	MCM22 modified with **Fe** by adsorption from the solution method and promoted with **Ce**
FeMCM22 impr	MCM22 modified with **Fe** by incipient wetness impregnation method

3. Characterization methods

The detailed characterization of the physicochemical properties of the materials enabled to correlate their structural properties with the catalytic behavior. Therefore, the materials were examined by the advanced instrumental techniques, such as:

- inductively coupled plasma atomic emission spectroscopy (ICP-OES),
- N_2 adsorption-desorption studies at 77 K,
- X-ray diffraction (XRD),
- scanning electron microscopy (SEM),
- temperature-programmed desorption of ammonia (NH_3-TPD),
- temperature-programmed reduction with hydrogen (H_2-TPR),

- thermogravimetric analysis (TGA),
- Fourier transform infrared spectroscopy (FT-IR),
- X-ray photoelectron spectroscopy (XPS),
- diffuse reflectance ultraviolet-visible spectroscopy (UV-Vis).

3.1 Inductively coupled plasma optical emission spectroscopy (ICP-OES)

Chemical composition of the catalysts is one of the crucial parameters influencing their performance in catalytic processes. Additionally, it can differ from the initially calculated one, based on the expected stoichiometry. Thus, determination of the elemental composition of the synthesis materials is essential for the comparative studies of the catalytic performance. The quantitative analysis of the materials was performed using inductively coupled plasma optical emission spectroscopy (ICP-OES). The method enables to determine more than 70 elements in the variety of matrices, even that of very low concentrations. In typical analysis, liquid samples are introduced into the instrument and converted into an aerosol form by nebulization. Afterwards, as obtained aerosol interacts with the plasma. Generation of plasma is provided by the ionization of argon inside an oscillating radio frequency (RF) field, created in a torch tube. High electron density of plasma at temperature of around 10,000 °C enables excitation of the chemical elements present in the analyzed sample. The investigated material in the aerosol form is introduced to the center of the torch tube by another, thin injector tube of typical aperture of 1-2 mm. After interaction with plasma, the sample is quickly dried, vaporized, atomized, and ionized or excited at high temperature. The characteristic radiation emitted by the excited atoms and ions is collected by the spectrometer, which separates the wavelengths of light, specific for the certain elements. The position of the photon rays and the content of each element is determined by their position and the intensity, respectively [503].

Experimental conditions: The weight percentages of the selected chemical elements (Si, Al, Fe, Cu, and Ce) in the investigated materials were determined using ICP-OES QTEGRA apparatus. In a typical procedure, 20-40 mg of the sample was dissolved in the mixture of hydrochloric, sulfuric, and phosphoric acid. Afterwards, the samples were supported to microwave digestion using the microwave-assisted sample preparation system Ethos Easy (Milestone).

3.2 N_2 adsorption-desorption studies at 77 K

The in-depth analysis of the behavior of the catalysts in heterogeneous catalytic reactions requires detailed knowledge of their textural parameters. One of the most important tools for the characterization of porous solids is gas sorption. In 1985, IUPAC presented the document reporting the conclusions and recommendations of the determination of specific surface area and porosity of the materials, called "Reporting Physisorption Data for Gas/Solid Systems" [504]. The document has been broadly accepted by the scientific and industrial communities and became a base for the investigations of the textural characteristics of porous materials. The characterization [504] involves experimental protocols for the adsorption of different subcritical fluids, such as nitrogen, argon, carbon dioxide, or organic vapors and supercritical gases. Among them, the most common is nitrogen adsorption-desorption measurement at 77 K [505].

Experimental conditions: N_2 adsorption-desorption experiments at 77 K were performed using Micromeritics 3Flex Surface Characterization gas adsorption analyzer. Prior to the analysis, the samples were degassed under vacuum at 90 ºC for 1 h and afterwards, at 350 ºC for 5 h. The specific surface area (S_{BET}) of the materials was calculated using the Brunauer-Emmet-Teller model, from the adsorption branch, according to the recommendations of Rouquerol et al. [506]. Taking into consideration the specific shape of the isotherms, pointing at the micro-mesoporous structure of the catalysts, the external surface area, surface of micro- and mesopores, their volume, and pore size distribution were calculated using additional methods, except of BET, such as *t-plot* and Barrett-Joyner-Halenda (BJH) method.

3.3 X-ray diffraction (XRD)

X-ray powder diffraction method (XRD) is a widespread method used to identify the crystalline features of the materials, such as crystalline phases, crystallite sizes, lattice parameters, and disorders occurring in the crystals. Diffraction occurs while light is scattered by a periodic array of long-range order and a constructive interference at specific angles is produced. The wavelength of the X-rays is similar to the distance between the atoms in the crystals and the scattering of X-rays from the atoms yields a diffraction pattern which includes information about the atomic arrangement in the crystals. In the case of amorphous materials, which are deprived of periodic array with long-range order, no

diffraction maxima can be observed in the XRD pattern [507]. Most of the crystals have many sets of planes passing through the atoms. Since each of the planes is characterized by a particular interplanar distance, it gives rise to a characteristic angle of the diffracted X-rays. The relationship between the wavelength, atomic spacing, and diffraction angle is represented by Bragg's law, mathematically described by **Equation (125):**

$$n \cdot \lambda = 2d \cdot sin\theta \quad \textbf{(125)}$$

where *n* is an integer related to the reflection order, λ is the wavelength of the incident X-ray beam, *d* is the distance between the parallel planes, and θ is so-called "Bragg's" diffraction angle. What is more, XRD method can be applied to determine size of the crystals within 3-100 nm. For the crystallites below 2-3 nm, the diffraction maxima are very broad, while for the ones above 100 nm, the reflection maxima is very narrow. The crystal size can be estimated by the means of Scherrer's formula, described by **Equation (126):**

$$d = \frac{K \cdot \lambda}{\beta \cdot cos\theta} \quad \textbf{(126)}$$

Where β (in radians) is the width of the diffraction maximum (FWHM – full width at half maximum) and *K* (typically between 0.8 and 1.39) corresponds to the Scherrer's constant and depends on the crystal shape, diffraction line indexes, and dispersion of the crystallite sizes of the analyzed powder [508].

Experimental conditions: The XRD patterns of the investigated materials were obtained using Empyrean (PANalytical) diffractometer (PANalytical, Almelo, UK). The diffractograms were collected using Cu-Kα radiation source (λ = 1.54184 Å) at a tube current of 40 mA and a voltage of 40 kV. The scanning range of 2θ was set for 2-40 º or 3-90 º, with a scan step of 0.02 º and counting time of 1 s per step. The recorded XRD data were analyzed using X'pert HighScore software plus (with database) (Malvern Panalytical, Malvern, UK).

3.4 Scanning electron microscopy (SEM)

Scanning electron microscopy (SEM) is one of the most powerful methods for the examination of the structure, morphology, and composition of materials. In general, SEM microscopes are used to investigate material surfaces and typically provide the magnification of 5-300,000 × and enable analysis

of inorganic and organic samples with diameters up to 200 mm. Additionally, energy dispersive X-ray spectroscopy (EDX) is a common mode working together with SEM, delivering quantitative and semi-quantitative information about the composition of the materials. The SEM analysis is usually performed according to the procedure described by Goldstein and co-workers [509]. Normally, a high-energy beam of electrons is emitted by the gun and directed into the system of lenses, than it is compressed, and transported into the spot with the sample. Subsequently, the electrons penetrate the sample to a depth of around 1 μm, in order to generate the signals used to record the SEM image. The image of the specimen is formed point by point and its quality is influenced by the movement of the scan coils, responsible for the ambulation of the electron beam. Formation of SEM images also depends on the acquisition of the signals produced from the interactions between the specimen and electron beam, which are divided into elastic and non-elastic. Elastic scattering is characterized by minor energy loss and a wide-angle directional change of the beam of the scattered electrons. Elastically scattered electrons are known as "backscattered electrons" (BSE). In the case of inelastic scattering, the energy loss depends on the binding energy of the electrons in the atoms and on the single or collective excitation of the specimen. Inelastic scattering produces secondary electrons (SE), which possess energies lower than 50 eV. Both BSE and SE are useful to produce SEM images. Additionally, apart from the signals generated by BSE and SE, X-rays or Auger electrons are produced while the electron beam strikes the sample. The signals emitted from the scanned material are finally collected on the detector to produce SEM image.

Experimental conditions: The morphology and shape of the catalysts' particles were investigated by scanning electron microscopy (SEM). High-magnification SEM micrographs of coated samples (20 nm of Cr) were obtained with a JSM-7500F (JEOL, Tokyo, Japan) field emission scanning electron microscope (SEM). The images were recorded using secondary electron detector, which provided SEI images.

3.5 Transmission electron microscopy (TEM)

Transmission electron microscopy (TEM) belongs to the groups of methods applied to analyze structural properties of materials, using a beam of electrons. Similarly to SEM, TEM microscopes generate a beam of electrons focused on a specimen inside the vacuum chamber. However, TEM

provides a detailed information on the internal structure of specimens, from the micrometer to the angstrom scale. In general, TEM allows to identify self-assembly of molecules into larger structures with defined microscopic features and macroscopic characteristics, such as layers, gels, films, membranes, solids, surfaces, etc. Typically, TEM microscope consists of an electron gun, electrostatic lenses, which focus the electrons before and after the specimen, and a detection system of the transmitted electrons. The electron gun is responsible for the production of the beam of electrons of the sufficient energy to pass through the material. The precise focus on the specimen is possible due to the system of lenses, such as the condenser lenses, which focus the beam on the specimen, the objective lens, which focuses the transmitted electrons to form the first image, and projector lenses, which magnify this image onto the detection system [510]. The path of the transmitted electrons through the post-specimen lenses and detection system and the geometry of the electron illumination determine the contrast in TEM images. Therefore, there are various modes of TEM imaging, which allow to obtain a great number of information from the specimen. The commonly used are bright-field (BF) imaging, high-resolution (HRTEM) imaging, and high angle annular dark field (HAADF) imaging. In the case of BF, the image is formed only from the non-scattered electrons, have darker contrast, and allow to detect the crystal orientation. Considering HRTEM, the electron waves interact with the crystal lattice and form complex interference patterns at very high magnifications. In this case, the elastic scattering of electrons dominates over the inelastic and this mode allows to determine position of the atoms in the material. Last, but not least, HAADF mode enables investigation of the materials chemistry on the atomic scale. Typically, it uses HAADF detector to collect incoherently scattered electrons through very high angles. Similarly to SEM, TEM microscopes can be equipped with EDS detectors [511].

Experimental conditions: Transmission electron microscopy (TEM) was performed on a Tecnai TF20 X-TWIN (FEG) microscope (Thermo Fisher Scientific) equipped with an EDS detector (EDAX), working at an accelerating voltage of 200 kV. The samples for TEM observations were prepared by drop-casting of powder/isopropyl alcohol suspensions on carbon coated copper TEM grids and were recorded in BF, HAADF, and HR modes.

3.6 Temperature-programmed desorption of ammonia (NH_3-TPD)

Characterization of the acidic properties of zeolites essential to understand their behavior in catalytic reactions. Temperature-programmed desorption of ammonia (NH_3-TPD) belongs to the group of the most frequently used methods to investigate density and strength of the acid centers. The standard conditions of NH_3-TPD involve out-gassing (evacuation), adsorption of ammonia, and its temperature-programmed desorption. Typically, NH_3-TPD patterns are composed of so-called low- (LT) and high-temperature (HT) desorption peaks. LT peaks correspond to weakly or physically adsorbed NH_3 molecules, while HT peaks are assigned to ammonia strongly bonded to the acid sites.

Experimental conditions: The concentration and strength of the acid sites present on the surface of the catalysts was determined by temperature programmed desorption of NH_3 using Autochem II (Micrometrics) apparatus. The experiments were performed in the temperature range of 100-800 ºC in a fixed-bed continuous flow microreactor. Prior to the measurement, 100 mg of the sample was pretreated at 100 ºC for 60 min with a stream of argon. Afterwards, the material was equilibrated at 100 ºC with a stream of helium and saturated for about 30 min in a flow of 1 vol.% of NH_3 in He. Subsequently, it was heated with a temperature ramp of 10 ºC · min^{-1}, up to 800 ºC in the stream of Ar. The desorbed amount of ammonia was analyzed by the means of a thermal conductivity detector (TCD) and coupled GC-MS mass spectrometer (OmniStar, Bazers Instruments).

3.7 Temperature-programmed reduction with hydrogen (H_2-TPR)

Temperature-programmed reduction with hydrogen (H_2-TPR) is a useful technique to examine reducibility of catalysts. Typically, the analyzed material is exposed to the flow of reducing gas (most often 0-10 vol.% of hydrogen in an inert gas) at linearly increasing temperature. The total consumption of H_2, calculated on the basis of its concentration in the gas at the outlet of the reactor, permits to determine the degree of reduction and average oxidation state of the active phase.

Experimental conditions: Temperature-programmed reduction (H_2-TPR) experiments were carried out in a Micromeritics Autochem 2910, equipped with a TCD detector for measuring H_2 consumption, in which the reducing gas was 10% H_2 in Ar (total flow rate of 50 $cm^3 \cdot min^{-1}$). The samples were heated from 40 to 800 °C at a heating rate of 10 °C · min^{-1}.

3.8 Thermogravimetric analysis (TG)

Thermal analysis enables investigation of the physicochemical characteristics of a material while it is heated, held at a constant temperature, or cooled. Thermogravimetric analysis or thermogravimetry (TGA), allows to determine the change of the sample mass in the function of temperature (scanning mode) or time (isothermal mode), in the certain, controlled atmosphere. Typically, the temperature range does not exceed 1000 °C, but it depends on the application of the analyzed material. The most important part of the thermogravimetric analyzer is thermobalance, sensitive for the changes of the mass as a function of temperature and time. Normally, thermobalance consists of electronic microbalance, sample holder, furnace, temperature programmer, and recorder. The atmosphere of the measurement is created by the purge gas flowing through the thermobalance. This atmosphere can be inert (nitrogen, argon, helium), oxidizing (oxygen), or reducing (8-10 vol.% of hydrogen in nitrogen). Therefore, since TGA studies are conducted under programmed conditions, it is used to examine certain thermal events, including adsorption, absorption, desorption, oxidation, reduction, sublimation, or decomposition. Moreover, it helps to predict thermal stability of the materials and detect if any volatile or gaseous products are generated by the samples [512].

Experimental conditions: Thermogravimetric analysis (TG) was performed using Q5000 IR thermobalance (TA Instruments). Typically, each sample was placed on a platinum holder, in the mixture of air and helium. The weight loss of the materials was monitored within the temperature range of 30-800 °C (with the temperature ramp of 10 °C · min^{-1}).

3.9 Fourier transform infrared spectroscopy (FT-IR)

Fourier-transform infrared spectroscopy (FT-IR) helps to identify functional groups in materials by using a beam of infrared radiation (IR). The region of infrared radiation can be divided into near (14000-4000 cm^{-1}), middle (4000-400 cm^{-1}), and far (400-40 cm^{-1}) IR. Determination of the functional groups using FT-IR is possible only for the materials which interact with IR radiation, thus, those which have a dipole moment. Therefore, symmetrical molecules cannot be excited and analyzed using IR beam. One of the biggest advantages of FT-IR spectroscopy is its versatility, since it enables analysis of solids, liquids, and gases with very high accuracy [513].

Absorption of energy cumulated in IR radiation causes oscillation of particular bonds in the molecules with the natural vibrational frequency, assigned to this particular bond. FT-IR spectra are presented as absorbance or % of transmittance in the function of wavenumber. Typically, the spectra recorded in absorbance mode are calculated from **Equation (127):**

$$A = log\ \frac{I_0}{I} \tag{127}$$

where A – absorbance, I_0 – intensity in the backgrounds spectrum, and I – intensity in the spectrum of the analyzed sample. Alternatively, absorbance can be expressed by the Lambert-Beer's law, represented by **Equation (128):**

$$A = \varepsilon \cdot l \cdot c \tag{128}$$

where ε - molar absorptivity, l – length of the path, c – concentration of the sample. Due to the fact that the area or the height of the peak in the absorbance spectrum is proportional to the sample concentration, Beer's law enables quantitative analysis of the investigated materials. Alternatively, the infrared spectra can be also exhibited using percent transmittance ($\%T$), which corresponds to the percentage of light transmitted by the material and can be calculated from **Equation (129):**

$$\%T = 100 \cdot \frac{I}{I_0} \tag{129}$$

where T – transmitance. One should note that in the case of absorbance, the absorption band of each characteristic functional group is pointed up, while in the $\%T$ spectra, the bands are pointed down. Absorbance and percent of transmittance are interconvertible and despite the *y*-axis are changed through the conversion, the positions of the observed peaks are not affected [514].

The majority of FT-IR spectrometers consists of a source of IR radiation, interferometer, sample compartment, detector, amplifier, and computer. Normally, the generated light strikes the sample and passes through the interferometer, finally reaching the detector. The initially obtained interferogram is quickly translated to FT-IR spectrum by the means of Fourier transform algorithm, performed by the computer software.

Experimental conditions: The FT-IR spectra of the analyzed materials were collected using Perkin Elmer Frontier spectrometer in the wavelength region of 4000-400 cm^{-1}, with a resolution of 4 cm^{-1}. Before each measurement, the analyzed sample was mixed with KBr at the ratio of 1:100 and pressed into a disk.

3.10 X-ray photoelectron spectroscopy (XPS)

X-ray photoelectron spectroscopy (XPS) belongs to the group of surface-sensitive methods used to investigate the quantity and oxidation state of chemical elements on the materials' surface. Due to its accuracy and the fact that it does not significantly damage the analyzed samples, XPS has been widely used especially for the analysis of heterogeneous catalysts [515]. In general, the method is based on the photoemission of electrons from surfaces irradiated with light (photoelectric effect). During the typical XPS measurement, the surface of a solid is irradiated with a beam of soft X-rays (energies below ~ 6 keV). In consequence, the electrons from the outer layers of the material (1-10 nm) are emitted, as the result of a complete transfer of the X-ray energy to a core level electron. The kinetic energies of the electrons ejected from the surface are characterized by various values, thus, the electrons follow different paths before they reach the detector. Basing on this, it is possible to differentiate between the certain electrons, which are identified in the resulting spectra by their binding energies. Additionally, intensity of the photoelectron peaks delivers an information on the quantity of all surface elements. XPS has been applied to study surfaces of many materials, since all chemical elements except of hydrogen and helium can be detected [516]. Due to the high surface sensitivity of XPS, preparation of the sample requires particular care, in order to avoid its contamination. One of the most common techniques used to remove surface impurities is bombardment with Ar^+ ion, so-called sputtering. However, this technique cannot be applied in the case of transition metals, which can exist on various oxidation states. Thus, prior to XPS measurement, such kind of samples are fractured under vacuum [517].

Experimental conditions: The X-ray photoelectron spectroscopy (XPS) experiments were conducted in a PHI VersaProbeII Scanning XPS system using monochromatic Al Kα (1486.6 eV) X-rays focused to a 100 μm spot and scanned over the area of 400 μm × 400 μm. The photoelectron take-off angle was 45 ° and the pass energy in the analyzer was set to 117.50 eV (0.5 eV step) for survey

scans and 46.95 eV (0.1 eV step) to obtain high energy resolution spectra for the C 1s, O 1s, Na 1s, Fe 2p, Al 2p and Si 2p regions. A dual beam charge compensation with 7 eV Ar^+ ions and 1 eV electrons were used to maintain a constant sample surface potential, regardless of its conductivity. All of the XPS spectra were charge-referenced to the unfunctionalized, saturated carbon (C-C) C 1s peak at 284.8 eV. The operating pressure in the analytical chamber was less than $3 \cdot 10^{-9}$ mbar. The spectra were deconvoluted using PHI MultiPak software (v.9.9.0.8). The spectrum background was subtracted by the Shirley method.

3.11 Diffuse reflectance ultraviolet-visible spectroscopy (UV-Vis-DRS)

UV-visible spectrophotometry ((UV-Vis) belongs to absorption spectroscopic methods, which covers a part of the ultraviolet and the full visible region of the electromagnetic spectrum (the wavelength range of 200-2500 nm). In this region, atoms, ions, or molecules absorb energy, which results in the electronic transitions from the ground state to the excited state. The parameters such as absorbance, transmittance, or reflectance (%*R*) in a function of the wavelength give an important information on the quality or/and quantity of the specific compound in the investigated material. In the case of heterogeneous catalysts, UV-Vis spectroscopy is used to study transition metal ion centers, especially d-d metal-to-ligand charge transfer or ligand-to-metal charge transfer. One should note that most of the catalysts are composed of the particles, which strongly scatter the beam of light, since their size corresponds to its wavelength. Therefore, the amount of light transmitted through the film of a catalyst is usually insufficient for transmission spectroscopy in the UV-Vis range. Due to that, it is recommended to use the diffuse reflectance technique (DRS), in which the particles of the catalysts are irradiated from all directions and the light is simultaneously absorbed and scattered in all possible directions. The part of the light, which is scattered is collected in an integrating sphere and detected by a photomultiplier or PbS cell (depending on the wavelength). Additionally, no light is transmitted by the particles of the investigated catalyst. The intensity of the detected light is described by the Kubelka-Munk (KM) formula, which correlates it with the KM absorption coefficient and KM scattering coefficient, as presented by **Equation (130)**:

$$F(R) = \frac{(1-R)^2}{2R} = \frac{K}{S} \quad \textbf{(130)}$$

where R – intensity of the light reflected from the infinitely thick sample, K – KM absorption coefficient, and S – KM scattering coefficient, which refers to the geometry of the investigated sample [518,519]. Typically, UV-Vis instrument is equipped with a source of radiation, monochromator, and photoelectric detector to transform the energy of electromagnetic radiation to the electric signal. There are various sources of radiation, such as deuterium lamp, which covers 180-380 nm combined with halogen lamp for the wavelength higher than 380 nm. The alternative is high-pressure xenon lamp, which emits stable and intense light with the wavelength range of 185-2000 nm. The advantage of xenon lamp over deuterium or halogen lamps is that it can reach a steady state in a shorter time and it covers the entire UV-Vis range. This fact allows to avoid interruptions in the spectra caused by switching from one lamp to another. Additionally, the lifetime of the xenon lamp is longer comparing to deuterium or halogen lamp.

Experimental conditions: The coordination and aggregation of transition metal species introduced into the zeolites were determined by ultraviolet diffuse reflectance spectra (UV-vis-DR). The analysis was conducted with Cary 5 spectrophotometer equipped with a diffuse reflectance accessory. The spectra were taken in the range of 200-900 nm, with a resolution of 2 nm.

4. Catalytic tests

4.1 Catalytic tests with model gas mixture

The catalytic activity of the analyzed materials in NH_3-SCR was investigated at atmospheric pressure in the fixed-bed flow microreactor containing 0.2 g of the catalyst (grain size between 0.09 and 0.16 mm). Temperature inside the reactor was measured using thermocouple with an electronic controller (Lumel RE19), positioned near the center of the catalyst. The model reaction mixture was composed of 800 ppm NO, 800 ppm of NH_3, 3.5 vol.% O_2, and He as an inert. The total gas flow was 100 $cm^3 \cdot min^{-1}$, which led to gas hourly space velocity (GHSV) of 30 000 $mL \cdot h^{-1}$. Prior to the catalytic reaction, the catalysts were outgassed at 400 °C for 1 h in He. The tests were conducted in the temperature range of 150-450 °C, for 1 h at every temperature, with a 50 °C step. The concentration of

NO and N_2O (selectivity to N_2O, treated as the by-product of the catalytic reaction) was analyzed by FT-IR detector (ABB 2000 AO series). The schematic experimental setup of NH_3-SCR used to perform the catalytic tests is illustrated in **Figure 39.** NO conversion was calculated according to **Equation (131):**

$$Conv_{NO}\ (\%) = \frac{C_{NO\ (in)} - C_{NO\ (out)}}{C_{NO\ (in)}} \times 100\% \qquad \textbf{(131)}$$

where $Conv_{NO}$ – total conversion of NO, $C_{NO\ (in)}$ – inlet concentration of NO, $C_{NO\ (out)}$ – outlet concentration of NO.

In order to further evaluate catalytic activity of the materials in NH_3-SCR reaction, kinetic parameters for NO conversion were calculated using **Equation (132)**, which is based on the theory that the process is first-order with respect to NO and zero-order to NH_3 [520]:

$$k = -\frac{V}{W} \times \ln(1 - x) \qquad \textbf{(132)}$$

where k – reaction rate constant ($cm^3 \cdot g^{-1} \cdot s^{-1}$), V – total gas flow rate ($cm^3 \cdot s^{-1}$), W – mass of catalyst in the reactor (g), x – NO conversion.

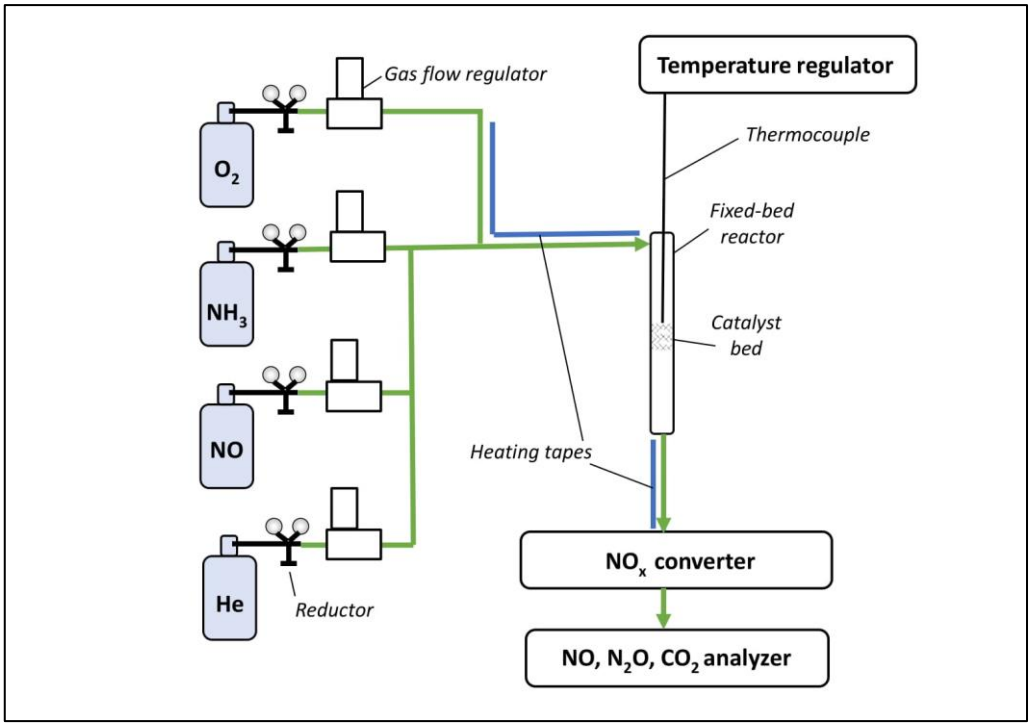

Figure 39. Schematic representation of NH_3-SCR experimental setup

4.2 Poisoning of the catalysts with sulfur dioxide

In order to analyze the resistance of the selected catalysts to the poisoning with sulfur dioxide, the materials were exposed to the gas mixture consisting of 1000 ppm of SO_2 in helium at 350 °C. The poisoning mode was maintained for 1 h and directly afterwards, the catalyst was subjected to NH_3-SCR tests, following the procedure described in the paragraph 4.1. Conversion of NO obtained for the poisoned catalysts was calculated according to **Equation (131)**.

4.3 Catalytic tests in the presence of sulfur dioxide in the gas mixture

To establish the influence of sulfur dioxide in the gas mixture on the catalytic performance, the selected materials were subjected to catalytic tests using gas mixture containing SO_2. Concentration of SO_2 was gradually increased during the measurement, following the values of 200 ppm, 400 ppm, 600 ppm, and 800 ppm. The catalytic tests were conducted at 350 °C and NO conversion was calculated using **Equation (131).**

Chapter IV: Results and discussion of the studies

1. Comparison of iron-modified zeolites prepared by various methods

1.1 Characterization of iron-modified clinoptilolite and MCM-22

Chemical composition and crystal structure of the materials

The content of Si, Al, and Fe in the investigated materials was determined by ICP-OES. The obtained results are collected in **Table 15**. The raw clinoptilolite exhibited considerable amount of aluminum and Si/Al molar ratio of 4.5, characteristic for the materials of HEU family [289]. The Si/Al molar ratio of the non-modified clinoptilolite confirms high concentration of acidic centers in the zeolite. Additionally, the analysis proved that the natural zeolite originally contained ca. 1.01 wt.% of iron, which is in agreement with the literature [521]. Pretreatment with HCl resulted in slight dealumination of clinoptilolite, thus, creation of vacant T-sites and the increase of Si/Al value. This effect has been earlier observed for other zeolites, for example BEA [418]. In general, the procedure aims to produce the vacant sites for the isomorphous incorporation of Fe^{3+} species. Additionally, modification with acid did not noticeably change Fe content, thus, probably Fe^{3+} cations are strongly built into clinoptilolite framework. In the case of MCM22 sample, the real Si/Al molar ratio is in very good agreement with the intended one, which suggests successful incorporation of the desired amounts of Si^{4+} and Al^{3+} into the zeolitic framework.

In the case of clinoptilolite, modification with iron did not change noticeably its Si/Al molar ratio. Therefore, the applied methods did not cause any significant interruptions in the chemical composition of the framework. It can be noticed that the real Fe loading is slightly higher than the calculated one, which was most likely caused by the presence of iron in the parent zeolite.

In contrast to clinoptilolite, iron loading in FeMCM22 samples was strongly affected by the modification method. The amount of Fe exceeded the calculated value especially in the case of FeMCM22 cop. Considering partial elimination of Si and Al from the sample, thus, the changed Si/Al molar ratio, it can be concluded that the aluminosilicate framework was partially dissolved and degraded during the modification. This observation was supported by the research of Schenkel and co-workers

[522]. The authors proved that the treatment with strong acids can lead to partial or even complete amorphization of MCM-22. Therefore, the affected chemical composition of the zeolite was the reason of strongly acidic, followed by strongly alkaline medium applied during co-precipitation procedure. In the case of FeMCM22 ads, the content of Al decreased comparing to the parent zeolite, however, not as much as in the case of FeMCM22 cop, due to the milder modification conditions. Furthermore, chemical composition of FeMCM22 impr was almost completely unaffected by the modification and Fe loading in the sample was the closest to the initial value.

Table 15. Chemical composition of the pristine and Fe-modified zeolites with the corresponding Si/Al molar ratio

Sample code	Si (wt.%)	Al (wt.%)	Fe (wt.%)	Si/Al
Clin	32.11	6.89	1.1	4.5
H-Clin	32.71	5.89	0.99	5.3
FeClin cop	30.01	5.33	8.01	5.4
FeClin ads	33.6	5.55	6.39	5.8
FeClin impr	32.52	5.83	5.79	5.4
MCM22	38.51	3.06	0	12.1
FeMCM22 cop	22.36	1.07	32.12	20.1
FeMCM22 ads	30.48	2.07	16.74	14.1
FeMCM22 impr	35.5	2.91	4.77	11.7

XRD analysis played a crucial role in the identification of the characteristic zeolitic structures of natural clinoptilolite and MCM-22. Additionally, the investigation enabled to determine some structural changes occurring in the materials after modification with iron.

XRD patterns obtained for the natural clinoptilolite and clinoptilolite-supported catalysts in the 2θ range of 3-75° are presented in **Figure 40.** The diffraction maxima at 2θ ca. 9.95, 11.37, 13.29, 19.1, 22.9, 30.14, 32.15, 32.97, and 33.79°, marked in the pattern with their corresponding plane (*hkl*) Miller's indices, are in agreement with those of clinoptilolite crystalline structure data (according to JCPDS No. 00-0025-1349) and the literature studies [296,523]. Additionally, it can be observed that the raw clinoptilolite contains some impurities in a form of stilbite [00-011-0695] and SiO_2 [00-046-1045]. The

reflection at *2θ* ca. 35.5° confirmed the presence of rhombohedral α-Fe_2O_3 phase in the natural clinoptilolite [524]. The broaden shape of this diffraction maxima suggests that iron oxide is originally present in the zeolite in the form of small particles. After protonation, XRD pattern of clinoptilolite remained almost unchanged, except of very slight decrease of the reflection intensity at *2θ* ca. 9.95°. The lack of structural changes after hydrogenation and dealumination of clinoptilolite is in line with the previous research conducted for the material [525–527]. The procedure of modification with iron had a noticeable impact on the crystallinity of the catalysts. In the case of FeClin cop, both the intensity and shape of the diffraction maxima were well-preserved. However, the characteristic clinoptilolite reflections were lower or even removed for FeClin ads and FeClin impr. Therefore, the modification method significantly influenced crystal structure of the support. What is more, iron introduced into the zeolitic structure is probably present in a form of well-dispersed species, since none of the diffraction maxima characteristic for Fe_2O_3 (expect from that detected for the parent material) have been found in the obtained XRD patterns.

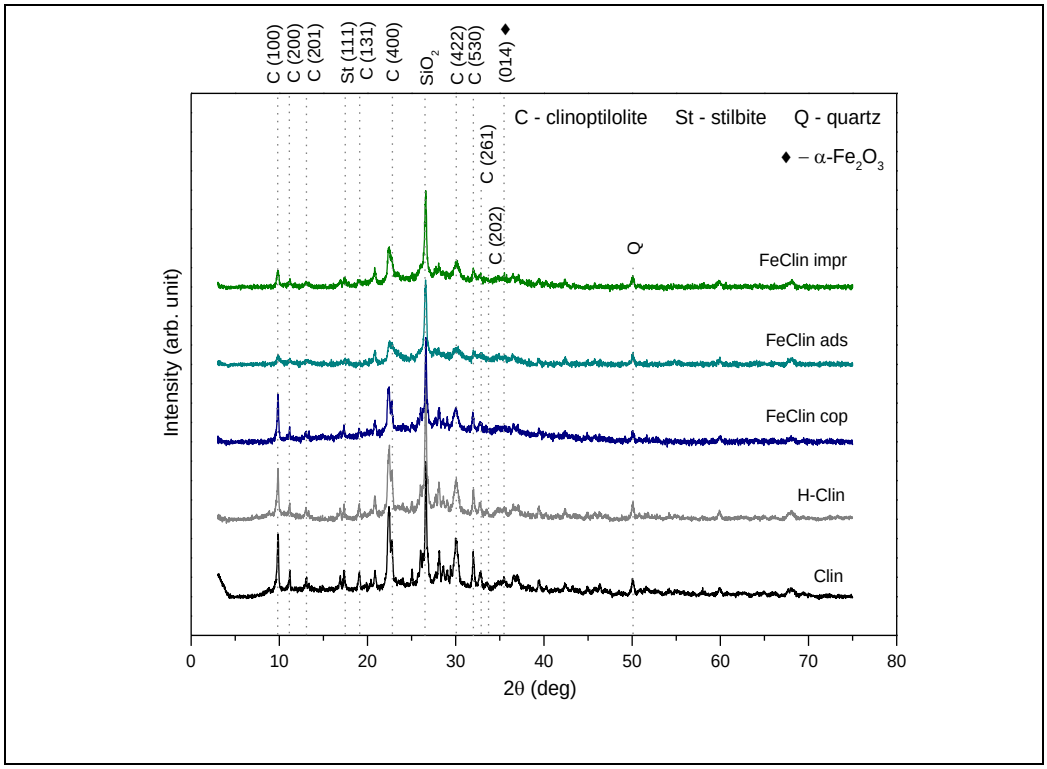

Figure 40. XRD patterns obtained for non-modified clinoptilolite (Clin), protonated clinoptilolite (H-Clin), and clinoptilolite-supported catalysts

The diffractograms obtained for MCM22 sample and its precursor, MCM-22 (P) are presented in **Figure 41**, while the comparative XRD pattens of the pristine MCM22 and FeMCM22 catalysts are collected in **Figure 42**. The most important reflections of MCM-22 are grouped at the *2θ* values of 6-10°. Thus, for better visibility of the structural differences between the zeolite and its precursor, the patterns obtained for the materials were collected in the range of *2θ* = 2-40°. The presence of so-called diagnostic reflections with their (*hkl*) indices at *2θ* of 6.6 (002), 7.1 (100), 8.0 (102), 9.8 (220), 25° (310), and 26 ° prove that the performed synthesis yielded highly crystalline layered precursor. Additionally, the relatively weak diffraction maximum at *2θ* ca. 3.1 °, marked in **Figure 41** as "≡", and detected for the precursor, confirms the formation of the MWW layers [350]. Another strong evidence of the formation of MCM-22 (P) can be found in the presence of the distinct doublet at 6.5-7.1°. The observation is significant due to the possibility of the generation of MCM-49 during the synthesis, which is typically proved by the presence of diffraction peak at 7.1° [528]. The inter-layer reflectance at *2θ* ~ 6.5 ° is ascribed to the regular separation between the adjacent MWW layers. Since the reflection corresponds to the *d*-spacing of 1.3 nm, the interlayer distance of the sheets, perpendicularly ordered to *c* axis can be estimated to around 2.6 nm. Calcination of the precursor resulted in the formation of 3D structure of MCM-22 zeolite. Analysis of the relative movement of the diffraction maxima, as well as their shape, indicated that (002) reflection overlapped with the intra-layer reflection (100). This phenomena is ascribed to the contraction of the zeolitic MWW layers, caused by the condensation between the opposite external silanol groups. The effect is characteristic for this material and results from the removal of the molecules of the organic template used for the synthesis of MCM-22 (P) [499]. In general, the position of the intra-layer (100) and the inter-layer mixed (101) and (220) diffraction maxima did not change after calcination, which indicates high crystallinity and phase purity of the zeolite. Additionally, the characteristic reflections became sharper after calcination, due to the removal of structure-directing agent molecules and crystallization of MCM-22.

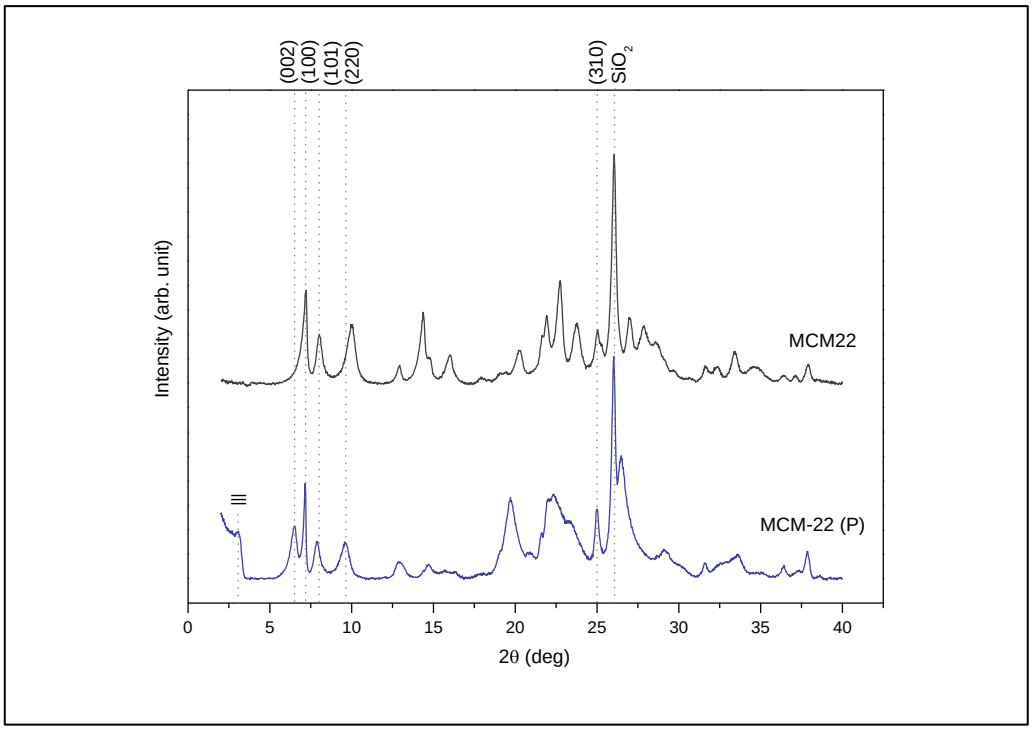

Figure 41. XRD patterns obtained for the pristine MCM22 sample and its precursor (MCM-22 (P)) before calcination

As can be seen in **Figure 42**, in the case of FeMCM22 catalysts, the position of the diffraction maxima did not change for any of the investigated materials and the ordered hierarchical structure of MCM-22 zeolite was preserved. However, the type of modification procedure had significant impact on the crystallinity. The most noticeable decrease of the reflections intensity for FeMCM22 cop is probably related to the degradation of the zeolitic structure and partial removal of Si and Al cations from the framework, confirmed by ICP-OES. On the contrary, crystallinity of FeMCM22 ads and FeMCM22 impr was only slightly lower than that of the support. Therefore, comparing to clinoptilolite, MCM-22 exhibits lower resistance to the influence of strongly acidic medium, applied during co-precipitation procedure.

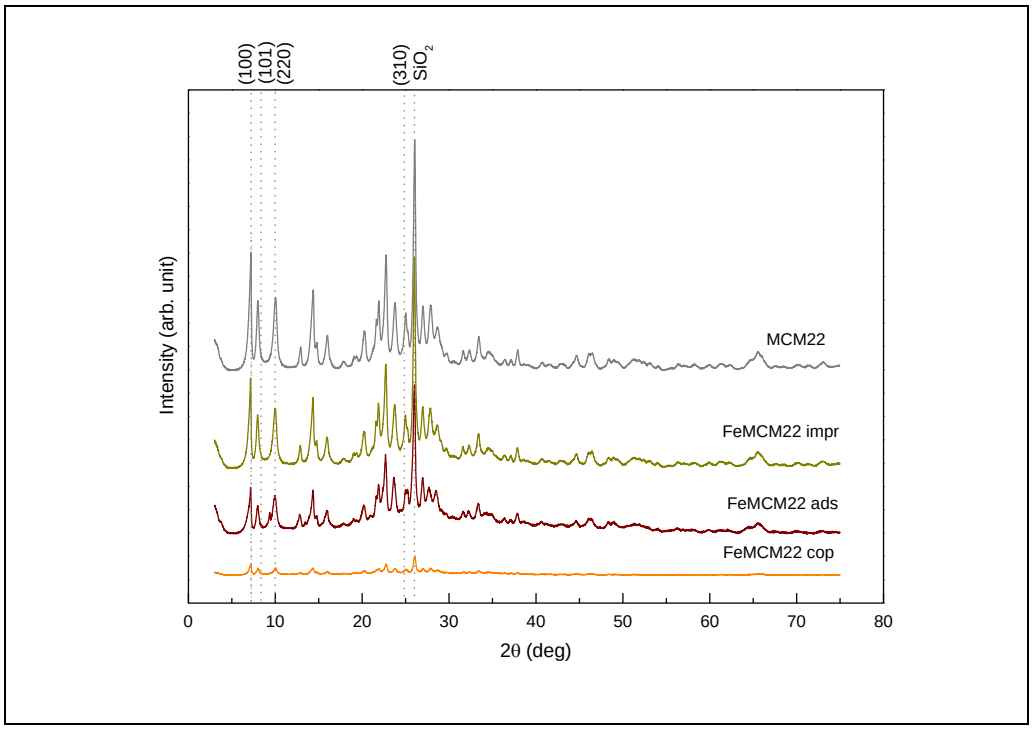

Figure 42. XRD patterns obtained for the pristine MCM22 and MCM-22-supported catalysts

Textural properties

Low-temperature N_2 sorption studies were conducted to determine structural and textural parameters of the investigated materials. The isotherms obtained for the samples supported on natural and synthetic zeolite are presented in **Figure 43** and **Figure 44**, respectively, while their structural characterizations are collected in **Table 17**.

Raw clinoptilolite demonstrated IV (a) type isotherm with the hysteresis loop H3, according to the IUPAC classification [505]. This type of isotherm is characteristic for the materials with non-rigid aggregates of plate-like particles and wedge-shaped mesopores [505,521]. Additionally, basing on the isotherm of Clin, it can be elucidated that the material contains both micro- and mesoporous nature. This postulate is confirmed by the presence of the monolayer-multilayer adsorption at $p/p_0 < 0.6$ and capillary condensation in mesopores at p/p_0 above 0.85 [529]. As can be seen in **Table 17,** the specific surface area of Clin is 13 $m^2 \cdot g^{-1}$, which is typical for this zeolite [530,531]. Vassileva and Voikova [521] suggested that the relatively low values of specific surface area and pore volume of non-modified clinoptilolite are caused by the limited access of N_2 molecule to its internal structure. As a result, the adsorbate was deposited mainly on the external surface of the material. Furthermore, Sprynskyy and co-

workers [532] linked low S_{BET} of natural clinoptilolite with the diffusion-hindering, exchangable cation complexes present in the micropores of the material. Another explanation of the low specific surface area of natural zeolite is strong interaction between highly polar structural water molecules and microporous structure of the material. After protonation, S_{BET} of clinoptilolite increased to 47 $m^2 \cdot g^{-1}$. The effect was probably caused by the penetration of the internal zeolitic structure by the acid molecules and the increase of the pore surface. Similar effects were observed by Stawiński et al. [201] for acid-modified vermiculites. The samples modified with iron were characterized by IV (a) type isotherm, thus, identical to raw and protonated clinoptilolite. However, introduction of the active phase resulted in the noticeable change of the shape of hysteresis loop, from H3 to H4 type. Therefore, the wedge-shaped mesopores were probably transformed into the slit-shaped ones. Furthermore, **Table 17** demonstrates a considerable difference in the S_{BET} of the catalysts modified with iron by various methods. In the case of FeClin cop and ads, the specific surface area increased, comparing to H-Clin, while for FeClin impr it was relatively lower. This difference results from the type of iron species introduced into the zeolitic structure. Therefore, impregnation caused deposition of bigger iron oxide particles near the pore openings and their partial blockage for the entrance of N_2 molecules [353]. On the contrary, in the case of the materials modified by co-precipitation and adsorption from the solution, the specific surface area increased comparing to the protonated zeolite. This result can be ascribed to the application of strongly acidic solutions required by the modification procedures. Moreover, basing on the values of S_{EXT}, it can the higher surface area is related to the development of the internal structure of the zeolites. Taking into consideration the increased total pore volume, co-precipitation and adsorption from the solution methods improved textural parameters of the zeolite by the formation of new pores. Additionally, the average pore diameter of the zeolite decreased from 17.04 nm to 7.22-7.36 nm (depending on the modification procedure) after introduction of iron. This effect has been already observed for other zeolite-supported catalysts after introduction of the active phase and corresponds to the deposition of clustered particles of metal oxides.

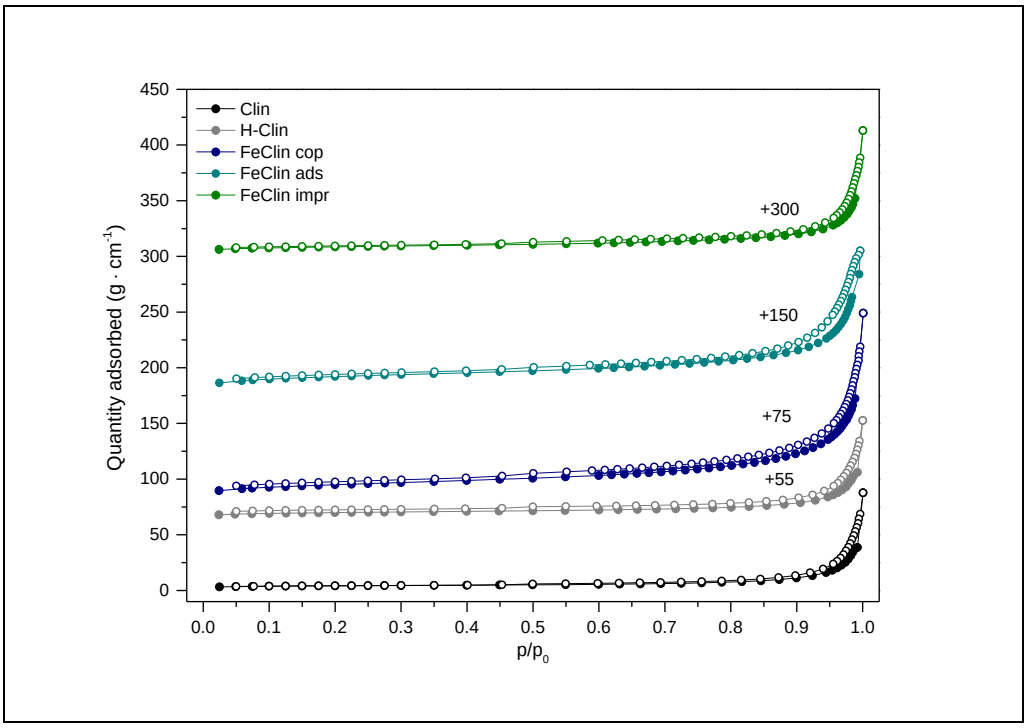

Figure 43. Nitrogen sorption isotherms obtained for non-modified clinoptilolite (Clin), protonated clinoptilolite (H-Clin), and the investigated clinoptilolite-supported catalysts with Fe (for better visibility, the isotherms were shifted by the values given in the figure)

Figure 44 presents the adsorption-desorption branches obtained for the pristine and Fe-modified MCM22 sample. The isotherm of the support is characterized by type I (b), according to IUPAC classification. The sudden increase of the adsorbed nitrogen at very low p/p_0 confirms that the material is microporous [533]. The formation of very narrow hysteresis loop of type H4, detected for the support at p/p_0 close to unity is assigned to the presence of secondary mesopores or narrow macropores [534]. Hence, the zeolite consists of plate-like particles and exhibits micro-mesoporous texture with slit-shaped pores, created by the internal parallel structure [350,353,535]. The uptake in N_2 adsorption in the range of $0.8 < p/p_0 < 1.0$ is ascribed to the stacked holes between MWW layers. Introduction of iron did not change the shape of the adsorption branch, comparing to the support. In the case of FeMCM22 cop and FeMCM22 impr, N_2 adsorption capacity at very low p/p_0 decreased almost doubly comparing to the support. In contrast, FeMCM22 ads showed almost identical adsorption behavior to the non-modified zeolite. Considering FeMCM22 cop, the observed effect could be correlated with amorphization of the sample and degradation of microporous structure. On the other hand, for FeMCM22 impr it can be explained by the formation of Fe_2O_3 particles and partial clogging of micropores. Therefore, the obtained

outcomes suggest that adsorption from the solution results in the incorporation of iron into extraframework positions of the zeolite. Besides, the hysteresis loop after modifications with metal was transformed from H4 into H3, regardless the applied method. Hence, introduction of the active phase caused aggregation of the plate-like particles of the zeolite into non-rigid structures [505]. According to the data collected in **Table 16**, MCM22 showed relatively high BET specific surface area, of the value comparable to that reported in the literature [352,353]. Introduction of iron decreased S_{BET}, regardless the modification procedure. What is interesting, co-precipitation significantly increased the external surface area, total pore volume, and pore diameter. In contrast, for FeMCM22 ads and FeMCM22 impr, the micropore area and volume only slightly decreased after introduction of iron. Therefore, the majority of micropores in the zeolite was preserved, even after deposition of the active phase. It can be noticed that the total pore volume of these samples was similar to that of the pristine MCM22, however, the summary volume of meso- and macropores moderately increased. Therefore, it is possible that modification with iron resulted in the development of meso- and macroporosity in the samples, which is in line with the change of the shape of hysteresis loop.

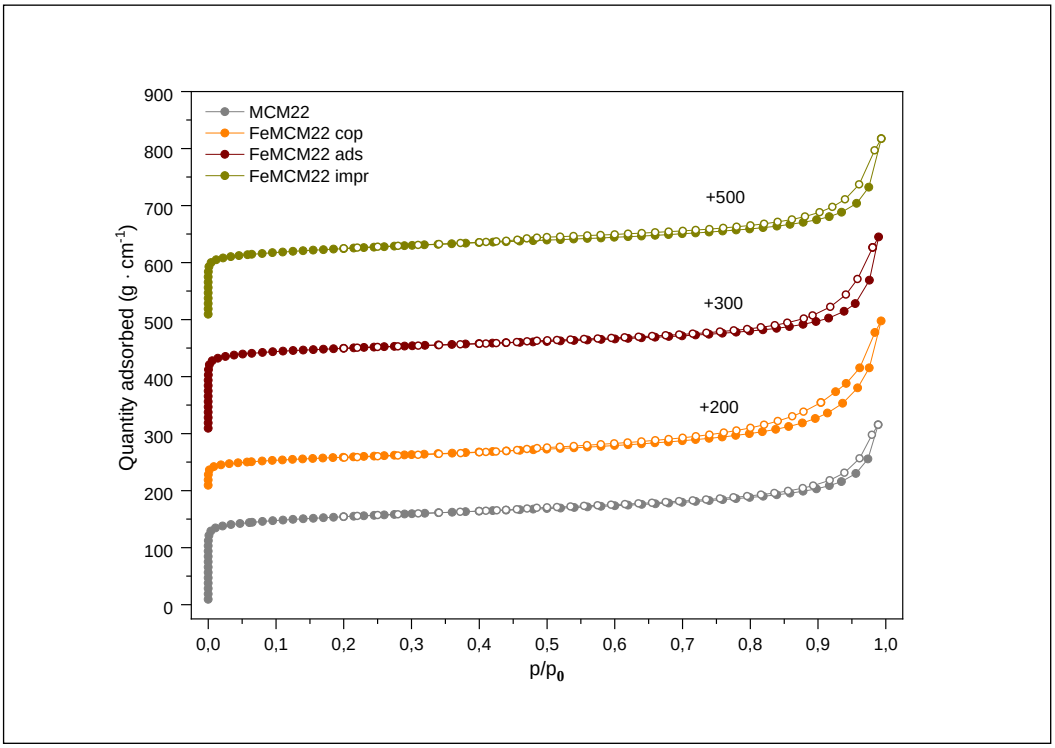

Figure 44. Nitrogen sorption isotherms obtained for the pristine MCM-22 and the investigated MCM-22-supported catalysts with Fe (for better visibility, the isotherms were shifted by the values given in the figure)

Table 16. Structural-textural properties of raw and protonated clinoptilolite and clinoptilolite-supported catalysts with Fe

Sample code	S_{BET} [a] ($m^2 \cdot g^{-1}$)	S_{EXT} [b] ($m^2 \cdot g^{-1}$)	S_{micro} [b] ($m^2 \cdot g^{-1}$)	V_{total} [c] ($cm^3 \cdot g^{-1}$)	V_{micro} [b] ($cm^3 \cdot g^{-1}$)	$V_{meso+macro}$ [d] ($cm^3 \cdot g^{-1}$)	D_{aver} [e] (nm)
Clin	13	8	6	0.059	0.003	0.056	17.04
H-Clin	47	17	30	0.079	0.016	0.063	11.44
FeClin cop	126	40	87	0.186	0.042	0.144	7.22
FeClin ads	133	48	84	0.203	0.044	0.159	7.18
FeClin impr	36	20	16	0.082	0.007	0.075	7.36
MCM22	425	62	363	0.432	0.178	0.254	7.62
FeMCM22 cop	370	189	181	0.677	0.085	0.592	9.34
FeMCM22 ads	372	109	264	0.418	0.129	0.289	5.89
FeMCM22 impr	399	75	325	0.426	0.156	0.270	7.17

[a] S_{BET} (BET surface area) was determined from the adsorption isotherm
[b] S_{EXT} (external surface area), S_{micro} (micropore surface area), and V_{micro} (micropore volume) were calculated using t-plot method
[c] V_{total} (total pore volume) was obtained at the relative pressure (p/p_0) = 0.99
[d] $V_{meso} = V_{total} - V_{micro}$ (mesopore volume)
[e] D_{aver} (average pore diameter) was determined by BJH method

Morphology of the materials analyzed by SEM microscopy

The morphology of the catalysts supports: natural clinoptilolite and MCM-22 and the catalysts was investigated by SEM microscopy at different magnification. The results of the analysis performed over Clin, H-Clin, and FeClin samples are presented in **Figure 45**, while **Figure 46** illustrates the SEM images of MCM22 and FeMCM22 catalysts.

As depicted in **Figure 45**, the raw clinoptilolite is a crystalline material, as confirmed by the results of XRD. The zeolite exhibits layered structure and does not consist of individual crystal grains, but characteristic heterogeneous flake- and plate-like particles, with small amount of impurities. This kind of particles have beneficial characteristics for the deposition of the catalytically active components [287,536]. What is more, protonation did not have significant influence on the morphology of clinoptilolite, since both crystallinity and the shape of the particles were well-preserved. After modification with iron, morphology of clinoptilolite remarkably changed and the observed differences

are correlated with the applied method. In the case of FeClin cop, the particles preserved their lamellar shape, however, their surface was covered with a layer consisting of small and aggregated particles. Atyam et al. [537] prepared iron oxide by-coprecipitation and calcination at 400 °C for 2 h. Since SEM results reported by the authors are very similar to that presented in **Figure 45,** new structures formed on the surface of clinoptilolite particles can be identified as the particles of iron oxide. Similar result was observed for FeClin ads and FeClin impr, however, the generated particles were less uniform than that of FeClin cop.

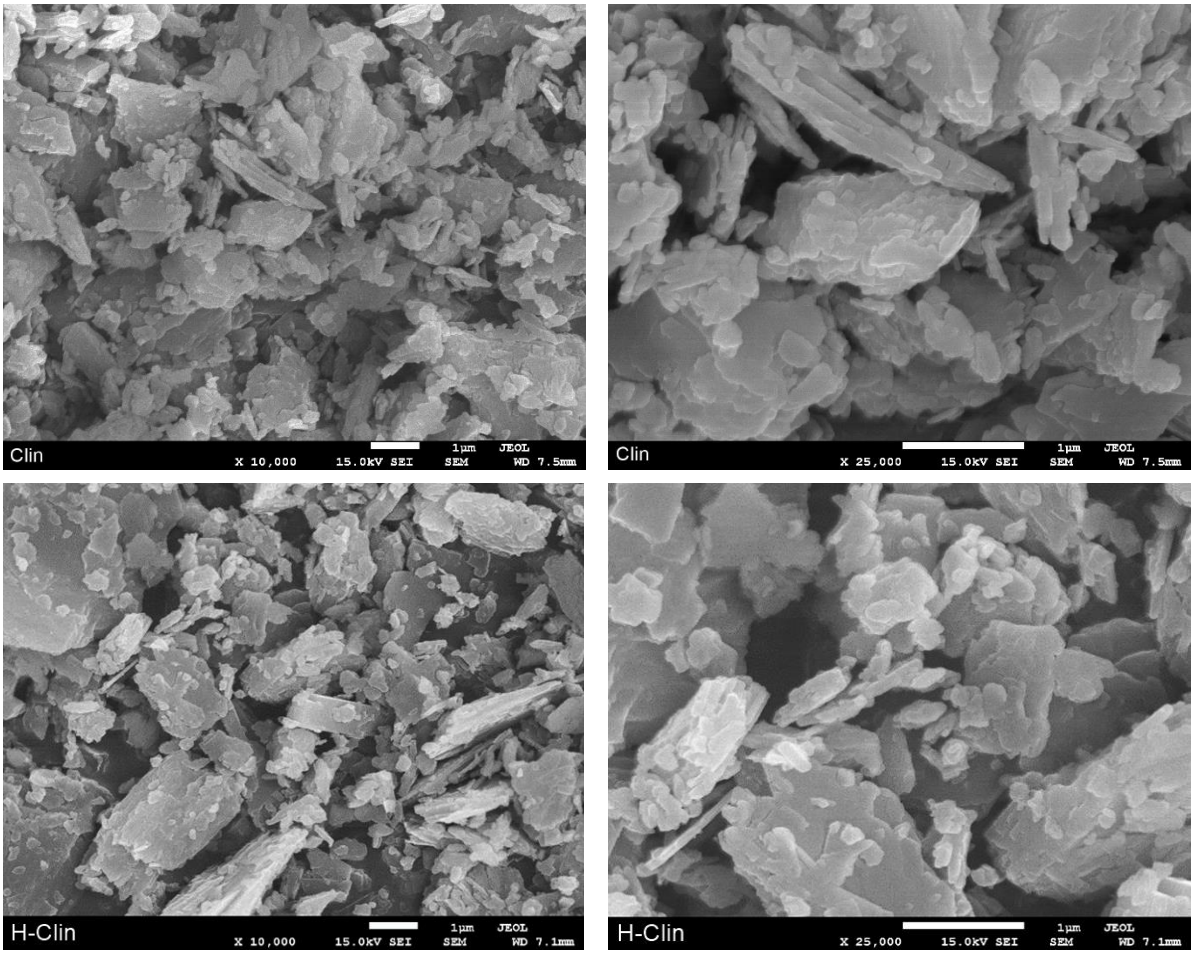

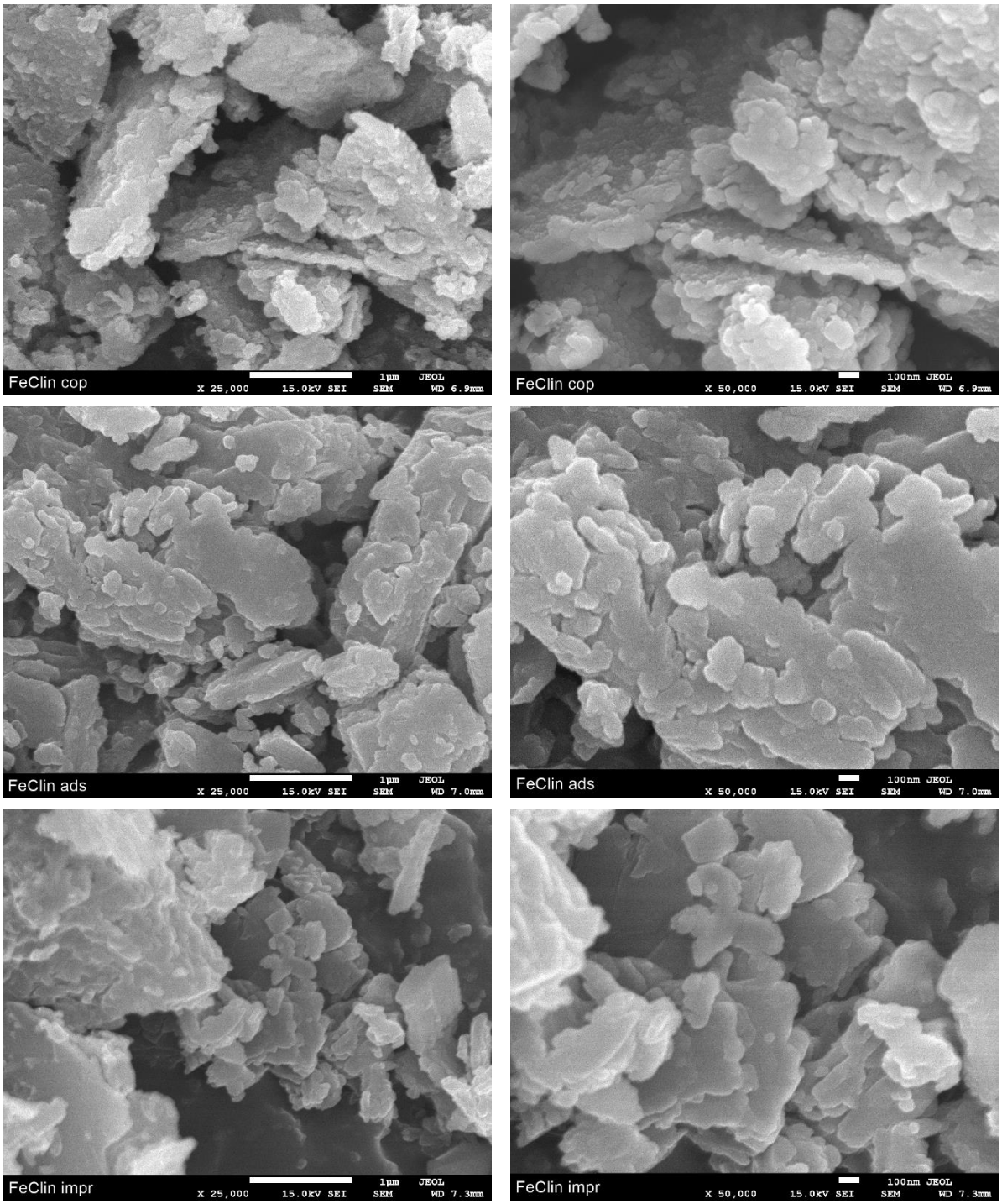

Figure 45. SEM images of clinoptilolite and clinoptilolite-supported catalysts

The particles of the pristine MCM22, presented in **Figure 46**, exhibited crystalline and sheet-like type. The presence of well-shaped crystals of the support was also confirmed by XRD studies. The small sheets formed relatively regular aggregates, reflecting donut-like structures. The observed result is typical for the lamellar materials of MWW family [349,538,539]. Modification of the layered zeolite with iron by co-precipitation method had a destructive impact on its crystallinity, as expected basing on

the XRD pattern obtained for that sample. The SEM image obtained for FeMCM22 cop shows partial degradation of the regularly arranged layers and the presence of aggregated, widely distributed particles of irregular shapes. The thin and well-developed nanolayers, characteristic for the pristine support, were transformed into bulky clusters of fine particles, of the size in range of 100-200 nm. However, despite the fact that the support lost its layered structure, SEM image showed that amorphization of the sample was only peripheral. On the contrary to FeMCM22 cop, the layered zeolite modified by adsorption from the solution or incipient wetness impregnation preserved its structural characteristics. The aggregation of the plate-like particles into donut shapes remained the same as in the case of the support and the morphological features of the zeolite were not changed.

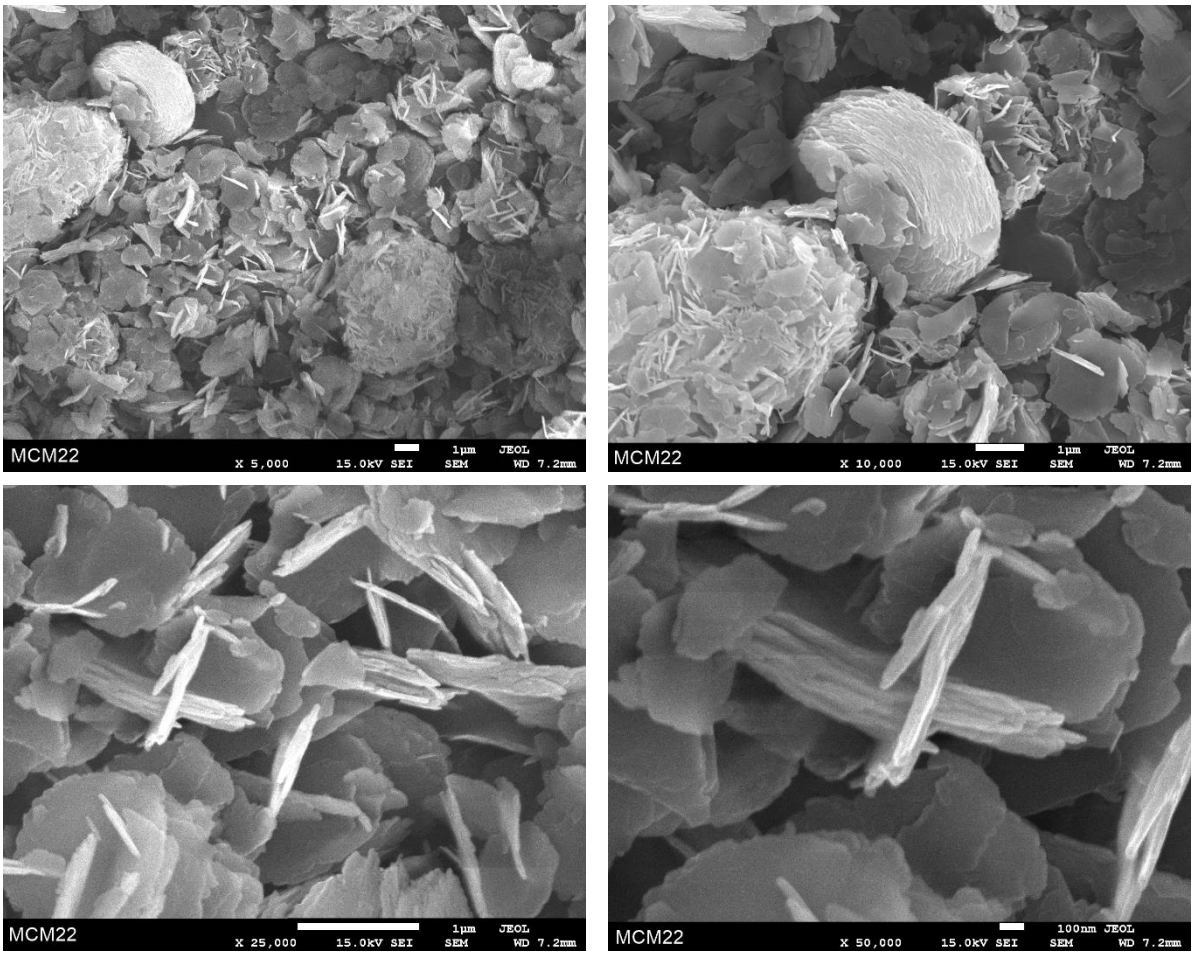

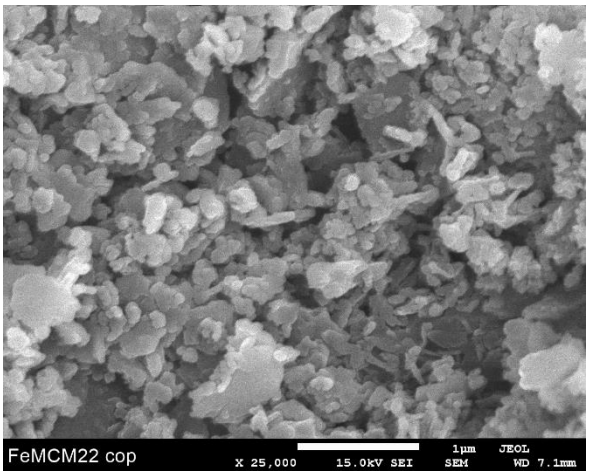
FeMCM22 cop
X 25,000 15.0kV SEI 1µm JEOL SEM WD 7.1mm

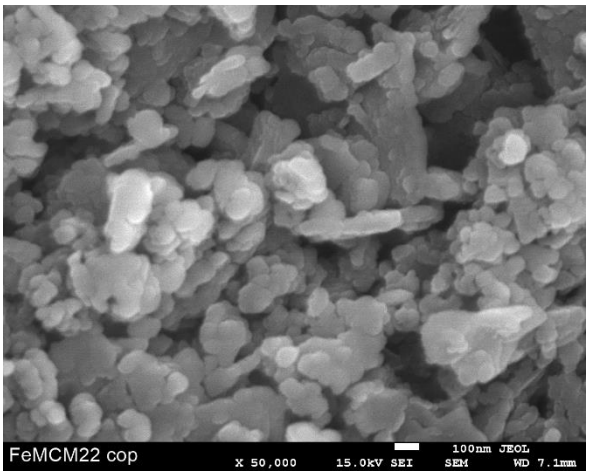
FeMCM22 cop
X 50,000 15.0kV SEI 100nm JEOL SEM WD 7.1mm

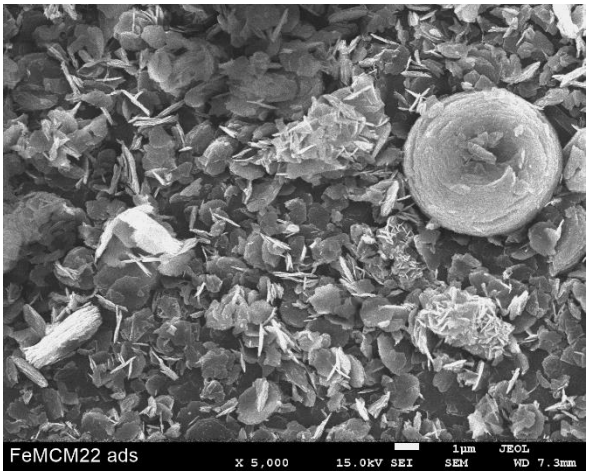
FeMCM22 ads
X 5,000 15.0kV SEI 1µm JEOL SEM WD 7.3mm

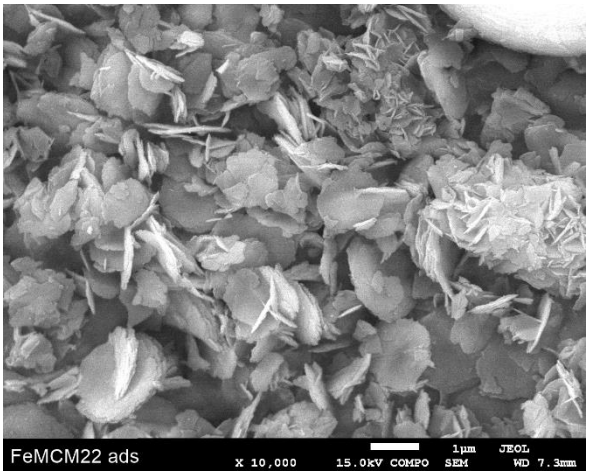
FeMCM22 ads
X 10,000 15.0kV COMPO 1µm JEOL SEM WD 7.3mm

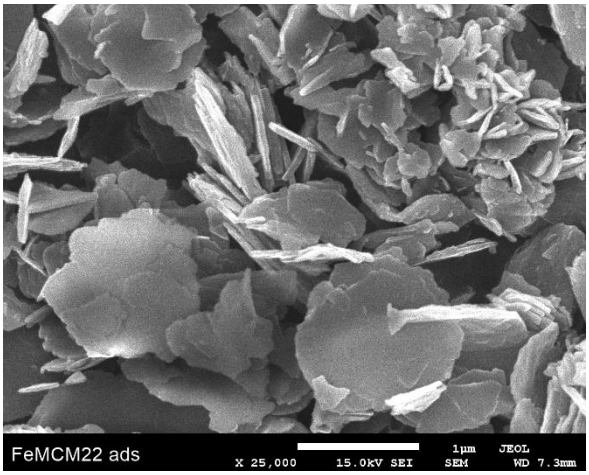
FeMCM22 ads
X 25,000 15.0kV SEI 1µm JEOL SEM WD 7.3mm

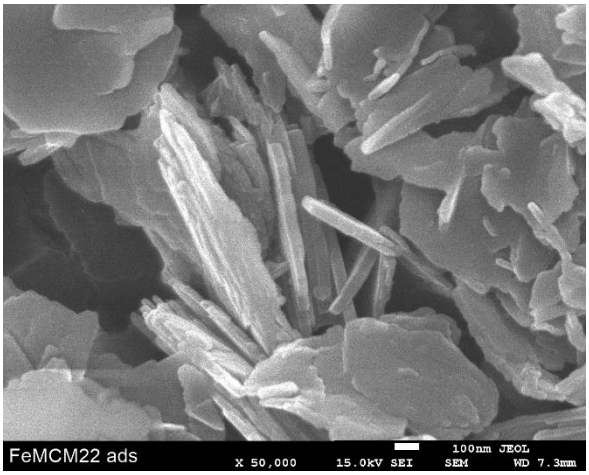
FeMCM22 ads
X 50,000 15.0kV SEI 100nm JEOL SEM WD 7.3mm

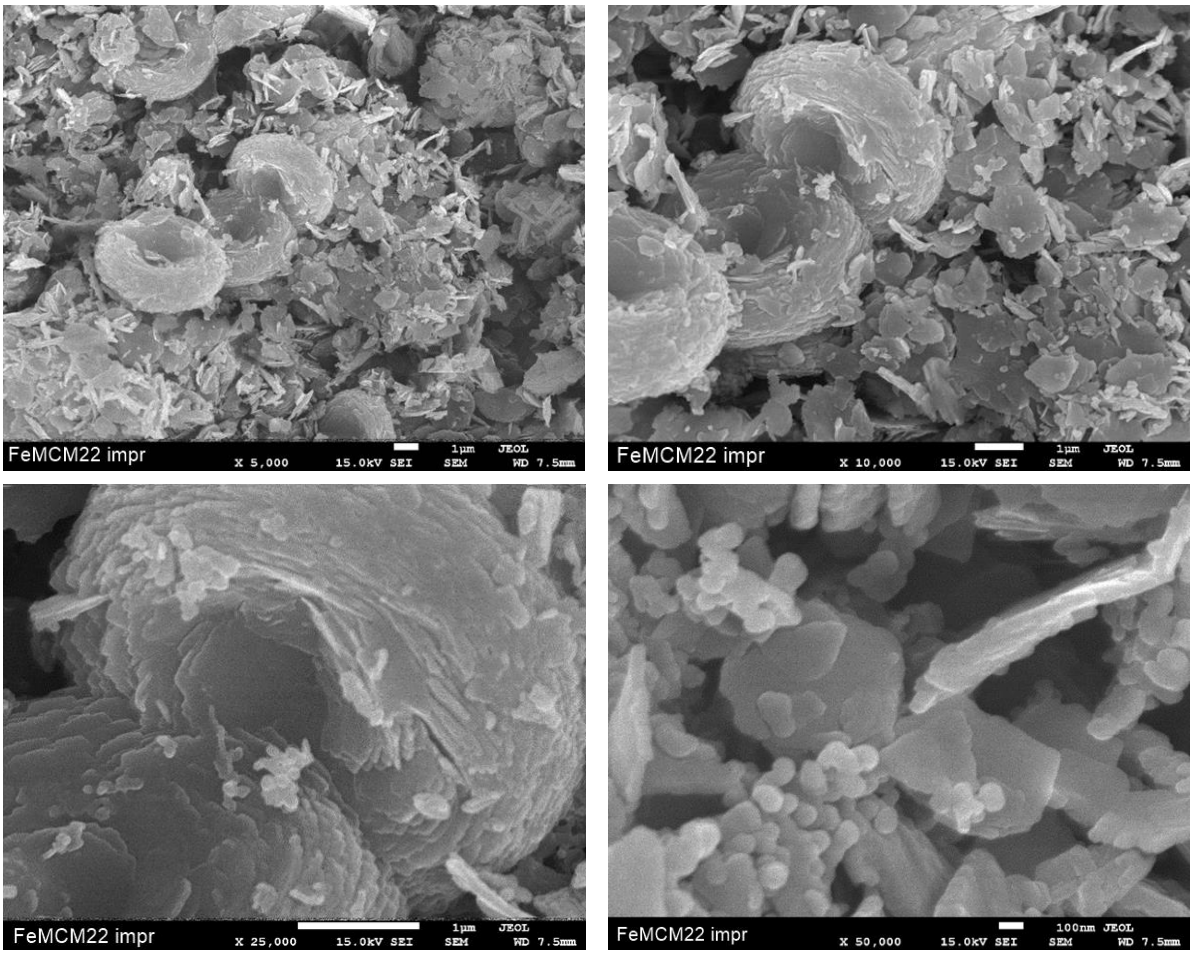

Figure 46. SEM images MCM-22 and MCM-22-supported catalysts

Morphology of the materials analyzed by TEM microscopy

Transition electron microscopy (TEM) was applied in order to analyze morphology of the supports and the catalysts in detail, on a nanoscopic scale. The micrographs recorded for the samples of clinoptilolite-catalysts are presented in **Figure 47**, while **Figure 48** presents the investigated Fe-derivatives of MCM-22. For the purpose of identification of the arrangement of the zeolite particles and the form of active phase, various modes were applied, including bright-field (BF), high-angle annular dark-field (HAADF), and high resolution (HR).

It can be observed in **Figure 47** that before modifications, clinoptilolite exhibits a regular lamellar structure with relatively smooth surface and irregular crystal size of ca. 100-500 nm. Additionally, it can be observed from HR micrographs that the zeolitic layers consist of piles of thin, flake-like plates, rather than separated individuals. Introduction of the active phase did not result in any significant changes in the morphology of the material and the characteristic zeolitic lamellae are still present in the

Fe-clinoptilolite samples. Regardless the modification route, one can notice the appearance of small particles of metal oxide, with the size of ca. 5 nm. Moreover, the black spots visible in the micrographs suggest that considerable amount of the active phase was located on the external surface of the zeolitic layers. Moreover, the preparation procedure remarkably influenced dispersion of iron species within the support. In the case of FeClin cop, iron species exhibited dual speciation, in which Fe_2O_3 was present in a dispersed or more aggregated form. In contrast, iron oxide in FeClin ads showed the highest degree of aggregation, which can be easily observed from HAADF micrograph. Last but not least, the most uniform dispersion of Fe_2O_3 was obtained for FeClin impr. All of the observations are in line with UV-Vis-DR and XRD analyses, which confirmed the presence of iron oxide particles in the catalysts.

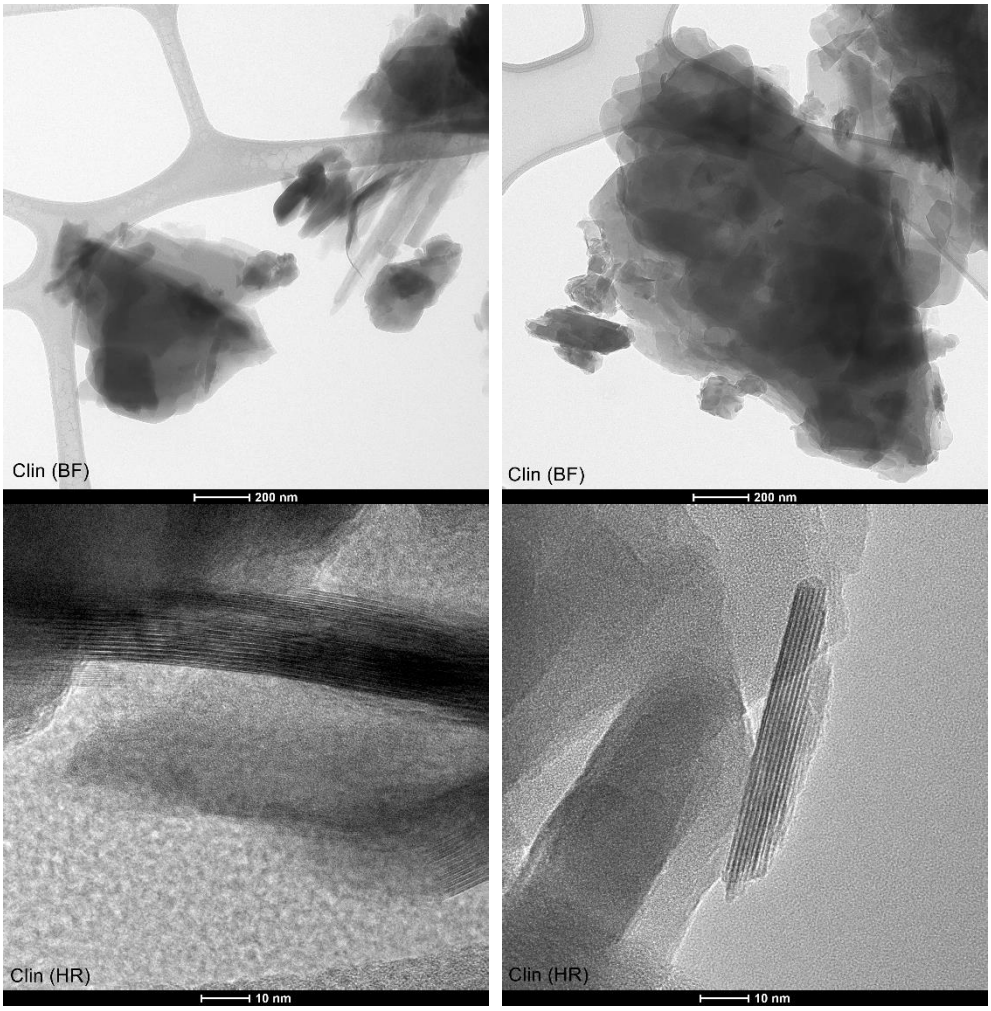

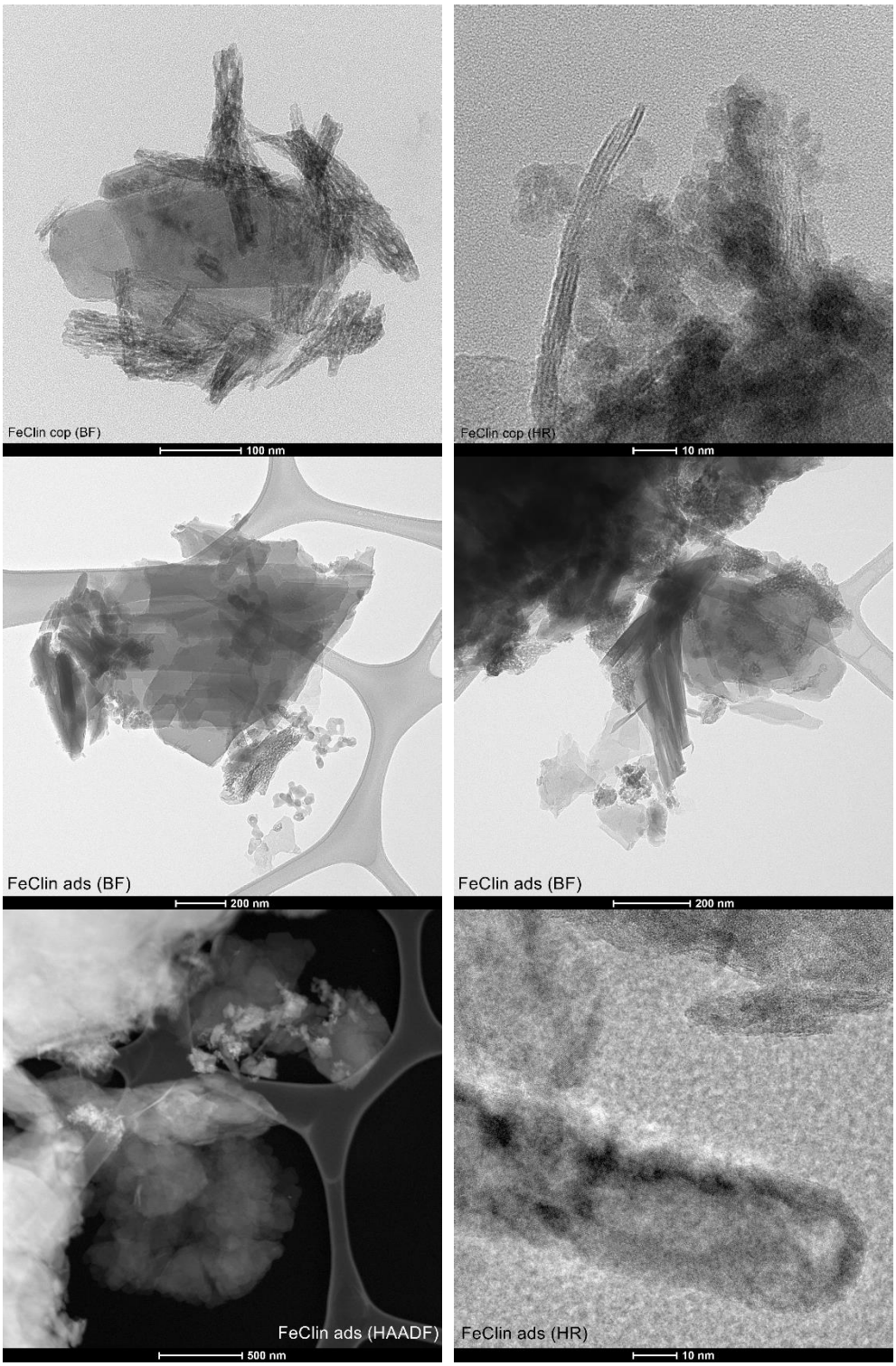
FeClin cop (BF)
100 nm
FeClin cop (HR)
10 nm
FeClin ads (BF)
200 nm
FeClin ads (BF)
200 nm
FeClin ads (HAADF)
500 nm
FeClin ads (HR)
10 nm

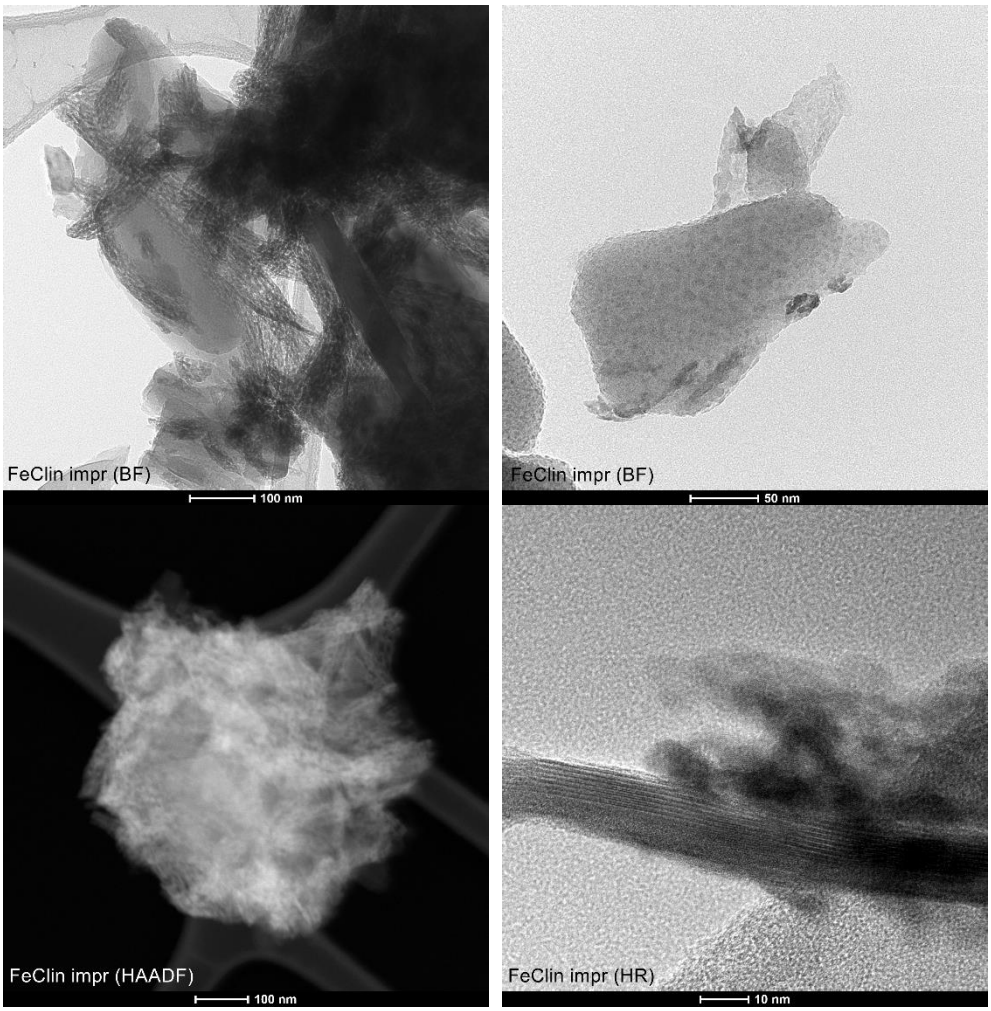

Figure 47. Bright-field (BF), high-angle annular dark-field (HAADF), and high resolution (HR) micrographs recorded for clinoptilolite-supported Fe-catalysts prepared by various methods (description of each sample with its code is present in the micrograph)

The morphology of the pristine MCM-22, presented in **Figure 48**, consisted of hexagonal, small plates. One can notice that the material exhibited irregular size and shape of particles, which is characteristic for this zeolite while HMI is used as a structure-directing agent [540]. The micrographs recorded in HR mode indicated that the MWW layers formed nanoscale crystallites, distinguished into the regular arrays of 0.7 × 0.7 nm cups and 10-MR channel system. Similarly to clinoptilolite-supported catalysts, deposition of iron species resulted in the appearance of distinct, bulky aggregates of iron oxide. However, as confirmed by XRD studies, in the case of FeMCM22 cop, the layered structure characteristic for MWW topology was almost completely degraded and substituted with big deposits of metal oxide. It is expected that the most uniform dispersion of iron and the lowest degree of aggregation was obtained for FeMCM22 ads, thus, adsorption from the solution seems to be beneficial method for

the introduction of iron in a form of isolated or oligonuclear species. In contrast, in the case of FeMCM22 impr iron was present in a form similar to FeMCM22 cop. However, impregnation did not result in any degradation of the layered structure. Additionally, it can be noticed that the majority of Fe_2O_3 particles in the sample is located on the external surface of MWW layers.

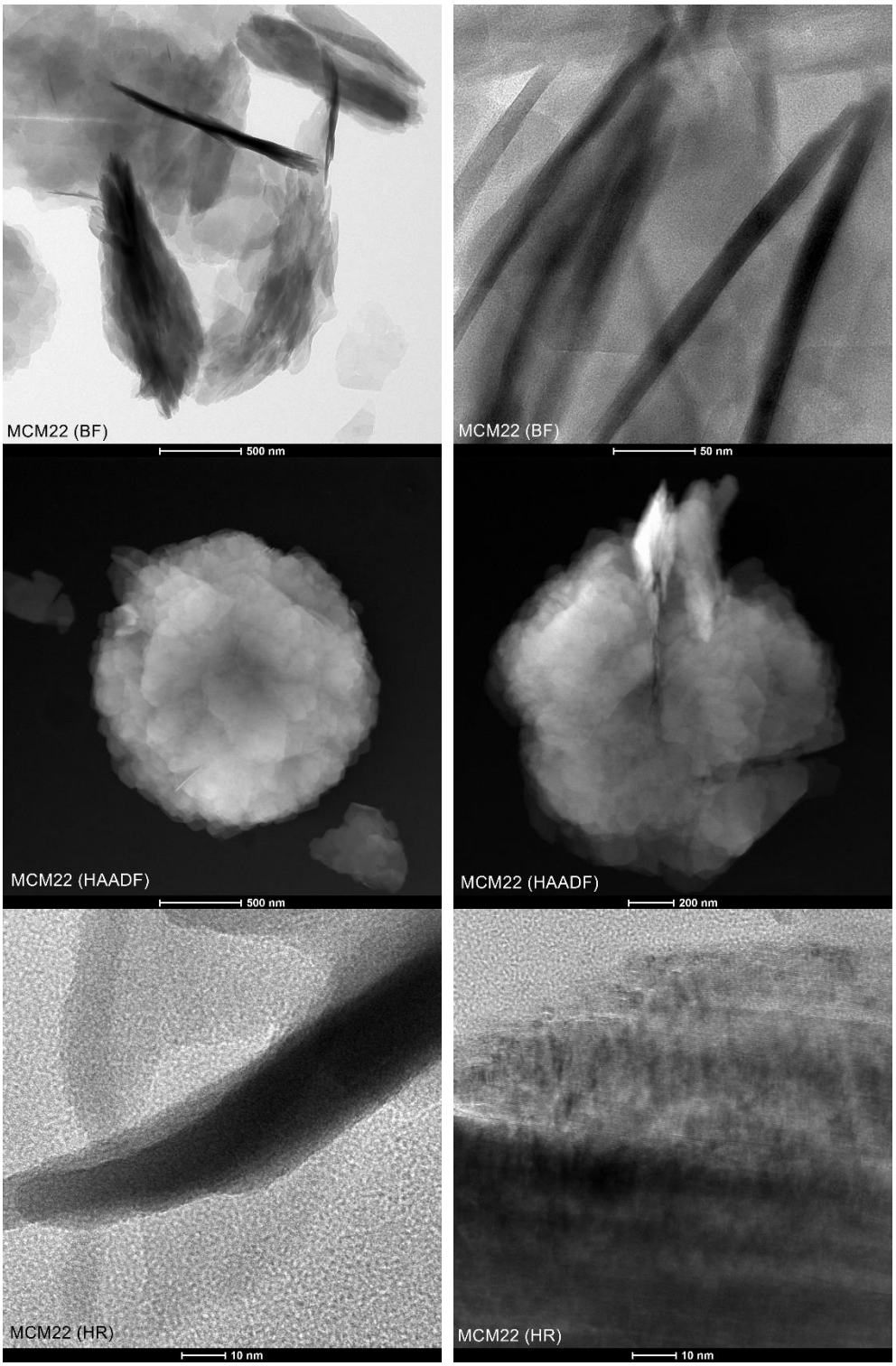

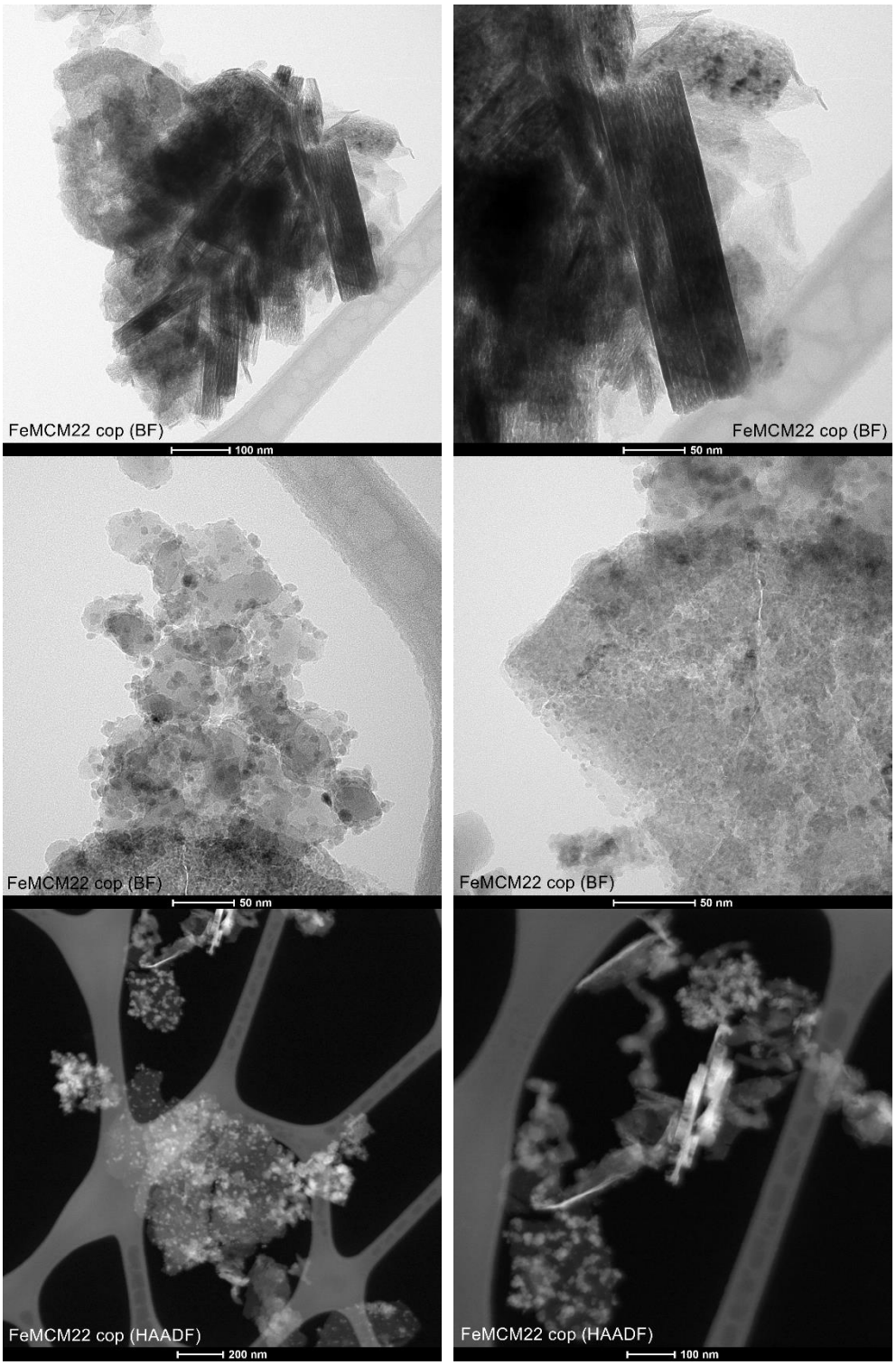
FeMCM22 cop (BF)
100 nm
FeMCM22 cop (BF)
50 nm
FeMCM22 cop (BF)
50 nm
FeMCM22 cop (BF)
50 nm
FeMCM22 cop (HAADF)
200 nm
FeMCM22 cop (HAADF)
100 nm

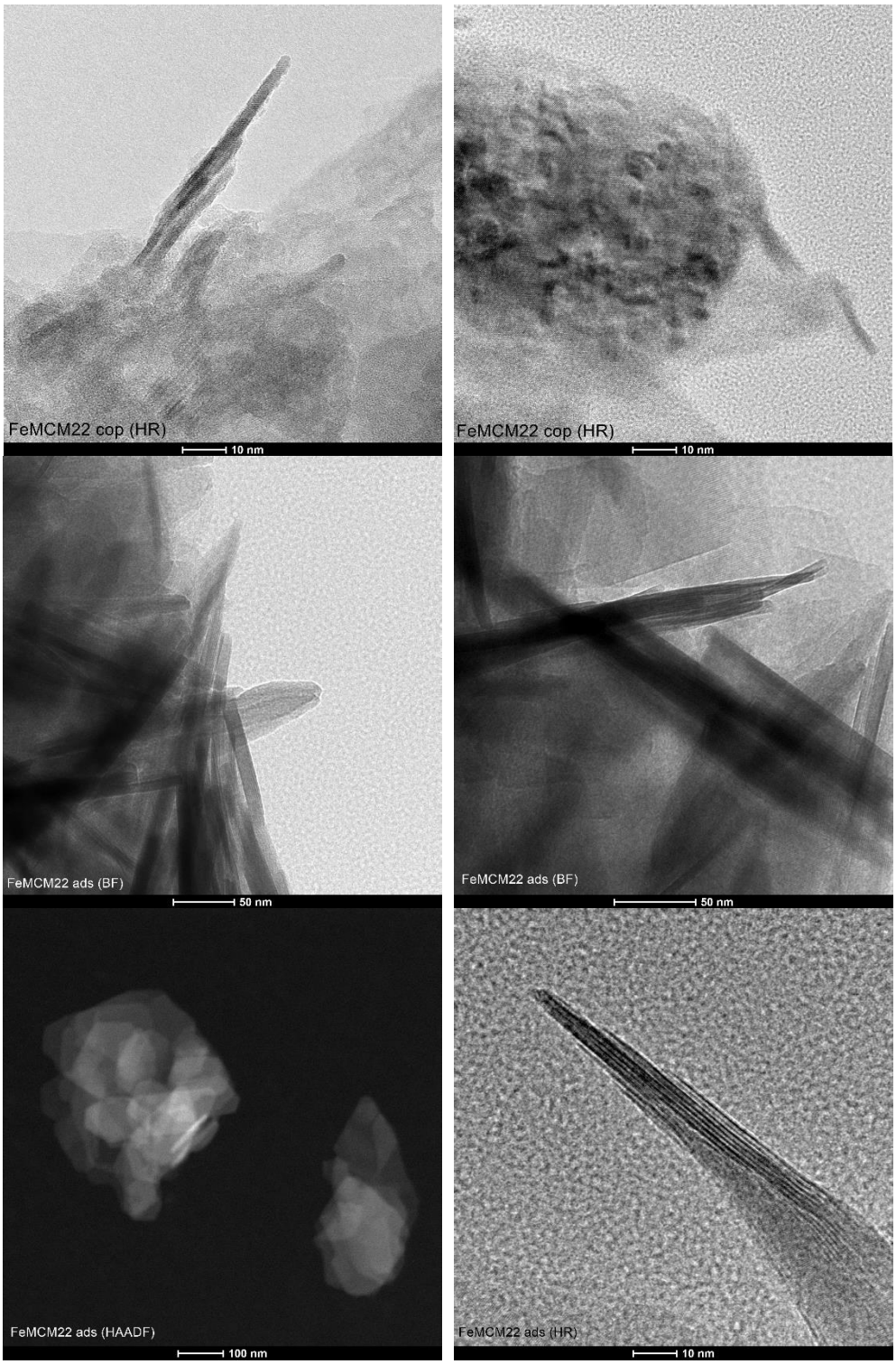
FeMCM22 cop (HR)
10 nm
FeMCM22 cop (HR)
10 nm
FeMCM22 ads (BF)
50 nm
FeMCM22 ads (BF)
50 nm
FeMCM22 ads (HAADF)
100 nm
FeMCM22 ads (HR)
10 nm

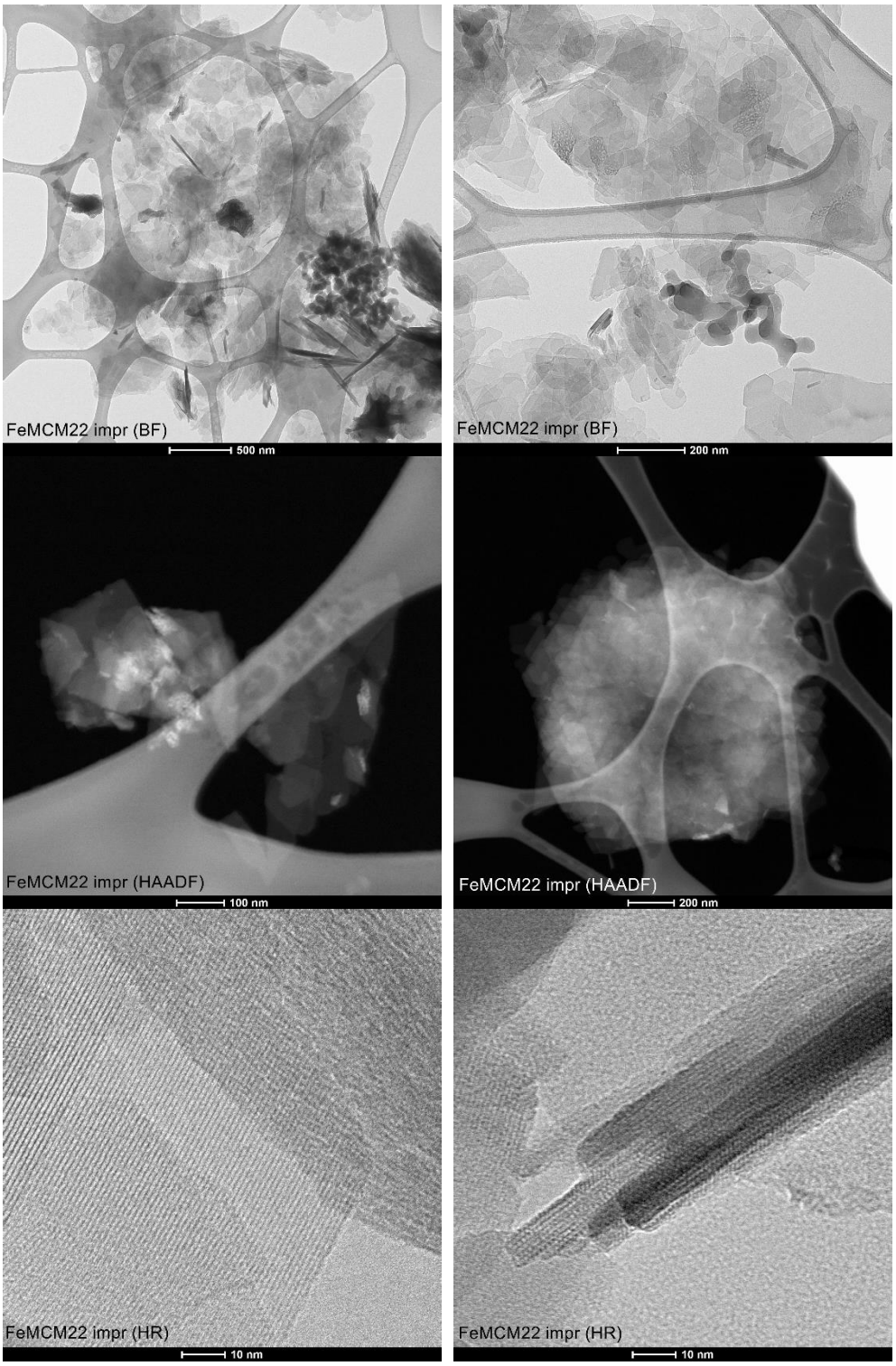

Figure 48. Bright-field (BF), high-angle annular dark-field (HAADF), and high resolution (HR) micrographs recorded for MCM-22-supported Fe-catalysts prepared by various methods (description of each sample with its code is present in the micrograph)

Acidity of the materials

Adsorption and activation of ammonia during NH_3-SCR requires the abundance of the acidic sites on the catalyst surface [81,541]. Therefore, the total acidity of the investigated materials, with the distinction to the weak, medium, and strong acid sites was determined by temperature-programmed desorption of ammonia (NH_3-TPD). In order to facilitate the assignment of the desorption peaks to the specific temperature, the obtained patterns were deconvoluted by fitting to Gaussian function. The results of NH_3 desorption rate in the temperature region of 100-800 °C are presented in **Figures 49-51.** The approximated number of the acid sites in the materials is summarized in **Table 17.**

Figure 49 presents the comparison of the NH_3-TPD patterns obtained for the catalysts supports: clinoptilolite before and after protonation and as-synthesized MCM-22. It can be observed that TPD profile of clinoptilolite exhibited desorption peaks with the maxima at 185, 255, and 600 °C. Therefore, the material contains acid centers of various strength: in the case of weak acid sites, ammonia is desorbed below 200 °C, the region between 200 and 400 °C corresponds to the centers of medium strength, while the sites desorbing NH_3 above 400 °C are characterized by strong strength [351]. According to the literature, these sites are mainly assigned to Lewis-type, represented by extra-framework ions [542]. After protonation, the intensity of the desorption peaks noticeably decreased, however, their position was only slightly shifted to lower temperature. Therefore, the acid centers of H-Clin exhibited lower affinity to the adsorption of NH_3 molecules. This effect is a consequence of the partial removal of Al^{3+} cations, considered as Lewis acid sites, which is in line with the results of ICP-OES.

The NH_3-TPD profile of MCM22 exhibited two intense desorption peaks at 195 °C and 340 °C, ascribed to the sites of weak and medium strength, respectively. Below 250 °C, the density of acid sites of the synthetic and protonated natural zeolite was similar, however, the peak corresponding to the sites of medium strength was located at higher temperature in the case of MCM22. Therefore, the acid sites of MCM22 created stronger chemical bonds with ammonia molecules, comparing to the protonated clinoptilolite. Nevertheless, as presented in **Table 17**, the total concentration of acid centers was similar for both supports. Additionally, MCM22 did not exhibit any desorption peak located above 400 °C. Therefore, the material contained exclusively acid centers of weak and medium strength.

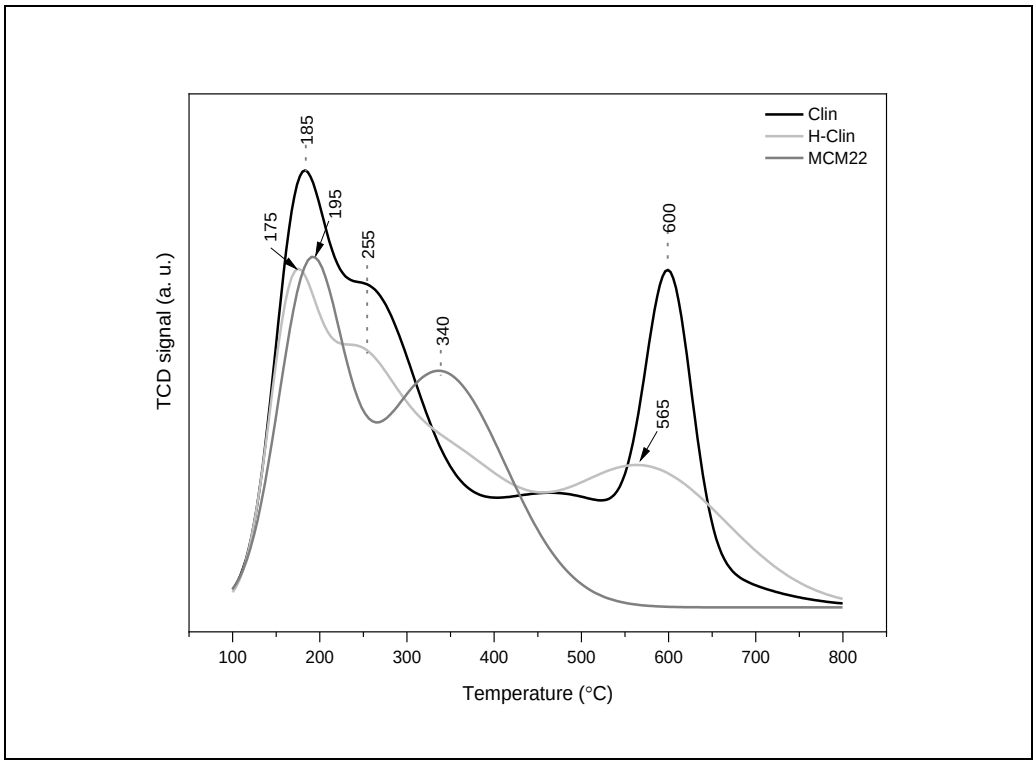

Figure 49. NH_3-TPD profiles obtained for non-modified clinoptilolite (Clin), protonated clinoptilolite (H-Clin), and as-synthesized MCM-22

Figure 50 and **Figure 51** show NH_3-TPD profiles obtained for FeClin and FeMCM22 catalysts, respectively. Similarly to the supports, all of the materials contained acidic centers of weak, medium, and strong strength. In the case of clinoptilolite-supported catalysts, the applied method of modification had a significant influence on the strength and the concentration of acid sites. According to the data collected in **Table 17**, the acidity followed the order of FeClin ads < FeClin cop < FeClin impr. According to the literature, the desorption peaks detected below 300 °C are ascribed to the sorption of NH_3 on Brönsted acid sites [543]. Since the intensity of this peak for FeClin ads is significantly diminished comparing to H-Clin, adsorption from the solution resulted in the destruction of some part of Brönsted sites in the zeolite. Alternatively, the decreased density of acid sites could result from the presence of Fe_2O_3 particles, as confirmed by UV-vis-DR studies (described in further part of the thesis). These species possibly covered the acidic centers of the zeolitic framework (Si(OH)Al, AlO^+, $Al(OH)_2^+$ $AlOH^{2+}$, etc.), simultaneously blocking the sites for effective adsorption of NH_3 molecules [543]. FeClin impr showed similar shape of TPD profile, and the same temperature values of NH_3 desorption as FeClin ads. However, total acidity of the impregnated sample was significantly higher, which was assigned

especially to its abundance in the sites of weak and medium strength. Furthermore, the total density of the acid sites of FeClin cop increased, and the desorption peak corresponding to the acid sites of medium strength was shifted to 395 °C. This result suggested that Fe^{3+} introduced into the framework and extraframework positions in this sample delivered new, stronger acid centers of Lewis type. Additionally, in the case of FeClin cop, the increased acidity can be related to the presence of sulfates in the precursor of the active phase. According to the literature [463,544], sulfation of Fe-zeolites increases NH_3 adsorption capacity and formation of ammonium sulfites or sulfates. Decomposition of these compounds above 325 °C results in their removal and generation of Fe-containing surface species, accessible for ammonia adsorption.

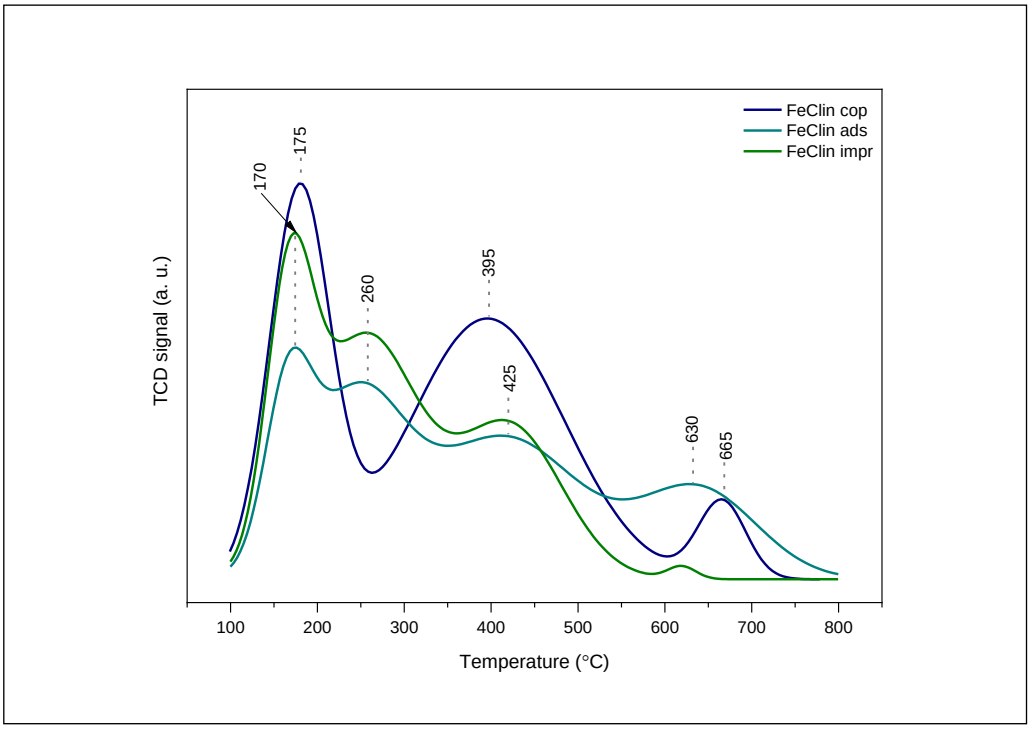

Figure 50. NH_3-TPD profiles obtained for clinoptilolite modified with Fe by various methods

NH_3-TPD profiles of FeMCM22 catalysts, presented in **Figure 51** revealed that modification with iron influenced on the layered zeolite differently than on the natural clinoptilolite. Comparing the results obtained for MCM22 and its Fe-derivatives, it can be noticed that the position of desorption peaks only slightly changed, regardless the modification procedure. However, there was a significant difference between the amount of acid centers between the pristine zeolite and the catalysts. It can be noted from **Table 17** that the density of the acid sites in the materials can be ordered as FeMCM22 impr <

FeMCM22 cop < FeMCM22 ads. Thus, in contrast to FeClin cop, FeMCM22 cop exhibited the lowest concentration of the acid centers among the catalysts. In this case, total concentration of the acidic sites diminished almost doubly, comparing to the support. This decrease can be assigned to the elimination of Si and Al form the zeolitic framework, and partial amorphization of the sample, confirmed by ICP-OES and XRD results, respectively. Additionally, referring to UV-vis-DR studies performed over the materials, FeMCM22 cop contained the highest amount of Fe_2O_3 particles, which could block the residual acid sites of the zeolite framework. Thus, modification of MCM22 with iron decreased total concentration of the acid sites, probably as the effect of the deposition of the particles of Fe_2O_3. Interestingly, in the case of FeMCM22 cop and FeMCM22 ads, introduction of iron led the formation of new strong acid centers, confirmed by the peaks at 635 and 655 °C, respectively. Kim and Yang [545] declared that desorption of ammonia occurring in this temperature region is ascribed to the presence of Fe_2O_3 particles. Therefore, in fact, the particles of iron oxide could partially cover weak acid sites, but delivered new, strong centers, confirmed by the peaks located above 600 °C.

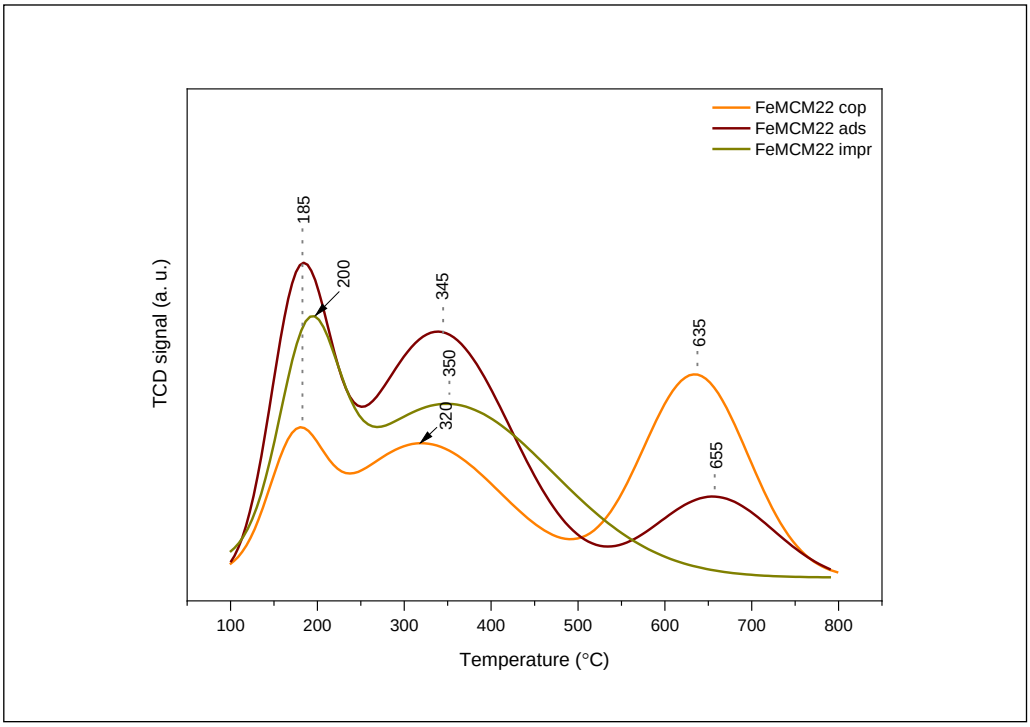

Figure 51. NH_3-TPD profiles obtained for MCM-22-modified with Fe by various methods

Table 17. Approximate concentration of the acid sites in the investigated materials

Sample code	Concentration of the acid sites (µmol · g^{-1})			
	Weak sites	**Medium sites**	**Strong sites**	**Total amount of sites**
Clin	887	661	689	**2237**
H-Clin	689	532	292	**1513**
FeClin cop	850	561	171	1582
FeClin ads	495	424	511	1430
FeClin impr	739	536	378	1653
MCM22	720	515	-	**1235**
FeMCM22 cop	319	288	438	1045
FeMCM22 ads	679	526	172	1377
FeMCM22 impr	555	380	-	935

Reducibility of the catalysts

Thermo-programmed reduction with H_2 (H_2-TPR) studies were conducted in order to elucidate reducibility of the active phase introduced into the zeolitic supports. The obtained profiles for FeClin and FeMCM22 catalysts are presented in **Figure 52** and **Figure 53**, respectively. All of the investigated materials revealed characteristic peaks assigned to the reduction of various iron species. In general, the isolated Fe^{3+} species are firstly reduced to Fe^{2+} at low temperature, while the reduction to Fe^0 takes place above 650 °C [455]. Basing on the similar intrazeolite environment of iron species, the differences between the reduction properties of the materials were explored after deconvolution of the obtained H_2-TPR profiles.

As can be seen in **Figure 52**, there is a strong correlation between the modification method and redox properties of FeClin catalysts. Generally, all of the materials exhibited intense reduction peak below 500 °C, attributed to the transfer of Fe^{3+} to Fe^{2+} [87]. Nevertheless, the reduction temperature differs for the materials, following the order of FeClin impr (325 and 440 °C) < FeClin ads (325 and 460 °C) < FeClin cop (360 and 490 °C). Thus, Fe^{3+} species introduced by impregnation were noticeably easier to reduce, comparing to other methods. Interestingly, on the contrary to FeClin ads and FeClin

impr, FeClin cop did not exhibit any reduction behavior of Fe_2O_3. Therefore, both of the peaks in H_2-TPR profile of the material can be ascribed to the presence of isolated Fe^{3+} species, which is consistent with UV-Vis-DR studies. Lower reduction temperature facilitates redox process and weaker binding energy of isolated iron species, thus, is beneficial for the efficiency of low-temperature NH_3-SCR [439]. Moreover, both FeClin ads and FeClin impr showed peaks at 670 and 660 °C, respectively, which correspond to the reduction of Fe_xO_y species to metallic iron (Fe^{2+} to Fe^0) [489]. Besides, the broad peak at 560 °C, detected only for FeClin impr is assigned to the binuclear or oligomeric Fe_xO_y cations in the zeolite [455]. Higher reduction temperature of these species is attributed to stronger "shielding effect", comparing to the isolated Fe^{3+} sites [455]. As a result, oligomeric clusters are expected to exhibit higher catalytic activity in NH_3-SCR in the high temperature range.

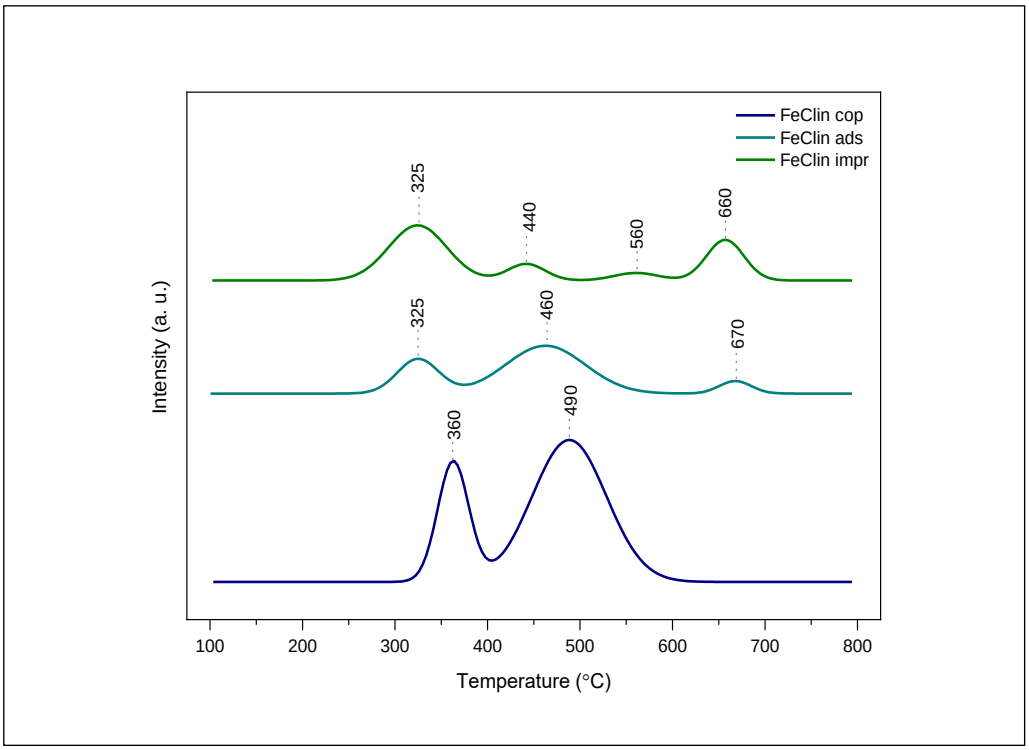

Figure 52. H_2-TPR profiles obtained for the investigated clinoptilolite-supported catalysts with Fe

From **Figure 53** it can be observed that FeMCM22 catalysts exhibited slightly different redox behavior than FeClin samples. The reduction temperature ascribed to the Fe^{3+} species introduced into the hierarchical support followed the order of FeMCM22 impr (270 and 460 °C) < FeMCM22 ads (300 and 410 °C) < FeMCM22 cop (345 °C). Thus, the influence of modification method on the reducibility of iron species was similar to the natural zeolite. Nevertheless, the reduction temperature of these species

was noticeably lower for FeMCM22 materials. This effect can be explained by their weaker interaction with MWW framework, comparing to the HEU structure. Surprisingly, FeMCM22 impr revealed the intense peak at 270 °C. This reduction temperature is rather unusual for iron-modified zeolites. It is expected that this phenomenon occurs due to the deposition of Fe^{3+} species on the external surface of the material, easily accessible for H_2. In contrast to FeClin cop and FeClin ads, FeMCM22 cop and FeMCM22 ads exhibited reduction peaks at 555 °C and 527, and 634 °C, respectively. The reduction peaks at 520, 550, 630, and 635 °C are the evidence of the presence of higher amount of oligomeric Fe-oxo cations in the hierarchical support [455]. What is more, the broad peak of relatively low intensity at 740 °C, detected for FeMCM22 cop is attributed to the reduction of large Fe_2O_3 clusters. It is possible that these particles contributed to the partial destruction of zeolitic framework, which was confirmed by other characterization methods [352].

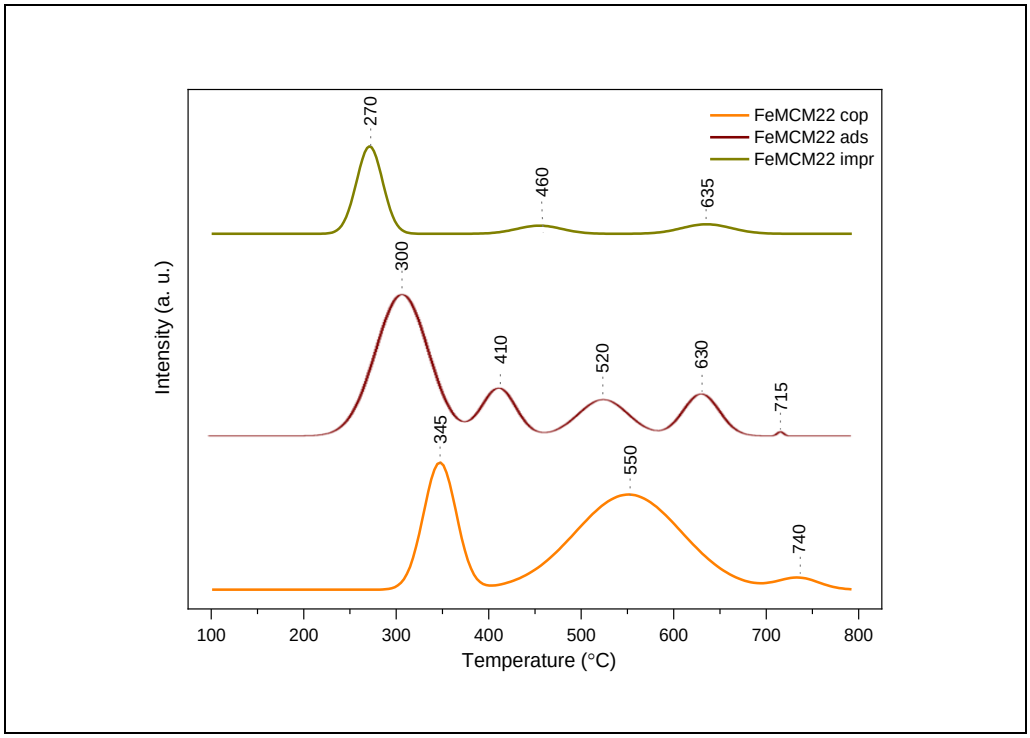

Figure 53. H_2-TPR profiles obtained for the investigated MCM22-supported catalysts with Fe

Thermogravimetric studies of the materials

Thermogravimetric studies of the catalysts within 30-800 °C were performed to investigate their thermal stability. Additionally, in the case of MCM22-supported materials, the analysis enabled to determine the efficiency of the structure-directing agent decomposition. The comparison of the

thermograms of the non-modified zeolites is presented in **Figure 54.** The outcomes of the measurements performed for clinoptilolite- and MCM22-supported catalysts are presented in **Figure 55** and **Figure 56**, respectively. Considering NH_3-SCR reaction, the most important temperature region is 150-450 °C, thus, it was marked in the thermograms by dotted lines. Furthermore, **Table 18** provides an overview of the percentage weight loss of the materials.

Figure 54 reveals that the weight loss of Clin and MCM22 was ca. 10 and 8% of the initial value, respectively. For both zeolites, it was related to the removal of the structural H_2O molecules. The weight of clinoptilolite was decreasing gradually in the temperature region of 30-650 °C, to finally stabilize above 650 °C. Generally, three weight losses can be distinguished in the curve of Clin, indicating three steps of H_2O and hydroxyl groups elimination from the zeolitic structure. The first step, below 300 °C, is assigned to the desorption of water attached to the surface by weak physical bonds. Subsequently, the framework hydroxyl groups were removed in the region of 300-650 °C. At least, above 650 °C, the slight weight loss was related to the elimination of strongly bounded structural water [531]. In contrast to Clin, the weight loss of MCM22 related to the desorption of H_2O occurred only within 30-200 °C and the increasing temperature did not result in any further weight changes. Additionally, since no weight loss was observed above 300 °C (temperature of HMI decomposition), the structure-directing agent of MCM22 was successfully removed during calcination. The noticeable change of the TGA curves obtained for the zeolites is a consequence of the differences between their structural characterizations. MCM-22, as the hierarchical zeolite with higher external surface area exhibits more uniform and well-developed mesoporosity, comparing to clinoptilolite. According to the literature, conventional zeolites with tetrahedral-octahedral morphology contain higher accumulation of H_2O molecules than the hierarchical zeolites [546]. What is more, the proceeding weight loss of clinoptilolite above 200 °C probably resulted from dehydroxylation of hydroxide complexes, generated due to the presence of various metal cations (for example Na, K, Fe), which are absent in the structure of pristine MCM-22 [547]. Additionally, dehydroxylation is associated with the creation of hydrogen bonds between the migrating hydroxyls and H_2O molecules. As a consequence, not only OH species, but also the chemically adsorbed water is removed from the internal zeolitic structure [546], which explains slightly higher weight loss of Clin.

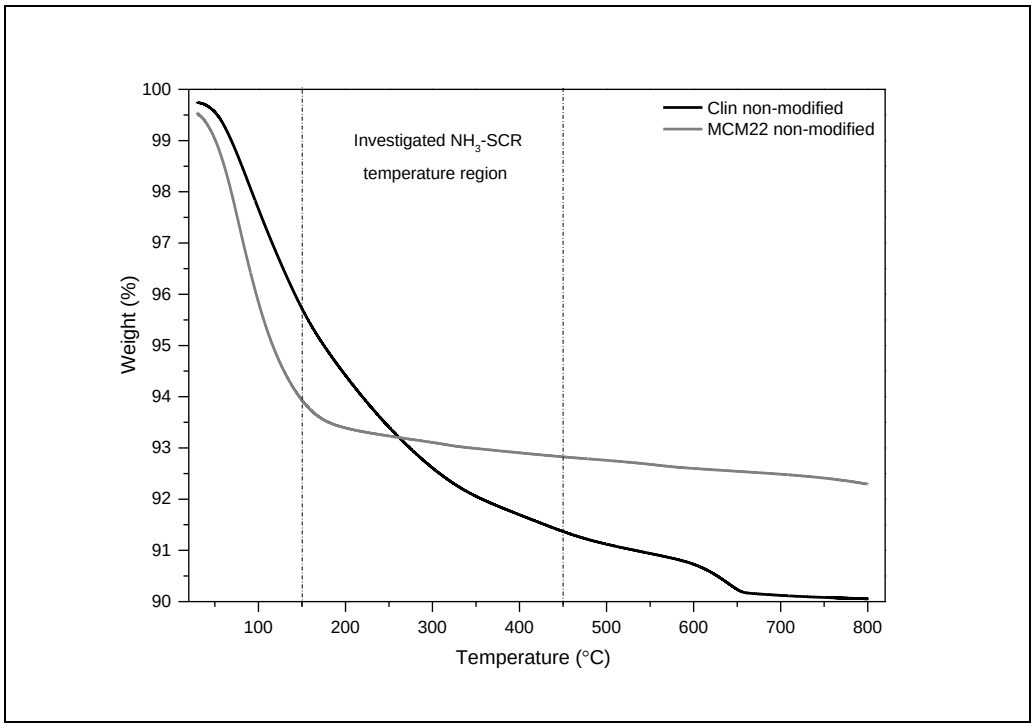

Figure 54. Results of TGA obtained for non-modified clinoptilolite (Clin), protonated clinoptilolite (H-Clin), and clinoptilolite-supported catalysts

The results of TGA obtained for clinoptilolite modified with Fe by various methods, presented in **Figure 55,** show that FeClin ads and FeClin impr exhibited slightly increased thermal stability comparing to FeClin cop, H-Clin, and Clin. This result can be explained by the higher amount of Fe^{3+} in the zeolitic structure, as well as Fe_xO_y aggregates, culminating on the external surface and in the internal structure of the zeolite. These species probably precluded unhampered migration of H_2O molecules by partial blockage of the pores. In the case of FeClin cop, the weight loss in the temperature range of 30-250 °C was similar to that of the support, while within 250-400 °C its thermal stability moderately increased. Furthermore, the weight loss of FeClin cop in range of 400-800 °C could result from the decomposition of the residual sulfate groups, remaining in the zeolitic framework after modification using $FeSO_4$ as Fe precursor [548]. In summary, the results of TGA obtained for FeClin catalysts indicated that the weight loss of the materials in the investigated temperature region of NH_3-SCR is related only to the removal of water molecules from the materials and the structure of the catalysts remains stable under the analyzed reaction conditions.

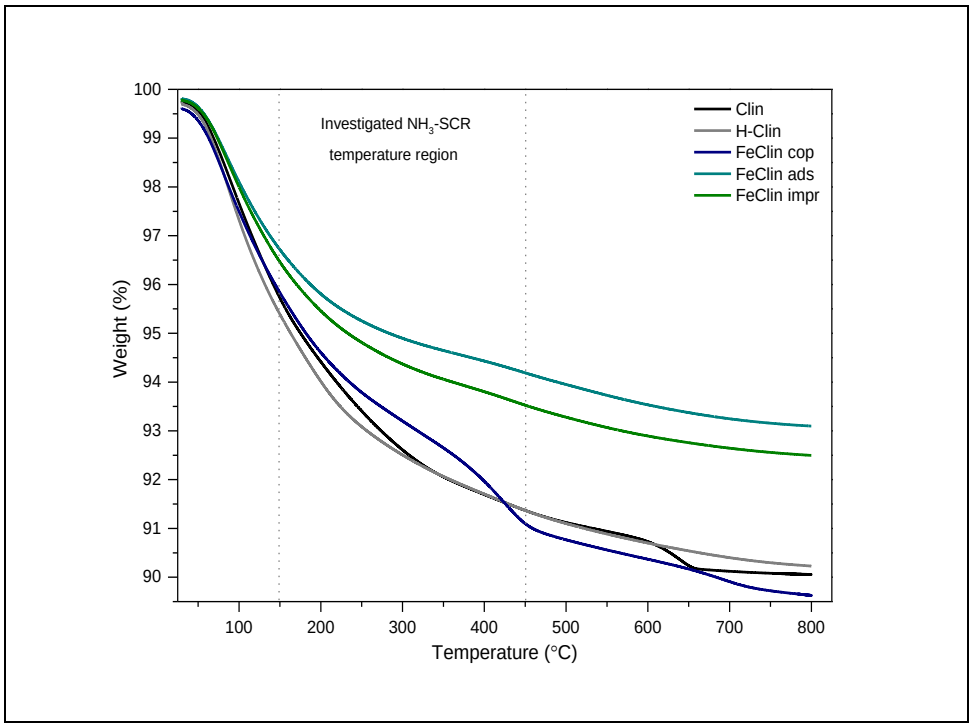

Figure 55. Results of TGA obtained for non-modified clinoptilolite (Clin), protonated clinoptilolite (H-Clin), and clinoptilolite-supported catalysts

The thermograms obtained for the pristine and iron-modified MCM22 are depicted in **Figure 56.** Similarly to FeClin catalysts, the modification method had a significant impact on thermal stability of the materials, however, the weight of the catalysts stabilized at lower temperature of ca. 175 °C and only two steps of weight loss can be distinguished in the curves. In the case of all iron-modified samples, the weight loss was lower than that of the pristine zeolite. The effect was related to the presence of iron oxide aggregates deposited around the pores of the materials, which hindered free migration of water molecules from the zeolite. Among the catalysts supported on MCM-22, the lowest weight loss was observed for FeMCM22 cop, which can be explain by the strongest penetration of the internal zeolitic structure and deposition of the highest amount of iron species around the pore openings. On the other hand, in the case of FeClin impr, exhibiting higher weight loss, the active phase was probably deposited on the external surface of the zeolite and did not act as a strong barrier for the effective desorption of H_2O molecules. Confirmation of this fact can be found in the lower value of S_{EXT} of FeMCM22 impr, comparing to the other catalysts, resulting from the presence of small Fe_xO_y clusters on the outer surface of the material. Overall, the TGA results obtained for FeMCM22 catalysts showed that the weight loss

of the materials in the analyzed temperature region of NH_3-SCR is related only to the removal of water and the structure of the catalysts preserves stability at the investigated reaction conditions.

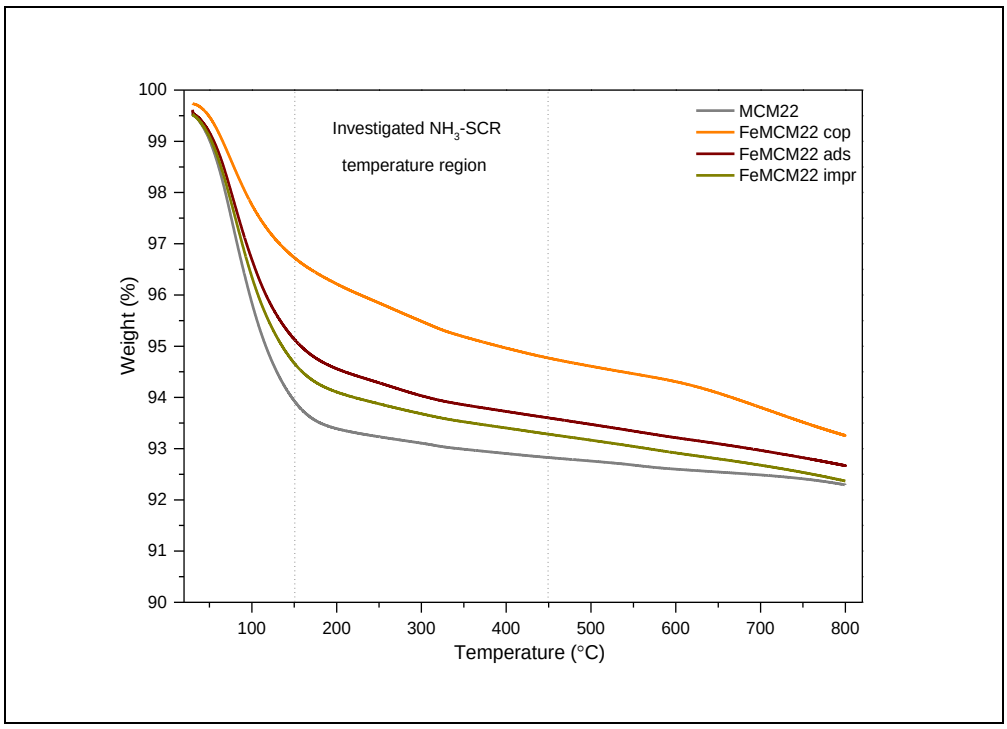

Figure 56. Results of TGA obtained for the pristine and Fe-modified MCM22

Table 18. Weight loss of the investigated materials in the temperature range of 30-800 °C

Sample code	Weight loss in the particular temperature range (%)			Total (%)
	30-200 °C	200-400 °C	400-800 °C	30-800 °C
Clin	5.54	2.76	1.63	9.93
H-Clin	6.18	2.22	1.41	9.81
FeClin cop	5.29	2.89	2.22	10.4
FeClin ads	4.32	1.25	1.38	6.95
FeClin impr	4.45	1.75	1.32	7.52
Sample code	**Weight loss in the particular temperature range (%)**			**Total (%)**
	30-175 °C	175-800 °C		30-800 °C
MCM22	6.51	1.25		7.76
FeMCM22 cop	3.53	3.24		6.77
FeMCM22 ads	5.29	2.07		7.36
FeMCM22 impr	5.74	1.92		7.66

FT-IR spectroscopic studies of the characteristic chemical groups

The characteristic chemical groups present in the zeolitic supports and the catalysts were examined using FT-IR spectroscopy. The results obtained for the pure and Fe-modified clinoptilolite and MCM-22 are presented in **Figure 57** and **Figure 58**, respectively. In general FT-IR spectra of zeolites can be divided into three characteristic regions, corresponding to the following wavelength ranges:

- 3800-3400 cm^{-1} – O-H stretching vibrations,
- 1700-700 cm^{-1} – Si-O stretching and Al-Me-OH bending vibrations (where Me = cation of metal, for example Ca^{2+}, Mg^{2+}), O-H bending vibrations from H_2O in the inner structure of zeolites,
- 700-450 cm^{-1} – pseudo-lattice vibrations of the zeolitic framework.

In the case of clinoptilolite, the peak at 1048 cm^{-1} corresponds to the asymmetric stretching vibrations and it is sensitive to the content of Si and Al in the framework [530]. It can be observed from **Figure 57**, that the position of this peak remained unchanged for all of the samples. Thus, composition of the aluminosilicate framework of the zeolite was not affected during modifications with iron. The peaks appearing at 3626 and 3444 cm^{-1} correspond to the bridging OH groups of ≡Al-OH-Si≡ and their shape depends on the location of hydrogen atoms bonded to oxygen atoms in the framework. Even though the above-mentioned peaks are present in the spectra of FeClin ads and FeClin impr, they are noticeably less intense than that FeClin cop. Therefore, both adsorption from the solution and impregnation methods resulted in the slight reconstruction of the zeolitic framework. According to the literature [549,550], ≡Al-OH-Si≡ surface groups, and the framework ≡Al-OH, and ≡Si-OH species are ion-exchange sites of the zeolites. Therefore, modification of the material by adsorption from the solution possibly resulted in the neutralization of ≡Si-O^-Al and ≡Al-O^- by Fe^{3+} cation. Additionally, the peak at 3444 cm^{-1}, intense for Clin, H-Clin, and FeClin cop, and almost absent for FeClin ads and FeClin impr, arises from monomeric hydrogen bonds. Thus, it can be expected that co-precipitation provided the formation of hydroxylated surface iron species, as presented in the reaction described by **Equation (133):**

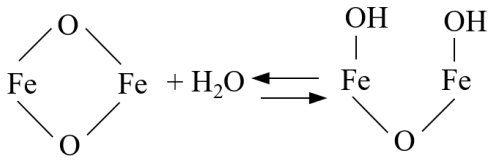

(133)

According to the literature, these species play a crucial role in NH_3-SCR, since they act as the Brönsted acid sites, which are indispensable for the effective course of the redox catalytic cycle [352,530]. Furthermore, it can be observed from **Figure 58** that similarly to clinoptilolite-supported samples, the form of chemical groups of Fe-derivatives of MCM-22 were determined by the modification procedure. The bands appearing within 4000-3000 cm^{-1} in the spectrum of the pristine zeolite exhibited two peaks: the sharp one at 3626 cm^{-1}, attributed to Brönsted acid sites of ≡Si-OH-Al≡ in the supercages at 10 member-ring channels [551,552] and the broad one at 3425 cm^{-1}, assigned to the hydrogen-oxygen bonds in the hydroxyl groups [296]. The former peak was preserved for FeMCM22 ads and it almost disappeared for FeMCM22 cop and FeMCM22 impr. This result suggests that the Brönsted acid sites present in the parent zeolite were well-preserved in the case of FeMCM22 ads.

The intense peak, appearing at 1636 cm^{-1} for both groups of the investigated catalysts is ascribed to the bending vibrations of hydroxyl groups of H_2O molecules in the internal zeolitic structure [320]. The bands at 1220 cm^{-1} and 1079 cm^{-1}, visible for clinoptilolite-supported catalysts, and at 1250 cm^{-1} and 1079 cm^{-1}, detected for MCM-22-supported materials are attributed to the Me-O asymmetric stretching vibrations of the tetrahedral groups (MeO_4) and O-Me-O stretching vibrations, respectively (where Me = Si or Al) [530]. The peak at 1015 cm^{-1}, detected for all of the analyzed Fe-modified materials and raw clinoptilolite can be considered as the evidence of the presence of iron in their structure. The obtained spectra of the samples with iron are in line with those obtained by Roth et al. [535] and Sahu et al. [553] for transition metal-modified zeolites. This result suggests that iron was successfully incorporated into the zeolitic frameworks. The peaks appearing for all of the materials at 788 and 794, and 602 cm^{-1} correspond to the symmetric O-Me-O stretching vibrations [530], while the bands at 679 and 525 cm^{-1} are attributed to so-called “pore-opening” vibration modes of the zeolites [554]. Due to the fact that the peak at 525 cm^{-1} is almost absent for FeClin catalysts, it is predicted that iron could somehow interact with the pore openings of the zeolite and slightly change structural features of the material. The well-shaped peak at 545 cm^{-1} and 595 cm^{-1}, detected for MCM22 is ascribed to the

double-six-ring (D6R) in the MWW structure of the zeolite [535,553]. It can be noticed that in the case of FeMCM22 cop these peaks are almost absent, which is in line with XRD results. Finally, the peak in the pseudo-lattice vibration region at 470 cm^{-1}, appearing for all of the analyzed materials, is assigned to the vibrations of the structural building blocks of zeolite, thus, MeO_4 tetrahedra [530].

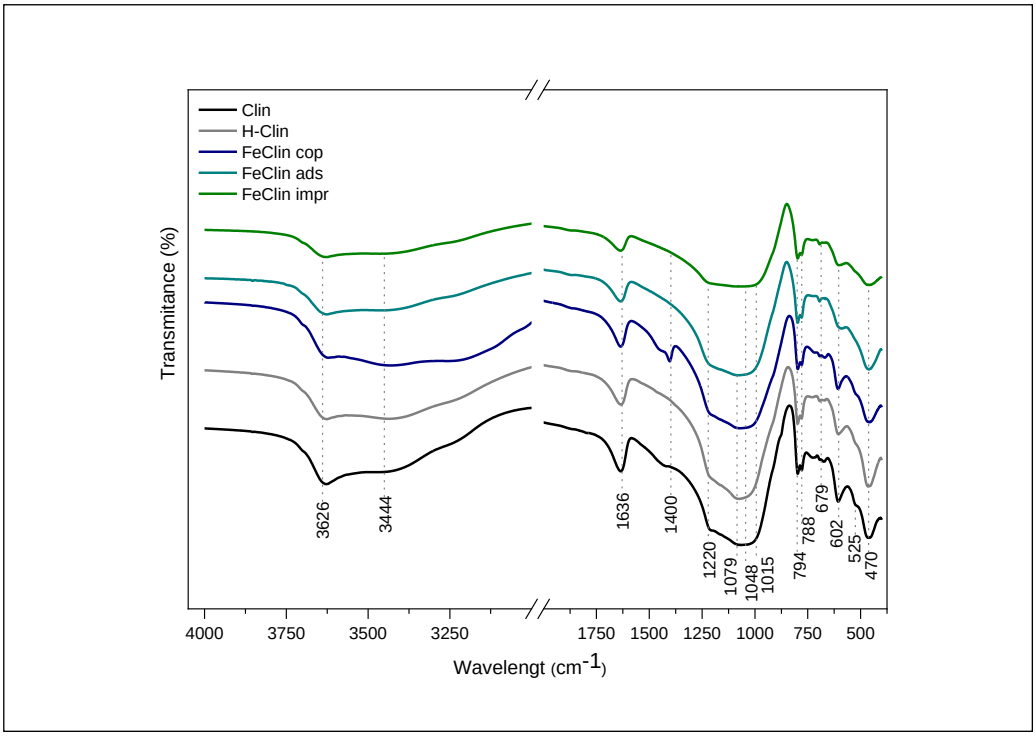

Figure 57. FT-IR spectra obtained for the raw, protonated and iron-modified clinoptilolite

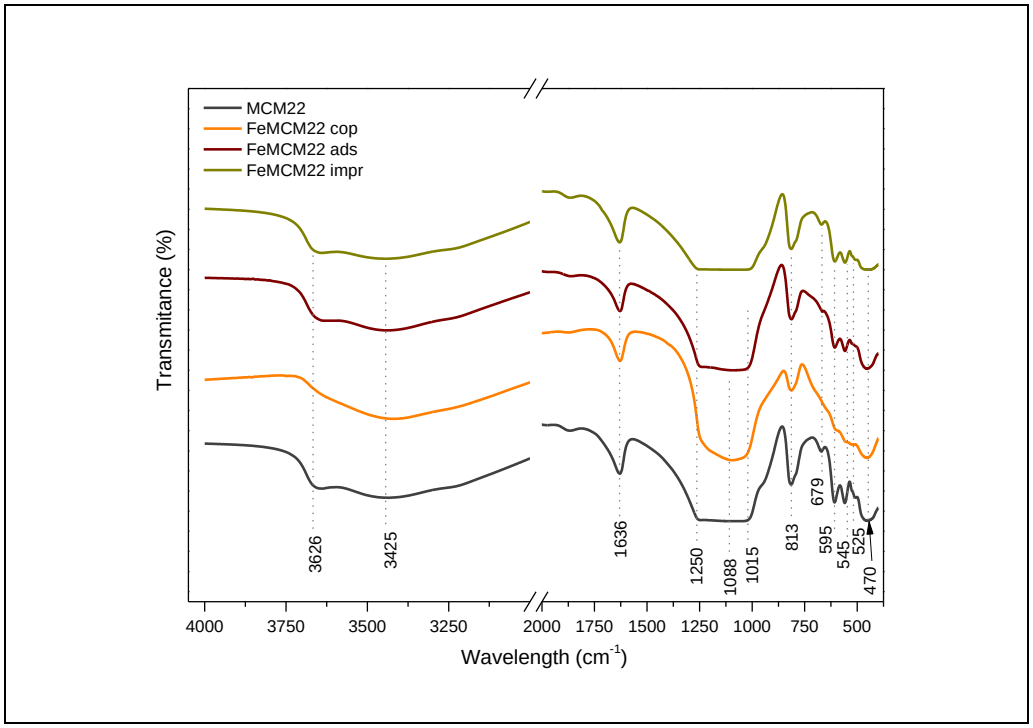

Figure 58. FT-IR spectra obtained for the pristine and Fe-modified MCM22

Speciation of iron in the catalysts determined by XPS

Surface chemistry (surface concentration and oxidation state) of clinoptilolite and MCM22 modified with iron were investigated by the means of XPS. The measurements were conducted in the binding energy (BE) regions of Si 2p, Al 2p, O 1s, C 1s, and Fe 2p and the obtained results are presented in **Figures 59-64.** Concentrations of chemical bonds on the catalysts surface, obtained from fitting XPS data for the analyzed samples are listed in **Table 19.**

Figure 59 presents the fragments of the spectra corresponding to the BE region of silicon. After deconvolution, the Si 2p spectra of all of the catalysts were very similar and could be perfectly fitted by a single doublet structure (doublet separation $p_{3/2} - p_{1/2}$ equals 0.6 eV) with the main line centered at 103.3 eV. This Si 2p BE value was reported earlier for many zeolitic structures and indicated the presence of tetrahedral Si (IV) [555].

The deconvoluted Al 2p spectra obtained for the catalysts, illustrated in **Figure 60,** were fitted with one doublet structure (doublet separation $p_{3/2} - p_{1/2}$ equals 0.4 eV). The main $2p_{3/2}$ line, located at 74.8 eV is characteristic for zeolites and corresponds to the presence of Al^{3+} ions in Al-O or Al-OH bondings [436]. Interestingly, the spectra of FeMCM22 cop in the Al 2p BE region remarkably differs from those of the other materials. The intensity of the recorded signal is almost on the verge of noise. Such effect is most likely caused by very low surface concentration of Al^{3+}) in the sample (see **Table 19**). This result is in a good agreement with ICP-OES and XRD experiments, which indicated that the severe conditions applied during co-precipitation method caused partial degradation of the MWW structure and dealumination caused by the interaction between iron oxide and the supporting zeolite.

The C 1s core lines depicted in **Figure 61** are similar for all of the samples and can be fitted with three components: aliphatic carbon (285.0 eV), C-O groups (286.8 eV), and C=O and/or O-C=O groups (289.0 eV) [555]. All of detected lines are typical for organic contamination present on the surface of air-handled samples.

The spectra recorded in the BE region of O 1s are presented in **Figure 62.** It can be observed that the main peak, related to O 1s is centered at ca. 532.6 eV for all of the samples and it can be deconvoluted into three Gaussian curves. The first one, located at 531.2-530.4 eV corresponds to oxygen-metal bonds

and exhibits the highest intensity for zeolites modified by co-precipitation method. This result is in line with the surface concentration of Fe^{3+} (see **Table 19**), indicating that this method favors formation of iron oxide species on the external surface of the support. The peak is the most pronounced for FeMCM22 cop, suggesting that the material was the most abundant in Fe_2O_3 particles. The second peak, which exhibited the highest intensity and appeared at ca. 532.6 eV is assigned to oxygen in the zeolitic framework. Last, but not least, the peak at ca. 534.0 eV, detected for all of the samples confirms the presence of H_2O molecules attached to the zeolitic framework and/or oxygen atoms originating from the organic contaminants [436,556].

In general, due to the spin-orbit coupling, the Fe 2p core level is splitted into Fe $2p_{3/2}$ and $2p_{1/2}$ doublet structure with binding energies strongly related to the oxidation state of iron [517]. The spectra collected in Fe $2p_{3/2}$ region, presented in **Figure 63**, are similar for all of Fe-catalysts. The BE value of Fe $2p_{3/2}$ peak is reported to be around 710.0-711.0 eV for Fe^{3+} and it was found to decrease while iron species are present in extraframework positions or in a form of Fe_2O_3 particles [436,556]. Such effect was noticed especially for the materials modified by co-precipitation method, for which the first line was centered at ca. 710.1 eV, thus contained the highest concentration of surface Fe^{3+} species in a form of iron oxide particles. The lines appearing within the energy range of 711.0-716.0 eV are due to the multiplet splitting phenomena and the position of the shake-up line at 718.4 eV is additional parameter that ensured Fe^{3+} oxidation state in the samples [557]. Besides, the presence of Fe $2p_{3/2}$ lines above BE 711.0 eV confirmed that many metal cations located in zeolite frameworks exhibit higher BE than their oxide forms. This result is correlated with dispersion of iron species and their interactions with the zeolite framework and chemical surroundings [436]. Additionally, the lack of the Fe $3p_{3/2}$ peak at the BE value of ca. 706 eV confirmed the absence of metallic Fe^0 in the catalysts.

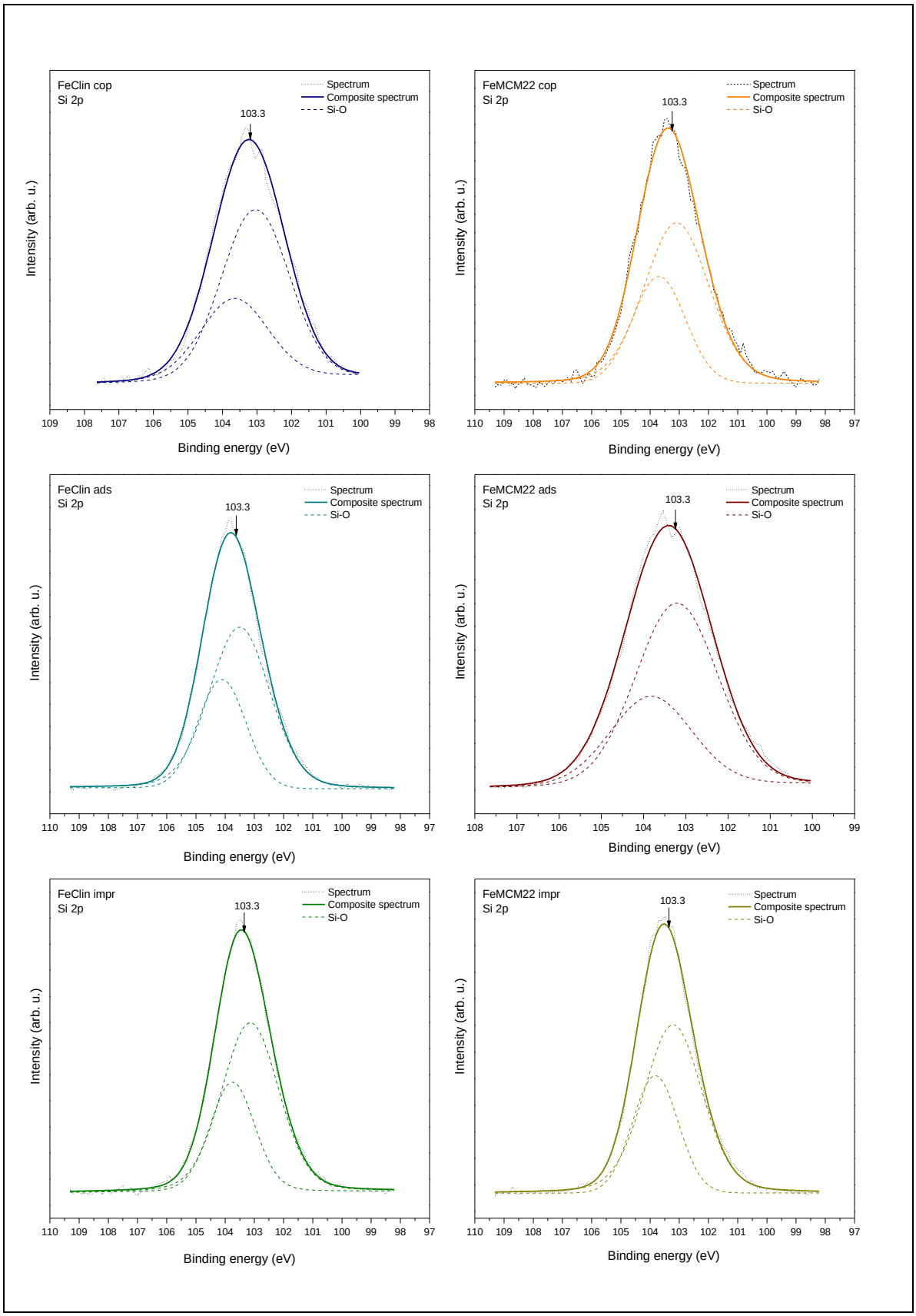

Figure 59. XPS spectra of FeClin and FeMCM22 catalysts in the BE region of Si 2p

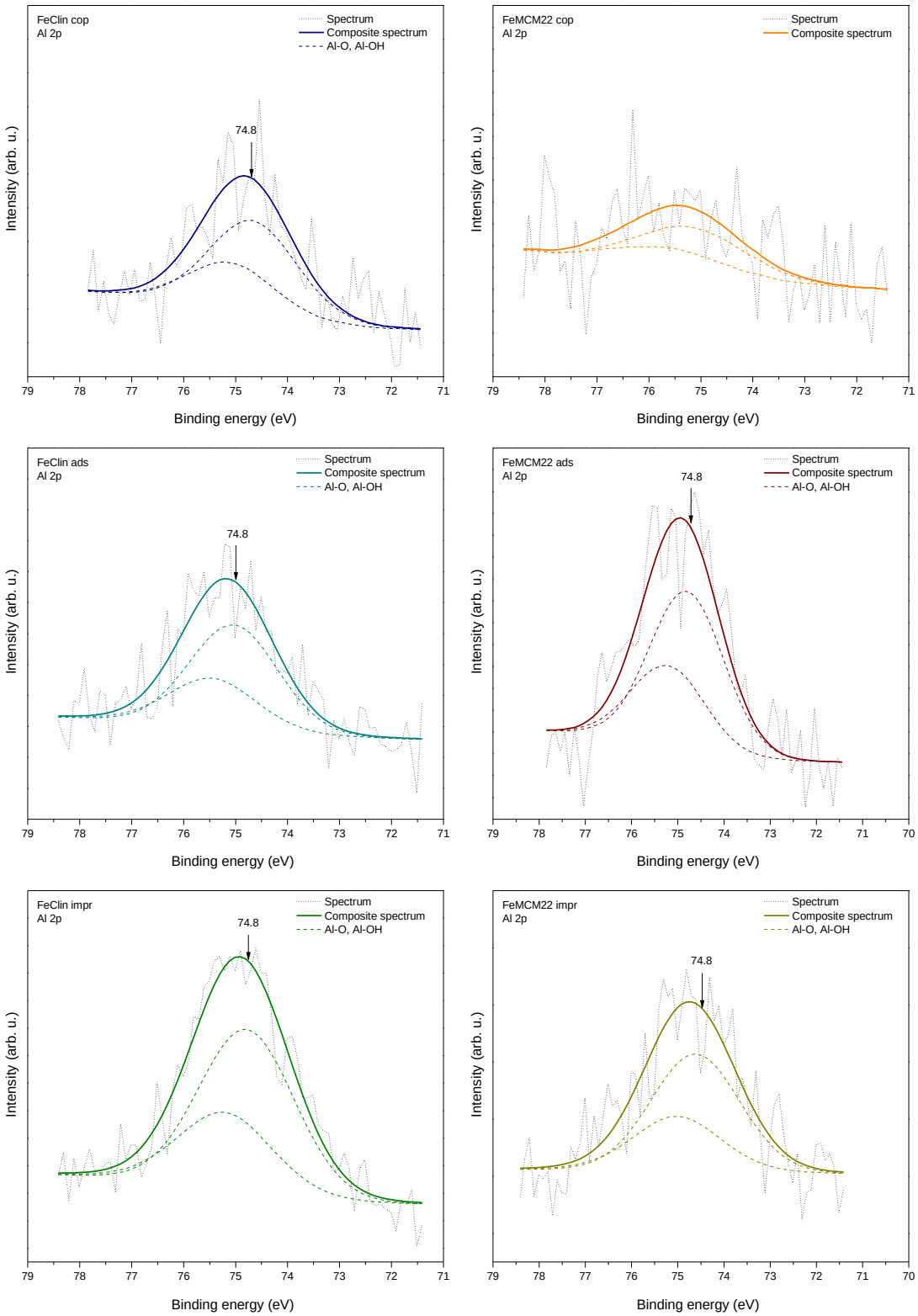

Figure 60. XPS spectra of FeClin and FeMCM22 catalysts in the BE region of Al 2p

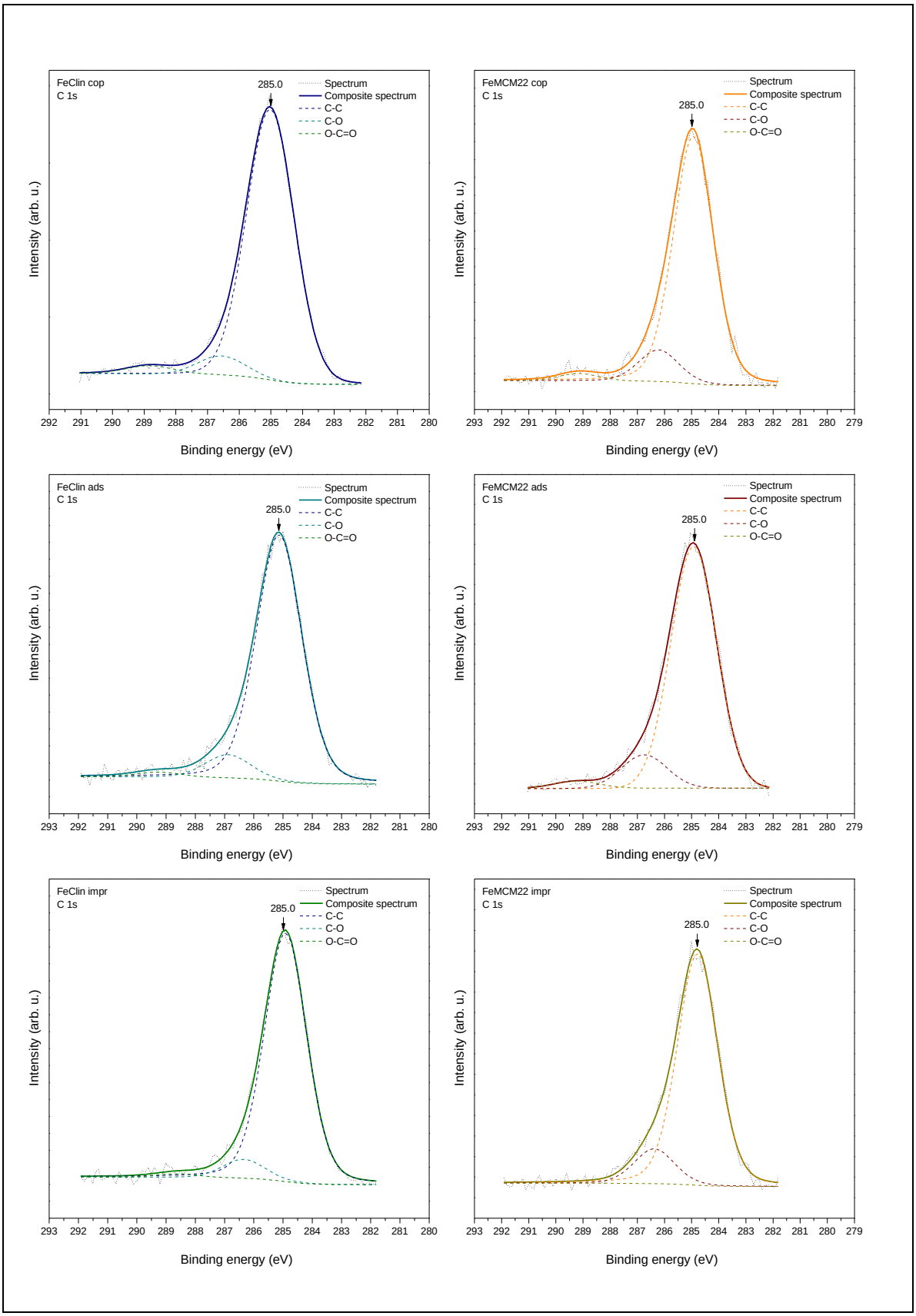

Figure 61. XPS spectra of FeClin and FeMCM22 catalysts in the BE region of C 1s

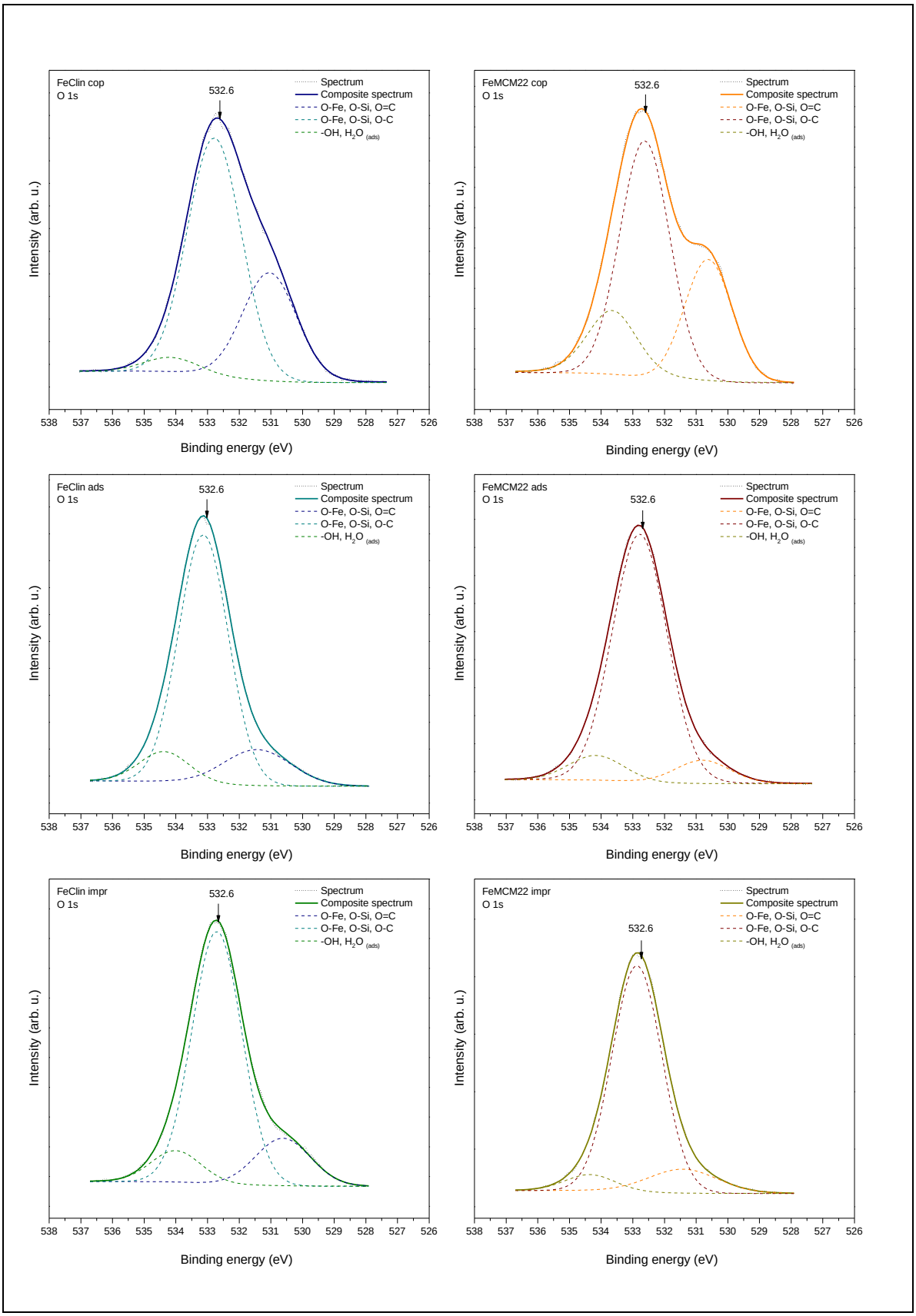

Figure 62. XPS spectra of FeClin and FeMCM22 catalysts in the BE region of O 1s

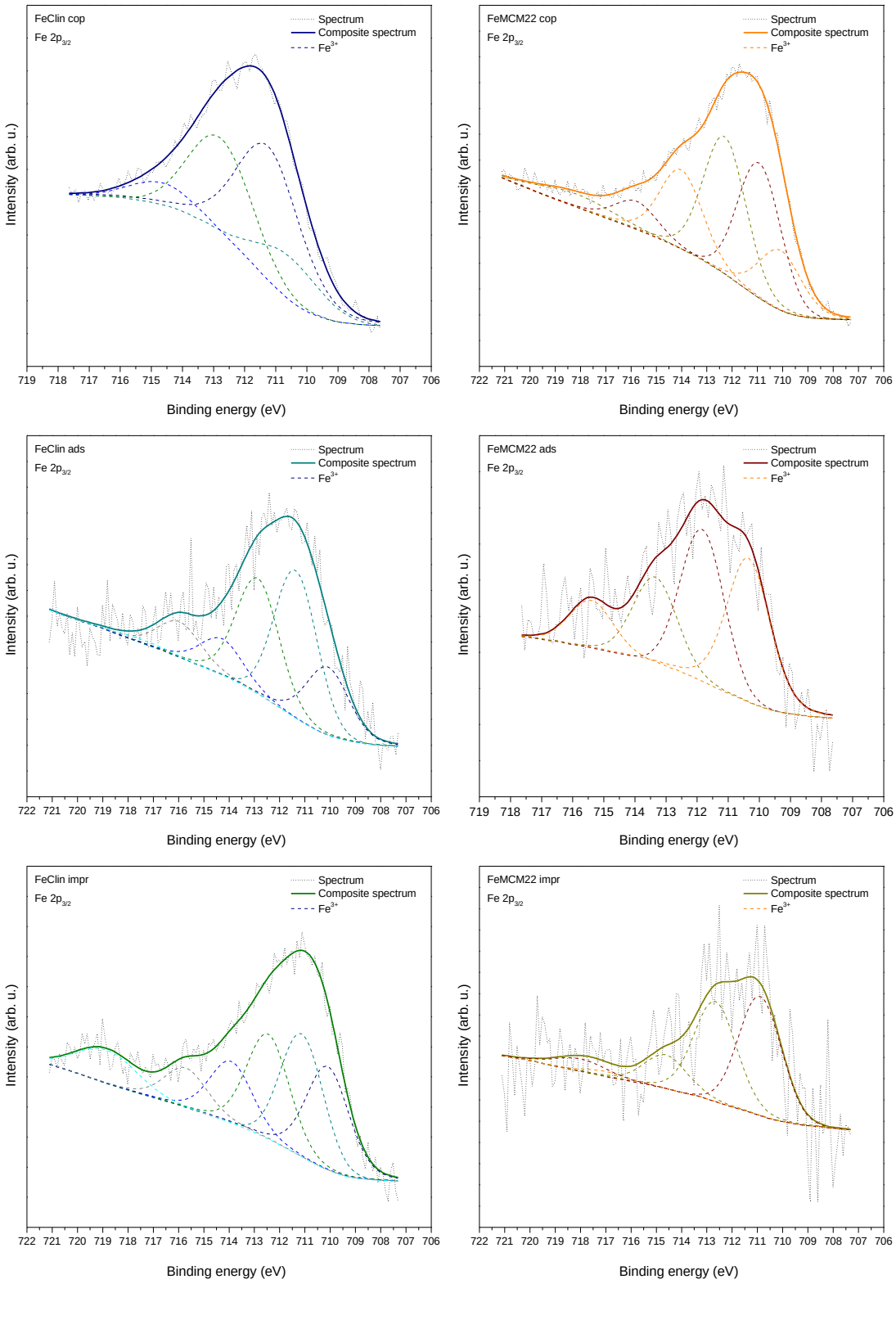

Figure 63. XPS spectra of FeClin and FeMCM22 catalysts in the BE region of Fe $2p_{3/2}$

Table 19. Surface compositions (in atomic %) determined by fitting XPS spectra of FeClin and FeMCM22 catalysts

	Si 2p	Al 2p	Fe $2p_{3/2}$	O 1s			C 1s		
Binding energy (eV)	103.3	74.8	711.0	530.7	532.6	534.0	285.0	286.6	289.0
Chemical groups or oxidation state	Si^{4+}	Al^{3+}	Fe^{3+}	O-Fe O-Si O-Al O=C	O-Fe O-Si O-Al O-C	-OH H_2O_{ads}	C-C	C-O	C=O O-C=O
FeClin cop	16.3	1.4	4.3	15.5	32.9	2.1	25.0	1.7	0.8
FeClin ads	25.4	1.3	1.2	7.9	40.0	5.0	17.3	1.6	0.4
FeClin impr	22.8	2.7	2.6	8.3	39.6	5.1	17.4	1.3	0.3
FeMCM22 cop	19.4	0.6	6.3	14.5	29.5	5.1	18.1	2.3	0.5
FeMCM22 ads	25.8	1.4	0.8	4.3	45.5	4.5	15.2	2.1	0.5
FeMCM22 impr	27.1	1.2	0.5	6.5	43.1	3.2	16.1	2.4	0

Speciation of iron in the catalysts determined by UV-vis-DRS

Information on the coordination, distribution, and nature of iron in the zeolites was provided by UV-vis-DRS, which is a suitable technique to study dispersed metal oxides on the solid surfaces. Typically, three characteristic wavelength regions can be distinguished in UV-vis-DR spectra of Fe-modified zeolites:

- 200-350 nm, corresponding to O → Fe^{3+} charge transfer of the isolated Fe^{3+} cations in the framework or extraframework positions,
- 350-450 nm, appearing due to the octahedral Fe^{3+} sites in the small extraframework clusters of Fe_xO_y,
- above 450 nm, ascribed to the large or more aggregated bulks of hematite (Fe_2O_3) [558].

The results of UV-vis-DRS obtained for the raw, protonated, and iron-modified clinoptilolite are presented in **Figure 64**. The line shape of the spectra is different for the materials, thus, modification procedure influenced on the form of the introduced active phase. In general, the structural SiO_4 units of tetrahedral silica layers in the zeolites do not absorb light within 200-800 nm. However, non-modified clinoptilolite exhibited three strong absorption bands centered at 225, 230, 265, and one, less intense at

375 nm. This result corresponds to that of ICP-OES and XRD and confirms the presence of iron species isomorphously incorporated into the framework of natural clinoptilolite. According to the literature, the absorption maxima at 225, 230 and 265 nm are assigned to the ligand (oxygen)-to-metal charge transfer (CT) transitions of mononuclear Fe^{3+}. Position of these bands in the spectra depends on the number of ligands attached to Fe^{3+}. Additionally, the band at 375 nm suggest the presence of iron species of higher nuclearity [559]. Protonation of clinoptilolite broadened and increased the intensity of the absorption band assigned to the isolated Fe^{3+} moieties. This effect is characteristic for the dealuminated zeolites and confirmed that protonation resulted in partial elimination of aluminum from clinoptilolite, as well as leaching of some part of iron species from the isolated octahedral positions to higher coordination. UV-vis-DR spectra obtained for the zeolite with Fe revealed the relationship between the modification method and speciation of the active phase. The results indicated that the highest variety of iron sites occurred in the sample treated by co-precipitation. FeClin cop exhibited the most intense absorption band among the samples, especially in the wavelength range of 230-300 nm, which suggests the presence of well-dispersed, pseudotetrahedral Fe^{3+} sites. In the case of FeClin ads and FeClin impr, the samples contained mainly octahedral extra-framework iron species (375 nm) and aggregated externa-surface particles of Fe_2O_3 (525 nm) [440]. In comparison to FeClin cop, the intensity of the bands attributed to the isolated Fe^{3+} cations was lower, especially for FeClin impr [352,555].

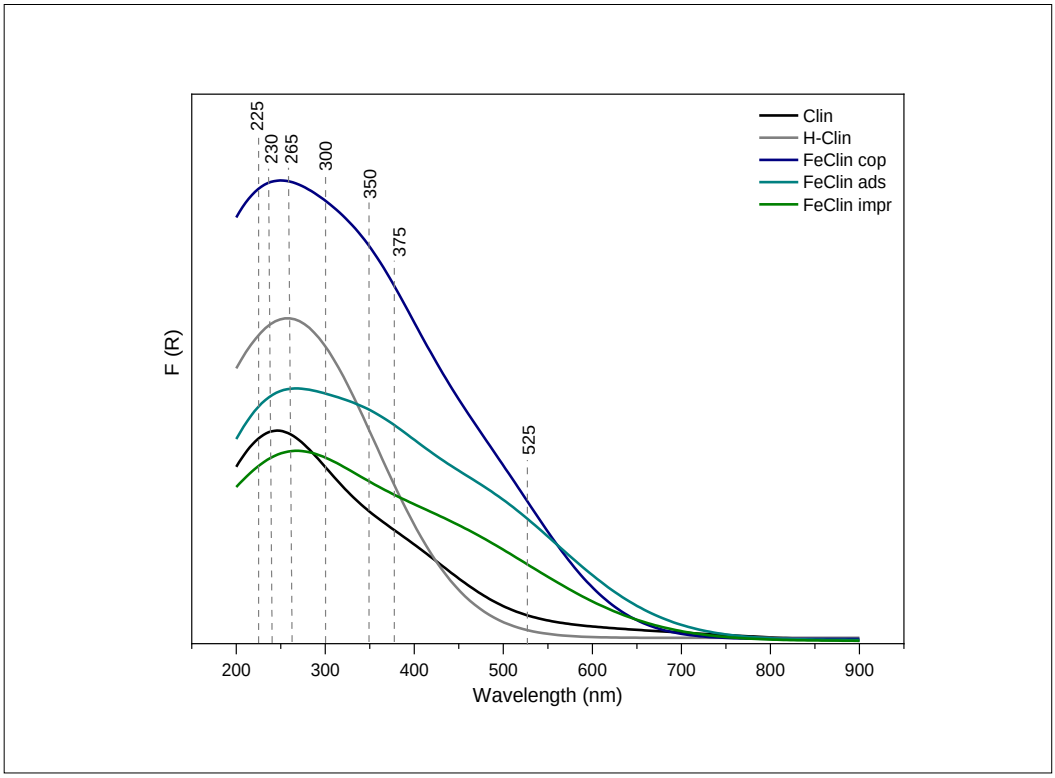

Figure 64. UV-vis spectra obtained for the raw, protonated and iron-modified clinoptilolite

As presented in **Figure 65,** introduction of iron resulted in the appearance of four absorption bands in the UV-vis-DR spectra of MCM22-supported catalysts. Similarly to FeClin catalysts, the applied modification method determined the speciation of iron. FeMCM22 cop exhibited strong absorption bands centered at 225, 250, 460, and 530 nm, which proved that co-precipitation yielded diversified speciation of iron in the material. The strong absorption bands at 460 and 530 nm suggested that Fe_xO_y oligomers and clustered iron oxide species dominated in the sample. On the other hand, FeMCM22 ads and FeMCM22 impr exhibited absorption band of relatively low intensity, located at 250 nm and more intense ones at 325 and 530 nm. Thus, the catalysts contained mainly iron species of higher nuclearity and aggregated iron oxide particles [555].

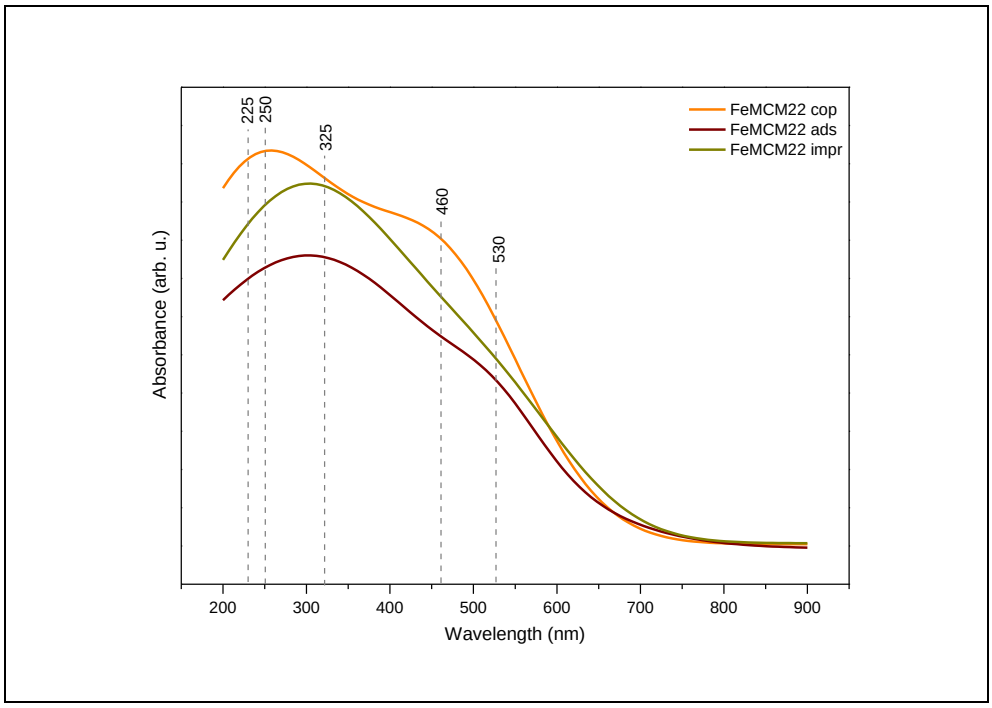

Figure 65. UV-vis spectra obtained for the pristine and Fe-modified MCM-22 zeolite

1.2 Catalytic performance of iron-modified clinoptilolite and MCM-22

The results of NH_3-SCR catalytic tests are presented in **Figure 66-67** and **Figure 68-79**, for natural and synthetic Fe-zeolites, respectively.

As presented in **Figure 66**, non-modified clinoptilolite has a very high potential to be a support of NH_3-SCR catalyst. It can be observed that ca. 58% of NO conversion was reached for the natural support at 450 °C. The effect was caused by the presence of iron species in the zeolite. Additionally, as confirmed by NH_3-TPD studies, both Clin and H-Clin contained considerable concentration of acidic sites, which provided active centers for adsorption of ammonia during the reaction. Despite satisfactory result of NO conversion, it can be noticed from **Figure 67** that N_2O concentration for Clin was almost the highest among the samples and increased with the increasing temperature. The production of N_2O during NH_3-SCR occurred mainly for the materials which contained the active phase in a form of more aggregated particles [145,352]. Therefore, the majority of iron species naturally present in clinoptilolite probably took the form of oligomers or iron oxide clusters, which is consistent with UV-vis-DRS studies. In general, introduction of iron considerably increased catalytic activity of clinoptilolite. Below 250 °C, all of the samples exhibited similar NO conversion, regardless the modification method. However, above this temperature and onwards, FeClin cop showed the highest catalytic activity. The

temperature of 50% conversion of NO (t_{50}) for this sample was ca. 260 °C, while for FeClin ads and FeClin impr the value was 280 and 290 °C, respectively. Besides, despite moderately higher activity of FeClin ads than that of FeClin impr, the difference was not significant. What is interesting, on the contrary to FeClin cop, the two other samples showed noticeable activity drop above 400 °C. According to the literature, this effect is related to the side reactions taking place during NH_3-SCR, such as direct oxidation of ammonia, thus undesired consumption of the reducing agent [555,559]. Importantly, this reaction is related to the presence of polynuclear species of iron or bulky Fe_2O_3, which are abundant in these materials, as confirmed by UV-vis-DRS and H_2-TPR studies.

The catalytic activity of the samples proved that modification of clinoptilolite by co-precipitation is the most beneficial for satisfactory conversion of NO. Additionally, the active species introduced by this procedure were inactive in direct NH_3 oxidation. There might be various reasons for this result. First of all, it is well known that acid sites are crucial in NH_3-SCR for the adsorption and activation of ammonia molecules [555]. As proved by NH_3-TPD, FeClin cop contained the highest concentration of weak and strong acid centers among the samples supported on clinoptilolite. The strongly acidic character of the sample can result from bridging OH groups in ≡Al(III)-O(H)-Si≡ or ≡Fe(III)-O(H)-Si≡ (Brönsted sites) and unsaturated Al or Fe atoms (Lewis sites) [436]. Basing on the NH_3-TPD pattern, the NH_3 desorption peak at 395 °C, detected for this sample, suggests that strong acid sites could assist in both high-temperature activity and formation of the desired reaction products. As postulated by Yuan et al. [560], the acid sites act in Fe-zeolites as the reservoir of ammonia molecules, however, too high concentration of NH_3 could lead to the side reactions. Therefore, the results of NH_3-SCR obtained for FeClin cop suggested that the presence of the adsorbed reducing agent was sufficient to provide high NO conversion, nevertheless, not too high to generate undesired products. It should be also noted that the acidity of this material can be correlated with the presence of residual SO_4^{2-} groups, derived from the precursor of iron, $FeSO_4$. As confirmed by TGA studies, possibly, $FeSO_4$ was not fully decomposed during calcination of the catalyst. Thus, the deposited sulfates could act as additional Brönsted acid sites and adsorb gas-phase ammonia during the reaction. Additionally, even though the amount of acid sites of FeClin impr was considerably higher than that of FeClin ads, the materials exhibited very similar catalytic activity. Hence, concentration and strength of acid centers was not essential for the catalytic

activity. The obtained result is in agreement with the findings of Brandenberger et al. [435], who proved that acidity of zeolite-supported catalysts is not a crucial factor influencing their activity in NH_3-SCR. Alternatively, the catalytic behavior of the materials could be a consequence of their redox properties. According to H_2-TPR studies, FeClin cop was the only sample, which did not exhibit reduction behavior above 500 °C. Thus, the majority of iron was possibly present in the sample in a form of monomeric and dimeric extraframework species: $[Fe(OH)_2]^+$ and $[HO\text{-}Fe\text{-}O\text{-}Fe\text{-}OH]^{2+}$. It was proved that these moieties are most active in the standard NH_3-SCR, especially below 300 °C [442,561]. As confirmed by UV-vis-DRS analysis, FeClin cop contained the highest concentration of the uniformly dispersed isolated iron sites. Therefore, its activity in the low-temperature region was higher comparing to the other catalysts. On the other hand, iron sites of higher nuclearity, present in greater amount in FeClin ads and FeClin impr, not only shifted the t_{50} but also contributed to NH_3 oxidation. Therefore, speciation of iron played a crucial role in the catalytic activity of FeClin catalysts.

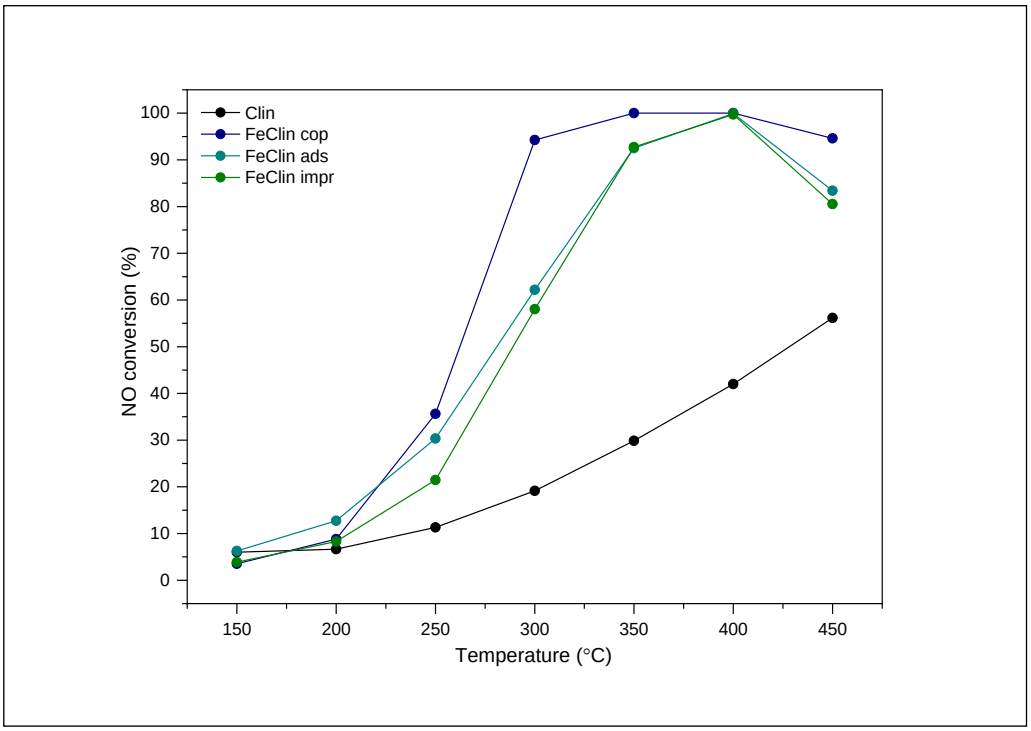

Figure 66. NO conversion obtained for raw and iron-modified clinoptilolite

Another important factor analyzed during NH_3-SCR is concentration of N_2O (common by-product of the reaction) at the reactor outlet. As presented in **Figure 67**, the emission of N_2O increased linearly with the reaction temperature and did not exhibit 50 ppm for any of the analyzed samples. The yield of N_2O produced during the reaction was higher in comparison to the raw zeolite only for FeClin ads, while

for FeClin cop and FeClin impr it was moderately lower. Taking into consideration that FeClin ads and FeClin impr exhibited similar NO conversion, it can be assumed that the former sample contained more iron sites, which induced the occurrence of undesired reactions of NH_3-SCR. Therefore, FeClin ads, as the sample with the highest concentration of iron sites of high nuclearity, is the most active in the production of N_2O. Zhang et al. [562] investigated the reaction pathway of N_2O formation over zeolite catalysts of NH_3-SCR. The authors proposed that generation of N_2O in the conditions reflecting that of the presented research can be described by **reactions (134-138)**:

$$4\ NO + 4\ NH_3 + 3\ O_2 \rightarrow 4\ N_2O + 6\ H_2O \quad \textbf{(134)}$$

$$2\ NH_3 + 2\ O_2 \rightarrow N_2O + 3\ H_2O \quad \textbf{(135)}$$

$$2\ NH_3 + 4\ NO \rightarrow 2\ N_2 + N_2O + 3\ H_2O \quad \textbf{(136)}$$

$$3\ NO \rightarrow N_2O + NO_2 \quad \textbf{(137)}$$

$$4\ NO \rightarrow 2\ N_2O + O_2 \quad \textbf{(138)}$$

As already mentioned, the tendency of Fe-zeolites to catalyze side-reactions, such as direct oxidation of NH_3 to N_2O **(reaction 135)** is strongly correlated with the speciation of iron. What is more, Cho and co-workers [563] mentioned that generation of N_2O results from the presence of NO_2 in the reaction mixture. Interaction of nitrogen dioxide and ammonia produces ammonium nitrate in a form of solid or liquid [564]. The process follows Langmuir-Hinshelwood mechanism, which assumes adsorption of the reactants on the catalyst, surface reaction, and formation of the products, as described by **reaction (139):**

$$2\ NO_2 + 2\ NH_3 \rightarrow NH_4NO_3 + N_2 + H_2O \quad \textbf{(139)}$$

Subsequently, NH_4NO_3 is thermally decomposed below 260 °C, according to **reaction (140):**

$$NH_4NO_3 \rightarrow N_2O + 2\ H_2O \quad \textbf{(140)}$$

Therefore, the increasing concentration of N_2O above 260 °C, detected for all of the materials, can be related to the thermal decomposition of ammonium nitrate produced on their surface during the catalytic reaction.

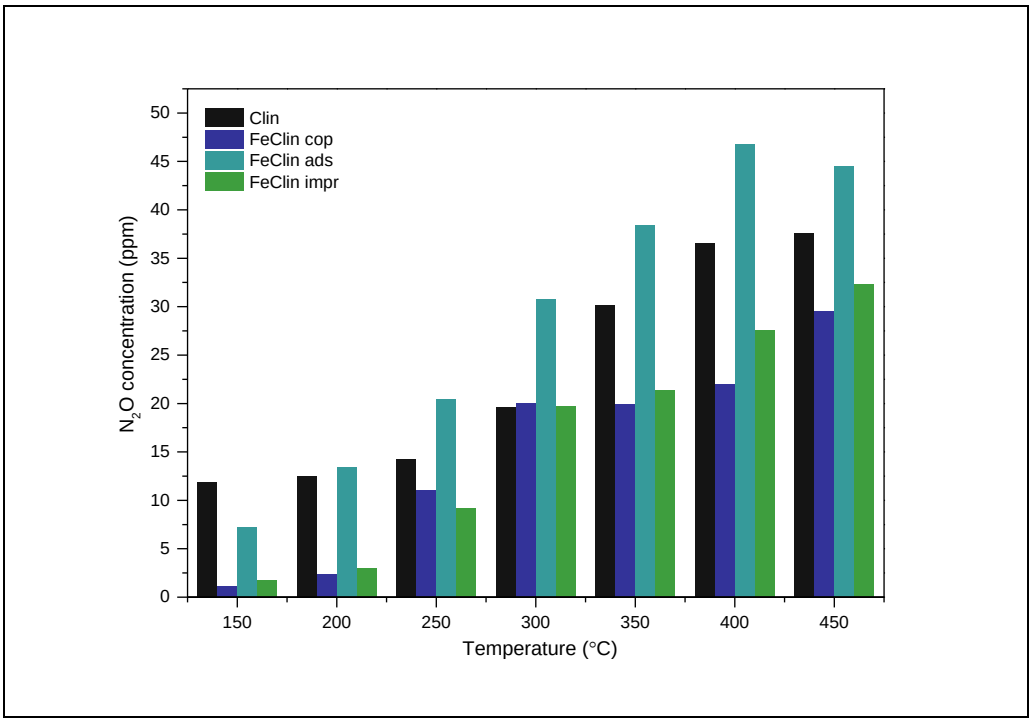

Figure 67. N_2O concentration in the flue gas during the catalytic reaction performed over raw and iron-modified clinoptilolite

The conversion of NO obtained for FeMCM22 catalysts is presented in **Figure 68**. In contrast to the raw clinoptilolite, the catalytic activity of MCM22 before introduction of Fe did not even exceed 20% in the investigated temperature range. The observed increase of NO reduction above 350 °C might be due to the promotion of NH_3-SCR by ammonia, adsorbed on the acid sites of medium strength. However, introduction of the active phase considerably promoted catalytic activity of the zeolite. Hence, the reaction over MCM-22 takes place exclusively with the participation of iron species. Similarly to FeClin, FeMCM22 catalysts showed the highest activity above 300 °C, which is characteristic for Fe-zeolites [85]. The most active materials, with t_{50} of 250 °C were FeMCM22 cop and FeMCM22 ads, while for FeMCM22 impr t_{50} was slightly higher (285 °C). Regardless the modification method, the activity diminished above 325 °C in the case of FeMCM22 cop and FeMCM22 ads and above 400 °C for FeMCM22 impr. Similarly to FeClin catalysts, this decrease is related to the presence of polynuclear iron sites or bulk particles of Fe_2O_3, as confirmed by UV-vis-DRS and H_2-TPR studies. Another confirmation of this result is that FeMCM22 cop contained the highest concentration of these species, thus its activity started to drop at the lowest temperature among all of the samples. Besides, as evidenced by H_2-TPR, FeMCM22 cop contained hardly reducible Fe_2O_3, which could be deposited near the pore

openings and thus, hinder sorption of gas molecules on the active centers. The collected data for NO reduction obtained for FeMCM22 catalysts support the hypothesis of Luo and co-workers [565] on the rate-determining step of standard NH_3-SCR over Fe-zeolite catalysts. The authors declared that adsorption of NO on the isolated iron species and its further oxidation is crucial to obtain high reduction rates, especially in the low temperature range. Insufficient concentration of these sites could lead to the adsorption of ammonia molecules on the acidic centers of the catalysts and its undesired oxidation in the high temperature region.

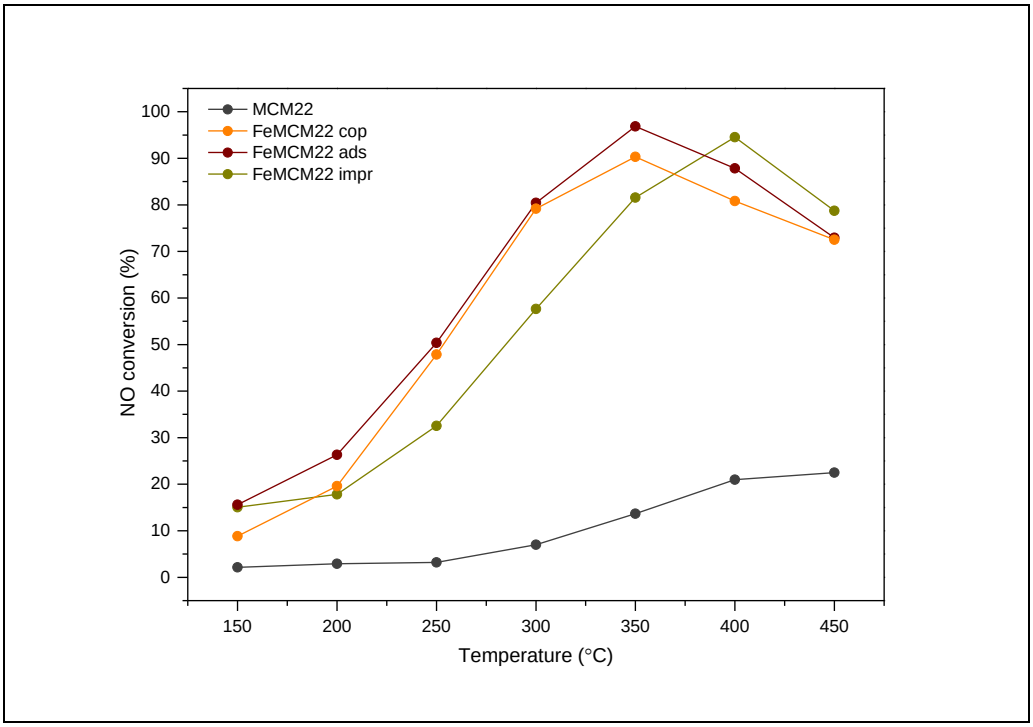

Figure 68. NO conversion obtained for the pristine and iron-modified MCM-22 zeolite

As already mentioned, one of the evidences of the occurrence of side reactions during NH_3-SCR is the increased concentration of N_2O, presented for FeMCM22 catalysts in **Figure 69.** Generally, comparing to the group of FeClin catalysts, the yield of nitrous oxide is considerably lower for the samples supported on MCM-22. The difference might be caused by more uniform porous structure of the hierarchical support, MCM-22, which facilitated the access of gas molecules to the active sites and desorption of the desired products. Interestingly, below 300 °C, all of the catalysts generated less than 10 ppm of N_2O, which is within the frames of analytical error of the apparatus. Nevertheless, in the range of 350-400 °C, selectivity of the materials to nitrous oxide slightly increased, suggesting the

occurrence of side reactions. However, as shown in **Figure 68,** conversion of NO in this temperature region raised as well. Therefore, correlating these two results, generation of N_2O can result from the non-selective reduction of NO, described by **reactions (132-136).** Additionally, similarly to FeClin catalysts, the presence of nitrous oxide within 300-350 °C could be a consequence of the formation and thermal decomposition of NH_4NO_3 [564].

What is interesting, the selectivity to N_2O of FeMCM22 cop and FeMCM22 ads gradually decreased above 350 °C, while for FeMCM22 impr this effect occurred above 400 °C. These result is in agreement with the findings reported by Delahay et al. [566], who postulated that N_2O can be reduced by ammonia to molecular nitrogen and water vapor, according to **reaction (141):**

$$2\ NH_3 + 3\ N_2O \rightarrow 4\ N_2 + 3\ H_2O \qquad \textbf{(141)}$$

The authors have found that the process takes place mainly on the isolated Fe^{3+} cations in the distorted tetrahedral environment. This explanation is in line with the decreasing NO conversion above 350 °C for FeMCM22 cop and FeMCM22 ads and above 400 °C for FeMCM22 impr. Since **reaction (141)** assumes consumption of NH_3, insufficient amount of the reducing agent declined the efficiency of NO reduction. The decreasing amount of N_2O above 350 °C (or 400 °C in the case of FeMCM22 impr) can be related to its decomposition at higher temperature as well. The catalytic activity of Fe-modified MCM-22 in this reaction was investigated by Rutkowska and co-workers [499]. The authors recognized Fe_xO_y oligomers as the most active centers of catalytic decomposition of N_2O. As evidenced by UV-vis-DRS, NH_3-TPD, and H_2-TPR studies, all of the analyzed FeMCM22 catalysts contained these species. Additionally, consumption of these sites, also active in the high-temperature NH_3-SCR, could result in the diminished conversion of NO. The effect of N_2O elimination was not observed for the pristine support, suggesting that it is correlated solely with the presence of iron centers.

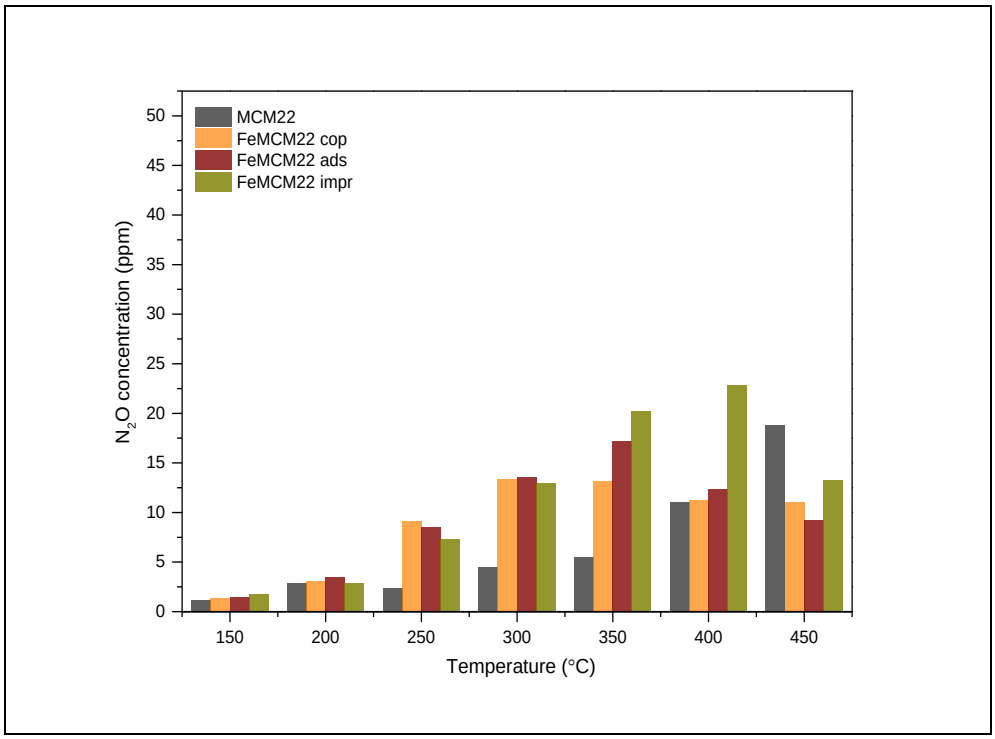

Figure 69. N_2O concentration in the flue gas during the catalytic reaction performed over pristine and iron-modified MCM-22

In order to discuss and compare the catalytic performance of the materials in detail, the reaction rate constants *k* of the catalysts were calculated at 250 and 450 °C (low and high temperature region of NH_3-SCR) according to **Equation (131).** Furthermore, since clinoptilolite and MCM-22 exhibit different structural parameters, the obtained values of *k* were normalized by the specific surface area of the catalysts, by calculating the per area (k/S_{BET}) constants. The results of these calculations are summarized in **Table 20.**

Table 20. Reaction rate constant *k* at 250 and 450 °C and *k* normalized by the specific surface area of the catalysts

Sample code	*k* ($cm^3 \cdot g^{-1} \cdot s^{-1}$)		$(10^2 \cdot k) / S_{BET}$ ($cm^3 \cdot m^2 \cdot s^{-1}$)		S_{BET} ($m^2 \cdot g^{-1}$)
	250 °C	450 °C	250 °C	450 °C	
Clin	1.0	6.9	7.7	52.9	13
FeClin cop	3.7	24.3	2.9	19.3	126
FeClin ads	3.0	15.0	2.3	11.3	133
FeClin impr	2.0	13.6	5.6	37.9	36
MCM22	0.3	2.1	0.1	0.5	425
FeMCM22 cop	5.4	10.8	1.5	2.9	370
FeMCM22 ads	5.8	10.9	1.6	2.9	372
FeMCM22 impr	3.3	12.9	0.8	3.2	399

The results displayed in **Table 20** show a clear correlation between temperature of the reaction and the *k* rate constant, regardless the catalyst support. According to the obtained outcomes, NH_3-SCR process over the investigated Fe-catalysts is the fastest in high-temperature range. In the case of clinoptilolite-supported materials, the highest reaction rate constant was exhibited by FeClin cop in both of the considered temperatures. This effect is related to the abundance of FeClin cop in various iron species, which influenced NO conversion in the entire temperature range. Interestingly, at 250 °C, *k* value of the samples increased almost linearly in the order of FeClin impr < FeClin ads < FeClin cop. It can be correlated with relatively lower concentration of isolated Fe^{3+} species on FeClin impr, as evidenced by H_2-TPR.

In contrast to FeClin catalysts, the reaction rate constants of FeMCM22 samples were influenced both by the modification method and temperature. Nevertheless, one should note that for FeMCM22 cop and FeMCM22 ads the values of *k* were only slightly different. The differences between *k* values for the catalysts might be a consequence of the accessibility of the gas molecules to the active centers of the materials, determined by the presence of iron oxide clusters on their external surface and near the pore openings. On the other hand, the highest reaction rate exhibited by FeMCM22 impr at 450 °C might

result from relatively high concentration of oligomeric Fe-oxo species, which are considered as the most active in high-temperature NH_3-SCR [439].

1.3 Comparison of the catalytic performance of Fe-zeolites to the commercial catalysts

In order to provide more comprehensive view on the catalytic performance of the examined zeolite-supported Fe-catalysts, the materials were compared to the literature studies on the commercial catalysts: promoted or non-promoted V_2O_5-TiO_2 and Cu-SSZ-13. The comparison included NO conversion and N_2O selectivity at 250 and 400 °C, thus in the low- and high-temperature region of NH_3-SCR. All of the results are collected in **Table 21.**

Table 21. Comparison of the catalytic performance of the investigated Fe-zeolite catalysts at 250 and 450 °C to the commercial catalysts reported in the literature

Sample code	NO conversion (%)		N_2O concentration (ppm)		Reference
	250 °C	400 °C	250 °C	400 °C	
FeClin cop	36	100	11	22	This thesis
FeClin ads	13	100	20	47	This thesis
FeClin impr	8	100	3	28	This thesis
FeMCM22 cop	48	81	9	11	This thesis
FeMCM22 ads	50	88	8	12	This thesis
FeMCM22 impr	32	95	7	23	This thesis
V_2O_5-TiO_2 [a]	70	78	18	42	[567]
V_2O_5-WO_3-TiO_2 [b]	85	90	5	65	[568]
Cu-SSZ-13 [c]	80	90	35	35	[569]

[a] 3.0 wt.% V_2O_5 [b] 1.6 wt.% V_2O_5 10 wt.% WO_3 [c] 2.4 wt.% Cu

In fact, the catalytic activity of iron-modified zeolites in low-temperature region of NH_3-SCR is lower comparing to the commercial systems. However, this result is typical for non-promoted Fe-zeolite catalysts [85]. One should note that the low-temperature activity was strongly influenced by the carrier, since MCM-22-supported materials showed 32-50% of NO conversion, depending on the modification method, thus, noticeably higher than that of Clin-supported catalysts. On the other hand, at 400 °C the

catalytic activity of all of the materials dramatically raised. This increase is especially noticeable for FeClin samples, while for FeMCM22 the activity was still lower than that of the industrial materials.

What is interesting, N_2O yield obtained for the analyzed samples (except of FeClin ads) was lower or comparable to that of the cited catalysts. In the case of the low-temperature region, this effect obviously results from lower catalytic activity. Nevertheless, in the high-temperature range, the production of N_2O still remained relatively low. Such different results of N_2O yield for the commercial catalysts and the samples might result from different mechanisms of nitrous oxide production. Cho et al. [563] compared emission of N_2O during NH_3-SCR over Fe-zeolite and V_2O_5-TiO_2 and found that in contrast to the zeolitic system, the latter catalyst does not generate N_2O through NH_4NO_3 decomposition. Martín et al. [570] suggested that generation of N_2O during NH_3-SCR over vanadia-titania catalysts is related to Lewis acid sites (V=O) which actively adsorb NO_2 and react with NH_3, yielding nitrous oxide. Furthermore, Zhu et al. [69] emphasized that transformation of Lewis to Brönsted centers by the addition of H_2O greatly hindered production of N_2O. Basing on the above-mentioned literature studies, it can be concluded that the investigated zeolites contained higher concentration of Brönsted acidity, which was beneficial for lower yield of the considered by-product of the process. In the case of the commercial zeolitic catalyst, Cu-SSZ-13, Liu and co-workers [569] distinguished two main pathways of N_2O formation, dependent on the temperature region: NH_4NO_3 decomposition below 300 °C and direct NH_3 oxidation above this temperature. Therefore, FeClin catalysts are speculated to produce N_2O according to these two reactions. In contrast, the negligible yield of nitrous oxide in low- and high- temperature region of the process supports the conclusion that MWW zeolite with Fe was active in the catalytic decomposition of this non-desired reaction product.

1.4 Conclusions on the comparison of natural and synthetic Fe-modified zeolites

In summary, in this chapter both physico-chemical and catalytic features of iron-modified zeolites were comprehensively investigated and compared. Two types of zeolites were considered: natural, represented by clinoptilolite, and synthetic layered MCM-22, belonging to the MWW family. The materials were modified with iron using three different post-synthesis procedures: co-precipitation,

adsorption from the solution, and incipient wetness impregnation. The amount of the active phase, for clinoptilolite-supported catalysts was slightly higher, due to the natural presence of iron in the material.

NO reduction obtained for the samples showed similar trend, which was gradual increase of the activity, linear to the reaction temperature. Such catalytic behavior, assigned to the activity of various types of iron species, is characteristic for Fe-zeolite catalysts. In order to investigate the contribution of the support to NO conversion, both materials were examined in NH_3-SCR before modifications. It was found that the pristine MCM-22 exhibited minimal activity, suggesting that the main role in the catalytic process is played by the Fe species. In contrast, raw clinoptilolite was moderately active, especially in the high-temperature range of NH_3-SCR. Therefore, naturally occurring iron sites were probably present in the zeolitic framework in a form of oligomers or small particles of higher nuclearity, which contributed to its activity above 350 °C.

Basing on the obtained results of the catalytic performance and characteristics of the catalysts, the following conclusions were drawn:

1. The investigated modification methods influenced both physico-chemical parameters of the zeolites and their catalytic features. The most active sample among clinoptilolite-supported catalysts was FeClin cop, while among MCM-222-supported it was FeMCM22 ads. This result suggests that formation of Fe active species in the zeolites was determined by the type of zeolite framework. However, regardless of the support, the catalyst obtained by incipient wetness impregnation exhibited the lowest NO conversion. This effect could result from partial pore blockage through the deposition of small particles of Fe_2O_3.
2. The most satisfactory catalytic activity of FeClin cop and FeMCM22 ads resulted mainly from the presence of isolated iron species with the beneficial redox features, which acted synergistically with the acid sites of the zeolites.
3. Regardless of the modification method, NO conversion in the low-temperature region was significantly higher for the catalysts supported on MCM-22, while the materials with clinoptilolite showed better activity in the high-temperature region (100% at 400 °C). Therefore, uniform and hierarchical porous structure probably promoted the NO reduction rate and formation of the desired reaction products, as confirmed by the minor N_2O yield.

4. Among all of the examined materials, only FeClin cop did not show the decrease of NO reduction in the high temperature region of NH_3-SCR. In contrast, this phenomenon could be observed for FeMCM22 cop, which suggests that co-precipitation method is preferable rather for heulandite, than for MWW topology.

5. Adsorption from the solution and incipient wetness impregnation methods influenced differently on the catalytic performance of clinoptilolite and MCM-22. The results obtained for these methods were almost identical for FeClin and noticeably differed for FeMCM22 catalysts. Aggregation of iron oxide clusters, characteristic for impregnation method, inhibited the access of the reactants to the isolated Fe^{3+} sites of FeMCM22 impr, which are active in low-temperature region of the process. As a result, activity of the sample was as high as that of the others only above 325 °C, when iron species of higher nuclearity contribute to NO conversion.

6. Formation of nitrous oxide, as one of the by-products of NH_3-SCR, was influenced by the type of the support, as well as by the modification method. However, irrespectively of the procedure of Fe deposition, MCM-22-supported catalysts exhibited significantly lower N_2O yield.

7. The production of N_2O increased linearly with temperature for all of the clinoptilolite-supported catalysts, especially in the case of FeClin ads. The decline of NO conversion for FeClin ads and FeClin impr above 400 °C suggests that nitrous oxide formation in the high-temperature region is a consequence of direct NH_3 oxidation, thus, consumption of the reducing agent. This explanation is supported by the lowest concentration of N_2O for FeClin cop, which remains highly active in the investigated temperature range.

8. The production of N_2O for FeMCM22 catalysts was increasing within 150-350 °C and above this temperature region, its concentration started to gradually decrease. Two possible explanations of this phenomenon concern reduction of N_2O by ammonia on isolated Fe^{3+} sites or its catalytic decomposition by oligomeric iron sites.

9. In comparison to the commercial vanadium-based systems, clinoptilolite- and MCM-22-supported catalysts exhibited lower conversion of NO in the low-temperature range, however, comparable concentration of N_2O. On the other hand, in the high-temperature region, activity of the zeolite-supported catalysts was considerably higher than that of V_2O_5-(WO_3)-TiO_2. Moreover, N_2O formation

detected for the majority of the investigated samples was negligible in comparison to the vanadia-titania catalyst. This effect was correlated with different mechanisms of N_2O formation during NH_3-SCR over zeolite-supported and vanadium-based catalysts.

10. The analyzed materials exhibited lower low-temperature activity comparing to the commercial Cu-SSZ-13. Nevertheless, in the high-temperature region, NO conversion obtained for FeClin exceeded that of Cu-zeolite. This result is assigned to different reduction ability of Cu and Fe in the zeolites, which determined activity of the catalysts in different temperature regions. Importantly, N_2O production during the catalytic reaction over the investigated samples was lower or comparable to that of Cu-SSZ-13. This effect can be explained by the strongly oxidative character of copper, resulting in the parallel, undesired reaction of ammonia oxidation, and increased N_2O concentration in the post-reaction gas mixture.

2. Influence of Cu or Ce on the physicochemical and catalytic features of the catalysts

In recent years, bimetallic dual- or single-layer catalysts with copper and iron have been tested in many catalytic reactions, including NH_3-SCR [472,475,480,571]. Fe-exchanged zeolites are highly active catalysts above 350 °C, which was proven by the results obtained within this thesis. On the other hand, Cu-zeolites show superior catalytic performance below 300 °C [572]. Moreover, copper and iron were confirmed to act synergistically in NH_3-SCR. There are literature reports describing the most efficient configuration and thickness of dual-layer Fe-Cu zeolite catalysts to provide high NO conversion [479,573]. However, so far, only few studies have examined single layer Cu-Fe-zeolites as catalysts of the reduction of NO with ammonia. Boroń et al. [476] analyzed the influence of 1 wt.% of Cu on the catalytic performance of Fe-BEA. It was found that the presence of copper decreased reducibility of iron and enhanced low-temperature activity in NO reduction. Furthermore, Zhang et al. [475] confirmed that Cu and Fe formed well-dispersed nanocomposites on the surface of ZSM-5. The authors declared that the presence of two metals expanded the temperature window of the catalyst to 200-475 °C. The satisfactory results obtained for other zeolites with Fe and Cu were the motivation to analyze how the addition of copper will influence the catalytic performance of iron-modified clinoptilolite and MCM-22.

Apart from copper, it was found that cerium dioxide, CeO_2, can have a beneficial influence on the catalytic properties of NH_3-SCR catalysts, due to its redox features [574]. To date, the research have been mainly focused on ceria with metal oxides [484,575] or activated carbon [213,576] used as a support of the catalyst. On the other hand, the area of the application of zeolite catalysts promoted with Ce has not been explored in depth. Jiang et al. [483] proved that Cu-modified ZSM-5, SSZ-13, SAPO-34, and Beta zeolites promoted with Ce show enhanced activity in low-temperature region of NH_3-SCR. Some researchers attempted to modify MCM-22 with Ce [535,553] and reported successful incorporation of the metal into the extraframework positions of the material. However, the studies were focused on catalytic reactions with organic molecules and none of them addressed the effect of Ce on Fe-clinoptilolite, nor MCM-22 as the catalysts of NH_3-SCR.

Therefore, this chapter provides an insight into the influence of copper or cerium promotion on clinoptilolite and MCM-22 modified with iron. The samples selected for the introduction of 1 wt.% of Cu or 0.5 wt.% of Ce were FeClin cop and FeMCM22 ads, due to their best catalytic performance among the two investigated groups of Fe-catalysts.

2.1 Characterization of the promoted zeolites

Chemical composition and crystal structure of the materials

The amount of copper or cerium introduced into the FeClin cop and FeMCM22 ads was determined by ICP-OES analysis. The obtained results, together with that obtained for the non-modified and Fe-zeolites are collected in **Table 22.** According to the presented data, Cu and Ce were successively deposited in the zeolitic structures. The amount of copper was in good agreement with the calculated value. However, concentration of cerium in the samples was noticeably lower than the desired, especially for FeCeMCM22 ads. This effect might result from the presence of aggregated particles of iron oxide in the catalysts, which inhibited the access and successful incorporation of cerium ions into the zeolitic framework. The negligible differences between the concentration of Si, Al, and Fe in the non-promoted and promoted samples might result from the analytical error of the apparatus.

Table 22. Chemical composition of Fe-modified zeolites promoted with Cu or Ce

Sample code	Si (wt.%)	Al (wt.%)	Fe (wt.%)	Cu (wt.%)	Ce (wt.%)
FeClin cop	30.01	5.33	8.01	0	0
FeCuClin cop	30.84	5.49	7.97	1.16	0
FeCeClin cop	31.33	5.60	8.21	0	0.36
FeMCM22 ads	30.48	2.07	16.74	0	0
FeCuMCM22 ads	31.57	2.19	15.16	0.70	0
FeCeMCM22 ads	30.28	2.11	15.20	0	0.13

XRD analysis was used to elucidate the influence of Cu and Ce species on the crystal structure of Fe-modified clinoptilolite and MCM-22. XRD patterns of the non-promoted and promoted FeClin cop are presented in **Figure 70**, while **Figure 71** demonstrates the patterns of FeMCM22 ads before and after introduction of Cu or Ce. For both zeolites, promotion with copper or cerium did not influence the position of the diffraction maxima characteristic for the zeolitic frameworks. Therefore, the promoters did not cause any structural changes. However, in the case of FeCuClin cop and FeCeClin cop, the intensity of the reflections at 2θ of 9.95, 11.37, and 13.29° decreased after promotion. Hence, the

presence of Cu or Ce species affected crystallinity of the zeolite. Similar effect can be observed after promotion with Cu for the diagnostic reflections of (*hkl*) (100), (101), and (220), ascribed to the layered structure of MCM-22. Possibly, small particles of copper oxide were deposited between the MWW layers, which resulted in their partial re-arrangement. However, the lack of characteristic diffraction maxima ascribed to the presence of copper oxide proved that Cu was present rather in a form of well-dispersed species, than clusters or bigger particles. In contrast, introduction of Ce did not cause such result, which was due to its lower loading.

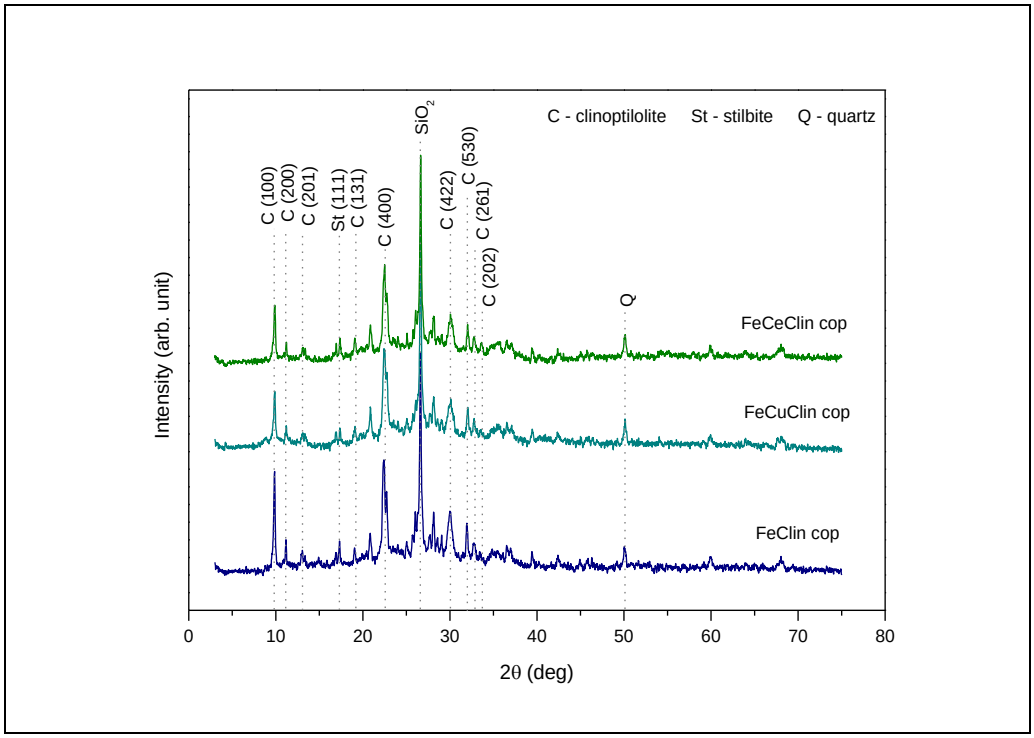

Figure 70. XRD patterns obtained for clinoptilolite-supported catalysts

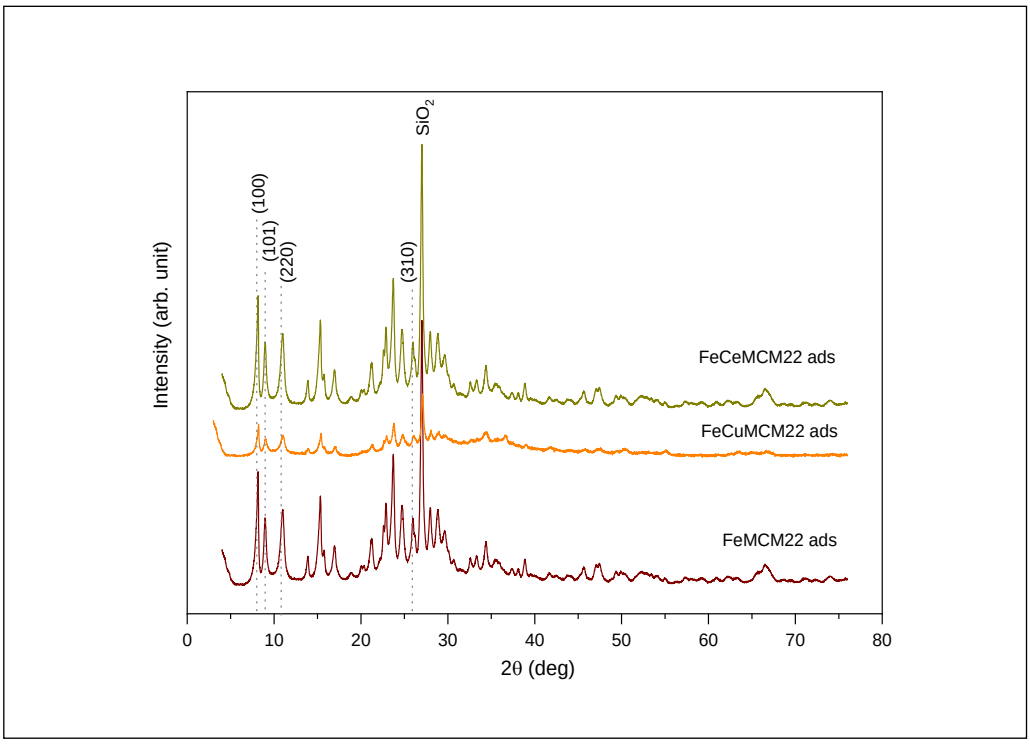

Figure 71. XRD patterns obtained for MCM22-supported catalysts

Textural properties

The nitrogen adsorption-desorption isotherms of the investigated Fe-catalysts before and after promotion with Cu or Ce are presented in **Figure 72** (clinoptilolite-supported samples) and **Figure 73** (MCM-22-supported samples). Furthermore, **Table 23** presents structural and textural parameters of the materials.

As showed in **Figure 72**, the catalysts supported on clinoptilolite exhibited isotherms of type IV (a) according to the IUPAC classification, with the hysteresis loop characteristic for type H4 [505]. The obtained results are in line with those reported in the literature [529,577]. This shape of adsorption-desorption branch suggests that after introduction of the promoters, the catalyst preserved its microporous nature and secondary mesoporosity. Nevertheless, the results collected in **Table 23** clearly indicate that the addition of Cu or Ce had a significant impact on the textural properties. The specific and external surface area, micropore surface area, and total pore volume decreased, following the order of FeCeClin cop < FeCuClin cop < FeClin cop. On the other hand, the average pore diameter was only slightly changed after introduction of the promoters to FeClin cop. The declining trend of the values can be ascribed to the formation of small aggregates of metal oxide particles. Another explanation of this

decrease can be found in moderately lower crystallinity of the promoted catalysts, confirmed by XRD studies.

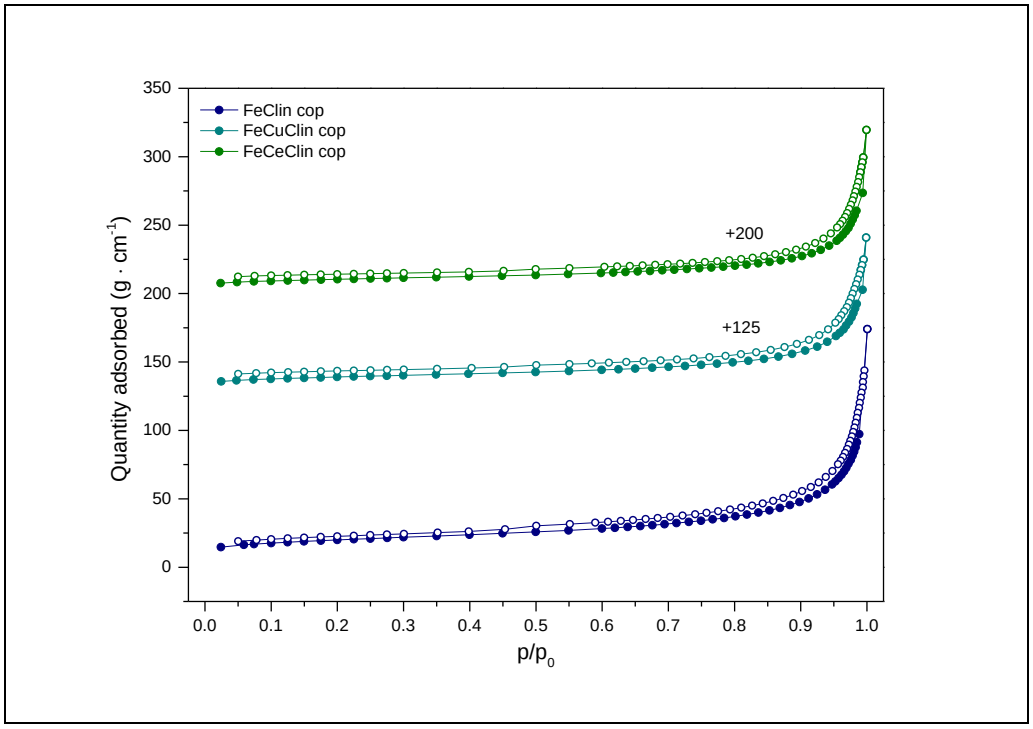

Figure 72. Nitrogen sorption isotherms obtained for clinoptilolite-supported catalysts (for better visibility, the isotherms were shifted by the values given in the figure)

N_2 sorption isotherms obtained for FeMCM22 ads before and after promotion with Cu or Ce are presented in **Figure 73**. As already mentioned, the adsorption branch of Fe-modified layered zeolite resembles that of the pure material and can be classified as type I (b) according to IUPAC. Additionally, non-rigid aggregates of the plate-like particles formed by the MWW layers contributed to the formation of H3 hysteresis loop [505]. However, its shape changed after introduction of Cu or Ce into the catalyst, since it was transformed from H3 into H4, suggesting aggregation of the zeolite crystals. What is more, similarly to the promoted clinoptilolite-supported catalysts, the values of the specific and external surface area, micropore surface area, and total volume of pores showed the following decreasing trend: FeCeMCM22 ads < FeCuMCM22 ads < FeMCM22 ads. This effect was likely caused by the aggregation of the particles of the active phase and the promoter (especially Cu, due to its greater loading), migration of iron oxide to the external surface of the zeolitic layers, or deposition of CuO or CeO_2 near the pore openings.

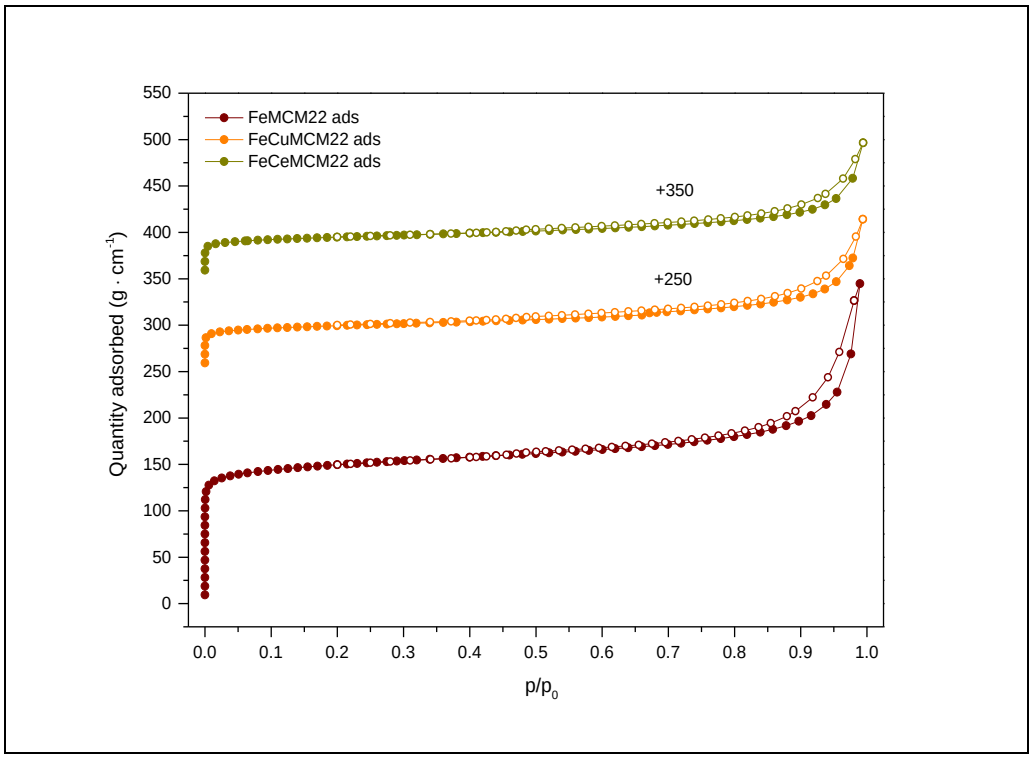

Figure 73. Nitrogen sorption isotherms obtained for MCM22-supported catalysts (for better visibility, the isotherms were shifted by the values given in the figure)

Table 23. Structural and textural properties of clinoptilolite- and MCM22-supported catalysts

Sample code	S_{BET} [a] ($m^2 \cdot g^{-1}$)	S_{EXT} [b] ($m^2 \cdot g^{-1}$)	S_{micro} [b] ($m^2 \cdot g^{-1}$)	V_{total} [c] ($cm^3 \cdot g^{-1}$)	V_{micro} [b] ($cm^3 \cdot g^{-1}$)	$V_{meso + macro}$ [d] ($cm^3 \cdot g^{-1}$)	D_{aver} [e] (nm)
FeClin cop	126	40	87	0.186	0.042	0.144	7.22
FeCuClin cop	69	28	41	0.151	0.021	0.130	8.34
FeCeClin cop	37	23	15	0.102	0.007	0.095	7.89
FeMCM22 ads	372	109	264	0.418	0.129	0.289	5.89
FeCuMCM22 ads	160	44	115	0.194	0.056	0.138	6.62
FeCeMCM22 ads	138	39	99	0.176	0.048	0.128	6.71

[a] S_{BET} (BET surface area) was determined from the adsorption isotherm

[b] S_{ext} (external surface area), S_{micro} (micropore surface area), and V_{micro} (micropore volume) were calculated using t-plot method

[c] V_{total} (total pore volume) was obtained at the relative pressure (p/p_0) = 0.99

[d] $V_{meso} = V_{total} - V_{micro}$ (mesopore volume)

[e] D_{aver} (average pore diameter) was determined by BJH method

Morphology of the materials determined by SEM microscopy

The morphological properties of FeClin cop and FeMCM22 ads promoted with Cu or Ce were investigated by SEM images, demonstrated in **Figure 74** and **Figure 75**, respectively.

It can be observed from **Figure 74** that introduction of Cu did not result in any changes of the structure of the Fe-modified natural zeolite. The small nano-sized particles were still present on the characteristic tubular crystals of clinoptilolite. Additionally, the sample with cerium showed similar morphology to the non-promoted catalyst. Moreover, the easily recognizable tubular crystals of clinoptilolite and clustering of the small particles suggested that the addition of Ce could lead to partial aggregation of the particles of iron oxide, which covered the zeolitic layers.

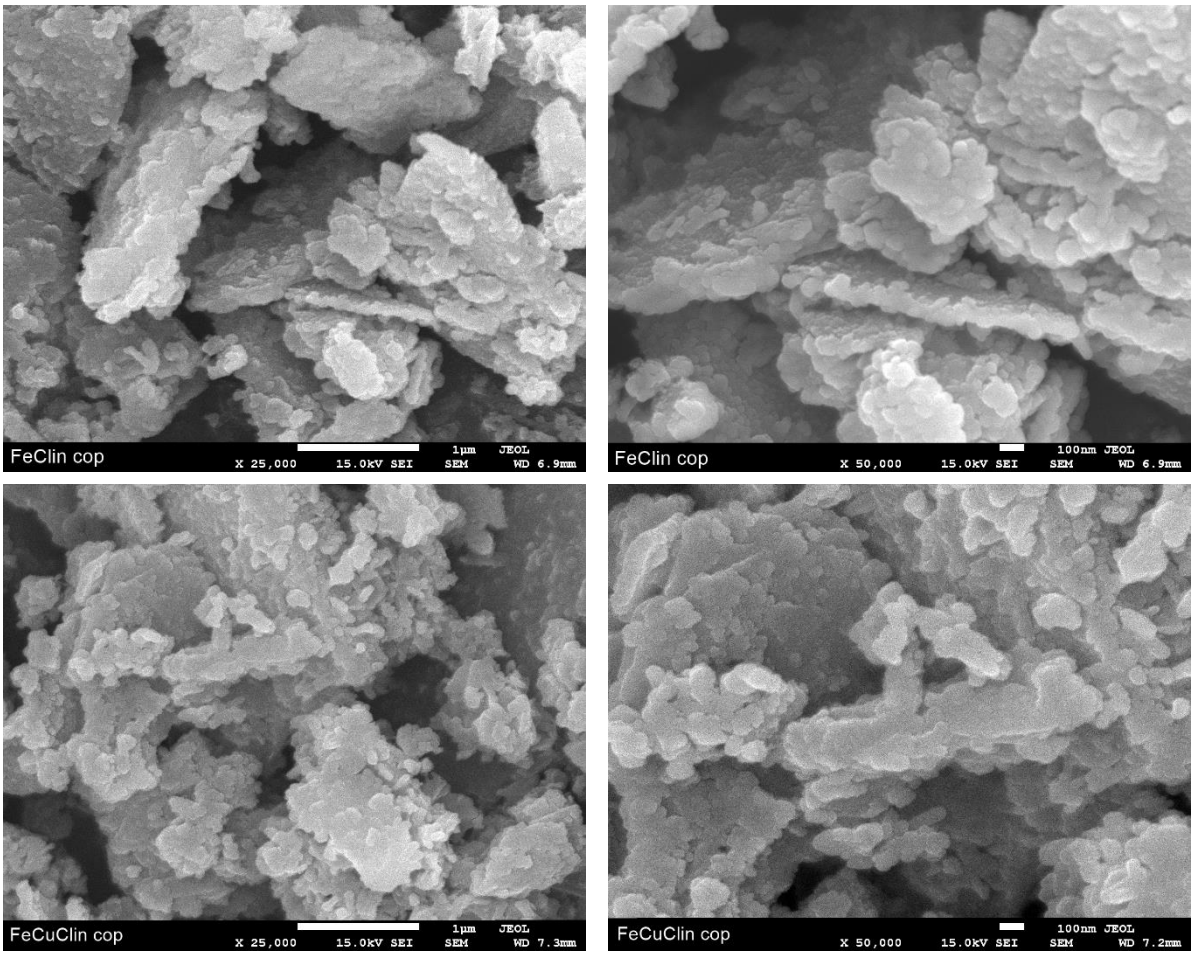

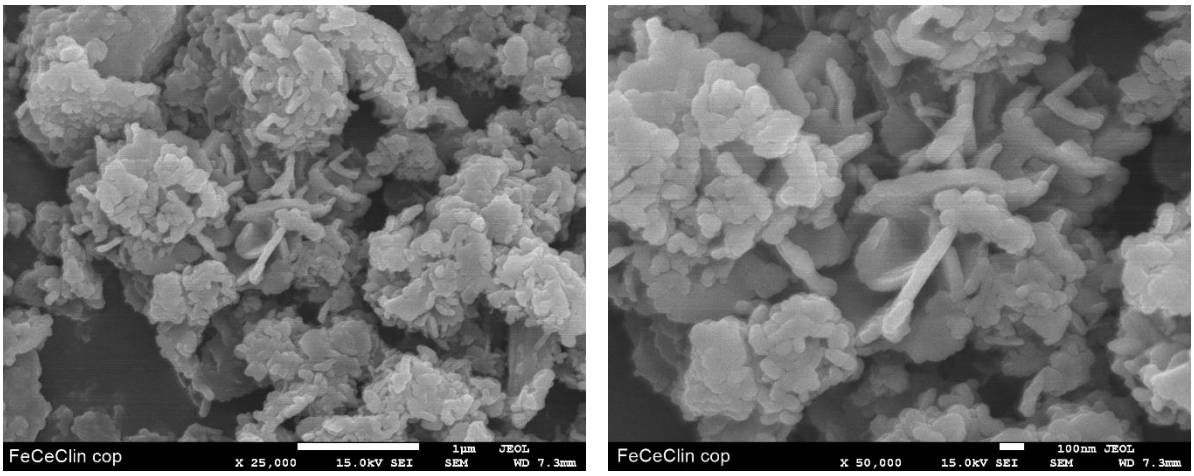

Figure 74. SEM images (at different magnification) of FeClin cop before and after promotion with Cu or Ce

SEM images recorded for FeMCM22 ads before and after promotion with Cu or Ce are presented in **Figure 75.** Introduction of the promoters did not have any influence on the morphology of the catalyst, since the characteristic plate-like particles of MWW layers were well-preserved. The nano-sized particles, detected in the images recorded for the promoted samples, can be assigned to the presence of bulk-like CuO or CeO_2 species, which is in line with the results of XRD. Nevertheless, it is predicted that the concentration of Ce was too low to form such amount of aggregated species, moreover, they were not detected by X-ray diffraction. Therefore, probably as in the case of FeCeClin cop, promotion of FeMCM22 ads with cerium caused clustering of the particles of iron oxide.

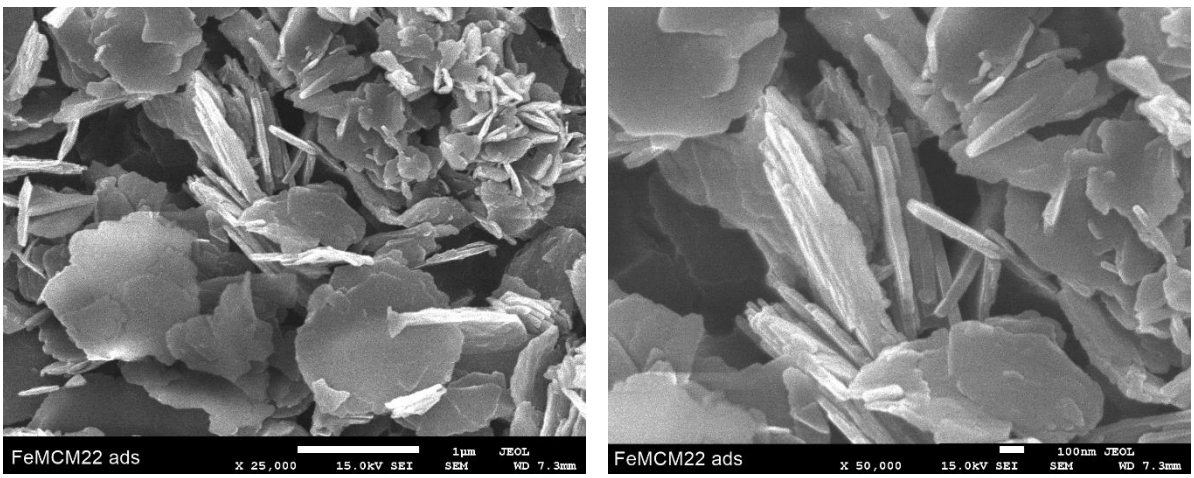

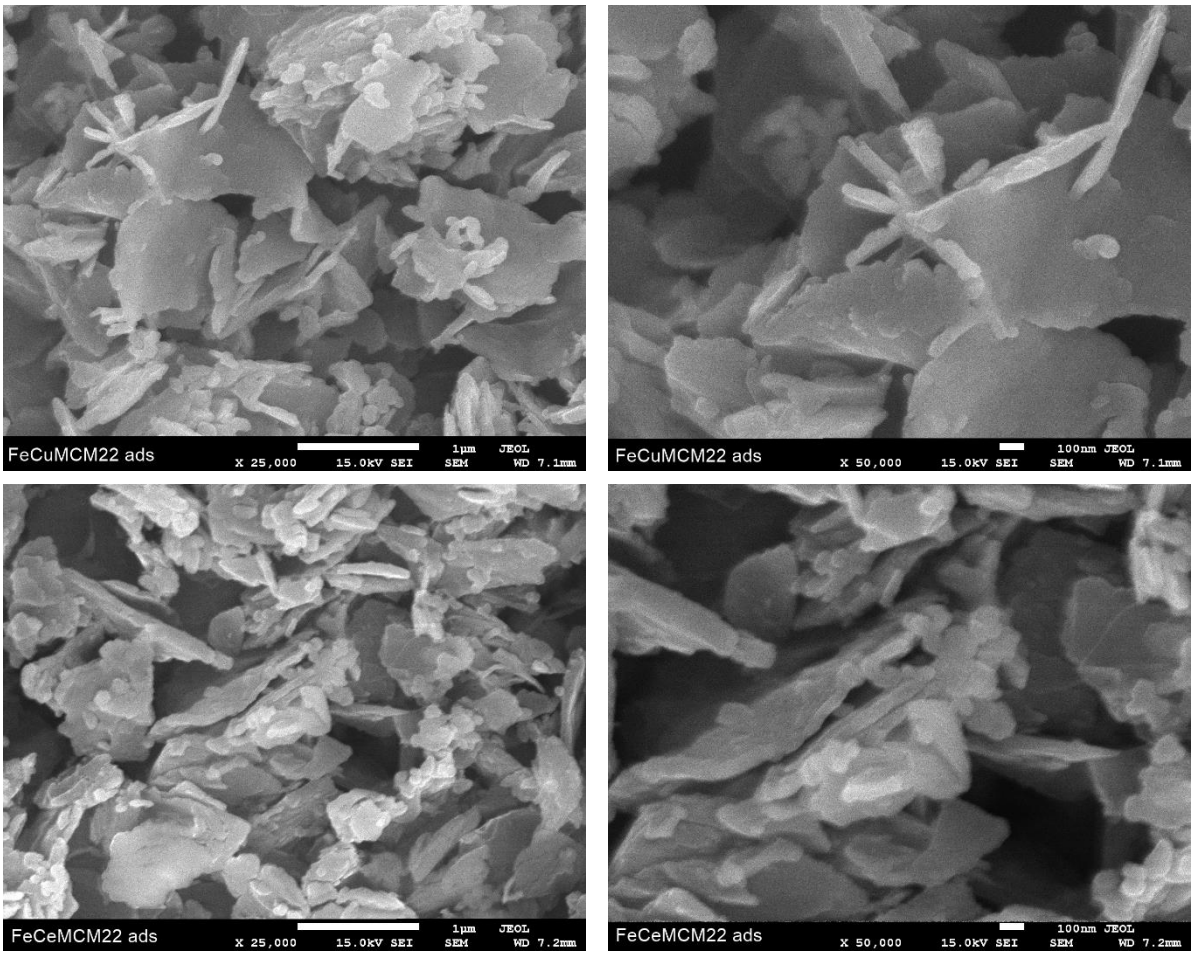

Figure 75. SEM images (at different magnification) of FeMCM22 ads before and after promotion with Cu or Ce

Morphology of the materials determined by TEM microscopy

The morphology of the catalysts after promotion with Cu or Ce, with the regard to metallic species and arrangement of zeolitic layers, was studied by transmission electron microscopy (TEM). The micrographs were recorded in bright-field (BF), high-angle annular dark-field (HAADF), and high resolution (HR) modes, as presented in **Figure 76** for Clin-supported and in **Figure 77** for MCM22-supported catalysts.

Figure 76 shows that any considerable differences occurred in the arrangement of tubular clinoptilolite layers after introduction of the promoters. However, uniformly distributed small particles of more bulky aggregates of metal oxides of the size ca. 10-20 nm can be easily found in the micrographs. The detected species can be considered as the reason of the decreased specific surface area and pore volume of the promoted catalysts. What is more, the effect of aggregation was more clearly visible in the case of FeCuClin cop, comparing to the sample promoted with Ce.

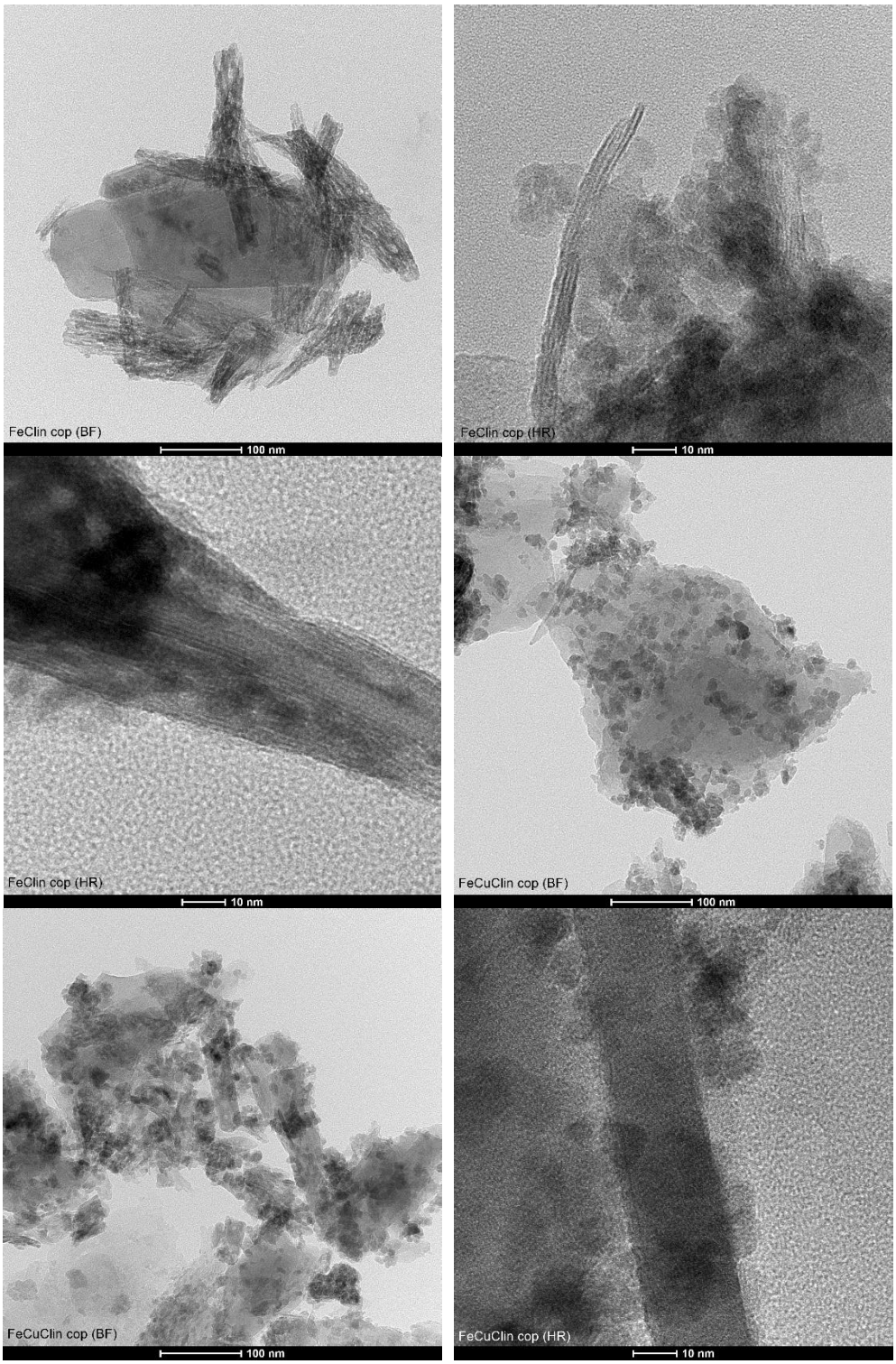
FeClin cop (BF)
100 nm
FeClin cop (HR)
10 nm
FeClin cop (HR)
10 nm
FeCuClin cop (BF)
100 nm
FeCuClin cop (BF)
100 nm
FeCuClin cop (HR)
10 nm

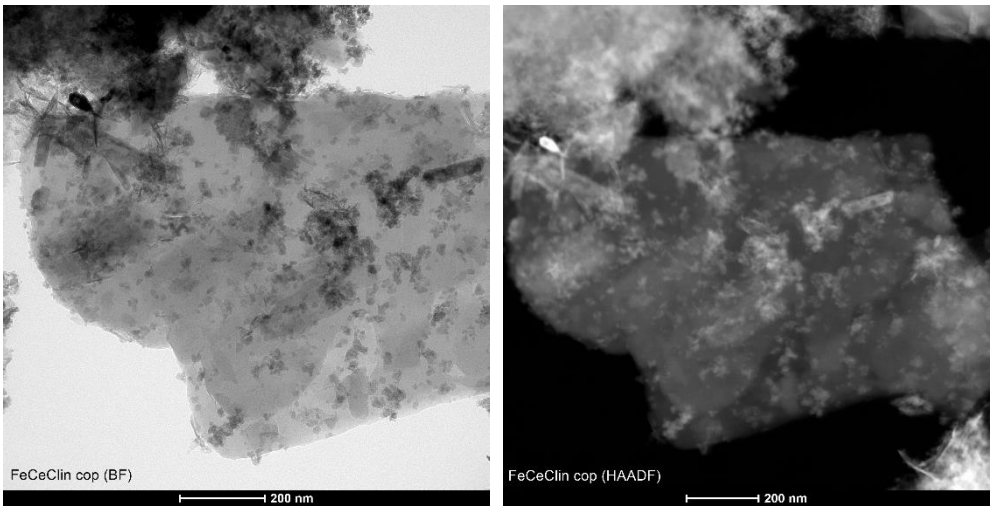

Figure 76. Bright-field (BF), high-angle annular dark-field (HAADF), and high resolution (HR) micrographs recorded for FeClin cop before and after promotion with Cu or Ce (description of each sample with its code is present in the micrograph)

The micrographs presented in **Figure 77** confirmed that the ordered, hexagonal, piled MWW-type layers of the support were preserved for FeCuMCM22 ads and FeCeMCM22 ads. Despite the fact that the arrangement of the layers did not noticeably change (see HAADF micrographs), introduction of the promoters resulted in the formation of agglomerated metal species. One can observe that some of the metal oxide particles have much higher dimension than the layers of the zeolitic support. Therefore, it can be concluded that they occupied rather the external surface of the material, than the inner structure. The formation of metal oxide particles on the surface of MWW layers was also observed by Lima and co-workers [378] for MCM-22 modified with cobalt. These results differ significantly from those obtained for clinoptilolite, which could result from different arrangement and nature of MWW and clinoptilolite layers.

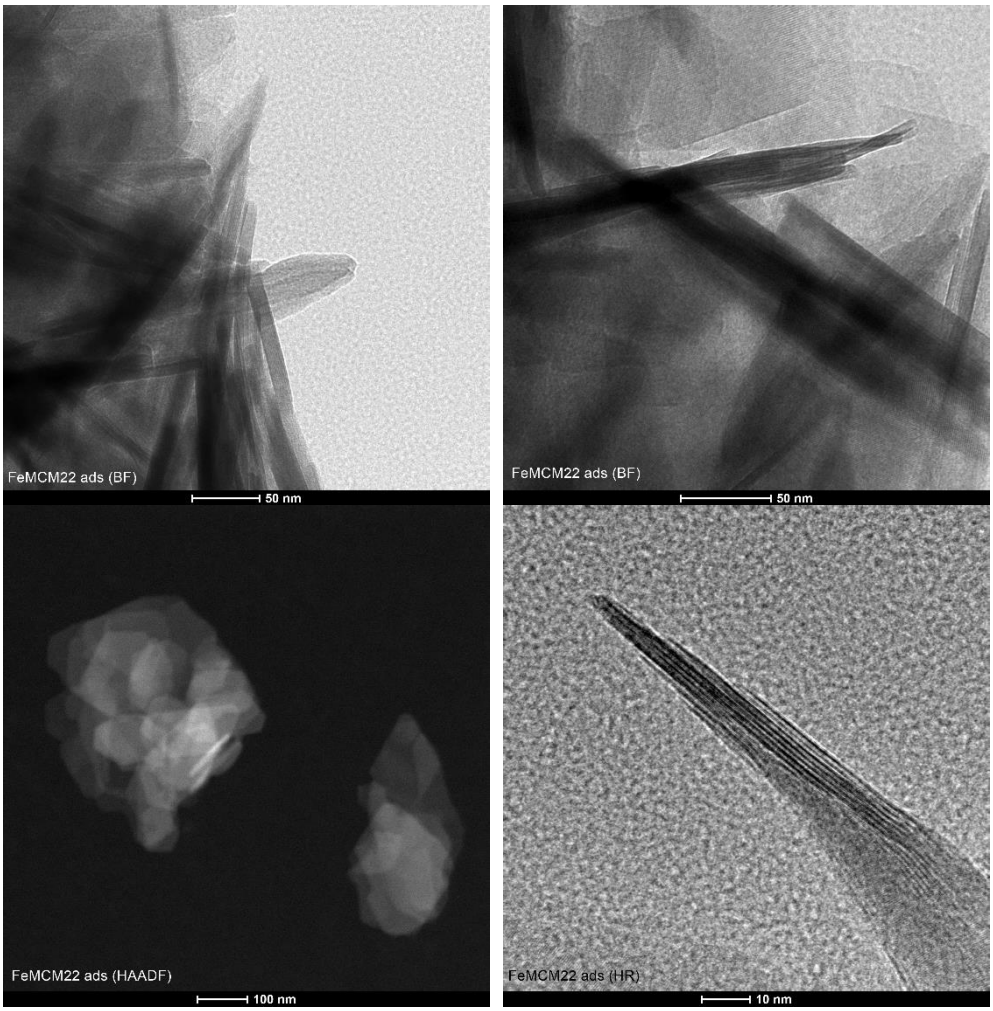
FeMCM22 ads (BF)
50 nm
FeMCM22 ads (BF)
50 nm
FeMCM22 ads (HAADF)
100 nm
FeMCM22 ads (HR)
10 nm

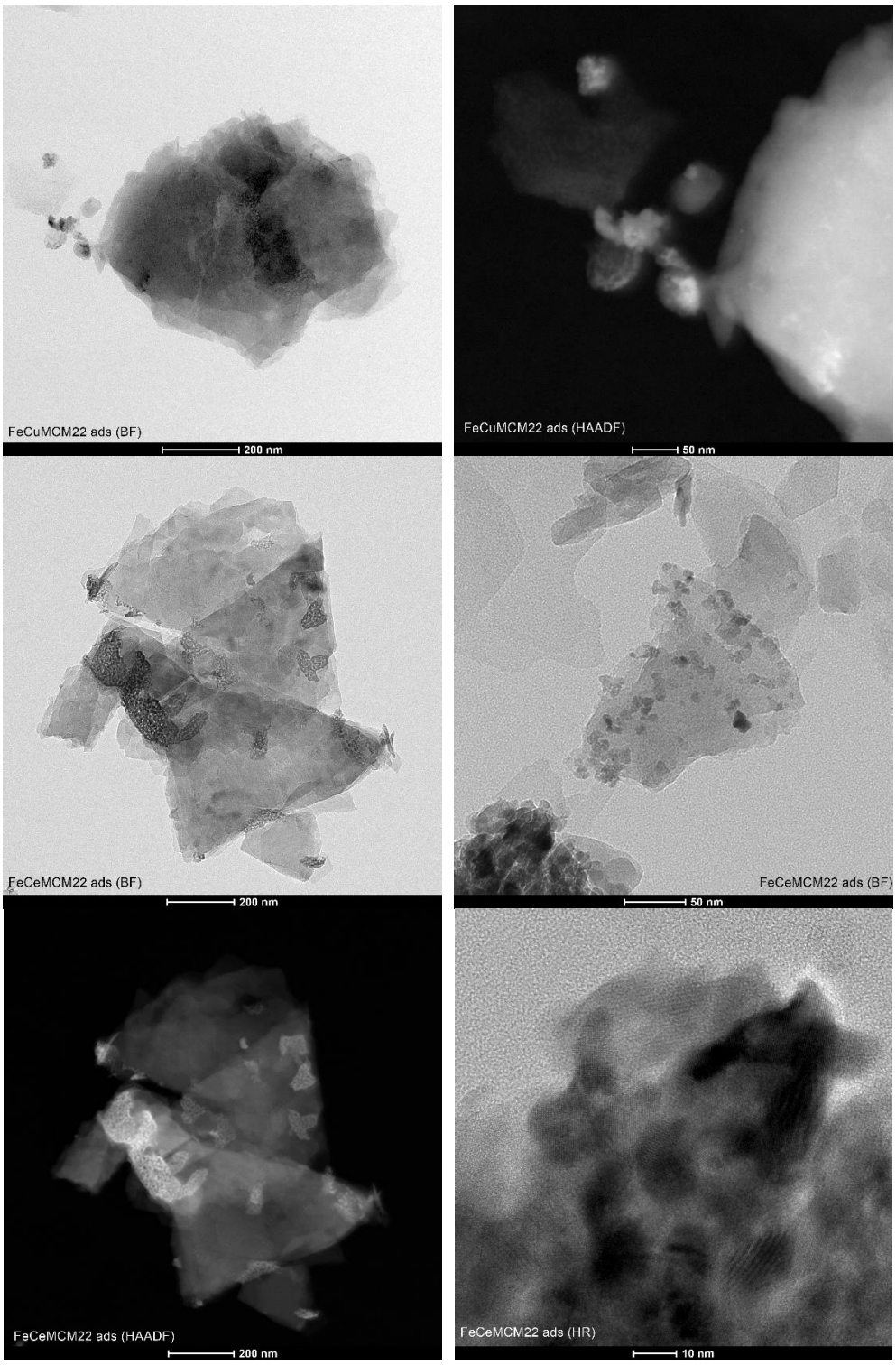

Figure 77. Bright-field (BF), high-angle annular dark-field (HAADF), and high resolution (HR) micrographs recorded for FeMCM22 ads before and after promotion with Cu or Ce (description of each sample with its code is present in the micrograph)

Acidity of the promoted catalysts

The total acidity of the catalysts promoted with Cu or Ce, with the distinction to the weak, medium, and strong acid sites was determined by NH_3-TPD in the temperature region of 100-800 °C. The obtained NH_3-TPD profiles are presented in **Figures 78-79**, for clinoptilolite- and MCM22-supported catalysts, respectively. In order to facilitate the assignment of the desorption peaks to the temperature, the patterns were deconvoluted by fitting to Gaussian function. Additionally, quantification of the acid sites is summarized in **Table 24.**

As depicted in **Figure 78,** the addition of Cu or Ce significantly influenced acidic characterization of FeClin cop. The copper-promoted catalyst exhibited slightly higher concentration of acidic centers of weak strength, however the desorption temperature was lowered by ca. 10 °C, comparing to the non-promoted material. Additionally, the broad and intense peak at 395 °C, detected for FeClin cop was divided into two more narrow, centered at 270 and 424 °C after promotion with Cu. The former one results from the generation of new acid sites of medium strength, while the latter corresponds to strong acid sites, due to the presence of Cu^{2+} [578]. Similar effect was observed by Zhang and co-workers [475] for Fe-Cu-modified HZSM-5. Furthermore, Chen et al. [579] characterized the acidity of Cu-CHA zeolite using NH_3-TPD and confirmed that the profiles of the catalysts are divided into three regions: low-, intermediate-, and high-temperature. The authors ascribed the appearance of the intermediate-temperature peak to NH_3 adsorbed on Cu sites. Moreover, the DFT calculations combined with kinetic simulations confirmed that NH_3 is desorbed from $[Cu(I)(NH_3)_2]^+$ and $[Cu(II)(NH_3)_3]^+$ complexes between 250-450 °C. Therefore, the demonstrated results indicated that copper had promoting impact on the development of new acid sites. On the other hand, the low-intense peak at 665 °C completely disappeared only in the case of FeCuClin cop. This phenomenon could be caused by the adsorption of aggregated copper oxide clusters on the acid sites responsible for the appearance of this desorption peak. According to the data presented in **Table 24**, the total acidity of FeCuClin cop was the highest among all of the clinoptilolite-supported catalysts. In contrast to FeCuClin cop, after promotion with Ce, the number of weakly adsorbed ammonia molecules decreased by around 25%. However, introduction of Ce resulted in the formation of a new desorption peak at ca. 300 °C, assigned to the acid sites of medium

strength. Additionally, the high temperature peak, ascribed to the chemisorbed ammonia, was shifted to 450 °C, while the position of the desorption maximum at 665 °C was not changed.

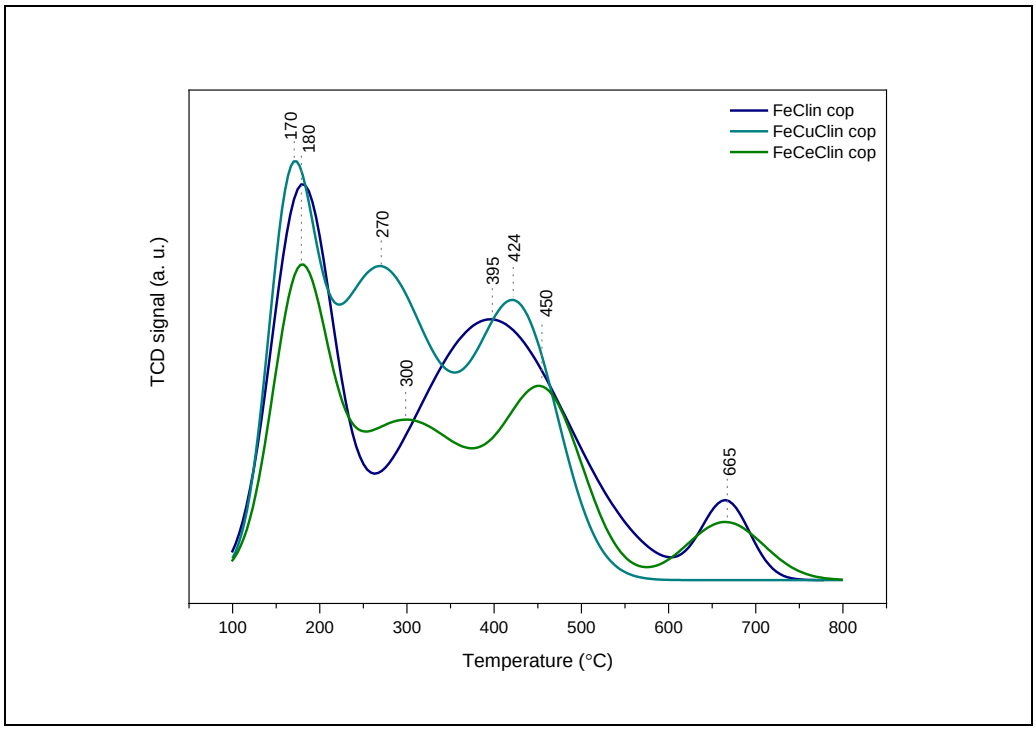

Figure 78. NH_3-TPD profiles obtained for clinoptilolite-supported catalysts

Acidic characterization of FeMCM22 ads after promotion with copper or cerium is demonstrated in **Figure 79.** In the case of the samples with MCM-22, the low temperature peaks remained almost unchanged, regardless the promoter used for the modification. However, promotion with Cu or Ce caused disappearance of the high-temperature peak located at 655 °C. Additionally, the changes of the shape of the patterns in the temperature region of 225-550 °C revealed important differences between the acidic features of the catalysts. Similarly to FeCuClin cop, after introduction of Cu, the desorption peak of FeCuMCM22 ads centered at 345 °C was divided into two separated ones. The newly formed peaks were shifted into lower and higher temperature: 300 and 445 °C, respectively. Rutkowska et al. [353] analyzed the acidity of Fe- and Cu-modified zeolites of MWW family by pyridine sorption. The authors recognized that copper present in MCM-22 acted as Lewis sites of two origins: extraframework cations and copper oxide species. Since in FeCuMCM22 copper was introduced by impregnation method, the newly formed Lewis centers, confirmed by the desorption peak at 300 °C, can be ascribed to the presence of well-dispersed particles of copper oxide. On the other hand, the peak at 445 °C results

from the decomposition of the complexes generated by Cu and NH_3 molecules, similarly as in the case of FeCuClin cop. Furthermore, as presented in **Table 24**, introduction of Ce decreased the total acidity of FeMCM22 ads noticeably more than in the case of FeClin cop. In fact, concentration of the acid sites, which desorbed ammonia in the low-temperature range was moderately lower for FeCeMCM22 ads, comparing to FeMCM22 ads. However, the amount of the sites desorbing NH_3 in the medium-temperature region decreased more remarkably, while the high-temperature peak located at 655 °C completely disappeared. Additionally, the low- and medium-temperature peaks of FeCeMCM22 ads were centered at 175 and 330 °C, respectively. Thus, the strength of the acidic sites after addition of Ce lowered.

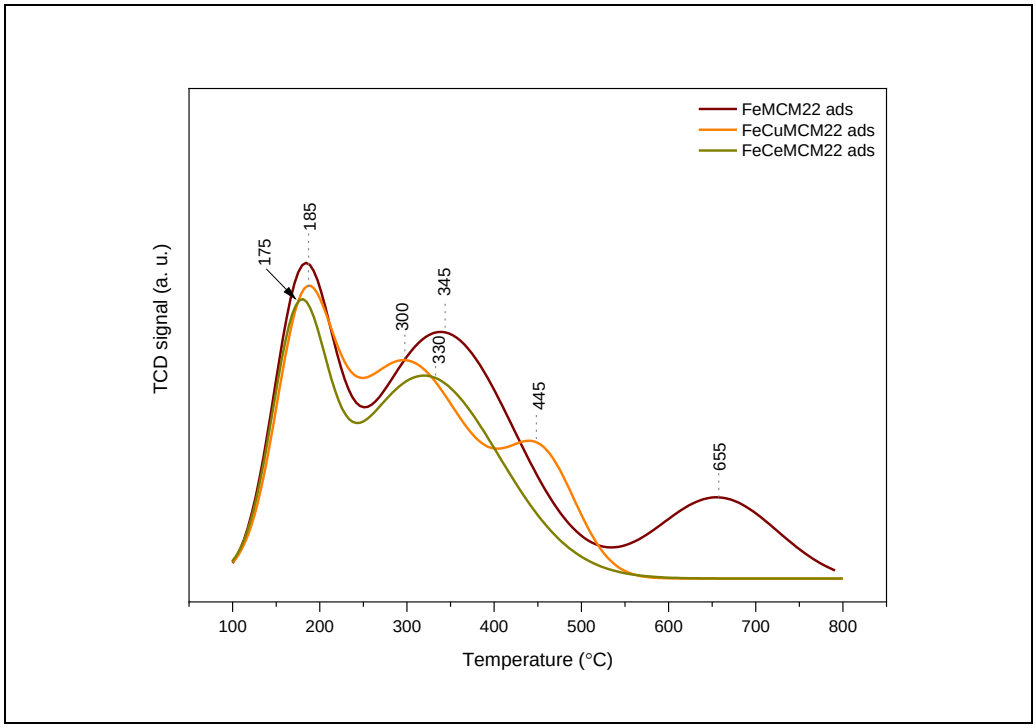

Figure 79. NH_3-TPD profiles obtained for MCM-22-supported catalysts

Table 24. Approximate concentration of the acid sites in the catalysts before and after promotion with Cu or Ce

Sample code	Concentration of the acid sites (μmol · g^{-1})			
	Weak sites	**Medium sites**	**Strong sites**	**Total amount of sites**
FeClin cop	850	561	171	1582
FeCuClin cop	899	673	606	2178
FeCeClin cop	679	348	538	1565
FeMCM22 ads	679	526	172	1377
FeCuMCM22 ads	626	467	292	1385
FeCeMCM22 ads	598	428	-	1026

Reducibility of the catalysts

The reducibility of Cu or Ce and their influence on the redox properties of iron was investigated by H_2-TPR. Assigning the H_2 consumption peaks to various Fe, Cu, and Ce species was a difficult task due to the interactions between the metals introduced into the zeolites. Therefore, interpretation of the obtained profiles was heavily relied on the extensive literature reports.

H_2-TPR profiles of the catalyst supported on clinoptilolite, presented in **Figure 80,** exhibited very similar shape before and after promotion with Cu or Ce. However, FeCuClin cop showed additional reduction peak centered at 200 °C. Łamacz et al. [580] declared that the reduction temperature of copper species depends on their dispersion on the catalyst surface. According to the authors, the peaks appearing below 190 °C correspond to well-dispersed isolated Cu^{2+} cations, while the peaks detected above this temperature are assigned to the reduction of small crystallites of CuO. On the other hand, Zhang et al. [581] investigated cupric sites located on HZSM-5 and reported that both Cu^{2+} and bulk-like CuO species are reduced at 200 and 330 °C, respectively. Nevertheless, the latter authors were focused on zeolitic catalysts, while the former ones at mixed metal oxides. Thus, it is more probable that the reduction peak at 200 °C, detected for FeCuClin cop, is assigned to the reduction of Cu^{2+} to Cu^{+}. Temperature of the reduction of the isolated Fe^{3+} (360 °C) and Fe_2O_3 to Fe^{2+} (500 °C) species slightly changed after introduction of copper. Therefore, promotion with Cu did not significantly improve the reduction behavior of iron species, but delivered additional centers, which facilitated redox properties

of the catalyst. In contrast to the promotion with Cu, any new reduction peaks were observed for FeCeClin cop. According to the literature, the reduction of pure CeO_2 can be divided into three stages: (1) the reduction of surface oxygen at 250-300 °C, (2) the reduction of surface lattice oxygen at 450-600 °C, (3) total reduction of the bulky species up to 900 °C [582]. Therefore, since the reduction of iron and cerium species occurs in similar temperature regions, the peaks could overlap and are not visible in the profiles. Additionally, promotion with Ce shifted the reduction temperature: from 365 to 335 °C and from 490 to 470 °C. Therefore, cerium could moderately improve redox ability of iron sites.

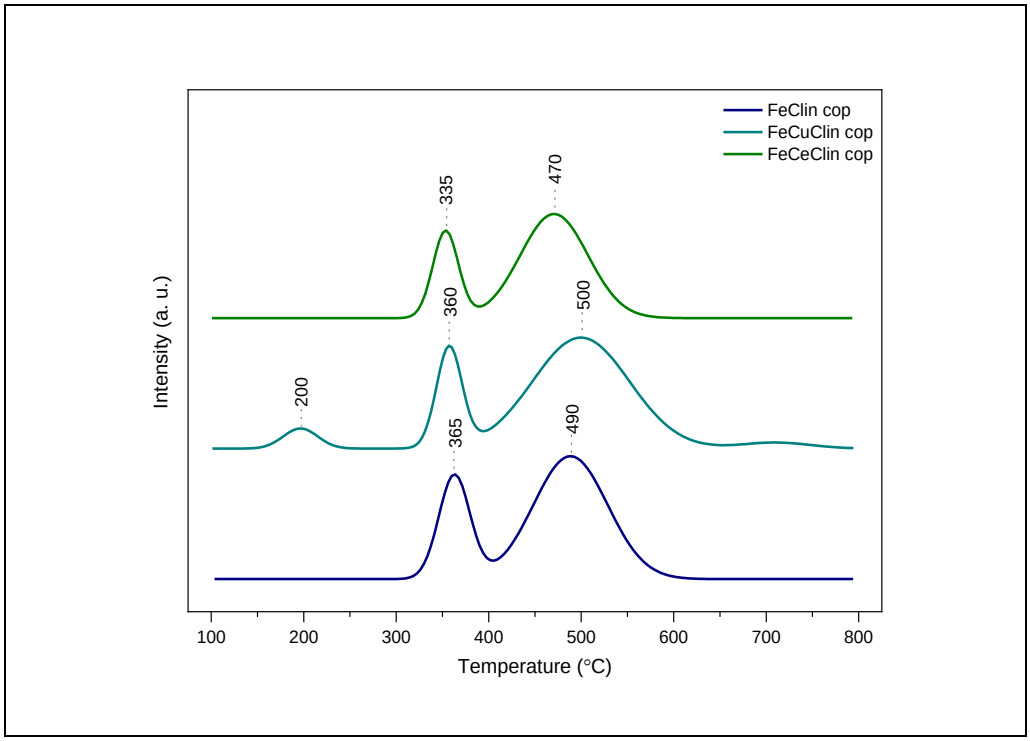

Figure 80. H_2-TPR profiles obtained for clinoptilolite-supported catalysts

In contrast to the clinoptilolite-supported catalysts, as presented in **Figure 81**, promotion with Cu or Ce observably changed the reduction properties of MCM-22-supported samples. The new reduction peak, appearing for FeCuMCM22 ads at 215 °C is a consequence of the reduction of Cu^{2+} to Cu^{+} [581]. Interestingly, FeCuMCM22 ads showed one, intense reduction peak at 405 °C. Therefore, the addition of copper increased the consumption of H_2 for the reduction of iron sites. On the other hand, the position of the peak at 635 °C, assigned to the reduction of Fe^{2+} to Fe^{0} remained unchanged. Similarly to FeCeClin cop, promotion with Ce slightly influenced the redox behavior of FeCeMCM22 ads. Two peaks at 415 and 530 °C, detected for FeMCM22 ads were replaced by one broad band centered at 450

°C. Nevertheless, it is not possible to assign accurately the reduction peaks to the specific metallic species. Besides, the peak at 635 °C was shifted to 600 °C, thus, the improvement of the high-temperature reduction ability of the catalyst was confirmed also for FeCeMCM22 ads.

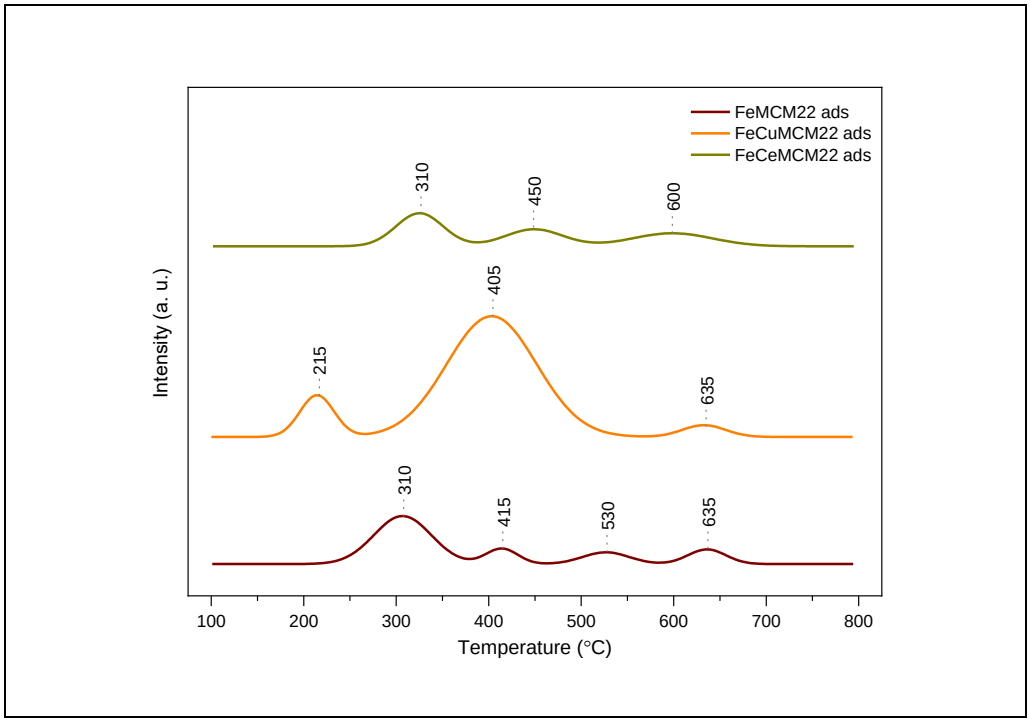

Figure 81. H_2-TPR profiles obtained for MCM-22-supported catalysts

Thermogravimetric studies of the materials

Thermogravimetric studies of the promoted catalysts in the temperature region of 30-800 °C were performed to observe the influence of Cu or Ce on thermal stability. The investigated temperature region of NH_3-SCR process was marked in the obtained thermograms by dotted lines. Additionally, the overview of the percentage weight loss of the catalysts is demonstrated in **Table 25**.

Figure 82 shows a trend of decreasing weight of the catalysts in the investigated temperature region. The effect is ascribed to the removal of water molecules, adsorbed physically or chemically to the surface of the materials [531]. The weight loss observed in the temperature region of 30-150 °C, ascribed to the elimination of weakly bonded H_2O is similar for all of the catalysts. However, above 150 °C the difference between the weight loss of the promoted and non-promoted samples became more remarkable. FeCuClin cop and FeCeClin cop showed moderately higher stability in the increasing temperature, which was likely caused by the presence of aggregated particles of the promoters. These

species inhibited the migration of the structural water from the zeolite. Slightly higher stability of FeCuClin cop can be explained by higher concentration of the promoter. Interestingly, both of the promoted samples did not show the sharp step of the weight loss above 400 °C, correlated with the decomposition of the residual sulfate groups of $FeSO_4$ (precursor of the active phase). The probable explanation of this phenomenon is that Cu^{2+} and Ce^{4+} could form small amounts of $CuSO_4$ and $Ce(SO_4)_2$, respectively. Copper sulfate decomposes to CuO at ca. 600-650 °C [583], while cerium sulfate to CeO_2 above 700 °C [584]. Thus, apart from the metal oxides, the sulfates could also contribute to the pore clogging and inhibition of the removal of water attached to the zeolite. Additionally, as a result, the promoted samples were more stable in the investigated temperature range of NH_3-SCR (150-450 °C).

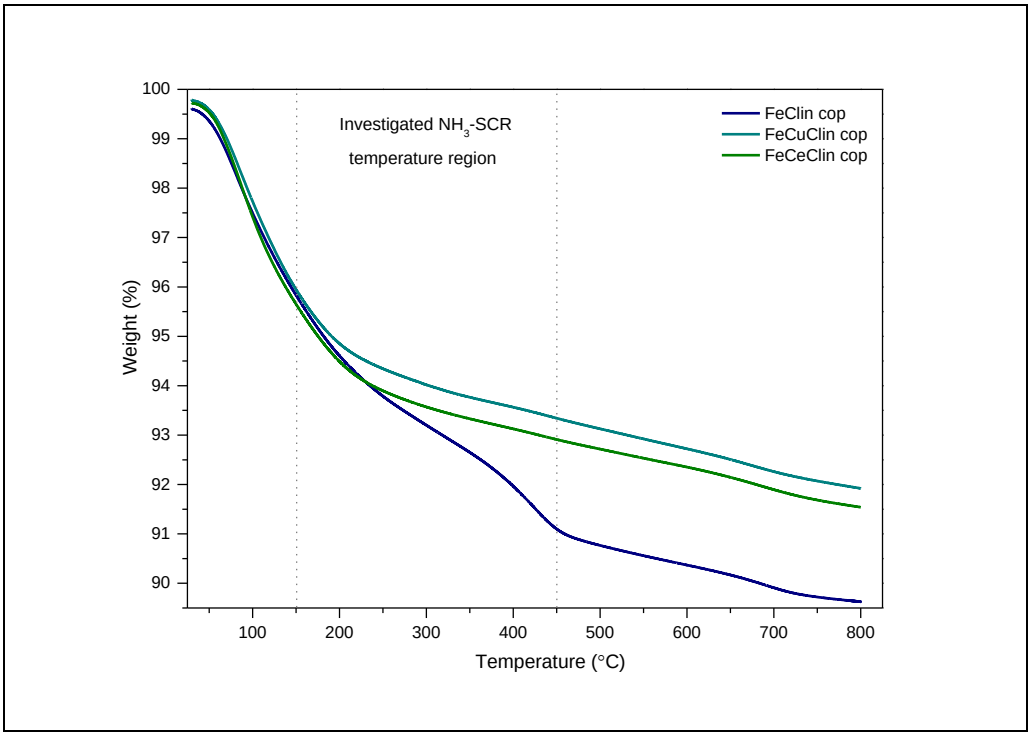

Figure 82. Results of TGA obtained for clinoptilolite-supported samples

In contrast to the catalysts supported on clinoptilolite, FeMCM22 ads and its derivatives exhibited very similar behavior at the increasing temperature. As presented in **Figure 83**, all of the weight losses of the catalysts were ascribed to the removal of the structural of physically adsorbed water [531]. Interestingly, introduction of Cu or Ce did not inhibit elimination of H_2O molecules, suggesting better dispersion of their species on MWW layers, comparing to the clinoptilolite-supported catalysts, which is in line with the results presented in SEM images of the materials.

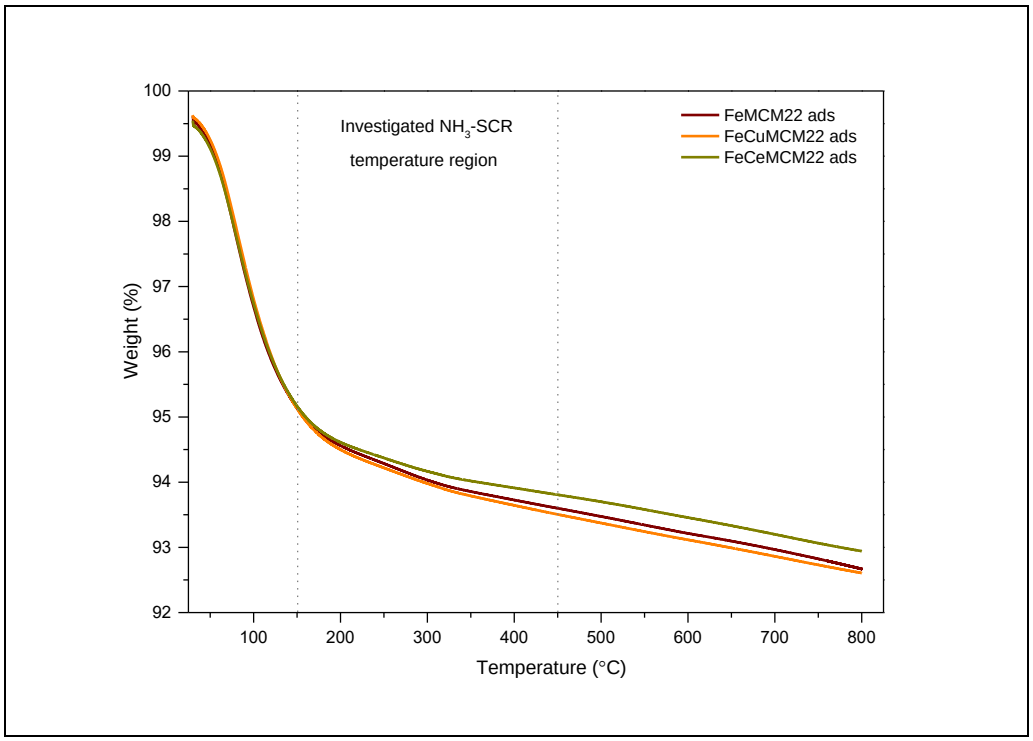

Figure 83. Results of TGA obtained for MCM-22-supported catalysts

Table 25. Weight loss of the analyzed catalysts within 30-800 °C

Sample code	Weight loss in the particular temperature range (%)			Total (%)
	30-200 °C	200-400 °C	400-800 °C	30-800 °C
FeClin cop	5.29	2.89	2.22	10.4
FeCuClin cop	5.25	1.43	1.41	8.09
FeCeClin cop	5.61	1.26	1.56	8.43
Sample code	**Weight loss in the particular temperature range (%)**			**Total (%)**
	30-175 °C	**175-800 °C**		**30-800 °C**
FeMCM22 ads	5.29	2.07		7.36
FeCuMCM22 ads	5.43	2.15		7.58
FeCeMCM22 ads	5.33	1.75		7.08

FT-IR spectroscopic studies of the characteristic chemical groups

FT-IR spectroscopy was applied in order to investigate if the introduction of Cu or Ce influenced on the chemical groups present in the materials. The comparative FT-IR spectra recorded for clinoptilolite- and MCM-22-supported catalysts are presented in **Figure 84** and **Figure 85**, respectively.

It can be noticed from **Figure 84**, that position of the peaks characteristic for the zeolitic framework vibrations were not changed after introduction of the promoters and the characteristic shape of the clinoptilolite spectrum was preserved. However, one of the peaks located at 1400 cm^{-1} was not detected in the spectra of FeCuClin cop and FeCeClin cop. Since the peak corresponds to Si-O stretching vibrations or Al-Me-OH bending vibrations, it can be concluded that the presence of the introduced metal oxides could cause some local interruptions in the framework of the zeolite.

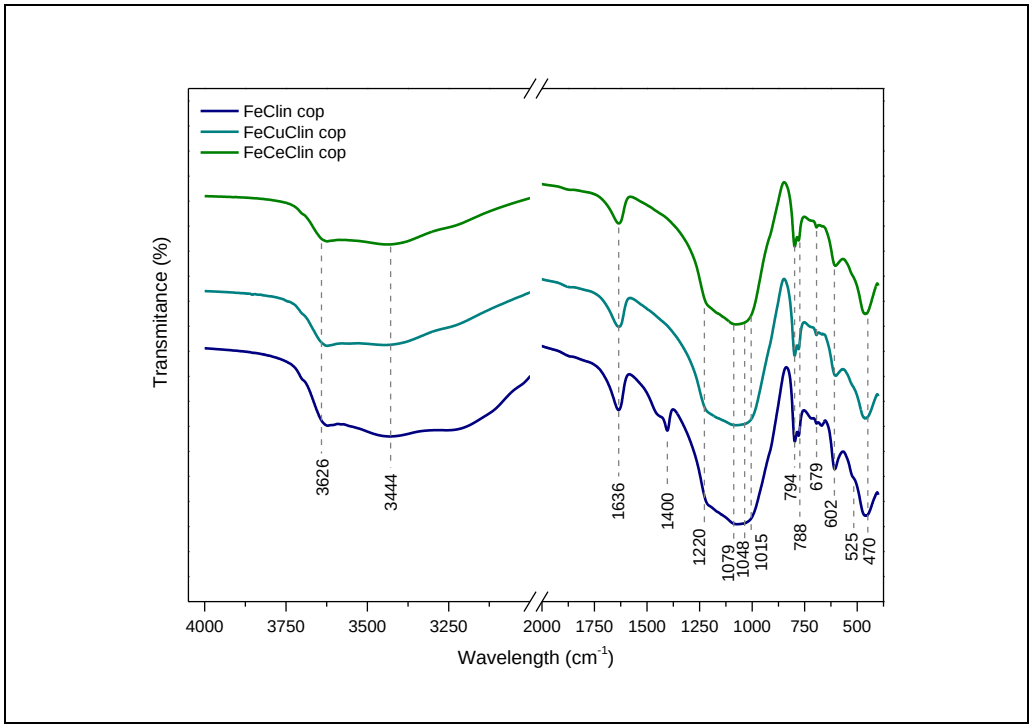

Figure 84. FT-IR spectra obtained for clinoptilolite-supported catalysts

As presented in **Figure 85**, the spectra obtained for FeMCM22 ads and FeCuMCM22 ads exhibited peaks which are similar with respect to their shape and position. Nevertheless, the form of the spectrum recorded for FeCeMCM22 ads in the wavelength region of 1250-1000 cm^{-1} was noticeably different, comparing to other materials. Additionally, the new peak, located at 1095 cm^{-1} appeared for this sample. Such result was reported in the literature [553] and is typical for MCM-22 modified with cerium. However, since the peaks at 595 and 545 cm^{-1} were preserved for both Cu- and Ce-promoted catalysts, it can be concluded that MWW structure of the zeolites was not affected by the modifications.

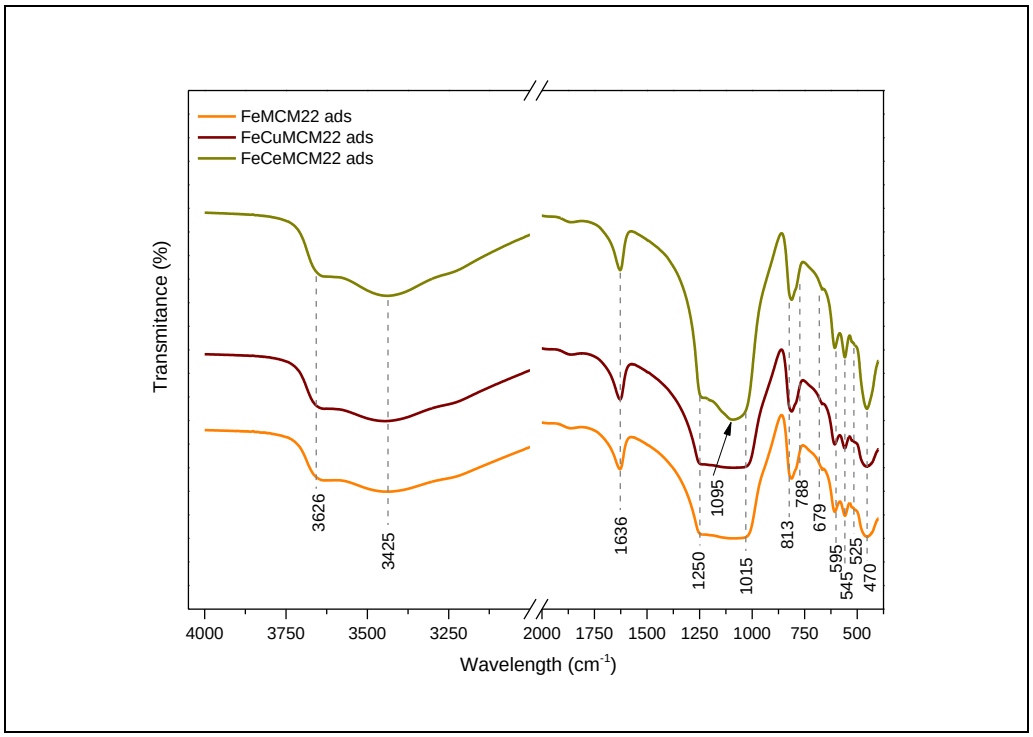

Figure 85. FT-IR spectra obtained for MCM-22-supported catalysts

Speciation of iron in the catalysts determined by XPS

The changes of the surface chemistry, which could possibly occur in the catalysts after promotion with Cu or Ce were investigated by the means of XPS spectroscopy. The measurements were conducted in the binding energy (BE) regions of Si 2p, Al 2p, O 1s, C 1s, and Fe 2p and the obtained results are presented in **Figures 86-90.** The detection limit of XPS instrument was ~ 0.1 at.%. Thus, the absence of the peaks in the binding energy regions characteristic for Cu 2p and Ce 3d suggests that the promoters were deposited in the inner structure of the zeolites. It can be observed from **Figure 86, Figure 87,** and **Figure 88** that introduction of the promoters did not change the characteristics of the spectra in the Si 2p, Al 2p, and C 1s regions. However, the spectra in the BE region of O 1s, depicted in **Figure 89,** changed after modification with Cu or Ce. The peak located at 532.6 eV, placed in the same position for all of the catalysts, was deconvoluted into three Gaussian curves. The first line, centered at 530.9 eV pointed out the existence of metal oxides (lattice oxygen, O_{α}), such as O-Fe and/or O-Si and/or O-Al and/or organic O=C type bonds in the materials. The intensity of this peak is higher for clinoptilolite-supported catalysts, thus the surface of the natural zeolite was more abundant in lattice oxygen than that of MCM-22. The second line, similar for all catalysts and centered at 533.0 eV, corresponds either to

defective oxygen in metal oxides (O-Fe, O-Si) or in organic species (O-C). Furthermore, the last line, found at 534.4 eV and similar for all of the samples, originated from -OH groups present as Al-OH, Si-OH, Fe-OH and/or H_2O, adsorbed during contact of the samples with atmospheric air [585].

Figure 90 shows fragments of the spectra corresponding to the binding energy of Fe $2p_{3/2}$. The first line, centered at 710.1 eV for all the catalysts, corresponds to the existence of Fe^{3+}. The lines observed within the binding energy range of 711-715 eV appeared due to the multiplet splitting phenomena. It can be observed that the position of the Fe $2p_{3/2}$ line was moderately shifted to lower BE values after promotion. According to Boroń et al. [555], higher BE values detected for Fe (III) reflect the presence of isolated metal cations. Furthermore, Gurgul and co-workers [556] postulated that lower binding energy peaks are given by extra-framework Fe_2O_3 species. Therefore, modification of the samples with Cu or Ce slightly changed distribution of iron in the materials, which is in line with the results of UV-vis-DRS experiments.

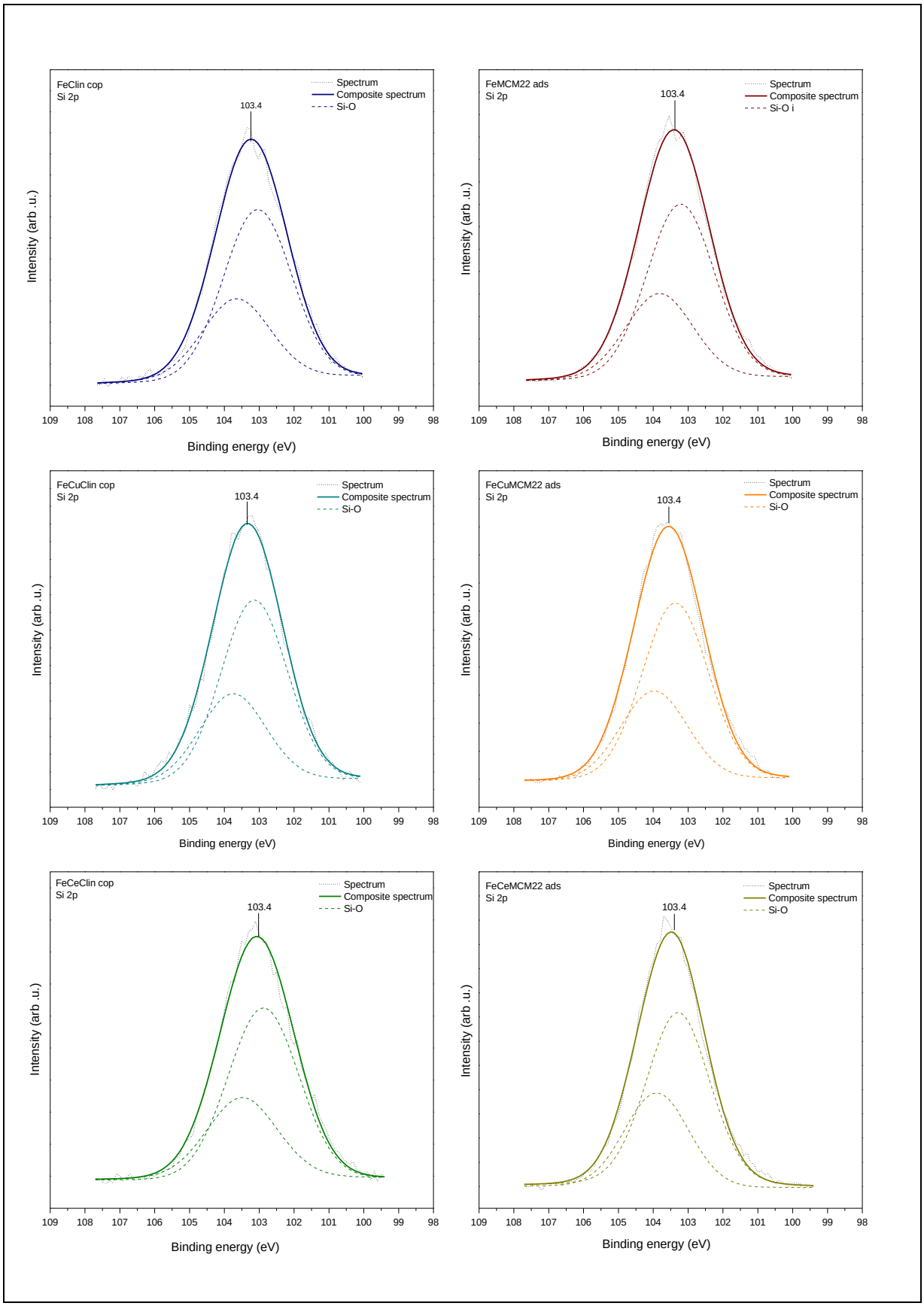

Figure 86. XPS spectra obtained for clinoptilolite- and MCM-22-supported catalysts in the BE region of Si 2p

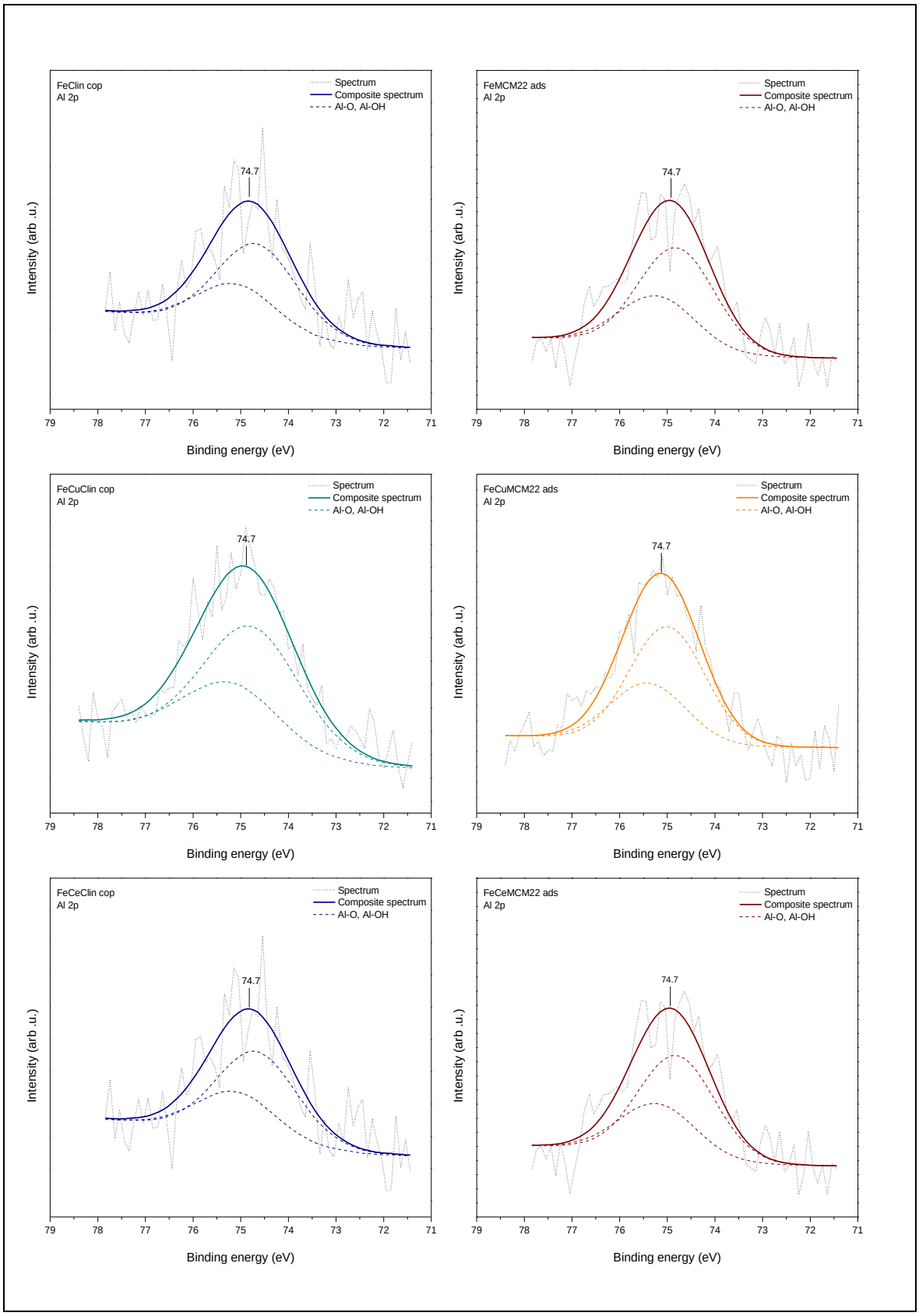

Figure 87. XPS spectra obtained for clinoptilolite- and MCM-22-supported catalysts in the BE region of Al 2p

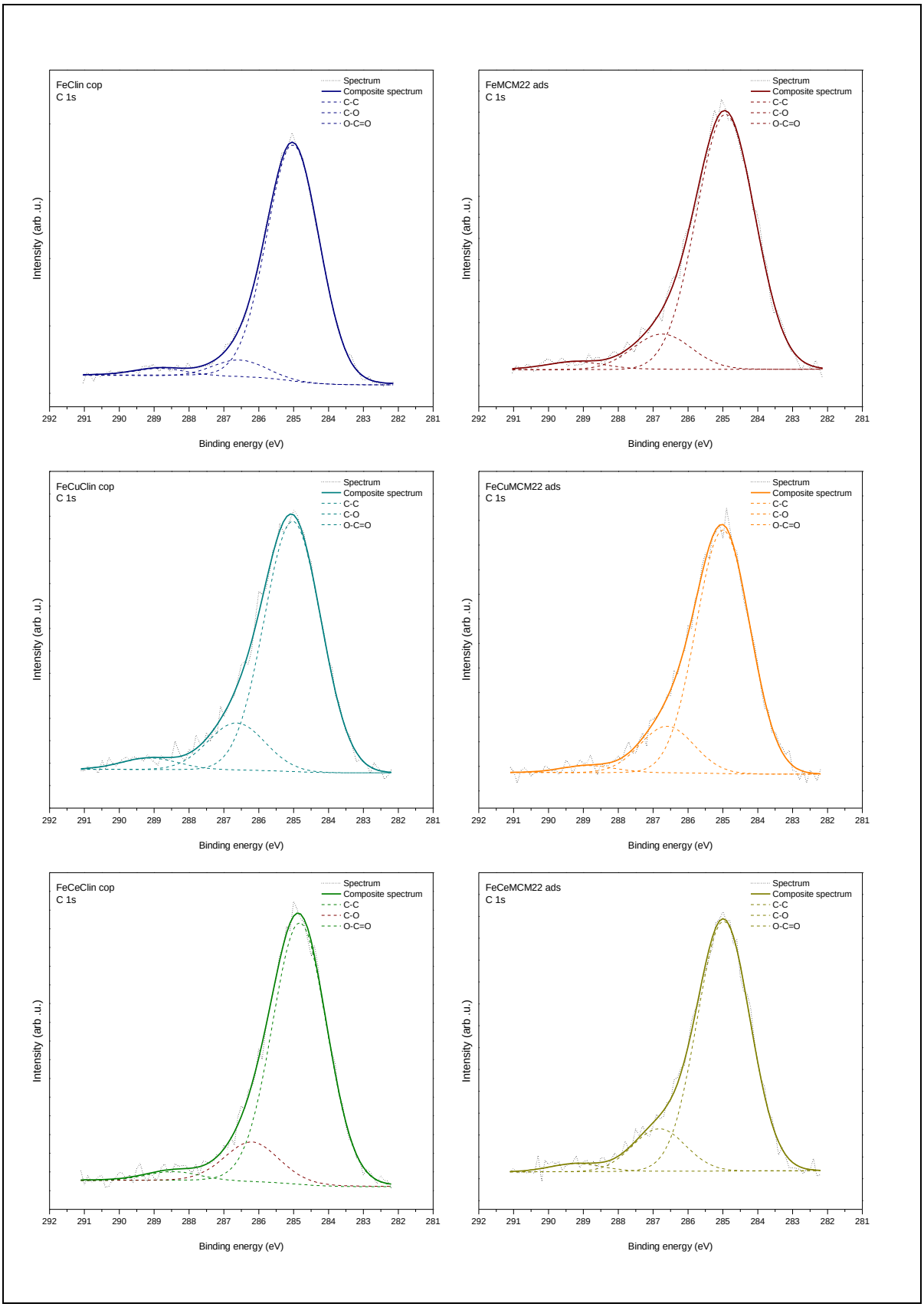

Figure 88. XPS spectra obtained for clinoptilolite- and MCM-22-supported catalysts in the BE region of C 1s

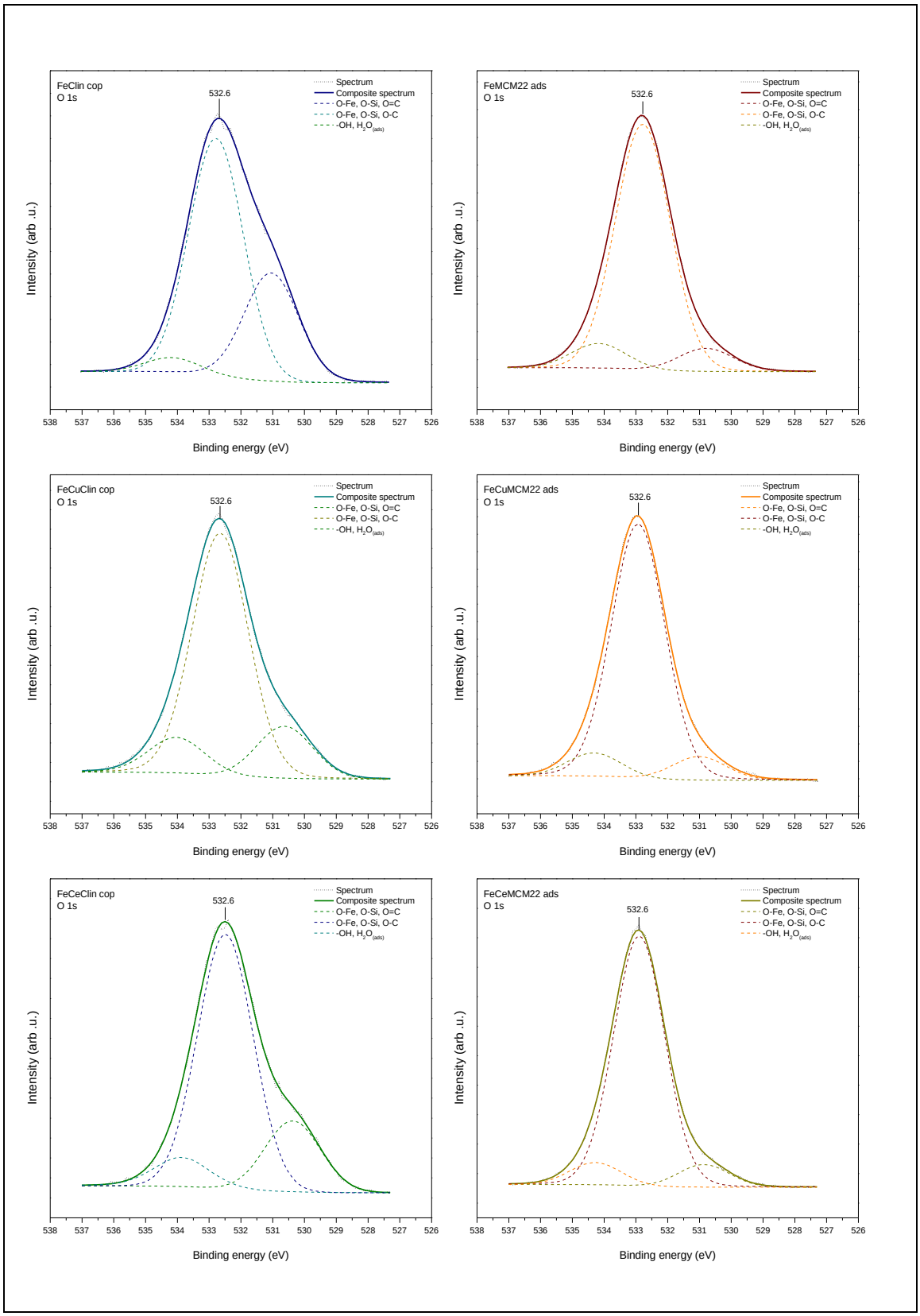

Figure 89. XPS spectra obtained for clinoptilolite- and MCM-22-supported catalysts in the BE region of O 1s

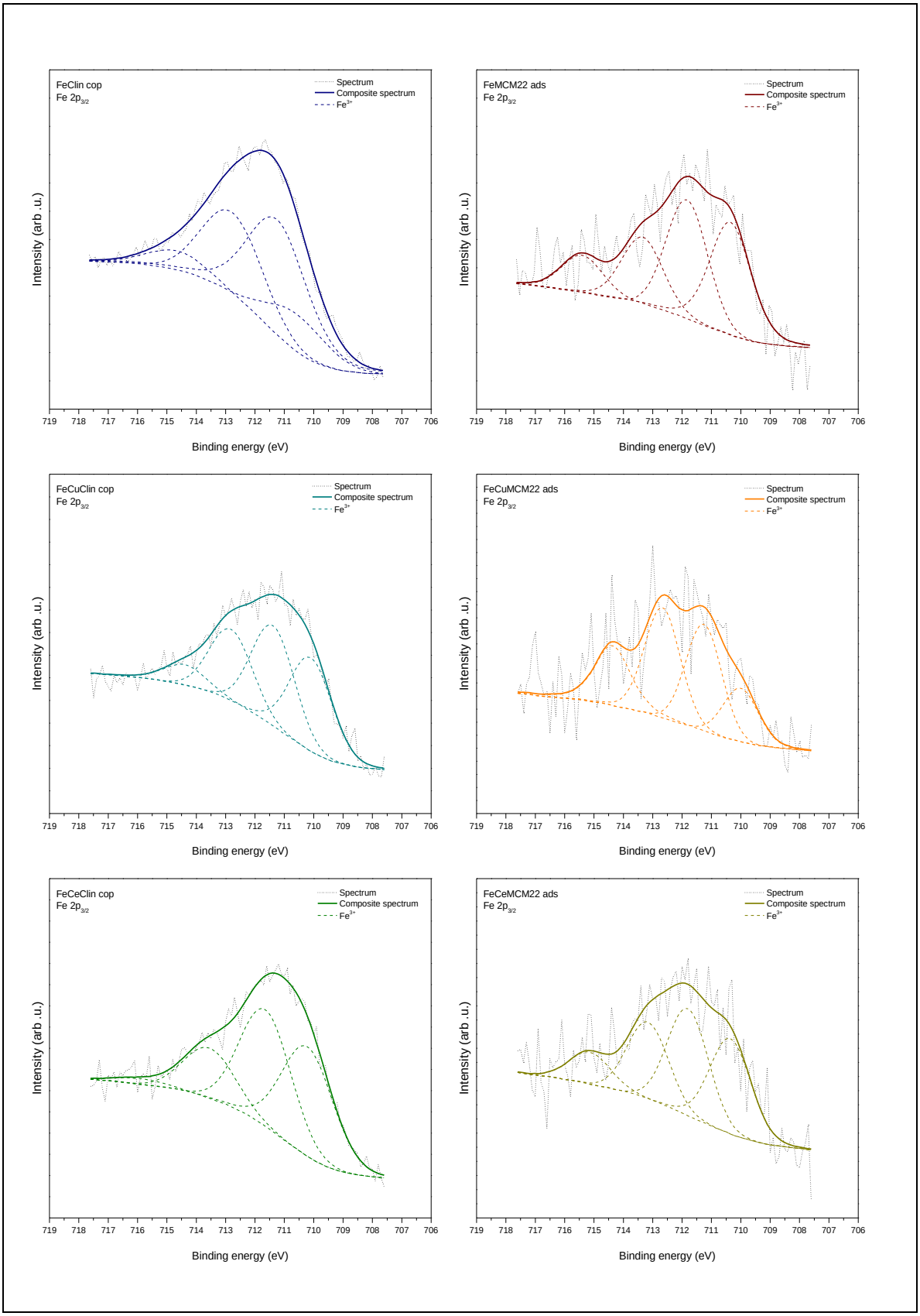

Figure 90. XPS spectra obtained for clinoptilolite- and MCM-22-supported catalysts in the BE region of Fe $2p_{3/2}$

The data presented in **Table 26** revealed that neither Cu, nor Ce was present on the surface of the catalysts. Therefore, the species of the promoters were incorporated into the inner structure of the zeolites, which is in line with the decreased surface and volume of micropores. Furthermore, surface composition of Cu- or Ce-promoted FeClin cop changed in terms of oxygen. One can notice that the samples were more abundant in the defective oxygen, while the concentration of the lattice oxygen decreased after promotion. The observed changes can be correlated with acidic character of the catalysts, which was affected by the introduction of copper or cerium. According to Osuga et al. [586], lattice oxygen in zeolites acts as Brönsted basic site in combination with Brönsted acid site. Therefore, since introduction of metal species affected the density of acid centers (see NH_3-TPD), concentration of lattice oxygen decreased as well. Additionally, such effect was stronger for FeCuClin cop, probably as the result of higher concentration of Cu comparing to Ce in FeCeClin cop. On the other hand, concentration of the lattice and defective oxygen remained almost unchanged after promotion of FeMCM22 ads, which can be correlated with similar distribution of the acid sites in MCM-22-supported samples. What is more, the surface concentration of Fe^{3+} species was lower for FeCuClin cop and FeCeClin cop in comparison to the non-promoted sample. One possible explanation is that iron species could migrate into the inner structure of clinoptilolite due to the modification with the promoters. Interestingly, such result was not observed for the catalysts supported on MCM-22 and the surface concentration of Fe remained on similar level regardless introduction of the promoters.

Table 26. Surface composition (in atomic %) determined by fitting XPS spectra of the catalysts

	Si 2p	**Al 2p**	**Fe $2p_{3/2}$**	**O 1s**			**C 1s**		
Binding energy (eV)	103.4	74.7	710.1	530.9	533.0	534.4	285.0	286.8	289.0
Chemical groups or oxidation state	Si^{4+}	Al^{3+}	Fe^{3+}	O-Fe O-Si O-Al O=C	O-Fe O-Si O-Al O-C	-OH H_2O_{ads}	C-C	C-O	C=O O-C=O
FeClin cop	25.0	1.7	0.8	15.5	32.9	2.1	1.4	16.3	4.3
FeCuClin cop	16.3	3.1	0.8	8.4	40.2	6.0	3.2	20.1	2.0
FeCeClin cop	19.2	3.1	0.7	10.7	38.3	4.8	0.0	20.7	2.5

FeMCM222 ads	15.2	2.1	0.5	4.3	45.5	4.5	1.4	25.8	0.8
FeCuMCM22 ads	14.2	2.7	0.4	4.4	46.5	4.1	1.8	25.3	0.7
FeCeMCM22 ads	14.7	2.5	0.5	4.1	46.7	4.1	0.0	26.9	0.7

Speciation of metals in the catalysts determined by UV-Vis-DRS

Information on the coordination environment of the promoters. as well as their influence on the speciation and distribution of iron sites in the catalysts were studied by UV-Vis-DRS. One should note that it is difficult to distinguish the individual contributions from the charge transfer of $Fe^{3+} \leftarrow O^{2-}$. $Cu^{2+} \leftarrow O^{2-}$. and $Ce^{3+} \leftarrow O^{2-}$, due to the mutual overlap of the transition regions. However. the shape of the UV-Vis-DR spectra have noticeably changed for both of the investigated Fe-catalysts after introduction of Cu or Ce. Therefore. the analysis clearly indicated that the nature of iron sites is different in comparison to the non-promoted catalysts.

Figure 91 compares UV-Vis-DR spectra recorded for FeClin cop catalysts. Both of the promoted samples exhibited strong absorption bands in the wavelength range of 200-650 nm, however, their intensity was lower in comparison to FeClin cop. In the case of FeCuClin cop, the main absorption bands appeared at around 250 nm and between 400 and 600 nm. The first, more intense band is assigned to the charge transfer from lattice oxygen O^{2-} to the isolated Cu^{2+} cations. Thereby, copper could be exchanged and incorporated into the extraframework positions in the form of isolated cations even in the impregnated Fe-clinoptilolite. The second, broader band, appearing between 300 and 600 nm corresponds to the presence of oligomeric Cu^{2+}-O^{2-}—Cu^{2+} chains. This wavelength region includes the charge transitions within Cu^{2+}−O^{2-}−Cu^{2+} (400-500 nm) and CuO particles in extraframework positions, in which electronic d-d transitions within a distorted octahedral structure take place (above 560 nm) [581]. What is interesting, introduction of Cu diminished the intensity of the absorption bands assigned to the isolated iron cations, $Fe^{3+} \leftarrow O^{2-}$ and the oligomeric clusters, such as $[HO{-}Fe{-}O{-}OH]^{2+}$. Thus, some of the isolated iron sites could be partially covered by the particles of the promoter. On the other hand, the intensity of the bands assigned to Fe_2O_3 increased, suggesting probable formation of iron oxide clusters resulting from the modification with Cu. Considering FeCeClin cop, introduction of cerium led to the appearance of characteristic absorption of UV light, even though the metal concentration was

relatively low. After promotion with Ce, the main absorption peak was shifted to the higher wavelength range, comparing to the non-promoted catalyst and showed two distinguishable bands at around 265 and 300 nm. Among them, the former one is related to the charge transfer transitions of $Ce^{3+} \leftarrow O^{2-}$, while the latter results from inter-band transitions, which raised due to the collective effects [590, 591]. Similarly to FeCuClin cop, the intensity of the band ascribed to Fe_2O_3 clusters increased, thus, even very low value of the promoter affected distribution of iron in the catalyst.

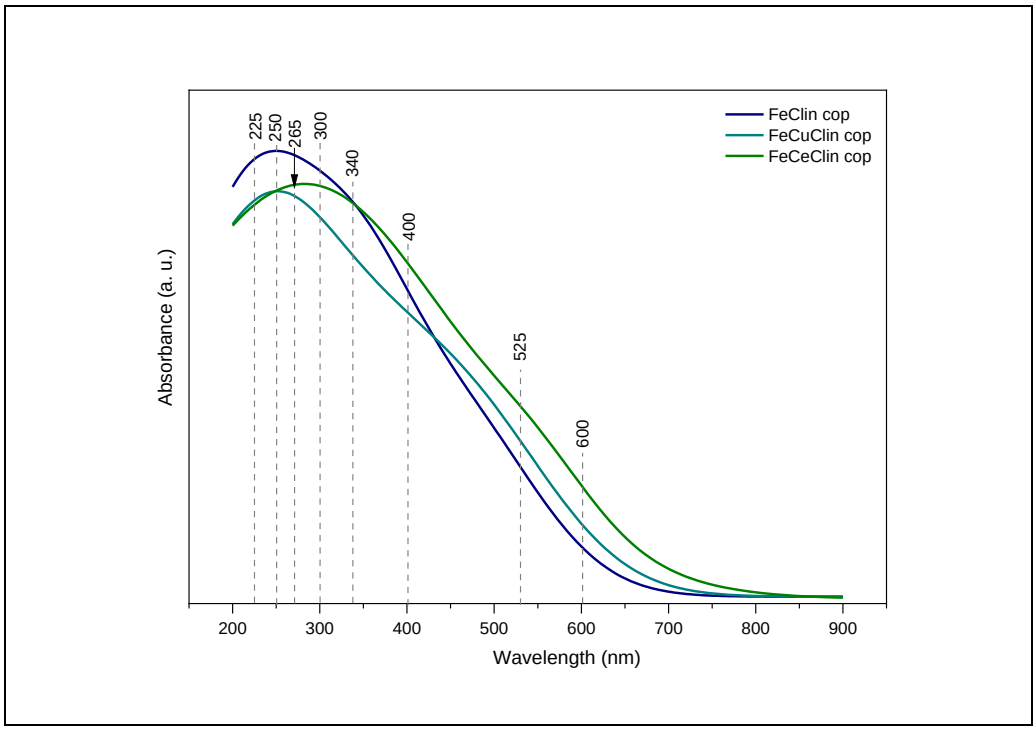

Figure 91. UV-Vis-DR spectra recorded for clinoptilolite-supported catalysts

As can be seen in **Figure 92**, the shape of UV-Vis-DR spectra for the MCM-22-supported catalysts changed as well after introduction of the promoters. The materials modified with Cu or Ce showed absorption bands in the wavelength range of 200-650 nm. However, for FeCuMCM22 ads the spectrum was more intense than that of FeMCM22 ads, while the opposite effect can be observed for FeCeMCM22 ads. Similarly to FeCuClin cop, introduction of copper resulted in the appearance of new absorption band in the spectrum of FeCuMCM22 ads in the wavelength range of 200-350 nm. It can be ascribed to the charge transfer from O^{2-} to well-dispersed Cu^{2+} cations. Furthermore. the intense band in the region of 400-600 nm points out the abundance of Cu_xO clusters. especially in the form of $[Cu{-}O{-}Cu]^{2+}$ species [359.583]. Additionally, comparing to FeCuClin cop, FeCuMCM22 ads showed

more intense band within 400-550 nm. One possible explanation is that the Cu_xO species were more aggregated on the surface of MWW layers than on the particles of clinoptilolite. In the case of FeCeMCM22 ads, introduction of the promoter resulted in the appearance of the new absorption peak at 265 nm, corresponding to the charge transfer from O^{2-} to Ce^{3+} [588]. Another band, located in the wavelength range of 460-650 nm is almost identical to that of FeMCM22 ads. Thus, on one hand, cerium could be located in the sample exclusively in the form of dispersed Ce^{3+} sites. Furthermore, the absorption bands assigned to CeO_2 could overlap with that of Fe_2O_3. Therefore, the distinguishment between these species in the sample using UV-Vis-DR spectroscopy is only approximate.

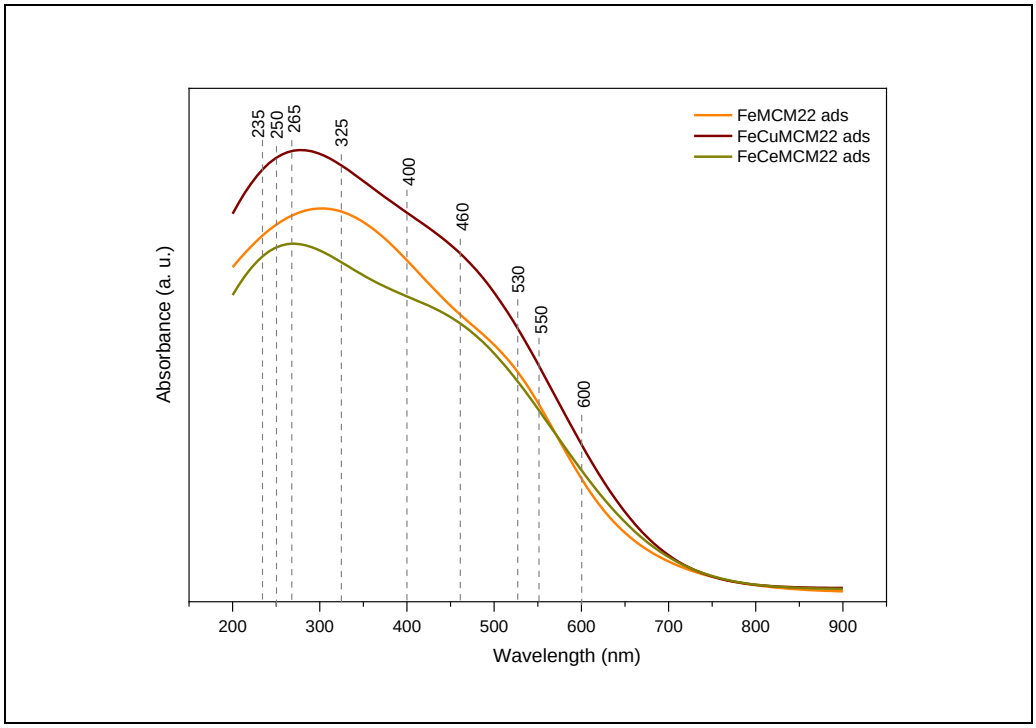

Figure 92. UV-Vis-DR spectra recorded for MCM-22-supported catalysts

2.2 Catalytic performance of copper- or cerium-promoted zeolites

NO conversion obtained for FeClin catalysts before and after promotion with Cu or Ce is presented in **Figure 93**. It can be observed that after introduction of copper, temperature window of the catalyst was shifted to lower region and T_{50} decreased for the sample to ca. 200 °C. In fact, textural parameters of the catalyst, such as the value of specific surface area or pore volume diminished after introduction of copper, which could potentially limit activity of the promoted catalyst. Nevertheless, as evidenced by H_2-TPR and UV-Vis studies, copper species in FeCuClin cop were present mainly in a

form of Cu^{2+} and Cu^{2+}-O^{2-}—Cu^{2+} oligomers. According to Pereda-Ayo and co-workers [589] low-temperature NO reduction over Cu-zeolites results from the abundance of oligomeric and more clustered copper species. Furthermore, Cu sites in ambient air are present in the hydrated state represented by $[Cu(OH)(H_2O)_5]^+$ and $[Cu(H_2O)_6]^{2+}$ [590]. Typically, the solvation effect of H_2O weakens the coordination between Cu ions and the zeolitic structure. However, increasing the temperature to ca. 250 °C results in the release of H_2O from copper species and formation of $[Cu(OH)]^+$-Al and Cu^{2+}-Al sites, in which Cu sites are solvated by NH_3 much stronger than by H_2O. According to the studies, [591–593] the generated Cu-NH_3 complexes are considered to be the active sites of low-temperature NH_3-SCR. What is more, basing on the outcomes of NH_3-TPD, the acidic character of Cu-promoted sample was noticeably enhanced. As a consequence, introduction of copper provided additional sites for NH_3 adsorption. As mentioned by Chen et al. [594], the binding enthalpy of these sites is lower comparing to that of Brönsted sites originating from the clinoptilolite framework. Thereby, adsorption of ammonia on the introduced copper sites can partially solve the problem of NH_3 inhibition effect, which is typical for Fe-zeolites in the low-temperature NH_3-SCR. Basing on the studies reported in the literature [595–597], Fe sites can interact competitively with NH_3 and NO below 300 °C. As postulated by Boubnov et al. [443] and Grossale et al. [598], the surface intermediates of NH_3-SCR generated on iron sites exhibit strong affinity to NH_3, which prevents them to react with gas-phase NO and complete the catalytic cycle. Thus, it is expected that introduction of copper as a promoter not only supplied the material with new catalytically active sites, but also reduced the inhibiting effect of NH_3 on Fe species. Importantly, the decreased NO conversion occurring above 400 °C is assigned to non-desired oxidation of NH_3, promoted by Cu in the high-temperature range [599,600]. Such effect was not observed for non-promoted catalyst, hence, oxidation of ammonia in the high-temperature range was caused exclusively by copper species. Given these points, it is expected that textural characterization was not the key factor, which determined NH_3-SCR activity of FeCuClin cop and the beneficial effect of copper on NO reduction can be linked with the multi-valence state of Cu^{2+}/Cu^+ couple, which provides new redox and acid sites of the catalyst and above all, mitigates the effect of NH_3 inhibition [590].

In contrast to Cu-promoted catalyst, introduction of Ce increased T_{50} to 270 °C and affected the overall catalytic performance. In fact, the conversion of NO gradually increased for the Ce-promoted

sample and reached its maximum of 95% at 350 °C. However, the catalytic activity in the high-temperature region was the lowest among clinoptilolite-supported catalysts. In general, there are various reasons for such catalytic performance of FeCeClin cop. On the one hand, as confirmed by H_2-TPR studies, introduction of Ce slightly improved reducibility of the catalyst, thus, theoretically it should also shift the temperature window to lower value. On the other hand, UV-Vis experiments indicated that most likely, introduction of ceria caused migration of isolated Fe^{3+} cations (active in low-temperature NH_3-SCR) and formation of more aggregated form of the active phase. It was found by Shi et al. [601] that the presence of Fe_xO_y clusters and Fe_2O_3 particles significantly affects Brönsted acidity, which is required for acid-catalyzed decomposition of the intermediate NH_4NO_2 species. The theory of the authors is supported by NH_3-TPD studies conducted over the clinoptilolite-supported catalysts, since indeed, FeCeClin cop exhibited relatively low acidity. Additionally, as confirmed by N_2 sorption studies, S_{BET} and the volume of pores were reduced after introduction of Ce into FeClin cop. This result was caused by the probable formation of Fe_2O_3 and CeO_2 aggregates and their deposition near the pore openings. Basing on kinetic and mechanistic study of NH_3-SCR over H-zeolites, Eng and Bartholomew [602] concluded that the fastest rates of the reaction are reached near the pore entrances. Thereby, the deposition of catalytically passive, and pore-blocking particles not only limited the diffusion of the gas mixture, but also hindered successful adsorption of the reacting molecules on the active sites. What is more, the drastic drop of catalytic activity above 350 °C can be explained by the side-reactions taking place on the catalyst surface, most likely oxidation of ammonia. Madia and co-workers [70] mentioned five possible reactions of NH_3 oxidation during NH_3-SCR **(Equations 142-146):**

$$4\ NH_3 + 3\ O_2 \rightarrow 2\ N_2 + 6\ H_2O \quad \textbf{(142)}$$

$$4\ NH_3 + 4\ O_2 \rightarrow 2\ N_2O + 6\ H_2O \quad \textbf{(143)}$$

$$4\ NH_3 + 5\ O_2 \rightarrow 4\ NO + 6\ H_2O \quad \textbf{(144)}$$

$$4\ NH_3 + 7\ O_2 \rightarrow 2\ NO_2 + 6\ H_2O \quad \textbf{(145)}$$

$$4\ NH_3 + 3\ O_2 + 4\ NO \rightarrow 4\ N_2O + 6\ H_2O \quad \textbf{(146)}$$

One can notice that the degree of ammonia oxidation increases in a systematic manner, linearly with the increasing amount of O_2 consumed for the process. Il'Chenko and Golodets [603] found that in the case of metal oxides, selectivity of ammonia oxidation to the specific products is correlated with the surface

oxygen bond energy. In general, low surface oxygen bond energy favours deep oxidation of NH_3 and the process follows reactions **(144)** and **(145),** producing NO or NO_2, respectively. According to the general agreement, the outstanding catalytic performance of Ce-catalysts in NH_3-SCR results from the presence of oxygen vacancies, which enhance NH_3 and NO adsorption capacity and accelerate acidic and redox cycle of the reaction [604]. Nevertheless, oxygen vacancies also promote the adsorption of O_2 from the gas-phase in order to complete the redox cycle. As postulated by Il'Chenko and Golodets [603], the strength of NH_3 oxidation during NH_3-SCR increases linearly with the increase in the surface coverage with oxygen and the oxidation is even stronger in the high-temperature region of the reaction. Therefore, it is expected that in the case of FeCeClin cop, cerium did not behave as a chemical promoter of the catalytic reaction. Alternatively, the decreased conversion of NO after introduction of Ce could be a consequence of limited access of the reacting molecules into the active sites, which were blocked by the metal oxide clusters. A somewhat remarkable was the fact that the results of TEM studies indicated stronger effect of aggregation for FeCuClin cop comparing to FeCeClin cop. Thereby, not only speciation and dispersion, but also synergistic effects between the components of the active phase and the promoter played a crucial role in the enhancement of NO reduction over bimetallic catalysts supported on clinoptilolite.

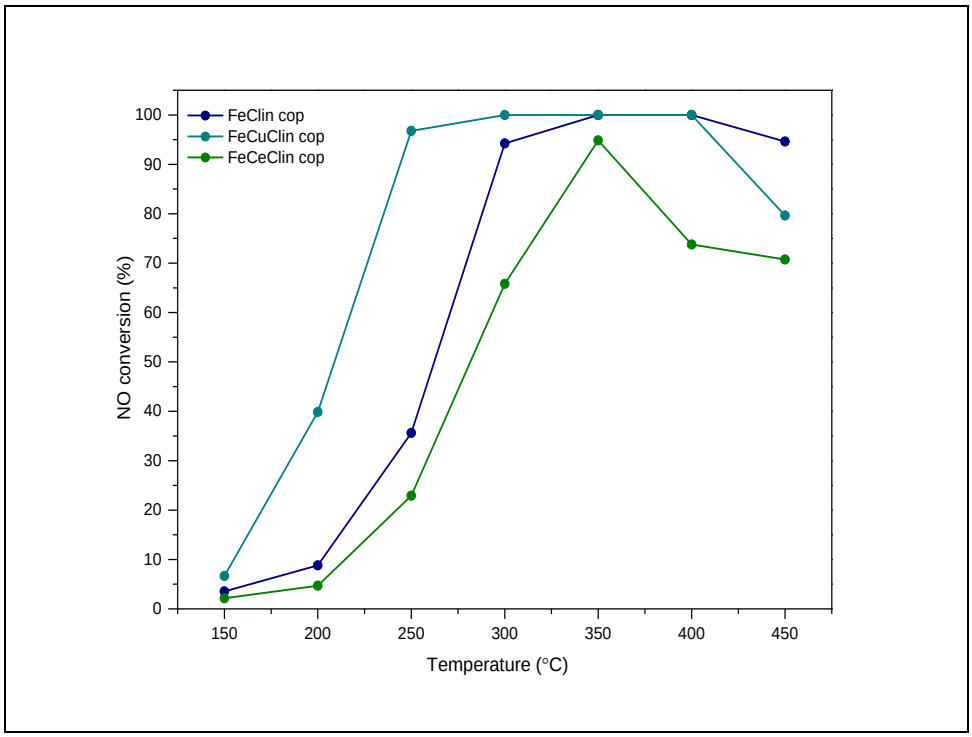

Figure 93. NO conversion obtained for clinoptilolite-supported catalysts

Concentration of N_2O emitted during the catalytic reaction over the promoted clinoptilolite-supported catalysts is presented in **Figure 94.** One can notice that there was a significant difference in the influence of Cu and Ce on the generation of nitrous oxide. Considering FeCuClin cop, the emission of N_2O decreased comparing to the non-promoted catalyst. In general, it was maintained on similar level within 250-450 °C and did not exceed 20 ppm, which is in line with the results reported by Shin et al. [605] for zeolite-supported catalyst with Fe and Cu. Additionally, the authors suggested that lower yield of N_2O for the catalyst containing copper was related to the presence of NO_2 generated in the mid-temperature region of the reaction (200-400 °C). According to the general agreement, formation and thermal decomposition of the intermediate nitrate species during NH_3-SCR is one of the main reasons of N_2O generation [563,564]. Typically, formation of ammonium nitrates is followed by reactions described by **Equations (147-148):**

$$2\ NO_2 + H_2O \leftrightarrow HNO_3 + HONO \quad \textbf{(147)}$$

$$HNO_3 + NH_3 \leftrightarrow NH_4NO_3 \quad \textbf{(148)}$$

Basing on temperature programmed desorption of NO_2 from Fe- or Cu-zeolites, it was found that the nitrates formed by disproportionation of NO_2 were more stable for copper active sites [606]. On the one site, such phenomenon mitigates formation of N_2O originating from NH_4NO_3 in the case of Fe-catalysts. Nevertheless, up to 350 °C the gas-phase NO_2 acts as an oxidant stronger than O_2 and can easily oxidize NH_3 to nitrous oxide, according to **Equations (149-151)** [605]:

$$6\ NH_3 + 8\ NO_2 \rightarrow 7\ N_2O + 9\ H_2O \quad \textbf{(149)}$$

$$4\ NH_3 + 4\ NO_2 + O_2 \rightarrow 4\ N_2O + 6\ H_2O \quad \textbf{(150)}$$

$$2\ NH_3 + 2\ NO_2 \rightarrow N_2 + N_2O + 3\ H_2O \quad \textbf{(151)}$$

Therefore, it is expected that some part of NO_2 produced during the catalytic reaction was strongly bonded to copper species, which limited its presence in the gas phase. Thus, undesired oxidation of NH_3 to nitrous oxide by NO_2 was reduced.

In contrast, to Cu-promoted sample, concentration of nitrous oxide for FeCeClin cop was determined by the temperature region of the reaction. It can be observed that the emission of N_2O exhibited gradual increase between 150 and 350 °C, simultaneously exceeding that of FeClin cop, while above 350 °C, concentration of N_2O was slightly reduced. The production of nitrous oxide up to 350 °C

can be ascribed to the thermal decomposition of NH_4NO_3. The expected source of N_2O above this value is oxidation of ammonia, however, one should note that it can proceed according to different reactions, depending on the temperature. As depicted in **Figure 93,** conversion of NO for FeCeClin cop considerably decreased above 350 °C and between 400 and 450 °C it was maintained on similar level. Therefore, oxidation of ammonia was most likely followed by the **reactions (150) and (151)** within 350-400 °C and reaction **(146)** above this region. Simultaneous increase of nitrous oxide concentration and reduction of the catalytic activity suggests that ammonia is oxidized to both N_2O and NO. As a result, generation of by-products and non-selective reactions of the reducing agent significantly decreased conversion of NO over FeCeClin cop. Moreover, since the catalytic activity of the material between 400 and 450 °C was stable, it can be expected that the produced NO was consumed for the production of N_2O in the high temperature range, according to the reaction **(146).** Besides, the highest concentration of N_2O within 200-400 °C might result from the presence of aggregated metallic species, which are considered as the limiting factor for selectivity of the heterogeneous catalysts [607]. On the other hand, as postulated by Delahay et al. [566], the decreased concentration of N_2O within 400-450 °C can be explained by the fact that N_2O can be reduced by NH_3 to nitrogen and water vapor, according to **Equation (152):**

$$2\ NH_3 + 3\ N_2O \rightarrow 4\ N_2 + 3\ H_2O \qquad \textbf{(152)}$$

The occurrence of reaction **(152)** is also confirmed by the decreased NO conversion resulting from the consumption of ammonia. Another possible explanation of the lower N_2O production in the high-temperature region was proposed by Rutkowska et al. [499], who found that N_2O can be decomposed by oligomeric iron species.

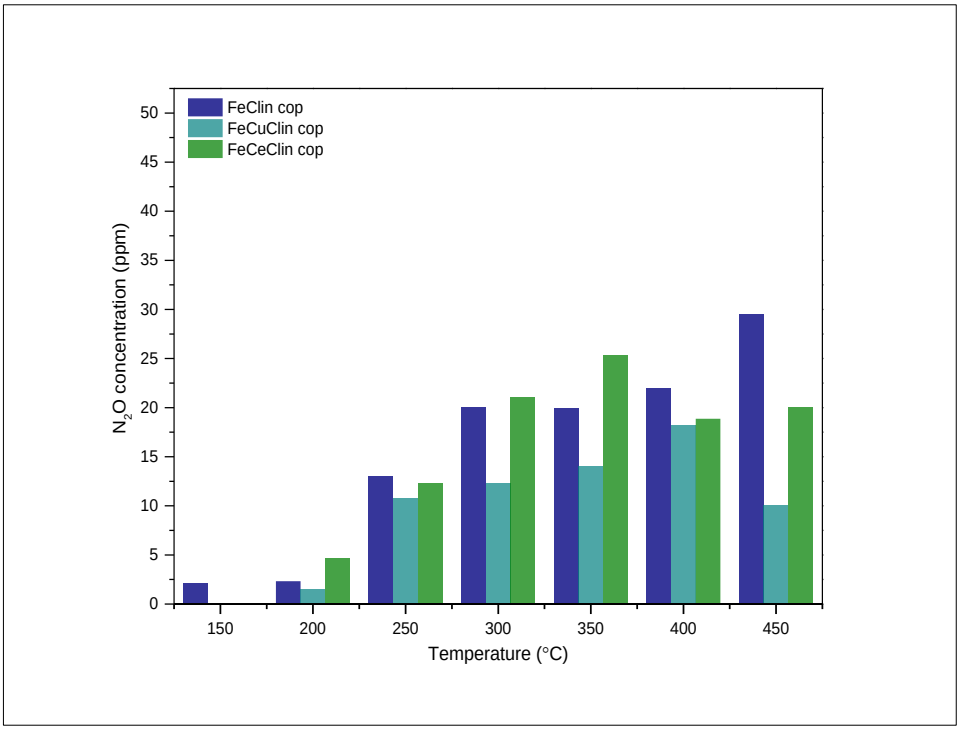

Figure 94. N_2O concentration in the flue gas during the catalytic reaction performed over clinoptilolite-supported catalysts

NO conversion obtained for FeMCM22 ads before and after promotion with Cu or Ce is presented in **Figure 95.** It can be observed that after introduction of copper, the catalytic behavior of the sample was almost identical to that of FeMCM22 ads. Surprisingly, the catalytic window was not shifted to lower values, as it typically occurs for Cu-promoted zeolites. In fact, according to the results of NH_3-TPD and H_2-TPR, FeCuMCM22 ads shows moderately higher acidity and improved reducibility, due to the presence of copper species. Additionally, according to TEM micrographs and UV-vis studies, Cu in the material was present mainly in a form of aggregated particles of CuO. According to the general agreement, CuO is responsible for low-temperature NH_3-SCR activity, while isolated Cu^{2+} cations promote high-temperature NO conversion [589]. Therefore, CuO present in FeCuMCM22 were expected to improve reduction of nitrogen oxide, at least within 150-300 °C. Nevertheless, as proved by N_2 sorption studies, introduction of copper significantly affected textural parameters of the catalyst. Thereby, CuO deposited near the pore openings blocked the access of the reagents to other active centers of the catalyst. As a consequence, the catalytic activity was not changed, since introduction of copper resulted in the consumption of other active sites of FeCuMCM22 ads. Last, but not least, similarly to

FeCuClin cop, co-existence of Fe and Cu in MCM22-supported catalyst did not improve high-temperature activity and susceptibility of the catalyst for ammonia oxidation.

On the other side, the effect of the promotion with Ce was very similar to that of FeCeClin cop. It can be observed that within 150-250 °C NO conversion obtained for the sample was almost equal to that of the non-promoted catalyst. Furthermore, above this region, it started to gradually decrease and was the lowest among the investigated MCM-22-supported samples. Identically to FeCeClin cop, NO reduction for FeCeMCM22 ads was maintained at similar level between 400 and 450 °C. In the main, the explanation of this phenomenon is similar to that for FeCeClin cop. First of all, the results of NH_3-TPD experiments indicated that acidity of the material was considerably lowered after introduction of cerium. Moreover, bulk particles of metal oxides detected in TEM micrographs and confirmed by UV-Vis were the main reason of the decreased values of textural parameters, evidenced by N_2 sorption studies. Besides, it is expected that as in the case of FeCeClin cop, introduction of Ce intro FeMCM22 ads resulted in the migration of isolated iron cations and formation of the species of higher nuclearity. Additionally, the presence of oxygen vacancies, promoted by Ce, enhanced O_2 adsorption capacity of the catalyst, resulting in the non-desired oxidation of ammonia and secondary production of NO in the high-temperature region [603]. Altogether, it is expected that the decreased activity of the material is a consequence of the changed speciation of the active phase, which inhibited diffusion and adsorption of the reacting molecules.

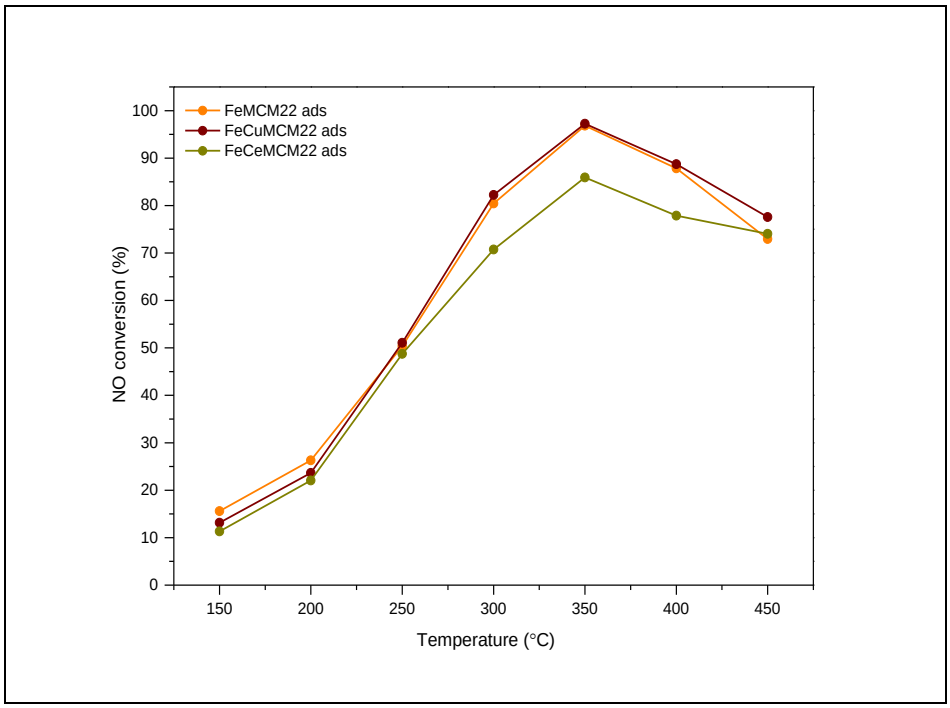

Figure 95. NO conversion obtained for MCM-22-supported catalysts

As presented in **Figure 96**, similarly to clinoptilolite-supported catalysts, concentration of N_2O for the samples supported on MCM-22 was lower than 35 ppm. It was observed that introduction of Cu or Ce increased production of nitrous oxide during the reaction, wherein in the case of FeCuMCM22 ads such effect was more clear. The emission of N_2O up to 350 °C can be linked with thermal decomposition of NH_4NO_3 produced on the catalyst surface [563,564]. Additionally, in the case of both Cu- and Ce-modified catalysts, the increased concentration of N_2O could result from the aggregation of metal oxide particles, which promote its formation [608]. Interestingly, in contrast to FeCuClin cop, the presence of Cu accelerated formation of the by-product during the reaction over FeCuMCM22 ads. According to the studies of Pereda-Ayo et al. [589], the abundance of CuO clusters not only enhances low-temperature activity of Cu-promoted zeolites, but also moves selectivity of the reaction not only toward N_2O, but also toward NO_2. Therefore, the presence of strongly oxidizing NO_2, desorbed from both Fe and Cu active sites was expected to accelerate oxidation of ammonia to nitrous oxide [605]. What is more, lower concentration of nitrous oxide in the case of FeCeMCM22 ads could originate from oxidation of NH_3 to NO, instead of N_2O, which is evidenced by the decreased activity of the catalyst within 350-450 °C. In addition, the production of nitrous oxide started to gradually drop in the high-temperature region. The observed decrease could be correlated with the possible decomposition of N_2O

on the iron species of higher nuclearity [499]. Since it was evidenced that the presence of Ce promoted clustering of the active phase, the amount of N_2O emitted during the reaction was lower for FeCeMCM22 ads comparing to FeCuMCM22 ads.

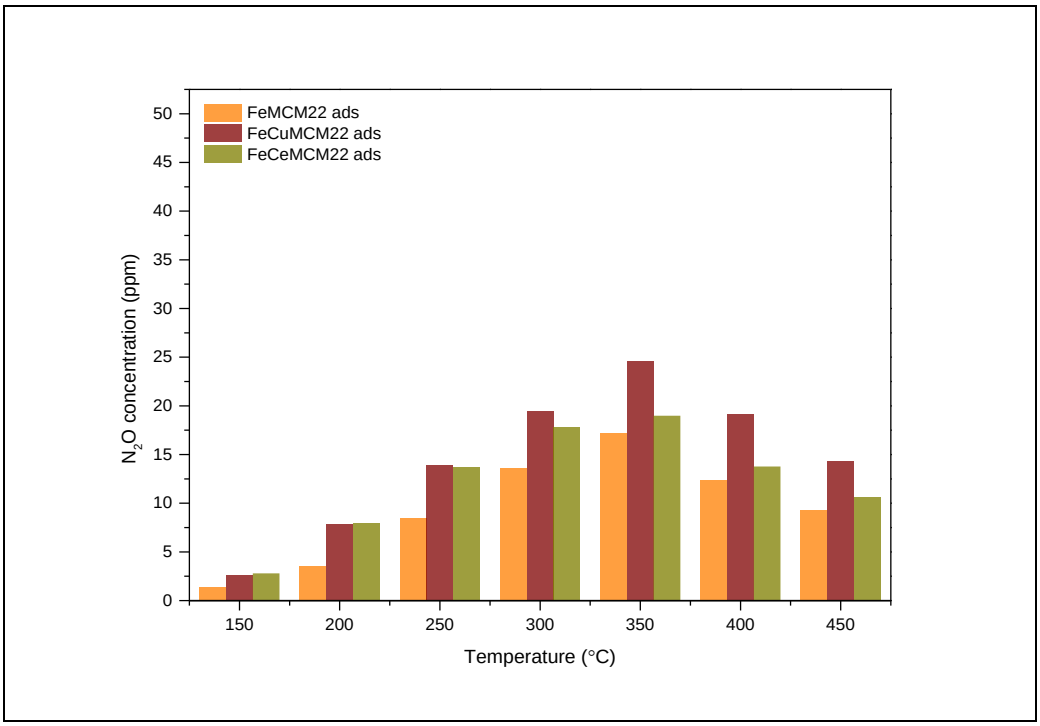

Figure 96. N_2O concentration in the flue gas during the catalytic reaction performed over MCM-22-supported catalysts

2.3 Conclusions on the copper or cerium promotion

Taken together, the investigations described in this chapter aimed to evaluate catalytic behavior of copper- or cerium-promoted FeClin cop and FeMCM22 ads and correlate it with their physicochemical characterization. In general, it was observed that introduction of the promoters influenced differently on the catalytic performance of clinoptilolite- and MCM-22-supported catalysts. The presence of copper shifted the temperature window of FeCuClin cop to lower region, however resulted in non-desired oxidation of NH_3. In contrast, FeCeClin cop exhibited lower activity than FeClin cop in the entire temperature range. In contrast, activity of the catalyst supported on MCM-22 remained almost unchanged after introduction of Cu and the only evidence of the presence of copper was higher concentration of N_2O in the gas exiting the reactor, comparing to FeMCM22 ads. Furthermore, FeCeMCM22 ads showed NO conversion identical to FeMCM22 ads up to 250 °C and above this value

its activity noticeably decreased. Thereby, the reported results of physicochemical characterization and catalytic performance indicated that:

1. The influence of copper on the catalytic behavior of the investigated Fe-zeolites was strongly determined by the type of framework. In fact, introduction of Cu affected textural parameters of both materials, however, its presence still promoted low-temperature activity of FeCuClin cop, which was not observed for FeCuMCM22 ads. Since both acidity and reducibility of Cu-promoted samples were enhanced, it is expected that in contrast to FeCuClin cop, the crucial factor for satisfactory NO conversion of MCM-22-supported catalyst was high value of specific surface area and well-developed pore texture.

2. Higher activity of clinoptilolite-supported catalyst after introduction of copper resulted from the introduction of new sites, which enhanced ammonia adsorption capacity and limited NH_3 inhibition effect, characteristic for Fe-catalysts of NH_3-SCR. In contrast, the unchanged NO conversion of MCM-22-supported catalyst after promotion with Cu was mainly caused by the presence of aggregated copper species, which not only blocked the pores of the zeolite, but also were more active in NH_3 oxidation than in NO reduction.

3. Introduction of cerium decreased catalytic activity of the catalysts, regardless the type of the support. The inhibiting effect was mainly caused by aggregation of the active phase after deposition of Ce and formation of Fe_2O_3 particles, which set diffusion limits and blocked acid sites of the materials required to complete the catalytic cycle. What is more, oxygen vacancies present in CeO_2 increased adsorption of O_2 on the surface and consumption of the reducing agent for side reactions, such as oxidation to NO or NO_2.

4. The opposite impact of the introduction of Cu on the emission of N_2O during the catalytic reaction over FeCuClin cop and FeCuMCM22 ads was caused by different behavior of copper species in heulandite and MWW framework. Lower concentration of N_2O for FeCuClin cop resulted from strong affinity of Cu sites to NO_2, which limited oxidation of NH_3 to N_2O during the reaction. In contrast, Cu clusters introduced into MWW framework showed higher activity toward oxidation of NH_3 than toward NO reduction. Since textural parameters of both samples were affected after introduction of Cu, it is

expected that heulandite-type framework is less sensitive for deformations caused by the deposition of metal oxide species, comparing to MWW-type framework.

5. Introduction of Ce intro the catalysts had very similar influence on the emission of N_2O, regardless the type of the zeolitic framework. Almost identical concentration of nitrous oxide for Ce-containing and Ce-free catalysts below 250-300 °C suggested that the main source of N_2O was thermal decomposition of NH_4NO_3. Furthermore, the gradual decrease of N_2O production, linear with the increasing temperature, resulted from the production of oligonuclear iron species after introduction of Ce and possible catalytic decomposition of nitrous oxide.

3. Influence of sulfur dioxide on the catalytic performance

In the practical applications, the NH_3-SCR catalyst is under the risk of being deactivated by chemical compounds present in the exhaust gas. One of the most harmful are sulfur oxides (SO_x), which can interfere with the catalyst surface even at very low concentration. Considering the commercial vanadium-based catalyst, the poisoning effect is the most dominant in low-temperature range and results from the oxidation of SO_2 to SO_3 [129]. Interactions between SO_3, ammonia, and water vapor yield ammonium sulfates and bisulfates, which as sticky and corrosive species, cause pore clogging, block active sites of the catalyst, and gradually decrease activity and selectivity [74]. The accumulation of ammonium sulfates requires periodic regeneration of the catalytic system, however, the appropriate regeneration conditions are often drastic for the active sites. As a consequence, the overall quality of the catalyst is affected. Therefore, in order to avoid poisoning with SO_x, it is important to design a catalyst with the highest possible mechanical and chemical resistance.

Several studies have suggested modified zeolites as the materials exhibiting moderately good activity, even in the presence of SO_x [609,610]. For instance, Auvray and co-workers [609] investigated catalytic behavior of Cu-BEA and Cu-SSZ-13 in NH_3-SCR and found that the inhibiting impact of SO_2 was strongly correlated with the pore size. The obtained results were in line with those obtained by Hammershøi et al. [610], who proved that the zeolitic framework is the factor determining the SO_2 resistance. Furthermore, according to Cheng et al. [467] Fe-zeolites show higher tolerance to SO_2 comparing to Cu-zeolites, while Zhang et al. [611] and Xie et al. [612] observed that that promotion of Cu-zeolite with iron decreases the amount of ammonium sulfates on the catalysts surface and protects Cu species from the formation of metal sulfates and irreversible deactivation.

According to the above-mentioned, the great majority of the studies on SO_x-poisoning of zeolite-supported SCR catalysts is related to Cu-zeolites, rather than Fe-zeolites. Additionally, the type of the framework seems to be one of the crucial factors, which determines catalytic activity of SO_x-poisoned metal-zeolites in NH_3-SCR. Hence, this chapter will go on to investigate the behavior of the representative samples of clinoptilolite- and MCM-22-supported catalysts after poisoning with SO_2. The samples subjected to the investigations were selected basing on their best catalytic performance in NH_3-

SCR conducted using model gas mixture. The conditions of poisoning and catalytic tests over the poisoned samples are described in detail in **subsection 4.2** of **Chapter III** of the thesis. Furthermore, the materials were tested using gas mixture containing various concentration of SO_2. The catalytic studies were carried out at 350 °C, which was the temperature of the highest NO conversion obtained for the analyzed samples.

3.1 Catalytic performance of the catalysts after poisoning with SO_2

The comparison of the catalytic activity of fresh and SO_2-poisoned FeCuClin cop and FeCuMCM22 ads are presented in **Figure 97** and **Figure 98**, respectively. It can be observed that up to 300 °C, the difference between the catalytic activity of the fresh and poisoned sample is moderate for both catalysts. NO conversion after poisoning with SO_2 was more affected in the case of FeCuMCM22 ads and introduction of the sulfate species into the sample slightly increased activation energy to initiate the catalytic process. The reduced activity of SO_2-poisoned catalysts in the low-temperature range of NH_3-SCR is mainly ascribed to the competitive adsorption of SO_2 against NO and ammonia and formation of pore- and active sites-blocking deposits of ammonium bisulfates [609]. Hence, the reaction rate was limited as the consequence of lower specific surface area, pore volume, and pore size. Besides, one should note that ammonium sulfates are thermally decomposed at around 280 °C, thus, theoretically, their presence limited only low-temperature activity [613]. Basing on the physicochemical characterization of FeCuClin cop and FeCuMCM22 ads, the catalysts were abundant in various types of iron species, including oligonuclear sites and Fe_2O_3 particles. According to Song and co-workers [614], iron oxide is an advantageous catalysts for decomposition of ammonium bisulfates. The authors provided a detailed analysis of the mechanism of the process, which takes place stepwise and follows **reactions (153)-(156):**

$$6\ (NH_4)_2SO_4 + Fe_2O_3 \rightarrow 2\ (NH_4)_3Fe(SO_4)_3 + 6\ NH_3 \uparrow + 3\ H_2O \uparrow \quad \textbf{(153)}$$

$$4\ (NH_4)_3Fe(SO_4)_3 + Fe_2O_3 \rightarrow 6\ NH_4Fe(SO_4)_2 + 6\ NH_3 + 3\ H_2O \uparrow \quad \textbf{(154)}$$

$$6\ NH_4Fe(SO_4)_2 \rightarrow 3\ Fe_2(SO_4)_3 + 6\ NH_3 \uparrow + N_2 \uparrow + 6\ H_2O \uparrow + 3\ SO_2 \uparrow \quad \textbf{(155)}$$

$$2\ Fe_2(SO_4)_3 \rightarrow 2\ Fe_2O_3 + 6\ SO_2 \uparrow + 3\ O_2 \uparrow \quad \textbf{(156)}$$

Reactions (153) and (154) are initiated at around 250 and 285-340 °C, respectively and both of them generate ammonia, water vapor, and $(NH_4)_3Fe(SO_4)_3$ or $NH_4Fe(SO_4)_2$. The oxidation-reduction

reaction (155), which takes place within 355-440 °C forms NH_3, N_2, H_2O and solid deposit of iron (III) sulfate. Last, but not least, **reaction (156)** describes thermal decomposition of $Fe_2(SO_4)_3$, proceeding within 470-650 °C, thereby, outside the investigated temperature region of NH_3-SCR. As a consequence, it is expected that formation of iron (III) sulfates could partially block the active sites of the catalysts and inhibit the access of the reacting molecules to the pore openings. Therefore, on the one site, the presence of Fe_2O_3 in the catalysts could be beneficial for elimination of ammonium sulfates, nevertheless, $Fe_2(SO_4)_3$ produced during decomposition of $(NH_4)_2SO_4$ inhibited adsorption of NO and cut off the Langmuir-Hinshelwood reaction pathway. Moreover, the additional portion of NH_3 produced via **reactions (153)-(156)** could be non-selectively oxidized to N_2O under SCR conditions.

The second possible pathway of partial deactivation of the catalysts is related to the presence of copper. Shen et al. [133] found that the amount of Cu participating in redox cycle of NH_3-SCR is lower for SO_2-poisoned Cu-catalyst. Furthermore, Wijayanti et al. [615] observed that concentration of Cu^{2+} in Cu-zeolite significantly decreased after SO_2 exposure. Due to the fact that high-temperature activity of the catalyst was partially promoted by the monomeric Cu^{2+} sites, the decreased activity of FeCuClin cop and FeCuMCM22 ads can be linked with the consumption of the active species through SO_2 adsorption. Poisoning of the catalysts resulted most likely during the reaction of sulfur dioxide with $[Cu^{II}(OH)]^+$ species, which actively captured SO_2 to form Cu-HSO_3 complexes. Subsequently, O_2 present in the gas mixture produced thermally stable copper sulfates (Cu-SO_4). As a consequence, copper species active in the high-temperature region were blocked and the reoxidation half cycle ($Cu^+ \rightarrow Cu^{2+}$), taking place during NH_3-SCR, was hindered, which severely lowered the reaction rate. Additionally, Yang et al. [616] suggested that copper sulfate species are more stable in 8MR, which can partially explain more pronounced deactivation of FeCuClin cop at 400 °C. Last, but not least, NO conversion for both catalysts is maintained on similar and stable level within 400-450 °C. This effect can correlated with the partial blockage of Fe- and Cu-sites which normally catalyze deep oxidation of NH_3 to nitrogen oxide. Given these points, the influence of SO_2 poisoning on the catalytic activity of the materials was independent on the type of zeolitic framework and resulted mainly from the interactions of sulfur dioxide with the metallic active phase of the catalysts. More remarkable deactivation of the catalysts in the high-temperature region is expected to result from the presence of

thermally stable copper and iron (III) sulfates, which blocked the porous texture and active centers of the zeolites, hence, inhibited the proceeding of the catalytic process.

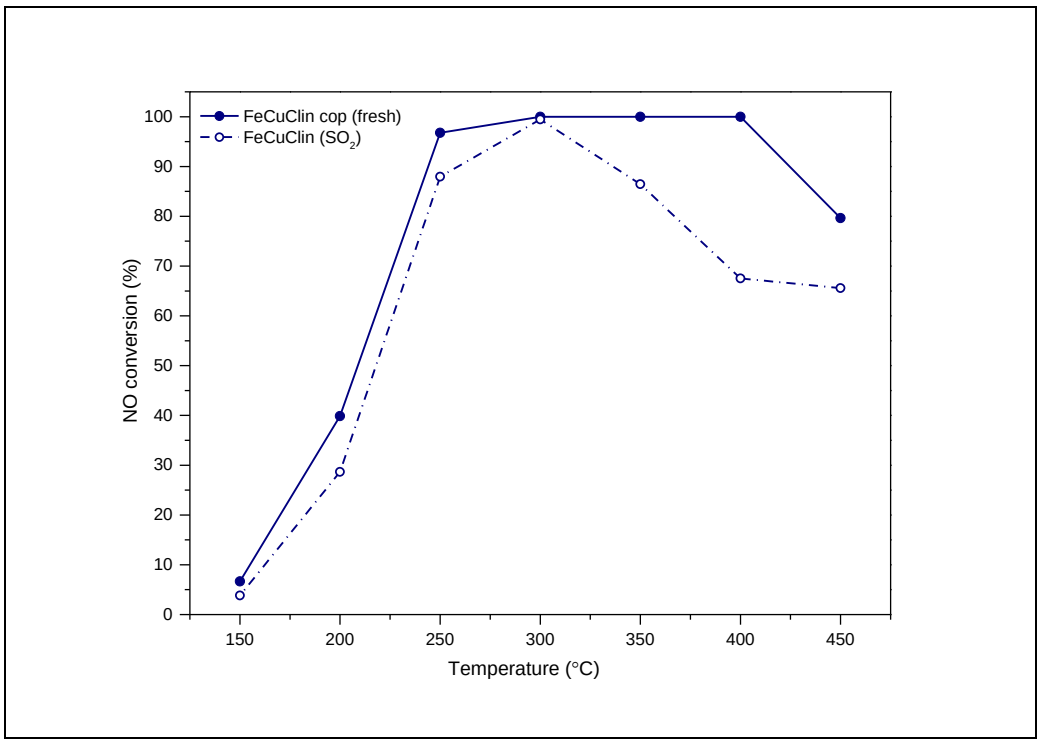

Figure 97. NO conversion obtained for fresh- and SO_2-poisoned FeCuClin cop

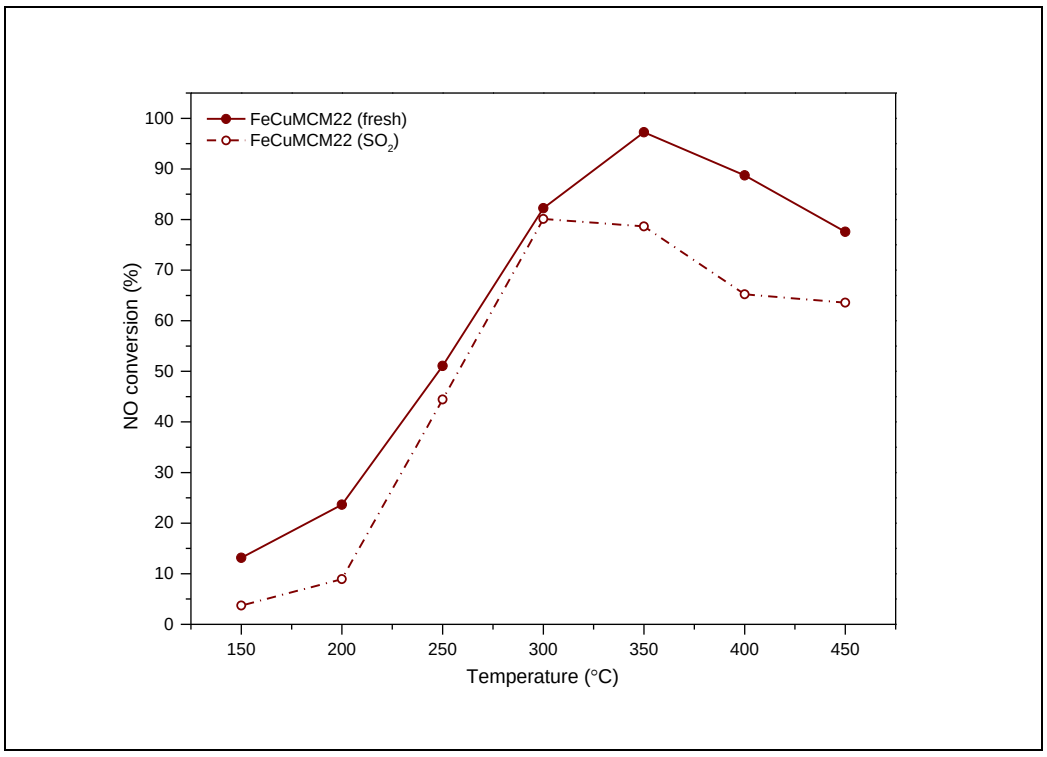

Figure 98. NO conversion obtained for fresh- and SO_2-poisoned FeCuMCM22 ads

Concentration of N_2O in the flue gas exiting the catalytic reactor is presented in **Figure 99** and **Figure 100** for FeCuClin cop and FeCuMCM22 ads, respectively. In can be observed that the influence of the exposition on SO_2 on the emission of N_2O was dependent on the type of the catalyst.

Basing on the data depicted in **Figure 99**, generation of nitrous oxide between 200 and 450 °C was higher for SO_2-poisined FeCuClin cop comparing to the fresh sample. Additionally, in contrast to the non-poisoned material, concentration of N_2O did not decrease with the increasing temperature. One possible explanation of the excessive emission of nitrous oxide was simultaneous decomposition of the reaction intermediates, NH_4NO_3 combined with emission of ammonia through the **reactions (153)-(156)** and its non-selective oxidation. Moreover, occupation of the active centers for NO reduction by metal sulfates could promote side-reactions in the gas phase, including undesired production of nitrous oxide.

As depicted in **Figure 100**, in contrast to FeCuClin cop, SO_2 poisoning of FeCuMCM22 ads did not accelerate formation of N_2O, which was even lower comparing to the fresh catalyst. Correlating the decreased emission of nitrous oxide at 350 °C with the remarkably lower activity of the material at this temperature, most probably deposition of the metal sulfates inhibited not only desired, but also side reactions of NH_3-SCR over FeCuMCM22 ads. Besides, relatively constant concentration of N_2O in the flue gas suggests that polynuclear iron sites, possibly responsible for decomposition of nitrous oxide in the high-temperature region, were occupied by metal sulfate deposits.

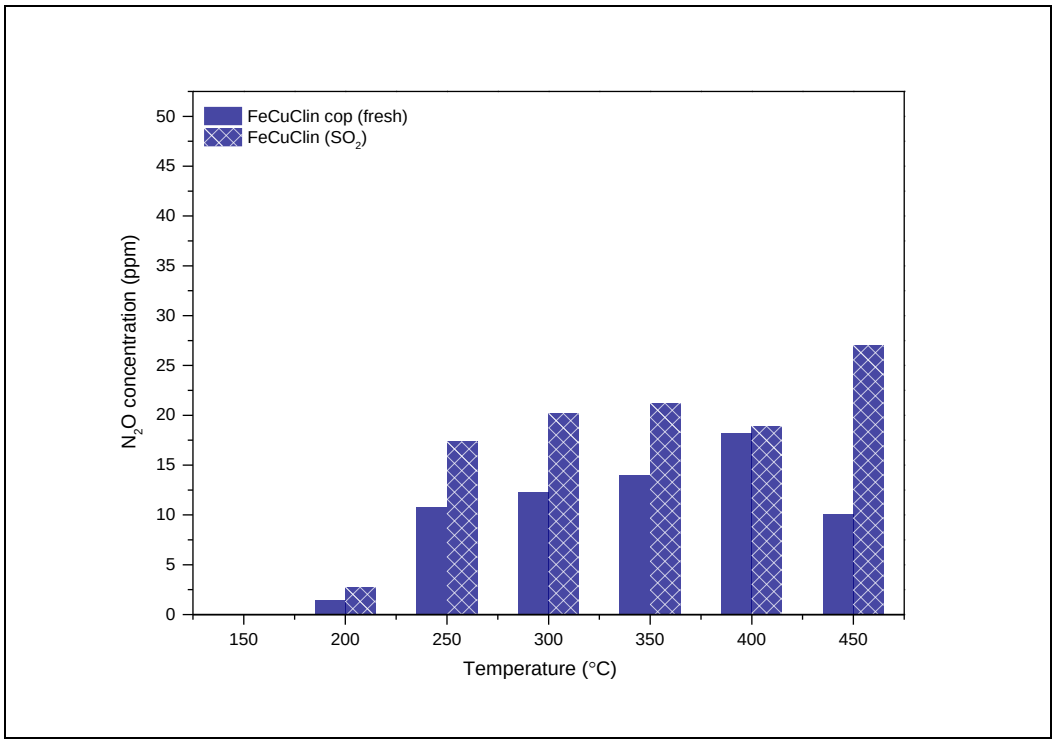

Figure 99. N_2O concentration in the flue gas during the catalytic reaction performed over fresh- and SO_2-poisoned FeCuClin cop

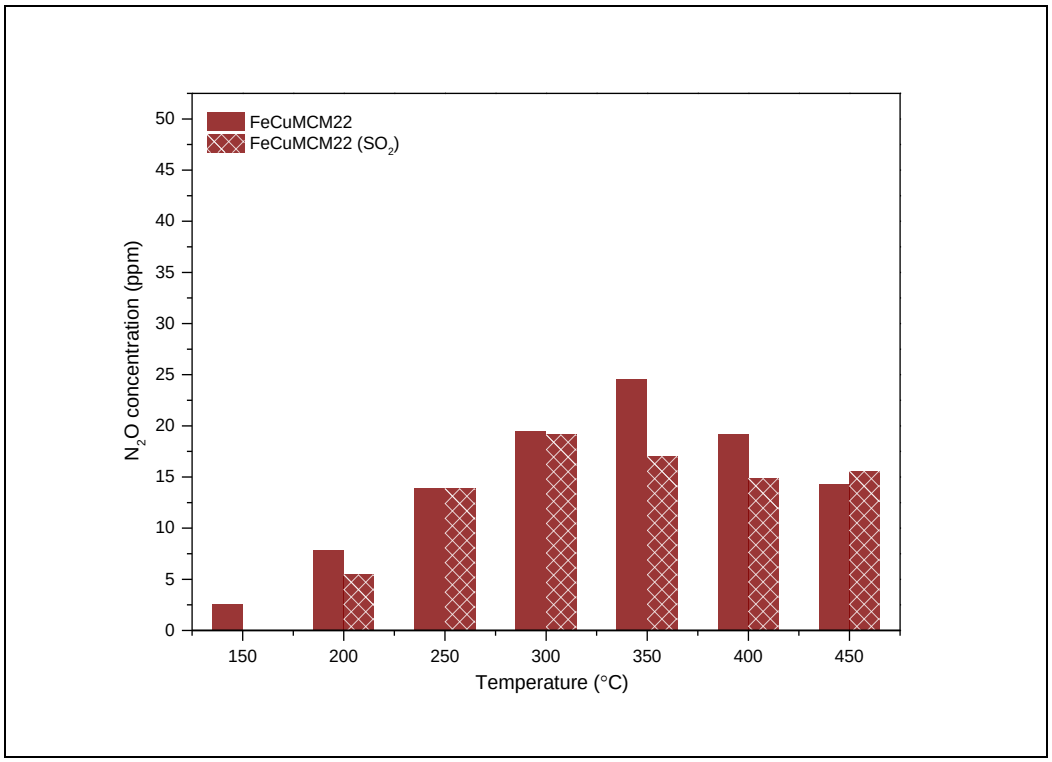

Figure 100. N_2O concentration in the flue gas during the catalytic reaction performed over fresh- and SO_2-poisoned FeCuMCM22 ads

3.2 Catalytic performance in the presence of SO_2 in the gas mixture

In order to investigate the influence of SO_2 in the gas mixture on the catalytic performance of the most active catalysts, sulfur dioxide was introduced into the gas mixture and the reaction was carried out at 350 °C. **Figure 101** illustrates NO conversion obtained for FeCuClin cop and FeCuMCM22 ads, while N_2O concentration produced during the reaction is presented in **Figure 102.**

In general, it can be observed from **Figure 101** that NO conversion for the samples drastically decreased after introduction of SO_2 into the reacting gas mixture. This effect was related to the formation of metal sulfates on the catalysts surface, thus coverage of the active species and hindered diffusion. Interestingly, the increase of SO_2 concentration did not influence remarkably on NO conversion, regardless the type of the sample. Moreover, one can notice that catalytic activity in the presence of sulfur dioxide was slightly higher for FeCuMCM22 ads comparing to FeCuClin cop. One possible explanation for this phenomenon is that clinoptilolite-supported catalyst was more abundant in iron species (see ICP-OES results), which exhibited high affinity to the surface interaction with SO_2, which resulted in more severe deactivation of the material.

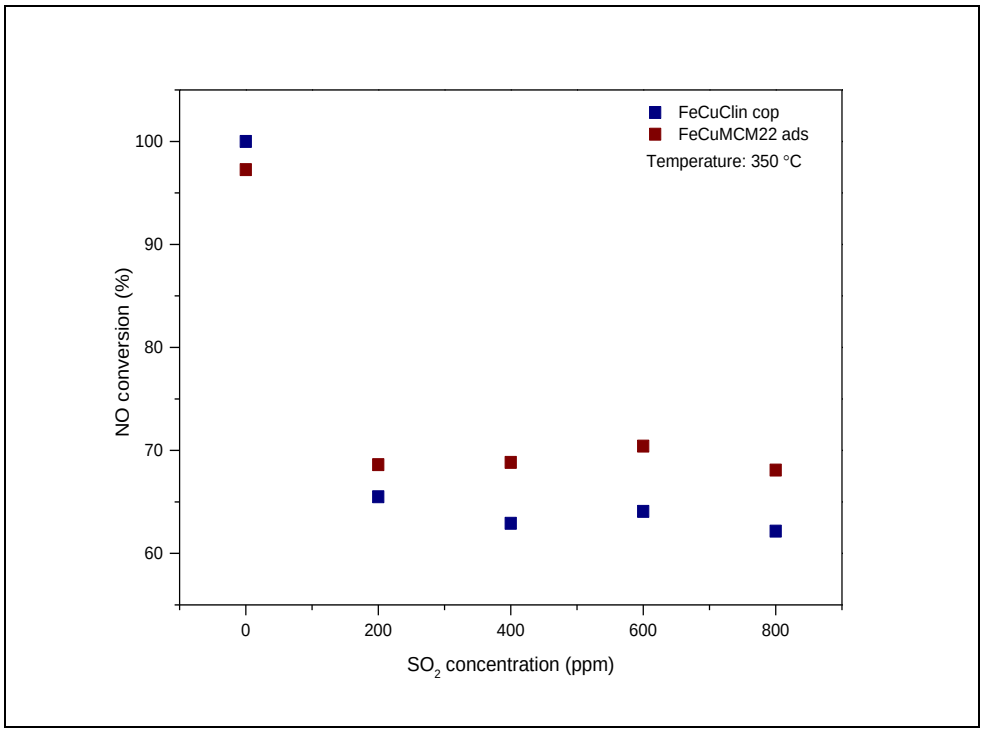

Figure 101. NO conversion obtained for FeCuClin cop and FeCuMCM22 ads in the presence of SO_2 in the gas mixture

As depicted in **Figure 102**, in contrast to NO conversion, there was a significant difference between the concentration of N_2O generated during the reaction over the materials. In the case of FeCuClin cop, production of nitrous oxide before introduction and in the presence of 200 ppm of SO_2 was very similar. However, while SO_2 concentration increased to 400-800 ppm, the emission of N_2O during the reaction noticeably decreased. The inhibiting effect of SO_2 on the production of nitrous oxide was observed by Bai and co-workers [617] for the hollow Co_3O_4@$CoMn_2O_4$ catalyst. According to the authors, the hindered production of N_2O in the presence of SO_2 results from inhibited dehydrogenation of NH_2 to NH during the catalytic reaction. On the contrary, the production of the by-product significantly increased for FeCuMCM22 ads while the reaction was conducted in the presence of SO_2. Furthermore, one can notice that N_2O emission was almost doubled while SO_2 was introduced into the gas mixture comparing to that observed for SO_2-poisined FeCuMCM22 ads. Such result might be related to the oxidation of NH_3, unreacted during the catalytic test. Therefore, the promoting effect of sulfur dioxide on the lower concentration of the produced N_2O was strongly related to the type of the zeolitic framework and active phase distribution.

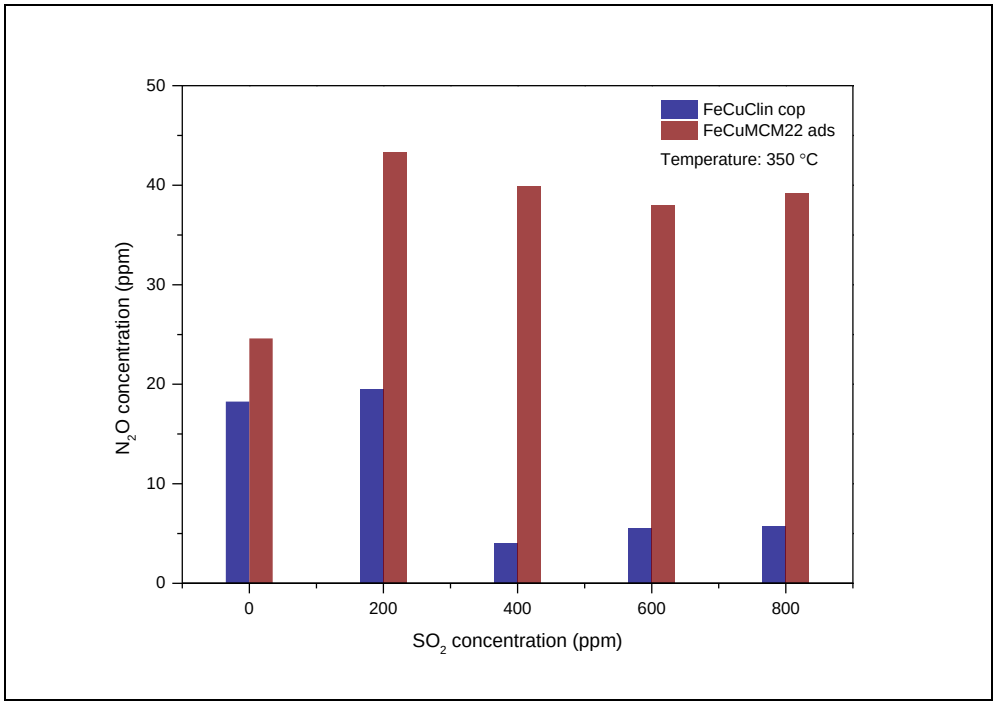

Figure 102. N_2O concentration in the flue gas during the catalytic reaction over FeCuClin cop and FeCuMCM22 ads in the presence of SO_2 in the gas mixture

3.3 Conclusions on the influence of SO_2 on the catalytic performance

In order to investigate the impact of SO_2 on the catalytic performance, FeCuClin cop and FeCuMCM22 ads, as two of the most active catalysts were selected to be poisoned with sulfur dioxide and afterwards, subjected to the catalytic tests with model gas mixture. Alternatively, the fresh samples were subjected to the catalytic tests at 350 °C using gas mixture containing various concentrations of sulfur dioxide. Basing on the obtained results, the following conclusions were drawn:

1. Poisoning with SO_2 did not remarkedly affect low-temperature NO conversion, however, it strongly influenced catalytic activity in the high-temperature region, while the effect was dependent on the type of zeolitic support.

2. Clinoptilolite-supported catalyst was more resistant to the poisoning with SO_2, probably due to higher acidity, which limited the adsorption of acidic sulfur dioxide.

3. It is expected that ammonium sulfate species, produced in the low-temperature region of NH_3-SCR, were catalytically decomposed over Fe_2O_3 particles present in the catalysts. As a consequence, iron (III) sulfates produced in the reaction partially blocked the pores of the zeolites, simultaneously hindering the access of the reacting molecules to the active sites of the catalysts and limiting the reaction rate at high temperature.

4. Interaction of SO_2 with Cu resulted in the consumption of monomeric copper species, thus, decreased high-temperature NO reduction.

5. Poisoning with SO_2 did not influence significantly on N_2O concentration in the flue gas during the catalytic reaction, independently on the type of the zeolitic support. However, emission of nitrous oxide within 300-400 °C could result not only from decomposition of NH_4NO_3, but also from the oxidation of additional portion of NH_3 emitted during catalytic decomposition of ammonium sulfates over Fe_2O_3.

6. The promoting effect of SO_2 on the generation of N_2O was more pronounced for FeCuClin cop comparing to FeCuMCM22 ads.

7. Elimination of nitrous oxide over polynuclear iron species and Fe_2O_3 particles above 400 °C was hindered due to the consumption of those sites on the formation of iron (III) sulfates and decomposition of ammonium sulfates, respectively. As a consequence, concentration of N_2O emitted in the high-temperature range over the poisoned catalysts was maintained on similar level.

8. The limiting influence of sulfur dioxide on NO conversion was more severe while SO_2 was present in the reacting gas mixture than while the catalysts were poisoned before the catalytic reaction. Additionally, increasing of SO_2 concentration to 800 ppm did not affect remarkably the activity of the catalysts at 350 °C.

9. The poisoning effect of SO_2 present in the gas mixture was slightly stronger in the case of FeCuClin cop, most likely due to the higher concentration of iron species comparing to FeCuMCM22 ads.

10. The decreasing concentration of N_2O with the increasing concentration of SO_2 observed for FeCuClin cop was related to the deactivation of the active centers in which N_2O formation takes place. The opposite effect was observed for FeCuMCM22 ads, for which concentration of N_2O noticeably increased, probably as the result of the oxidation of NH_3, unreacted during the catalytic reaction.

Chapter V: General conclusions

The results reported in this PhD thesis evidenced that natural clinoptilolite and layered zeolite belonging to MWW family, MCM-22, are advantageous supports of new catalysts for selective catalytic reduction of nitrogen oxides with ammonia. The conducted studies aimed to achieve the following goals:

- evaluate which support (natural or synthetic) is more beneficial to obtain satisfactory NO conversion and relatively low generation of N_2O during the reaction,
- compare three methods of the introduction of iron as the active phase in reference to the physicochemical and catalytic properties of the materials,
- investigate the influence of copper or cerium as promoters on the physicochemical and catalytic features of Fe-zeolites, which exhibited the best catalytic performance in NH_3-SCR,
- analyze NH_3-SCR catalytic performance of two most active representatives of clinoptilolite- and MCM-22-supported catalysts after their exposition on sulfur dioxide,
- analyze NH_3-SCR catalytic performance of two most active representatives of clinoptilolite- and MCM-22-supported catalysts in the presence of various concentrations of sulfur dioxide in the reacting gas mixture.

It was found that clinoptilolite-supported catalysts showed satisfactory high-temperature performance in NH_3-SCR, while MCM-22-supported samples were more active in low-temperature region of the reaction. Additionally, selectivity of the materials to N_2O was strongly correlated with the zeolitic framework, since regardless the modification method, concentration of N_2O in the post-reaction gas mixture was remarkably lower in the case of MCM-22-supported catalysts. Such effect was related to the speciation of iron species in the Fe-zeolites and possible decomposition of N_2O in the high-temperature range.

Furthermore, it was found that the procedure of modification with Fe had crucial impact on the physicochemical and catalytic features of the zeolites. In the case of clinoptilolite, the most active sample was that modified by co-precipitation, while the most beneficial method for MCM-22-supported catalysts was adsorption from the solution. Therefore, it can be assumed that the efficiency of the modification procedure was strongly related to the type of zeolitic framework. Additionally, in the case

of both zeolites, impregnation method resulted in clustering of iron species and formation of Fe_2O_3 particles, which inhibited low-temperature activity of the catalysts.

In order to investigate the influence of copper or cerium as promoters on the catalytic features of the analyzed materials, two most active representatives of clinoptilolite- and MCM-22-supported catalysts were modified with Cu or Ce by impregnation method. It was found that introduction of copper shifted temperature window to lower value only in the case of FeClin cop, while for FeMCM22 ads Cu species promoted formation of N_2O. The positive effect of Cu on the catalytic activity of FeClin cop resulted from the introduction of new sites for adsorption of NH_3 and improved reducibility, while excessive formation of nitrous oxide observed for FeCuMCM22 ads was a consequence of the formation of CuO aggregates, which are active in NH_3 oxidation reaction. In contrast to Cu, introduction of cerium hindered NO conversion in the case of both zeolites. The limiting influence was assigned to aggregation of iron species caused by introduction of Ce and formation of catalytically inactive Fe_2O_3 particles. Besides, oxygen vacancies in CeO_2 promoted adsorption of O_2 from the gas phase and consumption of NH_3 for side-reactions of NH_3-SCR.

FeCuClin cop and FeCuMCM22 ads were poisoned with SO_2 and subjected to catalytic tests. Alternatively, the materials were tested in NH_3-SCR using gas mixture containing various concentrations of sulfur dioxide. It was observed that poisoning with SO_2 had minor impact on low-temperature activity, however, strongly affected high-temperature NO conversion. This effect was explained by the possible formation of metal sulfates in the materials, pore blocking and occupation of the active sites of the catalysts. Higher acidity of clinoptilolite was the reason of better resistance of FeCuClin cop to the poisoning comparing to FeCuMCM22 ads. However, in the presence of SO_2 in the gas mixture, clinoptilolite-supported catalyst was slightly less active.

Taken together, the reported findings indicated that utility of each zeolite in NH_3-SCR is strongly determined by the temperature region of the reaction. Additionally, modification procedure should be adjusted with caution, taking into account specification of the zeolitic framework. It was also found that the promoting effect of Cu was dependent on the type of zeolite, while cerium was not beneficial for the catalytic performance of the investigated Fe-modified zeolites. Moreover, the obtained results indicated that both FeCu-clinoptilolite and MCM-22 were not severely deactivated by sulfur dioxide.

Nevertheless, still closer inspection is needed to improve SO_2 resistance of the materials. All in all, the results of this study highlight that both natural clinoptilolite and hierarchical mesoporous layered MCM-22 have a great potential to be the supports of new NH_3-SCR catalysts.

References

[1] BP Energy Outlook, Statistical Review of World Energy globally consistent data on world energy markets . and authoritative publications in the field of energy, BP Energy Outlook 2021. 70 **(2021)** 8–20.

[2] International Energy Agency Global Energy Review 2021, *Glob. Energy Rev.* 2021. **(2021)**. https://doi.org/10.1787/90c8c125-en.

[3] WHO, Ambient air pollution: A global assessment of exposure and burden of disease. [Online] http://apps.who.int/iris/bitstream/handle/10665/250141/9789241511353-eng.pdf?sequence=1, Accessed date: 10th of January 2022.

[4] S. Z. Azmi, M. T. Latif, A. S. Ismail, L. Juneng, A. A. Jemain, Trend and status of air quality at three different monitoring stations in the Klang Valley, Malaysia, *Air Qual. Atmos. Heal.* 3 **(2010)** 53–64. https://doi.org/10.1007/s11869-009-0051-1.

[5] J. Brodny, M. Tutak, Analysis of the diversity in emissions of selected gaseous and particulate pollutants in the European Union countries, *J. Environ. Manage.* 231 **(2019)** 582–595. https://doi.org/10.1016/j.jenvman.2018.10.045.

[6] K. Skalska, J.S. Miller, S. Ledakowicz, Trends in NOx abatement: A review, *Sci. Total Environ.* 408 **(2010)** 3976–3989. https://doi.org/10.1016/j.scitotenv.2010.06.001.

[7] M. Mladenović, M. Paprika, A. Marinković, Denitrification techniques for biomass combustion, *Renew. Sustain. Energy Rev.* 82 **(2018)** 3350–3364. https://doi.org/10.1016/j.rser.2017.10.054.

[8] M. Zheng, N. Zhou, S. He, F. Chang, J. Zhong, S. Xu, Z. Wang, T. Liu, Nitrous oxide (N_2O) emissions from a pilot-scale oxidation ditch under different COD/N ratios, aeration rates and two shock-load conditions, *J. Environ. Manage.* 280 **(2021)** 111657. https://doi.org/10.1016/j.jenvman.2020.111657.

[9] F. Ferella, A review on management and recycling of spent selective catalytic reduction catalysts, *J. Clean. Prod.* 246 **(2020)**. https://doi.org/10.1016/j.jclepro.2019.118990.

[10] S. Saravanan, G. Nagarajan, S. Anand, S. Sampath, Correlation for thermal NOx formation in compression ignition (CI) engine fuelled with diesel and biodiesel, *Energy* 42 **(2012)** 401–410. https://doi.org/10.1016/j.energy.2012.03.028.

[11] T. V Guseva, E. N. Potapova, I. O. Tichonova, K. A. Shchelchkov, Nitrogen oxide emissions reducing in cement production, *IOP Conf. Ser. Mater. Sci. Eng.* 1083 **(2021)** 012083.

https://doi.org/10.1088/1757-899x/1083/1/012083.

[12] Sources of NOx emission in 2019 (https://www.mybacharach.com/sources-nox-emissions/), Accessed date: 25th of February 2022.

[13] K. A. Yu, B. C. McDonald, R. A. Harley, Evaluation of Nitrogen Oxide Emission Inventories and Trends for On-Road Gasoline and Diesel Vehicles, *Environ. Sci. Technol.* 55 **(2021)** 6655–6664. https://doi.org/10.1021/acs.est.1c00586.

[14] P. Tan, J. Yao, C. Yao, Z. Hu, D. Lou, S. Lu, D. Li, Study of Real-road Nitrogen Oxide Emissions of Non-road Vehicles, *J. Phys. Conf. Ser.* 2160 **(2022)** 012050. https://doi.org/10.1088/1742-6596/2160/1/012050.

[15] D. Wang, Q. Chen, X. Zhang, C. Gao, B. Wang, X. Huang, Y. Peng, J. Li, C. Lu, J. Crittenden, Multipollutant control (mpc) of flue gas from stationary sources using scr technology: A critical review, *Environ. Sci. Technol.* 55 **(2021)**. https://doi.org/10.1021/acs.est.0c07326.

[16] M. Vascellari, NOx Emission and Mitigation Technologies , *Handb. Clean Energy Syst.* **(2015)** 1–23. https://doi.org/10.1002/9781118991978.hces118.

[17] B. Zhao, S. X. Wang, H. Liu, J. Y. Xu, K. Fu, Z. Klimont, J. M. Hao, K. B. He, J. Cofala, M. Amann, NOx emissions in China: Historical trends and future perspectives, *Atmos. Chem. Phys.* 13 **(2013)** 9869–9897. https://doi.org/10.5194/acp-13-9869-2013.

[18] Q. Zhang, Y. Pan, Y. He, W.W. Walters, Q. Ni, X. Liu, G. Xu, J. Shao, C. Jiang, Substantial nitrogen oxides emission reduction from China due to COVID-19 and its impact on surface ozone and aerosol pollution, *Sci. Total Environ.* 753 **(2021)** 142238. https://doi.org/10.1016/j.scitotenv.2020.142238.

[19] European Council, Directive 2010/75/EU Industrial Emissions, Off. J. Eur. Union. L334 (2010) 17–119. https://doi.org/10.3000/17252555.L_2010.334.eng.

[20] A. Soni, A Brief Study of Acid Rain, *Int. J. Innow. Res.* 1 **(2019)** 6–8.

[21] S. A. Ali, Ozone Depletion, a Big Threat to Climate Change: What can be Done?, *Glob. J. Pharm. Pharm. Sci.* 1 **(2017)** 1–5. https://doi.org/10.19080/gjpps.2017.01.555556.

[22] R. Zhang, G. Wang, S. Guo, M. L. Zamora, Q. Ying, Y. Lin, W. Wang, M. Hu, Y. Wang, Formation of Urban Fine Particulate Matter, *Chem. Rev.* 115 **(2015)** 3803–3855. https://doi.org/10.1021/acs.chemrev.5b00067.

[23] M. C. Turner, Z. J. Andersen, A. Baccarelli, W. R. Diver, S. M. Gapstur, C. A. Pope, D. Prada,

J. Samet, G. Thurston, A. Cohen, Outdoor air pollution and cancer: An overview of the current evidence and public health recommendations, *CA. Cancer J. Clin.* 70 **(2020)** 460–479. https://doi.org/10.3322/caac.21632.

[24] S. Paraschiv, L. S. Paraschiv, The role of NO_2 in ozone formation chemistry in the polluted urban troposphere, *Int. Multidiscip. Sci. GeoConference Surv. Geol. Min. Ecol. Manag.* SGEM. 19 **(2019)** 1125–1134. https://doi.org/10.5593/sgem2019/4.1/S19.143.

[25] J. M. Gaffin, M. Hauptman, C. R. Petty, W. J. Sheehan, P. S. Lai, J. M. Wolfson, D. R. Gold, B. A. Coull, P. Koutrakis, W. Phipatanakul, Nitrogen dioxide exposure in school classrooms of inner-city children with asthma, *J. Allergy Clin. Immunol.* 141 **(2018)** 2249-2255.e2. https://doi.org/10.1016/j.jaci.2017.08.028.

[26] R. Rahman Khan, M. Siddiqui, Review on effects of Particulates; Sulfur Dioxide and Nitrogen Dioxide on Human Health, *Int. Res. J. Environ. Sci. Int. Sci. Congr. Assoc.* 3 **(2014)** 70–73.

[27] S. E. Wing, G. Bandoli, D. Telesca, J. G. Su, B. Ritz, Chronic exposure to inhaled, traffic-related nitrogen dioxide and a blunted cortisol response in adolescents, *Environ. Res.* 163 **(2018)** 201–207. https://doi.org/10.1016/j.envres.2018.01.011.

[28] L. J. Muzio, G. C. Quartucy, F. Energy, C. S. Pointe, L. Hills, Implementing NOx Control: Research to Application, *Prog. Energy Combust. Sci.* 23 **(1997)** 233–266. https://doi.org/10.1016/S0360-1285(97)00002-6.

[29] M. Greenstone, The impacts of environmental regulations on industrial activity: Evidence from the 1970 and 1977 Clean Air Act Amendments and the Census of Manufactures, *J. Polit. Econ.* 110 **(2002)** 1175–1219. https://doi.org/10.1086/342808.

[30] M. Gemmer, B. Xiao, Air quality legislation and standards in the European Union: Background, status and public participation, *Adv. Clim. Chang. Res.* 4 **(2014)** 50–59. https://doi.org/10.3724/sp.j.1248.2013.050.

[31] European Parliament and Council, Directive (EU) 2016/2284 of the European Parliament and of the Council of 14 December 2016 on on the reduction of national emissions of certain atmospheric pollutants, amending Directive 2003/35/EC and repealing Directive 2001/81/EC, Off. *J. Eur. Union.* L 344 **(2016)** 1–31. https://doi.org/http://eur-lex.europa.eu/pri/en/oj/dat/2003/l_285/l_28520031101en00330037.pdf.

[32] E.E. Agency, National Emission reduction Commitments Directive reporting status 2022: https://www.eea.europa.eu/publications/national-emission-reduction-commitments-directive-2022. Accessed date: 12th of October 2022.

[33] E. Commission, Report from the Commision to the European Parliament and Council on the progress made on the implementation of Directive (EU) 2016/2284 on the reduction of natuonal emissions of certain atmospheric pollutants, **2020**.

[34] E. Commision, Annexes to the Report from the Commision to the European Parliament and Council on the progress made on the implementation of Directive (EU) 2016/2284 on the reduction of natuonal emissions of certain atmospheric pollutants, **2020**.

[35] European Comission, Commission Implementing Decision (EU) 2017/1442, *Off. J. Eur. Union.* **(2017)** L 212/1-L 212/82.

[36] A. Pinasseau, B. Zerger, J. Roth, M. Canova, S. Soudier, Best Available Techniques (BAT) Reference Document for Waste Treatment. Industrial Emissions Directive 2010/75/EU (Integrated Pollution Prevention and Control), **2018.**

[37] R. by the H.-L.G. on E. Industries, Masterplan for a Competitive Transformation of EU Energy-intensive Industries. Enabling a Climate-neutral, Circular Economy by 2050, Luxembg. Publ. Off. Eur. Union. **(2019)**. https://op.europa.eu/en/publication-detail/-/publication/be308ba7-14da-11ea-8c1f-01aa75ed71a1/language-en. Accessed date: 15th May 2022.

[38] G. Stupar, D. Tucaković, T. Živanović, S. Belošević, Assessing the impact of primary measures for NOx reduction on the thermal power plant steam boiler, *Appl. Therm. Eng.* 78 **(2015)** 397–409. https://doi.org/10.1016/j.applthermaleng.2014.12.074.

[39] T. Chae, J. Lee, Y. Lee, W. Yang, C. Ryu, Pilot-scale experimental study on impacts of biomass cofiring methods to nox emission from pulverized coal boilers - Part 2: NOx reduction capability through reburning versus cofiring, *Energies*. 14 **(2021)**. https://doi.org/10.3390/en14206552.

[40] L. A. Nikolaeva, A. N. Khusnutdinov, A Study of the Absorption of Nitrogen Oxides from the Boiler Flue Gases, *Therm. Eng.* 65 **(2018)** 575–579. https://doi.org/10.1134/S0040601518080049.

[41] F. Gao, T. J. Toops, Selective Catalytic Reduction: From Basic Science to deNOx Applications, *Catalysts.* 11 **(2021)** 250. https://doi.org/10.3390/catal11020250.

[42] V. A. Sadykov, V. A. Matyshak, Selective Catalytic Reduction of Nitrogen Oxides by Hydrocarbons in an Excess of Oxygen, Russ. *J. Phys. Chem. A.* 95 **(2021)** 475–491. https://doi.org/10.1134/S0036024421030183.

[43] S. Yang, Y. Fu, Y. Liao, S. Xiong, Z. Qu, N. Yan, J. Li, Competition of selective catalytic reduction and non selective catalytic reduction over MnO_x/TiO_2 for NO removal: The

relationship between gaseous NO concentration and N_2O selectivity, *Catal. Sci. Technol.* 4 **(2014)** 224–232. https://doi.org/10.1039/c3cy00648d.

[44] J. Van Caneghem, J. De Greef, C. Block, C. Vandecasteele, NOx reduction in waste incinerators by selective catalytic reduction (SCR) instead of selective non catalytic reduction (SNCR) compared from a life cycle perspective: A case study, *J. Clean. Prod.* 112 **(2016)** 4452–4460. https://doi.org/10.1016/j.jclepro.2015.08.068.

[45] A. Ściubidło, I. Majchrzak-Kucęba, Exhaust gas purification process using fly ash-based sorbents, *Fuel.* 258 **(2019)** 116126. https://doi.org/10.1016/j.fuel.2019.116126.

[46] S. H. Jo, K. M. Kim, S. H. Seo, T. H. Kim, S. Yu, T. H. Kim, Y. S. Son, A study on additives to improve electron beam technology for NOx and SO_2 reduction, *Radiat. Phys. Chem.* 183 **(2021)** 109397. https://doi.org/10.1016/j.radphyschem.2021.109397.

[47] R. M. Heck, Catalytic abatement of nitrogen oxides-stationary applications, *Catal. Today.* 53 **(1999)** 519–523. https://doi.org/10.1016/S0920-5861(99)00139-X.

[48] W. Fan, T. Zhu, Y. Sun, D. Lv, Effects of gas compositions on NOx reduction by selective non-catalytic reduction with ammonia in a simulated cement precalciner atmosphere, *Chemosphere.* 113 **(2014)** 182–187. https://doi.org/10.1016/j.chemosphere.2014.05.034.

[49] A. G. Chmielewski, E. Zwolińska, J. Licki, Y. Sun, Z. Zimek, S. Bułka, A hybrid plasma-chemical system for high-NOx flue gas treatment, *Radiat. Phys. Chem.* 144 **(2018)** 1–7. https://doi.org/10.1016/j.radphyschem.2017.11.005.

[50] D. Damma, P. R. Ettireddy, B. M. Reddy, P. G. Smirniotis, A review of low temperature NH_3-SCR for removal of NOx, *Catalysts*. 9 (4) (**2019)** 349. https://doi.org/10.3390/catal9040349.

[51] E. S. Rubin, M. R. Taylor, S. Yeh, D. A. Hounshell, Learning curves for environmental technology and their importance for climate policy analysis, *Energy.* 29 **(2004)** 1551–1559. https://doi.org/10.1016/j.energy.2004.03.092.

[52] Z. H. B. Guan, R. Zhan, H. Lin, Review of state of the art technologies of selective catalytic reduction of NOx from diesel engine exhaust, *Appl. Therm. Eng.* 66 **(2014)** 395–414. https://doi.org/10.1016/j.applthermaleng.2014.02.021.

[53] I. Lezcano-Gonzalez, U. Deka, B. Arstad, A. Van Yperen-De Deyne, K. Hemelsoet, M. Waroquier, V. Van Speybroeck, B. M. Weckhuysen, A.M. Beale, Determining the storage, availability and reactivity of NH_3 within Cu-Chabazite-based Ammonia Selective Catalytic Reduction systems, *Phys. Chem. Chem. Phys.* 16 **(2014)** 1639–1650.

https://doi.org/10.1039/c3cp54132k.

[54] B. Wu, L. Deng, Y. Liu, D. Sun, W. Su, Urea injection control strategy in urea-selective catalytic reduction for heavy-duty diesel engine under transient process, *Int. J. Engine Res.* **(2019)** 1–12. https://doi.org/10.1177/1468087419860633.

[55] H. Kim, C. Yoon, J. Lee, H. Lee, A study on the solid ammonium SCR system for control of diesel NOx emissions, *SAE Tech. Pap.* 1 **(2014)**. https://doi.org/10.4271/2014-01-1535.

[56] Y. Kim, H. Raza, S. Lee, H. Kim, Study on the thermal decomposition rate of ammonium carbamate for a diesel NOx reducing agent-generating system, *Fuel.* 267 **(2020)** 117306. https://doi.org/10.1016/j.fuel.2020.117306.

[57] G. Fulks, G.B. Fisher, K. Rahmoeller, M.C. Wu, E. D'Herde, J. Tan, A review of solid materials as alternative ammonia sources for lean NOx reduction with SCR, *SAE Tech. Pap.* **(2009)**. https://doi.org/10.4271/2009-01-0907.

[58] I. Heo, S. Sung, M. B. Park, T. S. Chang, Y. J. Kim, B. K. Cho, S. B. Hong, J. W. Choung, I. S. Nam, Effect of Hydrocarbon on DeNOx Performance of Selective Catalytic Reduction by a Combined Reductant over Cu-Containing Zeolite Catalysts, *ACS Catal.* 9 **(2019)** 9800–9812. https://doi.org/10.1021/acscatal.9b02763.

[59] I. A. Resitoglu, A. Keskin, H. Özarslan, H. Bulut, Selective catalytic reduction of NOx emissions by hydrocarbons over Ag–Pt/Al_2O_3 catalyst in diesel engine, *Int. J. Environ. Sci. Technol.* 16 **(2019)** 6959–6966. https://doi.org/10.1007/s13762-019-02266-x.

[60] H.L. Fang, H.F.M. DaCosta, Urea thermolysis and NOx reduction with and without SCR catalysts, *Appl. Catal. B Environ.* 46 **(2003)** 17–34. https://doi.org/10.1016/S0926-3373(03)00177-2.

[61] J. Xu, G. Chen, F. Guo, J. Xie, Development of wide-temperature vanadium-based catalysts for selective catalytic reducing of NOx with ammonia: *Review, Chem. Eng. J.* 353 **(2018)** 507–518. https://doi.org/10.1016/j.cej.2018.05.047.

[62] M. Fu, C. Li, P. Lu, L. Qu, M. Zhang, Y. Zhou, M. Yu, Y. Fang, A review on selective catalytic reduction of NOx by supported catalysts at 100-300 °C - catalysts, mechanism, kinetics, *R. Soc. Chem.* 3 **(2015)** 10715–10722. https://doi.org/10.1039/b000000x.

[63] F. J. J. G. Janssen, F. M. G. Van Den Kerkhof, H. Bosch, J. R. H. Ross, Mechanism of the reaction of nitric oxide, ammonia, and oxygen over vanadia catalysts. 2. Isotopic transient studies with oxygen-18 and nitrogen-15, *J. Phys. Chem.* 91 **(1987)** 6633–6638.

https://doi.org/10.1021/j100311a016.

[64] J. Zhang, X. Li, P. Chen, B. Zhu, Research status and prospect on vanadium-based catalysts for NH_3-SCR denitration, *Materials (Basel)*. 11 **(2018)**. https://doi.org/10.3390/ma11091632.

[65] Y. Liu, J. Zhao, J. M. Lee, Conventional and New Materials for Selective Catalytic Reduction (SCR) of NOx, *ChemCatChem.* 10 **(2018)** 1499–1511. https://doi.org/10.1002/cctc.201701414.

[66] M. Koebel, M. Elsener, M. Kleemann, Urea-SCR: a promising technique to reduce NOx emissions from automotive diesel engines, *Catal. Today.* 59 **(2000)** 335–345. https://doi.org/10.1016/S0920-5861(00)00299-6.

[67] M. Salazar, S. Hoffmann, V. Singer, R. Becker, W. Grünert, Hybrid catalysts for the selective catalytic reduction (SCR) of NO by NH_3. On the role of fast SCR in the reaction network, *Appl. Catal. B Environ.* 199 **(2016)** 433–438. https://doi.org/10.1016/j.apcatb.2016.06.043.

[68] M. Jabłońska, R. Palkovits, Copper based catalysts for the selective ammonia oxidation into nitrogen and water vapour-Recent trends and open challenges, *Appl. Catal. B Environ.* 181 **(2016)** 332–351. https://doi.org/10.1016/j.apcatb.2015.07.017.

[69] M. Zhu, J. K. Lai, I. E. Wachs, Formation of N_2O greenhouse gas during SCR of NO with NH_3 by supported vanadium oxide catalysts, *Appl. Catal. B Environ.* 224 **(2018)** 836–840. https://doi.org/10.1016/j.apcatb.2017.11.029.

[70] G. Madia, M. Koebel, M. Elsener, A. Wokaun, Side reactions in the selective catalytic reduction of NOx with various NO_2 fractions, *Ind. Eng. Chem. Res.* 41 **(2002)** 4008–4015. https://doi.org/10.1021/ie020054c.

[71] L. Sheng, Z. Ma, S. Chen, J. Lou, C. Li, S. Li, Z. Zhang, Y. Wang, H. Yang, Mechanistic insight into N_2O formation during NO reduction by NH_3 over Pd/CeO_2 catalyst in the absence of O_2, *Chinese J. Catal.* 40 **(2019)** 1070–1077. https://doi.org/10.1016/S1872-2067(19)63328-0.

[72] L. Muzio, S. Bogseth, R. Himes, Y.C. Chien, D. Dunn-Rankin, Ammonium bisulfate formation and reduced load SCR operation, *Fuel.* 206 **(2017)** 180–189. https://doi.org/10.1016/j.fuel.2017.05.081.

[73] Y. Yu, W. Tan, D. An, X. Wang, A. Liu, W. Zou, C. Tang, C. Ge, Q. Tong, J. Sun, L. Dong, Insight into the SO_2 resistance mechanism on γ-Fe_2O_3 catalyst in NH_3-SCR reaction: A collaborated experimental and DFT study, *Appl. Catal. B Environ.* 281 **(2021)** 119544. https://doi.org/10.1016/j.apcatb.2020.119544.

[74] S. Youn, I. Song, H. Lee, S.J. Cho, D.H. Kim, Effect of pore structure of TiO_2 on the SO_2

poisoning over V_2O_5/TiO_2 catalysts for selective catalytic reduction of NOx with NH_3, *Catal. Today.* 303 **(2018)** 19–24. https://doi.org/10.1016/j.cattod.2017.08.015.

[75] M. Takagi, T. Kawai, M. Soma, T. Onishi, K. Tamaru, The mechanism of the reaction between NOx and NH_3 on V_2O_5 in the presence of oxygen, *J. Catal.* 50 **(1977)** 441–446. https://doi.org/10.1016/0021-9517(77)90056-2.

[76] M. Inomata, A. Miyamoto, Y. Murakami, Mechanism of the reaction of NO and NH_3 on vanadium oxide catalyst in the presence of oxygen under the dilute gas condition, *J. Catal.* 62 **(1980)** 140–148. https://doi.org/10.1016/0021-9517(80)90429-7.

[77] G. T. Went, L .J. Leu, R. R. Rosin, A. T. Bell, The effects of structure on the catalytic activity and selectivity of V_2O_5/TiO_2 for the reduction of NO by NH_3, *J. Catal.* 134 **(1992)** 492–505. https://doi.org/10.1016/0021-9517(92)90337-H.

[78] N.-Y. Topsoe, J. A. Dumesic, H. Topsøe, Vanadia/Titania Catalysts for Selective Catalytic Reduction of NItric Oxide by Ammonia II. Studies of Active Sites and Formulation of Catalytic Cycles, *J. Catal.* 151 **(1995)** 241–252.

[79] T. V. W. Janssens, H. Falsig, L. F. Lundegaard, P. N. R. Vennestrøm, S. B. Rasmussen, P. G. Moses, F. Giordanino, E. Borfecchia, K. A. Lomachenko, C. Lamberti, S. Bordiga, A. Godiksen, S. Mossin, P. Beato, A consistent reaction scheme for the selective catalytic reduction of nitrogen oxides with ammonia, *ACS Catal.* 5 **(2015)** 2832–2845. https://doi.org/10.1021/cs501673g.

[80] C. Doornkamp, V. Ponec, The universal character of the Mars and Van Krevelen mechanism, *J. Mol. Catal. A Chem.* 162 **(2000)** 19–32. https://doi.org/10.1016/S1381-1169(00)00319-8.

[81] A. Marberger, D. Ferri, M. Elsener, O. Kröcher, The Significance of Lewis Acid Sites for the Selective Catalytic Reduction of Nitric Oxide on Vanadium-Based Catalysts, *Angew. Chemie.* 128 **(2016)** 12168–12173. https://doi.org/10.1002/ange.201605397.

[82] J. Due-Hansen, S. B. Rasmussen, E. Mikolajska, M. A. Bañares, P. Ávila, R. Fehrmann, Redox behaviour of vanadium during hydrogen-oxygen exposure of the V_2O_5-WO_3/TiO_2 SCR catalyst at 250°C, *Appl. Catal. B Environ.* 107 **(2011)** 340–346. https://doi.org/10.1016/j.apcatb.2011.07.034.

[83] E. W. Kuipers, A. Vardi, A. Danon, A. Amirav, Surface-Molecule Proton Transfer: A Demonstration of the Eley-Rideal Mechanism, *Phys. Rew. Lett.* 66 **(1990)** 116.

[84] L. Lisi, S. Cimino, Poisoning of scr catalysts by alkali and alkaline earth metals, *Catalysts.* 10 **(2020)** 1–24. https://doi.org/10.3390/catal10121475.

[85] Q. Liu, C. Bian, S. Ming, L. Guo, S. Zhang, L. Pang, P. Liu, Z. Chen, T. Li, The opportunities and challenges of iron-zeolite as NH_3-SCR catalyst in purification of vehicle exhaust, *Appl. Catal. A Gen.* 607 **(2020)** 117865. https://doi.org/10.1016/j.apcata.2020.117865.

[86] B. Samojeden, M. Motak, T. Grzybek, The influence of the modification of carbonaceous materials on their catalytic properties in SCR-NH_3. A short review, *Comptes Rendus Chim.* 18 **(2015) 1049–1073.** https://doi.org/10.1016/j.crci.2015.04.001.

[87] J. Zeng, S. Chen, Z. Fan, C. Wang, H. Chang, J. Li, Simultaneous selective catalytic reduction of NO and N_2O by NH_3 over Fe-zeolite catalysts, *Ind. Eng. Chem. Res.* 59 **(2020)** 19500–19509. https://doi.org/10.1021/acs.iecr.0c02909.

[88] G. Ramis, G. Busca, F. Bregani, P. Forzatti, Fourier transform-infrared study of the adsorption and coadsorption of nitric oxide, nitrogen dioxide and ammonia on vanadia-titania and mechanism of selective catalytic reduction, *Appl. Catal.* 64 **(1990)** 259–278. https://doi.org/10.1016/S0166-9834(00)81565-1.

[89] R. Qu, Y. Peng, X. Sun, J. Li, X. Gao, K. Cen, Identification of the reaction pathway and reactive species for the selective catalytic reduction of NO with NH_3 over cerium-niobium oxide catalysts, *Catal. Sci. Technol.* 6 **(2016)** 2136–2142. https://doi.org/10.1039/c5cy01220a.

[90] J. Liu, X. Li, R. Li, Q. Zhao, J. Ke, H. Xiao, L. Wang, S. Liu, M. Tadé, S. Wang, Facile synthesis of tube-shaped Mn-Ni-Ti solid solution and preferable Langmuir-Hinshelwood mechanism for selective catalytic reduction of NOx by NH_3, *Appl. Catal. A Gen.* 549 **(2018)** 289–301. https://doi.org/10.1016/j.apcata.2017.10.010.

[91] Z. Zhao, E. Li, Y. Qin, X. Liu, Y. Zou, H. Wu, T. Zhu, Density functional theory (DFT) studies of vanadium-titanium based selective catalytic reduction (SCR) catalysts, *J. Environ. Sci. (China).* 90 **(2020)** 119–137. https://doi.org/10.1016/j.jes.2019.11.008.

[92] G. Busca, L. Lietti, G. Ramis, F. Berti, Chemical and mechanistic aspects of the selective catalytic reduction of NO(x) by ammonia over oxide catalysts: A review, *Appl. Catal. B Environ.* 18 **(1998)** 1–36. https://doi.org/10.1016/S0926-3373(98)00040-X.

[93] L. Chen, V. Agrawal, S.L. Tait, Sulfate promotion of selective catalytic reduction of nitric oxide by ammonia on ceria, *Catal. Sci. Technol.* 9 **(2019)** 1802–1815. https://doi.org/10.1039/c8cy02590h.

[94] T. Komatsu, M. Nunokawa, I. S. Moon, T. Takahara, S. Namba, T. Yashima, Kinetic studies of reduction of nitric oxide with ammonia on Cu2+-exchanged zeolites, *J. Catal.* 148 **(1994)** 427–437. https://doi.org/10.1006/jcat.1994.1229.

[95] C. Liu, J. W. Shi, C. Gao, C. Niu, Manganese oxide-based catalysts for low-temperature selective catalytic reduction of NOx with NH_3: A review, *Appl. Catal. A Gen.* 522 **(2016)** 54–69. https://doi.org/10.1016/j.apcata.2016.04.023.

[96] M. Y. Mihaylov, V. R. Zdravkova, E. Z. Ivanova, H. A. Aleksandrov, P. S. Petkov, G. N. Vayssilov, K. I. Hadjiivanov, Infrared spectra of surface nitrates: Revision of the current opinions based on the case study of ceria, *J. Catal.* 394 **(2021)** 245–258. https://doi.org/10.1016/j.jcat.2020.06.015.

[97] S. Yang, C. Wang, J. Li, N. Yan, L. Ma, H. Chang, Low temperature selective catalytic reduction of NO with NH3 over Mn-Fe spinel: Performance, mechanism and kinetic study, *Appl. Catal. B Environ.* 110 **(2011)** 71–80. https://doi.org/10.1016/j.apcatb.2011.08.027.

[98] W. S. Kijlstra, D. S. Brands, H. I. Smit, E. K. Poels, A. Bliek, Mechanism of the Selective Catalytic Reduction of NO with NH_3 over MnO_x/Al_2O_3, *J. Catal.* 171 **(1997)** 219–230. https://doi.org/10.1021/jp031113i.

[99] Y. Tian, J. Yang, L. Liu, Q. Liu, B. Kong, F. Lin, M. Kong, G. Hu, Insight into regeneration mechanism with sulfuric acid for arsenic poisoned commercial SCR catalyst, *J. Energy Inst.* 93 **(2020)** 387–394. https://doi.org/10.1016/j.joei.2019.02.002.

[100] L. Arnarson, H. Falsig, S.B. Rasmussen, J. V. Lauritsen, P.G. Moses, The reaction mechanism for the SCR process on monomer V^{5+} sites and the effect of modified Brønsted acidity, *Phys. Chem. Chem. Phys.* 18 **(2016)** 17071–17080. https://doi.org/10.1039/c6cp02274j.

[101] G. Ramis, L. Yi, G. Busca, M. Turco, E. Kotur, R.J. Willey, Adsorption, activation, and oxidation of ammonia over SCR catalysts, *J. Catal.* 157 **(1995)** 523–535. https://doi.org/10.1006/jcat.1995.1316.

[102] M. Gruber, K. Hermann, Elementary steps of the catalytic NOx reduction with NH_3: Cluster studies on reaction paths and energetics at vanadium oxide substrate, *J. Chem. Phys.* 139 **(2013)** 244701. https://doi.org/10.1063/1.4849556.

[103] M. Zhu, J.K. Lai, U. Tumuluri, Z. Wu, I.E. Wachs, Nature of Active Sites and Surface Intermediates during SCR of NO with NH_3 by Supported V_2O_5-WO_3/TiO_2 Catalysts, *J. Am. Chem. Soc.* 139 **(2017)** 15624–15627. https://doi.org/10.1021/jacs.7b09646.

[104] Y. Inomata, S. Hata, M. Mino, E. Kiyonaga, K. Morita, K. Hikino, K. Yoshida, H. Kubota, T. Toyao, K.I. Shimizu, M. Haruta, T. Murayama, Bulk Vanadium Oxide versus Conventional V_2O_5/TiO_2: NH_3-SCR Catalysts Working at a Low Temperature below 150 °C, *ACS Catal.* 9 **(2019)** 9327–9331. https://doi.org/10.1021/acscatal.9b02695.

[105] K. Lee, B. Choi, C. Lee, K. Oh, Effects of SiO_2/Al_2O_3 ratio, reaction atmosphere and metal additive on de-NOx performance of HC-SCR over Cu-based ZSM-5, *J. Ind. Eng. Chem.* 90 **(2020)** 132–144. https://doi.org/10.1016/j.jiec.2020.07.005.

[106] W. Held, A. König, T. Richter, L. Puppe, Catalytic NOx reduction in net oxidizing exhaust gas, *SAE Tech. Pap.* **(1990)**. https://doi.org/10.4271/900496.

[107] M. Iwamoto, H. Yahiro, K. Tanda, Catalytic decomposition of nitrogen monoxide over copper ion-exchanged zeolites. Influence of zeolite structure and aluminum content on the catalytic activity, *Surf. Sci. Catal.* 44 **(1989)** 219-226. https://doi.org/10.1016/S0167-2991(09)61296-9.

[108] R. Mrad, A. Aissat, R. Cousin, D. Courcot, S. Siffert, Catalysts for NOx selective catalytic reduction by hydrocarbons (HC-SCR), *Appl. Catal. A Gen.* 504 **(2015)** 542–548. https://doi.org/10.1016/j.apcata.2014.10.021.

[109] A. Łamacz, A. Krztoń, G. Djéga-Mariadassou, Study on the selective catalytic reduction of NO with toluene over $CuO/CeZrO_2$. A confirmation for the three-function model of HC-SCR using the temperature programmed methods and in situ DRIFTS, *Appl. Catal. B Environ.* 142–143 **(2013)** 268–277. https://doi.org/10.1016/j.apcatb.2013.05.030.

[110] N. Wen, R. Lin, Y. Su, W. Deng, H. Zhou, B. Zhao, SCR of NO with CH_4 over Fe/Ga_2O_3-Al_2O_3 and the mechanism, J. Environ. Chem. Eng. 9 **(2021)** 105014. https://doi.org/10.1016/j.jece.2020.105014.

[111] A. M. Dakdareh, C. Falamaki, N. Ghasemian, Hydrothermally grown nano-manganese oxide on clinoptilolite for low-temperature propane-selective catalytic reduction of NOx, *J. Nanoparticle Res.* 20 **(2018)** 309**.** https://doi.org/10.1007/s11051-018-4414-0.

[112] M. Yuan, W. Deng, S. Dong, Q. Li, B. Zhao, Y. Su, Montmorillonite based porous clay heterostructures modified with Fe as catalysts for selective catalytic reduction of NO with propylene, *Chem. Eng. J.* 353 **(2018)** 839–848. https://doi.org/10.1016/j.cej.2018.07.201.

[113] T. Guo, H. Pan, E. Gao, X. Zhang, Y. He, Mechanism of Propane Adsorption and the Following NOx Reduction over an In/BEA Catalyst: A Computational Study, *ACS Omega* **7 (2022)** 4501-4513. https://doi.org/10.1021/acsomega.1c06414.

[114] L. Li, N. Guan, HC-SCR reaction pathways on ion exchanged ZSM-5 catalysts, *Microporous Mesoporous Mater.* 117 **(2009)** 450–457. https://doi.org/10.1016/j.micromeso.2008.07.021.

[115] G. Djéga-Mariadassou, From three-way to deNOx catalysis: A general model, *Catal. Today*. 90 **(2004)** 27–34. https://doi.org/10.1016/j.cattod.2004.04.004.

[116] Y. H. Yeom, M. Li, W.M.H. Sachtler, E. Weitz, A study of the mechanism for NOx reduction with ethanol on γ-alumina supported silver, *J. Catal.* 238 **(2006)** 100–110. https://doi.org/10.1016/j.jcat.2005.11.036.

[117] H. Gu, K.M. Chun, S. Song, The effects of hydrogen on the efficiency of NOx reduction via hydrocarbon-selective catalytic reduction (HC-SCR) at low temperature using various reductants, *Int. J. Hydrogen Energy*. 40 **(2015)** 9602–9610. https://doi.org/10.1016/j.ijhydene.2015.05.070.

[118] Z. Liu, J. Wu, C. Hardacre, Research Progress in the Selective Catalytic Reduction of NOx by H_2 in the Presence of O_2, *Catal. Surv. from Asia.* 22 **(2018)** 146–155. https://doi.org/10.1007/s10563-018-9248-3.

[119] K. Liu, Q. Yu, Q. Qin, C. Wang, Selective catalytic reduction of nitric oxide with carbon monoxide over alumina-pellet-supported catalysts in the presence of excess oxygen, *Environ. Technol. (United Kingdom)* 39 **(2018)** 1878–1885. https://doi.org/10.1080/09593330.2017.1341554.

[120] H. Hamada, M. Haneda, A review of selective catalytic reduction of nitrogen oxides with hydrogen and carbon monoxide, *Appl. Catal. A Gen.* 421–422 **(2012)** 1–13. https://doi.org/10.1016/j.apcata.2012.02.005.

[121] Z. Gholami, G. Luo, F. Gholami, F. Yang, Recent advances in selective catalytic reduction of NOx by carbon monoxide for flue gas cleaning process: a review, *Catal. Rev. - Sci. Eng.* 63 **(2021)** 68–119. https://doi.org/10.1080/01614940.2020.1753972.

[122] X. Yan, J. Liu, Y. Yang, Z. Wang, Y. Zheng, A catalytic reaction scheme for NO reduction by CO over Mn-terminated $LaMnO_3$ perovskite: A DFT study, *Fuel Process. Technol.* 216 **(2021)** 106798. https://doi.org/10.1016/j.fuproc.2021.106798.

[123] Z. Hu, X. Yong, D. Li, R. T. Yang, Synergism between palladium and nickel on Pd-Ni/TiO_2 for H_2-SCR: A transient DRIFTS study, *J. Catal.* 381 **(2020)** 204–214. https://doi.org/10.1016/j.jcat.2019.11.006.

[124] B. Frank, G. Emig, A. Renken, Kinetics and mechanism of the reduction of nitric oxides by H_2 under lean-burn conditions on a Pt-Mo-Co/α-Al_2O_3 catalyst, *Appl. Catal. B Environ.* 19 **(1998)** 45–57. https://doi.org/10.1016/S0926-3373(98)00057-5.

[125] K. Duan, B. Chen, T. Zhu, Z. Liu, Mn promoted Pd/TiO_2-Al_2O_3 catalyst for the selective catalytic reduction of NOx by H_2, *Appl. Catal. B Environ.* 176–177 **(2015)** 618–626. https://doi.org/10.1016/j.apcatb.2015.04.048.

[126] M. Komatsubara, A. Koga, M. Tanaka, R. Hagiwara, M. Iwamoto, Three pathways to selective catalytic reduction of NO over Pt/Nb-AlMCM-41 under H2 with excess O_2, *Catal. Sci. Technol.* 6 **(2016)** 7398–7407. https://doi.org/10.1039/c6cy01166g.

[127] R. Wu, L. Li, N. Zhang, J. He, L. Song, G. Zhang, Z. Zhang, H. He, Enhancement of low-temperature NH_3-SCR catalytic activity and H_2O & SO_2 resistance over commercial V_2O_5-MoO_3/TiO_2 catalyst by high shear-induced doping of expanded graphite, *Catal. Today.* 376 **(2021)** 302–310. https://doi.org/10.1016/j.cattod.2020.04.051.

[128] D. Zengel, M. Stehle, O. Deutschmann, M. Casapu, J.D. Grunwaldt, Impact of gas phase reactions and catalyst poisons on the NH_3-SCR activity of a V_2O_5-WO_3/TiO_2 catalyst at pre-turbine position, *Appl. Catal. B Environ.* 288 **(2021)** 119991. https://doi.org/10.1016/j.apcatb.2021.119991.

[129] A. Szymaszek, B. Samojeden, M. Motak, The Deactivation of Industrial SCR Catalysts—A Short Review, *Energies.* 13 **(2020)** 3870. https://doi.org/10.3390/en13153870.

[130] C. Chen, Y. Cao, S. Liu, J. Chen, W. Jia, Review on the latest developments in modified vanadium-titanium-based SCR catalysts, *Chinese J. Catal.* 39 **(2018)** 1347–1365. https://doi.org/10.1016/S1872-2067(18)63090-6.

[131] Y. Qiu, B. Liu, J. Du, Q. Tang, Z. Liu, R. Liu, C. Tao, The monolithic cordierite supported V_2O_5-MoO_3/TiO_2 catalyst for NH_3-SCR, *Chem. Eng. J.* 294 **(2016)** 264–272. https://doi.org/10.1016/j.cej.2016.02.094.

[132] C. Zheng, T. Cheng, L. Yang, H. Wu, H. Fan, Effect of SiO_2 addition on NH_4HSO_4 decomposition and SO_2 poisoning over V_2O_5–MoO_3/TiO_2–CeO_2 catalyst, *J. Environ. Sci. (China).* 91 **(2020)** 279–291. https://doi.org/10.1016/j.jes.2020.01.011.

[133] Y. K. Yu, C. He, J. S. Chen, X. R. Meng, Deactivation mechanism of de-NOx catalyst (V_2O_5-WO_3/TiO_2) used in coal fired power plant, *J. Fuel Chem. Technol.* 40 **(2012)** 1359–1365. https://doi.org/10.1016/s1872-5813(13)60003-1.

[134] M. Zyrkowski, M. Motak, B. Samojeden, K. Szczepanek, Deactivation of V_2O_5-WO_3/TiO_2 DeNOx Catalyst under Commercial Conditions in Power Production Plant, *Energies.* 13 **(2020)** 1–2.

[135] M. Li, B. Liu, X. Wang, X. Yu, S. Zheng, H. Du, D. Dreisinger, Y. Zhang, A promising approach to recover a spent SCR catalyst: Deactivation by arsenic and alkaline metals and catalyst regeneration, *Chem. Eng. J.* 342 **(2018)** 1–8. https://doi.org/10.1016/j.cej.2017.12.132.

[136] M. Kiełtyka, A. P. Soares Dias, H. Kubiczek, B. Sarapata, T. Grzybek, The influence of poisoning on the deactivation of DeNOx catalysts, *Comptes Rendus Chim.* 18 **(2015)** 1036–1048. https://doi.org/10.1016/j.crci.2015.05.004.

[137] Y. Zheng, A.D. Jensen, J.E. Johnsson, Deactivation of V2O5-WO3-TiO2 SCR catalyst at a biomass-fired combined heat and power plant, *Appl. Catal. B Environ.* 60 **(2005)** 253–264. https://doi.org/10.1016/j.apcatb.2005.03.010.

[138] L. Deng, X. Liu, P. Cao, Y. Zhao, Y. Du, C. Wang, D. Che, A study on deactivation of V_2O_5–WO_3–TiO_2 SCR catalyst by alkali metals during entrained-flow combustion, *J. Energy Inst.* 90 **(2017)** 743–751. https://doi.org/10.1016/j.joei.2016.07.003.

[139] Y. Xu, Y. Zhang, F. Liu, W. Shi, J. Yuan, CFD analysis on the catalyst layer breakage failure of an SCR-DeNOx system for a 350 MW coal-fired power plant, *Comput. Chem. Eng.* 69 **(2014)** 119–127. https://doi.org/10.1016/j.compchemeng.2014.07.012.

[140] X. Liu, H. Chen, X. Wu, L. Cao, P. Jiang, Q. Yu, Y. Ma, Effects of SiO_2 modification on the hydrothermal stability of the V_2O_5/WO_3-TiO_2 NH_3-SCR catalyst: TiO_2 structure and vanadia species, *Catal. Sci. Technol.* 9 **(2019)** 3711–3720. https://doi.org/10.1039/c9cy00385a.

[141] J.K. Lai, N.R. Jaegers, B.M. Lis, M. Guo, M.E. Ford, E. Walter, Y. Wang, J.Z. Hu, I.E. Wachs, Structure-Activity Relationships of Hydrothermally Aged Titania-Supported Vanadium-Tungsten Oxide Catalysts for SCR of NOxEmissions with NH_3, *ACS Catal.* 11 **(2021)** 12096–12111. https://doi.org/10.1021/acscatal.1c02130.

[142] A. Marberger, M. Elsener, R.J.G. Nuguid, D. Ferri, O. Kröcher, Thermal activation and aging of a V_2O_5/WO_3-TiO_2 catalyst for the selective catalytic reduction of NO with NH_3, *Appl. Catal. A Gen.* 573 **(2019)** 64–72. https://doi.org/10.1016/j.apcata.2019.01.009.

[143] A. Marberger, M. Elsener, D. Ferri, O. Kröcher, VOx surface coverage optimization of V_2O_5/WO_3-TiO_2 SCR catalysts by variation of the V loading and by aging, *Catalysts.* 5 **(2015)** 1704–1720. https://doi.org/10.3390/catal5041704.

[144] D. Damma, B.M.R. Padmanabha R. Ettireddy, Panagiotis G. Smirniotis, A Review of Low Temperature NH_3-SCR for Removal of NOx, *Catalysts.* 9 **(2019)** 349. https://doi.org/10.3390/catal9040349

[145] D. Wierzbicki, R. Dębek, J. Szczurowski, S. Basąg, M. Włodarczyk, M. Motak, R. Baran, Copper, cobalt and manganese: Modified hydrotalcite materials as catalysts for the selective catalytic reduction of NO with ammonia. the influence of manganese concentration, *Comptes Rendus Chim.* 18 **(2015)** 1074–1083. https://doi.org/10.1016/j.crci.2015.06.009.

[146] B. Samojeden, T. Grzybek, The influence of the promotion of N-modified activated carbon with iron on NO removal by NH_3-SCR, *Energy*. 116 **(2016)** 1484–1491.

[147] J. Li, Y. Peng, H. Chang, X. Li, J.C. Crittenden, J. Hao, Chemical poison and regeneration of SCR catalysts for NOx removal from stationary sources, *Front. Environ. Sci. Eng.* 10 **(2016)** 413–427. https://doi.org/10.1007/s11783-016-0832-3.

[148] S. Li, W. Huang, H. Xu, T. Chen, Y. Ke, Z. Qu, N. Yan, Alkali-induced deactivation mechanism of V_2O_5-WO_3/TiO_2 catalyst during selective catalytic reduction of NO by NH_3 in aluminum hydrate calcining flue gas, *Appl. Catal. B Environ.* 270 **(2020)**. https://doi.org/10.1016/j.apcatb.2020.118872.

[149] Z. Ali, Y. wen Wu, Y. Wu, Z. Arain, M. xin Xu, Q. Lu, H. Ma, H. yu Zhao, Inhibition effects of Pb species on the V_2O_5-MoO_3/TiO_2 catalyst for selective catalytic reduction of NOx with NH_3: A DFT supported experimental study, *Appl. Surf. Sci.* 525 **(2020)**. https://doi.org/10.1016/j.apsusc.2020.146582.

[150] Y. Chai, G. Zhang, H. He, S. Sun, Theoretical study of the catalytic activity and anti-SO_2 poisoning of a MoO_3/V_2O_5 selective catalytic reduction catalyst, *ACS Omega.* 5 **(2020)** 26978–26985. https://doi.org/10.1021/acsomega.0c00018.

[151] B. Samojeden, T. Grzybek, The influence of nitrogen groups introduced onto activated carbons by high- or low-temperature NH_3 treatment on SO_2 sorption capacity, *Adsorpt. Sci. Technol.* 35 **(2017)** 572–581.

[152] C. Erust, A. Akcil, Z. Bedelova, K. Anarbekov, A. Baikonurova, A. Tuncuk, Recovery of vanadium from spent catalysts of sulfuric acid plant by using inorganic and organic acids: Laboratory and semi-pilot tests, *Waste Manag.* 49 **(2016)** 455–461. https://doi.org/10.1016/j.wasman.2015.12.002.

[153] J. Svachula, L.J. Alemany, N. Ferlazzo, P. Forzatti, E. Tronconi, F. Bregani, Oxidation of SO2 to SO_3 over Honeycomb DeNoxing Catalysts, *Ind. Eng. Chem. Res*. 32 **(1993)** 826–834. https://doi.org/10.1021/ie00017a009.

[154] J.P. Dunn, H.G. Stenger, I.E. Wachs, Oxidation of sulfur dioxide over supported vanadia catalysts: Molecular structure - Reactivity relationships and reaction kinetics, *Catal. Today*. 51 **(1999)** 301–318. https://doi.org/10.1016/S0920-5861(99)00052-8.

[155] L. Xu, C. Wang, H. Chang, Q. Wu, T. Zhang, J. Li, New insight into SO2 poisoning and regeneration of CeO_2-WO_3/TiO_2 and V_2O_5-WO_3/TiO_2 catalysts for low-temperature NH_3-SCR, *Environ. Sci. Technol.* 52 **(2018)** 7064–7071.

[156] T. H. Kang, S. Youn, D. H. Kim, Improved catalytic performance and resistance to SO_2 over V_2O_5-WO_3/TiO_2 catalyst physically mixed with Fe_2O_3 for low-temperature NH_3-SCR, *Catal. Today.* 376 **(2021)** 95–103. https://doi.org/10.1016/j.cattod.2020.07.042.

[157] Y. Bu, L. Wang, X. Chen, X. Wei, L. Deng, D. Che, Numerical analysis of ABS deposition and corrosion on a rotary air preheater, *Appl. Therm. Eng.* 131 **(2018)** 669–677. https://doi.org/10.1016/j.applthermaleng.2017.11.082.

[158] M. Qing, S. Lei, F. Kong, L. Liu, W. Zhang, L. Wang, T. Guo, S. Su, S. Hu, Y. Wang, J. Xiang, Analysis of ammonium bisulfate/sulfate generation and deposition characteristics as the by-product of SCR in coal-fired flue gas, *Fuel.* 313 **(2022)** 122790. https://doi.org/10.1016/j.fuel.2021.122790.

[159] Z. Ma, X. Wu, Y. Feng, Z. Si, D. Weng, L. Shi, Low-temperature SCR activity and SO_2 deactivation mechanism of Ce-modified V_2O_5-WO_3/TiO_2 catalyst, *Prog. Nat. Sci. Mater. Int.* 25 **(2015)** 342–352. https://doi.org/10.1016/j.pnsc.2015.07.002.

[160] Y.K. Bae, T.W. Kim, J.R. Kim, Y. Kim, K.S. Ha, H.J. Chae, Enhanced SO2 tolerance of V_2O_5-Sb_2O_3/TiO_2 catalyst for NO reduction with co-use of ammonia and liquid ammonium nitrate, *J. Ind. Eng. Chem.* 96 **(2021)** 277–283. https://doi.org/10.1016/j.jiec.2021.01.029.

[161] D. Ren, K. Gui, S. Gu, Comparison of sulfur poisoning resistance of Ce/Mn doped γ-Fe_2O_3 (0 0 1) surface in NH_3-SCR reaction with DFT method, *Appl. Surf. Sci.* 561 **(2021)** 149847. https://doi.org/10.1016/j.apsusc.2021.149847.

[162] Q. Liang, J. Li, T. Yue, Promotional effect of CeO_2 on low-temperature selective catalytic reduction of NO by NH_3 over V_2O_5-WO_3/TiO_2 catalysts, *Environ. Technol. Innov.* 21 **(2021).** https://doi.org/10.1016/j.eti.2020.101209.

[163] A.D. Phule, J.H. Choi, J.H. Kim, High performance of catalytic sheet filters of V_2O_5-WO_3/TiO_2 for NOx reduction, *Environ. Sci. Pollut. Res.* 28 **(2021)** 34009–34016. https://doi.org/10.1007/s11356-020-10552-2.

[164] L. Jiang, Q. Liu, G. Ran, M. Kong, S. Ren, J. Yang, J. Li, V_2O_5-modified Mn-Ce/AC catalyst with high SO_2 tolerance for low-temperature NH_3-SCR of NO, *Chem. Eng. J.* 370 **(2019)** 810–821. https://doi.org/10.1016/j.cej.2019.03.225.

[165] X. Guo, C. Bartholomew, W. Hecker, L.L. Baxter, Effects of sulfate species on V_2O_5/TiO_2 SCR catalysts in coal and biomass-fired systems, *Appl. Catal. B Environ.* 92 **(2009)** 30–40. https://doi.org/10.1016/j.apcatb.2009.07.025.

[166] X. Du, J. Xue, X. Wang, Y. Chen, J. Ran, L. Zhang, J., Oxidation of sulfur dioxide over VO/TiO catalyst with low vanadium loading: a theoretical study, *J. Phys. Chem.* 122 **(2018)** 4517–4523. https://doi.org/10.1002/9783527809080.cataz12094.

[167] T. Lee, H. Bai, Metal Sulfate Poisoning Effects over $MnFe/TiO_2$ for Selective Catalytic Reduction of NO by NH_3 at Low Temperature, *Ind. Eng. Chem. Res.* 57 **(2018)** 4848–4858. https://doi.org/10.1021/acs.iecr.8b00511.

[168] Y. Xu, X. Wu, Q. Lin, J. Hu, R. Ran, D. Weng, SO_2 promoted V_2O_5-MoO_3/TiO_2 catalyst for NH_3-SCR of NOx at low temperatures, *Appl. Catal. A Gen.* 570 **(2019)** 42–50. https://doi.org/10.1016/j.apcata.2018.10.040.

[169] J. Miao, H. Li, Q. Su, Y. Yu, Y. Chen, J. Chen, J. Wang, The combined promotive effect of SO_2 and HCl on Pb-poisoned commercial NH_3-SCR V_2O_5-WO_3/TiO_2 catalysts, *Catal. Commun*. 125 **(2019)** 118–122. https://doi.org/10.1016/j.catcom.2019.03.030.

[170] R. Khodayari, C.U.I. Odenbrand, Regeneration of commercial SCR catalysts by washing and sulphation: Effect of sulphate groups on the activity, *Appl. Catal. B Environ.* 33 **(2001)** 277–291. https://doi.org/10.1016/S0926-3373(01)00193-X.

[171] Y. Peng, J. Li, W. Shi, J. Xu, J. Hao, Design strategies for development of SCR catalyst: Improvement of alkali poisoning resistance and novel regeneration method, *Environ. Sci. Technol.* 46 **(2012)** 12623–12629. https://doi.org/10.1021/es302857a.

[172] F. Moradi, J. Brandin, M. Sohrabi, M. Faghihi, M. Sanati, Deactivation of oxidation and SCR catalysts used in flue gas cleaning by exposure to aerosols of high- and low melting point salts, potassium salts and zinc chloride, *Appl. Catal. B Environ.* 46 **(2003)** 65–76. https://doi.org/10.1016/S0926-3373(03)00179-6.

[173] T. Lei, Q. Li, S. Chen, Z. Liu, Q. Liu, KCl-induced deactivation of V_2O_5-WO_3/TiO_2 catalyst during selective catalytic reduction of NO by NH_3: Comparison of poisoning methods, *Chem. Eng. J.* 296 **(2016)** 1–10. https://doi.org/10.1016/j.cej.2016.03.095.

[174] F. Tang, B. Xu, H. Shi, J. Qiu, Y. Fan, The poisoning effect of Na^+ and Ca^{2+} ions doped on the V_2O_5/TiO_2 catalysts for selective catalytic reduction of NO by NH_3, *Appl. Catal. B Environ.* 94 **(2010)** 71–76. https://doi.org/10.1016/j.apcatb.2009.10.022.

[175] Y. Yu, J. Wang, J. Chen, X. Meng, Y. Chen, C. He, Promotive effect of SO_2 on the activity of a deactivated commercial selective catalytic reduction catalyst: An in situ DRIFT study, *Ind. Eng. Chem. Res.* 53 **(2014)** 16229–16234. https://doi.org/10.1021/ie502065b.

[176] Z. Ali, Q. Lu, T. Iqbal, Z. Arain, J. Han, Y. wen Wu, D. jia Liu, Y. Ping Yang, Poisoning effects of lead species on the V_2O_5-WO_3/TiO_2 type NH_3-selective catalytic reduction catalyst, *Asia-Pacific J. Chem. Eng.* 14 **(2019)** 1–8. https://doi.org/10.1002/apj.2309.

[177] Y. Jiang, X. Gao, Y. Zhang, W. Wu, Z. Luo, K. Cen, $PbCl_2$-poisoning kinetics of V_2O_5-TiO_2 catalysts for the selective catalytic reduction of NO with NH_3, *Environ. Prog. Sustain. Energy.* 34 **(2015)** 1085–1091. https://doi.org/10.1002/ep.

[178] J. Miao, X. Yi, Q. Su, H. Li, J. Chen, J. Wang, Poisoning Effects of Phosphorus, Potassium and Lead on V_2O_5-WO_3/TiO_2 Catalysts for Selective Catalytic Reduction with NH_3, *Catalysts.* 10 **(2020)**. https://doi.org/10.3390/catal10030345

[179] L. Qi, J. Li, Y. Yao, Y. Zhang, Heavy metal poisoned and regeneration of selective catalytic reduction catalysts, *J. Hazard. Mater.* 366 **(2019**) 492–500. https://doi.org/10.1016/j.jhazmat.2018.11.112.

[180] Q. Lu, X.Q. Pei, Y.W. Wu, M.X. Xu, D.J. Liu, L. Zhao, Deactivation Mechanism of the Commercial V_2O_5-MoO_3/TiO_2 Selective Catalytic Reduction Catalyst by Arsenic Poisoning in Coal-Fired Power Plants, *Energy* and Fuels. 34 **(2020)** 4865–4873. https://doi.org/10.1021/acs.energyfuels.0c00066.

[181] M. Kong, Q. Liu, X. Wang, S. Ren, J. Yang, D. Zhao, W. Xi, L. Yao, Performance impact and poisoning mechanism of arsenic over commercial V_2O_5-WO_3/TiO_2 SCR catalyst, *Catal. Commun.* 72 **(2015)** 121–126. https://doi.org/10.1016/j.catcom.2015.09.029.

[182] X. Fang, Y. Liu, L. Chen, Y. Cheng, Influence of surface active groups on SO_2 resistance of birnessite for low-temperature NH3-SCR, *Chem. Eng. J.* 399 **(2020)** 125798. https://doi.org/10.1016/j.cej.2020.125798.

[183] Z.G. Liu, N.A. Ottinger, C.M. Cremeens, Vanadium and tungsten release from V-based selective catalytic reduction diesel aftertreatment, *Atmos. Environ*. 104 **(2015)** 154–161. https://doi.org/10.1016/j.atmosenv.2014.12.063.

[184] I. Zwolak, Vanadium carcinogenic, immunotoxic and neurotoxic effects: A review of in vitro studies, *Toxicol. Mech. Methods.* 24 **(2014)** 1–12. https://doi.org/10.3109/15376516.2013.843110.

[185] EPA United States Environmental Protection Agency: Technical Fact Sheet - Tungsten (January 2014). https://www.epa.gov/sites/default/files/201403/documents/ffrrofactsheet_contaminant_tungsten_january2014_final.pdf. Accessed date: 16th of June 2022.

[186] L. Han, S. Cai, M. Gao, J.Y. Hasegawa, P. Wang, J. Zhang, L. Shi, D. Zhang, Selective Catalytic Reduction of NOx with NH_3 by Using Novel Catalysts: State of the Art and Future Prospects, *Chem. Rev.* 119 **(2019)** 10916–10976. https://doi.org/10.1021/acs.chemrev.9b00202.

[187] W. Stawiński, A. Węgrzyn, T. Dańko, O. Freitas, S. Figueiredo, L. Chmielarz, Acid-base treated vermiculite as high performance adsorbent: Insights into the mechanism of cationic dyes adsorption, regeneration, recyclability and stability studies, *Chemosphere.* 173 **(2017)** 107–115. https://doi.org/10.1016/j.chemosphere.2017.01.039.

[188] T.T. Zhu, C.H. Zhou, F.B. Kabwe, Q.Q. Wu, C.S. Li, J.R. Zhang, Exfoliation of montmorillonite and related properties of clay/polymer nanocomposites, *Appl. Clay Sci.* 169 **(2019)** 48–66. https://doi.org/10.1016/j.clay.2018.12.006.

[189] C.H. Zhou, An overview on strategies towards clay-based designer catalysts for green and sustainable catalysis, *Appl. Clay Sci.* 53 **(2011)** 87–96. https://doi.org/10.1016/j.clay.2011.04.016.

[190] L. Chmielarz, P. Kuśtrowski, M. Zbroja, A. Rafalska-Łasocha, B. Dudek, R. Dziembaj, SCR of NO by NH_3 on alumina or titania-pillared montmorillonite various modified with Cu or Co: Part I. General characterization and catalysts screening, *Appl. Catal. B Environ.* 45 **(2003)** 103–116. https://doi.org/10.1016/S0926-3373(03)00121-8.

[191] A. Amari, H. Gannouni, M.I. Khan, M.K. Almesfer, A.M. Elkhaleefa, A. Gannouni, Effect of structure and chemical activation on the adsorption properties of green clay minerals for the removal of cationic dye, *Appl. Sci.* 8 **(2018)** 2302. https://doi.org/10.3390/app8112302.

[192] P. Komadel, Acid activated clays: Materials in continuous demand, *Appl. Clay Sci.* 131 **(2016)** 84–99. https://doi.org/10.1016/j.clay.2016.05.001.

[193] A. Gil, S. A. Korili, R. Trujillano, M. A. Vincente, Pillared Clays and Related Catalysts, Springer 2010^{th} Edition, ISBN: 978-1-4419-6669-8. https://doi.org/10.1007/978-1-4419-6670-4.

[194] T. Grzybek, Layered clays as SCR deNOx catalysts, *Catal. Today*. 119 (**2007)** 125–132. https://doi.org/10.1016/j.cattod.2006.08.006.

[195] J. H. Park, H. J. Shin, M. H. Kim, J. S. Kim, N. Kang, J.Y. Lee, K.T. Kim, J. I. Lee, D.D. Kim, Application of montmorillonite in bentonite as a pharmaceutical excipient in drug delivery systems, *J. Pharm. Investig.* 46 **(2016)** 363–375. https://doi.org/10.1007/s40005-016-0258-8.

[196] L. Chmielarz, P. Kuśtrowski, Z. Piwowarska, M. Michalik, B. Dudek, R. Dziembaj, Natural micas intercalated with Al2O3 and Modified with transition metals as catalysts of the selective

oxidation of ammonia to nitrogen, *Top. Catal.* 52 **(2009)** 1017–1022. https://doi.org/10.1007/s11244-009-9263-8.

[197] Lucjan Chmielarz, M. Wojciechowska, M. Rutkowska, A. Adamski, A. Węgrzyn, A. Kowalczyk, B. Dudek, P. Boroń, M. Michalik, A. Matusiewicz, Acid-activated vermiculites as catalysts of DeNOx process, *Catal. Today.* 191 **(2012)** 25–31. https:// 10.1016/j.clay.2010.04.020

[198] L. Chmielarz, A. Kowalczyk, M. Wojciechowska, P. Boroń, B. Dudek, M. Michalik, Montmorillonite intercalated with SiO_2, SiO_2-Al_2O_3 or SiO_2-TiO_2 pillars by surfactant-directed method as catalytic supports for DeNOx process, *Chem. Pap.* 68 **(2014)** 1219–1227. https://doi.org/10.2478/s11696-013-0463-0.

[199] S.S.G. Santos, H.R.M. Silva, A.G. de Souza, A.P.M. Alves, E.C. da Silva Filho, M.G. Fonseca, Acid-leached mixed vermiculites obtained by treatment with nitric acid, *Appl. Clay Sci.* 104 **(2015)** 286–294. https://doi.org/10.1016/j.clay.2014.12.008.

[200] B. Samojeden, T. Grzybek, J. Kowal, A. Szymaszek, M. Jabłońska, R. Gläser, M. Motak, The influence of holmium on catalytic properties of Fe or Cu-modified vermiculites, *Physicochem. Probl. Miner. Process.* 55 **(2019)** 1484–1495. https://doi.org/10.5277/ppmp19074.

[201] W. Stawiński, O. Freitas, L. Chmielarz, A. Węgrzyn, K. Komędera, A. Błachowski, S. Figueiredo, The influence of acid treatments over vermiculite based material as adsorbent for cationic textile dyestuffs, *Chemosphere.* 153 **(2016)** 115–129. https://doi.org/10.1016/j.chemosphere.2016.03.004.

[202] L. Chmielarz, M. Rutkowska, A. Kowalczyk, Advances in Functionalization of Inorganic Porous Materials for Environmental Catalysis, *Adv. Inorg. Chem.* 72 **(2018)** 323–383. https://doi.org/10.1016/bs.adioch.2018.05.005.

[203] L. Chmielarz, R. Dziembaj, Modified layered silicas as catalysts for conversion of nitrogen pollutants in flue gases—a review, *Catalysts.* 11 **(2021)**. https://doi.org/10.3390/catal11050644.

[204] P. Ziemiański, K. Kałahurska, B. Samojeden, Selective catalytic reduction of NO with NH_3 on mixed alumina–iron (III) oxide pillared montmorillonite "Cheto" Arizona, modified with hexamminecobalt (III) chloride, *Adsorpt. Sci. Technol.* 35 **(2017)** 825–833. https://doi.org/10.1177/0263617417710141.

[205] L. Chmielarz, M. Zbroja, P. Kuśtrowski, B. Dudek, A. Rafalska-Łasocha, R. Dziembaj, Pillared montmorillonites modified with silver: Temperature programmed desorption studies, *J. Therm. Anal. Calorim.* 77 **(2004)** 115–123. https://doi.org/10.1023/B:JTAN.0000033194.99509.c5.

[206] A. Galarneau, A. Barodawalla, T.J. Pinnavaia, Porous clay heterostructures formed by gallery-templated synthesis, *Nature.* 374 **(1995)** 529–531. https://doi.org/10.1038/374529a0.

[207] S. Chotiradsirikun, R. Guo, A.S. Bhalla, H. Manuspiya, Novel synthesis route of porous clay heterostructures via mixed surfactant template and their dielectric behavior, *J. Porous Mater.* 28 **(2021)** 117–128. https://doi.org/10.1007/s10934-020-00971-4.

[208] L. Chmielarz, A. Kowalczyk, M. Skoczek, M. Rutkowska, B. Gil, P. Natkański, M. Radko, M. Motak, R. Dębek, J. Ryczkowski, Porous clays heterostructures intercalated with multicomponent pillars as catalysts for dehydration of alcohols, *Appl. Clay Sci.* 160 **(2018)** 116–125.

[209] L. Chmielarz, B. Gil, P. Kuśtrowski, Z. Piwowarska, B. Dudek, M. Michalik, Montmorillonite-based porous clay heterostructures (PCHs) intercalated with silica-titania pillars-synthesis and characterization, *J. Solid State Chem.* 182 **(2009)** 1094–1104. https://doi.org/10.1016/j.jssc.2009.02.017.

[210] S. Ren, F. Guo, J. Yang, L. Yao, Q. Zhao, M. Kong, Selection of carbon materials and modification methods in low-temperature sintering flue gas denitrification, *Chem. Eng. Res. Des.* 126 **(2017)** 278–285. https://doi.org/10.1016/j.cherd.2017.08.022.

[211] J. Yang, J. Zhou, W. Tong, T. Zhang, M. Kong, S. Ren, Low-temperature flue gas denitration with transition metal oxides supported on biomass char, *J. Energy Inst.* 92 **(2019)** 1158–1166. https://doi.org/10.1016/j.joei.2018.06.002.

[212] M. Saad, A. Szymaszek, A. Białas, B. Samojeden, M. Motak, SO_2 poisoning and recovery of copper-based activated carbon catalysts for selective catalytic reduction of no with NH_3 at low temperature, *Catalysts.* 10 **(2020)** 1–21. https://doi.org/10.3390/catal10121426.

[213] M. Saad, A. Szymaszek, A. Białas, B. Samojeden, M. Motak, The enhanced performance of n-modified activated carbon promoted with ce in selective catalytic reduction of NOx with NH_3, *Catalysts.* 10 **(2020)** 1–20. https://doi.org/10.3390/catal10121423.

[214] J. Chen, J. Chen, B. Yang, Y. Zhao, Y.D. Lim, Y. Li, A primary understanding of field emission from superhigh specific surface area activated carbon with interconnection structure, *Appl. Surf. Sci.* 553 **(2021)** 149583. https://doi.org/10.1016/j.apsusc.2021.149583.

[215] K. Silas, W.A.W.A.K. Ghani, T.S.Y. Choong, U. Rashid, Carbonaceous materials modified catalysts for simultaneous SO_2/NOx removal from flue gas: A review, *Catal. Rev. - Sci. Eng.* 61 **(2019)** 134–161. https://doi.org/10.1080/01614940.2018.1482641.

[216] Y. Guo, Y. Li, T. Zhu, M. Ye, Investigation of SO_2 and NO adsorption species on activated carbon and the mechanism of NO promotion effect on SO_2, *Fuel.* 143 **(2015)** 536–542. https://doi.org/10.1016/j.fuel.2014.11.084.

[217] P.J.F. Harris, Z. Liu, K. Suenaga, Imaging the atomic structure of activated carbon, *J. Phys. Condens. Matter.* 20 **(2008)** 362201. https://doi.org/10.1088/0953-8984/20/36/362201.

[218] J. Klinik, B. Samojeden, T. Grzybek, W. Suprun, H. Papp, R. Gläser, Nitrogen promoted activated carbons as DeNOx catalysts. 2. the influence of water on the catalytic performance, *Catal. Today.* 176 **(2011)** 303–308. https://doi.org/10.1016/j.cattod.2010.12.009.

[219] Y. Lin, Y. Li, Z. Xu, J. Xiong, T. Zhu, Transformation of functional groups in the reduction of NO with NH_3 over nitrogen-enriched activated carbons, *Fuel.* 223 **(2018)** 312–323. https://doi.org/10.1016/j.fuel.2018.01.092.

[220] W. Li, S. Jin, R. Zhang, Y. Wei, J. Wang, S. Yang, H. Wang, M. Yang, Y. Liu, W. Qiao, L. Ling, M. Jin, Insights into the promotion role of phosphorus doping on carbon as a metal-free catalyst for lowerature selective catalytic reduction of NO with NH_3, *RSC Adv.* 10 **(2020)** 12908–12919. https://doi.org/10.1039/d0ra01654c.

[221] Q. Guo, W. Jing, Y. Hou, Z. Huang, G. Ma, X. Han, D. Sun, On the nature of oxygen groups for NH_3-SCR of NO over carbon at low temperatures, *Chem. Eng. J.* 270 **(2015)** 41–49. https://doi.org/10.1016/j.cej.2015.01.086.

[222] Y. Li, Y. Lin, C. Cheng, J. Hao, T. Zhu, On the Nature of Nitrogen-Containing Groups in the SCR of NO Over Functionalized Activated Coke, *Waste and Biomass Valorization.* 11 **(2020)** 1691–1699. https://doi.org/10.1007/s12649-018-0428-1.

[223] L. Yao, Q. Liu, S. Mossin, D. Nielsen, M. Kong, L. Jiang, J. Yang, S. Ren, J. Wen, Promotional effects of nitrogen doping on catalytic performance over manganese-containing semi-coke catalysts for the NH_3-SCR at low temperatures, *J. Hazard. Mater.* 387 **(2020)**. https://doi.org/10.1016/j.jhazmat.2019.121704.

[224] J. Yang, S. Ren, T. Zhang, Z. Su, H. Long, M. Kong, L. Yao, Iron doped effects on active sites formation over activated carbon supported Mn-Ce oxide catalysts for low-temperature SCR of NO, *Chem. Eng. J.* 379 **(2020)**. https://doi.org/10.1016/j.cej.2019.122398.

[225] J. Xu, H. Liu, Y. Sun, H. Zhao, L. Lv, Y. Wu, X. Zhang, Enhancing low-temperature SCR deNOx MnCe catalyst based on rice husk char by KOH and H_3PO_4 activation, *J. Chem. Technol. Biotechnol.* **(2021)** 749-758**.** https://doi.org/10.1002/jctb.6962.

[226] Y. Qin, C. Wang, X. Sun, Y. Ma, X. Song, F. Wang, K. Li, P. Ning, Defects on activated carbon determine the dispersion of active components and thus the simultaneous removal efficiency of SO_2, NOx and Hg^0, Fuel. 293 **(2021)** 120391. https://doi.org/10.1016/j.fuel.2021.120391.

[227] Y. Ye, J. Xie, D. Fang, X. Wang, F. He, Q. Jin, Effect of acid treatment on surfaces of activated carbon supported catalysts for NO and SO_2 removal, Fullerenes Nanotub. Carbon Nanostructures. 30 **(2021)** 297-305. https://doi.org/10.1080/1536383X.2021.1938000.

[228] Y. Guo, Y. Li, T. Zhu, M. Ye, Effects of concentration and adsorption product on the adsorption of SO_2 and NO on activated carbon, *Energy and Fuels*. 27 **(2013)** 360–366. https://doi.org/10.1021/ef3016975.

[229] S. Ren, S. Li, Z. Su, J. Yang, H. Long, M. Kong, J. Yang, Z. Cai, Poisoning effects of KCl and As2O3 on selective catalytic reduction of NO with NH_3 over Mn-Ce/AC catalysts at low temperature, *Chem. Eng. J.* 351 **(2018)** 540–547. https://doi.org/10.1016/j.cej.2018.06.085.

[230] Z. hui Su, S. Ren, T. shi Zhang, J. Yang, Y. han Zhou, L. Yao, Effects of PbO poisoning on Ce–Mn/AC catalyst for low-temperature selective catalytic reduction of NO with NH_3, *J. Iron Steel Res. Int.* 28 **(2021)** 133–139. https://doi.org/10.1007/s42243-020-00420-1.

[231] H. Chen, Y.J. Zhang, P.Y. He, C.J. Li, L.C. Liu, Facile synthesis of cost-effective iron enhanced hetero-structure activated carbon/geopolymer composite catalyst for NH_3-SCR: Insight into the role of iron species, *Appl. Catal. A Gen.* 605 **(2020)** 117804. https://doi.org/10.1016/j.apcata.2020.117804.

[232] J. Li, H. Chang, L. Ma, J. Hao, R.T. Yang, Low-temperature selective catalytic reduction of NOx with NH_3 over metal oxide and zeolite catalysts-A review, *Catal. Today*. 175 **(2011)** 147–156. https://doi.org/10.1016/j.cattod.2011.03.034.

[233] H. Jiang, C. Wang, H. Wang, M. Zhang, Synthesis of highly efficient MnOx catalyst for low-temperature NH_3-SCR prepared from Mn-MOF-74 template, *Mater. Lett.* 168 **(2016)** 17–19. https://doi.org/10.1016/j.matlet.2015.12.150.

[234] L. Ma, C.Y. Seo, M. Nahata, X. Chen, J. Li, J.W. Schwank, Shape dependence and sulfate promotion of CeO_2 for selective catalytic reduction of NOx with NH_3, *Appl. Catal. B Environ.* 232 **(2018)** 246–259. https://doi.org/10.1016/j.apcatb.2018.03.065.

[235] C. xu Li, Z. bo Xiong, Y. ping Du, X. Ning, Z. zhuang Li, J. fei He, X. ke Qu, W. Lu, S. mu Wu, L. zhi Tan, Promotional effect of tungsten modification on magnetic iron oxide catalyst for selective catalytic reduction of NO with NH_3, *J. Energy Inst. 93* **(2020)** 1809–1818. https://doi.org/10.1016/j.joei.2020.03.012.

[236] G. Huan Yao, F. Wang, X. Bo Wang, K. Ting Gui, Magnetic field effects on selective catalytic reduction of NO by NH_3 over Fe_2O_3 catalyst in a magnetically fluidized bed, *Energy.* 35 **(2010)** 2295–2300. https://doi.org/10.1016/j.energy.2010.02.017.

[237] M. D. Amiridis, I. E. Wachs, G. Deo, J. M. Jehng, D.S. Kim, Reactivity of V_2O_5 catalysts for the selective catalytic reduction of NO by NH_3: Influence of vanadia loading, H_2O, and SO_2, *J. Catal.* 161 **(1996)** 247–253. https://doi.org/10.1006/jcat.1996.0182.

[238] S. Wu, L. Zhang, X. Wang, W. Zou, Y. Cao, J. Sun, C. Tang, F. Gao, Y. Deng, L. Dong, Synthesis, characterization and catalytic performance of FeMnTiOx mixed oxides catalyst prepared by a CTAB-assisted process for mid-low temperature NH_3-SCR, *Appl. Catal. A Gen.* 505 **(2015)** 235–242. https://doi.org/10.1016/j.apcata.2015.08.009.

[239] G.S. Parkinson, Iron oxide surfaces, *Surf. Sci. Rep.* 71 **(2016)** 272–365. https://doi.org/10.1016/j.surfrep.2016.02.001.

[240] C. Liu, S. Yang, L. Ma, Y. Peng, A. Hamidreza, H. Chang, J. Li, Comparison on the performance of α-Fe_2O_3 and γ-Fe_2O_3 for selective catalytic reduction of nitrogen oxides with ammonia, *Catal. Letters.* 143 **(2013)** 697–704. https://doi.org/10.1007/s10562-013-1017-3.

[241] G.H. Yao, K.T. Gui, F. Wang, Low-temperature De-NOx by selective catalytic reduction based on iron-based catalysts, *Chem. Eng. Technol.* 33 **(2010)** 1093–1098. https://doi.org/10.1002/ceat.201000015.

[242] Y. Peng, H. Chang, Y. Dai, J. Li, Structural and Surface Effect of MnO_2 for Low Temperature Selective Catalytic Reduction of NO with NH_3, *Procedia Environ. Sci.* 18 **(2013)** 384–390. https://doi.org/10.1016/j.proenv.2013.04.051.

[243] X. Tang, J. Li, L. Sun, J. Hao, Origination of N_2O from NO reduction by NH_3 over β-MnO_2 and α-Mn_2O_3, *Appl. Catal. B Environ.* 99 **(2010)** 156–162. https://doi.org/10.1016/j.apcatb.2010.06.012.

[244] H. Liu, Y. Wu, L. Liu, B. Chu, Z. Qin, G. Jin, Z. Tong, L. Dong, B. Li, Three-dimensionally ordered macroporous Fe-doped ceria catalyst with enhanced activity at a wide operating temperature window for selective catalytic reduction of NOx, *Appl. Surf. Sci.* 498 **(2019)** 143780. https://doi.org/10.1016/j.apsusc.2019.143780.

[245] Y. Ma, X. Tang, F. Gao, H. Yi, S. Zhao, Y. Shi, C. Wang, Selective catalytic reduction of NOx with NH_3 over iron-cerium mixed oxide catalyst prepared by different methods, *J. Chem. Technol. Biotechnol.* 95 **(2020)** 232–245. https://doi.org/10.1002/jctb.6226.

[246] S. Yang, C. Liu, H. Chang, L. Ma, Z. Qu, N. Yan, C. Wang, J. Li, Improvement of the activity of γ-Fe_2O_3 for the selective catalytic reduction of NO with NH_3 at high temperatures: NO reduction versus NH_3 oxidization, *Ind. Eng. Chem. Res.* 52 **(2013)** 5601–5610. https://doi.org/10.1021/ie303272u.

[247] Z. Liu, H. Su, B. Chen, J. Li, S.I. Woo, Activity enhancement of WO3 modified Fe_2O_3 catalyst for the selective catalytic reduction of NOx by NH_3, *Chem. Eng. J.* 299 **(2016)** 255–262. https://doi.org/10.1016/j.cej.2016.04.100.

[248] A. Stahl, Z. Wang, T. Schwämmle, J. Ke, X. Li, Novel Fe-W-Ce mixed oxide for the selective catalytic reduction of NOx with NH_3 at low temperatures, *Catalysts.* 7 **(2017)** 71. https://doi.org/10.3390/catal7020071.

[249] A. Szymaszek, M. Motak, B. Samojeden, The application of modified layered double hydroxides in selective catalytic reduction of nitrogen oxides by ammonia (NH_3-SCR), *Polish J. Chem. Technol.* 22 **(2020)** 61–67. https://doi.org/10.2478/pjct-2020-0009.

[250] P. Summa, B. Samojeden, M. Motak, D. Wierzbicki, I. Alxneit, K. Świerczek, P. Da Costa, Investigation of Cu promotion effect on hydrotalcite-based nickel catalyst for CO_2 methanation, *Catal. Today.* 384–386 **(2022)** 133–145. https://doi.org/10.1016/j.cattod.2021.05.004.

[251] T. Baskaran, J. Christopher, A. Sakthivel, Progress on layered hydrotalcite (HT) materials as potential support and catalytic materials, *RSC Adv.* 5 **(2015)** 98853–98875. https://doi.org/10.1039/c5ra19909c.

[252] R. Wang, X. Wu, C. Zou, X. Li, Y. Du, Nox removal by selective catalytic reduction with ammonia over a hydrotalcite-derived NiFe mixed oxide, *Catalysts.* 8 **(2018)**. https://doi.org/10.3390/catal8090384.

[253] Y.S. Wei, M. Zhang, R. Zou, Q. Xu, Metal-Organic Framework-Based Catalysts with Single Metal Sites, *Chem. Rev.* 120 **(2020)** 12089–12174. https://doi.org/10.1021/acs.chemrev.9b00757.

[254] G. Cai, P. Yan, L. Zhang, H.C. Zhou, H.L. Jiang, Metal-Organic Framework-Based Hierarchically Porous Materials: Synthesis and Applications, *Chem. Rev.* 121 **(2021)** 12278–12326. https://doi.org/10.1021/acs.chemrev.1c00243.

[255] MIL-53, https://en.wikipedia.org/wiki/MIL-53. Accessed: 15th of February 2022.

[256] HKUST-1, https://en.wikipedia.org/wiki/HKUST-1. Accessed: 15th of February 2022.

[257] MOF-5, https://en.wikipedia.org/wiki/MOF-5. Accessed: 15th of February 2022.

[258] C. Li, Y. Shi, H. Zhang, Q. Zhao, F. Xue, X. Li, Cu-BTC metal-organic framework as a novel catalyst for low temperature selective catalytic reduction (SCR) of NO by NH_3: Promotional effect of activation temperature, *Integr. Ferroelectr.* 172 **(2016)** 169–179. https://doi.org/10.1080/10584587.2016.1177385.

[259] Q. Wang, H. Xu, W. Huang, Z. Pan, H. Zhou, Metal organic frameworks-assisted fabrication of CuO/Cu_2O for enhanced selective catalytic reduction of NOx by NH_3 at low temperatures, *J. Hazard. Mater.* 364 **(2019)** 499–508. https://doi.org/10.1016/j.jhazmat.2018.10.067.

[260] X. Sun, Y. Shi, W. Zhang, C. Li, Q. Zhao, J. Gao, X. Li, A new type Ni-MOF catalyst with high stability for selective catalytic reduction of NOx with NH_3, *Catal. Commun.* 114 **(2018)** 104–108. https://doi.org/10.1016/j.catcom.2018.06.012.

[261] S. Smolders, J. Jacobsen, N. Stock, D. De Vos, Selective catalytic reduction of NO by cerium-based metal-organic frameworks, *Catal. Sci. Technol.* 10 **(2020)** 337–341. https://doi.org/10.1039/c9cy02029b.

[262] P. Wang, H. Sun, X. Quan, S. Chen, Enhanced catalytic activity over MIL-100(Fe) loaded ceria catalysts for the selective catalytic reduction of NOx with NH_3 at low temperature, *J. Hazard. Mater.* 301 **(2016)** 512–521. https://doi.org/10.1016/j.jhazmat.2015.09.024.

[263] M. Zhang, B. Huang, H. Jiang, Y. Chen, Metal-organic framework loaded manganese oxides as efficient catalysts for low-temperature selective catalytic reduction of NO with NH_3, *Front. Chem. Sci. Eng.* 11 **(2017)** 594–602. https://doi.org/10.1007/s11705-017-1668-5.

[264] H. Sun, Z. Liu, Y. Wang, X. Quan, G. Zhao, Novel metal-organic framework supported manganese oxides for the selective catalytic reduction of NOx with NH_3: Promotional role of the support, *J. Hazard. Mater.* 380 **(2019)** 120800. https://doi.org/10.1016/j.jhazmat.2019.120800.

[265] S. Das, S. Xu, T. Ben, S. Qiu, Chiral Recognition and Separation by Chirality-Enriched Metal–Organic Frameworks, *Angew. Chemie - Int. Ed.* 57 **(2018)** 8629–8633. https://doi.org/10.1002/anie.201804383.

[266] D.G. Parker, Working with Zeolites: A Reflection on Catalyst Development in Industry, *Top. Catal.* 64 **(2021)** 889–895. https://doi.org/10.1007/s11244-021-01446-9.

[267] R. Bulanek, Catalysis in Zeolites and Zeotypes - Cornerstone of Chemical Industry and Permanent Subject of Research, *Catalysts*. 12 **(2022)** 53. https://doi.org/10.3390/catal12010053.

[268] J. Čejka, R. Millini, M. Opanasenko, D.P. Serrano, W.J. Roth, Advances and challenges in

zeolite synthesis and catalysis, *Catal. Today.* 345 **(2020)** 2–13. https://doi.org/10.1016/j.cattod.2019.10.021.

[269] D.H. Baerlocher, C.; McCusker, L. B.; Olson, Atlas of Zeolite Framework Types; Elsevier: Amsterdam, 2007, http://www.iza-structure.org/. Accesed date: 17th of March 2022.

[270] M.E. Davis, Zeolites from a materials chemistry perspective, *Chem. Mater.* 26 **(2014)** 239–245. https://doi.org/10.1021/cm401914u.

[271] J. Szerement, A. Szatanik-Kloc, R. Jarosz, T. Bajda, M. Mierzwa-Hersztek, Contemporary applications of natural and synthetic zeolites from fly ash in agriculture and environmental protection, *J. Clean. Prod.* 311 **(2021)** 127461. https://doi.org/10.1016/j.jclepro.2021.127461.

[272] S. Mohan, P. Dinesha, S. Kumar, NOx reduction behaviour in copper zeolite catalysts for ammonia SCR systems: A review, *Chem. Eng. J.* 384 **(2020)** 123253. https://doi.org/10.1016/j.cej.2019.123253.

[273] B. Jha, D.N. Singh, Fly Ash Zeolites Innovation, Applications, and Directions, Advanced Structured Materials (Strucmat) Springer Singapore. 78 **(2016).** https://doi.org/10.1007/978-981-10-1404-8.

[274] M. Noviello, C.E. Gattullo, M. Faccia, V.M. Paradiso, G. Gambacorta, Application of natural and synthetic zeolites in the oenological field, *Food Res. Int.* 150 **(2021)** 110737. https://doi.org/10.1016/j.foodres.2021.110737.

[275] A. Damodara Kannan, P. Parameswaran, Ammonia adsorption and recovery from swine wastewater permeate using naturally occurring clinoptilolite, *J. Water Process Eng.* 43 **(2021)** 102234. https://doi.org/10.1016/j.jwpe.2021.102234.

[276] A. Shamshiri, V. Alimohammadi, M. Sedighi, E. Jabbari, M. Mohammadi, Enhanced removal of phosphate and nitrate from aqueous solution using novel modified natural clinoptilolite nanoparticles: process optimization and assessment, *Int. J. Environ. Anal. Chem.* 00 **(2020)** 1–20. https://doi.org/10.1080/03067319.2020.1807525.

[277] M. Shamzhy, B. Gil, M. Opanasenko, W.J. Roth, J. Čejka, MWW and MFI frameworks as model layered zeolites: Structures, transformations, properties, and activity, *ACS Catal.* 11 **(2021)** 2366–2396. https://doi.org/10.1021/acscatal.0c05332.

[278] C. J. Plank, E.J. Rosinski, Catalytic cracking of hydrocarbons with a crystalline zeolite catalyst composite, United States Pat. Off. **(1964)**. https://www.freepatentsonline.com/3140249.html. Accessed date: 5th of April 2022.

[279] E. G. Derouane, J. C. Védrine, R. Ramos Pinto, P. M. Borges, L. Costa, M. Lemos, F. Lemos, F. Ramôa Ribeiro, The acidity of zeolites: Concepts, measurements and relation to catalysis: A review on experimental and theoretical methods for the study of zeolite acidity, *Catal. Rev. - Sci. Eng.* 55 **(2013)** 454–515. https://doi.org/10.1080/01614940.2013.822266.

[280] S. Prodinger, M.A. Derewinski, Synthetic zeolites and their characterization, Nanoporous Materials for Molecule Separation and Conversion, **(2020)**. https://doi.org/10.1016/b978-0-12-818487-5.00003-0.

[281] M. Niwa, N. Katada, Measurements of acidic property of zeolites by temperature programmed desorption of ammonia, *Catal. Surv. from Japan*. 1 **(1997)** 215–226. https://doi.org/10.1023/A:1019033115091.

[282] B. Jha, D. N. Singh, A review on synthesis, characterization and industrial applications of Flyash zeolites, *J. Mater. Educ.* 33 **(2011)** 65–132. https:// 10.1002/chin.201225227.

[283] L. B. McCusker, C. Baerlocher, Zeolite structures, *Stud. Surf. Sci. Catal.* 157 **(2005)** 41–64. https://doi.org/10.1016/s0167-2991(05)80005-9.

[284] I. Ore, I.O. Pigments, P. Rock, Q. Crystal, R. Earths, S. Ash, Mineral Commodity Summaries **(2021)**. https://pubs.usgs.gov/periodicals/mcs2021/mcs2021.pdf. Accessed date: 27th of April 2022.

[285] E. Cataldo, L. Salvi, F. Paoli, M. Fucile, G. Masciandaro, D. Manzi, C.M. Masini, G.B. Mattii, Application of zeolites in agriculture and other potential uses: A review, *Agronomy*. 11 **(2021)** 1–14. https://doi.org/10.3390/agronomy11081547.

[286] G. D. Gatta, P. Lotti, Systematics, crystal structures, and occurrences of zeolites, *Modified Clay and Zeolite Nanocomposite Materials*, Elsevier Inc., **(2018)**. https://doi.org/10.1016/B978-0-12-814617-0.00001-3.

[287] N. Mansouri, N. Rikhtegar, H.A. Panahi, F. Atami, B.K. Shahraki, Porosity, characterization and structural properties of natural zeolity - clinoptilolite - as a sorbent, *Environ. Prot. Eng.* 39 **(2013)**. https://doi.org/10.1002/9780470114735.hawley03904.

[288] J. Mačala, I. Pandová, A. Panda, Zeolite as a prospective material for the purification of automobile exhaust gases, *Gospod. Surowcami Miner. - Miner. Resour. Manag.* 33 **(2017)** 125–138.

[289] M. Ramishvili, V.G. Tsitsishvili, N.G. Kokiashvili, V.M. Gabunia, N.M. Inanashvili, Modified Forms of Natural Zeolites – Clinoptilolite and Heulandite as an Effective Catalysts for Synthesis

of Acetylsalicylic Acid, *AJST*. 08 **(2019)** 4985-4995. https://shorturl.at/fuAGP. Accessed date: 5th of May 2022.

[290] S.K. Pavelić, J.S. Medica, D. Gumbarević, A. Filošević, N. Pržulj, K. Pavelić, Critical review on zeolite clinoptilolite safety and medical applications in vivo, *Front. Pharmacol.* 9 **(2018)** 1–15. https://doi.org/10.3389/fphar.2018.01350.

[291] D.L. Bish, J.M. Boak, Clinoptilolite-heulandite nomenclature, *Rev. Mineral. Geochemistry*. 45 **(2001)** 206–216. https://doi.org/10.2138/rmg.2001.45.5.

[292] P. Ambrozova, J. Kynicky, T. Urubek, V. D. Nguyen, Synthesis and Modification of Clinoptilolite, *Molecules.* 22 **(2017)** 1–13. https://doi.org/10.3390/molecules22071107.

[293] S. Wang, Z.H. Zhu, Characterisation and environmental application of an Australian natural zeolite for basic dye removal from aqueous solution, *J. Hazard. Mater.* 136 **(2006)** 946–952. https://doi.org/10.1016/j.jhazmat.2006.01.038.

[294] Y. Li, P. Bai, Y. Yan, W. Yan, W. Shi, R. Xu, Removal of Zn^{2+}, Pb^{2+}, Cd^{2+}, and Cu^{2+} from aqueous solution by synthetic clinoptilolite, *Microporous Mesoporous Mater.* 273 **(2019)** 203–211. https://doi.org/10.1016/j.micromeso.2018.07.010.

[295] J.F. Gelves, L. Dorkis, M.A. Márquez, A.C. Álvarez, L.M. González, A.L. Villa, Activity of an iron Colombian natural zeolite as potential geo-catalyst for NH_3-SCR of NOx, *Catal. Today.* 320 **(2019)** 112–122. https://doi.org/10.1016/j.cattod.2018.01.025.

[296] E. P. Favvas, C. G. Tsanaktsidis, A. A. Sapalidis, G.T. Tzilantonis, S.K. Papageorgiou, A.C. Mitropoulos, Clinoptilolite, a natural zeolite material: Structural characterization and performance evaluation on its dehydration properties of hydrocarbon-based fuels, *Microporous Mesoporous Mater.* 225 **(2016)** 385–391. https://doi.org/10.1016/j.micromeso.2016.01.021.

[297] R. Świderska-Dąbrowska, R. Schmidt, A. Sikora, Physical and chemical properties of the zeolite iron modified [in polish] Właściwości fizykochemiczne zeolitu modyfikowanego jonami żelaza, *Inżynieria Ekol.* 24 **(2011)** 195–204. http://www.archive.ecoeet.com/pdf/24/19.pdf. Accessed: 10th of May 2022.

[298] O. Korkuna, R. Leboda, J. Skubiszewska-Zięba, T. Vrublevs'ka, V.M. Gun'ko, J. Ryczkowski, Structural and physicochemical properties of natural zeolites: Clinoptilolite and mordenite, *Microporous Mesoporous Mater.* 87 **(2006)** 243–254. https://doi.org/10.1016/j.micromeso.2005.08.002.

[299] C. Cobzaru, A. Marinoiu, C. Cernatescu, Sorption of vitamin C on acid modified clinoptilolite,

Rev. Roum. Chim. 60 **(2015)** 241–247. http://web.icf.ro/rrch/. Accessed: 19th of May 2022.

[300] W. Baek, S. Ha, S. Hong, S. Kim, Y. Kim, Cation exchange of cesium and cation selectivity of natural zeolites: Chabazite, stilbite, and heulandite, *Microporous Mesoporous Mater.* 264 **(2018)** 159–166. https://doi.org/10.1016/j.micromeso.2018.01.025.

[301] F. Taghavi, C. Falamaki, Purity P -Aminophenol Through P-Nitrophenol, *React. Kinet. Mech. Catal.* 109 **(2013)** 91–104. https://doi.org/10.1007/s11144-013-0539-4.

[302] N. Lihareva, L. Dimowa, O. Petrov, Y. Tzvetanova, Evaluation of Bulgarian clinoptilolite as ion-exchanger for Cs^+ removal from water solutions, *J. Radioanal. Nucl. Chem.* 316 **(2018)** 37–47. https://doi.org/10.1007/s10967-018-5715-6.

[303] Z. Yuna, Review of the natural, modified, and synthetic zeolites for heavy metals removal from wastewater, *Environ. Eng. Sci.* 33 **(2016)** 443–454. https://doi.org/10.1089/ees.2015.0166.

[304] V. C. de Souza, J. Villarroel-Rocha, M. J. G. de Araújo, K. Sapag, S. B. C. Pergher, Basic treatment in natural clinoptilolite for improvement of physicochemical properties, *Minerals.* 8 **(2018)** 1–14. https://doi.org/10.3390/min8120595.

[305] Y. Garcia-Basabe, I. Rodriguez-Iznaga, L.C. De Menorval, P. Llewellyn, G. Maurin, D.W. Lewis, R. Binions, M. Autie, A.R. Ruiz-Salvador, Step-wise dealumination of natural clinoptilolite: Structural and physicochemical characterization, *Microporous Mesoporous Mater.* 135 **(2010)** 187–196. https://doi.org/10.1016/j.micromeso.2010.07.008.

[306] M. Moradi, R. Karimzadeh, E. S. Moosavi, Modified and ion exchanged clinoptilolite for the adsorptive removal of sulfur compounds in a model fuel: New adsorbents for desulfurization, *Fuel.* 217 **(2018)** 467–477. https://doi.org/10.1016/j.fuel.2017.12.095.

[307] M. Z. Kussainova, R. M. Chernyakova, U. Z. Jussipbekov, S. Paşa, Structural investigation of raw clinoptilolite over the Pb^{2+} adsorption process from phosphoric acid, *J. Mol. Struct.* 1184 **(2019)** 49–58. https://doi.org/10.1016/j.molstruc.2019.02.012.

[308] K. Stocker, M. Ellersdorfer, A. Lechleitner, J. Lubensky, J. G. Raith, Impact of concentrated acid, base and salt pretreatments on the characteristics of natural clinoptilolite and its ammonium uptake from model solution and real effluents, *Microporous Mesoporous Mater.* 288 **(2019)** 109553. https://doi.org/10.1016/j.micromeso.2019.06.015.

[309] N. Ghasemian, C. Falamaki, M. Kalbasi, Clinoptilolite zeolite as a potential catalyst for propane-SCR-NOx: Performance investigation and kinetic analysis, *Chem. Eng. J.* 236 **(2014)** 464–470. https://doi.org/10.1016/j.cej.2013.10.061.

[310] A. S. M. Junaid, M. Rahman, H. Yin, W. C. McCaffrey, S.M. Kuznicki, Natural zeolites for oilsands bitumen cracking: Structure and acidity, *Microporous Mesoporous Mater.* 144 **(2011)** 148–157. https://doi.org/10.1016/j.micromeso.2011.04.007.

[311] S. M. Hosseinifard, M. A. Aroon, B. Dahrazma, Application of PVDF/HDTMA-modified clinoptilolite nanocomposite membranes in removal of reactive dye from aqueous solution, *Sep. Purif. Technol.* 251 **(2020)** 117294. https://doi.org/10.1016/j.seppur.2020.117294.

[312] S. Salehi, M. Anbia, Performance comparison of chitosan–clinoptilolite nanocomposites as adsorbents for vanadium in aqueous media, *Cellulose.* 26 **(2019)** 5321–5345. https://doi.org/10.1007/s10570-019-02450-9.

[313] P. Misaelides, Application of natural zeolites in environmental remediation: A short review, *Microporous Mesoporous Mater.* 144 **(2011)** 15–18. https://doi.org/10.1016/j.micromeso.2011.03.024.

[314] G. M. Haggerty, R. S. Bowman, Sorption of Chromate and Other Inorganic Anions by Organo-Zeolite, *Environ. Sci. Technol.* 28 **(1994)** 452–458. https://doi.org/10.1021/es00052a017.

[315] V. A. Nikashina, P. A. Gembitskii, E. M. Kats, L. F. Boksha, A .K. Galuzinskaya, Organomineral sorbents based on clinoptilolite-containing tuffs and polyethylenimime, *Russ. J. Appl. Chem.* 74 **(2001)** 1450–1452. https://doi.org/10.1023/A:1013728412590.

[316] S. Zaremotlagh, A. Hezarkhani, Removal of textile dyes from aqueous solution by conducting polymer modified clinoptilolite, *Environ. Earth Sci.* 71 **(2014)** 2999–3006. https://doi.org/10.1007/s12665-013-2676-5.

[317] A. Olad, S. Ahmadi, A. Rashidzadeh, Removal of Nickel (II) from aqueous solutions with polypyrrole modified clinoptilolite: Kinetic and isotherm studies, *Desalin. Water Treat.* 51 **(2013)** 7172–7180. https://doi.org/10.1080/19443994.2013.771285.

[318] H. Derikvandi, A. Nezamzadeh-Ejhieh, An effective wastewater treatment based on sunlight photodegradation by SnS_2–ZnS/clinoptilolite composite, *Solid State Sci.* 101 **(2020)**. https://doi.org/10.1016/j.solidstatesciences.2020.106127.

[319] E. Zanin, J. Scapinello, M. de Oliveira, C. L. Rambo, F. Franscescon, L. Freitas, J. M. M. de Mello, M. A. Fiori, J. V. Oliveira, J. Dal Magro, Adsorption of heavy metals from wastewater graphic industry using clinoptilolite zeolite as adsorbent, *Process Saf. Environ. Prot.* 105 **(2017)** 194–200. https://doi.org/10.1016/j.psep.2016.11.008.

[320] A. Nezamzadeh-Ejhieh, M. Kabiri-Samani, Effective removal of Ni(II) from aqueous solutions

by modification of nano particles of clinoptilolite with dimethylglyoxime, *J. Hazard. Mater.* 260 **(2013)** 339–349. https://doi.org/10.1016/j.jhazmat.2013.05.014.

[321] M. R. Abukhadra, M. G. Basyouny, A. M. El-Sherbeeny, M. A. El-Meligy, The effect of different green alkali modification processes on the clinoptilolite surface as adsorbent for ammonium ions; characterization and application, *Microporous Mesoporous Mater.* 300 **(2020)** 110145. https://doi.org/10.1016/j.micromeso.2020.110145.

[322] S. Wasielewski, E. Rott, R. Minke, H. Steinmetz, Application of natural clinoptilolite for ammonium removal from sludge water, *Molecules.* 26 **(2021)** 1–22. https://doi.org/10.3390/MOLECULES26010114.

[323] A. V. Voronina, M.O. Blinova, V.S. Semenishchev, D.K. Gupta, Returning land contaminated as a result of radiation accidents to farming use, *J. Environ. Radioact.* 144 **(2015)** 103–112. https://doi.org/10.1016/j.jenvrad.2015.03.012.

[324] M. Madej, K. Fendrych, R. Porada, M. Flacha, J. Kochana, B. Baś, Application of Fe(III)-exchanged clinoptilolite/graphite nanocomposite for electrochemical sensing of amitriptyline, *Microchem. J.* 160 **(2021).** https://doi.org/10.1016/j.microc.2020.105648.

[325] B. de Gennaro, L. Catalanotti, P. Cappelletti, A. Langella, M. Mercurio, C. Serri, M. Biondi, L. Mayol, Surface modified natural zeolite as a carrier for sustained diclofenac release: A preliminary feasibility study, *Colloids Surfaces B Biointerfaces.* 130 **(2015)** 101–109. https://doi.org/10.1016/j.colsurfb.2015.03.052.

[326] A. Mastinu, A. Kumar, G. Maccarinelli, S.A. Bonini, M. Premoli, F. Aria, A. Gianoncelli, M. Memo, Zeolite clinoptilolite: Therapeutic virtues of an ancient mineral, *Molecules.* 24 **(2019)**. 1517. https://doi.org/10.3390/molecules24081517.

[327] A. Szymaszek, B. Samojeden, M. Motak, Selective catalytic reduction of NOx with ammonia (NH_3-SCR) over transition metal-based catalysts - influence of the catalysts support, *Physicochem. Probl. Miner. Process.* 55 **(2019)** 1429–1441. https://doi.org/10.5277/ppmp19066.

[328] M. Saramok, A. Szymaszek, M. Inger, K. Antoniak-jurak, B. Samojeden, M. Motak, Modified Zeolite Catalyst for a NOx Selective Catalytic Reduction Process in Nitric Acid Plants, *Catalysts.* 11 **(2021)** 450. https://doi.org/10.3390/catal11040450.

[329] M. Sardar, M. Maharana, M. Manna, S. Sen, 2D Zeolites, Layer. 2D *Adv. Mater. Their Allied Appl.* **(2020)** 193–210. https://doi.org/10.1002/9781119655190.ch9.

[330] F. García-Villén, E. Flores-Ruíz, C. Verdugo-Escamilla, F.J. Huertas, Hydrothermal synthesis of zeolites using sanitary ware waste as a raw material, *Appl. Clay Sci.* 160 **(2018)** 238–248. https://doi.org/10.1016/j.clay.2018.02.004.

[331] S.K. Kirdeciler, B. Akata, One pot fusion route for the synthesis of zeolite 4A using kaolin, *Adv. Powder Technol.* 31 **(2020)** 4336–4343. https://doi.org/10.1016/j.apt.2020.09.012.

[332] E. Ofer-Rozovsky, G. Bar-Nes, A. Katz, M. Arbel Haddad, Alkali Activation of Fly Ash in the Presence of Sodium Nitrate, *Waste and Biomass Valorization.* **(2021)**. https://doi.org/10.1007/s12649-021-01584-x.

[333] B. Makgabutlane, L. N. Nthunya, N. Musyoka, B. S. Dladla, E. N. Nxumalo, S. D. Mhlanga, Microwave-assisted synthesis of coal fly ash-based zeolites for removal of ammonium from urine, *RSC Adv.* 10 **(2020)** 2416–2427. https://doi.org/10.1039/c9ra10114d.

[334] M. Król, Natural vs. Synthetic zeolites, *Crystals.* 10 **(2020)** 1–8. https://doi.org/10.3390/cryst10070622.

[335] U. Díaz, Layered Materials with Catalytic Applications Pillared and Delaminated Zeolites, *Int. Sch. Res. Netw.* **(2012)** ID 537164.

[336] L. Bacakova, M. Vandrovcova, I. Kopova, I. Jirka, Applications of zeolites in biotechnology and medicine-a review, *Biomater. Sci.* 6 **(2018)** 974–989. https://doi.org/10.1039/c8bm00028j.

[337] D. M. Flanagan, R. D. Crangle, 2017 Minerals Yearbook-Zeolites, 2017 *Miner. Yearb.* **(2017)** 77.1-77.5. https://www.usgs.gov/media/files/zeolites-2017-tables-only-release. Accessed date: 20th of June 2022.

[338] B. Kozera-Sucharda, B. Gworek, I. Kondzielski, The simultaneous removal of zinc and cadmium from multicomponent aqueous solutions by their sorption onto selected natural and synthetic zeolites, *Minerals.* 10 **(2020)** 343. https://doi.org/10.3390/min10040343.

[339] C. Fan, Z. Chen, L. Pang, S. Ming, X. Zhang, K.B. Albert, P. Liu, H. Chen, T. Li, The influence of Si/Al ratio on the catalytic property and hydrothermal stability of Cu-SSZ-13 catalysts for NH_3-SCR, *Appl. Catal. A Gen.* 550 **(2018)** 256–265. https://doi.org/10.1016/j.apcata.2017.11.021.

[340] T. Lu, W. Yan, R. Xu, Chiral zeolite beta: Structure, synthesis, and application, *Inorg. Chem. Front.* 6 **(2019)** 1938–1951. https://doi.org/10.1039/c9qi00574a.

[341] S. Van Minnebruggen, T. De Baerdemaeker, K. Y. Cheung, A.-N. Parvulescu, U. Müller, P. Tomkins, R. de Oliveira-Silva, X. Meng, F.-S. Xiao, T. Yokoi, W. Zhang, D. Sakellariou, D. De

Vos, Alkylation of isobutane with butenes using OSDA-free zeolite beta, *J. Catal.* 406 **(2022)** 206–212. https://doi.org/10.1016/j.jcat.2022.01.007.

[342] Y. Shi, X. Wang, L. Chen, S. Li, C. Wu, S. Shan, W. Li, In situ DRIFT study on NH_3 selective catalytic reduction of NOx over HBEA zeolite doped with CeO_2, *Appl. Surf. Sci.* 506 **(2020)** 144715. https://doi.org/10.1016/j.apsusc.2019.144715.

[343] Y. Liao, H. Xu, Z. Li, L. Ji, L. Wang, G. Gao, W. Huang, Z. Qu, N. Yan, Boosting RuO2Surface Reactivity by Cu Active Sites over Ru/Cu-SSZ-13 for Simultaneous Catalytic Oxidation of CO and NH_3, *J. Phys. Chem. C.* 125 **(2021)** 17031–17041. https://doi.org/10.1021/acs.jpcc.1c04100.

[344] T. Zhang, Y. Qiu, G. Liu, J. Chen, Y. Peng, B. Liu, J. Li, Nature of active Fe species and reaction mechanism over high-efficiency Fe/CHA catalysts in catalytic decomposition of N_2O, *J. Catal.* 392 **(2020)** 322–335. https://doi.org/10.1016/j.jcat.2020.10.015.

[345] J. Wan, J. Chen, R. Zhao, R. Zhou, One-pot synthesis of Fe/Cu-SSZ-13 catalyst and its highly efficient performance for the selective catalytic reduction of nitrogen oxide with ammonia, *J. Environ. Sci. (China).* 100 **(2021)** 306–316. https://doi.org/10.1016/j.jes.2020.08.003.

[346] A.H. Clark, R.J.G. Nuguid, P. Steiger, A. Marberger, A.W. Petrov, D. Ferri, M. Nachtegaal, O. Kröcher, Selective Catalytic Reduction of NO with NH_3 on Cu−SSZ-13: Deciphering the Low and High-temperature Rate-limiting Steps by Transient XAS Experiments, *ChemCatChem.* 12 **(2020)** 1429–1435. https://doi.org/10.1002/cctc.201901916.

[347] E. Kianfar, Investigation of the Effect of Crystallization Temperature and Time in Synthesis of SAPO-34 Catalyst for the Production of Light Olefins, *Pet. Chem.* 61 **(2021)** 527–537. https://doi.org/10.1134/S0965544121050030.

[348] S. Andonova, S. Tamm, C. Montreuil, C. Lambert, L. Olsson, The effect of iron loading and hydrothermal aging on one-pot synthesized Fe/SAPO-34 for ammonia SCR, *Appl. Catal. B Environ.* 180 **(2016)** 775–787. https://doi.org/10.1016/j.apcatb.2015.07.007.

[349] A. Ahmad, S. R. Naqvi, M. Rafique, H. Nasir, A. Sarosh, Synthesis, characterization and catalytic testing of MCM-22 derived catalysts for n-hexane cracking, *Sci. Rep.* 10 **(2020)** 1–11. https://doi.org/10.1038/s41598-020-78746-9.

[350] M.B. dos Santos, H.M.C. Andrade, A.J.S. Mascarenhas, Oxidative dehydration of glycerol over alternative H,Fe-MCM-22 catalysts: Sustainable production of acrylic acid, *Microporous Mesoporous Mater.* 278 **(2019)** 366–377. https://doi.org/10.1016/j.micromeso.2019.01.016.

[351] M. Marosz, B. Samojeden, A. Kowalczyk, M. Rutkowska, M. Motak, U. Díaz, A.E. Palomares,

L. Chmielarz, MCM-22, MCM-36, and ITQ-2 zeolites with different Si/Al molar ratios as effective catalysts of methanol and ethanol dehydration, *Materials (Basel).* 13 **(2020).** https://doi.org/10.3390/ma13102399.

[352] J. Chen, G. Peng, W. Zheng, W. Zhang, L. Guo, X. Wu, Excellent performance of one-pot synthesized Fe-containing MCM-22 zeolites for the selective catalytic reduction of NOx with NH_3, *Catal. Sci. Technol.* 10 **(2020)** 6583–6598. https://doi.org/10.1039/d0cy00989j.

[353] M. Rutkowska, U. Díaz, A.E. Palomares, L. Chmielarz, Cu and Fe modified derivatives of 2D MWW-type zeolites (MCM-22, ITQ-2 and MCM-36) as new catalysts for DeNOx process, *Appl. Catal. B Environ.* 168–169 **(2015)** 531–539. https://doi.org/10.1016/j.apcatb.2015.01.016.

[354] I. Kaskow, A. Wojtaszek-Gurdak, I. Sobczak, Methanol oxidation on AuAg-Zn-MCM-36 - the effect of catalyst components and pretreatment, *Catal. Today.* 345 **(2021)** 123-132. https://doi.org/10.1016/j.cattod.2019.04.010.

[355] A. Jankowska, A. Kowalczyk, M. Rutkowska, W. Mozgawa, B. Gil, L. Chmielarz, Silica and silica-Titania intercalated MCM-36 modified with iron as catalysts for selective reduction of nitrogen oxides-The role of associated reactions, *Catal. Sci. Technol.* 10 **(2020)** 7940–7954. https://doi.org/10.1039/d0cy01415j.

[356] H.K. Min, M.B. Park, S.B. Hong, Methanol-to-olefin conversion over H-MCM-22 and H-ITQ-2 zeolites, *J. Catal.* 271 **(2010)** 186–194. https://doi.org/10.1016/j.jcat.2010.01.012.

[357] Y. Ma, T. Xu, X. Zhang, J. Wang, H. Xu, W. Huang, H. Zhang, Excellent adsorption performance and capacity of modified layered ITQ-2 zeolites for elemental mercury removal and recycling from flue gas, *J. Hazard. Mater.* 423 **(2022)** 127118. https://doi.org/10.1016/j.jhazmat.2021.127118.

[358] M. F. Alotibi, B. A. Alshammari, M. H. Alotaibi, F. M. Alotaibi, S. Alshihri, R. M. Navarro, J. L. G. Fierro, ZSM-5 Zeolite Based Additive in FCC Process: A Review on Modifications for Improving Propylene Production, *Catal. Surv. from Asia.* 24 **(2020)** 1–10. https://doi.org/10.1007/s10563-019-09285-1.

[359] T. Zhao, F. Li, H. Yu, S. Ding, Z. Li, X. Huang, X. Li, X. Wei, Z. Wang, H. Lin, Synthesis of mesoporous ZSM-5 zeolites and catalytic cracking of ethanol and oleic acid into light olefins, *Appl. Catal. A Gen.* 575 **(2019)** 101–110. https://doi.org/10.1016/j.apcata.2019.02.011.

[360] E. A. Uslamin, H. Saito, Y. Sekine, E. J. M. Hensen, N. Kosinov, Different mechanisms of ethane aromatization over Mo/ZSM-5 and Ga/ZSM-5 catalysts, *Catal. Today*. 369 **(2021)** 184–192. https://doi.org/10.1016/j.cattod.2020.04.021.

[361] J. Shi, Y. Zhang, Y. Zhu, M. Chen, Z. Zhang, W. Shangguan, Efficient Fe-ZSM-5 catalyst with wide active temperature window for NH_3 selective catalytic reduction of NO: Synergistic effect of isolated Fe3+ and Fe_2O_3, *J. Catal.* 378 **(2019)** 17–27. https://doi.org/10.1016/j.jcat.2019.08.003.

[362] X. tao Wang, H. peng Hu, X. yu Zhang, X. xin Su, X. dong Yang, Effect of iron loading on the performance and structure of Fe/ZSM-5 catalyst for the selective catalytic reduction of NO with NH_3, *Environ. Sci. Pollut. Res.* 26 **(2019)** 1706–1715. https://doi.org/10.1007/s11356-018-3513-x.

[363] K. Qian, L. Li, P. Chen, Y. Xiu, Y. E, H. Gies, Copper-nickel doped LTA zeolite as a high-efficiency methanol oxidation reaction catalyst in alkaline solution, Int. *J. Hydrogen Energy*. 46 **(2021)** 23898–23905. https://doi.org/10.1016/j.ijhydene.2021.04.155.

[364] D. Jo, G.T. Park, T. Ryu, S.B. Hong, Economical synthesis of high-silica LTA zeolites: A step forward in developing a new commercial NH_3-SCR catalyst, *Appl. Catal. B Environ.* 243 **(2019)** 212–219. https://doi.org/10.1016/j.apcatb.2018.10.042.

[365] T. Ryu, N.H. Ahn, S. Seo, J. Cho, H. Kim, D. Jo, G.T. Park, P.S. Kim, C.H. Kim, E.L. Bruce, P.A. Wright, I.S. Nam, S.B. Hong, Fully Copper-Exchanged High-Silica LTA Zeolites as Unrivaled Hydrothermally Stable NH_3-SCR Catalysts, *Angew. Chemie - Int. Ed.* 56 **(2017)** 3256–3260. https://doi.org/10.1002/anie.201610547.

[366] N. Czuma, K. Zarębska, M. Motak, M.E. Gálvez, P. Da Costa, Ni/zeolite X derived from fly ash as catalysts for CO_2 methanation, *Fuel.* 267 **(2020).** https://doi.org/10.1016/j.fuel.2020.117139.

[367] P. Bareschino, E. Mancusi, A. Forgione, F. Pepe, Biogas purification on Na-X Zeolite: Experimental and numerical results, *Chem. Eng. Sci.* 223 **(2020)** 115744. https://doi.org/10.1016/j.ces.2020.115744.

[368] J. Peréz-Ramírez, D. Verboekend, A. Bonilla, S. Abelló, Zeolite catalysts with tunable hierarchy factor by pore-growth moderators, *Adv. Funct. Mater.* 19 **(2009)** 3972–3979. https://doi.org/10.1002/adfm.200901394.

[369] M. E. Leonowicz, J. A. Lawton, S. L. Lawton, M. K. Rubin, MCM-22: A Molecular Sieve with Two Independent calcined, *Science* 264 **(1994)** 1910–1913. https://10.1126/science.264.5167.1910.

[370] R. Barakov, N. Shcherban, O. Petrov, J. Lang, M. Shamzhy, M. Opanasenko, J. Cejka, MWW-type zeolite nanostructures for a one-pot three-component Prins–Friedel–Crafts reaction, *Inorg. Chem. Front.* 9 **(2022)** 1244-1257. https://doi.org/10.1039/d1qi01497h.

[371] A. Corma, C. Corell, J. Pérez-Pariente, J. M. Guil, R. Guil-López, S. Nicolopoulos, J. Gonzalez Calbet, M. Vallet-Regi, Adsorption and catalytic properties MCM-22: The influence of zeolite structure, *Zeolites.* 16 **(1996)** 7-14. https://doi.org/10.1016/0144-2449(95)00084-4.

[372] I. Güray, J. Warzywoda, N. Baç, A. Sacco, Synthesis of zeolite MCM-22 under rotating and static conditions, *Microporous Mesoporous Mater.* 31 **(1999)** 241–251. https://doi.org/10.1016/S1387-1811(99)00075-X.

[373] O. Kikhtyanin, P. Chlubná, T. Jindrova, D. Kubicka, Peculiar behavior of MWW materials aldol condensation of furfural and acetone - MCM-22 MCM-36, *Dalt. Trans.* 43 **(2014)** 10628. https://doi.org/10.1039/C4DT00184B.

[374] W. J. Roth, D. L. Dorset, Expanded view of zeolite structures and their variability based on layered nature of 3-D frameworks, *Microporous Mesoporous Mater.* 142 **(2011)** 32–36. https://doi.org/10.1016/j.micromeso.2010.11.007.

[375] P. Xiao, Y. Wang, R. Osuga, J.N. Kondo, T. Yokoi, One-pot synthesis of highly active Fe-containing MWW zeolite catalyst: Elucidation of Fe species and its impact on catalytic performance, *Adv. Powder Technol.* 32 **(2021)** 1070-1080. https://doi.org/10.1016/j.apt.2021.02.014.

[376] A. Corma, C. Corell, Synthesis and characterization of the MCM-22 zeolite, *Zeolites.* 15 **(1995)** 2–8. https://doi.org/10.1016/0144-2449(94)00013-I.

[377] U. Díaz, Layered Materials with Catalytic Applications : Pillared and Delaminated Zeolites from MWW Precursors, 2012 **(2012)** 537164. https://doi.org/10.5402/2012/537164.

[378] W. S. Lima, G. M. de Paula, L. do Nascimento Rocha de Paula, P. H. L. Quintela, F. A. N. Fernandes, M.G.F. Rodrigues, Co-Ru/MCM-22 catalysts for application in Fischer–Tropsch synthesis, *React. Kinet. Mech. Catal.* 134 **(2021)** 441–458. https://doi.org/10.1007/s11144-021-02071-z.

[379] D. Karabulut, S. Akyalcin, Friedel-Crafts alkylation of benzene with benzyl alcohol over H-MCM-22, *Int. J. Chem. React. Eng.* 19 **(2021)** 541–551. https://doi.org/10.1515/ijcre-2020-0175.

[380] W. Zhang, Y. Zhou, M. Shamzhy, S. Molitorisová, M. Opanasenko, A. Giroir-Fendler, Total Oxidation of Toluene and Propane over Supported Co_3O_4Catalysts: Effect of Structure/Acidity of MWW Zeolite and Cobalt Loading, *ACS Appl. Mater. Interfaces*. 13 **(2021)** 15143–15158. https://doi.org/10.1021/acsami.0c21999.

[381] Y. Ma, T. Xu, X. Zhang, Z. Fei, H. Zhang, H. Xu, Y. Ma, Manganese bridge of mercury and

oxygen for elemental mercury capture from industrial flue gas in layered Mn/MCM-22 zeolite, *Fuel.* 283 **(2021)** 118973. https://doi.org/10.1016/j.fuel.2020.118973.

[382] Y. Ma, T. Xu, J. Wang, Y. Shi, H. Wang, F. Xiong, H. Xu, Y. Ma, H. Zhang, Superior Hg0 capture performance and SO_2 resistance of Co–Mn binary metal oxide-modified layered MCM-22 zeolite for SO_2-containing flue gas, Environ. *Sci. Pollut. Res.* 28 **(2021)** 16447–16457. https://doi.org/10.1007/s11356-020-12214-9.

[383] A. E. Palomares, C. Franch, A. Corma, Determining the characteristics of a Co-zeolite to be active for the selective catalytic reduction of NO x with hydrocarbons, *Catal. Today*. 176 **(2011)** 239–241. https://doi.org/10.1016/j.cattod.2010.11.092.

[384] V. A. Ostroumova, A. L. Maksimov, MWW-Type Zeolites: MCM-22, MCM-36, MCM-49, and MCM-56 (A Review), *Pet. Chem.* 59 **(2019)** 788–801. https://doi.org/10.1134/S0965544119080140.

[385] S. T. Yang, J. Y. Kim, J. Kim, W. S. Ahn, CO_2 capture over amine-functionalized MCM-22, MCM-36 and ITQ-2, *Fuel.* 97 **(2012)** 435–442. https://doi.org/10.1016/j.fuel.2012.03.034.

[386] T. Wang, F. Jin, X. Yi, G. Wu, A. Zheng, Atom-planting synthesis of MCM-36 catalyst to investigate the influence of pore structure and titanium coordination state on epoxidation activity, *Microporous Mesoporous Mater.* 310 **(2021)** 110645. https://doi.org/10.1016/j.micromeso.2020.110645.

[387] C. C. Chang, J. F. Lee, S. Cheng, Highly catalytically active micro/meso-porous Ti-MCM-36 prepared by a grafting method, *J. Mater. Chem. A.* 5 **(2017)** 15676–15687. https://doi.org/10.1039/c7ta01792h.

[388] M. Jaroniec, T. U. Miinchen, New modifications of layered MCM-36 molecular sieve pillared with various mixed oxides facts and perspectives, *Surf. Sci. Catal.* 156 **(2005)** 349–356. https://doi.org/10.1016/S0167-2991(05)80228-9.

[389] J. Barth, A. Jentys, J. Kornatowski, J. A. Lercher, Control of Acid - Base Properties of New Nanocomposite Derivatives of MCM-36 by Mixed Oxide Pillaring, *Chem. Mater*. 16 **(2004)** 724–730. https://doi.org/10.1021/cm0349607.

[390] A. Corma, U. Diaz, V. Fornés, J.M. Guil, J. Martínez-Triguero, E.J. Creyghton, Characterization and catalytic activity of MCM-22 and MCM-56 compared with ITQ-2, *J. Catal.* 191 **(2000)** 218–224. https://doi.org/10.1006/jcat.1999.2774.

[391] D. V. Wieslaw J. Roth, P. Chlubna, M. Kubu, Swelling of MCM-56 and MCM-22P with a new

medium — surfactant – tetramethylammonium hydroxide mixtures, 204 **(2013)** 8–14. https://doi.org/10.1016/j.cattod.2012.07.040.

[392] A. Corma, V. Fornés, U. Díaz, ITQ-18 a new delaminated stable zeolite, *Chem. Commun.* 1 **(2001)** 2642–2643. https://doi.org/10.1039/b108777k.

[393] A. Corma, V. Fornés, J.M. Guil, S. Pergher, T.L.M. Maesen, J.G. Buglass, Preparation, characterisation and catalytic activity of ITQ-2, a delaminated zeolite, *Microporous Mesoporous Mater.* 38 **(2000)** 301–309. https://doi.org/10.1016/S1387-1811(00)00149-9.

[394] S. R. Naqvi, Y. Uemura, S. Yusup, N. Nishiyama, M. Naqvi, Catalytic Consequences of Micropore Topology on Biomass Pyrolysis Vapors over Shape Selective Zeolites, *Energy Procedia.* 105 **(2017)** 557–561. https://doi.org/10.1016/j.egypro.2017.03.356.

[395] S. R. Naqvi, M. Naqvi, A. Inayat, P. Blanco-Sanchez, Impact of layered and delaminated zeolites on catalytic fast pyrolysis of microalgae using fixed-bed reactor and Py-GC/MS, *J. Anal. Appl. Pyrolysis.* 155 **(2021)** 105025. https://doi.org/10.1016/j.jaap.2021.105025.

[396] S. R. Naqvi, M. Naqvi, T. Noor, A. Hussain, N. Iqbal, Y. Uemura, N. Nishiyama, Catalytic Pyrolysis of Botryococcus Braunii (microalgae) over Layered and Delaminated Zeolites for Aromatic Hydrocarbon Production, *Energy Procedia.* 142 **(2017)** 381–385. https://doi.org/10.1016/j.egypro.2017.12.060.

[397] S. R. Naqvi, M. Naqvi, Catalytic fast pyrolysis of rice husk: Influence of commercial and synthesized microporous zeolites on deoxygenation of biomass pyrolysis vapors, *Int. J. Energy Res.* 42 **(2018)** 1352–1362. https://doi.org/10.1002/er.3943.

[398] S. Kweon, Y. W. Kim, J. Bae, E.-J. Kim, M.B. Park, H.-K. Min, Nickel on two-dimensional ITQ-2 zeolite as a highly active catalyst for carbon dioxide reforming of methane, *J. CO_2 Util.* 58 **(2022)** 101921. https://doi.org/10.1016/j.jcou.2022.101921.

[399] J. Hao, Y. Wang, G. Liu, J. Zhang, G. Li, X. Ma, Synthesis of ITQ-2 zeolites and catalytic performance in n-dodecane cracking, *Chinese J. Chem. Eng.* 22 **(2014)** 869–874. https://doi.org/10.1016/j.cjche.2014.06.008.

[400] C. Wang, K. Lu, F. Jin, G. Wu, Y. Zhao, X. Yong, Modification of MWW Layer Structure to investigate the Effect of Acidity and Zn-type sites on Ethane Dehydroaromatization, *Catal. Today.* 368 **(2021)** 250–259. https://doi.org/10.1016/j.cattod.2020.03.056.

[401] M. Moreno-González, A. E. Palomares, M. Chiesa, M. Boronat, E. Giamello, T. Blasco, Evidence of a Cu^{2+}-Alkane Interaction in Cu-Zeolite Catalysts Crucial for the Selective

Catalytic Reduction of NOx with Hydrocarbons, *ACS Catal.* 7 **(2017)** 3501–3509. https://doi.org/10.1021/acscatal.6b03473.

[402] W. B. Zhang, J. L. Chen, L. Guo, W. Zheng, G.H. Wang, S. K. Zheng, X. Q. Wu, Research progress on NH_3-SCR mechanism of metal-supported zeolite catalysts, Ranliao Huaxue Xuebao/*Journal Fuel Chem. Technol.* 49 **(2021)** 1294–1315. https://doi.org/10.1016/S1872-5813(21)60080-4.

[403] Y. Mao, H.F. Wang, P. Hu, Theoretical investigation of NH_3-SCR processes over zeolites: A review, Int. J. Quantum Chem. 115 **(2015)** 618–630. https://doi.org/10.1002/qua.24844.

[404] F. Liu, Y. Yu, H. He, Environmentally-benign catalysts for the selective catalytic reduction of NOx from diesel engines: Structure–activity relationship and reaction mechanism aspects, *Chem. Commun.* 50 **(2014)** 8445–8463. https://doi.org/10.1039/c4cc01098a.

[405] L. Zhang, Q. Wu, X. Meng, U. Müller, M. Feyen, D. Dai, S. Maurer, R. McGuire, A. Moini, A.N. Parvulescu, W. Zhang, C. Shi, T. Yokoi, X. Pan, X. Bao, H. Gies, B. Marler, D.E. De Vos, U. Kolb, F.S. Xiao, Recent advances in the preparation of zeolites for the selective catalytic reduction of NOx in diesel engines, *React. Chem. Eng.* 4 **(2019)** 975–985. https://doi.org/10.1039/c8re00214b.

[406] M. Iwamoto, H. Furukawa, Y. Mine, F. Uemura, S.I. Mikuriya, S. Kagawa, Copper(II) Ion-exchanged ZSM-5 zeolites as highly active catalysts for direct and continuous decomposition of nitrogen monoxide, *J. Chem. Soc. - Ser. Chem. Commun.* **(1986)** 1272–1273. https://doi.org/10.1039/C39860001272.

[407] R. Burch, S. Scire, Selective catalytic reduction of nitric oxide with ethane and methane on some metal exchanged ZSM-5 zeolites, *Appl. Catal. B, Environ.* 3 **(1994)** 295–318. https://doi.org/10.1016/0926-3373(94)0004X-9.

[408] A. Corma, V. Fornés, E. Palomares, Selective catalytic reduction of NO(x) on Cu-beta zeolites, *Appl. Catal. B Environ.* 11 **(1997)** 233–242. https://doi.org/10.1016/S0926-3373(96)00042-2.

[409] G. Delahay, B. Coq, S. Kieger, B. Neveu, The origin of N2O formation in the selective catalytic reduction of NOx by NH_3 in O_2 rich atmosphere on Cu-faujasite catalysts, *Catal. Today.* 54 **(1999)** 431–438. https://doi.org/10.1016/S0920-5861(99)00206-0.

[410] B.M. Lok, C.A. Messina, R.L. Patton, R.T. Gajek, T.R. Cannan, E.M. Flanigen, Silicoaluminophosphate Molecular Sieves: Another New Class of Microporous Cristalline Inorganic Solids, *J. Am. Chem. Soc.* 106 **(1984)** 6092–6093. https://doi.org/10.1021/ja00368a062.

[411] S. I. Zones, Zeolite SSZ-13 and Its Method of Preparation, US Pat. **(1985)** 4, 544, 538. https://patents.google.com/patent/US4544538A/en.

[412] J. H. Kwak, R. G. Tonkyn, D. H. Kim, J. Szanyi, C. H. F. Peden, Excellent activity and selectivity of Cu-SSZ-13 in the selective catalytic reduction of NOx with NH_3, *J. Catal.* 275 **(2010)** 187–190. https://doi.org/10.1016/j.jcat.2010.07.031.

[413] D. W. Fickel, E. D'Addio, J. A. Lauterbach, R. F. Lobo, The ammonia selective catalytic reduction activity of copper-exchanged small-pore zeolites, *Appl. Catal. B Environ.* 102 **(2011)** 441–448. https://doi.org/10.1016/j.apcatb.2010.12.022.

[414] Z. Z. Ying Xin, Qian Li, Zeolitic Materials for DeNOx Selective Catalytic Reduction, *ChemCatChem.* 10 **(2017)** 29-41. https://doi.org/10.1002/cctc.201700854.

[415] H. Pan, Y. Guo, H. T. Bi, NOx adsorption and reduction with C_3H_6 over Fe/zeolite catalysts: Effect of catalyst support, *J. Chem. Eng.* 280 **(2015)** 66-73 https://doi.org/10.1016/j.cej.2015.05.093.

[416] N. Husnain, E. Wang, K. Li, M.T. Anwar, A. Mehmood, M. Gul, D. Li, J. Mao, Iron oxide-based catalysts for low-temperature selective catalytic reduction of NOx with NH_3, *Rev. Chem. Eng.* 35 **(2019)** 239–264. https://doi.org/10.1515/revce-2017-0064.

[417] G. Qi, Y. Wang, R.T. Yang, Selective catalytic reduction of nitric oxide with ammonia over ZSM-5 based catalysts for diesel engine applications, *Catal. Letters.* 121 **(2008)** 111–117. https://doi.org/10.1007/s10562-007-9306-3.

[418] M. Jabłońska, G. Delahay, K. Kruczała, A. Błachowski, K.A. Tarach, K. Brylewska, C. Petitto, K. Góra-Marek, Standard and fast selective catalytic reduction of NO with NH_3 on zeolites Fe-BEA, *J. Phys. Chem. C.* 120 **(2016)** 16831–16842. https://doi.org/10.1021/acs.jpcc.6b05692.

[419] S. Shwan, R. Nedyalkova, J. Jansson, J. Korsgren, L. Olsson, M. Skoglundh, Hydrothermal stability of Fe-BEA as an NH_3-SCR catalyst, *Ind. Eng. Chem. Res.* 51 **(2012)** 12762–12772. https://doi.org/10.1021/ie301516z.

[420] R. Nedyalkova, S. Shwan, M. Skoglundh, L. Olsson, Improved low-temperature SCR activity for Fe-BEA catalysts by H_2-pretreatment, *Appl. Catal. B Environ.* 138–139 **(2013)** 373–380. https://doi.org/10.1016/j.apcatb.2013.03.009.

[421] A. Ates, Characteristics of Fe-exchanged natural zeolites for the decomposition of N_2O and its selective catalytic reduction with NH_3, *Appl. Catal. B Environ.* 76 **(2007)** 282–290. https://doi.org/10.1016/j.apcatb.2007.06.005.

[422] R. Q. Long, R. T. Yang, Selective catalytic reduction of NO with ammonia over Fe^{3+}-exchanged mordenite (Fe-MOR): Catalytic performance, characterization, and mechanistic study, *J. Catal.* 207 **(2002)** 274–285. https://doi.org/10.1006/jcat.2002.3521.

[423] H. Mishima, K. Hashmoto, O. Takehiko, M. Anpo, Selective catalytic reduction of NO with NH_3 over natural zeolites and its application to stationary diesel engine exhaust, *Appl. Catal. B Environ.* 19 **(1998)** 119–126. https://doi.org/10.1016/S0926-3373(98)00071-X.

[424] R.Q. Long, R. T. Yang, Selective catalytic oxidation of ammonia to nitrogen over Fe_2O_3-TiO_2 prepared with a sol-gel method, *J. Catal.* 207 **(2002)** 158–165. https://doi.org/10.1006/jcat.2002.3545.

[425] R. Moreno-Tost, J. Santamaría-González, E. Rodríguez-Castellón, A. Jiménez-López, M. A. Autié, E. González, M. C. Glacial, C. D. Las Pozas, Selective catalytic reduction of nitric oxide by ammonia over Cu-exchanged Cuban natural zeolites, *Appl. Catal. B Environ.* 50 **(2004)** 279–288. https://doi.org/10.1016/j.apcatb.2004.01.019.

[426] R. Moreno-Tost, J. Santamaría-González, E. Rodríguez-Castellón, A. Jiménez-López, M.A. Autié, M.C. Glacial, G. A. Castro, M. Guerra, Selective catalytic reduction of nitric oxide by ammonia over Ag and Zn-exchanged Cuban natural zeolites, *Zeitschrift Fur Anorg. Und Allg. Chemie*. 631 **(2005)** 2253–2257. https://doi.org/10.1002/zaac.200570053.

[427] Q. Ye, L. Wang, R.T. Yang, Activity, propene poisoning resistance and hydrothermal stability of copper exchanged chabazite-like zeolite catalysts for SCR of NO with ammonia in comparison to Cu/ZSM-5, *Appl. Catal. A Gen.* 427–428 **(2012)** 24–34. https://doi.org/10.1016/j.apcata.2012.03.026.

[428] N. Martín, P.N.R. Vennestrøm, J.R. Thøgersen, M. Moliner, A. Corma, Iron-Containing SSZ-39 (AEI) Zeolite: An Active and Stable High-Temperature NH_3-SCR Catalyst, *ChemCatChem.* 9 **(2017)** 1754–1757. https://doi.org/10.1002/cctc.201601627.

[429] N. Martín, P.N.R. Vennestrøm, J.R. Thøgersen, M. Moliner, A. Corma, Fe-Containing Zeolites for NH_3-SCR of NOx: Effect of Structure, Synthesis Procedure, and Chemical Composition on Catalytic Performance and Stability, *Chem. - A Eur. J.* 23 **(2017)** 13404–1341. https://doi.org/10.1002/chem.201701742.

[430] Kristian R. Dixon, A. O. Z. Rodriguez, A.T. Steingrimsson, P.J. Rimmington, (12) Patent Application Publication (10) Pub. No. US 2015/0334785.

[431] H. Zhao, H. Li, X. Li, M. Liu, Y. Li, The promotion effect of Fe to Cu-SAPO-34 for selective catalytic reduction of NOx with NH_3, *Catal. Today*. 297 **(2017)** 84–91.

https://doi.org/10.1016/j.cattod.2017.05.060.

[432] T. Ryu, S.B. Hong, Iron-exchanged UZM-35: An active NH_3-SCR catalyst at low temperatures, *Appl. Catal. B Environ.* 266 **(2020)** 118622. https://doi.org/10.1016/j.apcatb.2020.118622.

[433] P. Wu, H. Lin, T. Komatsu, T. Yashima, Synthesis of ferrisilicate with the MCM-22 structure, *Chem. Commun.* **(1997)** 663–664. https://doi.org/10.1039/a607769b.

[434] J. Grzybek, B. Gil, W.J. Roth, M. Skoczek, A. Kowalczyk, L. Chmielarz, Spectrochimica Acta Part A: Molecular and Biomolecular Spectroscopy Characterization of Co and Fe-MCM-56 catalysts for NH_3-SCR and N_2O decomposition: An in situ FTIR study, *Spectrochim. Acta Part A Mol. Biomol. Spectrosc.* 196 **(2018)** 281–288. https://doi.org/10.1016/j.saa.2018.02.033.

[435] S. Brandenberger, O. Kröcher, A. Wokaun, A. Tissler, R. Althoff, The role of Brønsted acidity in the selective catalytic reduction of NO with ammonia over Fe-ZSM-5, *J. Catal.* 268 **(2009)** 297–306. https://doi.org/10.1016/j.jcat.2009.09.028.

[436] P. Boroń, L. Chmielarz, J. Gurgul, K. Łątka, B. Gil, J.M. Krafft, S. Dzwigaj, The influence of the preparation procedures on the catalytic activity of Fe-BEA zeolites in SCR of NO with ammonia and N_2O decomposition, *Catal. Today.* 235 **(2014)** 210–225. https://doi.org/10.1016/j.cattod.2014.03.018.

[437] F. Gao, M. Kollár, R.K. Kukkadapu, N.M. Washton, Y. Wang, J. Szanyi, C.H.F. Peden, Fe/SSZ-13 as an NH_3-SCR catalyst: A reaction kinetics and FTIR/Mössbauer spectroscopic study, *Appl. Catal. B Environ.* 164 **(2015)** 407–419. https://doi.org/10.1016/j.apcatb.2014.09.031.

[438] T. Ryu, S.B. Hong, Iron-exchanged UZM-35: An active NH_3-SCR catalyst at low temperatures, *Appl. Catal. B Environ.* 266 **(2020)** 118622. https://doi.org/10.1016/j.apcatb.2020.118622.

[439] S. Brandenberger, O. Kröcher, A. Tissler, R. Althoff, The determination of the activities of different iron species in Fe-ZSM-5 for SCR of NO by NH_3, *Appl. Catal. B Environ.* 95 **(2010)** 348–357. https://doi.org/10.1016/j.apcatb.2010.01.013.

[440] O. Kröcher, S. Brandenberger, Active sites, deactivation and stabilization of Fe-ZSM-5 for the selective catalytic reduction (SCR) of NO with NH_3, *Chimia (Aarau).* 66 **(2012)** 687–693. https://doi.org/10.2533/chimia.2012.687.

[441] J. Shi, Y. Zhang, Z. Zhang, Z. Fan, M. Chen, Z. Zhang, W. Shangguan, Water promotion mechanism on the NH_3-SCR over Fe-BEA catalyst, *Catal. Commun.* 115 **(2018)** 59–63. https://doi.org/10.1016/j.catcom.2018.07.012.

[442] F. Gao, Y. Zheng, R.K. Kukkadapu, Y. Wang, E.D. Walter, B. Schwenzer, J. Szanyi, C.H.F.

Peden, Iron Loading Effects in Fe/SSZ-13 NH_3-SCR Catalysts: Nature of the Fe Ions and Structure-Function Relationships, *ACS Catal.* 6 **(2016)** 2939–2954. https://doi.org/10.1021/acscatal.6b00647.

[443] A. Boubnov, H.W.P. Carvalho, D.E. Doronkin, T. Gu, E. Gallo, A.J. Atkins, C.R. Jacob, J. Grunwaldt, Selective Catalytic Reduction of NO Over Fe-ZSM-5 : Mechanistic, *J. Am. Chem. Soc.* 136 **(2014)** 13006–13015.

[444] R. Pérez Vélez, I. Ellmers, H. Huang, U. Bentrup, V. Schünemann, W. Grünert, A. Brückner, Identifying active sites for fast NH_3-SCR of NO/NO_2 mixtures over Fe-ZSM-5 by operando EPR and UV-vis spectroscopy, *J. Catal.* 316 **(2014)** 103–111. https://doi.org/10.1016/j.jcat.2014.05.001.

[445] X. Shi, F. Liu, L. Xie, W. Shan, H. He, NH_3-SCR performance of fresh and hydrothermally aged Fe-ZSM-5 in standard and fast selective catalytic reduction reactions, *Environ. Sci. Technol.* 47 **(2013)** 3293–3298. https://doi.org/10.1021/es304421v.

[446] M. Iwasaki, K. Yamazaki, K. Banno, H. Shinjoh, Characterization of Fe/ZSM-5 DeNOx catalysts prepared by different methods: Relationships between active Fe sites and NH_3-SCR performance, *J. Catal.* 260 **(2008)** 205–216. https://doi.org/10.1016/j.jcat.2008.10.009.

[447] J. Pérez-Ramírez, J.C. Groen, A. Brückner, M.S. Kumar, U. Bentrup, M.N. Debbagh, L.A. Villaescusa, Evolution of isomorphously substituted iron zeolites during activation: Comparison of Fe-beta and Fe-ZSM-5, *J. Catal.* 232 **(2005)** 318–334. https://doi.org/10.1016/j.jcat.2005.03.018.

[448] K. Niu, G. Li, J. Liu, Y. Wei, One step synthesis of Fe-SSZ-13 zeolite by hydrothermal method, J. Solid State Chem. 287 **(2020)** 121330. https://doi.org/10.1016/j.jssc.2020.121330.

[449] M. Schwidder, M.S. Kumar, K. Klementiev, M.M. Pohl, A. Brückner, W. Grünert, Selective reduction of NO with Fe-ZSM-5 catalysts of low Fe content: I. Relations between active site structure and catalytic performance, *J. Catal.* 231 **(2005)** 314–330. https://doi.org/10.1016/j.jcat.2005.01.031.

[450] M. Rauscher, K. Kesore, R. Mönnig, W. Schwieger, A. Tißler, T. Turek, Preparation of a highly active Fe-ZSM-5 catalyst through solid-state ion exchange for the catalytic decomposition of N_2O, *Appl. Catal. A Gen.* 184 **(1999)** 249–256. https://doi.org/10.1016/S0926-860X(99)00088-5.

[451] B.M. Abu-Zied, W. Schwieger, A. Unger, Nitrous oxide decomposition over transition metal exchanged ZSM-5 zeolites prepared by the solid-state ion-exchange method, *Appl. Catal. B*

Environ. 84 **(2008)** 277–288. https://doi.org/10.1016/j.apcatb.2008.04.004.

[452] E. Yuan, G. Wu, W. Dai, N. Guan, L. Li, One-pot construction of Fe/ZSM-5 zeolites for the selective catalytic reduction of nitrogen oxides by ammonia, *Catal. Sci. Technol.* 7 **(2017)** 3036–3044. https://doi.org/10.1039/c7cy00724h.

[453] A. Turrina, A.I. Dugulan, J.E. Collier, R.I. Walton, J.L. Casci, P.A. Wright, Synthesis and activation for catalysis of Fe-SAPO-34 prepared using iron polyamine complexes as structure directing agents, *Catal. Sci. Technol.* 7 **(2017)** 4366–4374. https://doi.org/10.1039/c7cy01269a.

[454] P. Boroń, M. Rutkowska, B. Gil, B. Marszałek, L. Chmielarz, S. Dzwigaj, Experimental Evidence of the Mechanism of Selective Catalytic Reduction of NO with NH_3 over Fe-Containing BEA Zeolites, *ChemSusChem.* 12 **(2019)** 692–705. https://doi.org/10.1002/cssc.201801883.

[455] Q. Liu, C. Bian, Y. Jin, L. Pang, Z. Chen, T. Li, Influence of calcination temperature on the evolution of Fe species over Fe-SSZ-13 catalyst for the NH_3-SCR of NO, *Catal. Today*. **(2020)** 388-389. https://doi.org/10.1016/j.cattod.2020.06.085.

[456] S. Lai, Y. She, W. Zhan, Y. Guo, Y. Guo, L. Wang, G. Lu, Performance of Fe-ZSM-5 for selective catalytic reduction of NOx with NH_3: Effect of the atmosphere during the preparation of catalysts, *J. Mol. Catal. A Chem.* 424 **(2016)** 232–240. https://doi.org/10.1016/j.molcata.2016.08.026.

[457] X. Shi, Y. Wang, Y. Shan, Y. Yu, H. He, Investigation of the common intermediates over Fe-ZSM-5 in NH_3-SCR reaction at low temperature by in situ DRIFTS, *J. Environ. Sci. (China)*. 94 **(2020)** 32–39. https://doi.org/10.1016/j.jes.2020.02.029.

[458] P. Chen, M. Jabłońska, P. Weide, T. Caumanns, T. Weirich, M. Muhler, R. Moos, R. Palkovits, U. Simon, Formation and Effect of NH4+ Intermediates in NH3-SCR over Fe-ZSM-5 Zeolite Catalysts, *ACS Catal.* 6 **(2016)** 7696–7700. https://doi.org/10.1021/acscatal.6b02496.

[459] P. Chen, U. Simon, In situ spectroscopic studies of proton transport in zeolite catalysts for NH_3-SCR, *Catalysts*. 6 **(2016)** 1–15. https://doi.org/10.3390/catal6120204.

[460] T. Jiang, R.F. Lobo, On the Mechanism of Ammonia SCR over Cu- and Fe-Containing Zeolite *Catalysts*, **(2018)** 155–178. https://doi.org/10.1007/430_2018_23.

[461] F. Gao, Y. Wang, M. Kollár, N.M. Washton, J. Szanyi, C.H.F. Peden, A comparative kinetics study between Cu/SSZ-13 and Fe/SSZ-13 SCR catalysts, *Catal. Today.* 258 **(2015)** 347–358. https://doi.org/10.1016/j.cattod.2015.01.025.

[462] M. Li, Y. Yeom, E. Weitz, W.M.H. Sachtler, An acid catalyzed step in the catalytic reduction of NO x to N_2, *Catal. Letters.* 112 **(2006)** 129–132. https://doi.org/10.1007/s10562-006-0191-y.

[463] X. Shi, H. He, L. Xie, The effect of Fe species distribution and acidity of Fe-ZSM-5 on the hydrothermal stability and SO_2 and hydrocarbons durability in NH_3-SCR reaction, Cuihua Xuebao/Chinese *J. Catal.* 36 **(2015)** 649–656. https://doi.org/10.1016/S1872-2067(14)60268-0.

[464] R. Yu, Z. Zhao, S. Huang, W. Zhang, Applied Catalysis B : Environmental Cu-SSZ-13 zeolite – metal oxide hybrid catalysts with enhanced SO 2 -tolerance in the NH_3 -SCR of NO x, *Appl. Catal. B Environ.* 269 **(2020)** 118825. https://doi.org/10.1016/j.apcatb.2020.118825.

[465] H. Liu, Z. Chen, H. Wang, C. You, Active centers response to SO_2 and H_2O poisoning over Fe-W-Ni exchanged zeolite for high-temperature NH_3-SCR: Experimental and DFT studies, *Appl. Surf. Sci.* 570 **(2021)** 151105. https://doi.org/10.1016/j.apsusc.2021.151105.

[466] Y. Tang, D. Wang, X. Wang, Y. Zha, H. An, K. Kamasamudram, A. Yezerets, Impact of low temperature sulfur exposure on the aging of small pore Cu-zeolite SCR catalyst, *Catal. Today.* 360 **(2021)** 234–240. https://doi.org/10.1016/j.cattod.2020.04.033.

[467] Y. Cheng, C. Montreuil, G. Cavataio, C. Lambert, Sulfur tolerance and DeSOx studies on diesel SCR catalysts, SAE Int. J. Fuels Lubr. 1 **(2009)** 471–476. https://doi.org/10.4271/2008-01-1023.

[468] L. Ma, H. Qu, J. Zhang, Q. Tang, S. Zhang, Q. Zhong, Preparation of nanosheet Fe-ZSM-5 catalysts, and effect of Fe content on acidity, water, and sulfur resistance in the selective catalytic reduction of NOx by ammonia, *Res. Chem. Intermed.* 39 **(2013)** 4109–4120. https://doi.org/10.1007/s11164-012-0927-9.

[469] R.Q. Long, R.T. Yang, Characterization of Fe-ZSM-5 catalyst for selective catalytic reduction of nitric oxide by ammonia, *J. Catal.* 194 **(2000)** 80–90. https://doi.org/10.1006/jcat.2000.2935.

[470] H. Pan, E. hao Gao, T. tuo Fang, Y. Mei, Y. He, Y. Shi, In situ treatment by high-temperature water vapor as a novel health-care approach for commercial SCR catalyst, *Appl. Surf. Sci*. 541 **(2021)**. https://doi.org/10.1016/j.apsusc.2020.148408.

[471] L. Ma, Y. Cheng, G. Cavataio, R.W. McCabe, L. Fu, J. Li, Characterization of commercial Cu-SSZ-13 and Cu-SAPO-34 catalysts with hydrothermal treatment for NH_3-SCR of NOx in diesel exhaust, *Chem. Eng. J.* 225 **(2013)** 323–330. https://doi.org/10.1016/j.cej.2013.03.078.

[472] H. I. Hamoud, V. Valtchev, M. Daturi, Selective catalytic reduction of NOx over Cu- and Fe-exchanged zeolites and their mechanical mixture, *Appl. Catal. B Environ.* 250 **(2019)** 419–428. https://doi.org/10.1016/j.apcatb.2019.02.022.

[473] A. Sultana, M. Sasaki, K. Suzuki, H. Hamada, Tuning the NOx conversion of Cu-Fe/ZSM-5 catalyst in NH_3-SCR, *Catal. Commun.* 41 **(2013)** 21–25. https://doi.org/10.1016/j.catcom.2013.06.028.

[474] P. S. Metkar, M. P. Harold, V. Balakotaiah, Experimental and kinetic modeling study of NH_3-SCR of NOx on Fe-ZSM-5, Cu-chabazite and combined Fe- and Cu-zeolite monolithic catalysts, *Chem. Eng. Sci.* 87 **(2013)** 51–66. https://doi.org/10.1016/j.ces.2012.09.008.

[475] T. Zhang, J. Liu, D. Wang, Z. Zhao, Y. Wei, K. Cheng, G. Jiang, A. Duan, Selective catalytic reduction of NO with NH_3 over HZSM-5-supported fe-cu nanocomposite catalysts: The Fe-Cu bimetallic effect, *Appl. Catal. B Environ.* 148–149 **(2014)** 520–531. https://doi.org/10.1016/j.apcatb.2013.11.006.

[476] P. Boroń, L. Chmielarz, S. Dzwigaj, Influence of Cu on the catalytic activity of FeBEA zeolites in SCR of NO with NH_3, *Appl. Catal. B Environ.* 168–169 **(2015)** 377–384. https://doi.org/10.1016/j.apcatb.2014.12.052.

[477] A. Shishkin, S. Shwan, T.N. Pingel, E. Olsson, A. Clemens, P.A. Carlsson, H. Härelind, M. Skoglundh, Functionalization of SSZ-13 and Fe-beta with copper by NH_3 and NO facilitated solid-state ion-exchange, *Catalysts.* 7 **(2017)** 7–14. https://doi.org/10.3390/catal7080232.

[478] T. Zhang, J. Li, J. Liu, D. Wang, Z. Zhao, K. Cheng, High activity and wide temperature window of Fe-Cu-SSZ-13 in the selective catalytic reduction of NO with ammonia, *AIChE J*. 61 (2015) 3825–3837. https://doi.org/10.1002/aic.

[479] B. M. Shakya, M.P. Harold, V. Balakotaiah, Simulations and optimization of combined Fe- and Cu-zeolite SCR monolith catalysts, *Chem. Eng. J.* 278 **(2015)** 374–384. https://doi.org/10.1016/j.cej.2014.11.029.

[480] I.A. Pankin, H. Issa Hamoud, K.A. Lomachenko, S.B. Rasmussen, A. Martini, P. Bazin, V. Valtchev, M. Daturi, C. Lamberti, S. Bordiga, Cu- And Fe-speciation in a composite zeolite catalyst for selective catalytic reduction of NOx: insights from operando XAS, *Catal. Sci. Technol.* 11 **(2021)** 846–860. https://doi.org/10.1039/d0cy01654c.

[481] J. Zhou, R. Guo, X. Zhang, Y. Liu, C. Duan, G. Wu, W. Pan, Cerium Oxide-Based Catalysts for Low-Temperature Selective Catalytic Reduction of NO x with NH_3: A Review , *Energy & Fuels.* **(2021)**. https://doi.org/10.1021/acs.energyfuels.0c04231.

[482] S.H. Begum, C. Te Hung, Y.T. Chen, S.J. Huang, P.H. Wu, X. Han, S. Bin Liu, Acidity-activity correlation over bimetallic iron-based ZSM-5 catalysts during selective catalytic reduction of NO by NH_3, *J. Mol. Catal. A Chem.* 423 **(2016)** 423–432.

https://doi.org/10.1016/j.molcata.2016.07.036.

[483] L. Jiang, Y. Cai, M. Jin, Z. Zhu, Y. Wang, The Influence of Ce or Mn Doping on Cu-Based Catalysts for De-NOx with NH_3-SCR, *J. Chem.* 2020 **(2020).** https://doi.org/10.1155/2020/1462801.

[484] T. Montini, M. Melchionna, M. Monai, P. Fornasiero, Fundamentals and Catalytic Applications of CeO_2-Based Materials, *Chem. Rev.* 116 **(2016)** 5987–6041. https://doi.org/10.1021/acs.chemrev.5b00603.

[485] T. Gu, Y. Liu, X. Weng, H. Wang, Z. Wu, The enhanced performance of ceria with surface sulfation for selective catalytic reduction of NO by NH_3, *Catal. Commun.* 12 **(2010)** 310–313. https://doi.org/10.1016/j.catcom.2010.10.003.

[486] L. Yan, Y. Ji, P. Wang, C. Feng, L. Han, H. Li, T. Yan, L. Shi, D. Zhang, Alkali and Phosphorus Resistant Zeolite-like Catalysts for NOxReduction by NH_3, *Environ. Sci. Technol.* 54 **(2020)** 9132–9141. https://doi.org/10.1021/acs.est.0c03290.

[487] X. Zhou, Z. Chen, Z. Guo, H. Yang, J. Shao, X. Zhang, S. Zhang, One-pot hydrothermal synthesis of dual metal incorporated CuCe-SAPO-34 zeolite for enhancing ammonia selective catalytic reduction, *J. Hazard. Mater.* 405 **(2021)** 124177. https://doi.org/10.1016/j.jhazmat.2020.124177.

[488] G. Carja, G. Delahay, C. Signorile, B. Coq, Fe–Ce–ZSM-5 a new catalyst of outstanding properties in the selective catalytic reduction of NO with NH_3, *Chem. Commun.* 4 **(2004)** 1404–1405. https://doi.org/10.1039/b402660h.

[489] L. Chen, X. Wang, Q. Cong, H. Ma, S. Li, W. Li, Design of a hierarchical Fe-ZSM-5@CeO_2 catalyst and the enhanced performances for the selective catalytic reduction of NO with NH_3, *Chem. Eng. J.* 369 **(2019)** 957–967. https://doi.org/10.1016/j.cej.2019.03.055.

[490] F. Lin, T. Andana, Y. Wu, J. Szanyi, Y. Wang, F. Gao, Catalytic site requirements for N_2O decomposition on Cu-, Co-, and Fe-SSZ-13 zeolites, *J. Catal.* 401 **(2021)** 70–80. https://doi.org/10.1016/j.jcat.2021.07.012.

[491] T. Zhang, X. Qin, Y. Peng, C. Wang, H. Chang, J. Chen, J. Li, Effect of Fe precursors on the catalytic activity of Fe/SAPO-34 catalysts for N_2O decomposition, *Catal. Commun.* 128 **(2019)** 105706. https://doi.org/10.1016/j.catcom.2019.05.013.

[492] B. Kang, M. Li, Z. Di, X. Guo, Y. Wei, J. Jia, R. Zhang, Role of Al pairs on effective N_2O decomposition over the ZSM-5 zeolite catalyst, *Catal. Today.* **(2022)**.

https://doi.org/10.1016/j.cattod.2022.01.018.

[493] A. Zecchina, M. Rivallan, G. Berlier, C. Lamberti, G. Ricchiardi, Structure and nuclearity of active sites in Fe-zeolites: Comparison with iron sites in enzymes and homogeneous catalysts, *Phys. Chem. Chem. Phys.* 9 **(2007)** 3483–3499. https://doi.org/10.1039/b703445h.

[494] H. Guesmi, D. Berthomieu, L. Kiwi-Minsker, Nitrous oxide decomposition on the binuclear [FeII(μ-O)(μ- OH)FeII] Center in Fe-ZSM-5 zeolite, *J. Phys. Chem. C.* 112 **(2008)** 20319–20328. https://doi.org/10.1021/jp808044r.

[495] H. Guesmi, D. Berthomieu, B. Bromley, B. Coq, L. Kiwi-Minsker, Theoretical evidence of the observed kinetic order dependence on temperature during the N_2O decomposition over Fe-ZSM-5, *Phys. Chem. Chem. Phys.* 12 **(2010)** 2873–2878. https://doi.org/10.1039/b918954h.

[496] E. V. Kondratenko, J. Pérez-Ramírez, Mechanism and kinetics of direct N_2O decomposition over Fe-MFI zeolites with different iron speciation from temporal analysis of products, *J. Phys. Chem. B.* 110 **(2006)** 22586–22595. https://doi.org/10.1021/jp063492w.

[497] S. Sklenak, P.C. Andrikopoulos, B. Boekfa, B. Jansang, J. Nováková, L. Benco, T. Bucko, J. Hafner, J. Ddeek, Z. Sobalík, N_2O decomposition over Fe-zeolites: Structure of the active sites and the origin of the distinct reactivity of Fe-ferrierite, Fe-ZSM-5, and Fe-beta. A combined periodic DFT and multispectral study, *J. Catal.* 272 **(2010)** 262–274. https://doi.org/10.1016/j.jcat.2010.04.008.

[498] M.L. Bols, B.E.R. Snyder, H.M. Rhoda, P. Cnudde, G. Fayad, R.A. Schoonheydt, V. Van Speybroeck, E.I. Solomon, B.F. Sels, Coordination and activation of nitrous oxide by iron zeolites, *Nat. Catal.* 4 **(2021)** 332–340. https://doi.org/10.1038/s41929-021-00602-4.

[499] M. Rutkowska, A. Jankowska, E. Różycka-Dudek, W. Dubiel, A. Kowalczyk, Z. Piwowarska, S. Llopis, U. Díaz, L. Chmielarz, Modification of mcm-22 zeolite and its derivatives with iron for the application in N_2O decomposition, *Catalysts.* 10 **(2020)** 1–17. https://doi.org/10.3390/catal10101139.

[500] N. Liu, R. Zhang, B. Chen, Y. Li, Y. Li, Comparative study on the direct decomposition of nitrous oxide over M (Fe, Co, Cu)-BEA zeolites, *J. Catal.* 294 **(2012)** 99–112. https://doi.org/10.1016/j.jcat.2012.07.008.

[501] E.M. El-Malki, R.A. Van Santen, W.M.H. Sachtler, Active sites in Fe/MFI catalysts for NOx reduction and oscillating N2O decomposition, *J. Catal.* 196 **(2000)** 212–223. https://doi.org/10.1006/jcat.2000.3034.

[502] G. Li, E.A. Pidko, I. A.W. Filot, R.A. Van Santen, C. Li, E. J. M. Hensen, Catalytic properties of extraframework iron-containing species in ZSM-5 for N_2O decomposition, *J. Catal.* 308 **(2013)** 386–397. https://doi.org/10.1016/j.jcat.2013.08.010.

[503] S. Ghosh, V.L. Prasanna, B. Sowjanya, P. Srivani, M. Alagaraja, D. Banji, Inductively Coupled Plasma - Optical Emission Spectroscopy: A Review, *Asian Pharma Press.* 3 **(2013)** 24–33. https://doi.org/10.1021/ac60349a023.

[504] K. S. W. Sing, D.H. Everett, R.A.W. Haul, L. Moscou, R.A. Pierotti, J. Rouquerol, T. Siemieniewska, Reporting physisorption data for gas/solid systems with special reference to the determination of surface area and porosity, *Pure Appl. Chem.* 57 **(1985)** 603–619.

[505] M. Thommes, K. Kaneko, A. V. Neimark, J.P. Olivier, F. Rodriguez-Reinoso, J. Rouquerol, K.S.W. Sing, Physisorption of gases, with special reference to the evaluation of surface area and pore size distribution (IUPAC Technical Report), *Pure Appl. Chem.* 87 **(2015)** 1051–1069. https://doi.org/10.1515/pac-2014-1117.

[506] G. M. J. Rouquerol, F. Rouquerol, K. S. W. Sing, P. Llewellyn, Adsorption by Powders and Porous Solids: Principles, Methodology and Applications, 2nd Edition **(2013)** eBook ISBN: 9780080970363.

[507] A. Chauhan, Powder XRD Technique and its Applications in Science and Technology, *J. Anal. Bioanal. Tech.* 5 **(2014)** 212. https://doi.org/10.4172/2155-9872.1000212.

[508] V. Uvarov, I. Popov, Metrological characterization of X-ray diffraction methods for determination of crystallite size in nano-scale materials, *Mater. Charact.* 58 **(2007)** 883–891. https://doi.org/10.1016/j.matchar.2006.09.002.

[509] J. I. Goldstein, D.E. Newbury, J.R. Michael, N.W.M. Ritchie, J.H.J. Scott, D.C. Joy, Scanning Electron Microscopy and X-Ray Microanalysis, Springer New York, 4th Edition **(2017)**. eBook ISBN: 978149396676-9. https://doi.org/10.1007/978-1-4939-6676-9.

[510] L.E. Franken, K. Grünewald, E.J. Boekema, M.C.A. Stuart, A Technical Introduction to Transmission Electron Microscopy for Soft-Matter: Imaging, Possibilities, Choices, and Technical Developments, Small. 16 *Wiley Online Library* 16 **(2020)** 1906198. https://doi.org/10.1002/smll.201906198.

[511] B. J. Inkson, Scanning Electron Microscopy (SEM) and Transmission Electron Microscopy (TEM) for Materials Characterization, *Materials Characterization Using Nondestructive Evaluation (NDE) Methods* **(2016)** 17-43. https://doi.org/10.1016/B978-0-08-100040-3.00002-X.

[512] S. Loganathan, R. B. Valapa, R. K. Mishra, G. Pugazhenthi, S. Thomas, Thermogravimetric Analysis for Characterization of Nanomaterials, *Micro and Nano Technologies* **(2017)** 67-108. https://doi.org/10.1016/B978-0-323-46139-9.00004-9.

[513] S. Y. Lin, C. W. Dence, *Methods in Lignin Chemistry*, Springer Berlin, Heidelberg **(1992)** eBook ISBN: 978364274067, https://doi.org/10.1007/978-3-642-74065-7.

[514] S. A. Khan, S. B. Khan, L. U. Khan, A. Farooq, K. Akhtar, A. M. Asiri, *Handbook of Materials Characterization*, Springer International Publishing AG, part of Springer Nature **(2018)** 317–344. eBook ISBN: 9783319929552. https://doi.org/10.1007/978-3-319-92955-2.

[515] A. G. Shard, A straightforward method for interpreting XPS data from core-shell nanoparticles, *J. Phys. Chem. C.* 116 **(2012)** 16806–16813. https://doi.org/10.1021/jp305267d.

[516] F. A. Stevie, C. L. Donley, Introduction to X-ray photoelectron spectroscopy, *J. Vac. Sci. Technol. A.* 38 **(2020)** 063204. https://doi.org/10.1116/6.0000412.

[517] T. Yamashita, P. Hayes, Analysis of XPS spectra of Fe^{2+} and Fe^{3+} ions in oxide materials, *Appl. Surf. Sci.* 254 **(2008)** 2441–2449. https://doi.org/10.1016/j.apsusc.2007.09.063.

[518] J. H. Nobbs, Kubelka—Munk Theory and the Prediction of Reflectance, *Rev. Prog. Color. Relat. Top.* 15 **(1985)** 66–75. https://doi.org/10.1111/j.1478-4408.1985.tb03737.x.

[519] R. A. Schoonheydt, UV-VIS-NIR spectroscopy and microscopy of heterogeneous catalysts, *Chem. Soc. Rev.* 39 **(2010)** 5051–5066. https://doi.org/10.1039/c0cs00080a.

[520] Y. Peng, C. Liu, X. ZHang, J. Li, The effect of SiO_2 on novel CeO_2-WO_3/TiO_2 catalyst for selective catalytic reduction of NO with NH_3, *Appl. Catal. B Environ.* 140–141 **(2013)** 276–282. https://doi.org/10.3390/catal8120592.

[521] P. Vassileva, D. Voikova, Investigation on natural and pretreated Bulgarian clinoptilolite for ammonium ions removal from aqueous solutions, *J. Hazard. Mater.* 170 **(2009)** 948–953. https://doi.org/10.1016/j.jhazmat.2009.05.062.

[522] R. Schenkel, J. O. Barth, J. Kornatowski, J. A. Lercher, Chemical and structural aspects of the transformation of the MCM-22 precursor into ITQ-2, *Stud. Surf. Sci. Catal.* 142 A **(2002)** 69–76. https://doi.org/10.1016/s0167-2991(02)80013-1.

[523] M. Nasiri-Ardali, A. Nezamzadeh-Ejhieh, A comprehensive study on the kinetics and thermodynamic aspects of batch and column removal of Pb(II) by the clinoptilolite–glycine adsorbent, *Mater. Chem. Phys.* 240 **(2020)** 122142. https://doi.org/10.1016/j.matchemphys.2019.122142.

[524] A. Lassoued, B. Dkhil, A. Gadri, S. Ammar, Control of the shape and size of iron oxide (α-Fe_2O_3) nanoparticles synthesized through the chemical precipitation method, *Results Phys.* 7 **(2017)** 3007–3015. https://doi.org/10.1016/j.rinp.2017.07.066.

[525] J. M. Müller, G. C. Mesquita, S. M. Franco, L. D. Borges, J. L. De Macedo, J. A. Dias, S. C .L. Dias, Solid-state dealumination of zeolites for use as catalysts in alcohol dehydration, *Microporous Mesoporous Mater.* 204 **(2015)** 50–57. https://doi.org/10.1016/j.micromeso.2014.11.002.

[526] L. E. Burris, M. C. G. Juenger, The effect of acid treatment on the reactivity of natural zeolites used as supplementary cementitious materials, *Cem. Concr. Res.* 79 **(2016)** 185–193. https://doi.org/10.1016/j.cemconres.2015.08.007.

[527] W. Wang, W. Zhang, Y. Chen, X. Wen, H. Li, D. Yuan, Q. Guo, S. Ren, X. Pang, B. Shen, Mild-acid-assisted thermal or hydrothermal dealumination of zeolite beta, its regulation to Al distribution and catalytic cracking performance to hydrocarbons, *J. Catal.* 362 **(2018)** 94–105. https://doi.org/10.1016/j.jcat.2018.03.002.

[528] E. Xing, Y. Shi, A. Zheng, J. Zhang, X. Gao, D. Liu, M. Xin, W. Xie, F. Zhang, X. Mu, X. Shu, Transformation from NaA to MCM-49 Zeolite and Its Catalytic Alkylation Performance, *Ind. Eng. Chem. Res.* 54 **(2015)** 3123-3135. https://doi.org/10.1021/ie5047736.

[529] J. F. Gelves, L. Dorkis, M. A. Márquez, A.C. Álvarez, L. M. González, A. L. Villa, Activity of an iron Colombian natural zeolite as potential geo-catalyst for NH_3-SCR of NOx, *Catal. Today.* 320 **(2019)** 112–122. https://doi.org/10.1016/j.cattod.2018.01.025.

[530] M. K. Doula, Synthesis of a clinoptilolite-Fe system with high Cu sorption capacity, *Chemosphere.* 67 **(2007)** 731–740. https://doi.org/10.1016/j.chemosphere.2006.10.072.

[531] N. Mortazavi, M. Bahadori, A. Marandi, S. Tangestaninejad, M. Moghadam, V. Mirkhani, I. Mohammadpoor-Baltork, Enhancement of CO_2 adsorption on natural zeolite, modified clinoptilolite with cations, amines and ionic liquids, *Sustain. Chem. Pharm.* 22 **(2021)** 100495. https://doi.org/10.1016/j.scp.2021.100495.

[532] M. Sprynskyy, R. Golembiewski, G. Trykowski, B. Buszewski, Heterogeneity and hierarchy of clinoptilolite porosity, *J. Phys. Chem. Solids.* 71 **(2010)** 1269–1277. https://doi.org/10.1016/j.jpcs.2010.05.006.

[533] Z. A. Alothman, A Review: Fundamental Aspects of Silicate Mesoporous Materials, *Materials.* 5 **(2016)** 2874-2902. https://doi.org/10.3390/ma5122874.

[534] C. Delitala, M. D. Alba, A. I. Becerro, D. Delpiano, D. Meloni, E. Musu, I. Ferino, Synthesis of MCM-22 zeolites of different Si/Al ratio and their structural, morphological and textural characterisation, *Microporous Mesoporous Mater.* 118 **(2009)** 1–10. https://doi.org/10.1016/j.micromeso.2008.07.047.

[535] W. J. Roth, B. Gil, W. Makowski, A. Sławek, A. Korzeniowska, J. Grzybek, M. Siwek, P. Michorczyk, Framework-substituted cerium MCM-22 zeolite and its interlayer expanded derivative MWW-IEZ, *Catal. Sci. Technol.* 6 **(2016)** 2742–2753. https://doi.org/10.1039/c5cy02074c.

[536] M. Ugrina, M. Gaberšek, A. Daković, I. Nuić, Preparation and Characterization of the Sulfur-Impregnated Natural Zeolite Clinoptilolite for Hg (II) Removal from Aqueous Solutions, *Processes*. 9 **(2021)** 217. https://doi.org/10.3390/pr9020217.

[537] K. K. Atyam, A. Ghosh, K. Mukherjee, S. B. Majumder, Hematite iron oxide nano-particles: Facile synthesis and their chemi-resistive response towards hydrogen, *Mater. Res. Express.* 2 **(2015)** 1–7. https://doi.org/10.1088/2053-1591/2/5/055901.

[538] M. Nawab, S. Barot, R. Bandyopadhyay, Solvent-free selective oxidation of toluene over metal-doped MCM-22, *New J. Chem.* 43 **(2019)** 4406–4412. https://doi.org/10.1039/C8NJ06247A.

[539] B. Mauricio, H. M. C. Andrade, A. J. S. Mascarenhas, Oxidative dehydration of glycerol over alternative H,Fe-MCM-22 catalysts : Sustainable production of acrylic acid, *Microporous Mesoporous Mater.* 278 **(2019)** 366–377. https://doi.org/10.1016/j.micromeso.2019.01.016.

[540] Y. Cheng, M. Lu, J. Li, X. Su, S. Pan, C. Jiao, M. Feng, Synthesis of MCM-22 zeolite using rice husk as a silica source under varying-temperature conditions, *J. Colloid Interface Sci.* 369 **(2012)** 388–394. https://doi.org/10.1016/j.jcis.2011.12.024.

[541] M. Aguilar-Romero, R. Camposeco, S. Castillo, J. Marín, V. Rodríguez-González, L.A. García-Serrano, I. Mejía-Centeno, Acidity, surface species, and catalytic activity study on V_2O_5-WO_3/TiO_2 nanotube catalysts for selective NO reduction by NH_3, *Fuel.* 198 **(2017)** 123–133. https://doi.org/10.1016/j.fuel.2016.11.090.

[542] N. Rajić, N. Z. Logar, A. Rečnik, P. Sprenger, P. Hannevold, M. Stöcker, Natural zeolite as a carrier for nano-oxide particles and a possible application of the oxide/clinoptilolite composite, *Proceedings of the 4th Slovenian-Croatian Symposium on Zeolites* **(2011)** 9-12.

[543] M. Hosseinpour, M. Akizuki, A. Yoko, Y. Oshima, M. Soltani, Novel synthesis and characterization of Fe-ZSM-5 nanocrystals in hot compressed water for selective catalytic reduction of NO with NH_3, *Microporous Mesoporous Mater.* 292 **(2020)** 109708.

https://doi.org/10.1016/j.micromeso.2019.109708.

[544] Y.J. Kim, H.J. Kwon, I. Heo, I.S. Nam, B.K. Cho, J.W. Choung, M.S. Cha, G.K. Yeo, Mn-Fe/ZSM-5 as a low-temperature SCR catalyst to remove NOx from diesel engine exhaust, *Appl. Catal. B Environ.* 126 **(2012)** 9–21. https://doi.org/10.1016/j.apcatb.2012.06.010.

[545] M. H. Kim, K. H. Yang, The Role of Fe_2O_3 Species in Depressing the Formation of N_2O in the Selective Reduction of NO by NH_3 over V_2O_5/TiO_2-Based Catalysts, *Catalysts.* 8 **(2018)** 134. https://doi.org/10.3390/catal8040134.

[546] N. M. Musyoka, L. F. Petrik, E. Hums, A. Kuhnt, W. Schwieger, Thermal stability studies of zeolites A and X synthesized from South African coal fly ash, *Res. Chem. Intermed.* 41 **(2015)** 575–582. https://doi.org/10.1007/s11164-013-1211-3.

[547] I. Edition, Thermal transformations in systems based on zeolites Y, X, and A containing zinc and sodium nitrates, *Russian Chemical Bulletin* 52 **(2003)** 1940–1949. https://doi.org/10.1023/B:RUCB.0000009636.89718.56.

[548] R. V Siriwardane, J. A. Poston, E. P. Fisher, M. Shen, A. L. Miltz, Decomposition of the sulfates of copper, iron (II), iron (III), nickel, and zinc: XPS, SEM, DRIFTS, XRD, and TGA study, *App. Surf. Sci.* 152 **(1999)** 219–236. https:// 10.1016/S0169-4332(99)00319-0.

[549] E. H. Oelkers, J. Schott, Experimental study of anorthite dissolution and the relative mechanism of feldspar hydrolysis, *Geochim. Cosmochim. Acta.* 59 **(1995)** 5039–5053. https://doi.org/10.1016/0016-7037(95)00326-6.

[550] A. Filippidis, A. Godelitsas, D. Charistos, P. Misaelides, A. Kassoli-Fournaraki, The chemical behavior of natural zeolites in aqueous environments: Interactions between low-silica zeolites and 1 M NaCl solutions of different initial pH-values, *Appl. Clay Sci.* 11 **(1996)** 199–209. https://doi.org/10.1016/S0169-1317(96)00025-7.

[551] B. Onida, F. Geobaldo, F. Testa, R. Aiello, E. Garrone, H-bond formation and proton transfer in H-MCM-22 zeolite as compared to H-ZSM-5 and H-MOR: An FTIR study, *J. Phys. Chem. B.* 106 **(2002)** 1684–1690. https://doi.org/10.1021/jp0122068.

[552] B. Onida, F. Geobaldo, F. Testa, F. Crea, E. Garrone, FTIR investigation of the interaction at 77 K of diatomic molecular probes on MCM-22 zeolite, *Microporous Mesoporous Mater.* 30 **(1999)** 119–127. https://doi.org/10.1016/S1387-1811(99)00033-5.

[553] P. Sahu, S. Eniyarppu, M. Ahmed, D. Sharma, A. Sakthivel, Cerium ion-exchanged layered MCM-22: preparation, characterization and its application for esterification of fatty acids, *J.*

Porous Mater. 25 **(2018)** 999–1005. https://doi.org/10.1007/s10934-017-0510-2.

[554] M. K. Doula, A. Ioannou, The effect of electrolyte anion on Cu adsorption-desorption by clinoptilolite, *Microporous Mesoporous Mater.* 58 **(2003)** 115–130. https://doi.org/10.1016/S1387-1811(02)00610-8.

[555] P. Boroń, L. Chmielarz, J. Gurgul, K. Łątka, B. Gil, B. Marszałek, S. Dzwigaj, Influence of iron state and acidity of zeolites on the catalytic activity of FeHBEA, FeHZSM-5 and FeHMOR in SCR of NO with NH_3 and N_2O decomposition, *Microporous Mesoporous Mater.* 203 **(2015)** 73–85. https://doi.org/10.1016/j.micromeso.2014.10.023.

[556] J. Gurgul, K. Łątka, I. Hnat, J. Rynkowski, S. Dzwigaj, Identification of iron species in FeSiBEA by DR UV-vis, XPS and Mössbauer spectroscopy: Influence of Fe content, *Microporous Mesoporous Mater.* 168 **(2013)** 1–6. https://doi.org/10.1016/j.micromeso.2012.09.015.

[557] A. P. Grosvenor, B. A. Kobe, M. C. Biesinger, N.S. McIntyre, Investigation of multiplet splitting of Fe 2p XPS spectra and bonding in iron compounds, *Surf. Interface Anal.* 36 **(2004)** 1564–1574. https://doi.org/10.1002/sia.1984.

[558] A. Kessouri, B. Boukoussa, A. Bengueddach, R. Hamacha, Synthesis of iron-MFI zeolite and its photocatalytic application for hydroxylation of phenol, *Res. Chem. Intermed.* 44 **(2018)** 2475–2487. https://doi.org/10.1007/s11164-017-3241-8.

[559] M. S. Kumar, M. Schwidder, W. Grünert, A. Brückner, On the nature of different iron sites and their catalytic role in Fe-ZSM-5 DeNOx catalysts: New insights by a combined EPR and UV/VIS spectroscopic approach, *J. Catal.* 227 **(2004)** 384–397. https://doi.org/10.1016/j.jcat.2004.08.003.

[560] E. Yuan, G. Wu, W. Dai, N. Guan, L. Li, One-pot construction of Fe/ZSM-5 zeolites for the selective catalytic reduction of nitrogen oxides by ammonia, *Catal. Sci. Technol.* 7 **(2017)** 3036–3044. https://doi.org/10.1039/c7cy00724h.

[561] L. Ma, H. Chang, S. Yang, L. Chen, L. Fu, J. Li, Relations between iron sites and performance of Fe/HBEA catalysts prepared by two different methods for NH_3-SCR, *Chem. Eng. J.* 209 **(2012)** 652–660. https://doi.org/10.1016/j.cej.2012.08.042.

[562] D. Zhang, R.T. Yang, N_2O Formation Pathways over Zeolite-Supported Cu and Fe Catalysts in NH_3-SCR, Energy and *Fuels.* 32 **(2018)** 2170–2182. https://doi.org/10.1021/acs.energyfuels.7b03405.

[563] C. P. Cho, Y. D. Pyo, J. Y. Jang, G. C. Kim, Y. J. Shin, NOx reduction and N_2O emissions in a

diesel engine exhaust using Fe-zeolite and vanadium based SCR catalysts, *Appl. Therm. Eng.* 110 **(2017)** 18–24. https://doi.org/10.1016/j.applthermaleng.2016.08.118.

[564] M. Koebel, G. Madia, M. Elsener, Selective catalytic reduction of NO and N_2O at low temperatures, *Catal. Today.* 73 **(2002)** 239–247. https:// 10.1016/S0920-5861(02)00006-8.

[565] J.Y. Luo, X. Hou, P. Wijayakoon, S.J. Schmieg, W. Li, W.S. Epling, Spatially resolving SCR reactions over a Fe/zeolite catalyst, *Appl. Catal. B Environ.* 102 **(2011)** 110–119. https://doi.org/10.1016/j.apcatb.2010.11.031.

[566] G. Delahay, M. Mauvezin, B. Coq, S. Kieger, Selective catalytic reduction of nitrous oxide by ammonia on iron zeolite beta catalysts in an oxygen rich atmosphere: Effect of iron contents, *J. Catal.* 202 **(2001)** 156–162. https://doi.org/10.1006/jcat.2001.3279.

[567] S. Youn, I. Song, D.H. Kim, Promotional Effect on Selective Catalytic reduction of NOx with NH_3 over Overloaded W and Ce V_2O_5/TiO_2 Catalysts, *J. Nanomater.* 54 **(2015)**. https://doi.org/10.1007/s10853-019-03369-z.

[568] M.H. Kim, K.H. Yang, The role of Fe_2O_3 species in depressing the formation of N_2O in the selective reduction of no by NH_3 over V_2O_5/TiO_2-based catalysts, *Catalysts.* 8 **(2018)** 1–17. https://doi.org/10.3390/catal8040134.

[569] B. Liu, D. Yao, F. Wu, L. Wei, X. Li, X. Wang, Experimental Investigation on N_2O Formation during the Selective Catalytic Reduction of NOx with NH_3 over Cu-SSZ-13, *Ind. Eng. Chem. Res.* 58 **(2019)** 20516–20527. https://doi.org/10.1021/acs.iecr.9b03294.

[570] J. A. Martín, M. Yates, P. Ávila, S. Suárez, J. Blanco, Nitrous oxide formation in low temperature selective catalytic reduction of nitrogen oxides with V_2O_5/TiO_2 catalysts, *Appl. Catal. B Environ.* 70 **(2007)** 330–334. https://doi.org/10.1016/j.apcatb.2005.11.026.

[571] P. S. Metkar, M.P. Harold, V. Balakotaiah, Selective catalytic reduction of NOx on combined Fe- and Cu-zeolite monolithic catalysts: Sequential and dual layer configurations, *Appl. Catal. B Environ.* 111–112 **(2012)** 67–80. https://doi.org/10.1016/j.apcatb.2011.09.019.

[572] K. Leistner, F. Brüsewitz, K. Wijayanti, A. Kumar, K. Kamasamudram, L. Olsson, Impact of copper loading on NH_3-selective catalytic reduction, oxidation reactions and N_2O formation over Cu/SAPO-34, *Energies.* 10 **(2017).** https://doi.org/10.3390/en10040489.

[573] P.S. Metkar, M.P. Harold, V. Balakotaiah, Selective catalytic reduction of NOx on combined Fe- and Cu-zeolite monolithic catalysts: Sequential and dual layer configurations, *Appl. Catal. B Environ.* 111–112 **(2012)** 67–80. https://doi.org/10.1016/j.apcatb.2011.09.019.

[574] Z. Song, P. Ning, Q. Zhang, H. Li, J. Zhang, Y. Wang, X. Liu, Z. Huang, Activity and hydrothermal stability of CeO_2-ZrO_2-WO_3 for the selective catalytic reduction of NOx with NH_3, *J. Environ. Sci. (China)*. 42 **(2016)** 168–177. https://doi.org/10.1016/j.jes.2015.06.010.

[575] Y. Zhang, X. Yue, T. Huang, K. Shen, B. Lu, In situ DRIFTS studies of NH_3-SCR mechanism over V_2O_5-CeO_2/TiO_2-ZrO_2 catalysts for selective catalytic reduction of NOx, *Materials.* 11 **(2018)** 1307. https://doi.org/10.3390/ma11081307.

[576] A. Athappan, M. L. Sattler, Selective catalytic reduction of nitric oxide over cerium-doped activated carbons, *J. Environ. Chem. Eng.* 3 (**2015)** 2502-2513. https://doi.org/10.1016/j.jece.2015.08.028.

[577] M. A. Hernández, F. Rojas, V. H. Lara, Nitrogen-sorption characterization of the microporous structure of clinoptilolite-type zeolites, *J. Porous Mater.* 7 **(2000)** 443–454. https://doi.org/10.1023/A:1009662408173.

[578] L. Ma, Y. Cheng, G. Cavataio, R. W. Mccabe, L. Fu, J. Li, Applied Catalysis B : Environmental In situ DRIFTS and temperature-programmed technology study on NH_3-SCR of NOx over Cu-SSZ-13 and Cu-SAPO-34 catalysts, *Applied Catal. B, Environ.* 156–157 **(2014)** 428–437. https://doi.org/10.1016/j.apcatb.2014.03.048.

[579] L. Chen, T. V. W. Janssens, M. Skoglundh, H. Grönbeck, Interpretation of NH_3-TPD Profiles from Cu-CHA Using First-Principles Calculations, *Top. Catal.* 62 (2019) 93–99. https://doi.org/10.1007/s11244-018-1095-y.

[580] A. Łamacz, A. Krztoń, G. Djéga-Mariadassou, Catalytic decomposition of nitrogen oxides from coal combustion flue gases on $CeZrO_2$ supported Cu catalysts, *Catal. Today.* 176 **(2011)** 126–130. https://doi.org/10.1016/j.cattod.2011.01.032.

[581] T. Zhang, J. Liu, D. Wang, Z. Zhao, Y. Wei, K. Cheng, G. Jiang, A. Duan, Selective catalytic reduction of NO with NH_3 over HZSM-5-supported fe-cu nanocomposite catalysts: The Fe-Cu bimetallic effect, *Appl. Catal. B Environ.* 148–149 **(2014)** 520–531. https://doi.org/10.1016/j.apcatb.2013.11.006.

[582] R. Dębek, M. Motak, M. E. Galvez, P. Da Costa, T. Grzybek, Catalytic activity of hydrotalcite-derived catalysts in the dry reforming of methane: on the effect of Ce promotion and feed gas composition, *React. Kinet. Mech. Catal.* 121 **(2017)** 185–208. https://doi.org/10.1007/s11144-017-1167-1.

[583] F. Habashi, S.A. Mikhail, K.V. Van, Reduction of sulfates by hydrogen, *Can. J.* Chem. 54 **(1976)** 3646–3650. https://doi.org/10.1139/v76-524.

[584] B. M. Casari, V. Langer, Two $Ce(SO_4)_2 \cdot 4\ H_2O$ polymorphs: Crystal structure and thermal behavior, *J. Solid State Chem.* 180 **(2007)** 1616–1622. https://doi.org/10.1016/j.jssc.2007.02.017.

[585] M. C. Biesinger, L. W. M. Lau, A. R. Gerson, R. S. C. Smart, Resolving surface chemical states in XPS analysis of first row transition metals, oxides and hydroxides: Sc, Ti, V, Cu and Zn, *Appl. Surf. Sci.* 257 **(2010)** 887–898. https://doi.org/10.1016/j.apsusc.2010.07.086.

[586] R. Osuga, T. Yokoi, J. N. Kondo, Probing the basicity of lattice oxygen on H-form zeolites using CO_2, *J. Catal.* 371 **(2019)** 291–297. https://doi.org/10.1016/j.jcat.2019.02.003.

[587] A. Bensalem, J.C. Muller, F. Bozon-Verduraz, Faraday communications. From bulk CeO_2 to supported cerium-oxygen clusters: A diffuse reflectance approach, *J. Chem. Soc. Faraday Trans.* 88 **(1992)** 153–154. https://doi.org/10.1039/FT9928800153.

[588] G. R. Rao, B. G. Mishra, A comparative UV-vis-diffuse reflectance study on the location and interaction of cerium ions in Al- And Zr-pillared montmorillonite clays, *Mater. Chem. Phys.* 89 **(2005)** 110–115. https://doi.org/10.1016/j.matchemphys.2004.08.037.

[589] J. R. G.-V. Benat Pereda-Ayo, Unai De La Torre, Maria Jose Illan-Gomez, Agustin Bueno-Lopez, Role of the different copper species on the activity of Cu/zeolite catalysts for SCR of NOx with NH_3, *Appl. Catal. B, Environ.* 147 **(2014)** 420–428. https://doi.org/10.1016/j.apcatb.2013.09.010.

[590] Y. Shan, J. Du, Y. Zhang, W. Shan, X. Shi, Y. Yu, R. Zhang, X. Meng, F.S. Xiao, H. He, Selective catalytic reduction of NOx with NH_3: Opportunities and challenges of Cu-based small-pore zeolites, *Natl. Sci. Rev.* 8 **(2021)**. https://doi.org/10.1093/nsr/nwab010.

[591] C. Paolucci, I. Khurana, A. A. Parekh, S. Li, A. J. Shih, H. Li, J. R. Di Iorio, J. D. Albarracin-caballero, A. Yezerets, J. T. Miller, W.N. Delgass, F. H. Ribeiro, W. F. Schneider, R. Gounder, Dynamic multinuckear sites formed by mobilized copper ions in NOx selective catalytic reduction, 903 **(2017)** 898–903. https:// 10.1126/science.aan5630.

[592] F. Gao, D. Mei, Y. Wang, J. Szanyi, C. H. F. Peden, Selective Catalytic Reduction over Cu/SSZ-13: Linking Homo- and Heterogeneous Catalysis, *J. Am. Chem. Soc.* 139 **(2017)** 4935–4942. https://doi.org/10.1021/jacs.7b01128.

[593] K. A. Lomachenko, E. Borfecchia, C. Negri, G. Berlier, C. Lamberti, P. Beato, H. Falsig, S. Bordiga, The Cu-CHA deNOx Catalyst in Action: Temperature-Dependent NH_3-Assisted Selective Catalytic Reduction Monitored by Operando XAS and XES, *J. Am. Chem. Soc.* 138 **(2016)** 12025–12028. https://doi.org/10.1021/jacs.6b06809.

[594] P. Chen, A. Khetan, M. Jabłońska, J. Simböck, M. Muhler, R. Palkovits, H. Pitsch, U. Simon, Local dynamics of copper active sites in zeolite catalysts for selective catalytic reduction of NOx with NH_3, *Appl. Catal. B Environ.* 237 **(2018)** 263–272. https://doi.org/10.1016/j.apcatb.2018.05.091.

[595] Z. Sobalík, K. Jíša, H. Jirglová, B. Bernauer, Simultaneous FTIR/UV-Vis study of reactions over metallo-zeolites. Approach to quantitative in situ studies, *Catal. Today.* 126 **(2007)** 73–80. https://doi.org/10.1016/j.cattod.2006.11.001.

[596] S. Malmberg, M. Votsmeier, J. Gieshoff, N. Söger, L. Mußmann, A. Schuler, A. Drochner, Dynamic phenomena of SCR-catalysts containing Fe-exchanged zeolites - Experiments and computer simulations, *Top. Catal.* 42–43 **(2007)** 33–36. https://doi.org/10.1007/s11244-007-0146-6.

[597] I. Nova, L. Lietti, E. Tronconi, P. Forzatti, Dynamics of SCR reaction over a TiO_2-supported vanadia-tungsta commercial catalyst, *Catal. Today.* 60 **(2000)** 73–82. https://doi.org/10.1016/S0920-5861(00)00319-9.

[598] A. Grossale, I. Nova, E. Tronconi, D. Chatterjee, M. Weibel, The chemistry of the NO/NO_2-NH_3 "fast" SCR reaction over Fe-ZSM5 investigated by transient reaction analysis, *J. Catal.* 256 **(2008)** 312–322. https://doi.org/10.1016/j.jcat.2008.03.027.

[599] J. Guo, Y. Peng, Y. Zhang, W. Yang, L. Gan, K. Li, J. Chen, J. Li, Comparison of NH_3-SCO performance over CuOx/H-SSZ-13 and CuOx/H-SAPO-34 catalysts, *Appl. Catal. A Gen.* 585 **(2019)**. https://doi.org/10.1016/j.apcata.2019.117119.

[600] M. Rutkowska, I. Pacia, S. Basąg, A. Kowalczyk, Z. Piwowarska, M. Duda, K.A. Tarach, K. Góra-Marek, M. Michalik, U. Díaz, L. Chmielarz, Catalytic performance of commercial Cu-ZSM-5 zeolite modified by desilication in NH_3-SCR and NH_3-SCO processes, *Microporous Mesoporous Mater.* 246 **(2017)** 193–206. https://doi.org/10.1016/j.micromeso.2017.03.017.

[601] X. Shi, F. Liu, W. Shan, H. He, Hydrothermal deactivation of Fe-ZSM-5 prepared by different methods for the selective catalytic reduction of NOx with NH_3, Cuihua Xuebao/Chinese *J. Catal.* 33 **(2012)** 454–464. https://doi.org/10.1016/S1872-2067(11)60326-4.

[602] J. Eng, C.H. Bartholomew, Kinetic and Mechanistic Study of NOx Reduction by NH_3 over H-Form Zeolites, *J. Catal.* 171 **(1997)** 27–44. https://doi.org/10.1006/jcat.1997.1769.

[603] N.I. Il'chenko, G.I. Golodets, Catalytic oxidation of ammonia. I. Reaction kinetics and mechanism, *J. Catal.* 39 **(1975)** 57–72. https://doi.org/10.1016/0021-9517(75)90282-1.

[604] B. Zhang, S. Zhang, B. Liu, Effect of oxygen vacancies on ceria catalyst for selective catalytic reduction of NO with NH3, *Appl. Surf. Sci.* 529 **(2020)** 147068. https://doi.org/10.1016/j.apsusc.2020.147068.

[605] Y. Shin, Y. Jung, C. P. Cho, Y. D. Pyo, J. Jang, G. Kim, T. M. Kim, NOx abatement and N_2O formation over urea-SCR systems with zeolite supported Fe and Cu catalysts in a nonroad diesel engine, *Chem. Eng. J.* 381 **(2020)** 122751. https://doi.org/10.1016/j.cej.2019.122751.

[606] A. Grossale, I. Nova, E. Tronconi, D. Chatterjee, M. Weibel, NH_3-NO/NO_2 SCR for diesel exhausts aftertreatment: Reactivity, mechanism and kinetic modelling of commercial Fe- and Cu-promoted zeolite catalysts, *Top. Catal.* 52 **(2009)** 1837–1841. https://doi.org/10.1007/s11244-009-9354-6.

[607] T. G. J. P. H. Papp, Supported manganese catalysts for the selective catalytic reduction of nitrogen oxides with ammonia: Part II. Catalytic experiments, *Phys. Chem. Chem. Phys.* 1 **(1999)** 341–348. https:// 10.1039/A806913A.

[608] T. Grzybek, J. Klinik, A. Krzyżanowski, H. Papp, M. Żyła, Selective catalytic reduction of nitric oxide with ammonia on Mn-promoted carbonized used silica-alumina sorbents, *Catal. Letters.* 63 **(1999)** 107–111. https://doi.org/10.1023/a:1019056718957.

[609] X. Auvray, M. Arvanitidou, Å. Högström, J. Jansson, S. Fouladvand, L. Olsson, Comparative Study of SO_2 and SO_2/SO_3 Poisoning and Regeneration of Cu/BEA and Cu/SSZ-13 for NH_3 SCR, *Emiss. Control Sci. Technol.* 7 **(2021)** 232–246. https://doi.org/10.1007/s40825-021-00203-4.

[610] P. S. Hammershøi, A. D. Jensen, T.V.W. Janssens, Impact of SO_2-poisoning over the lifetime of a Cu-CHA catalyst for NH_3-SCR, *Appl. Catal. B Environ.* 238 **(2018)** 104–110. https://doi.org/10.1016/j.apcatb.2018.06.039.

[611] R. Zhang, Y. Li, T. Zhen, Ammonia selective catalytic reduction of NO over Fe/Cu-SSZ-13, *RSC Adv.* 4 **(2014)** 52130–52139. https://doi.org/10.1039/c4ra09290b.

[612] L. Xie, C. Liu, Y. Deng, F. Liu, W. Ruan, Promotion Effect of Fe Species on SO_2 Resistance of Cu-SSZ-13 Catalysts for NOx Reduction by NH_3, *Ind. Eng. Chem. Res.* 61 **(2022)** 8698–8707. https://doi.org/10.1021/acs.iecr.2c00789.

[613] Y.J. Shi, H. Shu, Y.H. Zhang, H.M. Fan, Y.P. Zhang, L.J. Yang, Formation and decomposition of NH_4HSO_4 during selective catalytic reduction of NO with NH_3 over V_2O_5-WO_3/TiO_2 catalysts, *Fuel Process. Technol.* 150 **(2016)** 141–147. https://doi.org/10.1016/j.fuproc.2016.05.016.

[614] X. Song, J. Zhao, Y. Li, Z. Sun, J. Yu, Thermal decomposition mechanism of ammonium sulfate catalyzed by ferric oxide, *Front. Chem. Sci. Eng.* 7 **(2013)** 210–217. https://doi.org/10.1007/s11705-013-1320-y.

[615] K. Wijayanti, K. Leistner, S. Chand, A. Kumar, K. Kamasamudram, N.W. Currier, A. Yezerets, L. Olsson, Deactivation of Cu-SSZ-13 by SO_2 exposure under SCR conditions, *Catal. Sci. Technol.* 6 **(2016)** 2565–2579. https://doi.org/10.1039/c5cy01288k.

[616] G. Yang, X. Du, J. Ran, X. Wang, Y. Chen, L. Zhang, Understanding SO_2 Poisoning over Different Copper Species of Cu-SAPO-34 Catalyst: A Periodic DFT Study, *J. Phys. Chem. C.* 122 **(2018)** 21468–21477. https://doi.org/10.1021/acs.jpcc.8b06765.

[617] Y. Bai, Y. Hou, Y. Guo, N. Xiang, X. Han, H. Wang, Z. Wu, Z. Huang, Structure–activity relationship and the inhibitory effect of sulfur dioxide and water on nitrous oxide formation in selective catalytic reduction of nitrogen oxides by ammonia over hollow Co_3O_4@$CoMn_2O_4$ catalyst, *J. Colloid Interface Sci.* 616 **(2022)** 55–66. https://doi.org/10.1016/j.jcis.2022.01.034.

List of figures

List of tables

Academic achievements of the author

Publications in journals with Impact Factor

1. Agnieszka Szymaszek-Wawryca, Urbano Díaz, Bogdan Samojeden, Monika Motak: *Synthesis, Characterization, and NH_3-SCR Catalytic Performance of Fe-Modified MCM-36 Intercalated with Various Pillars,* Molecules **2023**, 28, 4960.

2. Agnieszka Szymaszek-Wawryca, Paulina Summa, Dorota Duraczyńska, Urbano Díaz, Monika Motak: *Hydrotalcite-modified Clinoptilolite as the Catalyst for Selective Catalytic Reduction of NO with Ammonia (NH_3-SCR),* Materials **2022**, 15, 7884.

3. Agnieszka Szymaszek-Wawryca, Urbano Díaz, Dorota Duraczyńska, Konrad Świerczek, Bogdan Samojeden, Monika Motak: *Catalytic Performance and Sulfur Dioxide Resistance of One-pot Synthesized Fe-MCM-22 in Selective Catalytic Reduction of Nitrogen Oxides with Ammonia (NH_3-SCR) – The Effect of Iron Content,* International Journal of Molecular Sciences **2022,** 23, 10754.

4. Agnieszka Szymaszek-Wawryca, Urbano Díaz, Bogdan Samojeden, Monika Motak: *Catalytic Performance of One-Pot Synthesized Fe-MWW Layered Zeolites (MCM-22, MCM-36, and ITQ-2) in Selective Catalytic Reduction of Nitrogen Oxides with Ammonia,* Molecules **2022**, 27, 2983.

5. Magdalena Saramok, Marek Inger, Katarzyna Antoniak-Jurak, Agnieszka Szymaszek-Wawryca, Bogdan Samojeden, Monika Motak: *Physicochemical Features and NH_3-SCR Catalytic Performance of Natural Zeolite Modified with Iron – The Effect of Fe Loading*, Catalysts **2022,** 12, 731.

6. Magdalena Saramok, Agnieszka Szymaszek, Marek Inger, Katarzyna Antoniak-Jurak, Bogdan Samojeden, Monika Motak: *Modified Zeolite Catalyst for a NO_x Selective Catalytic Reduction Process in Nitric Acid Plants,* Catalysts 11, **2021,** 450.

7. Marwa Saad, Agnieszka Szymaszek, Bogdan Samojeden, Monika Motak: *SO_2 poisoning of copper-based activated carbon catalyst for selective catalytic reduction of NO with NH_3 at low temperature,* Catalysts 10, **2020,** 1423.

8. Marwa Saad, Agnieszka Szymaszek, Bogdan Samojeden, Monika Motak: *The enhanced performance of Ce promoted N-modified activated carbon-based catalyst for selective catalytic reduction of NO_x with NH_3,* Catalysts 10, **2020,** 1426.

9. Agnieszka Szymaszek, Bogdan Samojeden, Monika Motak *The deactivation of industrial SCR catalysts – a short review. Energies* 13 (15), **2020,** 3870, s. 1-25.

10. Agnieszka Szymaszek, Bogdan Samojeden, Monika Motak: *The application of modified layered double hydroxides in selective catalytic reduction of nitrogen oxides by ammonia* (NH_3−SCR), Polish Journal of Chemical Technology 22 (1), **2020,** s. 61–67.

11. Agnieszka Szymaszek, Maciej Kubeł, Bogdan Samojeden, Monika Motak: *Modified bentonite-derived materials as catalysts for selective catalytic reduction of nitrogen oxides, Chemical and Process Engineering 41 (1),* **2020,** *s. 13-24.*

12. Agnieszka Szymaszek, Bogdan Samojeden, Monika Motak: *Selective catalytic reduction of NO_x with ammonia (NH_3-SCR) over transition metal-based catalysts – influence of the catalyst support,* Physicochemical Problems of Mineral Processing 55 (6), **2019**, s. 1429-1441.

13. Bogdan Samojeden, Teresa Grzybek, Joanna Kowal, Agnieszka Szymaszek, Magdalena Jabłońska, Roger Gläser, Monika Motak: *The influence of holmium on catalytic properties of Fe or Cu-modified vermiculites,* Physicochemical Problems of Mineral Processing 55 (6), **2019**, s. 1484-1495.

Chapters in monographs

1. Agnieszka Szymaszek-Wawryca, Urbano Díaz, Bogdan Samojeden, Monika Motak: *Application of Natural and Synthetic Pillared Aluminosilicates in Selective Catalytic Reduction of Nitrogen Oxides with Ammonia*, Contemporary Problems of Power Engineering and Environmental Protection 2021 (Post-conference Monograph) Silesian University of Technology 2022, **2022**, e-ISBN 978-83-964116-1-7, p. 7-16.

2. Agnieszka Szymaszek-Wawryca, Bogdan Samojeden, Monika Motak: *Catalytic Activity of Natural Clinoptilolite Modified with Iron by Various Methods in Selective Catalytic Reduction of Nitrogen Oxides with Ammonia (NH_3-SCR),* Modern Problems and Solutions in Environmental Protection – 2021 (Post-conference Monograph) University of Białystok, Białystok **2021**, ISBN 978-83-7431-692-7, p. 10-27.

3. Agnieszka Szymaszek, Bogdan Samojeden, Monika Motak: *Influence of SO_2 poisoning on catalytic performance of modified zeolites in selective catalytic reduction of nitrogen oxides with ammonia (NH_3-SCR),* Contemporary Problems of Power Engineering and Environmental Protection 2020, **2020**, e-ISBN: 978-83-950087-9-5, p. 15-25.

4. Agnieszka Szymaszek, Bogdan Samojeden, Monika Motak: *Solution combustion synthesis-derived materials in selective catalytic reduction of NO_x (NH_3-SCR): XRD analysis of Cu-Fe-Ce mixed oxides prepared by citric acid method,* Contemporary problems of power engineering and environmental protection 2019, **2019,** e-ISBN: 978-83-950087-6-4, p. 15–25.

5. Agnieszka Szymaszek, Bogdan Samojeden, Monika Motak: *Modified hydrotalcite-like derived materials as effective catalysts for $DeNO_x$ systems and N_2O decomposition,* Contemporary Problems of Power Engineering and Environmental Protection, Silesian University of Technology 2019, **2019**, e-ISBN: 978-83-950087-3-3, p. 349-357.

6. Agnieszka Szymaszek, Maciej Kubeł, Bogdan Samojeden, Monika Motak: *Modified bentonite-derived materials as catalysts for selective catalytic reduction of nitrogen oxides*, EYEC monograph*:* 8th European Young Engineers Conference, Warsaw University of Technology 2019, **2019,** e-ISBN: 978-83-936575-7-5, p. 162-173.

Presentations at polish and international conferences

- **Lectures**

1. Fizykochemia granic faz – metody instrumentalne, Lublin, 16-20.04.2023 – polish conference, „Porównanie właściwości fizykochemicznych i katalitycznych glinokrzemianów warstwowych na przykładzie bentonitu i MCM-36”

2. LV Ogólnopolskie Kolokwium Katalityczne, Instytut Katalizy i Fizykochemii Powierzchni im. Jerzego Habera PAN, 22-24.03.2023 – international conference, „Fe-modified MWW zeolites as catalysts for selective catalytic reduction of nitrogen oxides with ammonia”

3. 13th International Conference on Catalysis and Chemical Engineering, Orlando (USA), 21-22.10.2022 – international conference, „Catalytic performance of modified delaminated zeolite ITQ-2 in selective catalytic reduction of nitrogen oxides with ammonia”

4. The 3rd Advances in Green Chemistry Conference, Poznań, 26-30.09.2022 – international conference, „Catalytic performance of natural and synthetic zeolites modified by solution combustion synthesis in selective catalytic reduction of nitrogen oxides with ammonia”

5. Energy Fuels Environment International Conference, Kraków, 20-23.09.2022 – international conference, „Catalytic performance of Fe-modified delaminated zeolite in selective catalytic reduction of nitrogen oxides with ammonia”

6. XXIII Forum Zeolitowe, Niepołomice, 21-25.06.2022 – international conference, lecture „Comparison of the catalytic performance of modified natural and synthetic layered aluminosilicates in selective catalytic reduction of nitrogen oxides with ammonia”

7. Environmental Protection & Energy Conference EPAE 2021, Gliwice, 10.12.2021 – international conference, „Application of Natural and Synthetic Pillared Aluminosilicates in Selective Catalytic Reduction of Nitrogen Oxides with Ammonia”

8. Current Environmental Issues 2021, Wydział Chemii i Wydział Biologii Uniwersytetu w Białymstoku, Białystok, 22-24.09.2021 – international conference, „Catalytic activity in selective catalytic reduction of nitrogen oxides with ammonia (NH_3-SCR) of natural clinoptilolite modified with iron by various methods”

9. 63. Zjazd Naukowy Polskiego Towarzystwa Chemicznego, Polskie Towarzystwo Chemiczne, Łódź, 13-17.09.2021 – polish conference, „Influence of the preparation procedure of MCM-36 modified with iron on its catalytic activity in selective catalytic reduction of nitrogen oxides with ammonia”

10. 3rd European Mineralogical Conference EMC2020, Kraków, 29.08.-2.09.2021 – international conference, „Application of natural clinoptilolite modified with transition metals in selective catalytic reduction of nitrogen oxides with ammonia”

11. Fizykochemia granic faz – metody instrumentalne, Lublin, 22-26.08.2021 – polish conference, „Wpływ metody nanoszenia fazy aktywnej w zeolitach ITQ-2 na efektywność reakcji selektywnej redukcji katalitycznej tlenków azotu amoniakiem”

12. Balard Chemistry Conferences 2021, Montpellier, 15-18.06.2021 – international conference, „Catalytic activity of natural clinoptilolite and MWW-type zeolite modified with iron in selective catalytic reduction of nitrogen oxides with ammonia (NH_3-SCR)”

13. VII Edition of the Conference Young Researchers’ Innovative Ideas: Science | Start-ups | Industry, IATI Autostrada Technologii I Innowacji, Kraków, 27-28.05.2021 – international conference, „Natural zeolite as a precursor of the catalyst for the reduction of nitrogen oxides from tail gases in a nitric acid plant”

14. 8th Environmental Protection and Energy Conference, Silesian University of Science and Technology, Gliwice, 8.12.2020 – international conference, „Influence of SO_2 poisoning on catalytic

performance of modified zeolites in selective catalytic reduction of nitrogen oxides with ammonia (NH_3-SCR)”

15. Energy Fuels and Environment, AGH University of Science and Technology, Kraków, 1-4-12.2020 – international conference, „Clinoptilolite modified with iron and copper as catalysts for selective catalytic reduction of nitrogen oxides with ammonia”

16. Energy Fuels and Environment, AGH University of Science and Technology, Kraków, 1-4-12.2020 – international conference, co-authored lecture, „Modified zeolite catalyst for a NO_x selective catalytic reduction process in nitric acid plants”

17. International conference on the Clean Environment and Energy Research CEER 2020, Gdańsk, 2-4.12.2020 – international conference, „The application of modified green clay in selective catalytic reduction of nitrogen oxides with ammonia”

18. LII Ogólnopolskie Kolokwium Katalityczne, Instytut Katalizy i Fizykochemii Powierzchni im. Jerzego Habera PAN, Kraków, 25-27.11.2020 – international conference, „Modyfikowany klinoptylolit funkcjonalizowany żelazem i miedzią lub cerem jako katalizator selektywnej redukcji katalitycznej tlenków azotu amoniakiem (NH_3-SCR)”

19. LII Ogólnopolskie Kolokwium Katalityczne, Instytut Katalizy i Fizykochemii Powierzchni im. Jerzego Habera PAN, Kraków, 25-27.11.2020 – international conference, co-authored lecture, „Preparatyka i charakterystyka katalizatora do selektywnej redukcji katalitycznej NOx z gazów resztkowych w instalacji kwasu azotowego”

20. 7^{th} conference on Environmental protection and energy, Gliwice, 6.12.2019 – international conference, „Solution combustion synthesis-derived materials in selective catalytic reduction of NO_x (NH_3-SCR): XRD analysis of Cu-Fe-Ce mixed oxides prepared by citric acid method”

21. Sorbenty Mineralne Surowce, Energetyka, Ochrona środowiska, Nowoczesne technologie, Jerzmanowice k. Krakowa, 16-17.09.2019 – polish conference, „Porównanie właściwości

katalitycznych materiałów pochodzenia naturalnego jako nośników katalizatora procesu selektywnej redukcji katalitycznej tlenków azotu (NH_3-SCR)”

22. Sorbenty Mineralne Surowce, Energetyka, Ochrona środowiska, Nowoczesne technologie, Jerzmanowice k. Krakowa, 16-17.09.2019 – polish conference, co-authored lecture, „Wermikulity funkcjonalizowane metalami przejściowymi jako katalizatory w reakcji selektywnej redukcji katalitycznej NO amoniakiem”

23. Fizykochemia granic faz - metody instrumentalne, Lublin, 13-17.05.2019 – polish conference, „Aktywowane kwasowo i interkalowane wermikulity modyfikowane żelazem, kobaltem i miedzią jako efektywne katalizatory procesu NH_3-SCR”

24. Fizykochemia granic faz - metody instrumentalne, Lublin, 13-17.05.2019 – polish conference, co-authored lecture, „Wermikulity modyfikowane metalami d-elektronowymi jako katalizatory w procesach $DeNO_x$”

25. 8th European Young Engineers Conference, Warszawa, 8-10.04.2019 – international conference, „Modified bentonite-derived materials as catalysts for selective catalytic reduction of nitrogen oxides (SCR)”

26. LI Ogólnopolskie Kolokwium Katalityczne, Kraków, 20-22.03.2019 – international conference, „NH_3-SCR over hydrotalcite-derived mixed metal oxides containing manganese”

27. 6th Environmental Protection and Energy Conference, Gliwice, 7.12.2018 – international conference, „Modified hydrotalcite-like derived materials as effective catalysts for $DeNO_x$ systems”

28. VIII Ogólnokrajowej Konferencja Naukowa Młodzi Naukowcy w Polsce - Badania i rozwój, Wrocław, 21.11.2018 – polish conference, „Modyfikowane materiały warstwowe jako katalizatory selektywnej redukcji katalitycznej tlenków azotu”

- **Posters**

1. 15th European Congress on Catalysis EUROPACAT2023, Prague, 27.08.-1.09.2023 – international conference, „Natural and synthetic zeolites modified with Fe and Cu as the catalysts for selective catalytic reduction of nitrogen oxides with ammonia”

2. 15th European Congress on Catalysis EUROPACAT2023, Prague, 27.08.-1.09.2023 – international conference, „One-pot synthesized Fe-ITQ-2 as the catalyst for selective catalytic reduction of nitrogen oxides with ammonia – the effect of iron loading”

3. 15th European Congress on Catalysis EUROPACAT2023, Prague, 27.08.-1.09.2023 – international conference, „NH_3-SCR catalytic performance of natural clinoptilolite modified with hydrotalcite-like phase”

4. The 3rd Advances in Green Chemistry Conference, Poznań, 26-30.09.2022 – international conference, „Catalytic properties of one-pot synthesized layered zeolites”

5. 20th International Zeolite Conference, Walencja, 3-8.07.2022 – international conference, „Comparative study of the catalytic performance of natural and synthetic zeolites in selective catalytic reduction of nitrogen oxides with ammonia”

6. XXIII Forum Zeolitowe, Niepołomice, 21-25.06.2022 – international conference, „Catalytic performance of modified MCM-22 in selective catalytic reduction of nitrogen oxides with ammonia”

7. 63. Zjazd Naukowy Polskiego Towarzystwa Chemicznego, Polskie Towarzystwo Chemiczne, Łódź, 13-17.09.2021 – polish conference, „Catalytic properties of natural and synthetic layered aluminosilicates intercalated with metal oxide pillars in selective catalytic reduction of nitrogen oxides with ammonia”

8. 3rd European Mineralogical Conference EMC2020, Kraków, 29.08.-2.09.2021 – international conference, „Catalytic potential of modified natural clays in selective catalytic reduction of nitrogen oxides with ammonia”

9. Fizykochemia granic faz – metody instrumentalne, Lublin, 22-26.08.2021 – polish conference, „ITQ-2 modyfikowany metalami d-elektronowymi jako katalizator w reakcji selektywnej redukcji katalitycznej tlenków azotu amoniakiem”

10. Balard Chemistry Conferences 2021, Montpellier, 15-18.06.2021 – international conference, „Natural clinoptilolite modified with iron or/and copper as an effective catalyst of selective catalytic reduction of nitrogen oxides with ammonia (NH_3-SCR)”

11. IV edycja międzynarodowej konferencji „Innowacyjne pomysły młodych naukowców: nauka – startup – przemysł”, Kraków, 11-13.05.2020 – polish conference, „Katalizator komercyjny procesu selektywnej redukcji katalitycznej – współczesne wyzwania i nowoczesne rozwiązania”

12. IV edycja międzynarodowej konferencji „Innowacyjne pomysły młodych naukowców: nauka – startup – przemysł”, Kraków, 11-13.05.2020 – polish conference, „Porównanie właściwości katalitycznych zeolitów naturalnych i syntetycznych w procesie selektywnej redukcji katalitycznej tlenków azotu amoniakiem”

13. VII edycja konferencji naukowej KRK InnoTech Summit (KITS) 2019, Kraków, 25.10.2019 – polish conference, „Zastosowanie glinokrzemianów w redukcji tlenków azotu ze źródeł stacjonarnych”

14. Energetyka, Paliwa i Środowisko 2019, Kraków, 18.10.2019 – polish conference, „Rola miedzi w tlenkach pochodzenia hydrotalkitowego jako katalizatorów w reakcji selektywnej redukcji katalitycznej tlenków azotu amoniakiem (NH_3-SCR)”

15. Sorbenty Mineralne Surowce, Energetyka, Ochrona środowiska, Nowoczesne technologie, Jerzmanowice k. Krakowa, 16-17.09.2019 – polish conference, „The application of modified layered double hydroxides in selective catalytic reduction of nitrogen oxides by ammonia (NH_3-SCR)”

16. VSS Vienna Young Scientists Symposium, Wiedeń, 13-14.06.2019 – international conference, „Selective catalytic reduction of NO_x with ammonia over catalysts derived from fly ash”

17. VSS Vienna Young Scientists Symposium, Wiedeń, 13-14.06.2019 – international conference, „Comparison of structure of hydrotalcite materials prepared by different synthesis methods”

18. Fizykochemia granic faz - metody instrumentalne, Lublin, 13-17.05.2019 – polish conference, „Popioły lotne jako prekursory alternatywnych katalizatorów procesu selektywnej redukcji katalitycznej tlenków azotu amoniakiem (NH_3-SCR)”

19. V edycji konferencji Młodych Naukowców KRK InnoTech SUMMIT 2019, Kraków, 5.03.2019 – polish conference, „Selective catalytic reduction of nitrogen oxides with ammonia (NH_3-SCR) over fly ash-derived catalysts”

Patent application

Patent Application for an invention “Zeolitowy katalizator do selektywnej redukcji NOx amoniakiem i sposób jego wytwarzania”; Application no. P.441039 [WIPO ST 10/C PL441039]

Research projects

1. Principal Investigator of Preludium 19 financed by National Science Centre (nr 2020/37/N/ST5/00186) (2021-2024).

2. PhD candidate carrying out the tasks of the project „System grantów uczelnianych na prace badawcze realizowane z udziałem doktorantów” Excellence Initiative for AGH University of Science and Technology.

Internships and summer schools

1. Instituto de Tecnología Química, Universitat Politécnica de Valéncia, Valencia, Spain – Erasmus+ traineeship/realization of the tasks of the research projects **(2020-2023)**

2. Paul Scherrer Institut (PSI), Villigen, Switzerland – training **(2020)**

3. Université de Lyon, Lyon, Francja – summer school ELITECAT2019 **(2019)**

4. Sorbonne Université, Paris, France – training (international exchange of PhD candidates financed by PROM NAWA) **(2019)**

5. Centrum Badawczo-Rozwojowe Grupy Azoty, Tarnów, Poland – internship **(2019)**

Awards

1. Maspex Foundation Award for the best PhD candidates at AGH **(2022)**

2. Award for the best oral presentation at Fizykochemia granic faz – metody instrumentalne **(2022)**

3. Best Ambassador of Grupa Azoty S.A. **(2019)**

4. Award for the best poster at Fizykochemia granic faz – metody instrumentalne **(2019)**

5. Award for the best oral presentation at 6th Environmental Protection and Energy Conference **(2018)**

6. AGH Rector Scholarship for the best PhD candidates **(2020-2023)**